AD

PROCEEDINGS OF THE ARMY SYMPOSIUM ON SOLID MECHANICS, 1984 - ADVANCES IN SOLID MECHANICS FOR DESIGN AND ANALYSIS

19960315 013

October 1984

DEPARTMENT OF DEFENSE
PLASTICS TECHNICAL EVALUATION CENTER
ARRADCOM, DOVER, N. J.   07801

ARMY MATERIALS AND MECHANICS RESEARCH CENTER
Watertown, Massachusetts 02172-0001

DTIC QUALITY INSPECTED 1

The findings in this report are not to be construed as an official
Department of the Army position, unless so designated by other
authorized documents.

Mention of any trade names or manufacturers in this report
shall not be construed as advertising nor as an official
indorsement or approval of such products or companies by
the United States Government.

DISCLAIMER NOTICE

THIS DOCUMENT IS BEST QUALITY AVAILABLE. THE COPY FURNISHED TO DTIC CONTAINED A SIGNIFICANT NUMBER OF PAGES WHICH DO NOT REPRODUCE LEGIBLY.

TC 9-N

REPORT DOCUMENTATION PAGE		READ INSTRUCTIONS BEFORE COMPLETING FORM
1. REPORT NUMBER AMMRC MS 84-3	2. GOVT ACCESSION NO.	3. RECIPIENT'S CATALOG NUMBER
4. TITLE (and Subtitle) PROCEEDINGS OF THE ARMY SYMPOSIUM ON SOLID MECHANICS, 1984 - ADVANCES IN SOLID MECHANICS FOR DESIGN AND ANALYSIS		5. TYPE OF REPORT & PERIOD COVERED Final Report
		6. PERFORMING ORG. REPORT NUMBER
7. AUTHOR(s)		8. CONTRACT OR GRANT NUMBER(s)
9. PERFORMING ORGANIZATION NAME AND ADDRESS Army Materials and Mechanics Research Center ATTN: AMXMR-S Watertown, Massachusetts 02172-0001		10. PROGRAM ELEMENT, PROJECT, TASK AREA & WORK UNIT NUMBERS
11. CONTROLLING OFFICE NAME AND ADDRESS U.S. Army Materiel Command Alexandria, Virginia 22333		12. REPORT DATE October 1984
		13. NUMBER OF PAGES
14. MONITORING AGENCY NAME & ADDRESS(if different from Controlling Office)		15. SECURITY CLASS. (of this report) Unclassified
		15a. DECLASSIFICATION/DOWNGRADING SCHEDULE

16. DISTRIBUTION STATEMENT (of this Report)

Approved for public release; distribution unlimited.

17. DISTRIBUTION STATEMENT (of the abstract entered in Block 20, if different from Report)

18. SUPPLEMENTARY NOTES

19. KEY WORDS (Continue on reverse side if necessary and identify by block number)

Ballistics	Fatigue	Mechanical properties
Engineering	Impact	Mechanics
Failure (mechanics)	Ordnance	Shock

20. ABSTRACT (Continue on reverse side if necessary and identify by block number)

Proceedings of the Army Symposium on Solid Mechanics, 1984 - Advances in Solid Mechanics for Design and Analysis, held at Newport, Rhode Island, 1-3 October 1984.

PREFACE

The Army Symposium, 1984, was the ninth in a series of biennial meetings sponsored by the Army Materials and Mechanics Reseach Center (AMMRC), Watertown, Massachusetts. The symposium consisted of various types of presentations; namely, Keynote Themes; Overviews sof related federally sponsored research; full technical papers and a series of brief presentations and discussions of current, but not necessarily complete, research. This document contains the technical manuscripts and the abstracts for the various presentations.

Participation in these symposia has broadened with time. Starting with the 1972 meeting, papers have been solicited from in-house and contract researchers and designers for the Navy, Air Force, and other government agencies, in addition to those for the Army. The symposium committee has been expanded several times; its current membership is as shown on page v. These expansions were made in recognition of the fact that many mechanics research and/or design problems are not unique to a single service or government agency.

These symposia provide a forum for enhancing the responsiveness of mechanics research efforts for the design of advanced military systems. They also facilitate communications and coordination between and among researchers and designers having common applied mechanics theme interests, whether they work for a government service or agency, industry, or at some university or research institute.

No endeavor of the magnitude of this 1984 symposium could have been successfully conducted without the enthusiastic cooperation and support of many individuals and organizations. We greatfully acknowledge:

The speakers, authors, participants and session chairmen who made this conference such a success.

The manuscript reviewers from universities, industry and government organizations, for their diligence in carrying out a difficult task in a short time.

Finally, many thanks to the staff of the Battelle Columbus Laboratories and AMMRC for their efforts in the preparation and printing of numerous symposium materials.

DOCUMENTS IN THIS SYMPOSIA SERIES*

1968 Theme: (General – Solid Mechanics)
    Proceedings: AMMRC MS 68-09, September 1968, AD 675463

1970 Theme: Lightweight Structures
    Proceedings: AMMRC MS 70-05, December 1970, AD 883455L

1972 Theme: Role of Mechanics in Design – Ballistic Problems
    Proceedings: AMMRC MS 73-2, September 1973, AD 772827

1974 Theme: The Role of Mechanics in Design – Structural Joints
    Proceedings: AMMRC MS 74-8, September 1974, AD 786543
    Work-In-Progress: AMMRC MS 74-9, September 1974, AD 786524
    Bibliography: AMMRC MS 74-10, September 1974, AD 786520

1976 Theme: Composite Materials: The Influence of Mechanics of Failure on
             Design
    Proceedings: AMMRC MS 76-2, September 1976, AD A029735
    Work-In-Progress: AMMRC MS 76-3, September 1976, AD A029736

1978 Theme: Case Studies on Structural Integrity and Reliability
    Proceedings: AMMRC MS 78-3, September 1978, AD A059834/2G1
    Ongoing Case Studies: AMMRC MS 78-4, September 1978, AD A059605/6G1

1980 Theme: Designing for Extremes: Environment, Loading, and Structural
             Behavior
    Proceedings: AMMRC MS 80-4, September 1980, AD A090684
    Work-In-Progress: AMMRC MS 80-5, September 1980, AD A090685
    Opening Session Address: AMMRC MS 80-6, September 1980, AD A090686

1982 Theme: Critical Mechanics Problems in Systems Design
    Proceedings: AMMRC MS 82-4, September 1982
    Work-In-Progress: AMMRC MS 82-5, September 1982

1984 Theme: Advances in Solid Mechanics
    Proceedings:

---

* These documents may be ordered from the National Technical Information
  Service, U.S. Department of Commerce, Springfield, VA 22161.

SYMPOSIUM COMMITTEE

E. M. LENOE, Chairman, AMMRC
J. F. MESCALL, Vice Chairman, AMMRC
J. M. AYOUB, Coordinator, AMMRC

TECHNICAL PAPERS AND PROGRAM

J. ADACHI, Chairman, AMMRC
A. A. ANCTIL, AMMRC
R. BARSOUM, AMMRC
L. BERKE, NASA-Lewis Research Center
C. I. CHANG, Naval Research Laboratory
H. D. CURCHACK, Harry Diamond Laboratories
J. FALLER, Aberdeen Proving Ground
G. L. FILBEY, Jr., Ballistic Research Laboratories
R. FOYE, Navy Post Graduate School
C. E. FREESE, AMMRC
J. T. GARVIN, AMMRC
J. GASSNER, AMMRC
H. HATCH, AMMRC
G. E. MADDUX, Air Force Flight Dynamics Laboratory
J. F. MESCALL, AMMRC
D. R. MULVILLE, Naval Air Systems Command
D. M. NEAL, AMMRC
D. W. OPLINGER, AMMRC
R. P. PAPIRNO, AMMRC
R. QUATTRONE, Army Construction Engineering Research Laboratory
E. W. ROSS, Jr., Army Natick R&D Center
M. ROYLANCE, AMMRC
E. SAIBEL, Army Research Office
J. SCHAEFFEL, U.S. Army Missile Command
T. SIMKINS, Army Armament R&D Command
J. H. SMITH, National Bureau of Standards
D. TRACEY, AMMRC

WORK-IN-PROGRESS SESSION

G. E. MADDUX, Co-Chairman, Air Force Flight Dynamics Laboratory
R. P. PAPIRNO, Co-Chairman, AMMRC

CONTENTS

OPENING SESSION

SESSION I: OVERVIEWS OF SPONSORED RESEARCH

ANALYSIS AND DESIGN

SESSION VII: WORK IN PROGRESS

SESSION VIII: DESIGN & ANALYSIS OF PROJECTILES & MUNITIONS

MODERATOR: J. I. Bluhm, AMMRC

PROJECTILE DESIGN TECHNOLOGY FOR LAUNCH

    B. P. Burns & W. H. Drysdale, Ballistic Research Lab, Aberdeen, MD

PANEL DISCUSSION OF CRITICAL ISSUES IN ADVANCED SYSTEMS

    o FRACTURE MECHANICS CONSIDERATION

      J. Underwood, Benet Weapons Lab, Watervliet, NY

    o COMPOSITES & THEIR IMPLICATION FOR SPECIAL CONCLUSIONS
      IN PROJECTILES

      D. W. Oplinger, AMMRC

SESSION IX: SOLID MECHANICS IN PENETRATION PHENOMENA

MODERATOR: J. Mescall, AMMRC

COMPUTATIONAL ASPECTS OF PENETRATION MECHANICS — KINEMATICS &
MATERIALS ISSUES

    J. Mescall, AMMRC

EXPERIMENTAL TECHNIQUES IN PENETRATION MECHANICS

    S. Bless, University of Dayton Research Institute

BALLISTIC PENETRATION MODELS AS USED IN COMPUTER-AIDED-DESIGN
EVALUATIONS

    R. Recht, University of Denver Research Institute

A REVIEW OF SOME RECENT RESULTS IN DYNAMIC PLASTICITY

    J. Duffy, Brown University

THE SRI SNAG MODEL FOR SHEAR BANDING UNDER HIGH RATE LOADING

    D. Shockey, Stanford Research Instiute

OPENING SESSION

NEW COMPUTING SYSTEMS AND THEIR IMPACT ON STRUCTURAL CALCULATIONS

Ahmed K. Noor
George Washington University Center at
NASA Langley Research Center
Hampton, Virginia

A detailed review is given of the recent advances in computer technology that are likely to impact structures calculations. The characteristics of new and projected computing systems are summarized. At one end of the spectrum there are the large supersystems such as the CRAY-1S and the CDC CYBER 205. The performance of supersystems will continue to improve and their speed is likely to reach 20 GigaFLOPS before the end of the present decade. These supersystems will make possible new levels of sophistication in analytical modeling as well as in problem depth and scope which were not possible before. At the other end of the spectrum the small low-cost computer systems, particularly the microcomputers (handheld computers) and the desktop computers (engineering workstations) will provide a high degree of interactivity and free the analysts from constraints that are often imposed on them by large centralized computation centers. To improve the performance of the small systems, attached processors (some on single chips) will be combined with them to form high-performance duel-processor systems.

The special-purpose highly-parallel systems will occupy an intermediate position between the two extremes (the supersystems and the small systems). Special-purpose processors such as the Finite Element Machine, Navier-Stokes machines and Partial Differential Equation (PDE) machines will continue to be built for fast solution of engineering problems. However, their effectiveness will depend on the availability of software to exploit the parallelism in these processors (e.g., programming languages, operating systems and data management systems).

A scenario is presented for future hardware/software environment and structural analysis systems. In this scenario a broad spectrum of analysis software and firmware is projected ranging from stand-alone systems to modules in large integrated CAD/CAM systems. The user interface facilities (including geometric modeling, mesh generation, input facilities, graphics displays, etc.) will continue to improve. The networked computer hardware/software environment of the future will be more complex and offer many more choices to the user than are available today. This environment provides an opportunity for some very creative research on management-type methods for selecting the best combinations of hardware and software for cost-effective solutions to the problems. It is likely that the selection of the appropriate analysis software, firmware and hardware for the solution of an engineering problem will be done with the aid of artificial intelligence-based expert systems.

The discussion of the new computing systems presented herein is intended to give structural analysts some insight into the potential of these systems for providing cost-effective solutions of complex structural problems, and to stimulate research and development of the necessary numerical algorithms, firmware and software to realize this potential. The future offers exciting opportunities for new and innovative analytical research in exploiting the new computing environment.

CURRENT AND FUTURE DEVELOPMENTS OF EXPERIMENTAL MECHANICS

Fu-Pen Chiang
Professor of Mechanical Engineering
Director, Laboratory for Experimental Mechanics Research
State University of New York at Stony Brook
Stony Brook, New York 11794

The major achievement of experimental mechanics in th past decade is the development of a series of measurement methods using random patterns. Recent advances concerning these techniques will be reviewed together with other new developments such as fiber optics techniques, real time laser speckle photography, holo-speckle interferometry, etc. While no one can really predict the future, it is obvious that computer interfaced techniques will be playing a central role. Some trends of using computers to process directly optical information for strain measurement will be discussed.

SESSION I: OVERVIEWS OF SPONSORED RESEARCH

STRUCTURAL MECHANICS PROGRAM

Dr. Michael P. Gaus
Program Director
Directorate for Engineering
National Science Foundation

The Structural Mechanics Program of the National Science Foundation is concerned with supporting basic research aimed at providing a knowledge and data base related to the behavior of various types of structures. Because NSF is not an operating agency, the grant support provided is aimed at developing information which is perfectly general and the studies supported can have an impact on a large variety of structural types ranging from building structures, ship structures, aircraft, spacecraft, dams, structural behavior of pavements or the structual components of robots or equipment for automated assembly lines. Some specific areas in which studies are underway are the general area of structural loads and the mathematical techniques for their characterization for use in subsequent analysis procedures, mechanics of behavior of materials, mathematical approaches to structural mechanics analysis for linear or nonlinear behavior, effective use of supercomputers and microcomputers in analysis and simulation, experimental studies of structural behavior and acquisition of data from full-scale structures for use in validation of analytical and experimental methods.

Among the areas which are of particular interest at the present time are material related problems such as formulation of constitutive properties for numerical analysis, fatigue and fracture; improved methods for characterizing loadings used for analysis and the mathematical frameworks to incorporate these loadings in failure or acceptable performance approaches; computer methods including expert system methodology, improved opportunities offered by supercomputers for solid mechanics problems; development of nondestructive methods to acquire stress, displacement and response information from actual structures and mathematical optimization techniques for structural elements and configurtions.

A listing of some examples of Program activities is given in the attached table.

STRUCTURAL MECHANICS PROGRAM

1. Construction Materials

    High strength concrete
    Failure of glass
    Reflective cracking of pavement overlays
    Mechanics of wood behavior
    New high-technology wood composite materials
    Fatigue failure in construction materials

2. Loads

    Snow loads on structures
    Loads due to human movement
    Structural loads due to expansive soils
    Engineering characterization of natural winds
    Boundary layer wind tunnel techniques
    Internal pressures in buildings

3. Analytical Methods

    Fuzzy set theory in Civil Engineering
    Evaluation of existing structures
    Optimum design theory
    Response of structures to random loads
    Fluid-structure interaction
    Probabilistic methods for limit-states design
    Mathematical theories for load combinations
    High technology formulations for numerical analysis
    Methods for risk analysis for structures

4. Computer Methods

    Expert systems for structural design
    Decision logic for code formulation
    Consistent data base structures for microcomputers
    Breaking analytical barriers using supercomputers
    Computer graphics for optimum numerical analysis

5. Experimental Methods

    Non-destructive evaluation of structural deformation and performance
    Bond-slip in reinforced concrete
    Time dependent concrete deformation
    Fatigue strength of prestressed concrete members
    Behavior of partially-prestressed concrete members
    Stability theory for structural members

6. Field Data

    Multi-National engineering wind data collection
    Structural loads in tied-back walls
    Tall building data base
    Documenting structural failures

7. Equipment and Facilities

    Boundary layer wind tunnels
    Interactive computer analysis for optical experimental stress
        analysis
    Dynamic structural loading

8. International Travel

    Structural stability conference
    Partially prestressed concrete
    Wind loading and analysis of hyperbolic towers
    International Conference on Structural Serviceability and
        Reliability

STRUCTURAL MECHANICS PROGRAM - FY 1983

1. Construction Materials

      7 Grants $ 432,153   15.4%

2. Loads

      5 Grants $ 339,944   12.1%

3. Analytic Methods

      14 Grants $ 862,322   30.6%

4. Computer Methods

      6 Grants $ 325,055   11.6%

5. Laboratory Experiment

      9 Grants $ 605,285   21.5%

6. Field Data

      0 Grants

7. Equipment and Facilities

      6 Grants $ 220,545   7.8%

8. International Travel

      13 Grants $ 26,131   1.0%

                                             $2,811,435

AN OVERVIEW OF BASIC RESEARCH IN SOLID MECHANICS AND RELATED AREAS
SUPPORTED BY THE U. S. DEPARTMENT OF ENERGY

SEVERINO L. KOH*
Division of Engineering and Geosciences, ER-15
Office of Basic Energy Sciences
U. S. Department of Energy
Washington, DC 20545

EXTENDED ABSTRACT

Engineering Research in the U. S. Department of Energy is administered under the Office of Basic Energy Sciences of the Office of Energy Research. This program pursues two main objectives to meet the long-term basic research needs of energy technologies: (1) acquire a better understanding of the basic phenomena and processes underlying current energy-related engineering practice, and (2) expand the conceptual and technical base of engineering sciences for the initiation and advancement of emerging energy technologies. The program strives to identify and support fundamental research on generic subjects in areas of traditional engineering disciplines as well as in interdisciplinary areas, addressing problems related to energy production, distribution and utilization. Research projects are targeted to yield significant innovations important to meeting the Nation's energy needs.

The program has its focus on three categories: (1) Mechanical Sciences - including tribology, heat transfer, fluid mechanics, solid mechanics and structures; (2) Systems Sciences - including process control, large scale systems, intelligent machines in unstructured environment, and instrumentation; (3) Engineering Data and Analysis - including nonlinear dynamics and the development of critically-needed data bases for energy engineering systems.

A brief presentation of the development of the Engineering Research program in DOE will be given, tracing its history from its inception in 1979 to its current scope of activities. Budgetary information will be provided. The distribution of support under the three categories of engineering research will also be discussed.

The presentation will focus on sponsored research in solid mechanics and related areas with particular attention to ongoing work   on the following topics:

(1) Structural Mechanics and Mechanics of Materials -- dynamic plastic deformation of structures, stability control of fluid-conveying tubes, internal hysteresis of cord-rubber composites, stress creep of structural metals.

---

*Dr. S. L. Koh is currently on leave from the Department of Mechanical and Aerospace Engineering, West Virginia University, Morgantown, WV.

(2) Tribology -- mechanical interaction of rough surfaces, wear and friction-induced vibrations, mechanisms of friction and wear between lubricated surfaces, piston ring friction, effect of airflow inside a pneumatic tire on temperature buildup and rolling resistance.

(3) Damage, Fracture Mechanics and Failure Analysis -- continuous damage theories, damage accumulation under combined creep and fatigue, fatigue damage under multiaxial cyclic stress, crack-tip stress fields for materials with creep behavior, energy changes in transforming solids, elastic-plastic fracture.

(4) Nondestructive Evaluation -- scattering of ultrasonic waves, NDE characterization of cracks, instrumentation research: multiviewing ultrasonic transducer for QNDE, high-frequency transducers.

RESEARCH STUDIES IN SOLID MECHANICS SUPPORTED BY
THE ARMY RESEARCH OFFICE (ARO)

Dr. Edward Saibel
Chief, Solid Mechanics Branch
Engineering Sciences Division
Army Research Office
Research Triangle Park, NC 27709

The Army Research Office, Research Triangle Park, North Carolina, regularly supports a wide range of basic research programs conducted by research organiztions primarily at universities with some at non-profit research organizations and a few in industry.

In the engineering field, these programs include individual research programs on subjects such as finite element methods for metal forming problems, gun dynamics modeling, plasticity in fibrous composites, fracture of composites, armor/projectile response and penetration, friction and wear, helicopter dynamics, theory of machines and mechanisms with applications to robotics and others.

In addition, support is provided to conferences and workshops on subjects such as mechanics of materials behavior, rotordynamic instability in high performance turbomachinery and international research in plasticity. Equipment grants have also been provided under the DoD Research Instrumentation Program to a number of laboratories.

The presentation will provide specific information about ARO and the ARO sponsorship program as well as details of some of the research problems under study and results expected or obtained to date.

DIRECTIONS IN SOLID MECHANICS RESEARCH

AT THE OFFICE OF NAVAL RESEARCH

Alan S. Kushner
Program Manager
Solid Mechanics
Office of Naval Research

The Office of Naval Research (ONR) Solid Mechanics Program emphasizes basic research which broadens and deepens the scientific foundations of solid mechanics. Our aims are to provide a fundamental basis for describing the thermomechanical response of materials and to develop an understanding and predictive capability for the highly nonlinear regime of structural response. The ONR program is divided into five thrust areas; constitutive equations and micromechanics, fracture and NDE, fundamental structural response, mathematical and numerical aspects of solid mechanics, and structural acoustics.

Current thrust areas in the material response area are emphasizing the utilization of microstructurally based constitutive theories as the basis for improved phenomenological laws. In addition, a strong emphasis is being placed on utilizing inelastic constitutive laws to provide a sounder basis for describing the crack initiation and growth process. In composites, a primary goal is an understanding of the interacting damage and failure modes. ONR's computational program in solid mechanics is emphasizing error measures and solutions enhancement techniques. In addition, a broad based thrust exists in finite deformation shell theory and its computational implementation.

OVERVIEW OF AIR FORCE PROGRAMS

Dr. Anthony Amos
Air Force Office of Scientific Research

Abstract not available at time of publication.

BUCKLING AND POSTBUCKLING RESEARCH ON COMPOSITE STRUCTURES

Marshall Rouse
Aerospace Engineer
Structural Mechanics Branch
NASA Langley Research Center
Hampton, Virginia

Recent advances in applying composite materials to aircraft structures has led to several studies of buckling and postbuckling behavior of graphite-epoxy structural components. The Structural Mechanics Branch of NASA Langley Research Center is presently involved in a generic study of composite panels for potential transport applications.

This presentation will summarize some recent NASA in-house and contractor* studies of buckling and postbuckling behavior of flat and curved, stiffened and unstiffened graphite-epoxy panels loaded in compression and loaded in shear. Structural efficiency of graphite-epoxy panels will be compared with aluminum panels. Also, the structural efficiency of graphite-epoxy panels designed to be buckling resistant will be compared with graphite-epoxy panels designed to have postbuckling strength. Another area of research which will be discussed is the effect of low speed impact damage and circular cutouts on stiffened and unstiffened graphite-epoxy panels loaded into the postbuckling range.

In addition to experimental results, analytical results will be presented to describe the strucctural response of composite panels. Analytical results will be presented which predict the structural response of composite panels with arbitrary configurations that have complex buckling modes. Also, analytical correlations of the postbuckling response of stiffened and unstiffened graphite-epoxy panels loaded in compression will be presented. A brief outline of the presentation is given below:

I.   Buckling-resistant structures loaded in compression

    A. Structural efficiency
    B. Comparison of experiment and analysis

II. Compression-loaded structures with postbuckling strength

    A. Flat unstiffened panels
    B. Flat stiffened panels
    C. Curved unstiffened panels
    D. Curved stiffened panels

III. Shear-loaded structures with postbuckling strength

    A. Flat unstiffened shear webs
    B. Stiffened shear webs

SESSION II: EXPERIMENTAL METHODS

STRESS CONCENTRATION IN THE ELASTOPLASTIC STATE

AND RESIDUAL STRESS AFTER UNLOADING

Y. F. Cheng
U.S. Army Armament, Munitions, and Chemical Command
Armament Research and Development Center
Large Caliber Weapon Systems Laboratory
Benet Weapons Laboratory
Watervliet, NY 12189-5000

ABSTRACT

Photoplasticity and photoelastic coating have been employed successfully to study stress concentration in the elastoplastic state and residual stress after unloading. Principles are described. Examples of the application of both methods are given. The results show that stress concentration in the elastoplastic state is lower than that in the elastic state and decreases continuously as yielding progresses. A good agreement exists between results from both methods.

INTRODUCTION

It is well-known that in certain structural members an initial tensile overload produces a beneficial compressive residual stress ɹpon unloading. This fact has been utilized extensively in armament designs such as breech rings to reduce their operating stresses and to improve their fatigue liɣɛs. It is also known that stress concentrations in the elastoplastic state are different from those in the elastic state [1]. Thus, elastic stress concentration factors cannot be used to calculate the maximum stress at overload. This paper reports two experimental methods; namely, photoplasticity and photoelastic coatings, for determining stress concentration factors in the elastic and elastoplastic states. Principles are described. Examples of the application of both methods are given. Maximum free boundary stress at overload, elastic-plastic boundary, and residual stress after unloading are found. The results show that stress concentration in the elastoplastic state is lower than that in the elastic state and decreases continuously as yielding progresses.

PHOTOPLASTICITY

Experimental Method

Photoelastic stress analysis is based on the linear stress-optic law [2,3]. The discovery of the non-linear stress-optic law extends the photoelastic method to the plastic state [4]. Specifically, at any point in a model, the isochromatic fringe is related to the secondary principal stress difference $(\sigma_1' - \sigma_2')$, and the isoclinic parameter gives the directions of the secondary principal stresses σ_1' and σ_2'. In two-dimensional cases, the secondary principal stresses become principal stresses σ_1 and σ_2.

In this paper, we are interested only in the boundary stress and maximum shear in two-dimensional models. No attempts were made to determine the individual stress distribution, although techniques are readily available. On the free boundary, one of the principal stresses is identically zero, and the remaining principal stress tangent to the boundary is given by the boundary fringe order. It is known that the maximum shear, τ_{max}, equals one-half of the principal stress difference; i.e., $\tau_{max} = (\sigma_1 - \sigma_2)/2$. For a material obeying the yield condition of maximum shear, the elastic-plastic boundary is defined by the fringe having a maximum shear of $\sigma_y/2$, where σ_y is the yielding stress.

Model Material

Polycarbonate resin (ester of carbonic acid and bispherrol A) was first suggested by Ito [5] in 1962 for use as model material. It is ductile and has good transparency in both elastic and plastic states. Gurtman et al [6] conducted uniaxial tension tests on flat specimens of polycarbonate in 1965 and reported a Poisson's ratio of 0.38 in the elastic state and a limiting value of 0.5 in the plastic state. They also found that polycarbonate creeps optically and mechanically (birefringence and strain) at a stress of above 4000 psi.

The polycarbonate resin used in this work was supplied by the General Electric Company under the trade name LEXAN. It had a thickness of 0.12 inch. Calibration tests were made at a temperature of 73° ± 3°F and a relative humidity of 10% ± 5%. Strain was calculated from deformation readings obtained through a travelling telemicroscope. Birefringence was determined by means of Senarmont's principal of compensation with a collimated monochromatic light of 5461 Å. The results show that this material creeps both optically

25

and mechanically at a stress of above 4000 psi, confirming Gurtman's work, and that both creeps stabilize after 240 minutes. Figures 1 and 2 show the stress-fringe and stress-strain curves. It has an elastic material fringe value of 36 psi per inch, a Young's modulus E of 3.25×10^5 psi, a proportional limit stress of 6.2×10^3 psi, and a secant yield strength, σ_{sec}, defined by the point of intersection of secant modulus ($E_{sec} = 0.7E$) and the stress-strain curve of 8.7×10^3 psi. The non-dimensional stress-strain curve given by the Ramberg-Osgood equation [7] for this material has the following form

$$E\varepsilon/\sigma_{sec} = (\sigma/\sigma_{sec}) + (3/7)(\sigma/\sigma_{sec})^{11.5} \tag{1}$$

where ε denotes strain, and σ stress. During calibration, Luder's lines were observed, Figure 3, indicating that polycarbonate follows the yield condition of maximum shear.

Experiments and Results

1. Experiments on C-Shaped and Compact Tensile Specimens. The purposes of this series of experiments were to determine stress concentration factors in elastic and plastic states, and residual stresses after unloading. Three models each of the C-shaped and compact tensile specimens, Figures 4 and 5, were made. In order to minimize any effect of material nonhomogeneity, they were cut closely to the calibration specimens with their lines of loading parallel to each other. One model was tested in the elastic state. The other two models were tested in the elastoplastic state. Each elastoplastic test requires a new model. The load was applied through pins.

Photographs of isochromatic fringe pattern were taken for each load at 240 minutes after loading. The fringe and maximum shear distributions across the narrowest section were determined, Figures 6 and 7.

It was mentioned previously that for a material obeying the yield criterion of maximum shear, such as LEXAN, the elastic-plastic boundary is defined by the fringe having a maximum shear of $\sigma_y/2$. In this work, we chose the proportional limit stress of 6.2×10^3 psi as σ_y. Hence, the elastic-plastic boundary was given by the fringe having a maximum shear of 3.1×10^3 psi. The depth of the plastic region on the narrowest section AB, Figures 4 and 5, and its extended angle along the notch were found at two levels of load and shown in Table I.

TABLE I. SIZE OF PLASTIC REGION

Specimen	Load, Pound	Plastic Region	
		Depth, 1/AB	Extended Angle, Degrees
C-shaped	15.2	0.02	50
C-shaped	18.7	0.04	65
Compact	56	0.006	70
Compact	84	0.01	90

Boundary fringe order and stress σ were determined for end points A and B. Stress concentration factor K was defined as the ratio of σ/σ_{nom}, where

$$\sigma_{nom,A} = (P/td)(1+6D/d) \qquad (2)$$

and

$$\sigma_{nom,B} = (P/td)(1-6D/d) \qquad (3)$$

Subscripts refer to points A and B, respectively. These values are shown in Figure 8 and listed in Tables II and III.

The results show that as long as the material is in the elastic state, stress varies linearly with the load. Stress concentration factor K is a constant and the $K-\sigma_{nom}$ curve is straight and horizontal. When load is increased such that local yielding sets in, the linear stress-load relation breaks down and the stress concentration factor decreases continuously as

27

TABLE II.   STRESS CONCENTRATION FACTOR, PERCENTAGE OF OVERLOADING,

AND RESIDUAL STRESS IN POLYCARBONATE C-SHAPED SPECIMENS

Load (pounds)	Nominal Stress		Boundary Stress		Stress Concentration Factor		Percentage of Overloading	Residual Stress (psi)
	σ_{An} (psi)	σ_{Bn} (psi)	σ_A (psi)	σ_B (psi)	K_A	K_B		
3.84	1350	-1250	2040	-1050	1.51	0.84		
5.15	1810	-1670	2850	-1410	1.57	0.84		
6.45	2270	-2100	3450	-1710	1.52	0.81		
					Ave: 1.53			
15.2	5350	-4940	7000	-4200	1.31	0.85	32	-1190
18.7	6580	-6080	7850	-5000	1.19	0.82	63	-2220
						Ave: 0.83		

TABLE III. STRESS CONCENTRATION FACTOR, PERCENTAGE OF OVERLOADING, AND

RESIDUAL STRESS IN POLYCARBONATE COMPACT TENSILE SPECIMENS

Load (pounds)	Nominal Stress σ_{An} (psi)	Boundary Stress σ_A (psi)	Stress Concentration Factor K	Percentage of Overloading	Residual Stress (psi)
8	550	1190	2.16		
12	820	1790	2.18		
16	1090	2380	2.18		
20	1370	2980	2.18		
			Ave: 2.18		
56	3830	7500	1.96	35	-840
64	4370	8200	1.88	54	-1330

yielding progresses. The stress at point B in the C-shaped specimen is less than the nominal value. Hence, at this point the stress concentration factor is less than one. At 18.7 pounds of load, point B was still in the elastic state, although the plastic region had already progressed to a depth of 0.04 AB from point A. Assuming that the material property in compression is the same as in tension, point B would yield at a load of approximately $6200/(325 \times 0.83) = 23$ pounds.*

For the purpose of calculating residual stress, the usual assumption that unloading is inherently an elastic process was made. For example, an unloading from 18.7 pounds of load would reduce a stress of $(1.53)(352)(18.7) = 10.1 \times 10^3$ psi* at point A in the C-shaped specimen. Superposition of this value with 7.85×10^3 psi from elastoplastic load of 18.7 pound gives a residual stress of 2.22×10^3 psi compression, as shown in Table II.

The percentage of overloading was defined as $[(P/P_p) - 1] \times 100\%$ where P_p denotes the proportional limit load, the load produces the proportional limit stress. It has a value of 11.5 and 41.6 pounds for C-shaped and compact tensile specimens, respectively.

The residual stress and percentage of overloading were calculated for both specimens and listed in Tables II and III.

2. <u>Experiment on Breech Ring Section.</u> It is known that most breech ring failures are caused by the presence of high tensile stress at the lower fillet. It is also known that by introducing residual compressive stress at the lower fillet, ring failure can be delayed. The purpose of this experiment was to determine the residual stress at the lower fillet in an overloaded breech ring after unloading.

---

*In C-shaped specimens, real dimensions give $\sigma_{nom,A} = 352\ P$ and $\sigma_{nom,B} = 325\ P$, respectively.

30

A model of the meridian section of a breech ring was made, Figure 9. It was cut closely to the calibration specimens with their lines of loading parallel with each other. The block was made of aluminum. The top of the ring was fixed. The load was applied through a pin at the top of the block. Guide plates were used to prevent buckling.

Maximum fringe order at the lower fillet was closely watched during loading. The loads corresponding to the first four integral fringes were recorded, Table IV. It was found that in the elastic state a load of 27 pounds was necessary to raise one order of fringe, or 300 psi, at the fillet. After the elastic stress was determined, the load was increased to the elasto-plastic state of 1144 pounds and held for 240 minutes. Maximum fringe order at the fillet was measured intermittently. At 240 minutes it had an order of 43 indicating a plastic stress of 9.3×10^3 psi. A complete unloading would produce a stress reduction of $(1144)(300/27) = 12.7 \times 10^3$ psi giving a residual stress of 3.4×10^3 psi compression.

Transition to Prototype

Solutions of problems in stress distribution, whether elastic or plastic, must satisfy three conditions: equilibrium, compatibility, and boundary values. The elastic stresses, except those in the immediate vicinity of contact, are proportional directly to the loads and inversely to the square of the scale ratio. The transition of data from model to prototype can be made through the following equation:

$$\sigma_p/\sigma_m = (P_p/P_m)(L_m/L_p)^2 \tag{4}$$

where L is a characteristic length, and subscripts m and p refer to model and prototype, respectively.

TABLE IV. LOAD AND FRINGE ORDER AT LOWER FILLET

OF A POLYCARBONATE BREECH RING SECTION

Fringe Order	Load, pound	Remarks
1	23	Elastic
2	51	
3	78	
4	104	
43	1144	Elastoplastic

The transition of plastic stress from model to prototype requires at least three more conditions: the same shape of non-dimensional stress-strain curves of both materials, the same law of yielding, and the same Poisson's ratio in the plastic state. Elastoplastic data from polycarbonate model are transferable to prototype material having a Poisson's ratio of 0.5 in the plastic state and obeying the maximum shear yield criterion. By adjusting the temperature and relative humidity of the laboratory, the shape of non-dimensional stress-strain curve of polycarbonate can be altered to resemble closely to that of prototype.

PHOTOELASTIC COATING

Experimental Method

The photoelastic coating technique was initially introduced by Mesnager [8] in 1930. The method is based on the bonding of a thin layer of photoelastic material to the surface of the specimen. When load is applied to the specimen, strains are transmitted to the coating which then becomes birefringent. Polarized light is reflected from the surface of the specimen at normal incidence, and fringe patterns are obtained as in the photoelastic method.

Neglecting thickness effect of the reflective layer, the fringe order N is related to the principal strain difference $(\epsilon_1 - \epsilon_2)$ on the surface of the specimen as

$$N = 2c'_t(\epsilon_1 - \epsilon_2) \tag{5}$$

where c' denote the strain-fringe constant, and t thickness of the coating.

In this paper, we are interested only in the boundary stress in two-dimensional models, although techniques for separating individual strains and stresses are readily available.

In the elastic state, stress-strain relation has the following form:

$$\epsilon_1 - \epsilon_2 = (1+\mu)(\sigma_1 - \sigma_2)/E \tag{6}$$

33

where μ denotes Poisson's ratio. Combining Eqs. (5) and (6), we have

$$\sigma_1 - \sigma_2 = (N/2c'_t)[E/(1+\mu)] \tag{7}$$

On the free boundary one of the principal stresses is identically zero and the remaining principal stress tangent to the boundary can be readily found.

In the plastic state, in addition to Eq. (5), we have

$$\varepsilon_1 + \varepsilon_2 + \varepsilon_3 = 0 \tag{8}$$

where subscript 3 refers to the third principal component acting in the direction perpendicular to the surface. On the free boundary of a plane stress problem we have

$$\sigma_2 = \sigma_3 = 0 \tag{9}$$

and

$$\varepsilon_2 = \varepsilon_3 = -\varepsilon_1/2 \tag{10}$$

The principal strain ε_1 tangent to the free boundary becomes

$$\varepsilon_1 = N/3c't \tag{11}$$

and the corresponding principal stress σ_1 can be found from the uniaxial stress-strain relation of the material.

Model and Coating and Materials

Flat ground steel plate of 0.12-inch thickness with a chemical content of 0.85-0.95 C, 1.00-1.25 Mn, 0.20-0.40 Si, 0.40-0.60 Cr, 0.40-0.60 W, and 0.10-0.20 V was used as the model material. It was supplied by Simons Saw and Steel, Fitchburg, MA. Type PS-1 photoelastic sheet of 0.04-inch thickness was used as the coating material. It was supplied by Measurement Group, Raleigh, NC.

Tensile calibration specimens of steel were prepared with electric resistance strain gages (EA-13-015DJ-120, Micromeasurement) bonded at its midsection, one on each side. Coating was applied on the surface of the specimen. Figure 10 shows the stress-strain curve obtained from strain gage readings. It has a Young's modulus E of 30×10^6 psi, a proportional limit

34

stress of 51×10^3 psi, and a secant yield strength σ_{sec} of 60×10^3 psi.
Poisson's ratio was taken to be 0.3 in the elastic state. During calibration
the coating material registered one fringe per 1890×10^{-6} in./in. of axial
strain ε_1 or a principal strain difference of

$$\varepsilon_1 - \varepsilon_2 = 1.3\ \varepsilon_1 = 2460 \times 10^{-6}\ \text{in./in.}$$

Monochromatic light of 5461 Å was used.

Experiment and Result

Due to the limited availability of the material, a 55/65 scale,
two-dimensional model of the meridian section of a breech ring and block
was made with its line of loading parallel to those of the
calibration specimens. Photoelastic coating was bonded to both surfaces of
the lower part of the ring. The boundary of the coating was carefully
machined so as to coincide with the fillet. The model was mounted in the
Testing Machine (Baldwin-Tate-Emery) and the loads were applied through pins
at the top of the block and ring.

It was found that in the elastic state, 2100 pounds of load was required
to produce one-half of a fringe, or a principal strain difference $(\varepsilon_1-\varepsilon_2)$ of
1230×10^{-6} in./in. at the fillet. On the fillet boundary, $\sigma_2 = 0$, and the
maximum fillet stress from Eq. (6)

$$\sigma_1 = E(\varepsilon_1-\varepsilon_2)/(1+\mu) = (30)(1230)/1.3 = 28.4 \times 10^3\ \text{psi}$$

The average stress σ_{av} at the cross-section has a value of

$$\sigma_{av} = 2100/[(0.12)(5.75)(55/65)] = 3.6 \times 10^3\ \text{psi}$$

The stress concentration factor K, defined as the ratio of maximum fillet
stress to average stress is

$$K = \sigma_1/\sigma_{av} = 7.88$$

35

After the elastic solution was obtained, the model was loaded into the elastoplastic state. The loads corresponding to each increasing integral fringe order were recorded. Principal strain difference ($\epsilon_1 - \epsilon_2$), maximum principal strain ϵ_1 and stress σ_1, average stress σ_{av}, stress concentration factor K, and residual stress after unloading were calculated and shown in Table V.

Table V and Figure 11 show that as long as the model is in the elastic state, stress concentration factor is constant. When load is increased such that local yielding sets in, stress concentration factor decreases continuously as yielding progresses. These results are consistent with those obtained from photoplasticity experiments.

COMPARISON BETWEEN RESULTS FROM PHOTOELASTOPLASTICITY AND PHOTOELASTIC COATING

Table VI shows a comparison between results obtained from steel and polycarbonate models of breech ring.

In the elastic state, steel model has a stress concentration factor of 7.88 in comparison with 7.67 from a polycarbonate model. Also, the steel model shows a maximum fillet stress of 28.4×10^3 psi under a load of 2100 pounds in comparison with 27.6×10^3 psi obtained by means of transition, equation 4 , and data from polycarbonate model. A good agreement is established.

As mentioned earlier, the transition of data in the elastoplastic state requires at least three additional conditions: same Poisson's ratio, same law of yielding, and same shape of non-dimensional stress-strain curve. A comparison between figure 2 and 10 clearly shows the violation of the last condition. Specifically, steel and polycarbonate do not have the same shape of non-dimensional stress-strain curves at room temperature, although it is possible to match them closely by adjusting the temperature and relative humidity of the laboratory.

36

TABLE V. LOAD, MAXIMUM STRESS, STRESS CONCENTRATION FACTOR, AND RESIDUAL STRESS

AT THE LOWER FILLET OF A STEEL BREECH RING SECTION

Load P Pounds	Fringe Order N	Principal Strain Difference $(\epsilon_1-\epsilon_2)_s$ in./in.	Maximum Principal Strain $(\epsilon_1)_s$ in./in.	Maximum Principal Stress $(\sigma_1)_s$ psi	Average Stress σ_{av} psi	Stress Concentration Factor $K = (\sigma_1)_s/\sigma_{av}$	Percentage of Overloading $(P-3770)/3770$	Residual Stress psi
2100	0.5	1230×10^{-6}	950×10^{-6}	28.4×10^3	3.60×10^3	7.88	–	–
4100	1	2460×10^{-6}	1870×10^{-6}	54.9×10^3	7.02×10^3	7.63	9	-0.5×10^3
6000	2	4920×10^{-6}	3510×10^{-6}	61.2×10^3	10.3×10^3	5.96	59	-19.9×10^3
7000	3	7380×10^{-6}	5150×10^{-6}	63.1×10^3	12.0×10^3	5.26	86	-31.6×10^3
7600	4	9840×10^{-6}	6790×10^{-6}	64.7×10^3	13.0×10^3	4.97	102	-38.1×10^3
8000	5	12300×10^{-6}	8440×10^{-6}	66.3×10^3	13.7×10^3	4.84	112	-41.9×10^3

37

Nevertheless, the steel model at 102 percent overloading shows a stress concentration factor of 4.97 in comparison with 5.61 from a 105 percent overloading polycarbonate model. The difference is reasonable.

TABLE VI. COMPARISON BETWEEN STEEL AND POLYCARBONATE MODELS

		Steel	Polycarbonate
E S l t a a s t t e i c	Load	2100 pounds	27 pounds
	Maximum Fillet Stress	28.4×10^3 psi	300 psi
	Average Stress	3.6×10^3 psi	300 psi
	Stress Concentration Factor	7.88	7.67
E S l t a a s t t e o p l a s t i c	Load	7600 pounds	1144 pounds
	Maximum Fillet Stress	64.7×10^3 psi	9.3×10^3 psi
	Percentage of Over-loading	102	105
	Average Stress	13.0×10^3 psi	1.66×10^3 psi
	Stress Concentration Factor	4.97	5.61

CONCLUSIONS

Principles of photoplasticity and photoelastic coating have been described. Examples of the application of both methods to a C-shaped notched specimen, a compact tensile notched specimen, and a breech ring section in the elastoplastic state have been given. Maximum free boundary stress, stress concentration in the elastic and plastic state, elastic-plastic boundary, and residual stress after unloading have been determined.

In photoplastic analysis, data in the elastic state are transferable from model to prototype with usual consideration of load and scale ratios. In the plastic state, the transition of data requires at least the satisfaction of three additional conditions on material property: Poisson's ratio, yield criterion, and stress-strain relation. The coating method gives data in models of prototype material. The transition of data requires only the consideration of load and scale ratios.

Stress concentration is constant in the elastic state and decreases continuously as yielding progresses. Therefore, it is advisable to determine stress concentration factor at each load in the elastoplastic state.

Results from photoplasticity and photoelastic coating for a breech ring section have been compared. A reasonable agreement has been reached. The reliability and ease of photoplastic analysis and photoelastic coating technique in the elastoplastic state have been demonstrated.

ACKNOWLEDGEMENT
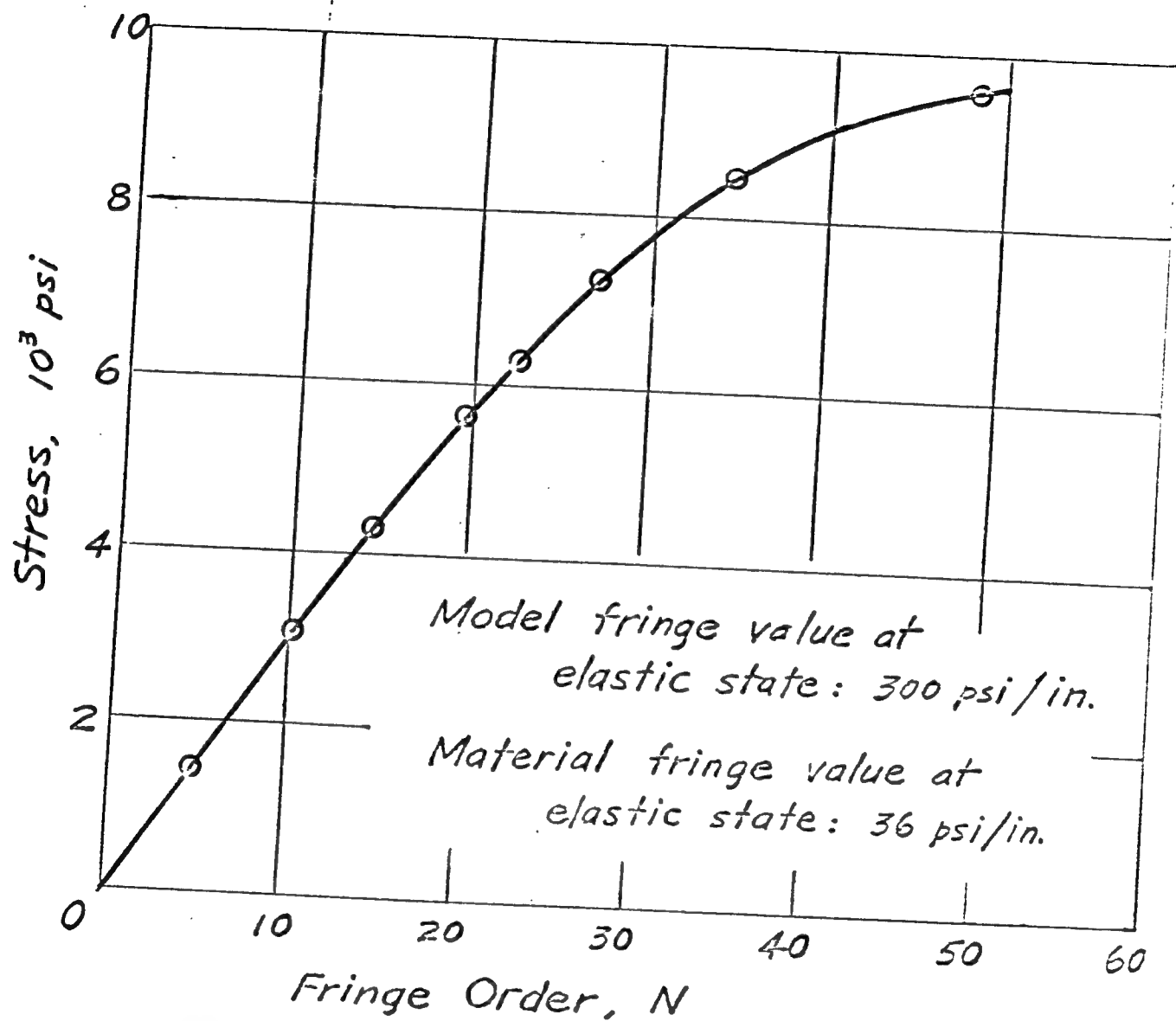
Fig. 1. Stress-Fringe Curve for Polycarbonate

Model fringe value at elastic state: 300 psi/in.

Material fringe value at elastic state: 36 psi/in.
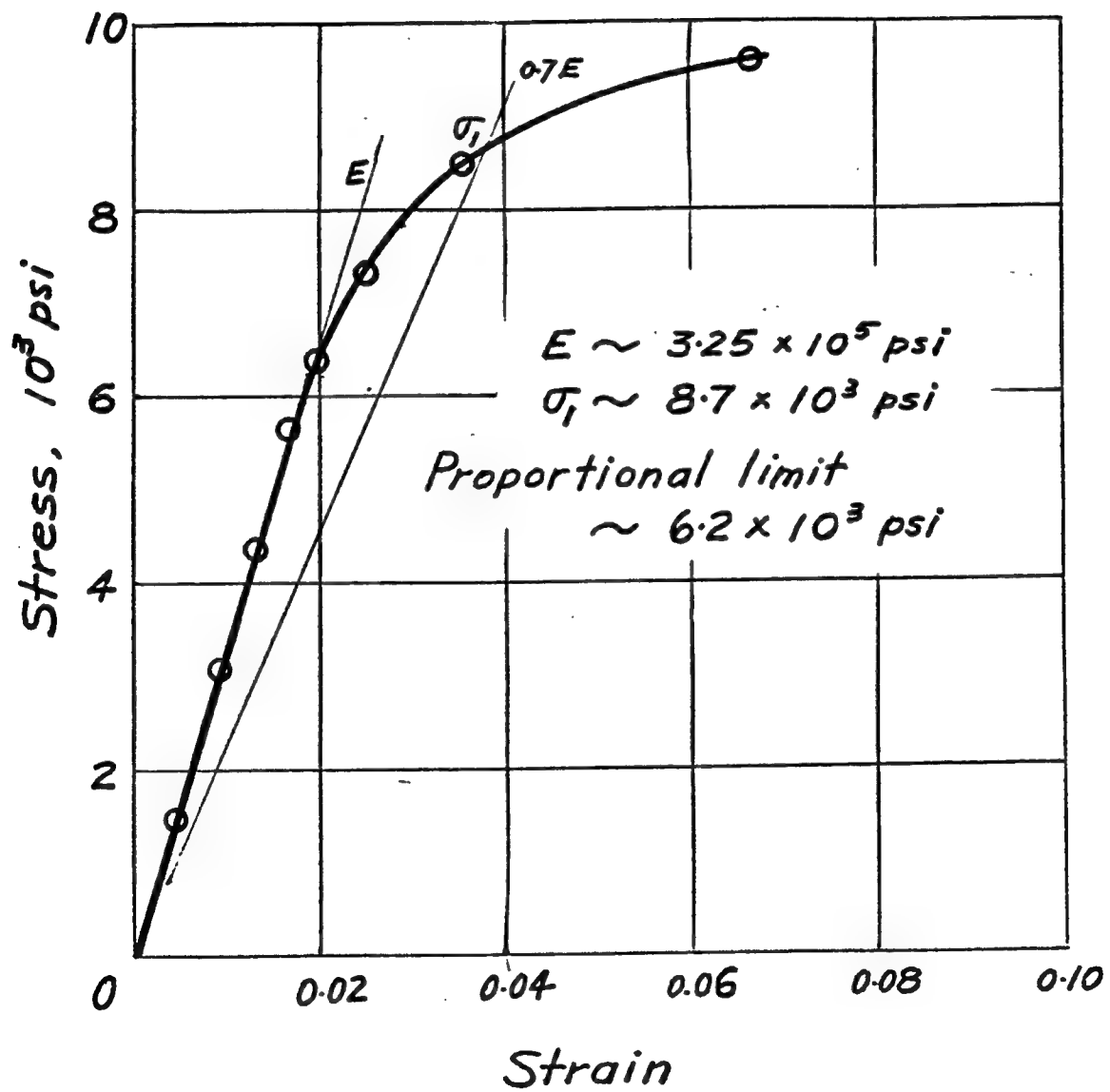
Fig. 2. Stress - Strain Curve for Polycarbonate

The figure shows a stress-strain curve with the following annotations:

- Vertical axis: Stress, 10^3 psi (marked 0, 2, 4, 6, 8, 10)
- Horizontal axis: Strain (marked 0, 0.02, 0.04, 0.06, 0.08, 0.10)
- Lines labelled E, 0.7E, and σ_1
- $E \sim 3.25 \times 10^5$ psi
- $\sigma_1 \sim 8.7 \times 10^3$ psi
- Proportional limit $\sim 6.2 \times 10^3$ psi

41

Fig.3. Photograph of Luder's Lines in Polycarbonate
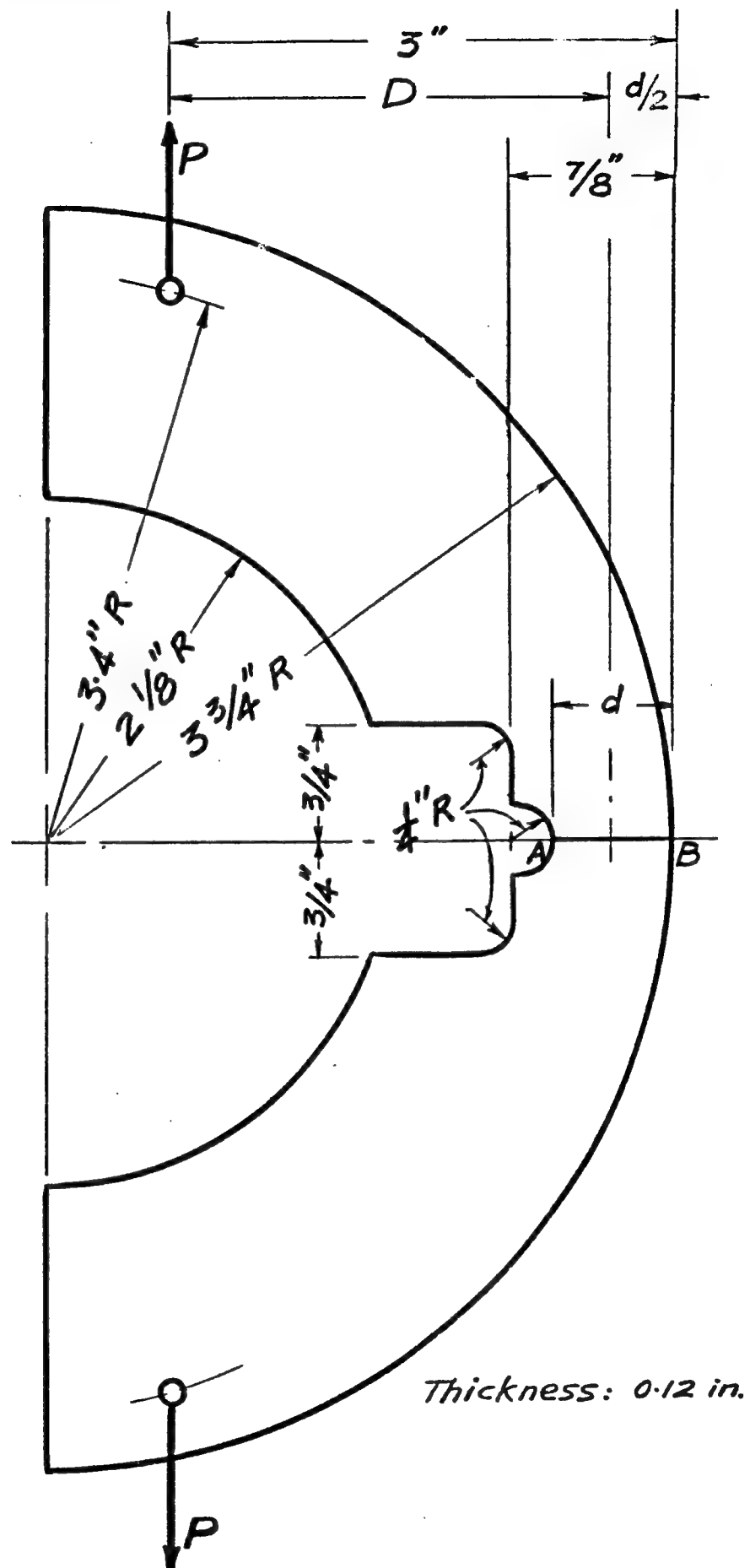
Fig. 4. Sketch of C-shape Specimen
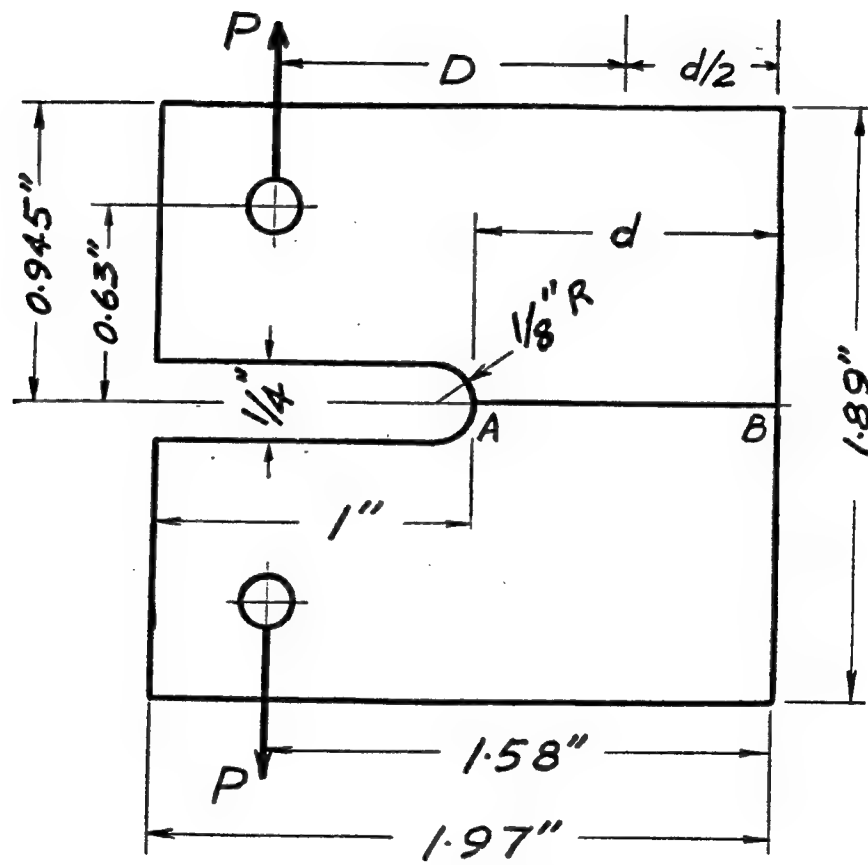
Fig. 5.   Sketch of Compact Tensile Specimen
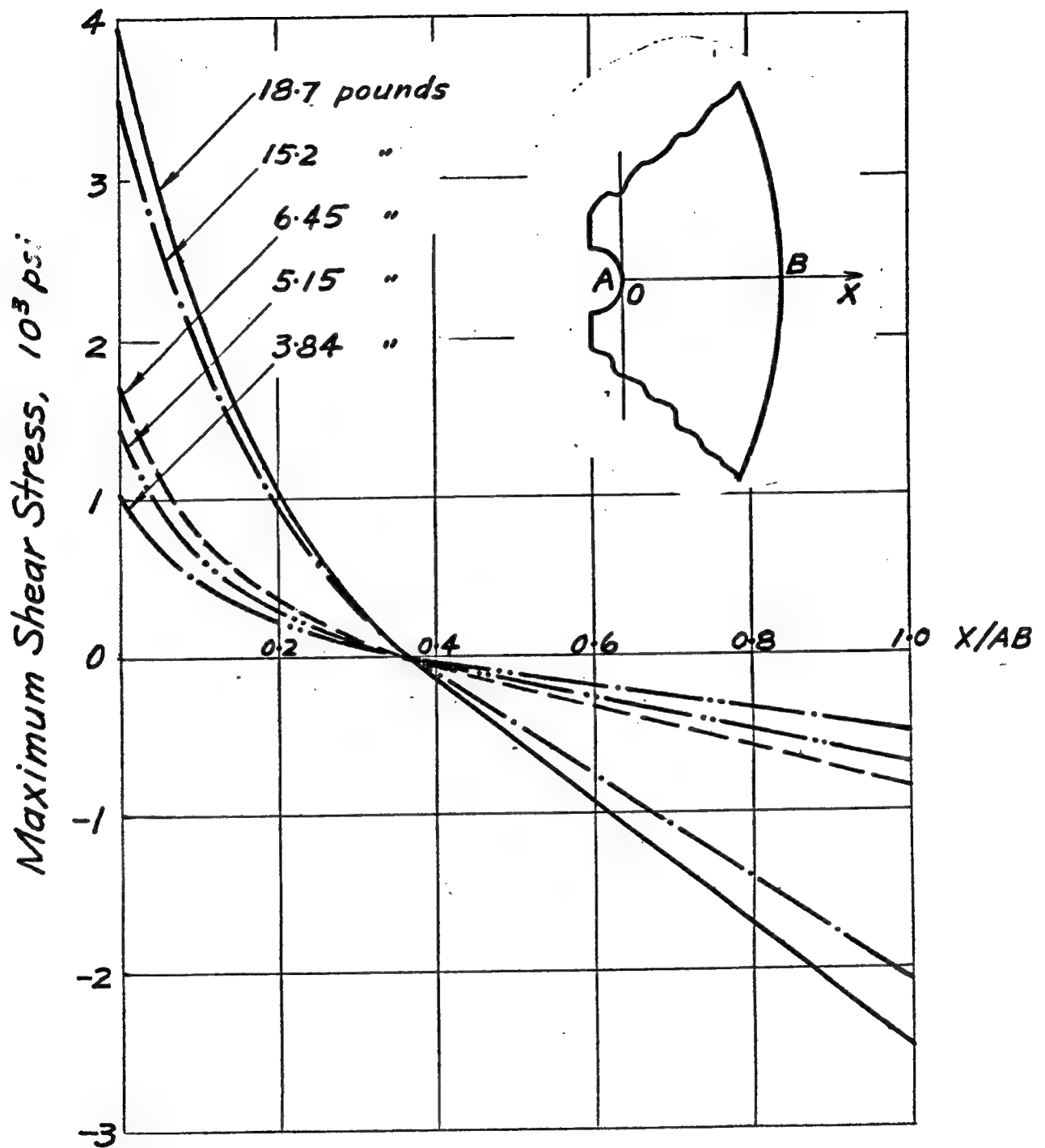
Fig. 6. Maximum Shear Stress Distribution Across Section AB in C-shape Specimen
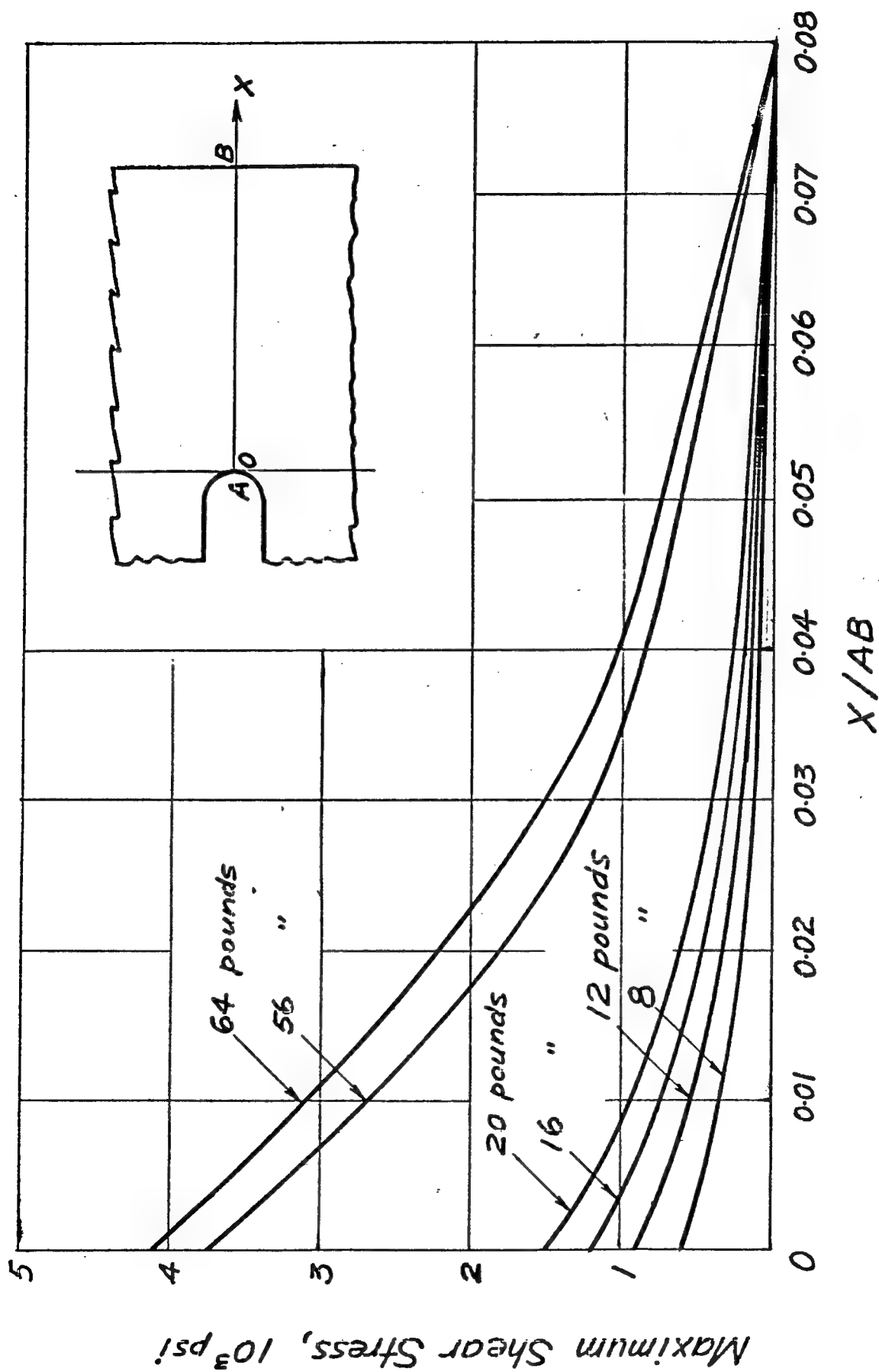
Fig. 7. Maximum Shear Stress Distribution Across Part of Section AB in Compact Tensile Specimen
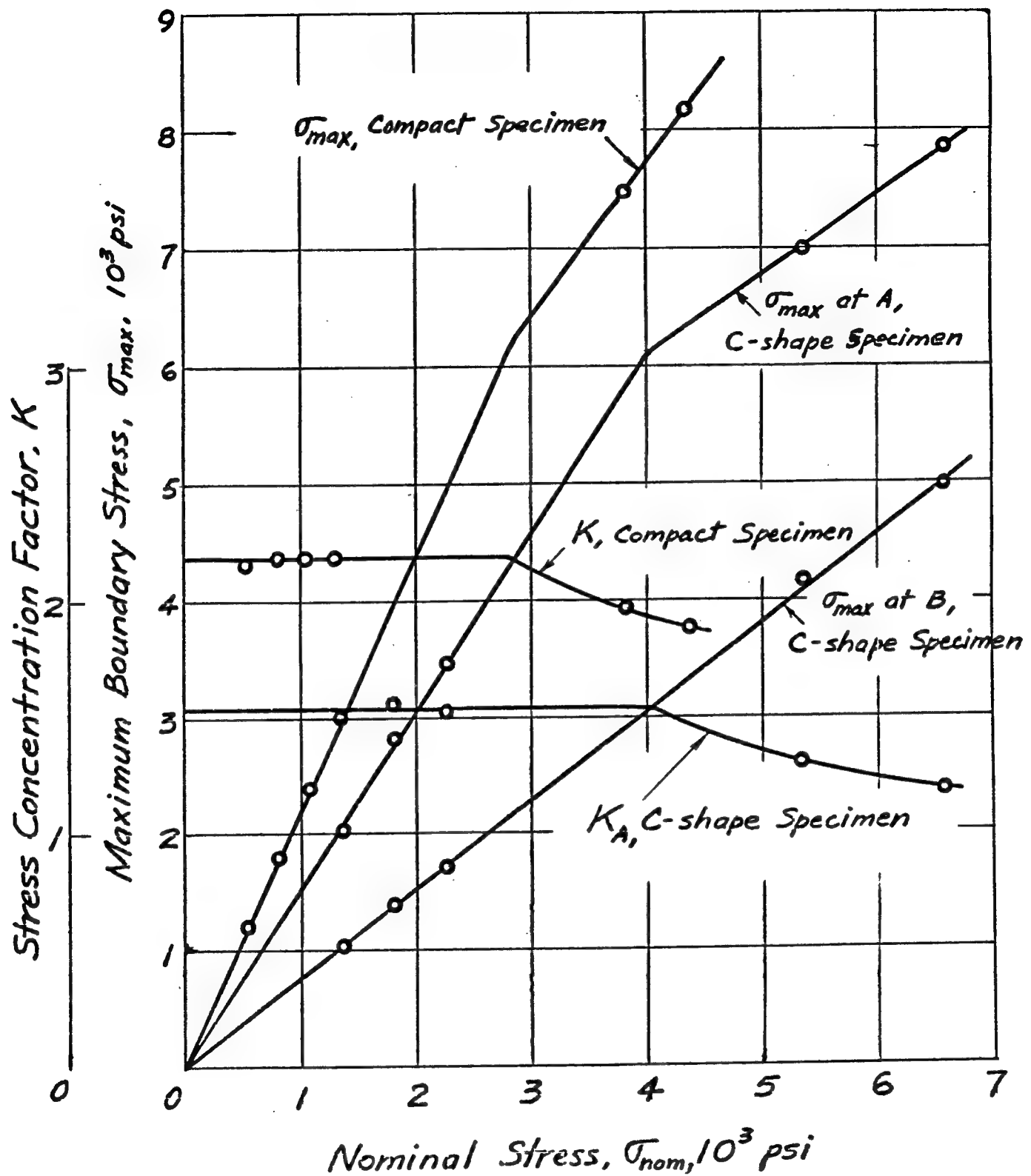
Fig.8. Curves of Stress Concentration Factor, K, and Maximum Boundary Stress, σ_{max}, Versus Nominal Stress, σ_{nom}, in C-shape and Compact Specimens

47
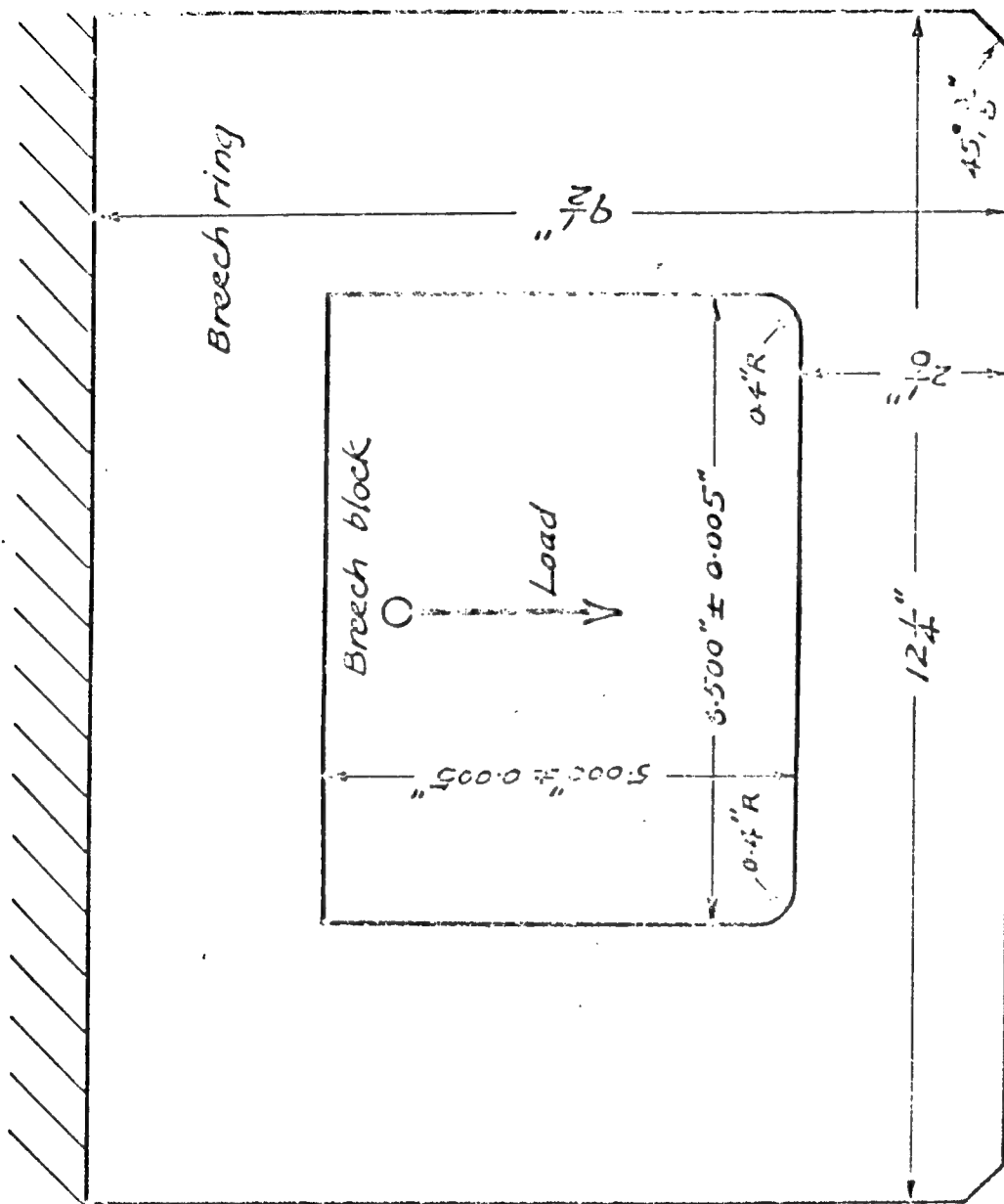
Fig. 9. Sketch of a Polycarbonate Breech Ring Section
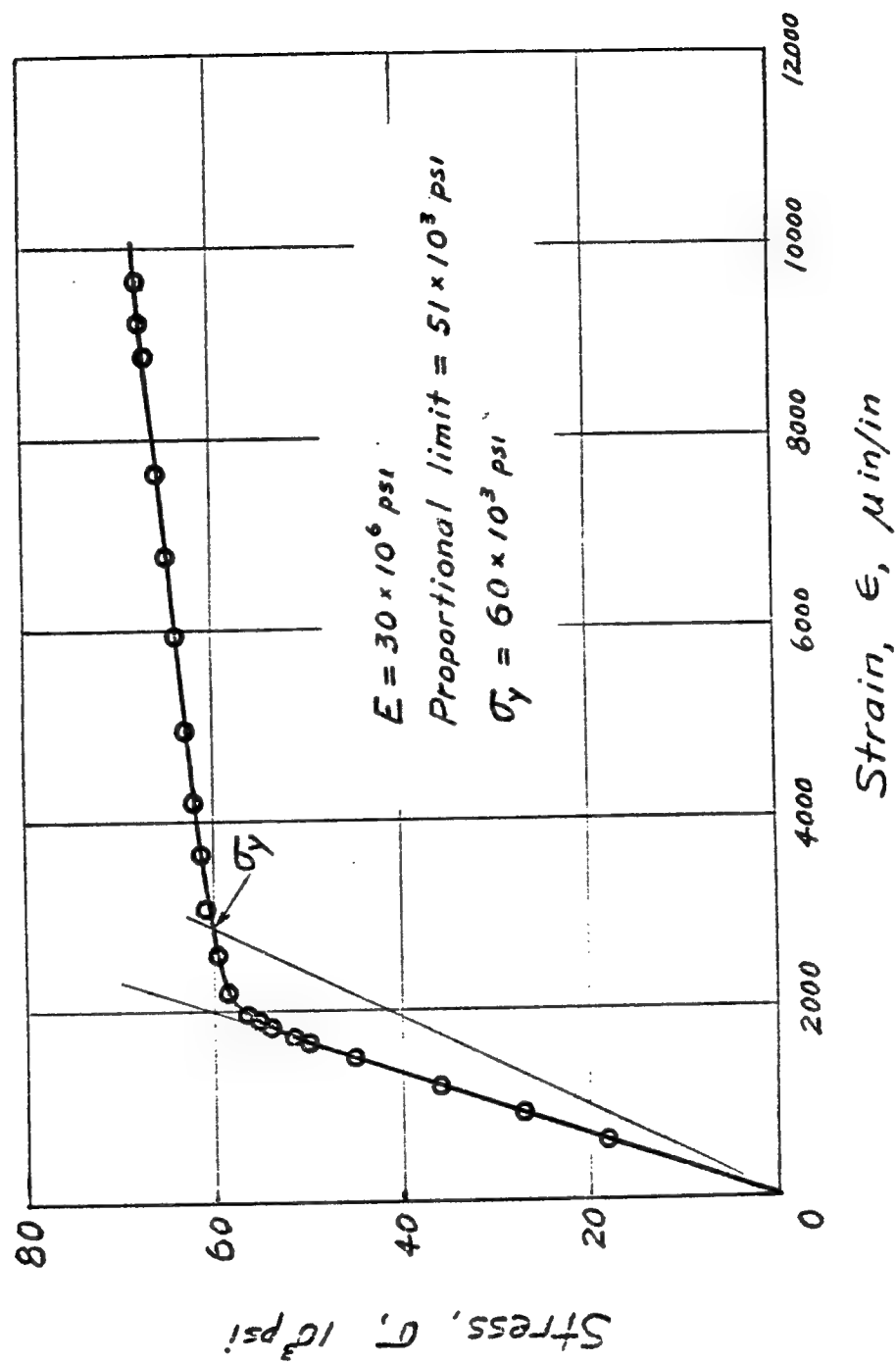
Fig. 10. Stress-Strain Curve for Steel

$E = 30 \times 10^6$ psi

Proportional limit = 51×10^3 psi

$\sigma_y = 60 \times 10^3$ psi

Strain, ϵ, μ in/in

Stress, σ, 10^3 psi
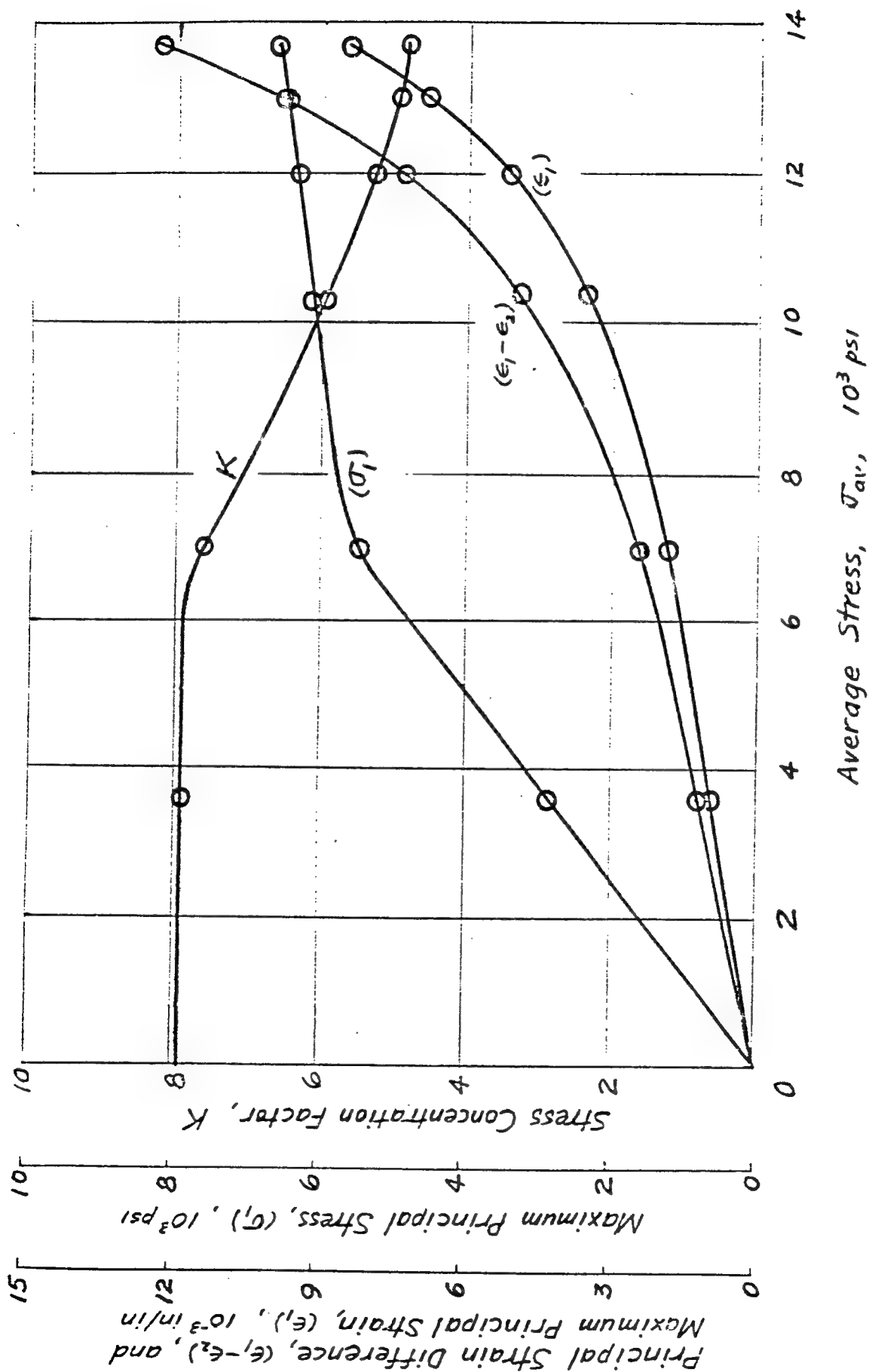
Fig. 11. Curves of $(\epsilon_1 - \epsilon_2)$, ϵ_1, σ_1, and K versus σ_{av} at Lower Fillet of a Steel Breach Ring Section

Average Stress, σ_{av}, 10^3 psi

Stress Concentration Factor, K

Maximum Principal Stress, (σ_1), 10^3 psi

Principal Strain Difference, $(\epsilon_1 - \epsilon_2)$, and Maximum Principal Strain, (ϵ_1), 10^{-3} in/in

50

EXPERIMENTAL BOUNDARY LAYER PHENOMENA IN HIGH POISSON RATIO FRACTURE MECHANICS

C. W. Smith, Alumni Professor, O. Olaosebikan, Assistant Professor
and J. S. Epstein[a], Visiting Scientist

Department of Engineering Science & Mechanics
Virginia Polytechnic Institute & State University
Blacksburg, Virginia 24061
a - Currently at Oxford University

ABSTRACT

After briefly reviewing the features of an optical method for measuring
boundary layer effects in cracked body problems, results of its application to
three problem geometries are presented. An interpretation of these results leads
to a suggestion for accounting for boundary layer effects in design rationale when
dealing with nearly incompressible materials such as rubbers, plastics and solid
rocket propellants.

NOMENCLATURE

u_z = displacement component normal to crack surface

λ_u; λ_σ = lowest eigenvalue in displacement; stress

Z = stress function

$(K_\lambda)_{AP}$; K_λ = Apparent; Actual "Eigenstress" factor

σ_{on}; τ_{nz}^{max} = Nonsingular normal; Maximum shear stress in nz plane

INTRODUCTION

Perhaps the major generic problem in the realm of stable crack growth can be
described as the initiation of a crack from a defect in the neighborhood of a
stress raiser which grows under cyclic or repeated mechanical and/or thermal load
until failure results. The stable growth regime often involves curved crack
fronts, non-planar crack surfaces and complex boundary conditions, all of which
lead to a non-uniform stress intensity factor (SIF) distribution along the crack
front. Such complications force analysts to use numerical methods of analysis,
often without adequate experimental computer code validation.

Beginning over a decade ago, the first author and his associates began a
study directed towards the development of experimental modelling methods which
could be employed to provide code verification for such models. Originally pro-
posed for Mode I only [1] the methods have been extended to include all three
modes of near tip analysis [2] photoelastically and currently also include auxil-
iary moire interferometric determination of displacements [3].

In 1970, G. C. Sih [4] and later E. S. Folias [5] focused attention on the
crack border-free surface intersection problem. Then, following two recent land-
mark papers by Prof. J. P. Benthem [6],[7], it has been verified both analytically
[8],[9],[10] and experimentally [11] that the inverse square root singularity com-
monly assumed in classical fracture mechanics is lost when a crack intersects a
free boundary at right angles. Very recently, Burton et al [12] have provided an

51

excellent overview of the analytical treatment of the problem. In thick bodies of incompressible materials, this effect may alter the stress intensification near the boundary by almost a factor of two but a smaller effect is even felt remote from the intersected boundary.

Using the ASTM E-399 Compact Bending Specimen Geometry as a model, the authors have been able to measure the order of the singularity and its variation through the beam thickness using frozen stress photoelasticity and high density moire interferometry. Results for incompressible materials, and also for a material with Poisson's Ratio $\approx$ 0.4, agree with Benthem's results to well within experimental error at the free surface intersection point. However, these results raise the issue of how the designer is to apply this knowledge to classical fracture mechanics in a rational design process.

After briefly reviewing the experimental methods and algorithms for converting data into stress intensity parameters, results obtained from three specific test configurations, namely the ASTM E-399 Compact Bending Specimen, part through cracks, and natural, semi-elliptic surface cracks all under Mode I loading are presented. The compact bending results are used to provide benchmark data, the part through cracks are used to indicate the effect of changing the boundary intersection angle as observed when crack growth occurs, and the semi-elliptic crack is used to model a typical service situation. Finally, a "corresponding" stress intensity factor (K_{cor}) is proposed for use by designers as a means of accounting for the complexities of the boundary layer effect in cracked bodies of substantial thickness made of nearly incompressible material.

<div align="center">EXPERIMENTAL METHODS</div>

As noted above, two experimental methods, frozen stress photoelasticity, and high density moire interferometry have been utilized in studying the above noted boundary layer effect as well as the variation in the SIF distribution in three dimensional cracked body problems. These methods have been described in detail elsewhere [2],[13] so will only be briefly reviewed here.

Frozen Stress Photoelasticity

This method capitalizes on the fact that the transparent model material exhibits diphase mechanical and optical behavior. At room temperature, it responds to load in a Kelvin-like manner (Fig. 1). However, when the model's temperature is raised to its "critical" value, the viscous coefficient vanishes and the mechanical response becomes linearly elastic with a corresponding reduction in material modulus of some two and a half orders of magnitude and an increase in optical sensitivity to stress fringes of about twenty five times the room temperature sensitivity. To take advantage of this behavior, we heat the cracked model to critical temperature, load and cool under load. Upon load removal, and even after slicing through the body after load removal, the deformations and stress fringes produced above critical temperature are retained and can be analyzed photoelastically in the usual way. The photoelastic fringes are proportional to the maximum shearing stress in the plane of the slice, and the algorithms for converting the data into stress intensity information are referred to a local cartesian coordinate system tnz (Fig. 2) with slices always taken parallel to the nz plane for Mode I loading [1],[2].

<div align="center">52</div>
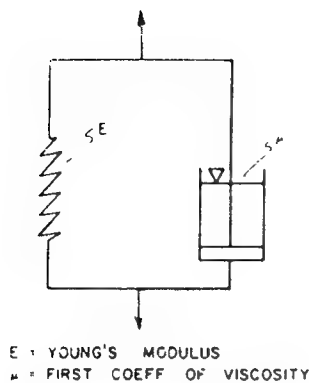
Fig. 1 Model of Kelvin
Material
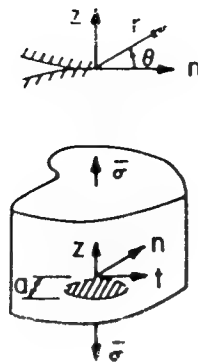
Fig. 2 General Prob-
lem Configura-
tion and Nota-
tion
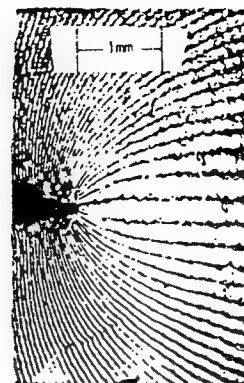
Fig. 3 Moiré Dis-
placement
Fringes for
U_z (Mode I)

High Density Moiré Interferometry

By assuming that the annealing of stress frozen slices reverses the effect of stress freezing (which has been approximately verified experimentally) one can deposit a grating of 1200 lines/mm on a slice surface and then anneal the slice, deforming the grating. By viewing this grating through a "virtual" master grating developed by Post [14], moire fringes which are proportional to the in-plane displacement components normal to the master grating can be obtained. The virtual grating is formed by splitting and recombining rays from a laser light source so as to form an optical grating of lines of constructive and destructive interference. It is important that rigid body motions be eliminated from the data used to compute SIF values. By following the photoelastic analysis of a slice with a moire analysis, two separate estimates of the SIF for that slice may be obtained.

ALGORITHMS FOR CONVERTING DATA INTO SIF VALUES

With the measuring techniques described above, we measure maximum shearing stress magnitude and displacement components in the slice plane. Generally, these data are collected close to the crack tip, but must exclude a very near tip non-linear zone. For problems in which boundary layer effects are not present (such as embedded flaws) or are neglected, algorithms are constructed from classical linear elastic fracture mechanics (LEFM) for converting optical data into SIF values. These algorithms have been discussed elsewhere [2,13] and will not be repeated here. In order to study the boundary layer effect, however, algorithms must be constructed which are outside the realm of LEFM.

Moiré Displacement Algorithm

Benthem's solution (loc. cit.) was a variable separable result which, for the displacement components, took the form of a series of eigenfunctions for a quarter infinite crack in a half space. Focusing on the lowest order eigenvalue term as is customary in such problems and noting that, for Mode I, moiré fringes (Fig. 3) are readily measurable along $\theta = \pm \pi/2$ we have near the crack tip:

53

$$u_z = Cr^{\lambda_u} \tag{1}$$

u_z = component of displacement normal to crack plane
C^z = coefficient of leading term in displacement series,
   constant for $\theta = \pm \pi/2$
λ_u = first or lowest order eigenvalue in solution for
   displacement

$$\therefore \log u_z = \log C + \lambda_u \log r \tag{2}$$

and λ_u may be determined as the slope of a plot of $\log u_z$ vs $\log r$. Fig. 4 shows a typical result from a slice removed from a compact bending specimen. The log r location for the slope measurement is in the linear range with the smallest slope and is common to all slices for a given crack border. In general the zone lies between $r = 0.1$mm and 1.0mm from the crack tip.

Photoelastic Algorithm

Since data from a stress frozen slice is averaged optically through the slice thickness, we can describe this data locally with a two dimensional function analagous to a Westergaard stress function for a small enough data zone taken so as to focus upon
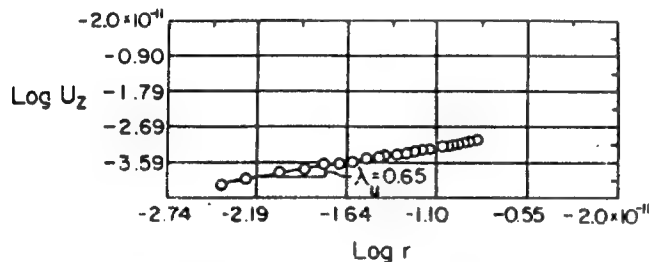
Fig. 4   Determination of λ_u from Moiré Data
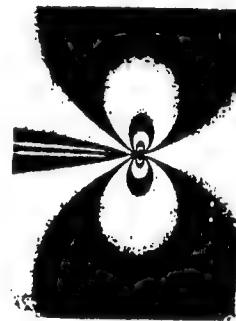
Fig. 5   Mode I Isochromatics Near Crack Tip

the in-plane singular effect. Using this approach, and again focusing upon the lowest order eigenvalue, we have, along $\theta = \pm \pi/2$ where the stress fringes spread the most for Mode I (Fig. 5)

$$\lim_{|\zeta| \to 0} [Z(\zeta)] = \frac{K_\lambda}{\sqrt{2\pi}\, r^{\lambda_\sigma}} \tag{3}$$

where

Z is the stress function
ζ is defined in Fig. 6
K_λ is a "stress eigenfactor"
λ_σ is the lowest order eigenvalue in the stress equations.

By computing σ_{ij} $(i,j = n,z)$ from Eq. (3) and τ_{nz}^{max} from these stresses, one arrives at the approximate expression [15]:

$$\tau_{nz}^{max} = \frac{K_\lambda f(\lambda_\sigma)}{r^{\lambda_\sigma}} + \sigma_{on} \qquad (4)$$

where σ_{on} represents the contribution of the nonsingular stresses in the measurement zone. By defining:

$$(K_\lambda)_{AP} = \tau_{nz}^{max} r^{\lambda_\sigma} \qquad (5)$$

then

$$\log(\tau_{nz}^{max}) = \log(K_\lambda)_{AP} - \lambda_\sigma \log r \qquad (6)$$

Thus, by plotting $\log(\tau_{nz}^{max})$ vs $\log r$, λ_σ can be determined. We note that $\lambda_\sigma = 1-\lambda_u$. However, they can be determined independently of this relation.

Fig. 6 ζ Coordinate

W = 51 ℓ = 38
d = 6   L = 64
a = 6   S = 238
B = 13   P = 22 25 N
e = 17

All dimensions in millimeter
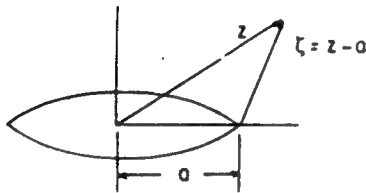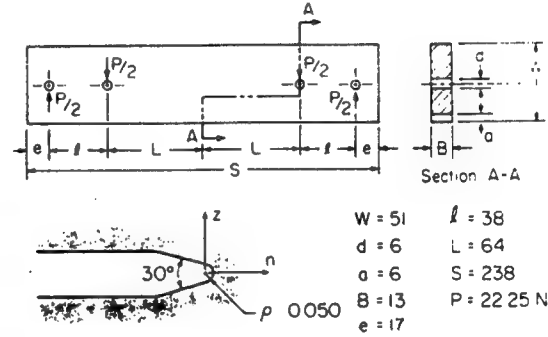
Fig. 7 Four Point Load Compact Bending Specimen

RESULTS

Compact Bending Experiments

The test specimen for these experiments is given in Fig. 7. Displacement fields obtained for each slice by moire interferometry using the aforementioned procedures were converted through the algorithm described above using Eq. (2) into values of λ_u. Stress fields obtained photoelastically were converted in a similar way also using the aforementioned procedures and the algorithm given by Eq. (6). Since Benthem's solution was for a half space, we compared our results with his only at the free surface. They were as follows:

Poisson's Ratio	λ_u (Expr.)	λ_u Benthem
0.40	0.58	0.59
0.48	0.63	--
0.50	--	0.65

Once our experimental results were benchmarked in this way, we then plotted the variation in λ_u across the beam half thickness for both moire and photoelastic data. For the photoelastic data $\lambda_u = 1-\lambda_\sigma$. The result is shown in Fig. 8. We

55

conclude that the methods yield reasonable results with good accuracy.
Part Through Crack Experiments

Benthem's solution and the compact bending results presented in the previous section are for straight front cracks which intersect free surfaces at right angles. When cracks grow, the boundary angle appears to change. In order to study the boundary layer effects for other boundary intersection angles, part through cracks were employed. Fig. 9 gives the distribution of λ_σ for such a geometry. However, in these studies, no moire data were taken on the free surface itself. Instead,
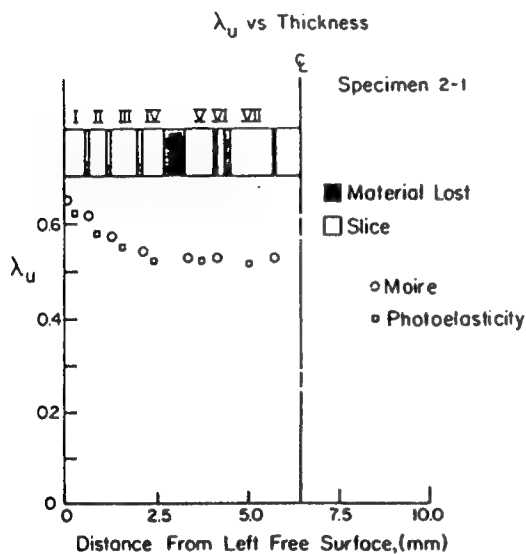
Fig. 8 λ_u Values from Moiré and Photoelastic Data
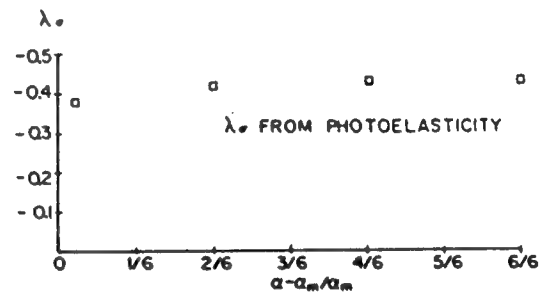
Fig. 9 λ_σ Distribution from Part Circular Flaw

slices positioned as shown in Fig. 10a were progressively reduced in thickness by sanding the surface furtherest from the free surface through which the crack entered. As shown in Fig. 10b, there is a severe reduction in the classical SIF as the slice thickness approaches zero. In fact, as shown by the dashed lines, the classical SIF could even vanish at the free surface.

Semi-Elliptic Surface Crack Experiments

Semi-elliptic surface cracks in wide plates were also studied (Fig. 11). This geometry was used because of its prevalence in structural elements in service in order to investigate the extent to which the aforementioned concepts might apply in a techologically important strongly three dimensional configuration. Moreover, in these experiments, only standard photoelastic methods were used so that boundary surface values of λ_σ were obtained only by extrapolation. However, this approach results in a signiffcant reduction (over 50%) in analysis time and, as seen in Fig. 8, would not appear to yield significant error.

The distribution of λ_σ along the flaw border for a semi-elliptic crack of moderate depth is compared with the λ_σ distribution for a compact bending specimen of about the same crack depth in Fig. 12. These results agree at the free surface

and at the crack mid-point. However, there is a substantial divergence between
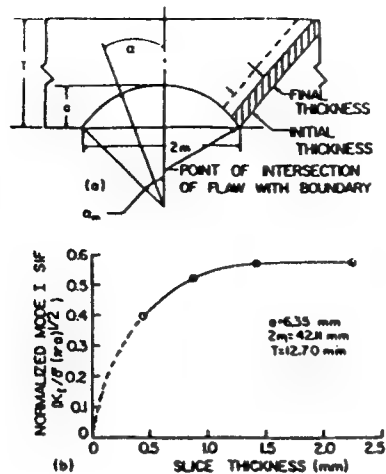
Fig. 10 (a) Thinning of Part Through Crack Slice Which Intersects the Free Surface. (b) Variation of Classical SIF with Slice Thickness (see Fig. (10a)

a = 6.95 mm $a/_C$ = 0.760
C = 9.17 mm $a/_T$ = 0.525
T = 13.23 mm
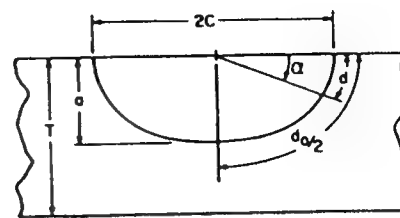
(d, do/2) are distances along flaw border
(α, π/2) are the corresponding angular 'spreads'

Fig. 11 Semi-Elliptic Surface Crack Geometry and Notation
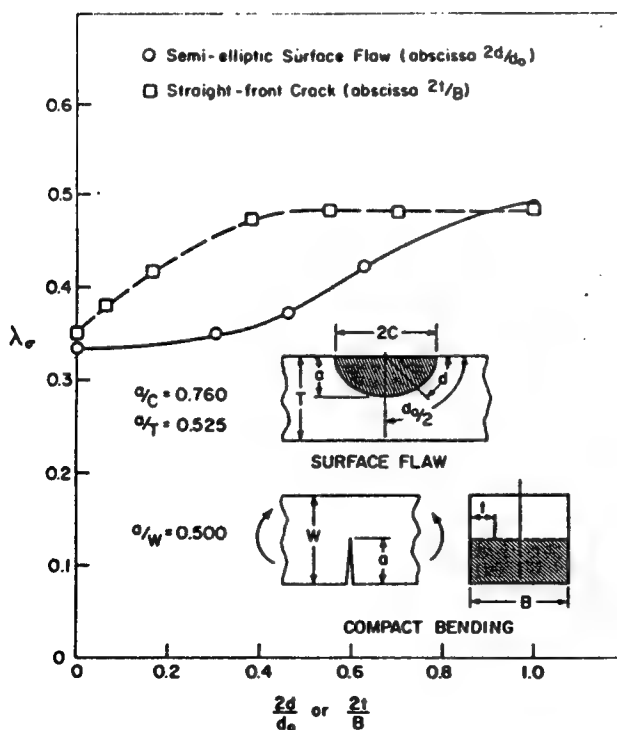
Fig. 12 Variation in λ_σ with Distance from Free Surface
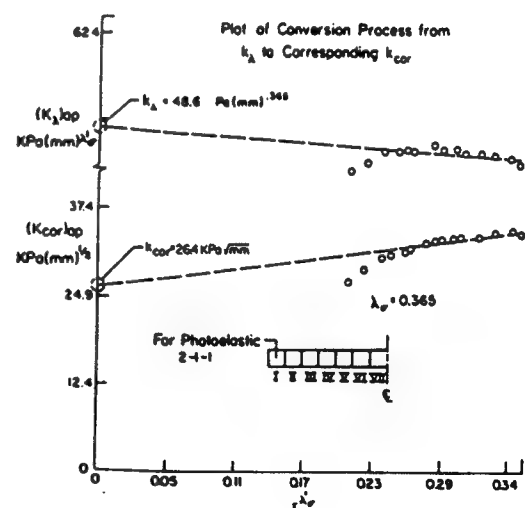
Fig. 13 Converting from $(K_\lambda)_{AP}$ to $(K_{cor})_{AP}$

57

these points suggesting that, for the surface flaw, the loss of the inverse square root singularity extends much further from the free surface than for the straight front crack. This latter trend was also observed for both shallower and deeper flaws. On the basis of these preliminary studies, we conjecture that the extended boundary layer effect is geometric, and results from the fact that a slice taken normal to the crack border in the surface flaw sees a much smaller a/T value than the compact bending slices and thus approaches the free surface condition over a larger portion of the plate thickness than for a straight front crack.

DISCUSSION

In the foregoing, experimental methods of analysis were used to measure the variation in the order of the lowest eigenvalue for cracks intersecting free surfaces. The effect is greatest for materials with high Poisson's ratio (rubbers, plastics, adhesives, rocket motor propellants) and, for such materials one raises the question as to how the effects should be accounted for by the fracture analyst in designing against fracture. Since K_λ, or $K_\lambda f(\lambda)$ do not have dimensions of the classical SIF, some additional interpretations are needed here.

When the frozen stress method is employed, the quantity measured is proportional to a stress averaged through the thickness in a local region near the crack tip. In this region we have obtained expressions for an apparent stress intensity value of both LEFM [3] and from Eq. (5) for the boundary layer algorithm. Since each describes the same quantity (in-plane maximum shear stress) we equate them in the measurement zone to obtain:

$$\tau_{nz}^{max} = \frac{K_{AP}}{r^{1/2}} = \frac{(K_\lambda)_{AP}}{r^{\lambda_\sigma}} \qquad AP \rightarrow \text{"apparent"} \qquad (7)$$

where K_{AP} "corresponds" to $(K_\lambda)_{AP}$ so we call it $(K_{cor})_{AP}$. Thus

$$(K_{cor})_{AP} = (K_\lambda)_{AP} \, r^{1/2-\lambda_\sigma} \qquad (8)$$

If we then use Eq. (8) on the boundary layer data, we can convert to a "corresponding" classical LEFM value. Once this is done, $(K_{cor})_{AP}$ values may be extrapolated to the origin on a plot of K_{AP} vs r^{λ_σ} to obtain K_{cor} values as is done to obtain K_I in LEFM [13]. Fig. 13 shows an example of this procedure. In Fig. 14 we compare the photoelastic data using an LEFM algorithm with the results obtained using the boundary layer algorithm and Eq. (8) for the compact bending specimen. We note that use of Eq. (8) essentially eliminates the influence of the free surface although the result is slightly higher than the two dimensional result. Thus the new algorithm, when modified by Eq. (8), yields a conservative result which could be employed within a two dimensional context by the designer. Fig. 15 shows a similar result for a part through crack. We again see an elevation of K_{cor} above the classical SIF as before. However, a large zone of variation in K_{cor} also appears which was not present for the straight front crack with a right angle free boundary intersection. Through conjecture, we now address the reason for the difference in the K_{cor} distributions in Figs. 14 and 15. If we conjecture that, when the 90° intersection angle is altered during crack growth,

the inverse square root singularity is being restored near the boundary, then the difference between the K_I and K_{cor} distributions in Fig. 15 should be small and, perhaps similar in shape. This is the effect we observe. Conversely, if the singularity is completely lost at the boundary in the limit as the slice thickness goes to zero, then this could also account for the larger gradient of both K_I and K_{cor} in Fig. 15. Another issue involves the applicability of the algorithm to the part through crack. Studies directed towards these issues are continuing. Fig. 16 shows that, for the semi-elliptic crack, K_{cor} is again elevated above K_I. As with the straight front crack, the greatest elevation occurs at the free surface.
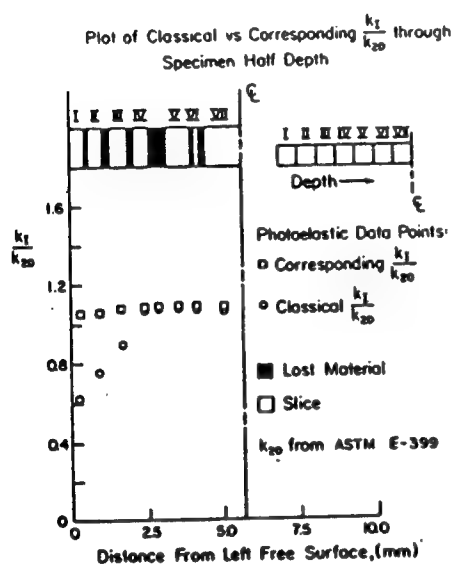
Fig. 14 K_I and K_{cor} Distributions in Compact Bending Specimens
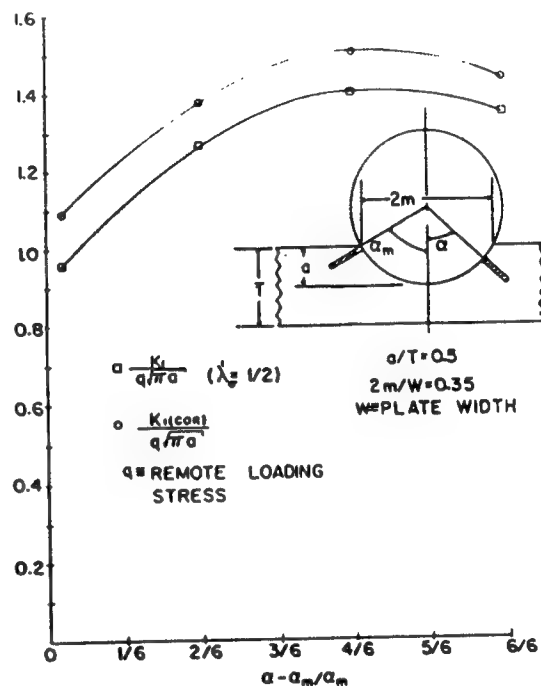
Fig. 15. K_I and K_{cor} Distributions in Part Through Crack in a Wide Plate
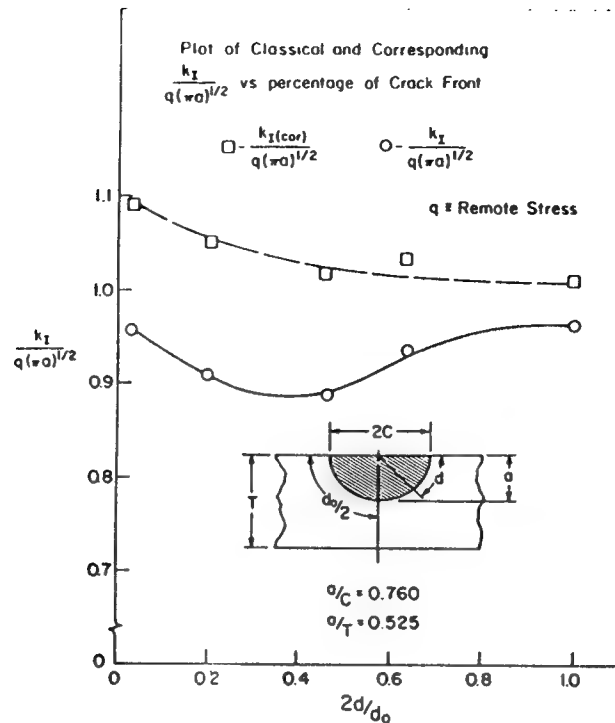
Fig. 16 K_1 and K_{cor} for Semi-Elliptic Crack

SUMMARY

Experimental methods of analysis and corresponding algorithms for converting data into fracture parameters were reviewed. Results obtained from applying the methods to an analysis of boundary layer effects in three different problem geometries were presented. Finally, a means for incorporating the new results into LEFM design rationale was suggested. Studies relating to this latter point are continuing.

ACKNOWLEDGMENTS

REFERENCES

[1]   Smith, C. W., "Use of Three Dimensional Photoelasticity and Progress in Related Areas", Experimental Techniques in Fracture Mechanics 2, SESA Monograph No. 2, A. S. Kobayashi, Ed., Ch. 1, 1975, pp. 3-58.

[2]   Smith, C. W., "Use of Photoelasticity in Fracture Mechanics", Experimental Evaluation of Stress Concentration and Intensity Factors, Mechanics of Fracture, Vol. 7, G. C. Sih, Ed., Martinus-Nijhoff, Ch. 2, 1981, pp. 162-187.

[3]   Smith, C. W., "Use of Optical Methods in Stress Analysis of Three Dimen-
        sional Cracked Body Problems", J. of Optical Engineering, Vol. 71, No. 4,
        1982, pp. 696-703.

[4]   Sih, G. C., "A Review of the Three-Dimensional Stress Problem for a Cracked
        Plate", Intl. J. of Fracture Mechanics, Vol. 7, No. 1, March 1971, pp. 39-
        61.

[5]   Folias, E. S., "On the Three Dimensional Theory of Cracked Plates", J. of
        Applied Mechanics, Vol. 42, Series E, No. 3, Sept. 1975, pp. 663-672.

[6]   Benthem, J. P., "On an Inversion Theorem for Conical Regions in Elasticity
        Theory", J. of Elasticity, Vol. 9, No. 2, 1979, pp. 159-169.

[7]   Benthem, J. P., "The Quarter Infinite Crack in a Half Space: Alternative and
        Additional Solutions", Intl. J. of Solids & Structures, Vol. 16, 1980, pp.
        119-130.

[8]   Bazant, Z. P. and Estenssoro, L. F., "Stress Singularity and Propagation of
        Cracks at Their Intersection with Surfaces", Northwestern Univ. Struct.
        Engr. Report No. 77-12/480, Dec. 1977.

[9]   Burton, W. S. and Sinclair, G. B., "On the 3D Implications of LEFM, An
        Intergral Equation Approach", 16th National Symposium on Fracture Mechanics,
        Battelle-Columbus, August 1983.

[10]   Solecki, J. S. and Swedlow, J. L., "On the 3D Implications of LEFM - Finite
        Element Analysis of Straight and Curved Through Cracks in a Plate" (see Ref.
        9).

[11]   Smith, C. W. and Epstein, J. S., "Measurements of Near Tip Fields Near the
        Right Angle Intersection of Straight Front Cracks" (In Press), Proc. of
        Tenth Canadian Fracture Conference, Waterloo, Canada, Aug. 1983.

[12]   Burton, W. S., Sinclair, G. B., Solecki, J. S., and Swedlow, J. L., "On the
        Implications for LEFM of the Three Dimensional Aspects in Some Crack/Surface
        Intersection Problems", Intl. Journal of Fracture, Vol. 25 (1984), pp. 3-32.

[13]   Smith, C. W., Post, D. and Nicoletto, G., "Experimental Stress Intensity
        Distributions in Three Dimensional Cracked Body Problems", Experimental
        Mechanics, Vol. 23, No. 4, Dec. 1983, pp. 378-382.

[14]   Nicoletto, G., Post, D. and Smith, C. W., "Moiré Interferometry for High
        Sensitivity Measurements in Fracture Mechanics", Proc. of 1982 Joint SESA-
        JSME Conference on Experimental Mechanics, 1982, pp. 258-262.

[15]   Smith, C. W. and Epstein, J. S., "Measurement of Three Dimensional Effects
        in Cracked Bodies" (In Press), Proc. of Vth Intl. Congress on Experimental
        Stress Analysis, June 1984, pp. 102-110.

Applications of Fiber Optics to Coherent Metrology for the Study of Material Deformations and Structural Mechanics

J. A. Gilbert[†]
and
*T. D. Dudderar**

ABSTRACT

In recent years there has been an explosion in fiber optic technology due to a rapidly growing interest in the application of optical fiber light guides to communications systems. Optical fiber research and development has now reached the point where low-loss/low-cost fiber optics suitable for a wide range of practical noncommunications applications have become readily available. At the same time, progress in the development of high quality flexible fiber optic imaging instruments, such as medical endoscopes and industrial boroscopes which use coherent bundles of many thousands of fibers, has provided additional tools with which to access remote or otherwise inaccessible subjects for viewing with exceptional accuracy and resolution. Concurrently, the development of the laser as an economical and reliable source of coherent illumination has given birth to the entire field of coherent light metrology, including holographic interferometry, laser speckle interferometry, laser speckle photography and laser doppler velocimetry. This paper discusses the synthesis of fiber optics and the two of these coherent light techniques most readily applied to studies of material deformation and structural mechanics; holographic interferometry and laser speckle photography.

† Dept. of Civil Engineering, University of Wisconsin - Milwaukee, Milwaukee, Wisconsin 53201

* AT&T Bell Laboratories, Murray Hill, New Jersey 07974

Applications of Fiber Optics to Coherent Metrology for the Study of Material Deformations and Structural Mechanics

J. A. Gilbert[†]

and

T. D. Dudderar[*]

Introduction

Over the last decade, the work of various investigations has demonstrated the practical uses of fiber optic elements for holography and holographic interferometry,[1]–[17] and in more recent years, for white light speckle photography[18]–[19] and coherent light objective speckle photography.[20]–[23] Experience has established that individual single mode optical fibers provide convenient, highly stable illuminators for holographic interferometry[9] and laser speckle photography,[20] while lensed coherent fiber optic bundles may be used to transmit holographic[3],[6],[9] or speckle "images"[18]–[20] for recording and analysis at locations remote from the actual test object. Moreover, unlensed fiber optic bundles may be used as flexible illuminators for pulsed laser holography.[12] Individual optical fibers and coherent fiber optic bundles may be used in both local and remote holographic systems, including double exposure,[6]–[9] time average[16] and real-time holographic interferometry. Procedures for recording both image plane ("white light") and Fraunhofer holograms through fiber optics have now been developed, as well as a method for greatly suppressing the inherent instability of commercially available multimode fiber optic image bundles through the use of an "ultra low spatial frequency" (ULF) holographic technique.[13]–[14]

Single fiber coherent light illuminators can be used to generate speckle fields whose movements are sampled either directly or by a fiber optic image bundle suitably oriented for remote access. At the present time the resolution limits of fiber optic image bundles strongly favor objective speckle systems,[20] which are fundamentally disposed towards data acquisition on a point wise rather than full field basis. However, displacement fields can be evaluated through the use of imaged "white light" or artificial speckle,[19] albeit at lower sensitivities than those possible with coherent light speckle.

Fiber Optics

An optical fiber may be described as a long (usually flexible) cylinder of dielectric materials designed to guide light by total internal reflection or refraction. The optical characteristics of a given fiber are largely determined by its refractive index distribution, and although there are many interesting designs, most (except for those designed to preserve polarization) are radially symmetric such that the index varies only with the distance from the fiber center, r. In the simplist case, a fiber may consist of a solid uniform core of highly transparent material whose index of refraction, n_{Co}, is slightly higher than the index of refraction, n_{Cl}, of the cladding which surrounds it such that $n_{Cl} = n_{Co}(1 - \Delta)$. (Usually the cladding itself is surrounded by an outer protective but lossy sheath.) In this "step-index" design a light ray traveling in the core will be guided so long as its incidence angle, θ, to the core-cladding interface is sufficiently shallow. For most practical fibers the index difference, Δ, is very small, varying between a few tenths of a percent to a few percent. In such cases a critical incidence angle (defined by Snell's law) may be taken as $(2\Delta)^{1/2}$. This means that all meridional rays propagating at $\theta \leqslant (2\Delta)^{1/2}$ will be totally internally reflected every time they intersect the core-cladding interface, and thus be guided, without loss, along a zig-zag path down the core. On the other hand, those meridional rays propagating at angles larger than $(2\Delta)^{1/2}$ will be at least partially refracted out into the cladding. Consequently, such rays are successively attenuated at each reflection and soon "disappear." Of course, light rays are not restricted to meridional paths (in a single plane) and many guided rays follow spiral paths down the fiber core. Similar arguments may be applied to fibers with more complex index distributions. In these fibers the guided rays follow curved paths as they are refracted back and forth (perhaps spiraling) down the fiber core. Again, rays propagating at too great an angle will be lost, while those at shallower

angles will be guided.

Regardless of the index configuration, all fibers exhibit a critical or maximum angle limiting the propagation directions of guided rays (waves). Translated into external angles for guidable rays entering or leaving the flat, squared off end of such a fiber, this critical angle defines its numerical aperture, NA. In air (a medium of $n \simeq 1$) $NA = n_{Co}(2\Delta)^{\frac{1}{2}}$. For a typical fiber with a Δ of around 0.01 the NA would be around 0.21, which means that it would "accept" or "radiate" light rays propagating within a 24° core angle. Actually, not every wavefront whose propagation direction lies within the NA will be guided. In a rigerous analysis of light propagation the wave (rather than ray) character of light must also be considered. This involves solving Maxwell's equations and yields a discrete family of guided wavefronts or modes whose number may be estimated from the theoretical relationship (Marcatili[24])

$$N = \frac{g\Delta}{2+g} \left[\frac{2\pi n_{Co}a}{\lambda} \right]^2 \qquad (1)$$

derived for a fiber whose core index varies in the radial direction according to the power law

$$n = n_{Co}[1 - \Delta(r/a)^g] \qquad (2)$$

Here a is the core diameter and g the profile parameter.* Theoretically, it is possible to design a fiber to guide any number of modes as desired, including just one,** by the proper choice of a, g and Δ for a given wavelength. In recent years the development of processes for the manufacture of practical, low loss optical fiber with the desired characteristics for telecommunications has been the focus of a highly successful technological effort by many parties (see Miller and Chynoweth,[24] Arnaud[25]). In telecommunications applications the choice between so called single mode and multimode optical fiber is, in a sense, a simple choice between one signal path and many. Since the many paths of a multimode fiber mean many differing travel times, the inevitable modal dispersion means a significant loss of bandwidth when compared with single mode fiber. Consequently, the superior performance of single mode fiber systems must be weighed against their greater cost. In these times of rapidly falling cost, single mode systems are becoming the predominant choice. When it comes to coherent metrology, our present topic, somewhat different considerations also lead to the identification of a very great advantage in using single mode fiber optics wherever possible, as will be explained.

Single Versus Multimode Fiber Optics

When a multimode optical fiber is excited by coherent light from a laser the far field radiation emitted at the output end*** appears as a rather coarse random speckle pattern, hardly a desirable field with which to illuminate a holographic or laser speckle test subject. Furthermore, it will be noticed that even if the input and output ends of the multimode fiber "illuminator" are held firmly, small movements of the fiber anywhere along its length generates a significant revision of this speckle pattern. This occurs because small changes in the bending induce significant changes in the modal propagation pattern. Unfortunately, such changes mean a significant loss of correlation. Consequently, unless they are fixed rigidly all along their length, such multimode fiber components are inherently unstable in the presence of even small motions — a severe problem when considering holographic applications, for example.

---

* Note that a step index fiber is described by a $g = \infty$, while a low dispersion "square-law" or parabolic graded index fiber is described by $g = 2$.

** Actually at $N = 1$ two modes of orthogonal polarization will propagate along the fiber.

*** Assumed to be polished flat and square to the fiber axis.

Of course, the coarse far field emission pattern can be made much finer by increasing the core diameter, but the motion related modal instability would remain. However, if a fiber of sufficiently small core diameter and index difference (say around 7 μm at a step-index Δ of perhaps 0.0017) were chosen, its operation would be single mode in the visible light range and the far field emission patterns would look like the output from a classical "objective and pinhole" spatial filter normally employed in CW holography. In a way, such a single mode fiber (SMF) may be thought of as an extremely long, flexible 7μ pin hole capable of delivering an intense beam of filtered coherent illumination anywhere desired — that is, an excellent coherent illuminator! Furthermore, because it is single mode, it has the advantage of being relatively stable — so long as its ends are fixed, mechanical disturbance along its length have little or no effect on the stability of the illumination.

Imaging Through Fiber Optics

Of course, illuminating the test subject with a SMF accomplishes only a part of the task of accessing a remote object for optical measurement. In applications to either holographic interferometry (including remote holography) or speckle photography it may be necessary to return an "image" of some sort from the illuminated remote test surface to a local test station for recording (as either a hologram or a speckle gram or whatever) and analysis. As it happens, individual SMFs do not readily transmit images - at least not as analog signals.* However, flexible coherent bundles of multimode optical fiber are now commercially available with the resolution (33 lines/mm or more) and size required for high quality remote imaging with coherent light and, as will be shown, application to holographic and speckle metrology.

Holographic Interferometry

Holography utilizes the optical interference which occurs between two intersecting beams of mutually coherent light to generate and record, in some amplitude sensing medium (e.g. a photographic emulsion), a complex diffraction pattern. If recorded correctly, this pattern, or "hologram" as it is commonly called, will have encoded within it all the information required to reconstruct either of the two original beams of coherent light (used to generate the interference pattern) whenever it is illuminated by the other. In other words, a hologram provides a practical means of reproducing an original coherent wave front, complete in terms of both amplitude and phase, at any time desired. Furthermore, this capacity to record and accurately reconstruct a field of phase information holographically provides the means of doing optical interferometry on arbitrary objects. Thus, holo-interferometry involves interfering coherent wavefronts recorded at different times and observing the development of interference fringes. These fringes are associated with the spatial distribution of phase differences between the two wavefronts, and may be uniquely related to the differences in optical path length between these wavefronts which arise because of changes imposed on the test subject, so long as they are the only changes affecting phase.

In a classical off-axis holographic system coherent light from a laser is divided by a beam splitter to provide one beam for the illumination of the test subject (called, naturally, the "illumination" beam) and another beam for illumination of the hologram (called the "reference" beam). The test subject and the hologram are arranged so that coherent light reflected from or transmitted through the test subject reaches the holograms as well. This is referred to as the "object" beam or "object" wavefront, and its combination with the reference beam produces the complex standing wave interference pattern that is to be recorded on the hologram. Subsequent reillumination of the processed hologram by the reference beam will generate, by diffraction, an exact optical replica of the original object wavefront. Consequently an observer looking through the hologram towards the original object will see that object just as it was when originally illuminated with coherent light *even if the illumination has been interupted or the object removed*! Of course the same thing might be

---

* Alternatively, a vidicon camera and digitizer might be used to generate a signal which could be encoded and transmitted over a digital single mode fiber optic communications link, but that is another story.

experienced in reverse if the reference beam were removed and the test subject reilluminated. In this situation part of the object wavefront would be diffracted by the hologram to reconstruct the original reference beam!

In addition to the need to achieve an appropriate intensity balance between the object wavefront and the reference beam so as to assure an appropriately modulated hologram, the holographer must consider a variety of additional factors affecting hologram quality. Naturally, when the object and reference beams meet at the hologram the two wavefronts must be mutually coherent or no standing wave interference patterns will be formed. As it happens, the coherent length of the illumination from a laser is not infinite, but may in fact be quite limited. For example, the popular HeNe CW laser has a coherence length of only 20 to 25 cm. Consequently, when using such a coherent light source, if the optical path length of the reference beam differs from the total optical path length of the illumination plus object beam by more than that distance when they reach the hologram plane, there will be no interference and *no hologram will be recorded*! In conventional (nonfiber optic) systems this need to match path lengths within a limited coherence length often leads to reference beams which must be folded back and forth on the optical bench in order to achieve the necessary optical path length. Moreover, even if the coherence conditions are satisfied, small motions anywhere in the system of optical components used to manipulate any of the beams can destroy the hologram completely if they induce a shift of as little as half a wavelength in the standing wave interference pattern during recording. Consequently, such holographic systems are generally mounted on sophisticated vibration isolated tables with numerous heavy rigid mounts for an often complex system of mirrors, prisms and lenses used to shape and manipulate the light. Moreover, long optical paths through air are frequently subjected to time varying phase shifts resulting from the integrated effects of thermal air currents, and which can also have a deleterious influence on stability.

Local Holographic Systems with Fiber Optics

While no panacea, the use of fiber optic components to transmit and manipulate the object illumination and/or reference beams can be very helpful in dealing with some of these problems. Figure 1 shows a diagram of a holographic system in which the use of SMF illumination for both beams provides a facility whose realization on the bench rivals a schematic in simplicity, which is rarely the case with non-fiber optic systems. Morever, in addition to the immediate improvement in simplicity and flexibility, the use of a fiber optic reference beam makes it easy to match optical path lengths simply by preparing SMFs of appropriate length. So long as (1) the beam splitter and system of launch optics are rigidly affixed to the laser, and (2) the two fiber outputs, the test subject and the hologram are firmly maintained in their relative positions; vibrations or displacements along the fiber paths will have little or no effect on the operation of the holographic system. Figure 2a shows a time averaged holographic interferogram of a vibrating cantilever beam recorded using just such a system, with the illumination and reference beam SMFs fixed only at their ends and otherwise "free in the breeze".[16] (Had multimode fibers been used in place of the SMF illuminators, the vibration in the table would have required providing either total vibration isolation or rigid support all along their lenghts to assure the stability needed to do time averaged holography.)

Recently Jones et al[15] have described a two SMF holography system in which an etched directional coupler was used to amplitude divide an SMF guided beam into the reference and object beam fibers, for which they claimed improved mechanical stability and convenience in comparison with a beam splitter system. They also described an electronic servo-system to assure the thermal stability required for very long exposures with thermally sensitive fibers, but application to interferometry was not discussed. However, most such single mode fiber optic local systems can be used for double exposure, time average, and real time holographic interferometry. Figure 3 shows doubly exposed holographic interferograms recorded during a study of the thermally induced out-of-plane warping of a multilayer board due to power dissipation from two different arrays of surface mounted microelectronics components. This study was made using a holo-interferometer with flexible SMF illumination beams simply to exploit their convenience and simplicity.

Remote Holographic Systems with Fiber Optics

In the preceding examples the object wavefront was transmitted by direct line-of-sight from the test subject to the hologram plane. However, many situations arise in which the test subject may not be so conveniently located, and it would be advantageous to use flexible fiber optics to both (1) illuminate the obscured or remote object and to (2) transmit the resulting object wavefront back to the hologram plane for recording and observation. In such a situation an SMF illuminator can be used in conjunction with a multimode imaging bundle (MMB) to provide "remote" holographic capability. Figure 4 shows a schematic diagram of the type of mixed mode fiber optic holographic system used to initially evaluate this concept.[9] Lenses were used to image the test subject onto one end of the imaging bundle and from the other end of the imaging bundle onto the hologram, thereby creating an image plane holographic system.[†] Figure 5 shows a white light reconstruction of a double exposed image plane holo-interferogram recorded using this system. The test subject was a clamped circular plate subjected to a central displacement towards the viewer so as to create a pattern of circular interference fringes. Each fringe represents a change in displacement of approximately half the wavelength of light. This particular image plane holo-interferogram was recorded through a flexible 2mm diameter MMB of a meters length. The pattern of individual 12μ diameter fibers in the bundle can be seen clearly in the reconstruction, which is quite typical of well focused reconstructions of remote image plane holograms. Furthermore, Figure 2b shows the vibrating cantilever beam reconstructed from a time-averaged holo-interferogram which was recorded successfully through a 10 mm diameter MMB with *no* output lens - thereby creating a Fraunhofer rather than image plane holo-interferogram! Because these experiments were carried out on a vibration shielded optical bench and because care was taken to assure that the MMB was unperturbed, the stability limitations of such a multimode component were of little consequence. However, it would be desirable to be able to combine the object illuminating and imaging fiber optics into a kind of holographic probe capable of functioning in more active environments. In this situation the MMB can be expected to experience some mechanical disturbance during operation.

A mixed mode fiber optic holographic system with a 4 mm diameter MMB several meters long was used to evaluate performance both on and off the vibration isolated optical bench and in air or under water.[11] In this case the test subject was a simple end loaded cantilever beam mounted, along with the necessary fiber optics for illumination and image transmission, in a moveable test fixture. This fixture could be mounted either on the vibration isolated optical bench with the rest of the system, or removed to an adjacent workbench (not vibration isolated). Furthermore, it could be submerged in a tank of water either on or off the vibration isolated optical bench as desired. Double exposed image plane holo-interferograms recorded and reconstructed for all four cases are shown in Figure 6. As might be expected, the best interference fringes were obtained, both in air and under water, from the tests run on the vibration isolated bench. On the other hand, the relative motion on the non-isolated bench perturbed the transmission through the MMB and greatly reduced the quality of those two interferograms, although useable fringes were obtained in all cases. It is interesting to note that, of the non-vibration isolated tests, those run under water gave somewhat better results than these obtained with the subject in air! Perhaps to a certain extent the water reduced the mechanical motion or in some way decreased the system's sensitivity to motion. It is also important to note that holo-interferograms with useable fringes were obtained in both cases where fiber optics were used to pierce the air-water interface. Had no fiber optics been available, surface motion would probably have made it very difficult to obtain a satisfactory result using a conventional holographic system, even on a conventionally isolated optical bench, and would have rendered it impossible elsewhere. Furthermore, any sort of flexing or vibration of the MMB during the recording process in any of these tests would have completely destroyed the hologram. Of

---

† If the MMB output lens is removed the resulting holograms are not "image plane" and require coherent light for proper reconstruction. Image plane holograms may be reconstructed with incoherent or "white" light.

course, one way of surpressing this problem would be to shorten the hologram recording time so as to effectively "stop" the motion. Figure 7 shows a white light reconstruction of two image plane holograms of a tape dispenser that were recorded using a ruby laser operating at 20 nanoseconds pulse duration.[12] The first of these was recorded using direct line-of-sight access between the test subject and the hologram plane (no image transmitting MMB), while the second was recorded with the image transmitted through a one meter long, 10 mm diameter MMB, Figure 8. In both cases the reference beam was transmitted through single 2 mm diameter MMBs of appropriate length and the object illumination was transmitted through a matched length pair of MMB's. While both these systems work quite well for holography - in both cases the images were bright and clear such that the tape was resolvable even though viewed edgewise - the pulsed laser approach will not work in remote applications to double exposure holo-interferometry unless the same stability conditions are met between exposures that would apply using a CW system. Consequently, it can be seen that a flexible multimode fiber optic "probe" with pulsed ruby laser excitation works very well for recording "remote" holograms. However unless the entire system is well stabilized mechanically, it doesn't work for interferometry because, if the system experiences any motion during the test, the images won't correlate well enough to produce useable interference fringes.

Ultra Low Frequency Holography and Holo-Interferometry

Another approach to achieving the required stability with flexible MMBs for remote holography is to transmit an image of the hologram, which is an intensity distribution with encoded phase information, rather than an image of the test subject, which involves both intensity and phase information and is, consequently, rather sensitive to the effects of any disturbance that effects the model propagation characteristics of the MMB. However, transmitting the image of a hologram requires transmitting a complex interference fringe pattern whose spatial frequency would normally lie well beyond the capabilities of all currently available MMB's. This means that the successful use of a flexible (and possibly moving) MMB to transmit a hologram requires generating a very low frequency interference fringe pattern. This in turn means that both the illumination and reference beams must be transmitted to the "remote" location and that the reference and object image beams must intersect at a very small angle wherever they are to be sampled by the MMB. The schematic shown in Figure 9 illustrates such an arrangement[13] with two SMFs of appropriate length used to carry coherent illumination and reference beams to the remote subject and a 10 mm diameter MMB (capable of resolving around 33 lines/mm) used to return the ultra low frequency interference pattern to the test station. In this system a hologram "image" is contact printed directly onto a high resolution film plate to produce a ULF hologram of 10 mm diameter. Figure 10 shows an enlarged portion of the resulting complex diffraction pattern as it appears in a remotely recorded hologram of the words REMOTE HOLO, a reconstruction of which is shown in Figure 11a. In this example the angle of intersection, θ, was around 0.25°. Figure 11b shows a reconstruction of a similar ULF hologram recorded directly (at the input rather than output end of the MMB). For comparison purposes this ULF hologram was reconstructed with a 10 mm reference beam, and as such it appears somewhat sharper than the reconstruction of the ULF hologram shown in Figure 11a, indicating that there is some loss of information associated with the use of the MMB. Never-the-less, the ULF hologram shown in 11a was recorded through a flexible MMB (held only at its ends) which could be displaced anywhere along its free length at any time during the experiment with little deterioration in the quality of the hologram image. In other words, the ULF technique confers motion insensitivity on the MMB as a hologram transmitter functionally comparable to the motion insensitivity of the SMFs used as illuminators. Consequently, not only can this ULF technique be used to record remote holograms in the presence of significant motion along the fiber optics, but unlike the pulsed ruby laser fiber optic technique it can also be used to do remote holographic interferometry.[14] Figures 12a and 12b show reconstructions of doubly exposed ULF holograms of an end loaded cantilever beam recorded directly and remotely through a flexible 10 mm dia MMB. Both examples show numerous useable fringes, although there is again some loss of resolution and contrast associated with transmission through the MMB. However, no motion isolation of the fiber optic components was required to achieve these results.

There are limitations to this technique in so far as a holographic probe is concerned. The need for a low angle reference beam configuration creates a geometrical complexity that makes design of a suitable probe head awkward to say the least. Moreover, the restriction on hologram bandwidth imposed by the restricted resolution of the MMB is limiting. This component functions as a low pass filter, effectively eliminating the higher frequency fringes in the standing wave interference pattern, and thereby restricting the range of possible propagation directions in any complex wavefront to be diffracted by a hologram recorded at the MMB output. This, in turn, limits both the size and complexity of any test subject to be recorded holographically, as well as the range and complexity of any deformation field to be measured interferometrically. As expected, direct observations at low magnification reveal that increases in either the area of illumination (subject size) or beam deflection (measurement range) act to increase the complexity of the standing wave interference pattern that must be transmitted. With any such increase there is an associated increase in the proportion of higher frequency components which will be cut off by the MMB and consequently cannot contribute to the formation of the hologram. Furthermore, the combination of a relatively small hologram (which of itself reduces the information available to reconstruct the image) with a large reconstructed image viewing distance (necessitated by the small reference-to-object beam angle) will result in the development of significant speckle noise in the reconstructed image, with an associated loss of resolution. This speckle noise is the result of a kind of self interference associated with coherent light, and is commonly manifest in the granular appearance of any diffusely reflecting surface when it is illuminated with such light. While the statistics of this interference can be fairly complicated (see Dainty[26]) the three-dimensional spatial distribution of laser speckle can be evaluated in terms of the conditions of its formation. Consider the relation given by Ennos in [26] for the characteristic (transverse) size, σ, of the objective speckle

$$\sigma \simeq 1.22\lambda \frac{L}{D} .$$ (3)

Here λ is the wavelength, D the diameter of the area under coherent illumination (which in the present case would be the diameter of the hologram) and L is the observation distance. At an object-to-reference beam angle of only 0.25°, the distance L must be nearly 230 cm to permit clear access to an image of one centimeter width. According to the relation given above, this means that the characteristic objective speckle in the reconstructed image at 230 cm from a 10 mm diameter hologram (contact printed from a 10 mm MMB) would be only 0.178 mm at $\lambda = 6328\text{Å}$. This is less than 2% of the image width and sufficiently small as to permit resolution of all the fringes shown in Figure 11. However, with an MMB of 4 mm diameter the smaller hologram would generate a σ of 0.42 mm, and with a 1 mm MMB σ would be almost 1.7 mm - large enough to completely obscure the interference fringes shown in the figure.

The use of a larger diameter (D > 10 mm) MMB would certainly reduce this speckle problem and improve the signal to noise ratio. Unfortunately, such a component would also be quite expensive. However, the same result might be achieved more efficiently through the use of a coherent array of far less expensive MMB's of smaller diameter. Indeed, effectively optimized fiber optic ULF holo-interferometric probe systems require both the largest practical MMB/hologram areas and significantly improved MMB resolution to reduce the limiting effects of restricted bandwidth.

Fiber Optic Speckle Photography

While laser speckle represents a problem in the area of fiber optic ULF holography and holo-interferometry, it also represents and opportunity in the general area of fiber optic coherent light metrology. Consider what happens if the reference beam is eliminated. In this case there will be no standing wave interference pattern to transmit, and consequently no diffraction pattern to record as a hologram. However, since the subject is still being illuminated with coherent light (via an SMF, naturally) there will still be laser speckle. Now this speckle may be thought of as a kind of random grating which moves with the surface as it moves or deforms. As surely as a distribution of holographically generated interference fringes can be related to the deformation of a surface, so also

71

can the movement of a laser generated speckle pattern be related to the deformation of a surface. In fact, this is the basis of the technique of coherent optical metrology commonly referred to as laser speckle photography or LSP, (see Erf,[27] Francon,[28]). Since a speckle pattern is simply an intensity distribution, it is quite reasonable to use an MMB to transmit such an image from a coherently illuminated remote test subject back to a test station for recording and analysis.

In a fiber optic setup like that shown schematically in Figure 4 (but with no reference beam) the image plane hologram becomes simply a photograph of an object illuminated with coherent light. The image of the object formed on the input end of the MMB carries with it a speckle pattern whose characteristic transverse size, σ, can be estimated by the relationship for subjective speckle* given by Ennos in [26] as

$$\sigma \cong 1.2\lambda f(m+1) \qquad (4)$$

Here f is the aperture ratio of the lens used to image the test subject into the end of the MMB and m is magnification at which this lens is operating. At the output end of the MMB a second lens images the transmitted image onto the recording plane where it will be seen with an associated speckle pattern which is really the superposition of several (at least two) such patterns. If σ of the input image is large enough to be resolved by the MMB it will be one of these. If it is too small, less than 30μ for an MMB with a 33 lines 1/mm resolution limit, then it won't be. On the other hand, there will be intrinsic speckle-like patterns associated with the far-field radiation from each multimode fiber individually, as well as a speckle-like pattern associated with the interference between the overlapping far-field illuminations from each fiber radiating as a separate coherent light source of many modes. Both of these patterns are very sensitive to movement or flexing anywhere along the MMB. However, since the fibers in the MMB are highly multimode, and since there are many many* fibers in a given MMB, the resulting intrinsic speckle pattern (which represents noise and moves with the bundle but not the test subject) is generally as fine as or finer than any pattern that can be resolved by or transmitted through the MMB. On the other hand, the subjective speckle pattern input to the MMB, which is the signal and moves with the test subject but not the bundle, is itself often too small to be resolved by or transmitted through the MMB. That is, with a lens at an f ratio of 1 operating at a magnification of 0.1 (necessary to image a 10cm test subject onto a 10 mm diameter MMB) the characteristic subjective speckle size, σ, as estimated by equation 4 would be less than 1μ - hardly resolvable by an MMB with a 30μ resolution limit. If the lens were stopped down to f/64, however, the speckle size would be increased to around 50μ - enough to be resolved at the output end of the MMB but at the cost of an enormous loss of intensity - so much so that even a contact print of the output speckle pattern would require a very long time exposure to yield a suitable speckle image. Even then the resulting "specklegram" will be difficult to analyze optically because of the relatively large characteristic speckle size. This can be understood in terms of the classical optical method of analyzing doubly exposed LSP specklegrams, which involves a point by point interrogation of the image (on the specklegram) with an unspread laser beam. If the image is covered with a fine speckle pattern the laser beam will be scattered into a large, bright diffraction halo. In addition if, in the region of the doubly exposed specklegram illuminated by the unspread laser interrogation beam, the recorded speckle pattern has shifted (in plane) some distance x, but otherwise remained locally the same (or nearly so), then by a generalization of the Young's fringe phenomena for two apertures a pattern of parallel equally spaced fringes will be found in the diffraction halo, Figure 13a. The parallel orientation of these fringes will lie normal to the direction of the local speckle shift, and their spacing will be inversely proportional to the magnitude of local speckle shift, x, thereby completely defining the in-plane speckle displacement at the point of

---

* For a hcp, fiber structure the number of fibers of radius d in a bundle of radius r may be estimated from the relationship $N = \frac{\pi r^2}{2\sqrt{3}d^2}$. Consequently there are over six thousand 12μ diameter fibers in a 1 mm diameter MMB, and over six hundred thousand such fibers in a 10 mm diameter MMB.

interrogation. A systematic point-by-point scan of such a specklegram can yield a field of speckle displacement information describing the deformation of the test subject between exposures. However, it happens that, because of the large characteristic speckle size, the area of the diffraction halo in which the fringes are to be observed will be exceptionally small, Figure 13b, severely limiting the range of measurements to be made from any given specklegram. Moreover, because the LSP technique works for only those cases where the in plane displacement magnitude exceeds the characteristic speckle size, the large speckle limitation renders such applications relatively insensitive. Fortunately, the availability of photo-electronic systems for image access and digitization as well as computer-based image processing and correlation techniques provides a means around these restrictions on range and sensitivity.

Fiber Optic Speckle Metrology with Photoelectronic Digitization and Numerical Correlation

Figure 14 shows a schematic arrangement for generating laser speckle using coherent SMF illumination and sampling the resulting field with an MMB coupled to a vidicon camera to generate the pattern of very coarse speckle shown in Figure 15. Digitization of this intensity pattern provides a record which can be compared with a succession of subsequently recorded speckle patterns obtained in the same way as the test surface is moved or deformed. Various approaches to making these comparisons numerically have been demonstrated. In the simplest case, ordinary correlations of systematic pairings of intensity samples from correlatable digitized speckle patterns have been used for the measurement of simple motions,[20] while Chu et al[29],[30] have employed techniques of digital image processing to evaluate more complex deformation fields using a surface fit and bi-linear interpolation technique for correlating directly recorded and digitized subjective speckle data.

It turns out that in order to generate the "large" speckle required by the MMB at sufficient intensity for it to register on a standard vidicon tube it is easier to use either (1) white light (or artifical) speckle or (2) objective (rather than subjective) laser speckle. In the latter case, no lens is used to image the test subject into the end of the MMB and the characteristic far field speckle size is given by the objective speckle relationship given in equation 3. Such systems give point-by-point information, rather than a full field of deformation. Specifically, for remote objective speckle the SMF is positioned at a distance ℓ to illuminate a small area of surface whose displacement is to be measured, Figure 14. If the SMF is unlensed it will scatter coherent light from an area of surface of diameter $\sim 2\ell \cdot NA$. Consequently, at an ℓ of 5 mm an SMF of NA = 0.11 will illuminate a spot only 1.1 mm in diameter which, in turn, will throw a very bright objective speckle field a considerable distance from the surface. Moreover, the transverse characteristic size of this field increases linearly with distance, reaching almost 70μ at 10cm ($\lambda = 0.633\mu$). Since the illumination is diverging, the wavefront radius-of-curvature, ρ, at the surface will be small compared to the speckle sampling distance, L. Consequently, the geometrical displacement gain, M, which is defined as the ratio of the transverse speckle motion as sampled at L to the inplane displacement of the illuminated point in the surface, will be large. By the relation[23]

$$M = \frac{\rho + Z}{\rho} \qquad (5)$$

for a normal sampling position, where $\rho \simeq \ell$ and $Z = L$, such a configuration would provide a geometrical gain of over 20 to 1! Such an objective speckle system can be optimized, by reducing ρ and increasing L, to provide geometrical gains of 500 or more before the loss of intensity becomes limiting. Unfortunately, this high sensitivity does have a price, in that with L/ρ so large the gain itself is very sensitive to out-of-plane surface displacements. Of course, if the transverse gain is reduced, so is this out-of-plane sensitivity. In fact, with collimated illumination it becomes zero. That is, the addition of a rod lens positioned to collimate the illumination (NA = 0.0) produces an objective speckle field whose transverse sensitivity would always be unity, regardless of any out-of-plane movement or where the speckle x field was sampled. In this case axial shifts would affect only the characteristic speckle size, σ. Moreover, if the lens were used to reduce the effective NA by a factor of around twenty, the sampling distance, L, and the radius of curvature, ρ, could be matched to yield a 70μ characteristic speckle size which would remain constant regardless of the out-of-plane

surface position or sampling position. By equation 5 the geometrical gain would always be two, while by equation 3, with $D = 2\ell \cdot NA$ and $\dfrac{L}{\ell} = 1$, the speckle size would depend only on the effective numerical aperture and wavelength, $\sigma = 0.61\ \lambda/NA$. Finally, since the output from the MMB is imaged through a lens into the vidicon camera/digitization system, there are always further opportunities for significantly increasing the overall system sensitivity by image magnification, if so desired.

Such a pointwise technique, however sensitive, has limitations when compared to a full-field technique. The use of a lens to image the test surface into the MMB would provide a full field of subjective speckle information about the surface, but at a speckle size too small or an intensity too low to be processed reliably by a fiber optic and vidicon/digitizer system, as described above. However, if the characteristic speckle size were independent of the illumination, then a full field of bright, "MMB resolvable" speckle could easily be acquired remotely, transmitted through a flexible MMB, digitized and analysed. "White-light" or artifical speckle provides such an opportunity.

Fiber Optic White Light Speckle Metrology with Photoelectronic Digitization and Numerical Correlation

Figure 16 shows a photograph of the remote speckle pattern (from the TV monitor) used to make full field measurements of the deformation of a beam painted* with artificial speckle.[19] Incoherent object illumination was provided by an incandescent lamp, although it could have as easily been provided via fiber optics.** A 4 mm diameter MMB nearly 3 meters long was used to transmit bright speckle pattern images of the beam from the remote location to the test station. At the test station the speckle pattern was imaged into the vidicon camera/digitizer system for recording under two slightly different loading conditions. Simple numerical correlation of small subsets of intensity data taken from appropriate pairs of digitized speckle patterns provided 95% valid displacement measurements along the beam, and the invalid measurements were easily identified by their poor correlation coefficients.

Summary

In holographic applications fiber optic components may be used in three ways. Individual single mode fibers (SMFs) may be used to provide object beam illumination for the test subject and/or reference beam illumination for the hologram itself. In either case, flexible optical fibers provide convenience and simplicity. Moreover, SMFs are considerably more effective than multimode fiber optics because of their far lower spatial noise and greater stability. In addition to their advantages as convenient illuminators, fiber optic components may also be used to transient the reflected wavefront back from the test object to the hologram. Adding this fiber optic link facilitates access to test surfaces that may otherwise be optically inaccessible or physically remote from the laser bench or test station where the hologram is to be recorded, and raises the prospects of designing a flexible holographic "probe". Such a sophisticated system would incorporate fiber optics for both illumination and return imaging, analogous to a medical endoscope but with holographic and even holo-interferometric capabilities of great potential value in experimental mechanics. Unfortunately, complete success is not yet here. The need to transmit an image requires that this third flexible fiber optic link be a coherent fiber optic image bundle. Since all such bundles presently available are constructed from thousands of fine *multimode* optical fibers, they are significantly less stable (for holographic applications) than are the SMFs used for illumination. This means that, with any combined single and multimode fiber optic holography system wherein the MMB must transmit both amplitude and phase information, considerable care must be taken to secure full length of the MMB

---

* A plexiglass beam is three point bending painted white and very lightly over sprayed with black paint.

** In fact, the painted on speckle could have being illuminated with coherent light transmitted through an SMF. With the SMF positioned to illuminate a large area of the sample and a lens positioned to image this area into the MMB, the laser speckle would have been far too small to be a problem.

against the deleterious effects of mechanical movement or vibration. Otherwise, such motions produce changes in the MMBs modal propagation characteristics during recording which degrade or completely eliminate the hologram. Nevertheless, such systems have been operated successfully both to record remote holograms and to make remote interferometric measurements by the time-averaged, double exposure and real time holo-interferometric techniques. The use of short exposure durations, as with a pulsed laser, has been demonstrated as another means of overcoming stability problems in so far as recording remote holograms is concerned, but cannot be expected to provide much relief when doing interferometry for all except those events which occur on a time scale shorter than that of the offending MMB disturbances. On the other hand, mixed mode holographic systems which do not entail the transmission of phase information via the MMB, such as remotely generated holograms of ultra-low spatial frequency, are quite stable and effective for both holography and holographic interferometry. However, a true ULF probe system would be geometrically challenging and require an MMB of both a large cross-section and the best possible resolution to provide both an acceptable signal-to-noise ratio and bandwidth needed for reconstructing complex wavefronts and/or interference patterns. Of course, the equivalent of a single mode flexible imaging bundle might be the best solution, but so far no one has demonstrated the ingenuity to produce one.

Speckle correlation techniques, like holographic interferometry, can also benefit from the use of SMF illuminators, although in this case only one such fiber optic link is required (there being no reference beam in speckle metrology). Indeed, many of the same things may be said about single versus multimode optical fibers for speckle applications that were said for holographic applications. However, speckle images may best be treated simply as intensity distributions which move with the test subject and nothing more. In this case the returning image stability requirements are greatly reduced and the MMB resolution becomes most important (as for the remote ULF holography). This is so because the resolution limit establishes the minimum useable characteristic speckle size of any remote speckle field to be transmitted via the MMB. Current experience with commercially available MMBs of intermediate cost and resolution require speckle patterns of relatively large characteristic size (at least 50μ) which can readily be generated using unimaged objective laser speckle at the input end and, on the output end, imaging into a vidicon camera/digitizer system for recording and numerical correlation. For a given objective speckle size, such a numerical correlation system can readily measure inplane displacements over a much wider range than can be achieved by optical correlation methods, but is limited to point-by-point studies (unless developed from arrays of illuminating SMFs or some sort of scanning illumination system). On the other hand, remote full field measurements can be made using coarse "white light" or artificially painted speckle fields. These can be imaged into an MMB and fed into the vidicon camera/digitizer for subsequent numerical analysis of displacements over a field of view. Both of these approaches permit making comparisons between a succession of states or surface positions so that time histories can be obtained. Furthermore, the use of higher resolution MMBs and more (light) sensitive vidicon camera systems should facilitate the application of fiber optics to *subjective* laser speckle metrology which would provide the advantages of both coherent light speckle and full field displacement measurement via a flexible probe system.

Acknowledgements

REFERENCES

[1] Nishida, N., Sakaguchi, M., and Saito, F., "Holographic Coding Plate: a New Application of Holographic Memory," Appl. Opt., 12, 7 (1973).

[2] Rosen, A. N., "Holographic Fundoscopy with Fiber Optic Illumination," Opt. and Laser Tech., 7, 3 (1975).

[3] Hadbawnik, D., "Holographische Endosckopie," Optik, 45, 1, 21-38 (1976).

[4] Suhara, T., Nishihara, H., and Koyama, J., "Far Radiation Field Emitted From an Optical Fiber and Its Applications to Holography," Trans. of the IECE of Japan. Sec E (Engl), 60, 10, 533-540 (1977).

[5] Leite, A.M.P.P., "Optical Fiber Illuminators for Holography," Opt. Commun., 28, 3, 303-306 (1979).

[6] Yonemura, M., Nishisaka, T., and Machida, H. "Endoscopic Hologram Interferometry Using Fiber Optics," Appl. Opt., 28, 9, 1664-1667 (1981).

[7] Gilbert, J. A., and Herrick, J. W., "Holographic Displacement Analysis with Multimode-Fiber Optics," Exp. Mech., 21, 8, 315-320 (1981).

[8] Gilbert, J. A., Schultz, M. E. and Boehnlein, A. J., "Remote Displacement Analysis Using Multimode Fiber-optic Bundles," Exp. Mech., 22, 10, 398-400 (1982).

[9] Gilbert, J. A., Dudderar, T. D., Schultz, M. E., and Boehnlein, A. J., "The Monomode Fiber - A new Tool for Holographic Interferometry," Exp. Mech., 23, 2, 190-195 (1983).

[10] Rowley, D., "The Use of a Fiber-Optic Reference Beam in a Focused Image Holographic Interferometer," Optics & Laser Tech., 15, 4, 194-198 (1983).

[11] Gilbert, J. A., Dudderar, T. D., and Nose, A., "Remote Displacement Analysis Through Different Media Using Fiber Optics," Proc. of the 1983 Spring Conf. on Exp. Mech., SESA, Cleveland, OH, May 15-19, 424-430 (1983).

[12] Dudderar, T. D. and Gilbert, J. A., "Fiber Optic Pulsed Laser Holography," Appl. Phys. Let., 43, 8, 730-732 (1983).

[13] Dudderar, T. D., Gilbert, J. A., and Boehnlein, A. J., "Achieving Stability in Remote Holography Using Flexible Multimode Image Bundles," Appl. Opt., 22, 7, 1000-1005 (1983).

[14] Gilbert, J. A., Dudderar, T. D., and Boehnlein, A. J., "Ultra Low-Frequency Holographic Interferometry Using Fiber Optics," Optics and Lasers in Eng. 5, 1, 29-40 (1984).

[15] Jones, J. D. C., Corke, M., Kersey, A. D., Jackson, D. A. J. Phys. E: Sci Instrum, 17, 271-273 (1984).

[16] Dudderar, T. D., Gilbert, J. A. Franzel, R. A., Schamell, J. H., "Remote Vibration Measurement by Time Averaged Holographic Interferometry," Proc. of the Fifth Int'l Cong. in Exp. Mech., Montreal, to be presented June 14, 1984.

[17] Hall, P. M., Dudderar, T. D., and Argyle, J. F., "Thermal Deformations Observed in Leadless Ceramic Chip Carriers Surface Mounted to Printed Wiring Boards," IEEE Trans. Components, Hybrids and Manufacturing Technology, CHMT-6, 4, 544-552 (1983).

[18] Gilbert, J. A., Dudderar, T. D. and Bennewitz, J. H., "The Application of Fiber Optics to Remote Speckle Metrology Using Incoherent Light," Optics and Lasers in Eng., 3, 3, 183-196, (1982).

[19] Dudderar, T. D., and Gilbert, J. A., "Fiber Optic Measurement of the Deformation Field on a Remote Surface Using Numerically Processed White-Light Speckle," Appl. Opt., 21, 19, 3520-3527 (1982).

76

[20] Dudderar, T. D., Gilbert, J. A., Boehnlein, A. J., and Schultz, M. E., "Application of Fiber Optics to Speckle Metrology - a Feasibility Study," Exp. Mech. 23, 3, 289-297 (1983).

[21] Bennewitz, J. H., Dudderar, T. D., and Gilbert, J. A., "Objective Speckle Measurement," Proc. of the 1983 Spring Conference on Exp. Mech., SESA, Cleveland, OH, May 15-19, 113-118 (1983).

[22] Dudderar, T. D., Gilbert, J. A. and Bennewitz, J. H., "Numerical Correlation of Remote Objective Speckle Patterns for Displacement Measurement," Proc. of the Fifth International Congress on Exp. Mech., Montreal, to be presented June 13, 1984.

[23] Dudderar, T. D., Gilbert, J. A. and Bennewitz, J. H., "Displacement Sensitivity in Remote Objective Speckle Metrology," (Submitted to Exp. Mech.).

[24] Marcatili, E. A. J., "Objectives of Early Fibers: Evolution of Fiber Types," Chapter 2 of Optical Fiber Telecommunications, Edited by S. E. Miller and A. G. Chynoweth, Academic Press, New York, 1979.

[25] Arnaud, J. A., Beam and Fiber Optics, Academic Press, New York 1976.

[26] Dainty, J. C., Topics in Applied Physics, Vol 9, Laser Speckle and Related Phenomena, Springer-Verlag, Berlin (1975).

[27] Erf, R. K., Speckle Metrology, Academic Press, New York (1978).

[28] Francon, M., Laser Speckle and Applications in Optics, Academic Press (1979).

[29] Peters, W. H. and Ransom, W. F., "Digital Imaging Techniques in Stress Analysis," Opt. Engrg., 21, 3, 427-435 (1982).

[30] Chu, T. C., Peters, W. H., Ransom, W. F. and Sutton, M. A., "Digital Image Processing of Finite Deformations," Proceedings of the 1983 Spring Conference of the SESA, Cleveland, OH, 223-227 (1983).
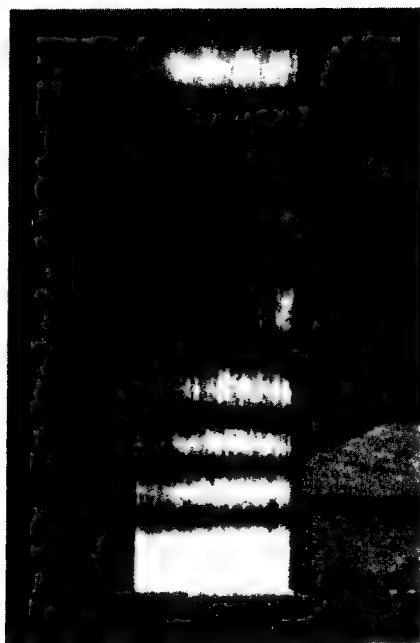
FIGURE CAPTIONS

Figure 1. Schematic Diagram of a Holographic System with Single Mode Fiber Optic Object and Reference Beams.

Figure 2. Time Averaged Holo-Interferograms for a Vibrating Cantilever Beam Recorded (a) Directly and (b) Through a Coherent Fiber Optic Bundle.

Figure 3. Reconstructions of Double-Exposed Holo-Interferograms Showing the Thermal Displacement Responses of Two Different Microelectronic Modules due to 0.75 watts of Power Dissipation with (a) Five Surface Mounted Ceramic Components and (b) One Surface Mounted Ceramic Component.

Figure 4. Schematic Diagram of a Holographic System for Recording Image Plane Holo-Interferograms through a Coherent Fiber Optic Bundle.

Figure 5. White-Light Reconstruction of an Image Plane Holo-Interferogram of a Centrally Loaded Disk Recorded Through a Coherent Fiber Optic Bundle.

Figure 6. Reconstructions of Four Holo-Interferograms Showing the Deformation Fringe Pattern for a Cantilever Beam as Recorded Through a Coherent Fiber Optic Bundle, both in Air and Under Water.

Figure 7. Reconstructions of Holograms of a Scotch Tape Dispenser Illuminated by Coherent Light Transmitted by Fiber Optics From a Pulsed Ruby Laser and Recorded (a) Directly and (b) Through a Coherent Fiber Optic Bundle.

Figure 8. Schematic of a Fiber Optic System for Pulsed Laser Holography.

Figure 9. Schematic of a Fiber Optic System for Remote Ultra-Low Spatial Frequency (ULF) Holography.

Figure 10. Magnified View of the ULF Interference Pattern Transmitted Through a Coherent Fiber Optic Bundle to Form a Remote ULF Hologram of the words "REMOTE HOLO."

Figure 11. Reconstructions of the Words "REMOTE HOLO" From ULF Holograms Recorded (a) Through a Coherent Fiber Optic Bundle and (b) Directly.

Figure 12. Reconstructions of ULF Holo-Interferograms of an End Loaded Cantilever Beam Recorded (a) Directly and (b) Through a Coherent Fiber Optic Bundle.

Figure 13. Diffraction Halos with Youngs Fringes From (a) a Small σ Specklegram and (b) a Large σ Specklegram.

Figure 14. Schematic of a Fiber Optic System for Coherent Light Speckle Metrology with Photo-Electronic Recording and Digital Processing.

Figure 15. Coarse Objective Speckle Field Transmitted Through a Coherent Fiber Optic Bundle into a Vidicon Camera and Photographed on the TV Display Monitor.

Figure 16. White Light Speckle Pattern for Full Field Numerical Correlation of Deformation Distribution Along a Beam in Three Point Bending.
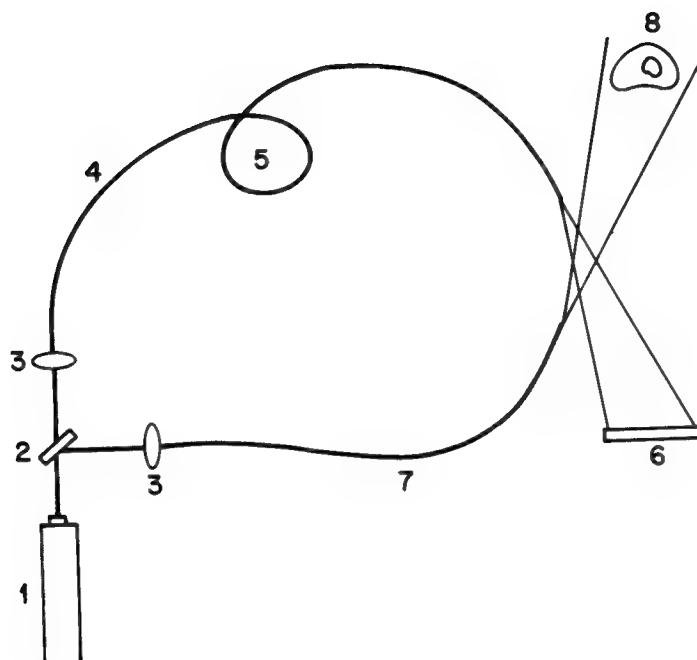
SET-UP FOR LOCAL FIBER OPTIC HOLOGRAPHY

1 - LASER
2 - VARIABLE BEAM SPLITTER
3 - LOW POWER OBJECTIVES
4 - REFERENCE BEAM
    SINGLEMODE OPTICAL
    FIBER (SMF)

5 - OPTICAL PATH LENGTH
    MATCHING LOOP
6 - HOLOGRAM
7 - OBJECT ILLUMINATION
    SINGLEMODE OPTICAL
    FIBER (SMF)
8 - TEST OBJECT

Figure 1

(a)   (b)

Figure 2

(a)   (b)

Figure 3

LOCAL STATION   REMOTE STATION

1 - CONTINUOUS WAVE LASER

2 - VARIABLE BEAM SPLITTER

3 - LOW POWER OBJECTIVE

4 - SINGLE MODE OPTICAL FIBER OBJECT ILLUMINATION BEAM
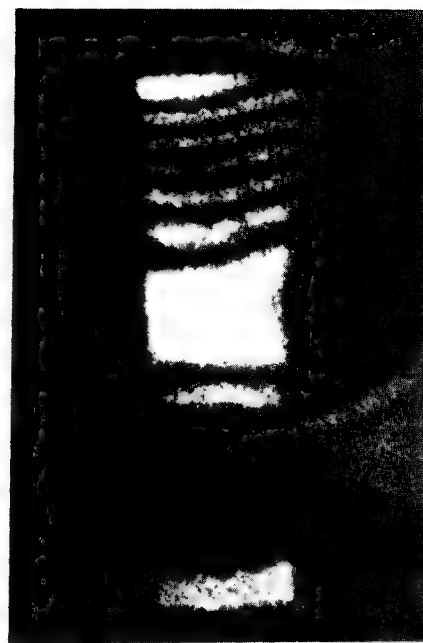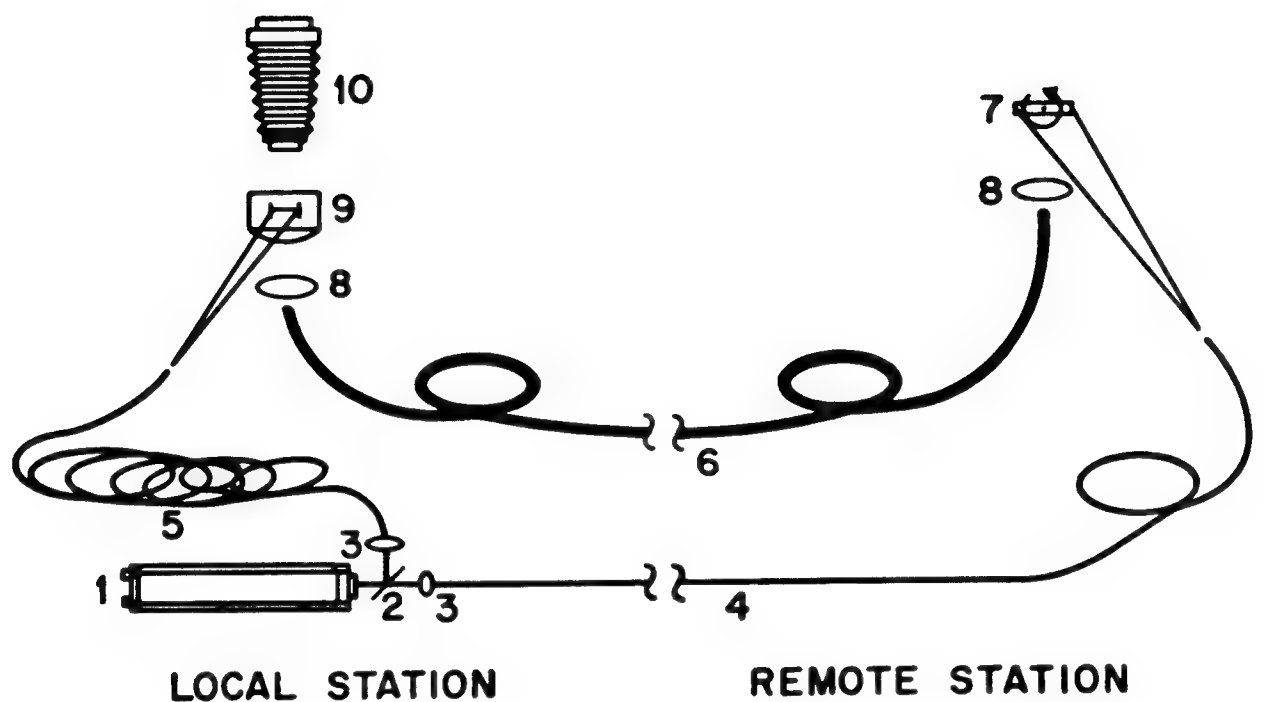
5 - SINGLE MODE OPTICAL FIBER REFERENCE BEAM

6 - MULTIMODE OPTICAL FIBER IMAGE TRANSMITTING BUNDLE

7 - TEST SUBJECT

8 - IMAGING LENS

9 - HOLOCAMERA

10 - INTERFEROGRAM CAMERA

Figure 4

81
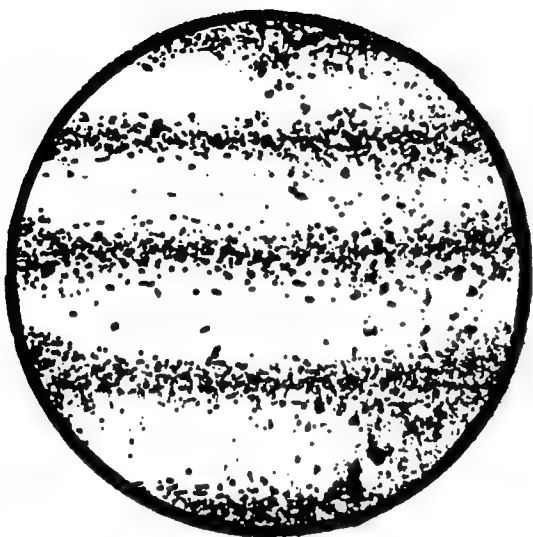
Figure 5

WATER & ISOLATED
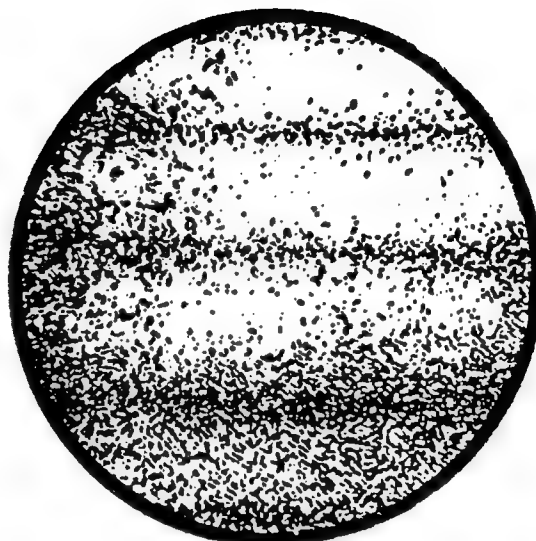
WATER & NON – ISOLATED
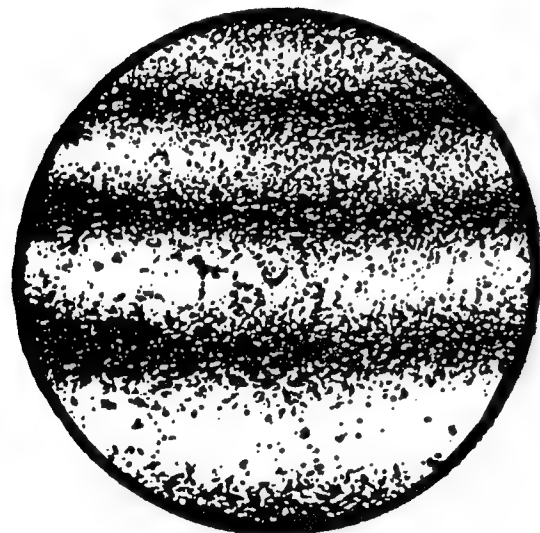
AIR & ISOLATED
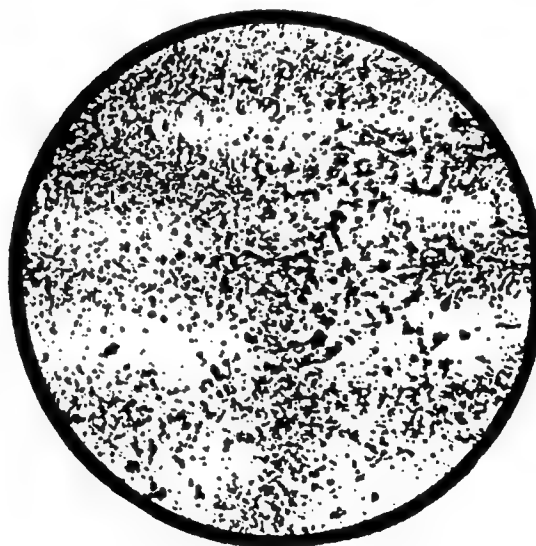
AIR & NON–ISOLATED

Figure 6

83

a

b

84
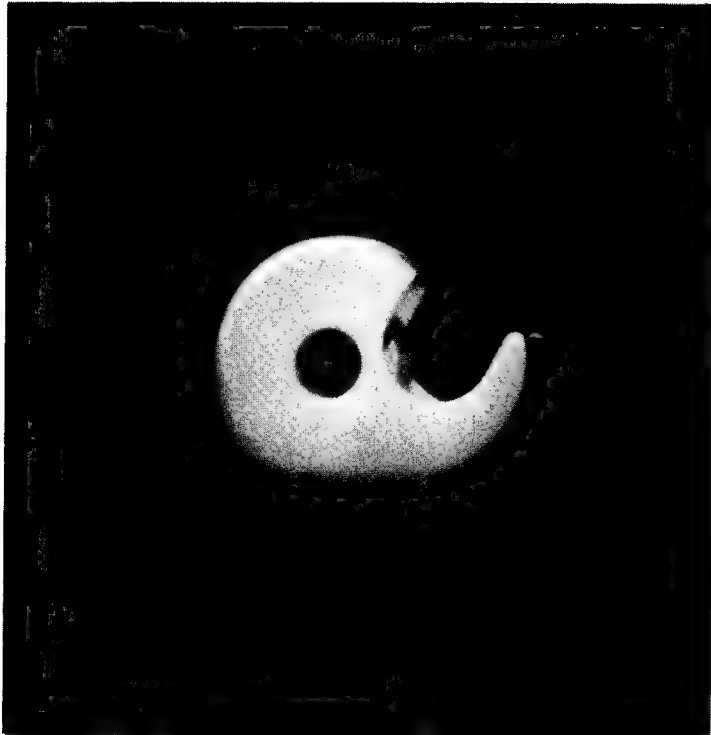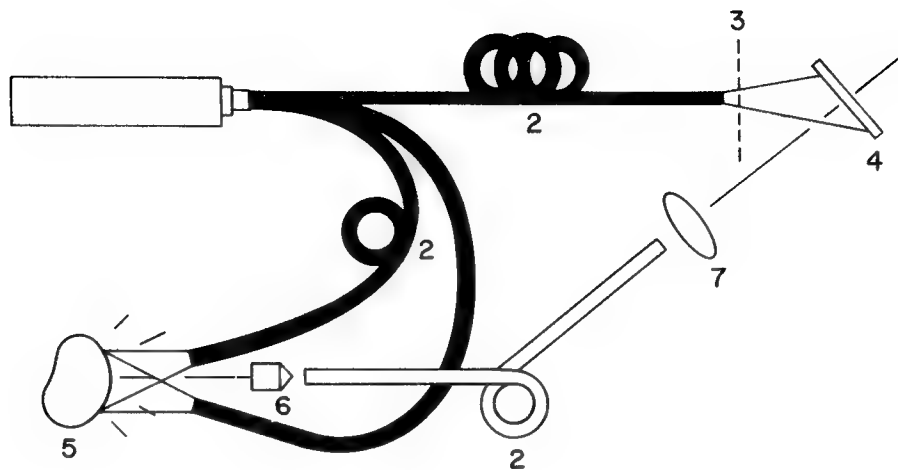
Figure 7

1- PULSED RUBY LASER
2- MULTIMODE OPTICAL FIBER
    BUNDLES
3- ATTENUATOR
4- PHOTOGRAPHIC PLATE
    (HOLOGRAM)

5- TEST OBJECT
6- ERFL LENS
7- IMAGING LENS

Figure 8

REFERENCE BEAM SMF (SINGLE MODE OPTICAL FIBER)

COLLIMATING LENS

GROUND GLASS SCREEN WITH TEST PATTERN

REMOTE STATION

FLEXIBLE MMB (MULTIMODE FIBER OPTIC IMAGE BUNDLE)

OBJECT BEAM SMF (SINGLE MODE OPTICAL FIBER)

10X OBJECTIVES

VARIABLE BEAM SPLITTER

LOCAL STATION

HOLOGRAM FILM PLATE

CW LASER

Figure 9

86

Figure 10

(a)

(b)

Figure 11

88

(a)

(b)

Figure 12

89

a   b

Figure 13

FLAT DIFFUSLY
REFLECTING SURFACE

COHERENT MULTIMODE
FIBER BUNDLE

OUTPUT TO DIGITIZER
& DATA PROCESSOR

IOX
OBJECTIVE

VIDICON
CAMERA

LIGHT SOURCE

HeNe LASER

SINGLE MONOMODE
OPTICAL FIBER

Figure 14

Figure 15

Figure 16

SESSION III: MODELING SPECIAL EFFECTS

DYNAMIC STABILITY OF A SPINNING TUBE CONVEYING A FLOWING FLUID

G. A. Benedetti
Sandia National Laboratories
Livermore, CA 94550

ABSTRACT

When a fluid flows inside a tube, the deformations of the tube can interact with the fluid flowing within it and these dynamic interactions can result in significant lateral motions of the tube and the flowing fluid.

The purpose of this report is to examine the dynamic stability of a spinning tube through which an incompressible fluid is flowing. The tube can be considered as either a hollow beam or as a hollow cable. The analytical results can be applied to spinning or stationary tubes through which fluids are transferred; e.g., liquid coolants, fuels and lubricants, slurry solutions, high explosives in paste form, etc.

The coupled partial differential equations are determined for the lateral motion of a spinning Bernoulli-Euler beam or a spinning cable carrying an incompressible flowing fluid. The beam, which spins about an axis parallel to its longitudinal axis and which can also be loaded by a constant axial force, is uniform, simply supported, and rests on a massless, uniform elastic foundation. Damping for the beam and foundation is considered by using a combined uniform viscous damping coefficient. The fluid, in addition to be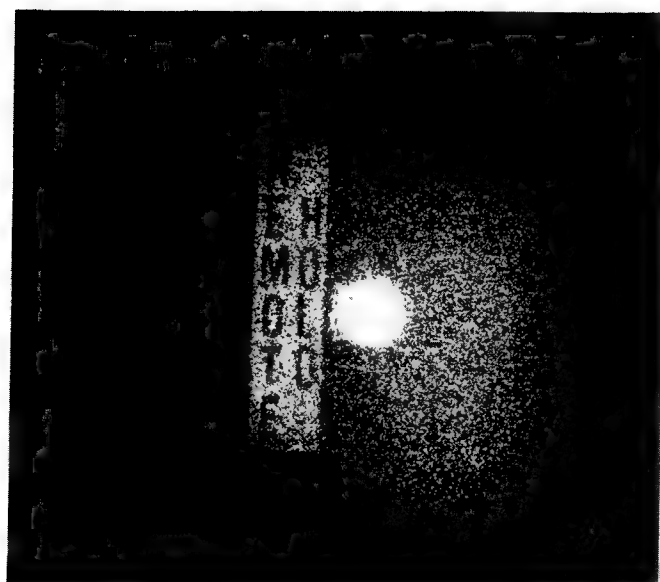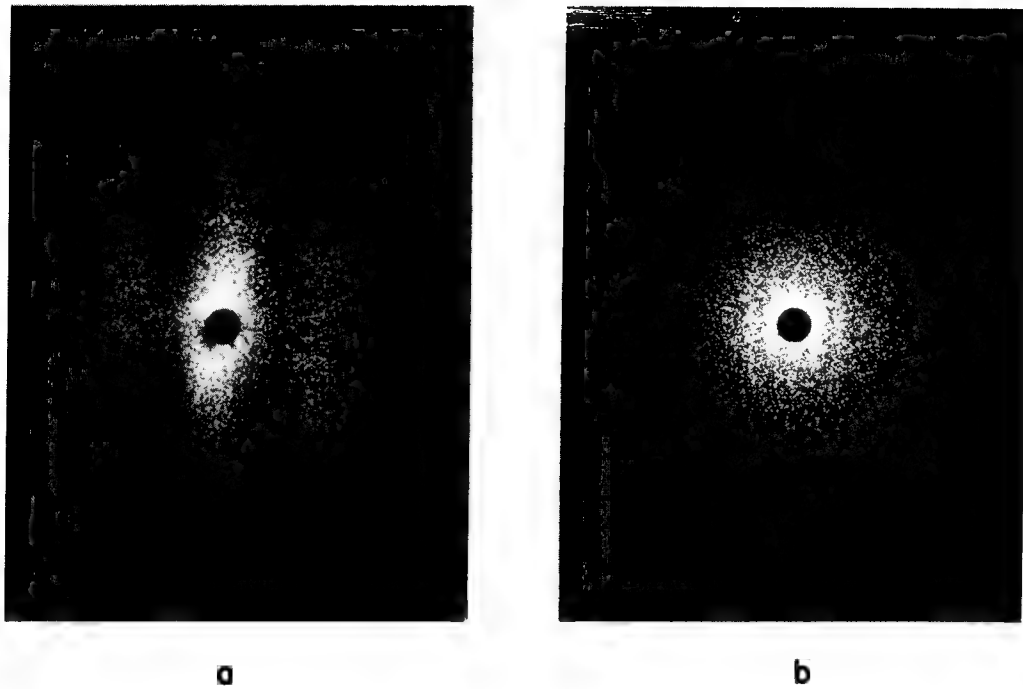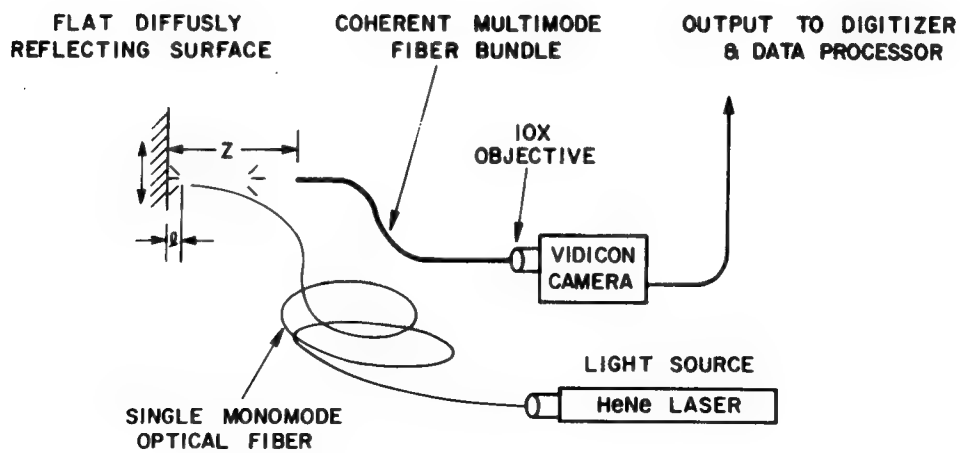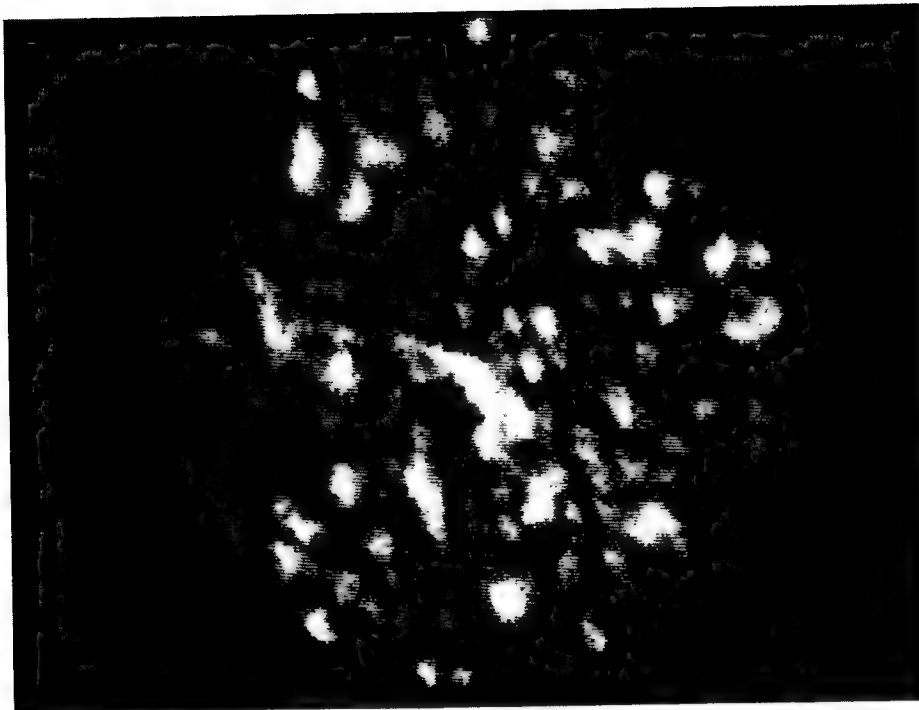ing incompressible, is frictionless, has a constant density, and flows at a constant speed relative to the longitudinal beam axis.

The Galerkin method is used to reduce the coupled partial differential equations for the lateral motion of the spinning beam to a coupled set of 2N, second order, ordinary differential equations for the generalized beam coordinates. By simplifying these equations and examining the roots of the characteristic equation, an analytical solution is obtained for the lateral dynamic instability of the beam or cable. The analytical solutions determine the critical fluid speed and the critical spin speeds, for a specified fluid speed, in terms of the physical parameters of the system.

When the beam is not spinning, a certain fluid speed results in a dynamic instability which is analogous to static buckling (divergence) and consequently, there are no oscillatory lateral motions associated with the dynamic instability. In this case, when the fluid speed equals (or exceeds) the critical fluid speed, the lateral stiffness of the beam is zero (or negative) and dynamic buckling occurs. For this case, the critical speed for the fluid is independent of the viscous damping ratio for the beam and foundation.

97

On the other hand, when the beam is spinning with a constant angular speed, the dynamic instability is identical to resonance. In this case, as the fluid speed increases, the natural frequencies associated with lateral motion of the beam decrease and small spin speeds of the beam can result in violent self-excited vibrations. When the fluid speed equals or exceeds the critical fluid speed, resonance occurs for any spin speed greater than zero.

A NONLINEAR SOLUTION FOR PARACHUTE SUSPENSION LINE DEFORMATION

By
EDWARD W. ROSS, JR.*

Aero-Mechanical Engineering Laboratory
US Army Natick Research & Development Center
Natick, Massachusetts 01760-5017

*Mathematician

Abstract

This paper presents a solution to the nonlinear equations for large deformation of the suspension lines in a flat, circular parachute. It is assumed that this normal force on a typical suspension line is the resultant of the fluid pressure forces on the gores adjoining the line. These pressure forces are taken as uniform between the vent and a variable leading edge and zero elsewhere. Elastic (not necessarily linear) behavior is assumed and the inertia of the cord and gores neglected. Examples of the deformed profile, strain and fluid pressure as functions of leading edge position are presented. Also, this is embedded in a very simple program for calculating the velocity and drag of a C-9 canopy as functions of time during opening.

1. Introduction

There is a voluminous literature dealing with the behavior of parachutes during opening e.g. O'Hara[1], Heinrich and Jamison[2], Heinrich and Saari[3], Berndt and Deweese[4], Wolf[5], Roberts and Reddy[6], Lingard[7], French[8], Ross[9] and many others. Recently the finite-element method has been used to model the evolution of parachute geometry during the inflation process, Sundberg[10] and Purvis[11].

Despite the large body of knowledge contained in these works, there are still open questions. In particular, the finite-element methods do not always reveal much about the essential nature of difficulties in solution. Moreover, nonlinear problems may evince unexpected behavior that is sometimes indistinguishable from that caused by errors in the code. For these reasons it is useful to have solutions to simple nonlinear problems that can be used to check the code and give insight into the character of the solution.

This paper presents an elementary nonlinear solution, applicable to the suspension lines in a parachute during opening. The problem is geometrically nonlinear and may also be used to model material nonlinearity, although the latter aspect is not emphasized. Because this solution may have applications in other contexts, we first present the well-known equations for large, plane motion of a perfectly flexible string under a band of uniform force perpendicular to the string. The force term is then specialized to the form appropriate for a suspension line in a canopy, and the resulting nonlinear ordinary differential equation is solved. The results are used to show predictions of the canopy line profile at various stages of opening and as part of a very simple program for estimating the opening force and deceleration.

2. Basic Equations For a String

We consider a perfectly flexible string of length L, initially unstressed and straight and lying along the X – axis. It is subjected to a combination of forces in the X – Y plane i.e. a distributed pressure force on the string and forces at the ends. No moments are applied and inertia forces are assumed negligible.

The motion of the string, see Figure 1, is taken to be

$$x = x(X), \quad y = y(X), \quad z = 0, \tag{1}$$

i.e. (x, y, 0) are the deformed coordinates of the particle that initially had coordinates (X, 0, 0). The displacements are

$$u_x = x - X, \quad u_y = y, \quad u_z = 0 \tag{2}$$

and $\theta(X)$ is the deformed slope angle of the particle initially at X, expressible as

$$\tan \theta(X) = dy/dx \tag{3}$$

$$= (dy/dX)/(dx/dX)$$

$$= \frac{d u_y/dX}{1 + d u_x/dX}$$

The strain in the string is

$$\epsilon = \frac{ds}{dX} - 1 \tag{4}$$

$$= \left[\left(1 + \frac{d u_x}{dX}\right)^2 + \left(\frac{d u_y}{dX}\right)^2 \right]^{1/2} - 1$$

The geometry of the deformed string gives

$$dy/dX = (dS/dX)\sin \theta = (1+\epsilon)\sin \theta \tag{5}$$

$$d u_y/dX = (1+\epsilon)\sin \theta$$

and similarly

$$dx/dX = (1+\epsilon)\cos\theta \qquad (6)$$

$$du_x/dX = -1 + (1+\epsilon)\cos\theta$$

The equilibrium equations are expressed in terms of the tensile force in the string, T, and the applied force normal to the string, p, (see Figure 2) as

$$dT/dx = 0 \qquad (7)$$

$$T\frac{d\theta}{dx} + p\frac{ds}{dx} = 0 \qquad (8)$$

$$\left(T\frac{d\theta}{dX} + p\frac{ds}{dX}\right)\frac{dX}{dx} = 0$$

Equation (7) implies that T is independent of x and so of X. Then (8) becomes

$$\frac{d\theta}{dX} + \frac{(1+\epsilon)}{T}p = 0 \qquad (9)$$

The constitutive relation can be written in the general form for an elastic body

$$T = \psi(\epsilon) \qquad (10)$$

We shall usually employ the linear law

$$T = E^*\epsilon \qquad (11)$$

but will occasionally digress to point out when solutions are conveniently obtainable for other forms.

The force function, p (X), is assumed to be a rectangular pulse in X,

$$p = p_0 \quad \text{in} \quad X_v \leq X \leq X_E \qquad (12)$$
$$p = 0 \quad \text{elsewhere}$$

See Figure 3.

103

3. Equation for a Parachute Suspension Line

We assume that the opening of the parachute proceeds symmetrically, that is, all lines and gores have the same shape at any stage, so it suffices to consider any one of them. Figure 3 shows the shape of a line before inflation and again in a partially open state. We seek a relation between the force, p, in Equation (9) and the fluid pressure, p_f , of the air acting on the gores.

Figures 4 and 5 show the geometry of a typical line-and-gore combination. We see from Figure 4 that $2 U_y \sin(\beta/2)$ is the distance between corresponding points on two adjacent lines. In Figure 5 the length of line C-D in section A-A is this distance. The fluid pressure, p_f , acting on the gore fabric, must be in equilibrium with p_f acting on line C-D. Thus, the total normal force transmitted by the adjacent gores to the line at this cross-section is

$$p = p_f \cdot 2 U_y \sin(\beta/2) \qquad (13)$$

where

$$\beta = 2\pi / N_g \qquad (14)$$

and N_g is the number of gores and lines in the canopy. Equation (9) for equilibrium of the line becomes

$$d\theta/dX + [2(1+\epsilon) p_f \sin(\beta/2)/T] U_y = 0 \qquad (15)$$

Differentiating Equation (15), combining with (5) and assuming that p_f is piecewise constant, we obtain the differential equation

$$d^2\theta/dX^2 + H \sin\theta = 0$$

$$H = 2 p_f \sin(\beta/2)(1+\epsilon)^2/T \qquad (16)$$

This is the familiar equation for the nonlinear, simple pendulum. Before presenting the solution, we put the problem into dimensionless form by setting

$$z = X/L \tag{17}$$

and using subscripts V, S and E to denote respectively the vent, skirt and forward edge of the pressurized region. Then $2Lz_V$ and $2Lz_S$ are the vent and skirt diameters in the flat circular state.

The problem is now to solve the nonlinear, ordinary differential equations

$$d^2\theta/dz^2 + \lambda^2 \sin\theta = 0 \tag{18}$$

$$\lambda^2 = c^2 = \left[2\rho_f L^2(1+\epsilon)^2 \sin(\beta/2)\right]/T \tag{19}$$
$$\text{for} \quad z_V \le z \le z_E$$

$$= 0 \qquad \text{elsewhere}$$

The deformed position of the string is found from Equations (5) and (6).

$$dw/dz = (1+\epsilon)\sin\theta, \quad dv/dz = (1+\epsilon)\cos\theta$$

$$w \equiv y/L \qquad\qquad v = X/L \tag{20}$$

The boundary conditions assume that the apex of the canopy is fixed, and there is no applied force there. Then from symmetry,

$$\theta = \pi/2, \qquad v = w = 0 \qquad \text{at} \quad z = 0 \tag{21}$$

For simplicity we assume that the payload coincides with the confluence point of the lines, initially at $z = 1$. Then

$$w(1) = 0 \tag{22}$$

The solution in the unpressurized region $0 \le z \le z_V$ is

$$\theta = \pi/2, \quad w = (1+\epsilon)z, \quad v = 0 \tag{23}$$

and in the unpressurized region $z_E \le z \le 1$ is

$$\theta = \theta_E = \theta(z_E)$$
$$w = -(1-z)(1+\epsilon)\sin\theta_E$$
$$v = v(z_E) + (z - z_E)(1+\epsilon)\cos\theta_E \tag{24}$$

105

The nonlinear equations in the pressurized region is known to be solvable in terms of Elliptic Functions, see Abramowitz and Stegun.[12] The solution that joins smoothly with that for $z \leq z_v$ is:

$$\sin(\theta/2) = m^{1/2} \, sn(\alpha|m)$$

$$W = 2m^{1/2}(1+\epsilon) G^{-1} \, cn(\alpha|m) \qquad (25)$$

$$V = 2(1+\epsilon) G^{-1} \left[E(\alpha_v|m) - E(\alpha|m) - G(z-z_v) \right]$$

where
$$m = \frac{1}{2} + (Gz_v/2)^2$$

$$\alpha = A - G(z-z_v) \qquad (26)$$

$$A = F\left[\sin^{-1}(2m)^{-1/2} \, | \, m \right]$$

and $E(\phi|m)$ and $F(\phi|m)$ are the incomplete elliptic integrals of the second and first kinds, respectively, with amplitude ϕ and modulus m.

If the pressurized region extends to the apex of the parachute, so that $z_v = 0$, the solution simplifies somewhat:

$$m = 1/2 \, ,$$

$$\alpha = A - Gz \, , \qquad (27)$$

$$A = F(\pi/2 \, | \, 1/2) = K(1/2) = 1.8547$$

To complete the solution, we must choose G

so that w is continuous across z_E . Equations (24) and (25) imply the

condition

$$G(1-z_E) + \frac{cn(\alpha_E|m)}{sn(\alpha_E|m)\,dn(\alpha_E|m)} \qquad (28)$$
$$\alpha_E = A - G(z_E - z_v)$$

This transcendental relation among G, z_E and z_v is not solvable in closed form

but can be treated numerically. Since the Jacobian Elliptic Functions are

periodic in α_E, infinitely many solutions are possible, but the physically

meaningful one in the present context has the smallest G such that

$$0 > sn(\alpha_E|m) > -\pi/2 , \qquad cn(\alpha_E|m) > 0$$

Figure (6) shows logarithmic plots of G as a function of z_E for $z_v = 0$, .025,

.05, found by solving (28) using the IMSL BRENT algorithm.

The relation (28) determines G as a function only of z_E and z_v and this

relation does not involve T or ϵ i.e. G is governed by the geometry and the

statics of the problem but is unaffected by the constitutive relations. Having

found G, we can now calculate various other quantities of interest, assuming

that ρ_f is known. The simplest constitutive relation is that of inextensionality,

i.e. $\epsilon = 0$, which yields via (19)

$$T = [2\rho_f L^2 \sin(\beta/2)]\,G^{-2} \equiv T_i \qquad (29)$$

A slightly more complicated situation results when we have linear elasticity,

with modulus E*,

$$T = E^* \epsilon \qquad (30)$$

In this case Equation (19) leads to a quadratic equation for ϵ , whose

solution is

$$\epsilon = \gamma - (\gamma^2 - 1)^{1/2} \qquad (31)$$

where

$$\gamma = -1 + E^*/(2T_i)$$

Then T is given by (30). the inextensional solution $T = T_i$ is obtained as the

limit of this solution as $E^* \to \infty$.

107

If a nonlinear elastic law of the form

$$T = \psi(\epsilon) \qquad (32)$$

is appropriate, then ϵ has to be found by solving

$$G^2 \psi(\epsilon) - 2\rho_f L^2 (1+\epsilon)^2 \sin(\beta/2) = 0$$

and T is found from (32).

The total drag exerted by the parachute on the payload is

$$R = N_g T \cos\Theta_E = N_g T \left[1 - 2m \, sn^2(\alpha_E|m)\right] \qquad (33)$$

In calculating the inflated volumes and areas of the canopy we assume that the deformed canopy has the shape generated by rotating a deformed cord about the canopy axis. The error committed by doing this, i.e. neglecting the contributions from bulging of this gore fabric, is small though not negligible (typically 10 - 15%) near the end of inflation, but perhaps larger in the early stages. It can be estimated from a separate calculation after the shape of the lines has been found, but we shall not do that here.

The maximum diameter of the inflated canopy occurs where $\Theta = \alpha = 0$, hence the initial position of the point where y attains its maximum is from (25) and (26)

$$z_{max} = z_v + A/G \qquad (34)$$

The dimensionless maximum radius is

$$W_{max} = 2m^{1/2}(1+\epsilon)/G \qquad (35)$$

and Equation (28) implies that the radius at the skirt is

$$W(z_s) = W_{max} \, cn(\alpha_E|m) \, (1-z_s)/(1-z_E) \qquad (36)$$

The projected and skirt areas are respectively

$$A_p = \pi L^2 W_{max}^2 \qquad (37)$$

$$A_s = \pi L^2 W^2(z_s) \qquad (38)$$

To calculate the volume, we compute separately the volumes of the pressurized

and unpressurized (conical) regions. The volume associated with the pressurized

region is

$$V_P = \pi L^3 \int_{x=0}^{x(z_E)} y^2 dx = \pi L^3 (1+\epsilon) \int_{z=z_v}^{z_E} y^2 \cos\theta \, dz$$

$$= 4\pi m \left[(1+\epsilon) L / G \right]^3 \int_{\alpha=\alpha_E}^{A} cu^2(\alpha|m) \left[1 - \right.$$

$$\left. - 2m \, sn^2(\alpha|m) \right] d\alpha \qquad (39)$$

where $\alpha_E = A - G(z_E - z_v)$. The unpressurized region has volume found

similarly to be

$$V_U = \pi L^3 (1+\epsilon) \cos(\theta_E) \, y^2(z_E) \, (1-z_E)^{-2} \int_{z_E}^{z_s} (1-z)^2 dz \qquad (40)$$

The latter integral can be evaluated easily, but the integral for V_P cannot

and was found numerically with the aid of the IMSL DCADRE subroutine. Finally,

the total volume, V_T, of the canopy is found from

$$V_T = V_P + V_U$$

$$(41)$$

4. Predictions of the Solution

In this Section we exhibit two kinds of predictions given by this solution.

In the first examples we show sequences of shapes taken by a typical canopy

at various stages of opening. For simplicity $z_v = 0$ was used in all these

cases, but Figure 6 suggests that the results would not be much different for

reasonable, nonzero values of z_v, say $z_v \leq .05$. Figures 7 and 8 depict the

inflation of two slightly different canopies, one with $z_s = .5$ and the other

with $z_s = .4$. Each Figure contains profiles of the canopy lines for five values

of z_E,

$$z_E = z_s \, j / 5 \qquad\qquad j = 1, 2, \ldots, 5$$

The calculations were done using the linear elastic law with $E^* = 1,500$ lbs and a uniform drag, $R = 200$ lbs. Equations (28), (29) and (31) imply that p_f and ϵ must change with z_E in order to preserve a uniform drag, and Figures 9 and 10 depict these variations.

The families of canopy shapes in Figures 7 and 8 predict that the maximum diameter at full inflation, $z_E = z_s$, is

$$Y_{max}/Y_s \approx .3/.5 = .6 \qquad \text{for} \quad z_s = .5$$
$$\approx .25/.4 = .625 \qquad \text{for} \quad z_s = .4$$

Thus the change from $z_s = .5$ to .4 does not have much effect on the ratio of maximum diameter to flat-circular diameter.

A second application consists of inserting this solution as a subroutine in a general program for predicting parachute opening. The general program accepts the system parameters and initial conditions, then integrates the equations of motion numerically over time, taking account of the interaction between the deforming canopy and changing fluid flow. The program calls subroutines that calculate (a) changes in the fluid field, given the state of the parachute, (b) changes in the parachute deformation, given the fluid field and (c) a mechanism for enforcing the consistency of the results of (a) and (b). The present solution furnishes part (b), but at present no comparable solution exists for the fluid flow subroutine.

Accordingly, a very limited version of this program was written in which the fluid subroutine simply calculates the fluid pressure, P_f, as a function of load velocity by means of

$$P_f = \rho U^2 / 2$$

$$U = \text{load velocity}$$

where ρ is the mass density of air. The differential equation of motion of a load, W_L, for a vertical launch is taken as

$$\frac{dU}{dt} = g \left\{ 1 - (R/W_L) \right\}$$

and the initial condition is

$$U = U_o \quad \text{at} \quad t = t_o.$$

The only consistency that is enforced between the fluid flow and the parachute deformations involves the canopy volume, V_T. The fluid equations give approximately

$$dV_T/dt = A_s U$$

and the same rate of volume increase can be calculated from (41) at two successive times. These are compared and t_E is chosen so that these agree within desired limits. The results of a calculation for a canopy with the parameters

$$L = 28 \text{ ft.,} \quad \rho = .002 \text{ lb sec}^2/\text{ft}^4, \quad Z_V = .05$$

and the conditions

$$W_L = 330 \text{ lbs} \qquad U_o = 73 \text{ ft./sec.}$$

produced the curves of velocity, and drag shown in Figure 11. The filling time

111

was approximately .8 seconds in this trial.

5. Discussion

The principal question about the solution obtained here concerns its behavior in the early stages of parachute opening, when $z_E - z_v$ is small. We shall examine the predictions of the solutions in this Section, but there are at least two reasons why the results may not be accurate. First, since bending effects have been neglected in this analysis, it is doubtful that the theory can be trusted in the vicinity of a narrow band of pressure. Second, the whole development has emphasized the action of the parachute suspension lines and ignored the effects of the fabric, except insofar as those effects can be represented by the pressure forces transmitted to the suspension lines. This viewpoint is probably deficient in the early stages of opening. Nevertheless, it is interesting to examine the predictions of this theory when $z_E - z_v \to 0$.

The main characteristics of the theory are determined by the dependence of G on z_E and z_v, as expressed in Equations (28) and (26). Figure 6 suggests that for $0 \le z_v \le .05$, which is roughly the range of interest for z_v, G is not much affected by z_v unless z_E is also small. Indeed, G is rather accurately represented by the approximate formula

$$G = 10^{f(z_E)}$$
$$f(z_E) = -.309 + .800 \, z_E^{-0.3}$$

except when $z_E \to 0$.

The behavior of G when

$$z_E = z_v + \Delta$$

and

$$\Delta \to 0$$

112

is somewhat complicated. In general, we see from Figure 6 that $G \gg 1$ as $\Delta \to 0$, and Equation (28) can be satisfied only if α_E becomes very small, in which case

$$sn(\alpha_E|m) \sim \alpha_E \qquad dn(\alpha_E|m) \sim cn(\alpha_E|m) \sim 1$$

The transcendental equation becomes approximately

$$G\alpha_E(1-z_E) \sim -1$$

To estimate α_E, we use Equation (28) in the form

$$\alpha_E = A - G\Delta$$

The estimation of A is different when $z_v = 0$ and $z_v > 0$. When $z_v = 0$, we have simply $A = 1.8547$, regardless of G, and the asymptotic relation between G and $z_E = \Delta$ is found to be

$$G \sim A/z_E \qquad as \qquad z_E \to 0 \qquad (42)$$

When $z_v > 0$, we have

$$m = \frac{1}{2} + \frac{1}{4}(Gz_v)^2$$

and $m \geq 1$ when $G > \sqrt{2}/z_v$. We have

$$A = F(\phi|m)$$

where

$$Sin\,\phi = (2m)^{-1/2},$$

but when $m > 1$

$$F(\phi|m) = m^{-1/2}F(\chi|m^{-1}); \quad sin\,\chi = m^{1/2}sin\,\phi$$

Then

$$\phi = \pi/4$$

$$F(\phi|m) = m^{-1/2}F(\pi/4|m^{-1}) \sim \pi/(2Gz_v).$$

Combining this with Equation (28), we obtain finally

$$G \sim (q/\Delta)^{1/2} \qquad as \qquad \Delta = z_E - z_v \to 0$$

$$(43)$$

where

$$q = \pi/(2z_v) + 1 - z_v - \Delta$$

113

There is quite good agreement between these asymptotic formulas and the results near $z_E = 0$ in Figure 6, which were found by using the IMSL BRENT algorithm and the IBM subroutines for Elliptic functions. This is reassuring, but less so is the fact that as $z_V \to 0$ the asymptotic approximation for $z_V > 0, E_q (43)$ does not approach that for $z_V = 0$. In fact, it is singular at $z_V = 0$, i.e. the asymptotic approximation (43) is not uniform in z_V.

It is possible to seek more refined approximations to the dependence of G on z_E and z_V when $z_E \to z_V \to 0$, but in view of the remarks at the beginning of the discussion it is more sensible simply to accept the fact that the solution does not predict the results well near the start of opening.

The predictions of canopy shape, and the ratio of maximum diameter to flat, circular diameter obtained in Figures 7 and 8 appear realistic. They are a little lower than the conventional estimates, but the latter usually include a contribution from the fully-opened gores, which is omitted here.

The predictions of drag and velocity are not in very good agreement with experiments as parachute opening conducted by Lee.[13] The test results showed an opening time of about 1.5 seconds and a maximum drag 1300 lbs in this case compared with about .8 seconds and 730 lbs, respectively. However, the results were quite sensitive to the initial conditions, and much different results were obtained from calculations starting at a slightly different z_E.

These results suggest that the solution given here for parachute behavior is a convenient and reasonable one for the deformation of the canopy. If it is to give satisfactory results for the opening problem, more realistic treatments of the fluid flow and initial stages of opening are needed.

References

[1] O'Hara, F., "Notes on the opening behavior and opening forces of Parachutes", J. Roy, Aeronautical Soc. 53, 1949, pp. 1053-1062.

[2] Heinrich, H.G. and Jamison, L.R., "Parachute stress analysis during inflation and at steady State", J. Of Aircraft 3, 1966, pp. 52-58.

[3] Heinrich, H.G. and Saari, D.P., "Parachute opening shock calculations with experimentally established input Functions", J. of Aircraft 15, 1978, pp. 100-105.

[4] Berndt, R.J. and DeWeese, J.H., "The opening Force of solid-cloth, personnel type Parachutes", AIAA Paper No. 70-1167, AIAA Aero Decel. Sys. Conf., Dayton, Ohio, September 1970.

[5] Wolf, D.F., "A simplified, dynamic Model of Parachute Inflation, 4th AIAA Aero Decel. Sys. Conf., Palm Springs, CA, May 1973.

[6] Roberts, B.W. and Reddy, K.R., "A Discussion of Parachute Inflation Theories", 5th AIAA Aero Decel. Sys. Conf, Albuquerque, November 1975.

[7] Linguard, J.S., "A Semi-Empirical Theory to predict the Load-Time History of an inflating Parachute", 8th AIAA Aero Decel. & Balloon Tech conf., Hyannis, MA, April 1984.

[8] French, K.E., "Inflation of a parachute", AIAA Journal 1, 1963, pp. 2615-2617

[9] Ross, E.W., "A general Theory of Parachute Opening", J. of Aircraft 9, 1972, pp. 257-258.

[10] Sundberg, W.D., "Finite Element Modeling of Parachute Deployment and Inflation", AIAA Paper No. 75-1380, November 1975.

[11] Purvis, J.W., "Numerical Prediction of Deployment, Initial Fill and Inflation of Parachute Canopies", 8th AIAA Aero Decel. & Balloon Tech Conf., Hyannis, MA, April 1984.

[12] Abramowitz, M., and Stegun, I.A., "Handbook of Mathematical Functions", Nat. Bur. of Stds., Washington, DC, 1967, pp. 567-626.

[13] Lee, C.K., "Experimental investigation of full-scale and model Parachute Opening", 8th AIAA Aero Decel. & Balloon Tech Conf., Hyannis, MA, April 1984.
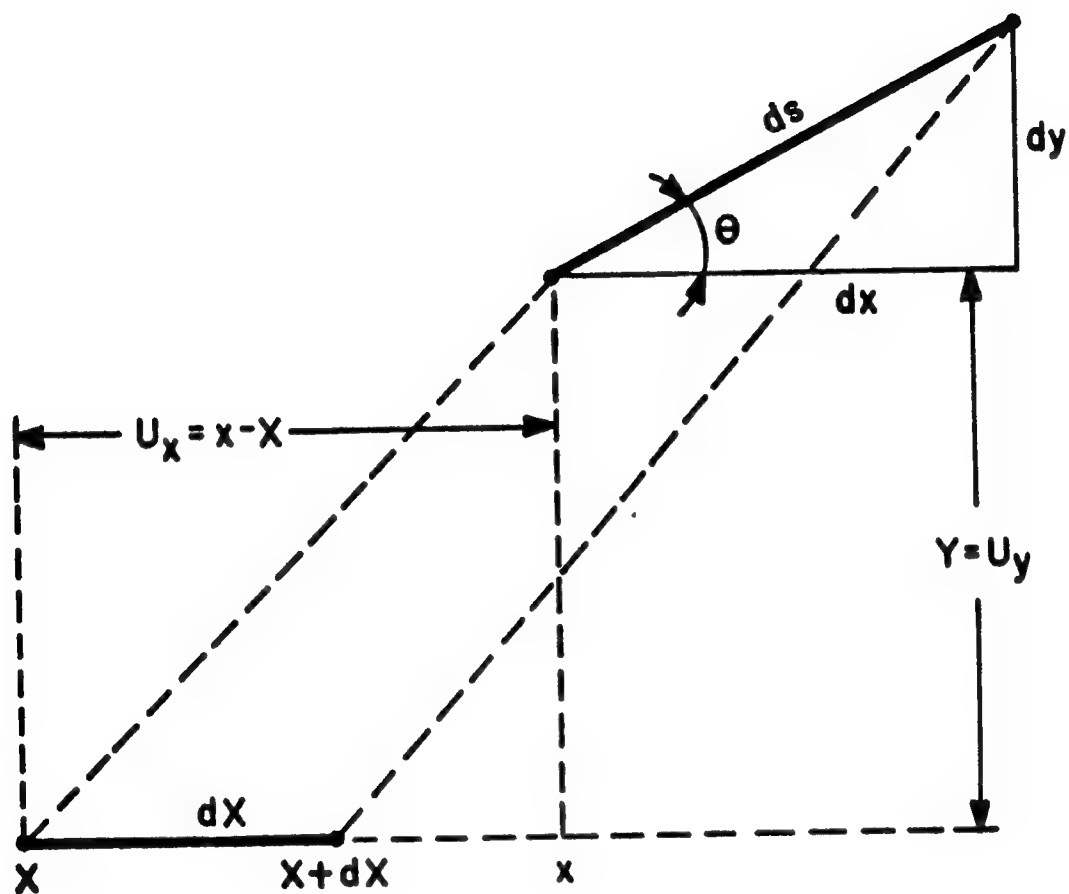
Figure 1: Geometry of Deformed Line

117
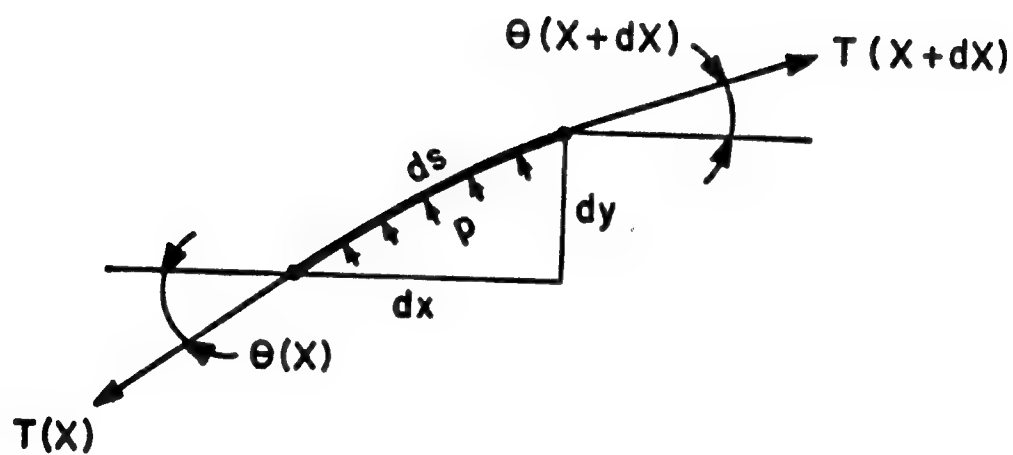
Figure 2: Forces on Deformed Line

118
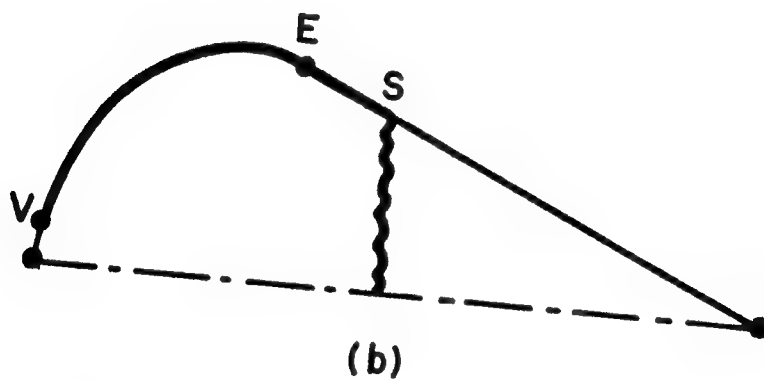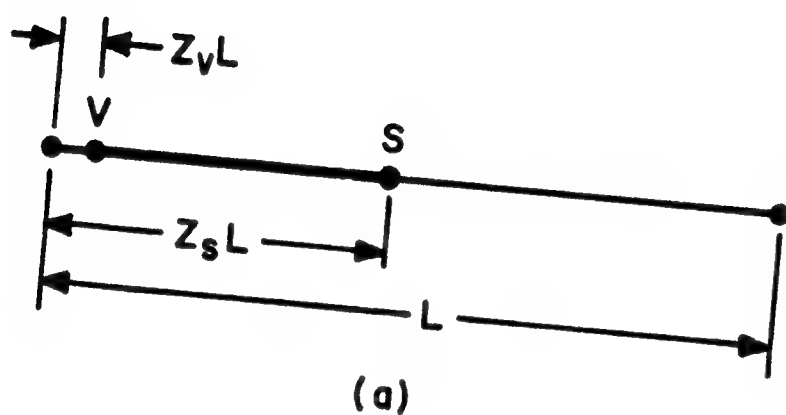
Figure 3: Line Configurations: (a) Initial (b) After partial Opening
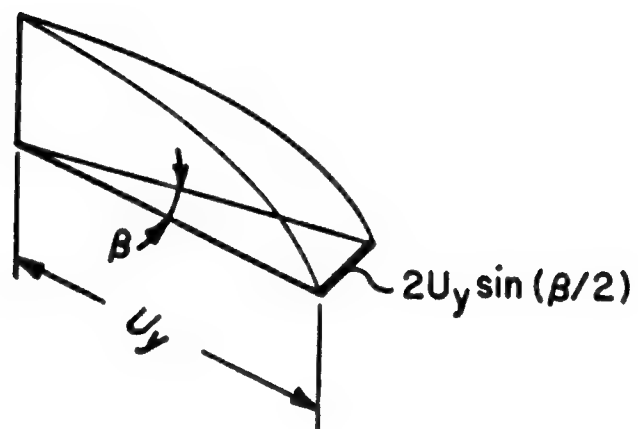
Figure 4: Gore and Line Geometry after partial Opening
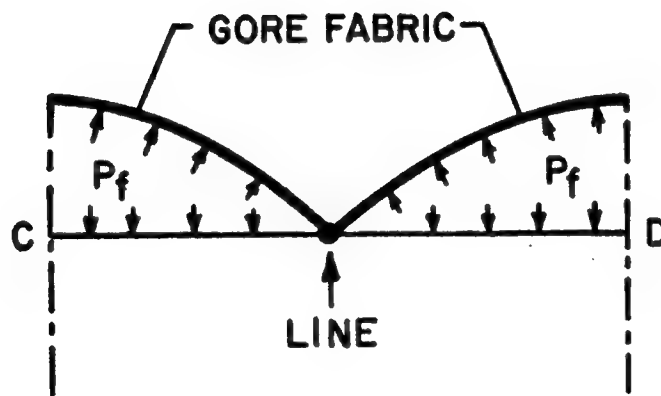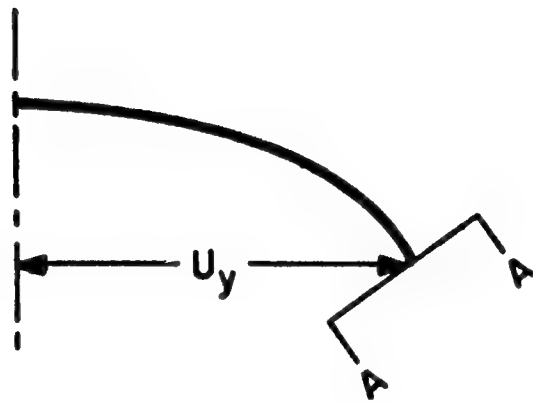
SECTION A-A

Figure 5: Section perpendicular to Lines after partial Opening.
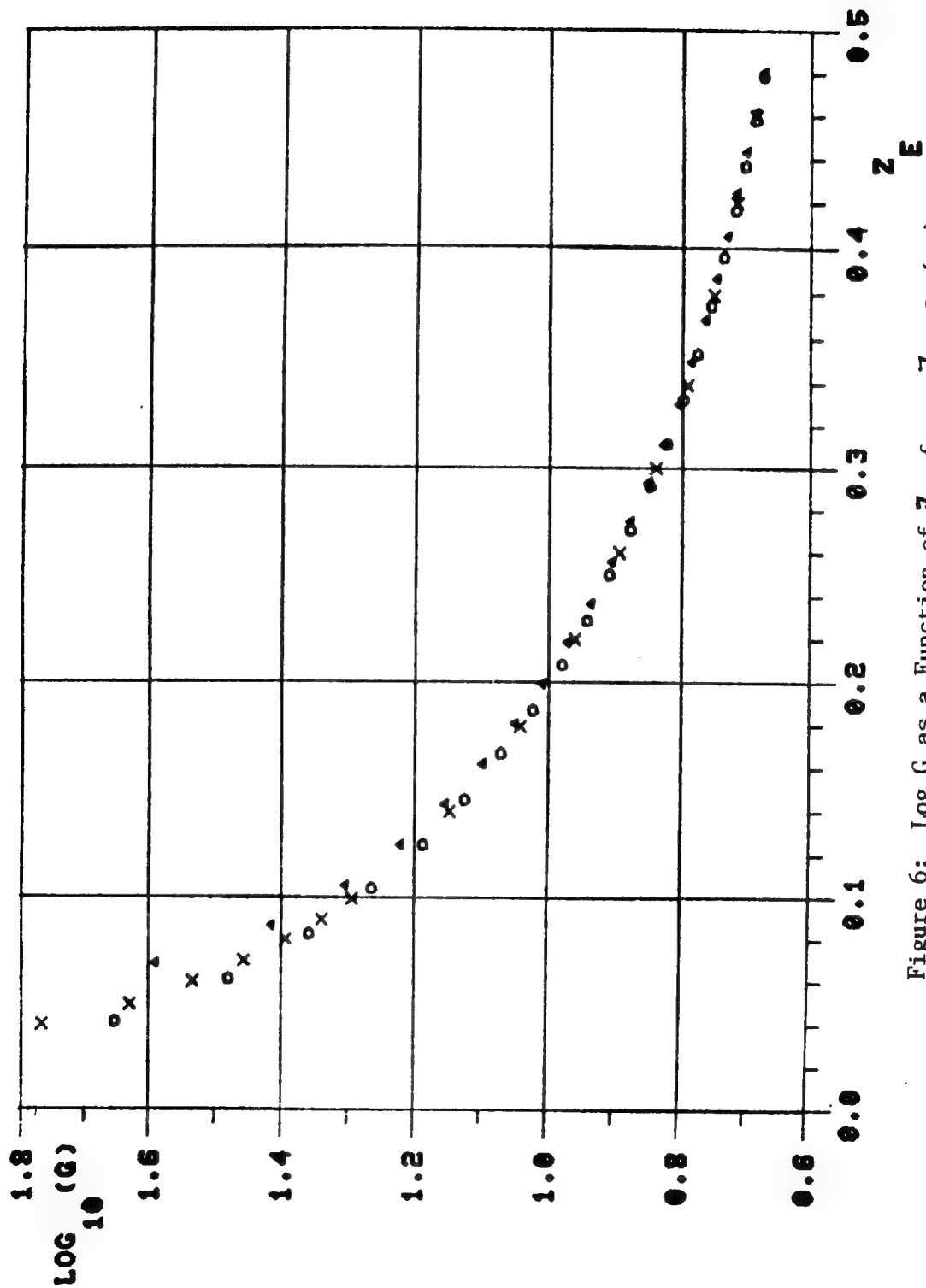
Figure 6: Log G as a Function of Z_E for $Z_V = 0$ ($\circ$)

$Z_V = .015$ (x) and $Z_V = .05$ (triangles)
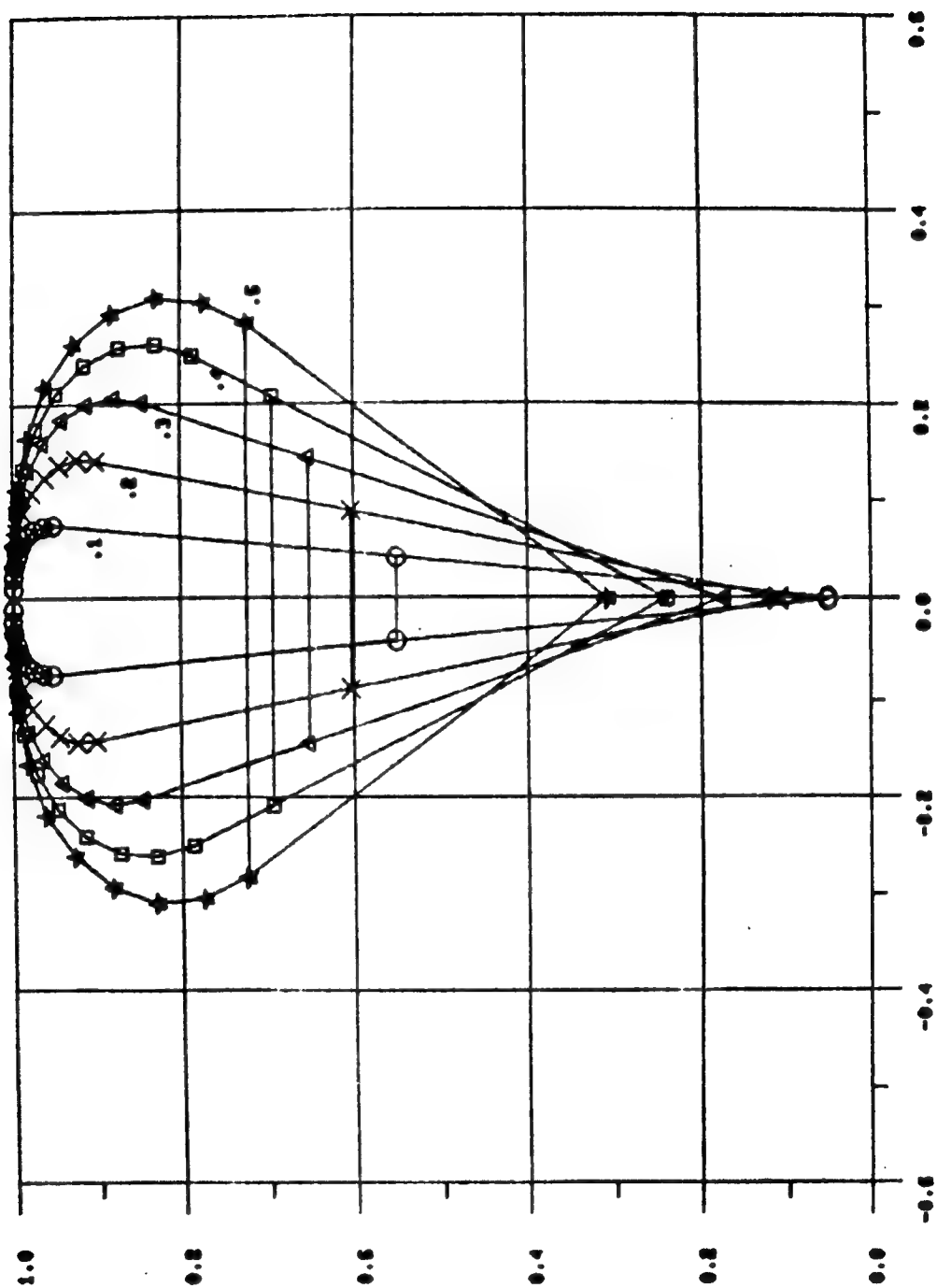
Figure 7: Profiles of Suspension Lines for R = 200 lbs, Z_s = .5, Z_v = 0
E* = 1,500 lbs. and z_E = 0.1, 0.2, ..., 0.5.

123
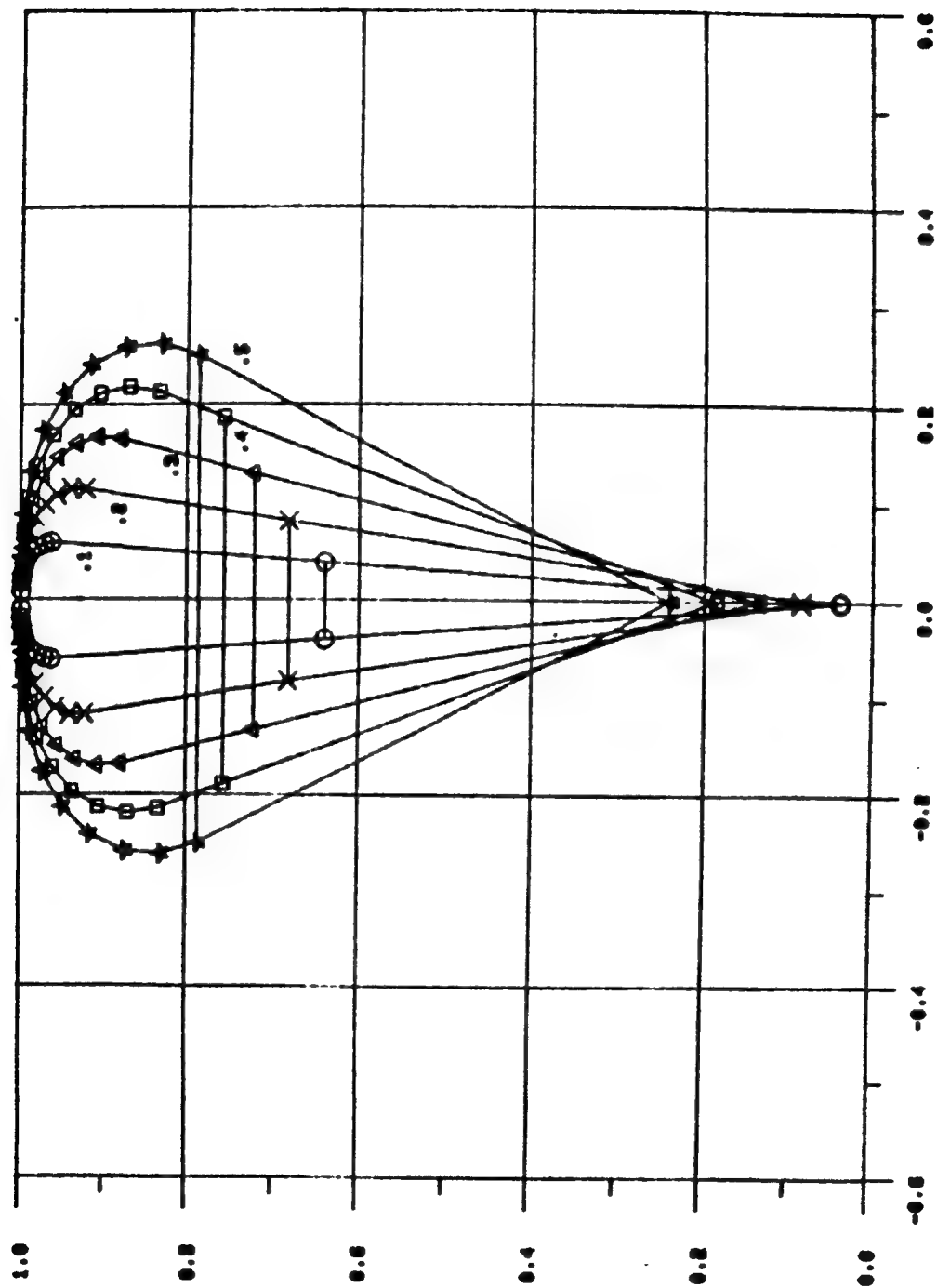
Figure 8: Profiles of Suspension Lines for R = 200 lbs, $\mathcal{Z}_S = .4$, $\mathcal{Z}_v = 0$

E* = 1,500 lbs and $\mathcal{Z}_E$ = 0.1, 0.2,....., 0.5.
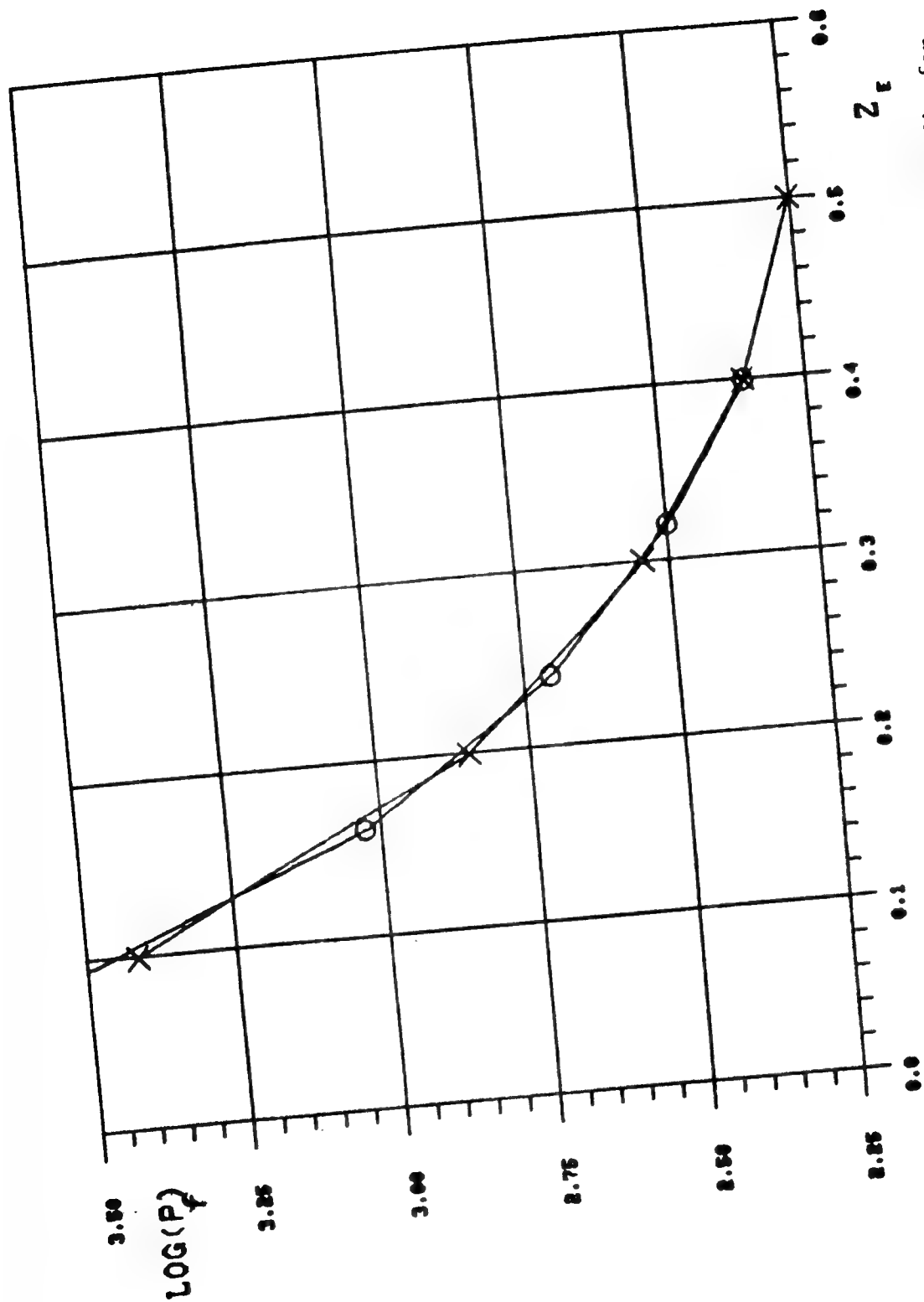
Figure 9: Dependence of P_f on z_e for R = 200 lbs, $z_v = 0$, E* = 1,500 lbs for $z_s = .4$ (o) and $z_3 = .5$ (x)
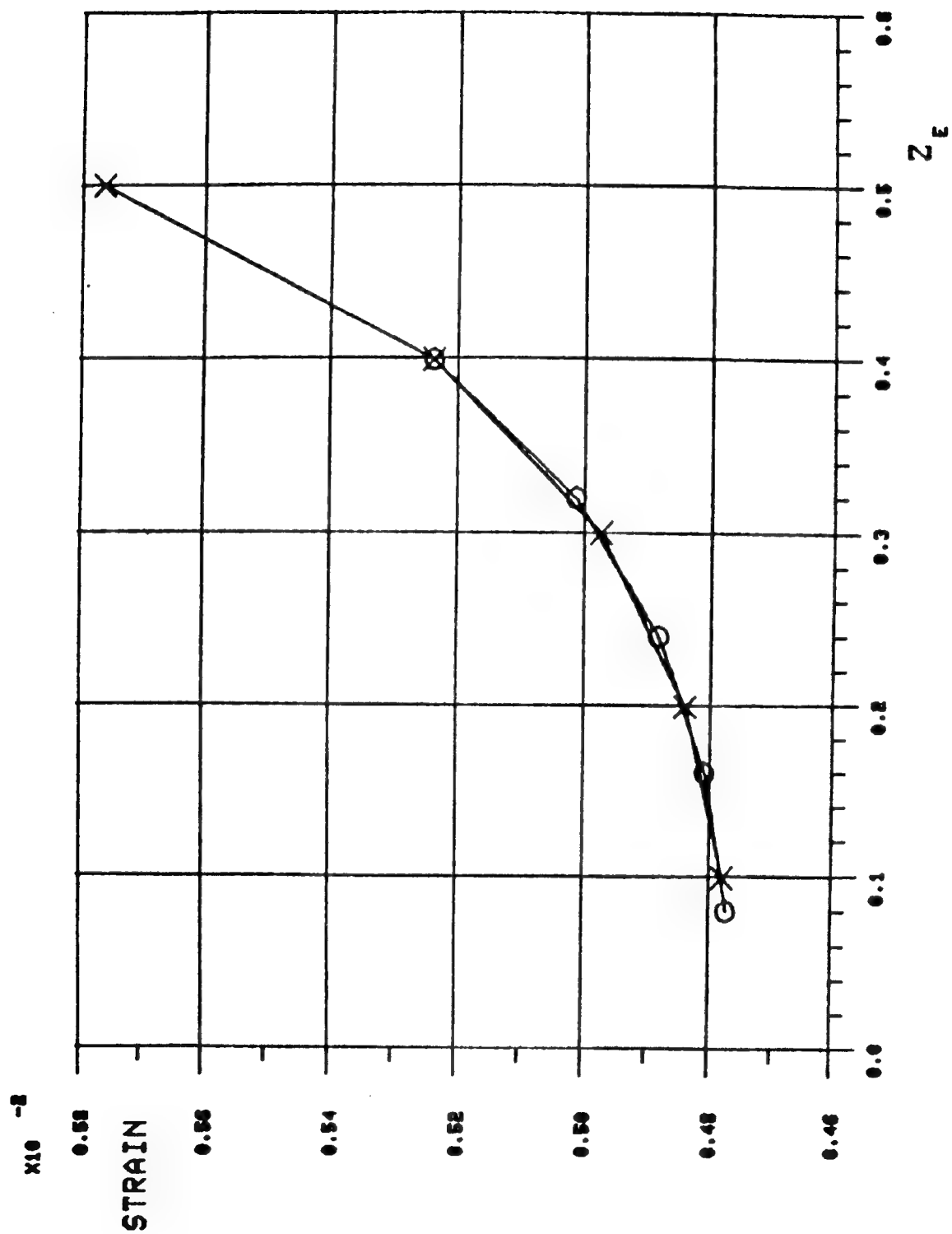
Figure 10: Dependence of ϵ on z_i for R = 200 lbs, $z_v = 0$, E* = 1,500 lbs for z_s = .4 (o) and z_s = .5 (x).
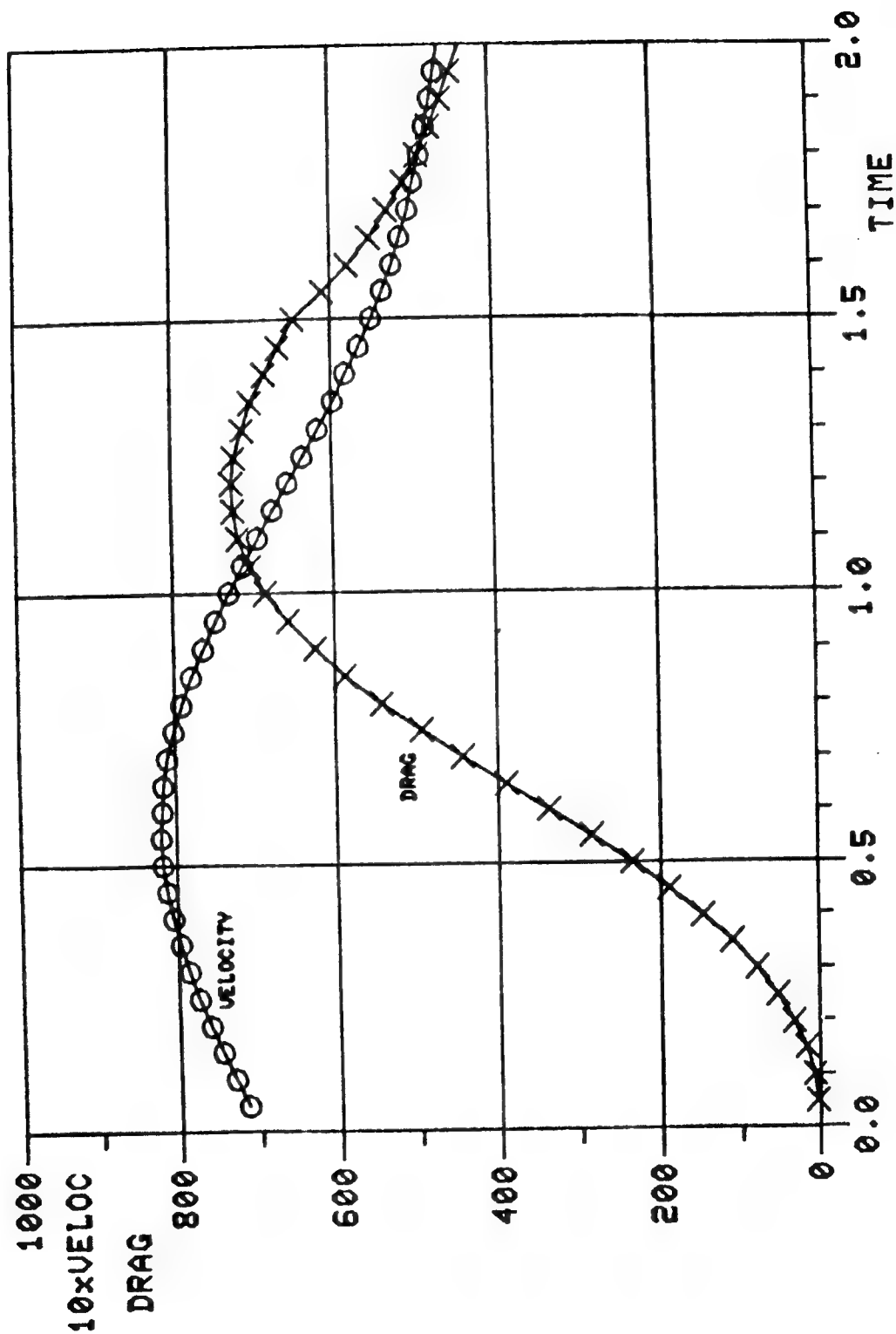
Figure 11: Time-dependence of Drag and (10 x Velocity) for a C-9 Canopy during

Opening with $\mathcal{V}_o$ = 73 ft/sec and W = 330 lbs.

FRICTION EFFECTS ON BEAM RESPONSE

NORRIS J. HUFFINGTON, JR.
Mechanical Engineer
US Army Ballistic Research Laboratory
Aberdeen Proving Ground, MD 21005

ABSTRACT

Previous predictions of the response of blast-loaded beams were found to greatly exceed corresponding experimental values. However, a subsequent re-examination of the test apparatus raised doubts that the intended boundary conditions of "simple supports" were even approximately achieved in the tests. In order to assess the importance of various possible contributors to the observed discrepancies (friction at unlubricated rotating and sliding surfaces, rotatory inertia of moving supports, and strain-rate effects in the specimens) the original dynamic response analysis was modified to include analytical modeling of these contributing factors. By variation of parameters associated with the cited contributing factors over plausible ranges in computer-based solutions it was possible to deduce that the overprediction of response was due almost entirely to neglect of Coulomb friction at support surfaces. For optimized input parameters the predicted final deformation of the beam is in excellent agreement with the experimental result.

INTRODUCTION

Air blast loading experiments [1] were conducted at BRL using a fixture and beam specimens provided by another agency. To aid in the selection of instrumentation and gage settings, some pre-test predictions of beam responses were made using a well-established finite difference response code [2]. When the tests were conducted these predictions were found to be gross overestimates of the physical response. In seeking an explanation of this disappointing performance two possible deficiencies in the analytical modeling were given serious consideration: strain rate effects in the specimen material and inadequate representation of the support conditions provided by the fixture.

It was suspected that the specimen material, 3003 aluminum alloy, might be significantly rate sensitive. Subsequent split Hopkinson bar tests [3] verified that this was true. However, as will be presently demonstrated, the strain-rate history of the response is not sufficiently large in magnitude to account for more than a small fraction of the discrepancy.

The beam specimens had rectangular cross-sections, 50.8mm (2 in) wide by 11.1mm (7/16 in) deep, and a span of 304.8mm (12 in). These specimens were slipped into steel rocker shafts at each end which were in turn supported in split bearing blocks. Had these shafts been massless and had all rubbing surfaces been frictionless this design should have provided a good simulation of the intended simply supported boundary conditions; i.e., no transverse displacement and no bending moment at either end of the beam. However, in view of the cited discrepancies between predictions for response of

simply supported beams and the experimental data and the discovery that the rocker shaft bearings had inadvertently been left unlubricated, it was decided that a more realistic modeling of the physical support conditions should be developed which includes the effect of Coulomb friction at all rubbing surfaces.

FRICTION AND ROTATORY INERIA MODELING

Since the blast loaded beams were expected to experience moderately large deflections the test fixture had been designed to permit one end of the beam to slide through its rocker shaft in order to avoid the occurrence of large membrane forces. Owing to this lack of symmetry of the boundary conditions a separate formulation was developed for each boundary.

FORMULATION FOR THE PINNED END CONDITION

One end of each beam specimen was bolted to its rocker shaft with a pair of force transducers sandwiched between the lower surface of the beam the attachment surface of the shaft. This end of the beam could only rotate, no translation being permitted in either the transverse or longitudinal direction. A drawing showing details of the pinned end rocker shaft is included as Figure 1. Free body diagrams showing the forces and moments acting on the rocker shaft and on the end segment of the beam are presented in Figure 2. The symbols have the following definitions:

θ = angle of rotation of rocker shaft and of normal to beam reference surface at $x = 0$.

$p(t)$ = blast pressure loading

P_0 = membrane force in beam at $x = 0$.

S_0 = transverse shear force in beam at $x = 0$.

M_0 = bending moment in beam at $x = 0$.[*]

R_0 = reactive force of bearing blocks on rocker shaft.

M_{f0} = frictional moment acting at bearing interface.

A = projected area of rocker shaft surface on which blast pressure acts.

---

[*] The small "overhang" of the beam is neglected except for its contribution to the moment of inertia of the rocker assembly.
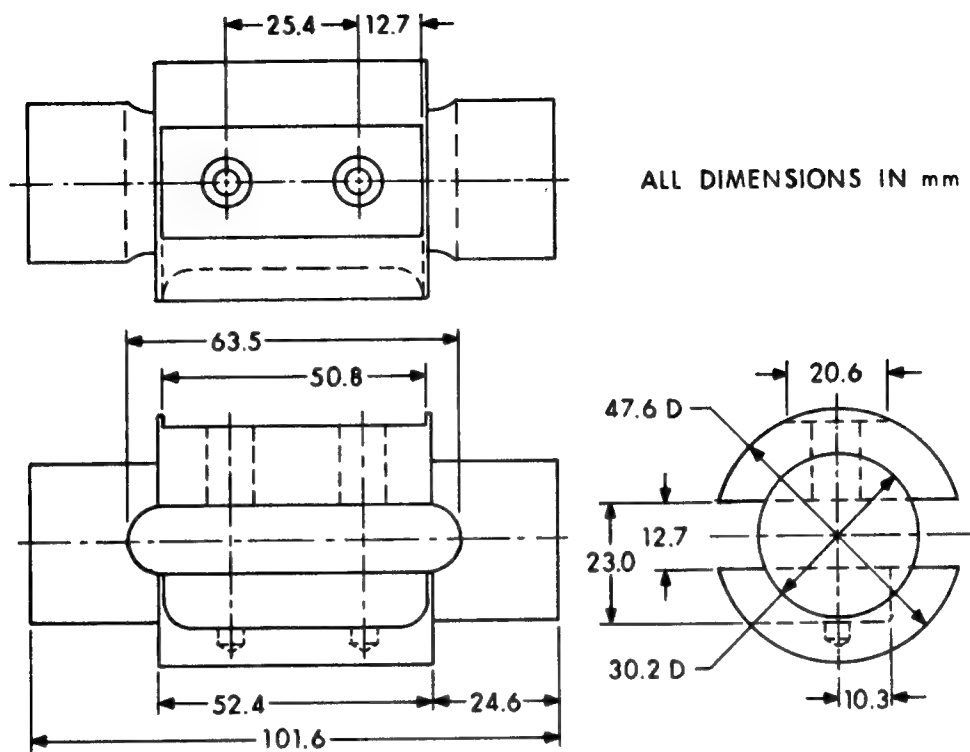
Figure 1. Pinned End Rocker Shaft Details

(a) Rocker Shaft

(b) Beam Segment
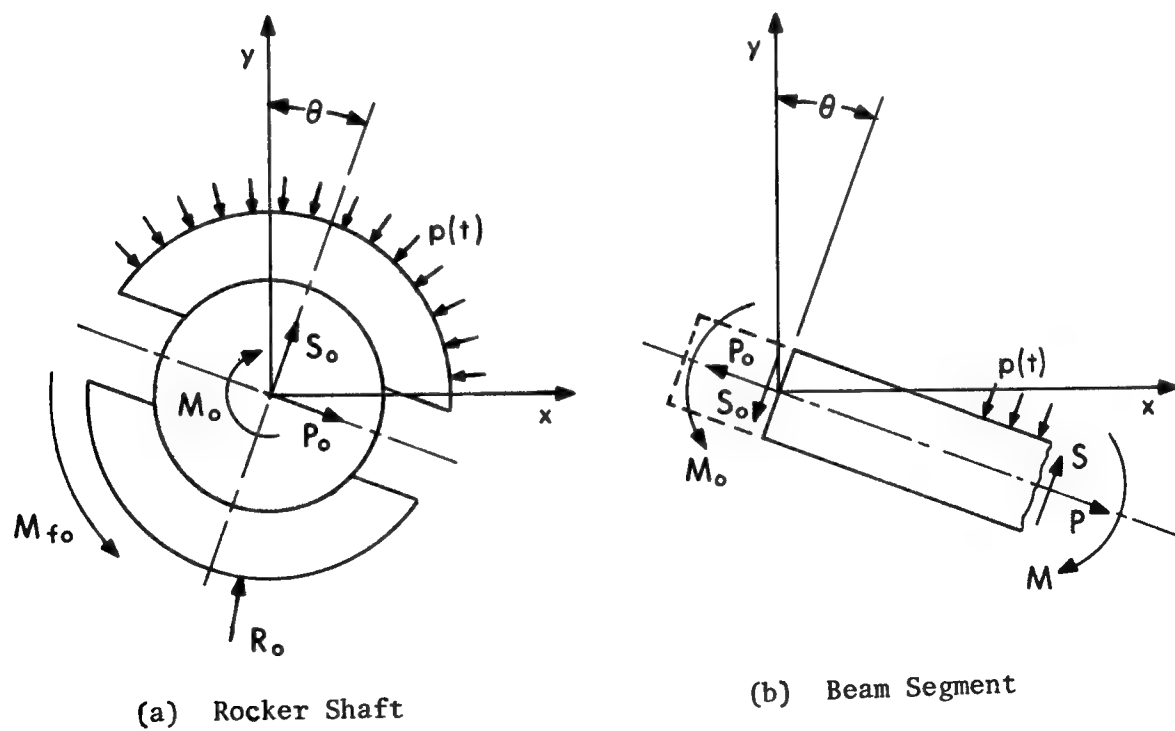
Figure 2. Free Body Diagrams at Pinned End

$$e \quad = \text{radius of bearing}$$

$$\mu \quad = \text{coefficient of Coulomb friction.}$$

The equilibrium equations for the rocker shaft are:

$$P_0 \cos \theta + S_0 \sin \theta + R_{0x} = 0 \tag{1}$$

$$-P_0 \sin \theta + S_0 \cos \theta + R_{0y} - pA = 0 \tag{2}$$

where R_{0x}, R_{0y} are the x- and y- components of R_0. These components can be combined to obtain

$$R_0 = \sqrt{R_{0x}^2 + R_{0y}^2} \tag{3}$$
$$= \left[P_0^2 + S_0^2 + 2pA \left(P_0 \sin \theta - S_0 \cos \theta \right) + p^2 A^2 \right]^{1/2}$$

The frictional moment can then be determined using

$$M_{f0} = \mu e \, R_0 \, C(\dot{\theta}) \tag{4}$$
$$= \mu e \, C(\dot{\theta}) \left[P_0^2 + S_0^2 + p^2 A^2 + 2pA \left(P_0 \sin \theta - S_0 \cos \theta \right) \right]^{1/2}$$

where $C\left(\dot{\theta}\right)$ is the nonlinear function which may be represented graphically as indicated and which presently will be formulated analytically.
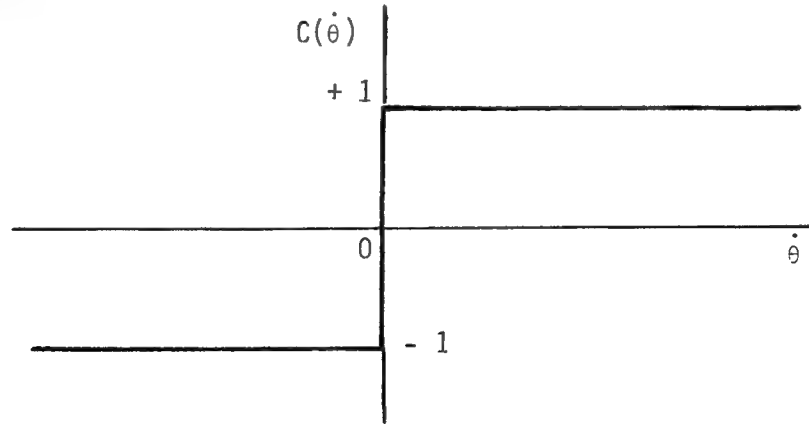
The rotational equation of motion from the free body diagram of figure 2(a) is:

$$M_0 - M_{f0} = I_0 \ddot{\theta} \tag{5}$$

where I_0 is the mass moment of inertia of the material which rotates with the angular acceleration $\ddot{\theta}$. This ordinary differential equation may be replaced by the customary

$O(\Delta t^2)$ central difference approximation consistent with the time integration algorithm employed in the REPSIL code [2]. Letting

$$\Delta\theta^+ = \theta\left(t_{j+1}\right) - \theta(t_j) \tag{6}$$

$$\Delta\theta^- = \theta\left(t_j\right) \quad - \theta\left(t_{j-1}\right) \tag{7}$$

where

$$t_{j+1} = t_j + \Delta t, \tag{8}$$

Equation (5) may be re-expressed as

$$\Delta\theta^+ = \Delta\theta^- + \frac{(\Delta t)^2}{I_0}\left(M_{0,j} - M_{f0,j}\right) \tag{9}$$

By use of Equation (9) a discrete numerical solution for $\theta(t)$ can be obtained concurrently with the marching out of the solution for the beam response. The initial conditions for $\theta(t)$ are $\theta(0) = 0$ and $\dot{\theta}(0) = 0$. In utilizing Equation (4) to obtain the value of $M_{f0,j}$ to employ in Equation (9), one must determine the value of $C\left(\dot{\theta}\right)$ in accordance with one of the following three possibilities:

1. $\dot{\theta} > 0$ or $\left(\dot{\theta} = 0, \ddot{\theta} > 0\right)$ for which $C\left(\dot{\theta}\right) = +1$

2. $\dot{\theta} = 0, \ddot{\theta} = 0$ for which $-1 < C\left(\dot{\theta}\right) < 1$ and $M_{f0} = M_0$

3. $\dot{\theta} < 0$ or $\left(\dot{\theta} = 0, \ddot{\theta} < 0\right)$ for which $C\left(\dot{\theta}\right) = -1$

Although somewhat awkward in appearance, these tests to determine which regime is operative can be readily programmed into the time marching algorithm of the response code.

FORMULATION FOR THE SLIDING-HINGED END CONDITION

The support condition at the other end of the beam is similar to that at the pinned end in that the rocker shaft (see Figure 3) does not translate but is complicated by the provision for the beam to slide through the slot in the rocker shaft as the lateral displacement of the beam varies.
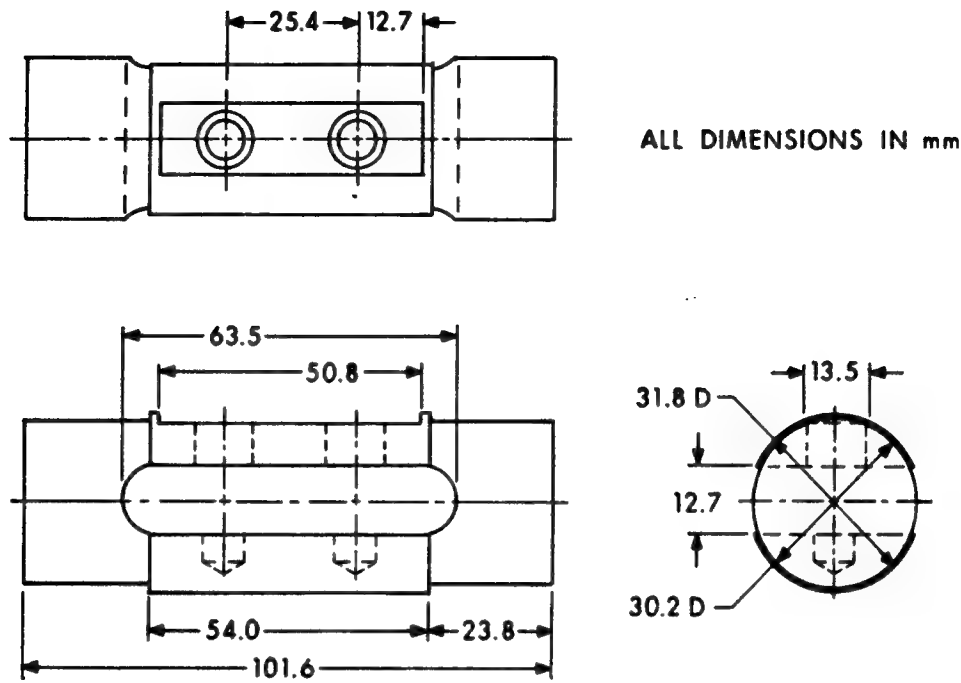
Figure 3. Sliding-Hinged End Rocker Shaft Details

The formulation of the boundary conditions at this end of the beam entails the introduction of two additional dependent variables:

ψ = angle of rotation of the rocker shaft

u = displacement of point in beam initially on axis of rocker shaft parallel to sliding interface

Other symbols employed in this formulation are:

S_N = transverse shear force in beam at x = N

F_f = frictional force at sliding interface

M_T = moment transmitted between beam and rocker shaft

M_{fN} = frictional moment acting at bearing interface

R_N = reactive force of bearing blocks on rocker shaft

B = projected area of rocker shaft surface upon which blast pressure acts

134

$$m \quad = \text{mass of beam considered in free body diagram, including overhang material}$$

$$h \quad = \text{depth of beam}$$

$$I_S \quad = \text{mass moment of inertia of rocker shaft}$$

Referring to Figure 4(a), we may write the equation of motion for the direction parallel to the sliding surface as

$$-P + F_f = m \ddot{u} \tag{10}$$
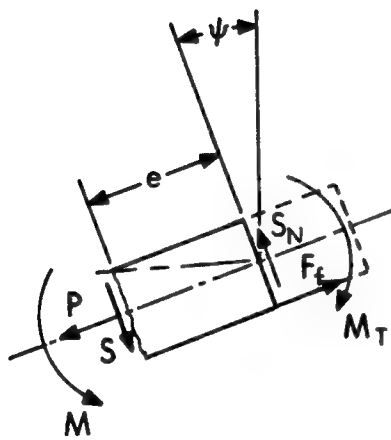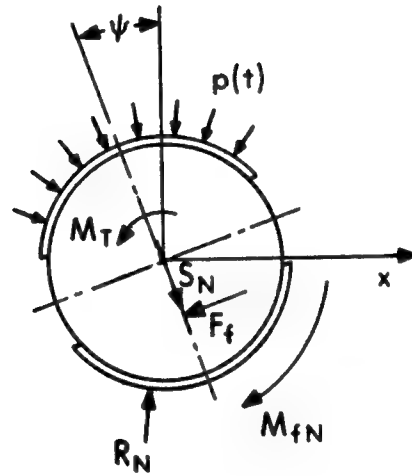
(a) Beam Segment   (b) Rocker Shaft

Figure 4. Free Body Diagrams at Sliding-Hinged End

where it is tacitly assumed that the angular velocity of the rocker shaft is never large enough that a distinction between relative and absolute acceleration of m is necessary. Defining incremental changes in u in the same manner as for θ, Equation (10) may be expressed in finite difference form as

$$\Delta u^+ = \Delta u^- + \frac{(\Delta t)^2}{m} \left(-P + \mu S_n C(\dot{u}) \right) \tag{11}$$

Since the REPSIL code employs Cartesian components of displacements increments, these can be obtained for the mesh location initially on the rocker shaft axis by use of

$$\Delta u_x = - \Delta u \cos \psi \tag{12}$$

$$\Delta u_y = - \Delta u \sin \phi \tag{13}$$

Also with respect to Figure 4(a) we may write the moment equation

$$M - M_T + Se + \frac{h}{2} F_f = I_B \ddot{\psi} \tag{14}$$

where I_B is the centroidal moment of inertia of m.

For the rocker shaft (see Figure 4(b)) we obtain the following equations of equilibrium and of motion:

$$-F_f \cos \psi + S_N \sin \psi + R_{Nx} = 0 \tag{15}$$

$$-F_f \sin \psi - S_N \cos \psi + R_{Ny} - pB = 0 \tag{16}$$

$$M_T - M_{fN} - \frac{h}{2} F_f = I_S \ddot{\psi} \tag{17}$$

Making use of Equations (15) and (16) the bearing reaction is obtained:

$$R_N = \sqrt{R_{Nx}^2 + R_{Ny}^2}$$
$$= [F_f^2 + S_N^2 + p^2 B^2 + 2pB (F_f \sin \psi + S_N \cos \psi)]^{1/2} \tag{18}$$

The frictional moment at the bearing is then

$$M_{fN} = \mu e \, R_N \, C (\dot{\psi}) \tag{19}$$
$$= \mu e \, C (\dot{\psi}) \, [F_f^2 + S_N^2 + p^2 B^2 + 2pB (F_f \sin \psi + S_N \cos \psi)]^{1/2}$$

Adding Equation (14) to Equation (17), one obtains

$$M - M_{fN} + Se = I_N \ddot{\psi} \tag{20}$$

where $I_N = I_S + I_B$ is the mass moment of inertia of the shaft and the contained beam. Equation (20) may be expressed as the difference equation

$$\Delta \psi^+ = \Delta \psi^- + \frac{(\Delta t)^2}{I_N} (M_{N,j} - M_{fN,j} + e \, S_{N,j}) \tag{21}$$

136

The formulation of the boundary conditions for the sliding-hinged end contains the two Coulomb functions $C(u)$, $C(\dot{\psi})$ which must be evaluated by tests analogous to those prescribed for $C(\dot{\theta})$; i.e., the possibilities of forward slip, no slip, or reverse slip must be considered at each sliding interface.

The foregoing boundary condition formulations, which take account of boundary friction and the rotatory inertias of boundary masses, have been incorporated into the REPSIL code as a temporary modification in order to perform an evaluation of the contribution of each of these effects.

APPLICATION OF THE GENERALIZED RESPONSE ANALYSIS

All calculations to be reported in sequel pertain to the case identified as Shot Number 5 in [1]. Static tensile stress-strain data for this material were reported in Figure A-2 of [1]. The blast loading, assumed uniformly distributed spatially, was the experimentally recorded pressure history shown in Figure 48 of the same reference. Other input parameters used in the calculation are:

$$A = 2419 \text{ mm}^2 \ (3.75 \text{ in}^2)$$

$$B = 1452 \text{ mm}^2 \ (2.25 \text{ in}^2)$$

$$e = 15.1 \text{ mm} \ (0.594 \text{ in})$$

$$I_0 = 0.15325 \text{ g·m}^2 \ (0.0013564 \text{ lb·in·s}^2)$$

$$I_N = 0.05360 \text{ g·m}^2 \ (0.0004744 \text{ lb·in·s}^2)$$

$$m = 0.0303 \text{ kg} \ (0.0001728 \text{ lb·s}^2/\text{in})$$

The computer runs of the REPSIL code which were made for correlation with the experimental data for Shot Number 5 are listed in Table I. A comparison of transient mid-span deflections for each run is shown in Figure 5 as well as the experimental final value of this quantity (unfortunately, the transient experimental data were lost). Damping was initiated in each run after the maximum displacement in order to obtain a predicted final deflection, which is listed in Table I. Runs A, B, and C were reported in [1] and are included for completeness. It is clear that use of simply supported end conditions (run A) results in a gross overprediction of the response. On the other hand, runs B and C which were made using fixed end conditions effectively bracket the experimental final deflection. However, run C employed a power law strain-rate model with parameters for a different aluminum alloy. When dynamic data for 3003 aluminum alloy became available these were used with a hyperbolic tangent strain-rate model [4] to make run D, also with fixed boundaries. This run provided excellent agreement with

TABLE I. EXPERIMENTAL/THEORETICAL CORRELATIONS FOR SHOT NO. 5

ITEM	CONSTITUTIVE MODEL	BOUNDARY CONDITIONS	FRICTION COEFFICIENT	MAXIMUM DEFLECTION (mm)	FINAL DEFLECTION (mm)	MAXIMUM STRAIN AT		
						16.2%Span	43.3%Span	82.3%Span
Exp.Data				----	11.2	.0020	.0152	.0025
Run A	EP-SH	Simply Supp.		54.6	45.7	.0036	.0598	.0034
Run B	EP-SH	Fixed		15.4	12.6	.0018	.0186	.0023
Run C	EP-SH-PLSR	Fixed		13.6	10.8	.0014	.0172	.0017
Run D	EP-SH-HTSR-I	Fixed		14.3	11.4	.0014	.0182	.0016
Run E	EP-SH	RM+F	0.5	37.9	32.2	.0022	.0311	.0023
Run F	EP-SH	RM+F	1.0	28.2	21.7	.0018	.0232	.0022
Run G	EP-SH-HTSR-I	RM+F	1.0	26.8	20.4	.0017	.0211	.0022
Run H	EP-SH-HTSR-II	RM+F	1.0	26.8	20.5	.0017	.0211	.0022
Run I	EP-SH-HTSR-I	0.1 RM+F	1.0	28.2	22.2	.0016	.0210	.0021
Run J	EP-SH-HTSR-I	RM+F	2.0	16.7	12.8	.0012	.0186	.0016
Run K	EP-SH-HTSR-I	RM+F	3.0	15.6	11.8	.0012	.0176	.0012

Constitutive Model abbreviations:

EP-SH   Elastoplastic strain-hardening
PLSR   Power Law strain-rate dependence
HTSR   Hyperbolic tangent strain-rate dependence [4]
I & II   Data fits of Hopkinson bar results [4]

Boundary condition abbreviation:

RM+F   Rotating masses plus friction (model formulated in this paper)

experimental final deflection. However, it was realized that the physical response did involve rotation of the rocker shafts and slippage of one end of the beam through the slotted rocker shaft so a more rational response modeling was sought.
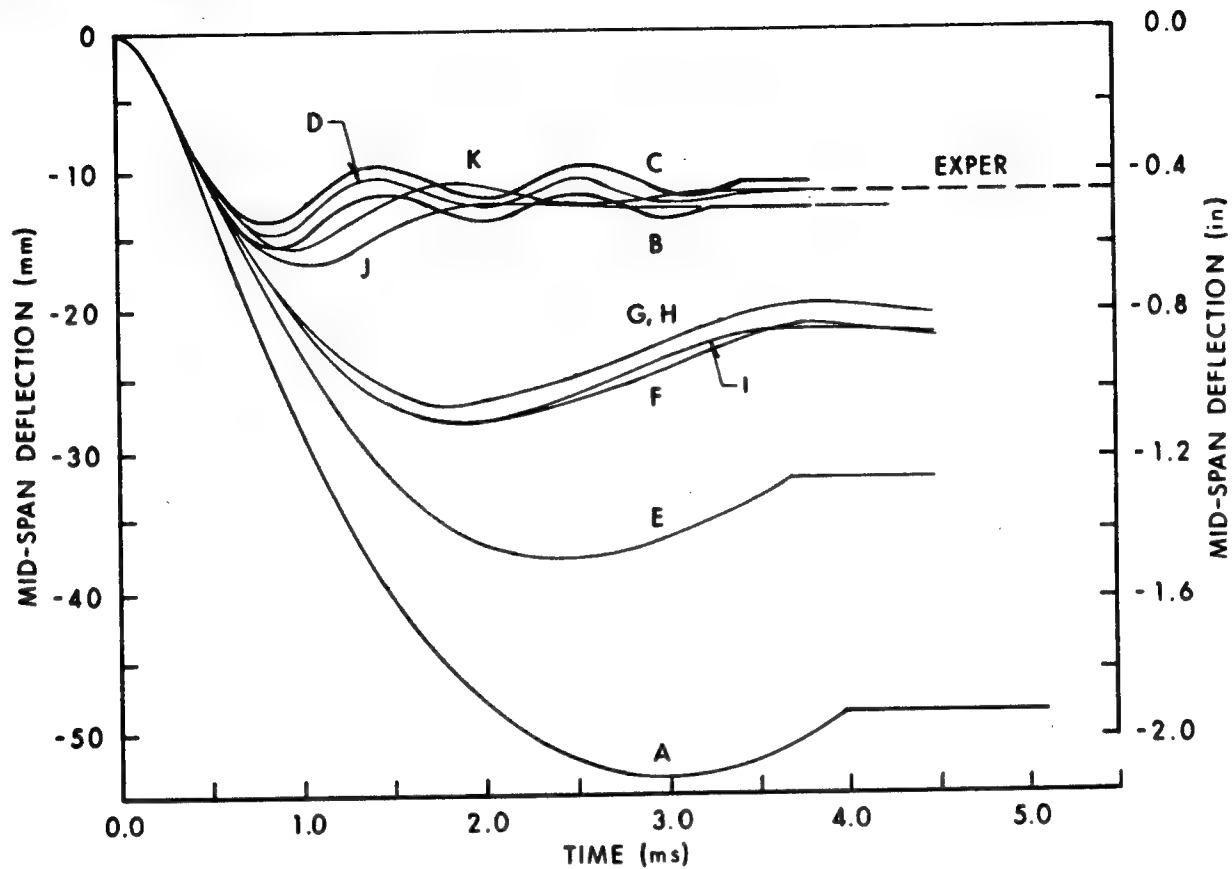
Figure 5. Comparison of Deflection Responses for Shot 5.

The remaining REPSIL runs employed the boundary condition formulations developed in this paper. Runs E and F were made using static material properties (no strain-rate dependence in the constitutive function) and illustrate the dominant effect of the friction coefficient μ on the response. Run G was then made using the same value of μ as Run F but employing the hyperbolic tangent strain-rate model and the data of Fit I. As may be seen from Figure 5, the inclusion of strain-rate dependence had a relatively small effect in this instance, amounting to a further decrease in the final deflection of 12% of the experimental value.

When additional dynamic material property data became available Fit II was effected and Run H was made, providing results almost identical to those of Run G. This was due to the relatively small strain-rates calculated for Shot No. 5: a maximum value of 120.8 s^{-1} at one location in the beam and for most of the response much smaller values throughout the beam. For tests involving higher strain-rates this effect could be expected to have a significantly greater importance for the response of blast loaded beams.

It is instructive to examine certain other results produced by the REPSIL program for Run G (to which results for other runs are qualitatively similar). Figure 6 shows the variation of the bending moment M_0 and the frictional moment M_{f0} at the pinned end while Figure 7 displays the transient rotation of the rocker shaft at the same location.
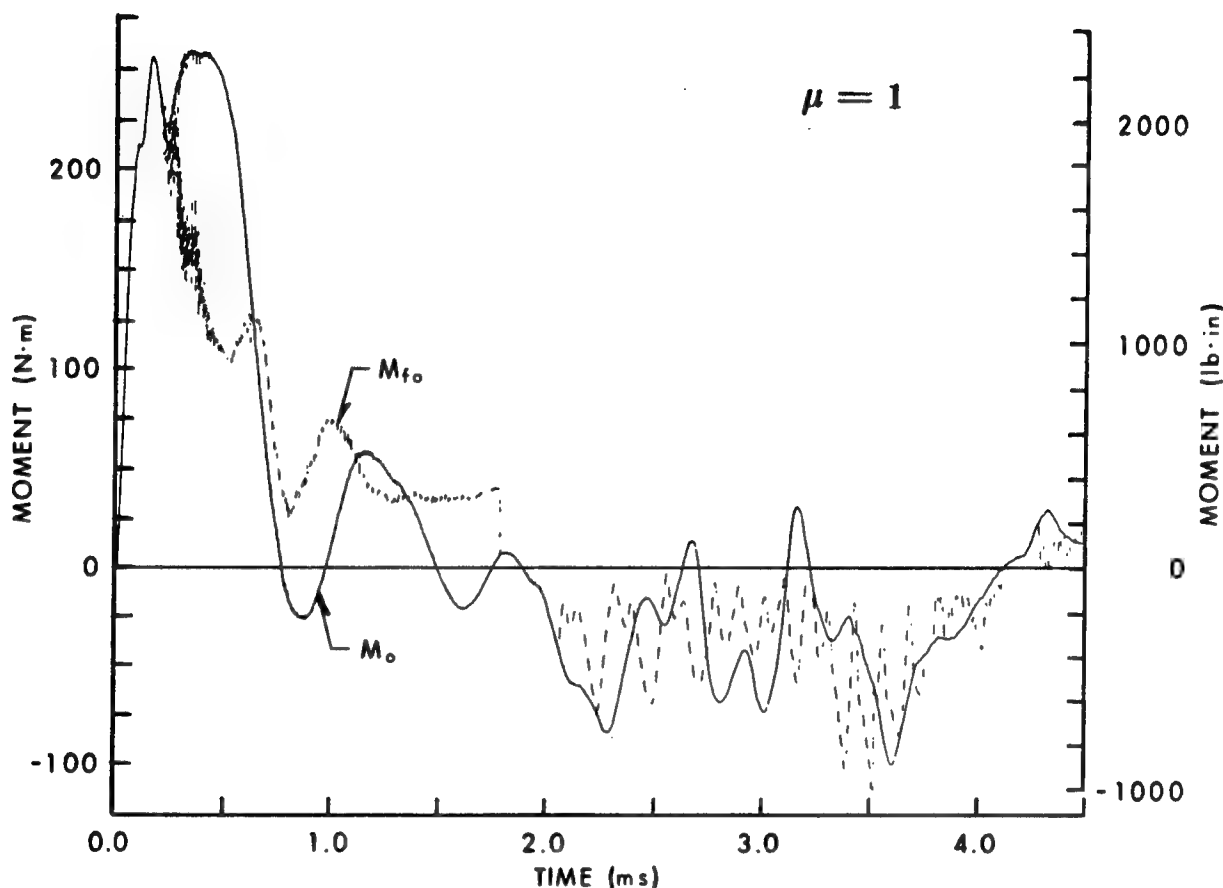
Figure 6. Transient Moments at Pinned End

It may be seen that no rotation occurs until about 0.23 ms when M_{f0} is no longer able to match M_0. Subsequently the end of the beam rotates until about 1.81 ms when the shaft "locks up" $(M_{f0} = M_0)$ and θ remains constant until the reversed bending moment becomes large enough to overcome the frictional resistance. Another brief period of ankylosis starts at about 4.13 ms.

It was desired to assess the importance of including the rotatory inertia of the end masses in the response formulation. This cannot be accomplished by simply making a run with the mass moments of inertia I_0 and I_N set equal to zero (see Equations (9) and (21)). Rather than program a special formulation for this case, the available program was used with the values of I_0 and I_N set to a small fraction of their actual values. This was done in Run I where the fraction employed was 1/10. The results should be compared with Run G since all other parameters were the same for these two runs. It may be seen from Figure 5 that the form of the response curve is somewhat altered for
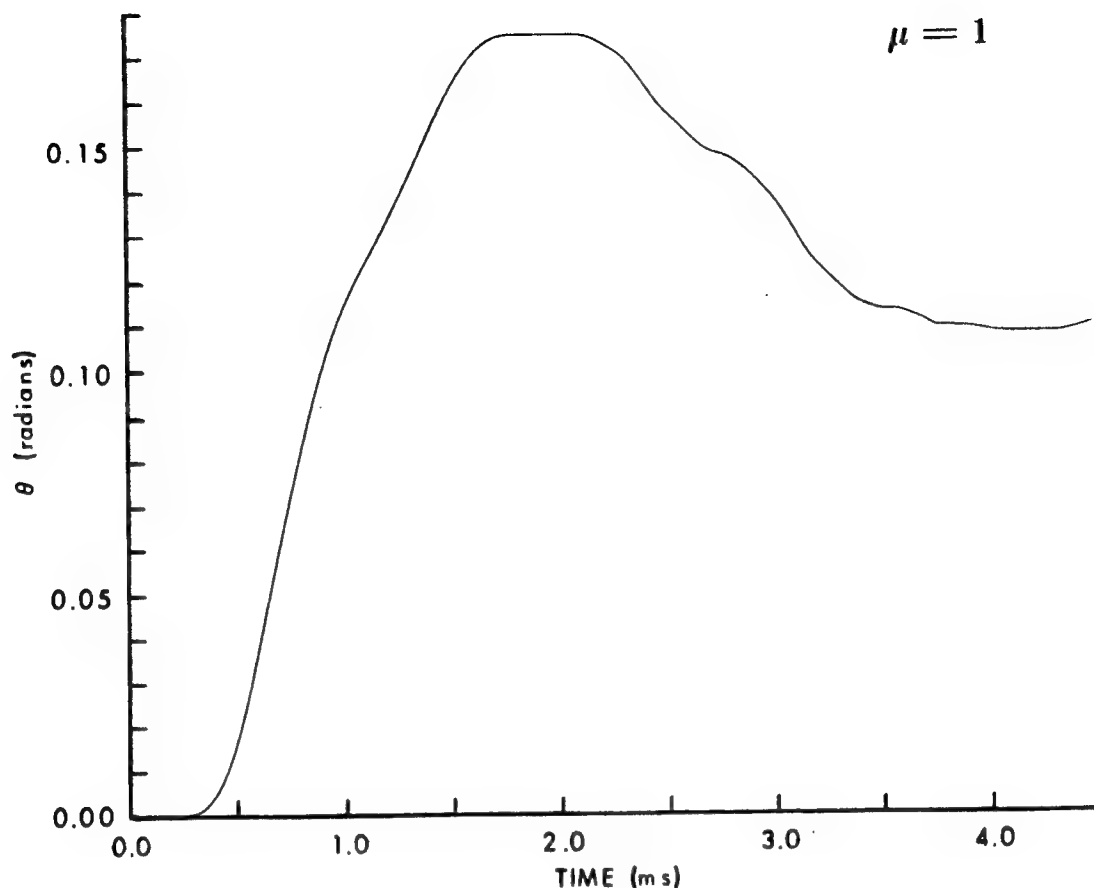
Figure 7. Predicted Rotation at Pinned End

Run I. The final displacement is about 16% (of the experimental value) greater when the rotatory inertia effect is minimized.

Since none of the cases examined for $\mu = 1$ resulted in a final displacement approximating the experimental value it was decided to explore further the effect of varying this parameter. This was done in Runs J and K using $\mu = 2$ and 3, respectively. Run K provided a very satisfactory correlation with respect to final deflections. In fact, further increase in μ would have little effect since, even for Run K, the end masses were "locked" during most of the run. The transient rotations of the rocker shafts for Run J are shown in Figure 8 and 9. Comparing Figure 7 and 8 one sees that for the larger μ the maximum positive θ is reduced to about 10% of that for $\mu = 1$ and that there are more "plateaus". Also, for Run J the residual value of both θ and ψ is negative (unlike Run G). Figure 10 presents the transient value of u for Run J which also exhibits several cycles of stick-slip motion. The use of such large values of friction coefficient may seem inappropriate but there is essentially no data on Coulomb friction under conditions where both driving force and the normal pressure are rapidly changing.

141
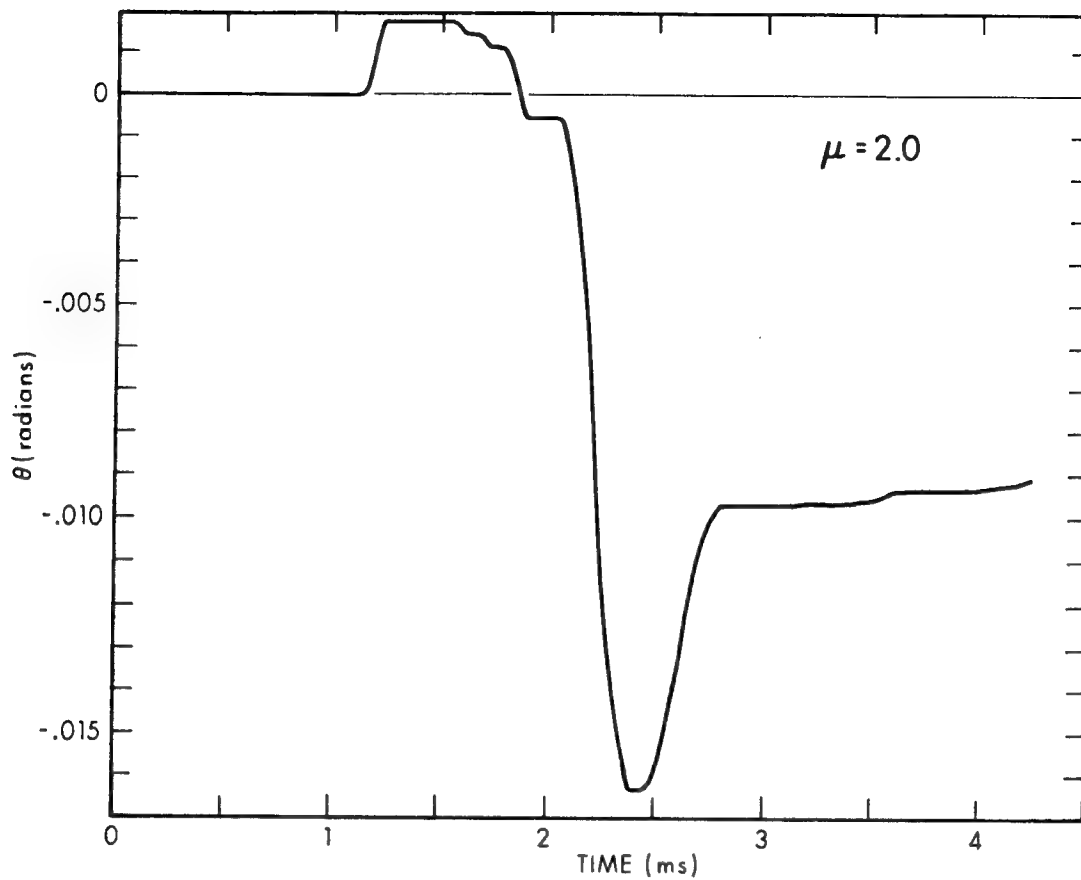
Figure 8. Rotation at Pinned End for Run J
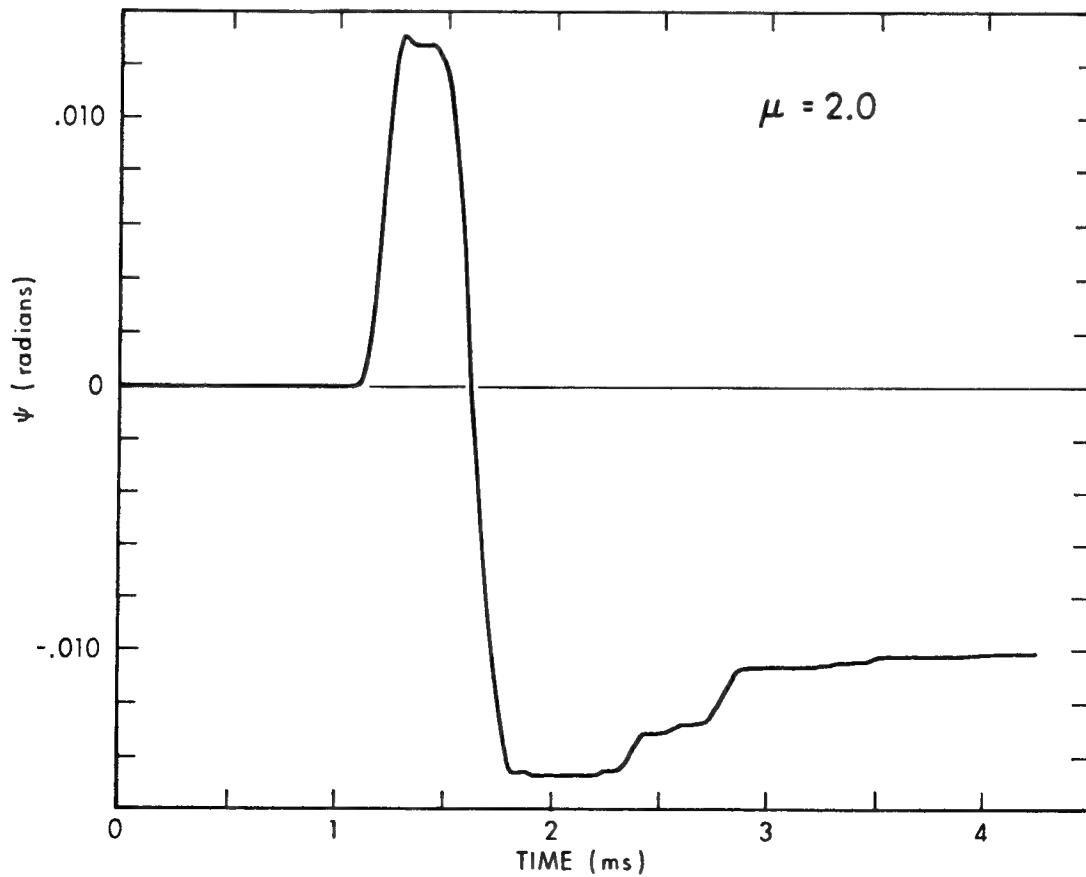
Figure 9. Rotation at Sliding-Hinged End for Run J

142
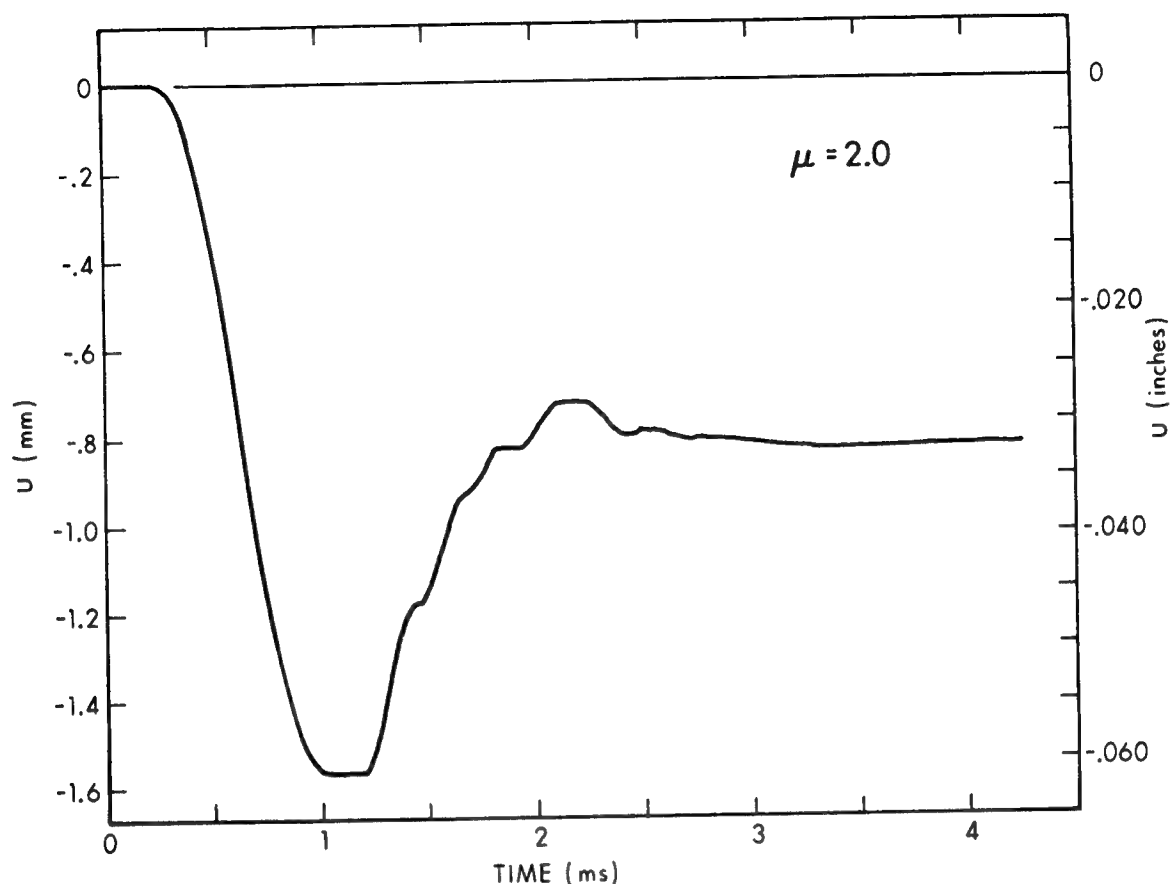
Figure 10. Displacement at Sliding-Hinged End for Run J

It is observed that strains, both experimental and analytical, vary directly with the transverse displacement amplitude. Thus, the best correlations with experimental strain data occur for runs which best match the experimental final deflection.

CONCLUSIONS

The foregoing analytical formulations for friction and rotatory inertia at supports have permitted a more rational interpretation of experimental data from blast loaded beam tests reported in [1]. Through use of selective computer runs of the modified REPSIL code it was possible to evaluate the relative importance of each of these effects on the overall response.

The 3003 aluminum alloy used in fabricating the beam specimens was determined by Hopkinson bar experiments to be significantly more strain-rate sensitive than most structural aluminum alloys. The use of a hyperbolic tangent function strain-rate model is believed perferable to the widely used power law model due to its more realistic behavior for small strain rates. Inclusion of strain-rate effects in the response calculations for Shot 5 produced only a small change in beam deflection due to the rather small

143

strain-rates which were associated with this shot. One should not conclude that strain-rate effects are always insignificant; for problems where strain-rates in the saturation region occur for an appreciable portion of the response, resisting stress increases of 40% and 78% would be available for Fits I and II, respectively.

Although the intended simply supported end conditions for the beam tests were not achieved experimentally the boundaries were certainly not completely fixed. The augmentation of REPSIL boundary conditions to account for support friction and rotatory inertia permitted the determination that the observed response was primarily due to large frictional forces at the boundaries. The relatively small effect of the rotatory inertial of the rocker shafts did alter the mathematical character of the problem and provided a smoothing effect on the response calculations. The results of this investigation provide further substantiation for the basic formulation employed in the REPSIL code and demonstrate that it can be adapted to treat a variety of physical boundary value problems.

ACKNOWLEDGEMENT

144

REFERENCES

1. C. N. Kingery, N. J. Huffington, Jr., and J. D. Wortman, "Response of Beams to Airblast Loading," Ballistic Research Laboratory Technical Report ARBRL-TR-02369, September 1981. (AD B060635L)

2. J. D. Wortman, "RPSL1D (A One-Dimensional Version of REPSIL)," Ballistic Research Laboratory Memorandum Report ARBRL-MR-03221, November 1982. (AD A122336)

3. Private communications from S. J. Bless and A. Challita, UDRI to N. J. Huffington, Jr., BRL.

4. N. J. Huffington, Jr. and J. D. Wortman, "Boundary Condition and Strain-Rate Effects on the Response of Blast-Loaded Beams," Ballistic Research Laboratory Technical Report ARBRL-TR-02551, March 1984 (AD A140428).

SESSION IV: ANALYSIS, DESIGN AND RELIABILITY

BOUNDARY INTEGRAL SOLUTIONS
TO CONTACT STRESS PROBLEMS

By
Marlin Brueggert

Garrett Turbine Engine Company
A Division of The Garrett Corporation

ABSTRACT

Boundary integral element presents a unique design method, wherein contact stress solutions are provided for general geometries, without classical restraints of quadratic boundaries or approximations thereto. The boundary integral method presented employs the Kelvin solution and is a relatively new approach to general stress solutions for elastostatic problems. Mathematically, the boundary integral and finite element methods are two different forms of weighted residual techniques. Comparisons are made with classical Hertz solutions and a more limited technique using Boussinesq solutions. The rationale for using boundary integral methods as opposed to finite element methods for contact stress solution is discussed. Because the boundary integral method discretizes only the boundary rather than the area of the domain, the modeling effort is reduced by one order. The advantages here are twofold; first, the modeling effort is reduced, and secondly, better solution to steep local gradients are obtained with the same number of degrees of freedom. This is shown to be especially important to the contact stress problem, which is characterized by high local stress gradients and the sensitivity of contact stress to small, local perturbations in geometry.

The boundary integral method is applied to a contact geometry and the resulting stresses are presented. This baseline geometry is then perturbed and the effect on contact stress is compared. These results demonstrate that a design criteria for contact stresses based on an average bearing stress can be highly misleading. The solution is then extended one step further by considering tolerancing and misalignment effects. Small misalignments are shown to have a dramatic effect on contact stress. Friction effects are demonstrated to be admissible in the boundary integral solution method, and their effects are presented for the example contact geometry. The importance of considering these friction effects when notches or fillets local to the contact area exaggerate the contact stresses is discussed.

APPLICATION OF FINITE ELEMENT MODELLING ANALYSIS
TO ACV STRUCTURAL HULL DESIGN

MICHAEL C. LOU
Member Technical Staff

PAUL M. RAPACZ
Member Techincal Staff
Jet Propulsion Laboratory
Pasadena, California 91109

ABSTRACT

This paper describes the application of the finite-element modelling method to the integrated design and analysis process of an ACV structural hull. MSC/NASTRAN static and dynamic models which accurately simulate geometry, materials, mass, and constraints of the hull were assembled. The analysis results of those models were used to guide the progress of structural design, test planning and other design and development activities. Included in this paper are discussions of the fundamental design philosophy for structural hulls, modelling techniques for lightweight hull structures, ACV hull design criteria and applicable load cases, stress and modal analysis results.

INTRODUCTION

In the past two decades the rapid advent of high-speed, large-core digital computers has prompted the widespread use of finite-element modeling (FEM) analysis methods. One of the most noticeable examples is the application of FEM analysis to the design of ground transportation vehicle structures. Since the early 1970's the domestic automotive companies, driven by the need to reduce vehicle weight for improved fuel economy, have spent hundreds of millions of dollars in facilities, equipment, software and training to develop their in-house FEM analysis capabilities. At present, FEM methods have become the most cost-effective tool for developing, assessing and optimizing complex vehicle structural systems. Passenger car and truck structures are routinely subjected to stress, dynamic and/or acoustic analyses at a component, subsystem and systems level.

Compared to their civilian counterparts, the military vehicle producers are using the FEM structural analysis techniques to a much lesser extent. This is particularly true in the design of hull structures for tank-type armored combat vehicles (ACV). These vehicles traditionally have an integrated structural/armored hull design, for which meeting the required level of threat protection usually produces a hull structure more than capable of withstanding loads caused by rough terrain and weapons firing. Therefore, very little structural analysis is required in the design stage of an ACV development program.

During the past few years, research and development efforts in new armor materials indicated that not all promising armor materials have mechanical properties suitable for ACV structural applications using conventional shaping and assembly processes. The intended use of these armor materials leads to the evolution of a "structural hull" with applique armor plates. Since the structural hull should be optimally designed to withstand terrain and weapons firing loads with minimum structural weight, more sophisticated structural analysis is required. The FEM method is a logical choice as the analysis tool to provide sufficiently accurate stress and deformation data in support of such a complicated structural system.

STRUCTURAL TEST MODEL (STM) HULL DESIGN

The Advanced Material Technology Development (AMDT) project was initiated, under the sponsorship of the Tank and Automotive Command (TACOM), in 1982. This project is concerned primarily with the development of design and fabrication techniques for a lightweight ACV hull and applique armor. Since the intent is not to design a complete vehicle, several sub-systems deemed representative were adapted from existing vehicles. The track and suspension systems chosen were originally used on the High Survivability Test Vehicle-Lightweight (HSTV-L). The designated propulsion system consists of an Allison DDA-250 gas turbine and the ATT-463 transmission. The gas turbine is a production item used primarily in aviation, but the transmission design is only in the conceptual stage. Sufficient information was gathered to configure the engine compartment of the hull to accommodate these components. The hull is also designed to accept a turret removed from a M551 Sheridan tank. Figure 1 depicts the outside configuration of the STM vehicle.
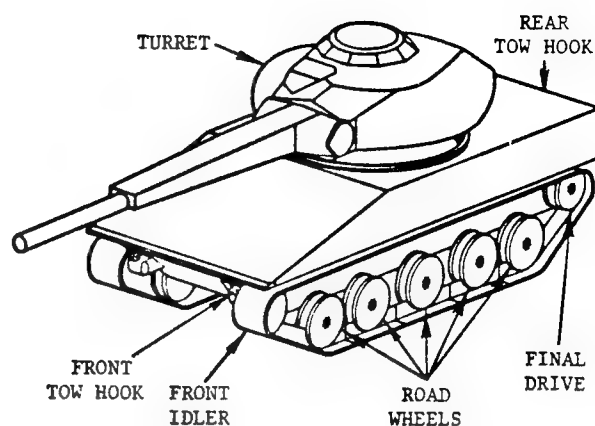
Fig. 1 - STM Configuration

The hull of the STM vehicle is basically an aluminum skin over rib structure with appropriate local reinforcements in highly loaded areas. These areas include the road wheel attachments, turret ring, idler/track tensioner mounts, drive sprocket mount, lifting and towing provisions, and the front nose area. Applique armor is attached to the skin using methods which do not add significantly to the structure of the hull. Since the skin becomes an active part of the armor protection, the hull is constructed of 5083 aluminum, a recognized armor alloy.

In the early phase of the design, a coarse finite-element model of the hull was assembled to facilitate iterative analysis aimed at preliminary selection of skin thicknesses. For most of the hull, the skin is 1/4-inch or less in thickness. To better utilize the material, the ribs, whenever possible, are located at the skin panel terminations and formed by rolling up the sheet edges.

Sizing of the hull is controlled primarily by external size limits dictated by expected transportation methods. The overall hull length does not exceed 220 inches, while hull

152

width is held to 106 inches at the sponson. The hull is configured such that it can act as an integrated carrier for the existing turret and suspension systems.

The interior of the hull has sufficient protected volume to accommodate the crew and items needed to assure operation and control of the vehicle. The only crew member to be located in the hull is the driver. Two additional crew members, the commander and gunner, are located in the turret. The final arrangement of internal components positions the driver on the forward left side of the hull surrounded by electronic equipment. The propulsion system is located in an engine compartment that forms the rear portion of the hull. Other internal items that account for the greatest mass and volume are the fuel and ammunition. The fuel capacity is designated to be approximately 240 gallons based on the requirement for a vehicle cruising range of 300 miles. Fuel is stored in plumbed tanks placed in the sponsons and the area just to the rear of the turret. Fifty rounds of 75 mm ammunition are considered a full load for the vehicle. Thirty of these are designated as "ready rounds" and must be located in the turret. The remaining twenty rounds are stored in canisters mounted to the forward right side floor .

STM HULL STRUCTURAL DESIGN SUPPORT AND ANALYSIS

To achieve a high degree of structural efficiency for the STM hull, an integrated design and analysis approach is employed to develop the hull structure. As the hull design progresses from concept through preliminary, detail, fabrication, and assembly stages, finite-element models are assembled and continuously updated. These finite-element models, supplemented by manual structural analysis, are used to guide the structural design effort.

In performing the FEM analysis, a set of STM operational load cases, see Table 1, are imposed on the models. These load cases are primarily applications of the design handbook recommendations [1] which are based upon experience gained from many years of ACV design, testing, and field usage. Although all of the design loads considered are of a dynamic nature, they are applied to the FEM analysis models as equivalent quasi-static forces. The load values listed in Table 1 are all design limit loads, based on which an ultimate safety factor of 1.5 is required as one of the STM structural design criteria.

Both static and dynamic (normal modes) analyses are performed on the STM system model with only minor modifications for both types of analyses. Static analysis is used to produce stress and deformation results, while the normal modes analysis determines the natural frequencies and mode shapes of the hull structure.

In static analysis, loads applied to the structure must be reacted by restraining forces. With each of the sub-system models used for local detailed analysis, rigid constraints in the appropriate degrees of freedom are imposed on the boundary to provide support for the model. This approach, although relatively simple, creates artificially high stresses in the vicinity of the supported edge. In reality any load of a dynamic nature applied to a vehicle is initially reacted by the inertia of the vehicle. Since most terrain and gun firing loads imposed on the STM are dynamic loads, an analysis algorithm in the MSC/NASTRAN Computer Code [2] called "inertia relief" is employed with the system model. The algorithm balances the applied forces, which are not in static equilibrium, with inertial loads due to the mass distribution of the vehicle. This is applicable to static analysis cases in

TABLE 1   STATIC ANALYSIS LOAD CASES

Case #	Force (lb.)	Description
1	119,000	Left idler horizontally rearward
2	89,250	Both idlers horizontally rearward
3	119,000	Left idlers vertically upward
4	89,250	Both idlers vertically upward
5	79,333	#1 road wheels and sponson vertically upward
6	39,667	Remaining road wheels and sponson vertically upward
7	11,333	All road wheels laterally
8	13,600	All road wheels vertically upward
	6,800	All road wheels laterally
9	55,533	Left final drive horizontally forward
10	41,650	Both final drives horizontally forward
11	55,533	Left final drive vertically upward
12	41,650	Both final drives vertically upward
13	23,250	Ft.-lb. moment both final drives
14	113,333	Front tow hook 60° upward
15	113,333	Front tow hook 60° downward
16	113,333	Rear tow hook 60° inboard
17	113,333	Rear tow hook 60° outboard
18	113,333	Lifting lugs vertically upward
19	100,000	Gun firing horizontally rearward

which the rate of change of the applied forces is sufficiently small compared to the lowest frequency of the structure.

In normal mode analysis, free-free eigenvalues and eigenvectors of an undamped structure are considered. To facilitate eigenvalue extraction, generalized dynamic reduction coupled with Modified Givens method [3] are used. Generalized dynamic reduction is preferred because of its high degree of accuracy for models of this size in which mutiple modes are required. Modified Givens method is used for its ability to overcome numerical problems associated with near sigularities in the mass matrix. The normal mode analysis results help identify the dynamic behavior of the hull and will be useful for firing control studies of the armament systems.

STM SYSTEM FINITE-ELEMENT MODEL

A three dimensional finite-element model representing the STM structure and mass is assembled for static and normal mode analyses by the MCS/NASTRAN general structural analysis computer code. The model corresponds to a fully loaded, combat ready condition including crew, armament, fuel, ammunition, armor, etc. The source data for modeling is primarily derived from design and fabrication drawings of the STM hull.

The system model, as shown in Figure 2, is composed of separate front, center, and rear hull sub-models joined together at their interfaces. The sub-models have been used in the design development phase to conduct structural analyses which helped guide design improvements of local structures. While the hull structures

154

are modeled elastically, the suspension components, turret, and non-structural masses are modeled rigidly. Shell-type elements are used to model not only the exterior skin of the hull, but also its internal bulkheads as shown in Figure 3.

Hull frames, stiffeners, and floor bars are represented by beam-type elements as shown in Figure 4. The hull model also includes major openings, such as the engine compartment opening, entry and escape hatches, engine air intake and exhaust vents, and the opening of the battery compartment. The removable covers of these openings are considered nonstructural masses which do not contribute to the hull stiffness. Similarly, the applique armor plates are also considered as nonstructural masses in the model. The model statistics consists of 1,299 grids, 1,146 shell elements, 429 bar elements, 231 rigid elements, and 40 concentrated masses. The total number of active degrees of freedom (DOF) is 5,241.

In general, modeling detail is relatively refined in areas where higher stress gradients are expected. These include the areas of external load application, such as the front idler attachment, road wheels, final drive, towing hooks, and lifting lugs.

The front idler attachment is considered one of the most critical areas due to the large idler impact loads. To facilitate the idler load input to the model, the idler shaft, housing and track adjustor are all rigidly modeled. Housing bolts designed to carry tension are connected only in the direction normal to the mating surface. A key down the center of the housing designed to carry shear is connected along the in-plane directions. Since the idler shaft is free to rotate in the housing, the shaft is connected to the housing in only 5 DOF. This rotation
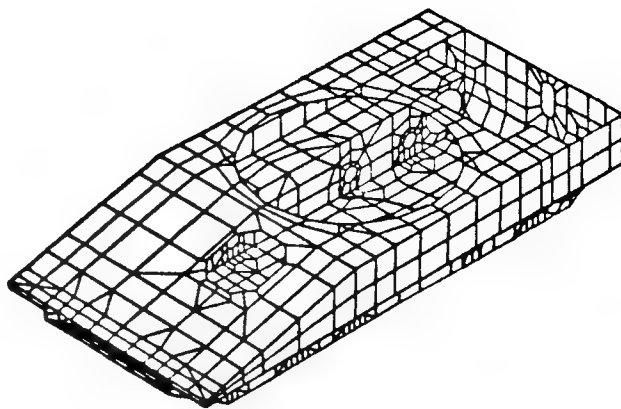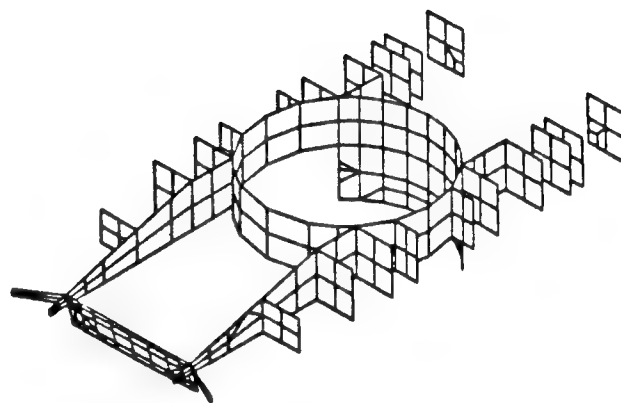

Fig. 2 – STM Hull System Model

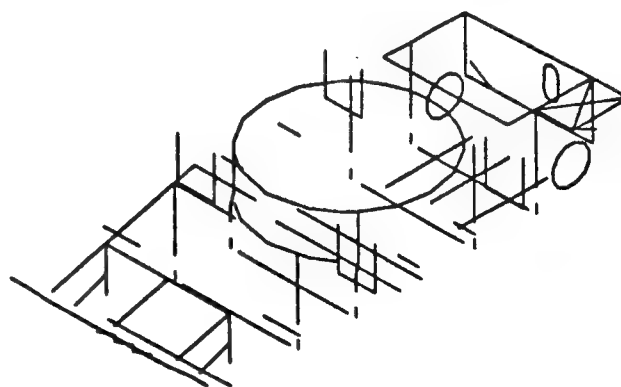Fig. 3 – STM Hull Internal Plates

Fig. 4 – STM Bar Structures

155

is prevented by a track adjustor represented by a pin-ended rod element connected to the lower side wall. Idler loads are applied to the end of the shaft.

The hull structure supporting the idler attachment includes a thick mounting plate between idlers. The center area is lightened by machining out 8 waffle pockets with the skin modelled by shell elments and the stiffeners by bars. A nose bar made of beam-type elements running the full width of the leading edge is connected rigidly to the upper and lower surfaces supporting one side of the mounting plate. The other side is supported by an internal nose bulkhead with a thickened triangular gusset at either end. The hull walls are also thickened locally in the track adjustor area and an internal stiffener modelled with bar elements is added to resist the track adjustor loads. Grid points for the outer walls are placed at the mid-plane of the thinnest plate. Since the outer surface was kept planar, locally thickened elements were offset inwards to represent their eccentricity.

Road wheel attachements are composed of rigid plugs representing heavy attachment rings connected to ground by rigid elements representing the suspension arms. Vertical supports extending up and down the inside sidewall surface at each plug are modelled by offset beam-type elements. Care was taken to rigidly connect the lower end of these beams to grids in the floor to realistically distribute the support beam torque into the floor. Four road wheel supports also act as turret supports feeding turret loads down to those wheels.

Though not part of the structural hull, the final drive housings provide a large degree of stiffness that can not be ignored. The housing is represented by a ring of beam-type

elements around the final drive opening whose properties closely match those of the housing. The load application point representing the sprocket wheel is modelled by an RBE3 type rigid element which imposes only averaged displacements. This allows forces to be transfered without creating undue restraint. A thickened sidewall to which the housing is mounted is also offset inward.

Towing and lifting hooks are included to allow realistic load distribution and hook offset. Rigid elements are used for all but the rear tow hooks where triangular shell elements are used to simulate local design details.

To eliminate the need of designing and fabricating a turret, an extisting lightweight M-551 turret is used in the STM vehicle. Because this turret is much stiffer than the hull, it is idealized by a series of semi-rigid rod elements. Bearing effects on the turret/hull interface are included since the ball bearings can only transmit compressive loads normal to the bearing races. Rod elements, connected to these points, intersect above and below the center of the turret ring. By rigidly connecting these two points, a rigid turret model consisting of two sets of eccentric rods is formed. Each rod is actually composed of two parallel bar elements, one made very stiff and the other very soft. This allows for adjusting the bearing distribution by iterating in critical load cases. Stiff elements are freed if in tension while the soft indicator elements are used to check load direction during successive iterations. This modeling arrangment will be particularly useful for studying the effect of turret flexibility on the hull.

Structural mass is included by specifying the mass density for all structural elements representing the aluminum hull. Non-structural mass is accounted for in one of two ways.

Applique armor takes advantage of the existing FEM by selectively increasing element density in those areas covered by armor. The remaining items shown in Table 2. are idealized as point masses at their C.G. connected rigidly to the hull. The turret mass is attached to the rigid turret structure while the power train is connected by an RBE3 to support beams along the engine compartment floor. Both include moments of inertia. The sprung portion of track and suspension is divided between idler, road wheels and final drive using the load application rigid elements. Fuel tanks are divided into 5 groups, each connected by weighted average constraint elements to the surrounding walls in directions normal to these surfaces. Track armor skirts are pinned to the lower outside corner of each sponson and attached normal to the bottom sidewall. The drive seat, ammo rack and controls are each attached to the foward floor area. Batteries and engine compartment cover are included in the rear. An externally mounted fuel tank is also attached to the outside rear wall.

ANALYSIS RESULTS

Stress and deformation results are obtained by imposing the above-decribed load cases on the system finite-element model. The analysis results indicate that only four areas appear to be critical. These include the front idler, tow hook (front and rear) and lifting lug loads. All load cases, however, produce only local areas of maximum stress.

The front idler load cases, shown in figures 5 and 6, produce stress levels up to 35 ksi in the lower sidewall, idler attachment pad, and escape hatch corners. Horizontal loading at the idler is carried, in part, through the track adjustor attached to the lower sidewall. Vertical loading at the idler, however, passes directly

TABLE 2   MASS SUMMARY

Description	Weight (lb.)
Turret (combat ready)	10,780
Spung suspension & track	4,586
Structural hull	3,476
Applique armor	3,152
Engine & transmission	2,500
Track armor skirts	1,600
Fuel	1,626
Ammunition	733
Reserve fuel tank (w/fuel)	427
Engine compartment cover (w/armor)	337
Batteries	300
Driver & seat	283
Converter, controller, amplifier & circuit breaker	128
	29,928

through the attachment pad causing compression in the sidewall and sponson bulkhead above.

Front tow hook load cases, shown in Figure 7 and 8, give results similar to the front idler load cases. This is expected since towing loads are transmitted to the hull through the idler housing.

The rear tow hook load case, shown in Figure 9, produces local stress levels as high as 25 ksi in the lower sidewall around the final drive attachment as well as 36 ksi in frame members located in the rear wall. The load case shown represents the worst case with regard to pull direction.

Lifting lug loads produce stresses up to 40 ksi in the frame structure surrounding the engine compartment opening. Only the rear two lugs are considered a problem and will require design changes to meet the loading conditions.
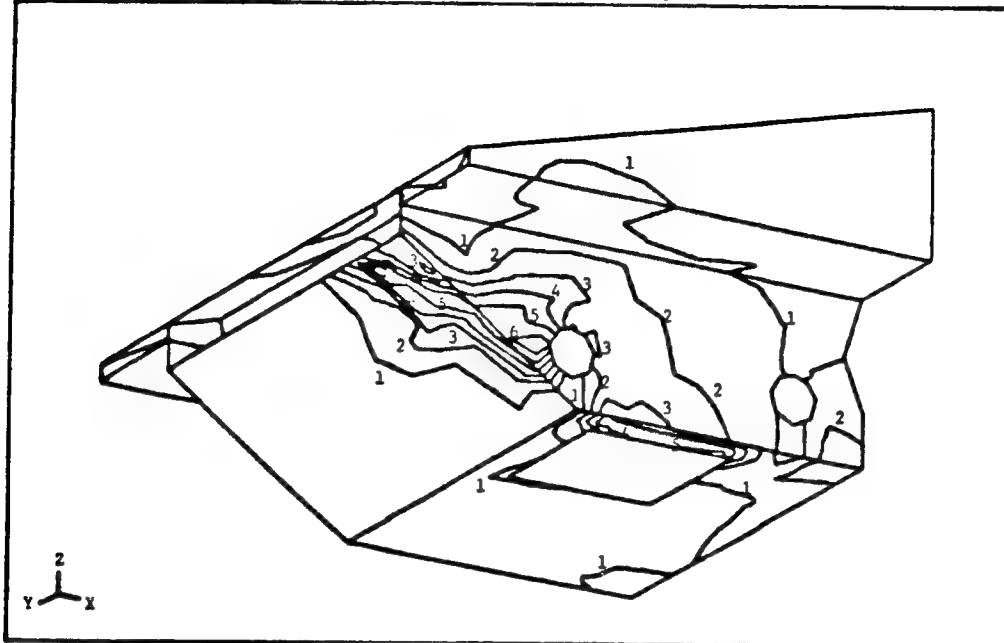
Fig. 5 - Front Idler Horizontal Load Case Stress Contours
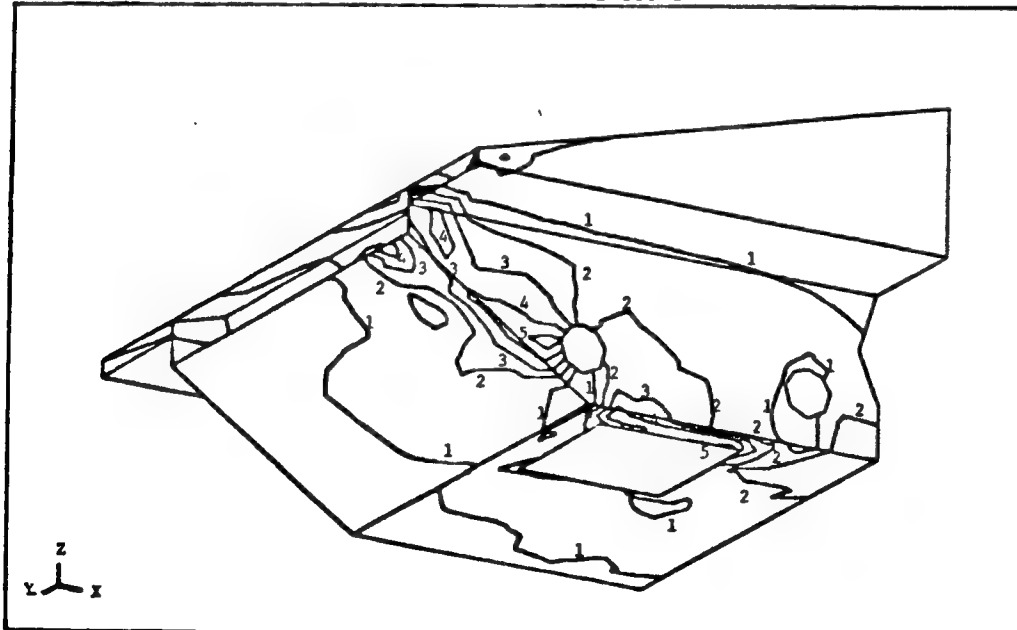
Fig. 6 - Front Idler Vertical Load Case Stress Contours
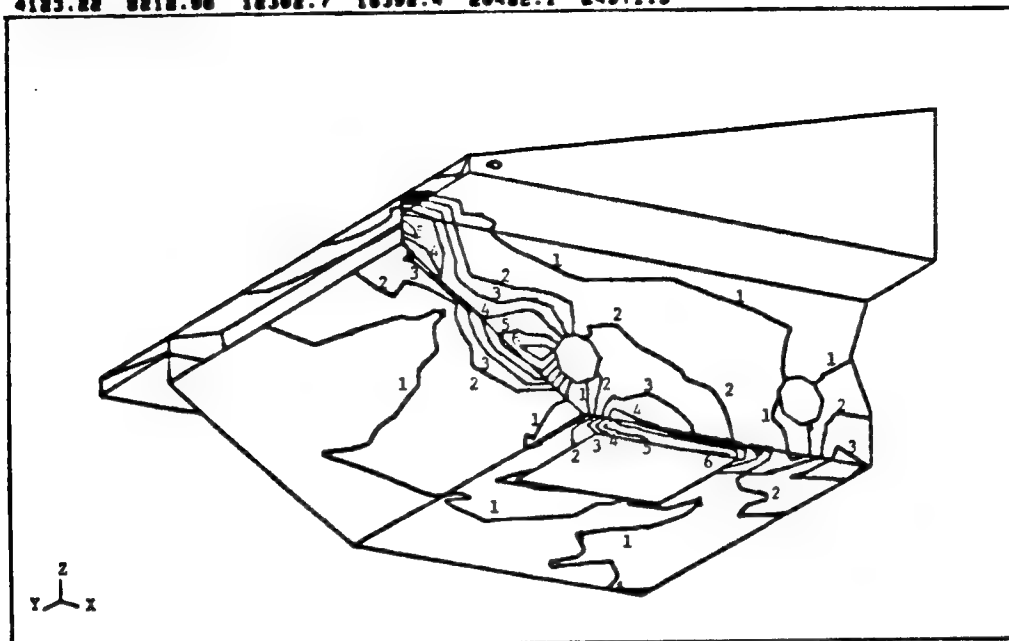
Fig. 7 - Front Tow Hook Upward Load Case Stress Contours
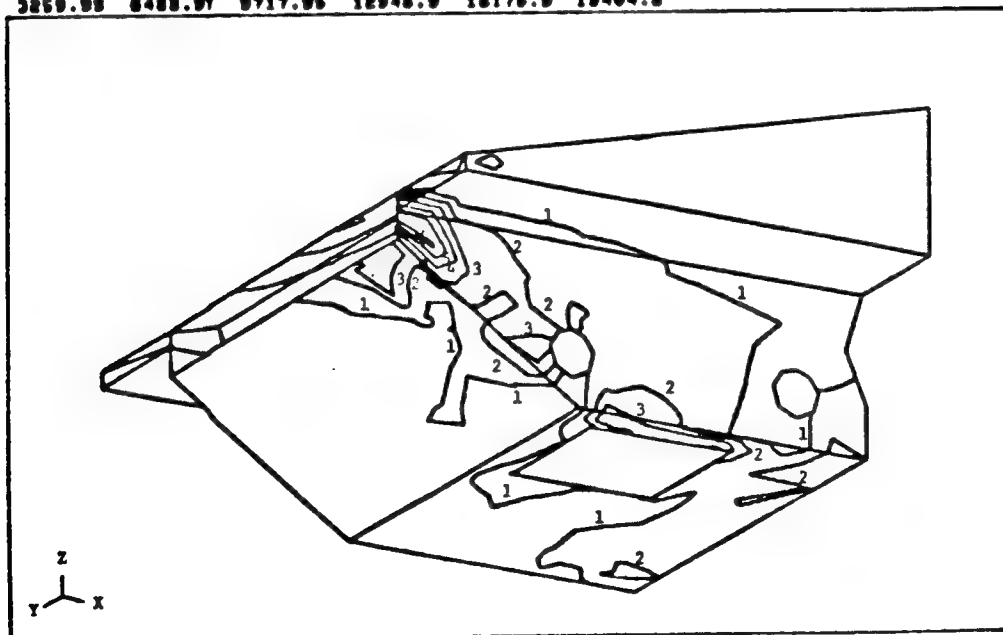
Fig. 8 - Front Tow Hook Downward Load Case Stress Contours
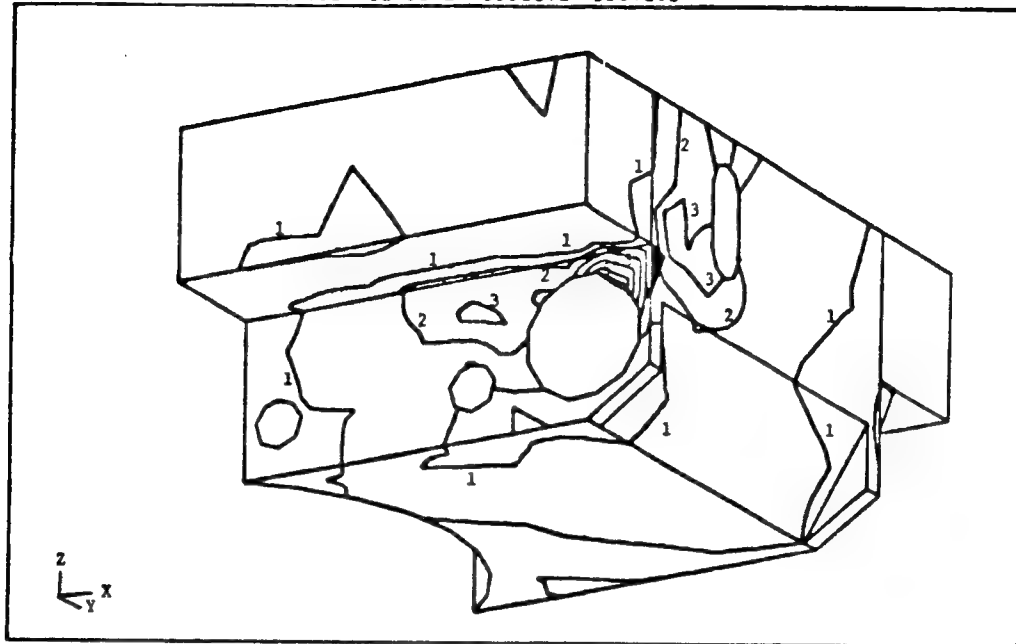
Fig. 9 - Rear Tow Hook Outboard Load Case Stress Contours

Subsequent to the static analyses, normal mode analysis using basically the same STM system finite-element model was performed. Results of this modal analysis indicate that, in addition to the six rigid-body modes, the free-free STM structure has ninteen elastic modes with frequencies under 50 Hz. However, close examination of the mode shapes revealed that most of these elastic modes involve only local deformation near concentrated masses representing some large non-structural items (e.g. the external fuel tank, ammunition carriers, engine compartment cover, etc).

Only two of them are global structural modes. The first structural mode, see Figure 10, is a combined turret/hull bending mode with the turret and gun bouncing out-of-phase with the hull at 37.3 Hz. The second structural mode, see Figure 11, is a hull torsional mode with the front and rear hull sections undergoing rolling motions in opposite directions at 41.5 Hz.
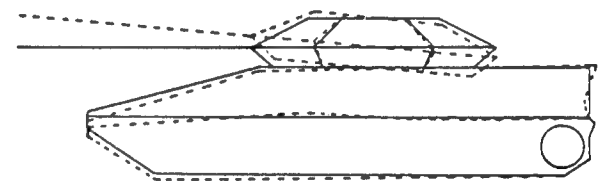
Fig. 10 - STM Bounce Mode @ 37.3 Hz
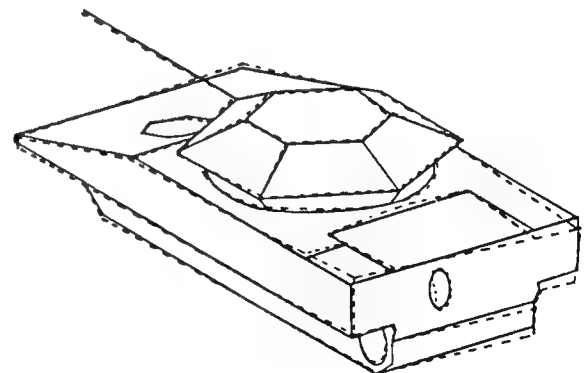
Fig. 11 - STM Torsion Mode @ 41.5 Hz

160

SUMMARY

Static and modal analyses of an experimental ACV were performed using the MSC/NASTRAN finite-element computer code. It was demonstrated that the application of FEM analysis procedures to supporting ACV design are highly beneficial. Structural deficiencies can be readily identified and redesign options evaluated in a timely and efficient manner.

REFERENCES

1. Engineering Design Handbook, U.S. Army Material Command Headquarters, AMCP 706-357, April 1970.

2. Schaeffer, H.G., MSC/NASTRAN Primer , Schaeffer Analysis Inc., New Hampshire, 1982, 309-10.

3. Gockel, M.A., ed., MCS/NASTRAN Handbook for Dynamic Analysis, MacNeal-Schwendler Corp., California, June 1983.

M60-TORSION BAR RELIABILITY

R. BARSOUM*, W. BETHANEY, R. BROCKLEMAN, H. HATCH, C. HICKEY, D. NEAL

Army Materials & Mechanics Research Center
Watertown, Massachusetts 02172

ABSTRACT

The life prediction and reliability assessment of the M60 tank torsion bars was obtained from a developed methodology using several disciplines of engineering and material science. The disciplines are: structural mechanics, fracture, statistical reliability, mechanical testing, non-destructive examination (NDE) quality assurance (QA) and metallurgical and fractorgraphic evaluations.

The methodology was applied in order to assess the means for increasing bar life and enhance the reliability of the tank. Usually, U.S. Army reliability performance is measured in mean miles between failures (MMBF). In order to introduce a more meaningful measure of component acceptability, this paper describes the means for obtaining minimum life estimate at a specified probability of survival using the Monte Carlo method. This includes predicting remaining life, with known risk and an approach to perform trade off costs or redesign against increased life. The result is a more meaningful measure of component acceptability. The reliability vs. bar life computation indicated a negligable amount of life after a bar flaw was initiated. The minimum life estimates for crack initiation were in good agreement with actual failure results at Aberdeen Proving Grounds.

INTRODUCTION

The M60 tank, which was developed in the 1960's, is still the principal Army heavy tank. It is currently undergoing a major "Rebuild" program to increase its effectiveness. The M60 program manager has expressed concern regarding the reliability of various components of the overhauled tanks as a result of failures experienced during proving ground tests. In a report to Congress, January 29, 1980, the GAO expressed a similar concern on the reliability of other systems. This study is an effort by an interdisciplinary task group assembled at AMMRC from specialists in material science, engineering, structural mechanics, nondestructive testing, and statistical analysis. The charter of the task group was to develop a methodology for life prediction of structural components in the M60 tank. The torsion bar (Figure 1) was chosen because of the availability of a fairly comprehensive history at AMMRC, proving grounds and overhaul depot. Torsion bar failure can lead to

---

*Principle Author

reduced mobility and track throwing or failure to other overloaded bars and eventual total loss of mobility of the tank.

Visits were made by the task group to include: manufacturing facilities, the overhaul depot, field test sites, AMSAA and TACOM, for data and information collection. Detailed failure analysis metallurgical examination, material testing, NDE, detailed stress analysis and a comprehensive probablistic analysis were completed by the group. The paper will discuss in details the above studies, tne major findings of the sensitivity analysis and final conclusions as to design improvements, material requirements and the feasibility of predictive methodology for torsion bars. The methodology used here circ umvents the present deterministic approaches used in establishing design life. It simulates variability of loading and material by introducing a probablistic design method.

RELIABILITY AND LIFE PREDICTION METHODOLOGY:

The approach taken to developing life prediction methodology was basically to obtain as much data about the torsion bar as the program would allow, analyze the data, perform the reliability study and make recommendations.

The M60-task group visited various manufactures of the torsion bars and obtained quality assurance procedures, test results, manufacturing procedures and machining methods (General Dynamics and FMC). Data obtained from the developer, the Army Tank and Automotive Command (TACOM), covered requirements and specifications, DMWR (1) and user experiences. Aberdeen Proving Ground (APG) test facilities and the Materials Testing Directorate provided data on loading from specific course and carefully monitored failure incidents. The Anniston Army overhaul depot provided inspection procedures information, NDE and replacement requirements. A major part of the material data generated involved mechanical and various metallurgical properties, and their relation to the specification. These properties were then incorporated with the data bank obtained from the QA testing of the manufacturer and published data on the material. The methodology then requires accurate analysis of the mechanical loading, stresses, fatigue and fracture evaluation of the torsion bar.

Finally, all the data is incorporated in a Monte Carlo method (2) for assessing the reliability of the torsion bar. Conceptually this method is quite simple, requiring modeling of the spectrum loads and the material fatigue life with respect to crack growth or stress/cycles to failure (S/N). The reliability of a single torsion bar (or system) can then be studied under various assumptions of terrain, speeds, improvement in designor material, inspection procedure, replacement period or any combinations.

MATERIAL CHARACTERIZATION DATA:

The metallurgical data reported here was obtained from analysis of the failed torsion bars obtained from Aberdeen Proving Grounds (APG) and bars from Anniston Army Depot.

METALLURGICAL EVALUATION AND OTHER MECHANICAL PROPERTIES:

A metallurgical evaluation was conducted on two failed M60 torsion bars, one produced by General Dynamics (GD) and the other by Machine Products Company (MPU). The parameters addressed in this evaluation are: chemical analysis, light microscopy, retained austinite, hardness traverse-spline and body, tensile properties (RT), Cv impact transition curve (longitudinal and transverse, and fracture toughness (RT & -40°)(LT & TL orientations).

Table I contains a near complete chemical analysis for the GD material plus a carbon and sulfur content for the MPU product. As can be seen the GD bar conforms to the specifications for AISI 8660, which is also shown in Table II. It also meets phosphorus and sulfur requirements (0.040% each) in MIL-5-45387BAT.

Table II shows the results of a hardness traverse in both a spline and body location for the GD material and the spline location for the MPU bar. It can be stated that both companies meet the hardness requirements of HRC 47-51 per MIL-5-45387BAT.

Tensile data from the GD bar are shown in Table III; Duplicate tests were conducted and the data is consistent. Longitudinal and transverse V-notch charpy impact energy and fibrosty data for the GD material are shown in Table IV. Based on a 100% fibrosity criterion the transitive temperature for the longitudinal orientation is about 400°F. The impact energy at this temperature is 9 ft-lbs. Room temperature fibrosity is about 10% with an energy level of 7 ft-lbs. Transverse data were obtained at room temperature and -40°F and are lower than the longitudinal values.

Fracture toughness data Table V (K_O) were obtained at room temperature and -40°F in both a LR and TR orientative from a GD bar and room temperature TR from a MPU. Room temperature LR values are higher than TR, 43 vs. 38.3 ksi in. GD TR data is slightly higher than MPU, 38.3 vs. 34.2 ksi in.

Microstructural and retained austenite studies were also conducted on the GD material. The microstructure consisted of primarily tempered martensite and the retained austenite was 3% or less.

Based on the tests conducted on both of these torsion bars it was concluded that each meet the specifications. However, it is highly recommended that a V-notch charpy energy requirement be added to the specification. It is further felt that the 4350 should be explored as a coandidate replacement for the torsion bar application in the M60 tank.

FAILURE ANALYSIS:

In addition to the metallurgical investigations which were performed on the failed torsion bar, fractographic examination was also performed. One of the basic principles of failure analysis is the preservation of the fracture surface in a condition as close as possible to that at the time of failure. Another is a compilation of historic data concerning the failed component.

165

The first principle issue was not achievable since, the available torsion bars were found in scrap bins at either the depot or testing grounds, resulting in fracture surfaces with some rust on them. The second issue was resolved by using statistical random loading spectrum which will be discussed later.

Figure 2a shows a typical field failure which was obtained from Anniston. Other failed bars detained from APG, Ft. Knox and GD exhibited similar failure. They obviously initiated within the splines at the ends of the bar, and in most cases at the wheel arm end, with the exception of one case that was observed at APG where the failure was at the anchor block end. These observations are supported by three other reports obtained from the Measurement and Analysis Division at APG, Ref. 4.

Light microscopy and Scanning Electron Microscopy (SEM) were used in the examination of the fracture surfaces. The failed bar in Fig. 2a was cut open and examined, figures 2b, c show the origin of the fracture. The arrow on figure 2b shows the surface of the serration which experienced surface plastic flow at the initiation site. This indicates high stresses at the inner end of the splines. In figure 2c, there is a slight indication of fatigue marking but not as large as usual. The SEM examination, figure 2d, however did not show the usual striation bench marks associated with fatigue crack growth. This indicated that once fatigue crack initiation has occured the propagation stage was very short. Further away from the initiation site, the fracture surface showed signs of corrosion hydrogen embrittlement. It should be noted here that the fracture surface was old and could have been contaminated by the environment after failure.

STRESS ANALYSIS:

The stress analysis of the splines was performed to evaluate various probable modes of failure. For the spline teeth, the possible modes of cracking are; longitudinal, inclined, and transverse, w.r.t. the axis. Such cracks are associated with various stress states, where the predominant are torsional shear stresses, Hertzian stresses, and bending stresses. Such stress state is three dimensional in nature and is very expensive to analyze. Therefore, three types of stress models were chosen to simplify the problem. The final results were combined.

i.   Bearing Stresses on Spline Teeth

Due to the existence of a missing tooth in the spline, it is suspected that the highest stressed area in bearing would be in that location. The bearing stresses were evaluated assuming that the load on the missing tooth is distributed equally on both neighboring teeth (Case 1) or only on the forward tooth (Case 2). The analysis was carried out using substructuring and super position of the two load cases.

The stresses produced by the contact forces depend on the number of teeth in contact, and the distribution of contact force along the teeth. The number of teeth in contact depends on the tolerances, misalignment and load, while

the distribution of the contact force depends on the teeth shape and moments of inertia of the axal and block. Figures 3a-b show the finite element model used and the stresses resulting from bearing forces (case 1).

ii. Torsion of Non-Uniform Bar

The enlargement of the ends of the torsion bar, leads to stress concentrations at the fillets. The solution of this problem was carried out using the finite element method using a heat transfer analogy of the classical Michell torsion problem [1]. The finite element mesh and the results of this analysis are shown in figure 4a.

iii. Evaluation of Stress Intensities

In the fracture analysis, four crack locations were considered:

1) Surface crack in the shaft (Mode III)
2) Subsurface crack in the shaft (Mode III)
3) Surface crack in the spline area away from the missing tooth (Modes I and III)
4) Same as 3, but at the missing tooth (Mode I)

The Mode I analysis used the results of the finite element model in figure 5. Mode III results of Cases 1 to 3 were obtained by the solution of a St. Venant problem, figure 4b. The finite element penalty method was used for the a multiply connected region case. In all the above fracture analyses the quarter point crack tip elements were used, Ref. 5. More details about the methods used in the analysis and the results can be found in Ref. 11.

iv. Reduction of Stresses in Spline

As demonstrated from the failure analysis and from the bearing stress and fracture analysis, the splines are the most highly stressed region in the torsion bar. A reduction of the contact stresses can be accomplished through a more uniform distribution of the stresses by redesigning the splines. Figure 5 shows the bearing stress distribution from current spline design (uniform teeth). Using tapered teeth permits intensional redistribution of the contact stresses between the splines and end blocks. From the deformation of the splines it was calculated that a 0.005 in. tapering, increases the contact zone and reduces the maximum bearing stresses by more than 25%. Machining of such tapered teeth is accomplished using a gear shaper.

SIMULATION PROCESS AND RELIABILITY EVALUATION DUE TO RANDOM LOADING:

i. Amplitude Displacement Model

The angular amplitude distributions of three bars from tests conducted at Aberdeen Proving Grounds (APG) is shown in figure 6. Positive and negative angular displacements of the bars as function of tank travel, are shown in figure 6. In figure 6 the amplitude distributions are listed in a manner describing percent time less than by a plus sign (+) and percent time greater

than by a minus sign (-), (e.g. 25% level equals a -75% level). The + peak represents maximum angular displacement under load, the negative peak is maximum rewind angular measurement. The range of angular rotation $\Delta\theta$ is defined as follows,

$$\Delta\theta = \theta + |\theta^-|$$

where θ^- = maximum negative angular displacement   (1)

θ = displacement from figure 2b

The Beta distribution provided the best representation of the skewed amplitude distribution. The dampening effects that occured under load resulting from a stop used in preventing further angular twist of the bar producing a highly skewed discrete cumulative probability values. The Beta function is defined as:

$$f(\Delta\theta) = \frac{\Gamma(P+Q)}{\Gamma(P)\Gamma(Q)} (\Delta\theta)^{P-1} (1-\Delta\theta)^{Q-1}$$

$$0 \leq \Delta\theta \leq 1 \quad P, Q > 0$$

         (2)

The P and Q values are selected in a manner that provides the best Probability Density Function (PDF) for representing the data. Figure 7 describes a typical distribution. Angles less than 20° represent stresses sufficiently low that infinite torsion bar life could be expected, therefore, a good representation below this angle is not essential.

In figure 8, a typical result of M60 A3 torsion bar, positive and negative angular displacements vs. time are shown. The results were obtained for a DADS simulation process at TACOM. A stochastic model was introduced in order to simulate the bar response. Included in the figure are tabulated absolute amplitude values.

In order to represent the amplitude distributions, uniform probability density function was selected. The selection process involved evaluating an informative quantile (IQ) plot [9] of the amplitude data. In figure 9a, the IQ plot of data tabulated in figure 8 is shown, the straight line represents an exact uniform distriubtion with disjointed line representing actual data. Figure 9b is a schematic of a typical distribution model for DADS simulation data.

ii. Crack Growth Law for Estimating Torsion Bar Life

Initial efforts in applying the Monte Carlo Method for determining reliability vs. cycles to failure of the torsion bar involved using the crack propagation laws indicated a very short life. Due to the short life expended in crack propagation because of the operating stress levels, the results are not given here. Details can be found in Ref. 11.

iii. S/N Curve Analysis

Torsional bar life expectancy was obtained using the Monte Carlo process applied to the S/N Curve relationship. The procedure provided a method for obtaining life time estimates of the bar by combining the effects of crack initiation and propagation. A description of the S/N Curve is shown in figure 10, where the base line data was obtained from a literature survey for material metallurgically similar to the torsion bar material. The survey provided a set of S/N Curves for torsional fatigue shown below for best representing the current materials used in the bar.

$$\text{Log}_{10}N = B + .068 \, \Delta \theta \tag{2}$$

$$\text{where } B = 7.70$$

The slope value of .068 was essentially the same for all curves in the set. The adjustment in B from 7.70 to 8.06 is made on the basis of M60 torsion bar quality assurance tests at a single value performed at the Scranton manufacturing facility (see figure 11). A single load equivalent to a 42° angular displacement was applied during the quality assurance torsional fatigue test. Using the mean value and the cycles to failure in figure 11 provided a more accurate estimate of (B). The curves representing a range of 10 and 20 percent reduction in bar stress are shown in figure 10.

The S/N Curve Monte Carlo process uses Models for (B) and $\Delta \theta$ from figure 12a and 7 or 9b respectively. A schematic of the basic S/N representation is shown in figure 12a. In figure 12b simulation of S/N curve variability is shown for a specific value. Figure 12a describes probability density function (PDF) for (B). A random selection of a discrete set of numbers from $\Delta \theta$ and (B) distributions is then applied to equation 2 in order to obtain $\text{Log}_{10}N$ value. The process is repeated until all values from the two distributions are selected. This process will then provide a PDF to represent $\text{Log}_{10}N$.

iv. Reliability of Operation After Specific Number of Cycles

The reliability of operating an additional number of cycles when a specified number of cycles of operation has been completed is obtained using conditional probability. See details in Ref. 11.

v. Results of the Reliability Study

The proper number of simulations for the Monte Carlo Method depended on the models under consideration. For example 5000 and 3000 were required for the da/dN and S/N curve models respectively. Using a convergence rate criteria for the calculated 1 percent values and recognition of the third and fourth moment stability of the $\text{Log}_{10}N$ distribution provided an excellent method for determining required number of simulations. Differences in percentile values for coefficient of variation (C.V.) of 10 and 15 percent were minimum for da/dN simulation of parameters. The 10 percent value was used for all calculations.

169

The torsion bar reliability results from the da/dN relationship are given in Ref. 11. They indicated relative limited lifetime range of 14 to 500 miles, with a probability of survival values of .99 and .01 respectively. Analysis shows that an improvement in material will not significantly improve bar performance. On the other hand, a 25 and 50% reduction in K_I (stress intensity) leads to considerable increase in propagation life.[I] These reductions represent improvements in the design of spline section of the bar as shown in figure 5. Ref. 11 gives detials of K_I and K_{III} reliability figures as related to spline and shaft failure.

In figure 13, the failure probability obtained from S/N curve - Monte Carlo application is shown. The resultant exponential form is consistent with that expected from the S/N modeled in the analysis.

A graphical display of P_s vs. miles to failure is shown in figure 13 for the 25 mph tank velocity. The life expectancy of the bar is much greater than that obtained from the da/dN analysis. The minimum life estimates (.99P_s) of 292 miles is 21 times greater than 14 miles determined from the da/dN results. This result indicates that most of bar life occurs prior to crack initiation. Therefore the torsion bar should be manufactured in such a manner that flaws are minimized. The current shot peening used in the manufacture of the bar indicated recognition of this fact by the manufacturer. The bar reliability estimate obtained after an assumed 741 miles of tank travel are shown in figure 13. The increase of the Probability of Survival (PS) from .90 to .99 if the bar survives the initial 741 miles does not provide a sufficient gain to warrant re-using bars since the minimum increase in expected life is reduced very rapidly. The results from a 20 percent reduction in design stress of 865 miles for a PS of .99, is a considerable improvement when comparing that of 292 of the current design. In Ref. 11, the results from velocity ranging from 5 mph to 25 mph in increments of 5 mph are given with respect to current 10 and 20 percent improvements in design. Reducing velocies of tank operation obviously improves reliability of the torsion bar. Note, in this paper, the experimental data and reliability calculations refer to failure of the first bar.

Examination of current design mileage capability of the bar for 20 and 25 mph indicates a range from 276 to 292 miles. These results agree with 262 miles minimum life obtained from Aberdeen Proving Ground (APG) test results (Report MT-5376 of bar failure from 3 mile test course), (see figure 14). This course and tank velocity were similar to those used in obtaining the spectrum load results. The excellent agreement between the predicted and actual life expectancy of the bar indicates the desirability of Monte Carlo Process for modelling variability of spectrum loads (design stress) and S/N curve (material capability) results.

Although excellent agreement has been obtained, the authors would have preferred representing the spectrum load consistent with an individual peak to peak angular displacement. The simplification applied using the negative peak as base and representing the displacement relative to this value was a good approximation to the available individual displacements. This approximation would provide a slightly conservative estimate in the reliability values.

Using the ASTM recommended practice of representing lower 3 standard deviation band of the S/N curve as measure of material fatigue loading capability combined with maximum angular displacement (46 degrees) for 25 mph; the tank operation resulted in a minimum life estimate of 112 miles for the bar. Selecting this number as a design value could result in an overly conservative estimate. The chance that this maximum displacement could occur and the S/N curve was the actual lower band described above is extremely small.

A minimum life of 575 miles was obtained from using the maximum displacement value with original S/N curve where B = 8.06. This result is obviously wrong since in the limited samples of 23 bar failures two of them failed at mileage less than 400 miles (see figure 14).

Results from application of the Monte Carlo for DADS simulation data is shown in table VI. Probability of survival (PS) percentages and their corresponding miles of tank travel are tabulated for road arms 1L, 2L and 6L at 5, 18 and 25 miles per hour. The APG 12 (18 mph) course was the most severe according to the TACOM representative. The results from table V reflect this, since .99 percent PS of 14 miles was the lowest obtained from any of the computed life estimates at that PS value.

Since this course introduces unusually large angular displacements of the bar (1L) (see figure 3a) and requirements are only one failure in a hundred, this is not an unrealistic estimate of bar life. It is obvious from examination of table 4 that road arm 6L will survive much longer than either 1L or 2L. Traveling at 5 mph in such severe course will also increase bar life considerably.

NONDESTRUCTIVE TESTING CONSIDERATIONS:

Review of torsion bar field failure reports and examination of a number of fractured bars clearly illustrated that fatigue failures predominately initiate in the spline ends rather than in the reduced cross-section central gage length. Based on these data, it was initially considered that a periodic magnetic particle inspection for fatigue cracks in the spline surfaces would provide a technique for predicting premature failures. However, results of the subsequent fracture mechanics analysis reported herein has identified critical crack size as .019 inch. Furthermore, the analysis shows that an existing fatigue crack, .005 inch deep, will propagate to critical size within only a few miles. Therefore, if a fatigue crack equal to or less than .019 inch exists, failure is imminent.

It has been shown, Ref. 10, that a fatigue crack in steel must be greater than .030 inch for a 90% probability of detection at 95% confidence using the conventional magnetic particle inspection method. Significantly smaller cracks are indeed detectable using the technique, but probability of detection will be low in a production environment. Inasmuch as the torsion bar must be removed from the vehicle to conduct and inspection at some arbitrary time, detection of a crack less than .019 inch would be only by chance. It was therefore concluded that, in the case of the M60 torsion bar, even the most

sophisticated nondestructive crack detection scheme will not provide an effective life prediction technique. Once a fatigue crack initiates and could be detected, service life of the torsion bar has essentially ended.

CONCLUSIONS AND RECOMMENDATIONS:

1. A methodology for obtaining reliability of the M60 tank torsion bar subjected to cyclic random loads has been developed where probability of survival is represented as function miles of tank travel.

2. The developed methodlogy could be applied to other structures with cyclic random loads.

3. The use of the method appears justified from recognition of the excellent agreement between predicted reliability estimates and those obtained from the actual bar life (miles to failure) experienced during the tank operation.

4. Determination of minimum bar life was 21 times greater from application of S/N curve model than that of the assumed da/dN model. This indicates most of the bar life is expended in crack initiation.

5. Application of deterministic procedures, (use of lower 3 S.D bound for S/N curve (ASTM method) and mean S/N curve providing over and under design value estimates while Monte Carlo method outlined in the text accurately described acceptable design values.

6. Redesigning of the bars to reduce the stresses increases the life considerably. A slight improvement by 20%, is much more effective than requiring a higher toughness.

7. Recommendation of a revision to MIL-S-45387A, by requiring aircraft quality material and including requirements for grain size, cleanliness, and V-notch Charpy energy for room temperature and -40°C, can lead to longer life, but may be costly.

8. For new bars, it is recommended that materials other than 8660, such as 4350 steel be considered and the necessary data package generated. Also, induction hardening followed by shot peening should be explored.

9. Explore use of the torsion bar presetting operation at the depot as a proof test for re-used bars, and follow it by 100% magnetic flux inspection. Also, explore reshot peening of the whole bar, or replacement of the pinion and anchor blocks at the depot.

REFERENCES

1. Depot Maintenance Work Requirement, USATACOM, DMWR9-2350-253-1-5 "Suspension System Components for M60".

2. D.M. Neal and D.S. Mason, "Determination of Structural Reliability Using a Flaw Simulation Scheme", Army Materials and Mechanics Research Center TR81-53, 1981.

3. J.F. Lawless, "Construction of Tolerance Bounds for the Extreme Value and Weibull Distributions", Technometrics, Vol. 17 No. 2, May 1975.

4. Measurement and Anal. Div., Phys. Test Branch, APG, Report Nos. 78-M-4, 79-M-9, 80-M-34, and 82-M-57-STEAP-MT-G.

5. R.S. Barsoum, "On the Use of Isoparametric Finite Elements in Linear Fracture Mechanics", Int. J. Num. Meth. Eng., Vol. 10, pp. 25-37, 1976.

6. "Damage Tolerant Design Handbook", Metals and Ceramics Information Center, Battelle Columbus Laboratories, MCIC-HB-01, Page 8.2-D, 1975.

7. Ibid. Page 8.2-E.

8. J.M. Barsom, Transactions of the ASME, Journal of Engineers for Industry, Series B, 93, No. 4, Nov. 1971.

9. E. Parzen, "Entropy Interpretation of Tests for Normality by Shapiro-Wilk Statistics", presented at the Twenty-Eight Conference on the Design of Experiments in Army Research, Development and Testing, 20-22 Oct, 1982, Monteray, CA.

10. W. Rummel, et al., "Detection of Tightly Closed Flaws by Nondestructive Testing Methods in Steel and Titanium", Martin Marietta, Denver, Final Report MCR-76-476, NAS 9-14653, Sept. 1976.

11. R.S. Barsoum, et al., "Reliability and Life Prediction Methodology for M60 Torsion Bars", AMMRC-TR-to be published.

TABLE I

CHEMICAL COMPOSITION

SOURCE/MARKING	GD/JN	MPU/#5399	SPECIFICATION AISI 8660	
	WEIGHT PERCENT			
			MINIMUM	MAXIMUM
CARBON	0.63	0.54	0.55	0.65
MANGANESE	0.87		0.75	1.00
PHOSPHORUS	0.009		- - -	0.040
SULFUR	0.02	0.02	- - -	0.040
SILICON	0.21		0.20	0.35
NICKEL	0.58		0.040	0.70
CHROMIUM	1.02		0.04	0.60
MOLYBDENUM	0.15		0.15	0.25

TABLE II

ROCKWELL C HARDNESS

SOURCE/MARKING	GD/JN		MPU #5399
LOCATION	SPLINE TRAVERSE	BODY TRAVERSE	SPLINE
HRC	(48.0 - 50.3)	(48.5 - 49.9)	50.0

TABLE III

TENSILE PROPERTIES OF GD/JN TORSION BAR

ORIENTATION	0.2%YS KSI	UTS KSI	ELON %	RA %
LONG	231.4	257.2	8.3	28.4
	229.6	258.1	8.7	28.5
	230.5	257.7	8.5	28.5

TABLE V
FRACTURE TOUGHNESS

SOURCE/MARKING	ORIENTATION	K_Q, KSI $\sqrt{IN}$ TEST TEMP °C RT	K_Q, KSI $\sqrt{IN}$ TEST TEMP °C -40
GD/JN	LR	45.7	32.2
		40.3	24.7
		43.0	28.5
	TR	38.9	32.1
		37.7	31.8
		38.3	32.0
MPU #5399	TR	34.5	
		33.9	
		34.2	

TABLE IV
ENERGY AND FIBROSITY DATA FOR GD/JN

LONGITUDINAL ORIENTATION (LR)

TESTING TEMP °C	CHARPY IMPACT ENERGY FT-LBS	FIBROSITY %
-40 (-40F)	5.5	5
+22 (+72F)	7.7	10
+100 (+212F)	7.9	15
+160 (+320F)	8.8	50
+180 (+356F)	11.0	80
+220 (+428F)	9.0	100
+240 (+464F)	8.5	100

TRANSVERSE ORIENTATION (TR)

TEST TEMP °C	CHARPY IMPACT ENERGY FT-LBS	FIBROSITY %
+22 (+72F)	3.5	5
+22 (+72F)	1.8	5
	2.7	5
-40 (-40F)	2.8	5
-40 (-40F)	3.0	5
	2.9	5

PROBABILITY OF SURVIVAL VS. MILES
TACOM Simulation Course

			5mph (38 displ)			5mph (12 disp)	10mph			18mph			25mph		
	PS %		1L	2L	6L	1L	1L	2L	6L	1L	2L	6L	1L	2L	6L
Original Design	99		1467	8	8	2702	8	8	8	14	16	1324	620	1060	2289
	95		4859	8	8	5032	8	8	8	37	45	3107	1478	2594	5441
	90		12550	8	8	7433	8	8	8	70	89	5032	2471	4157	8777
	80		13900			11210	8	8	8	176	238	9502	4701	7827	17160
	70						8	8	8	398	590	18350	8354	13930	29280
10% Design Improvement	99		1618	8	8	3742	8	8	8	32	37	1941	1010	1660	3363
	95		3527	8	8	7694	8	8	8	85	101	4617	2424	3951	7981
	90		5487	8	8	11390	8	8	8	159	191	7290	3935	6245	12580
	80		9693			18760	8	8	8	359	467	13680	7246	11570	24010
	70					27860	8	8	8	792	1082	21980	12490	20130	29280
20% Design Improvement	99		2222	8	8	5107	8	8	8	65	74	2757	1523	2336	4686
	95		4732	8	8	10350	8	8	8	166	193	6321	3618	5623	10590
	90		7359	8	8	15420	8	8	8	301	361	9990	5717	8831	16910
	80		12910			25160	8	8	8	652	818	18420	10320	16020	29280

Table VI

SHOT PEEN SERRATIONS & BODY-SEE MFG NOTE

BEFORE SHOT PEENING

AT NO TIME SHALL THE TANGENT TO THE
BLEND RADIUS EXCEED 15°

CUTTER

$H_2 \pm .005$

$K_2°$
$\pm 0° 30'$

¢ REMOVED
TOOTH

F_2-APPROX
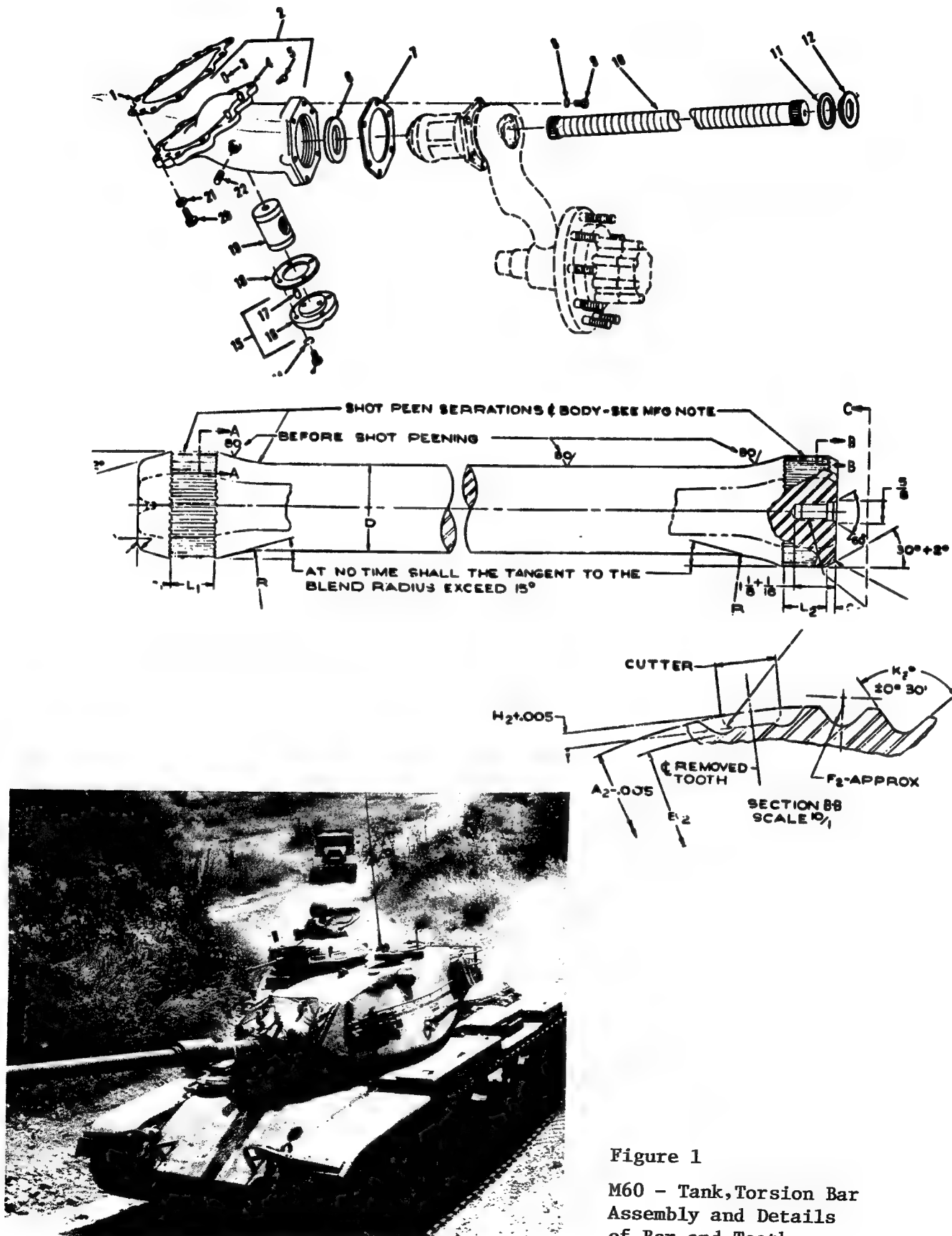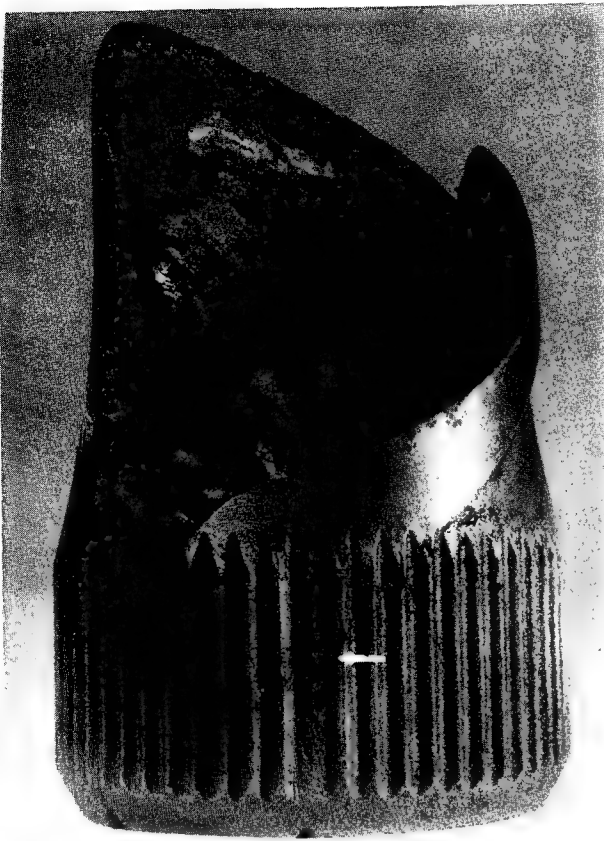
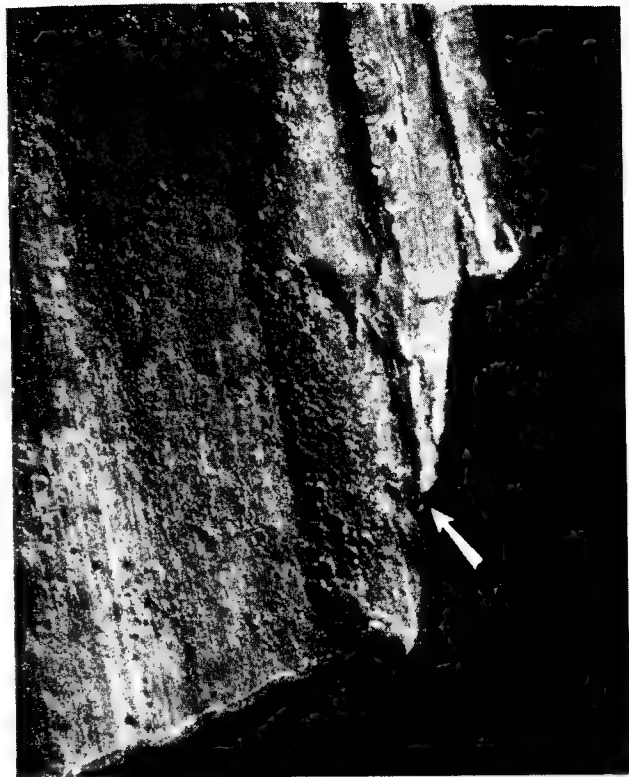$A_2 -.005$

E_2

SECTION BB
SCALE 10/1

Figure 1

M60 – Tank, Torsion Bar
Assembly and Details
of Bar and Teeth

(a) Origin

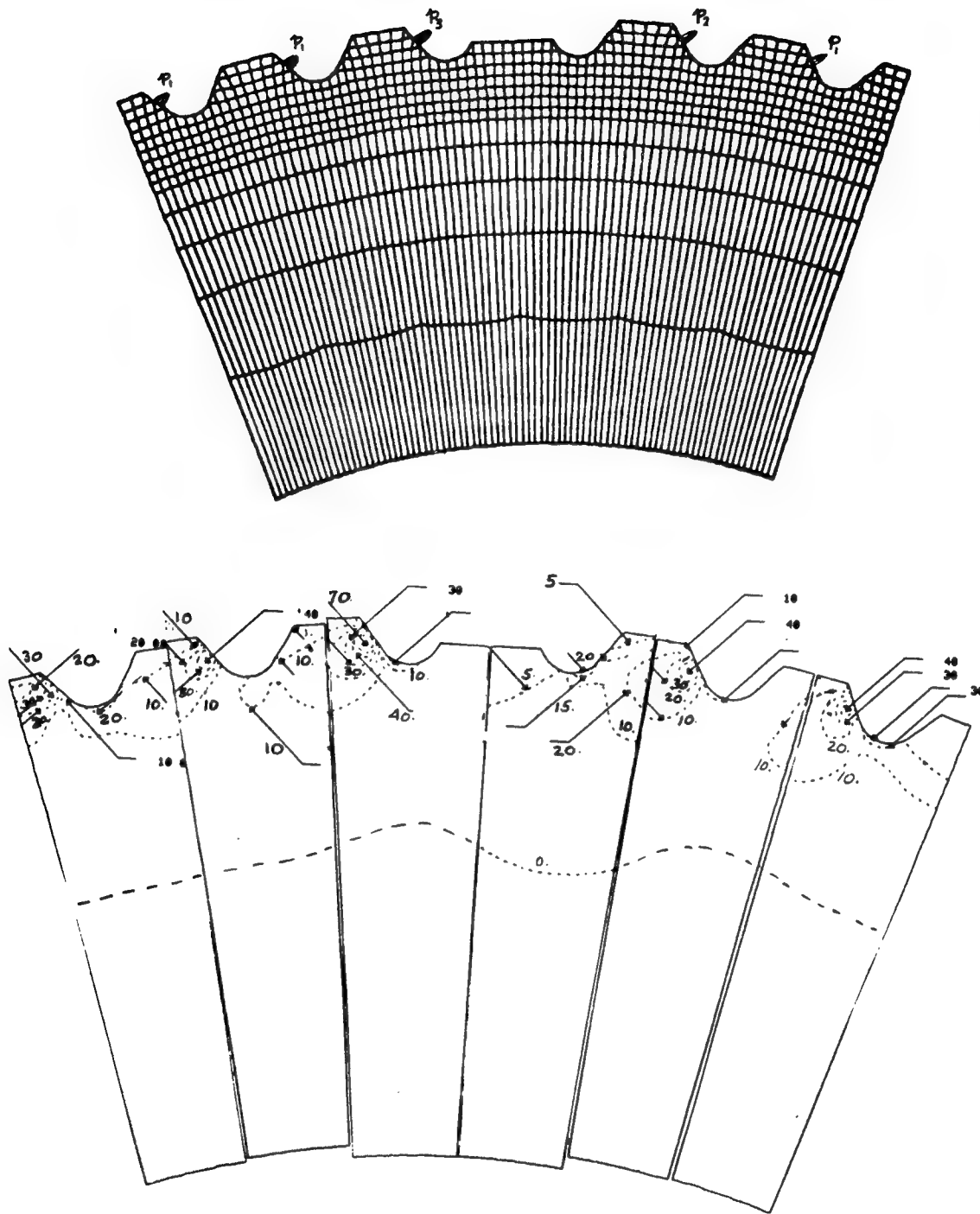(b) Plastic Flow of Teeth

(c) Initial Site

(d) SEM 500X – Corrosion

Figure 2   Field Failure

177

CONTACT STRESSES:
EFFECTIVE STRESS CONTOURS CASE 1

Figure 3   Finite Element Model and Contact Stresses

178

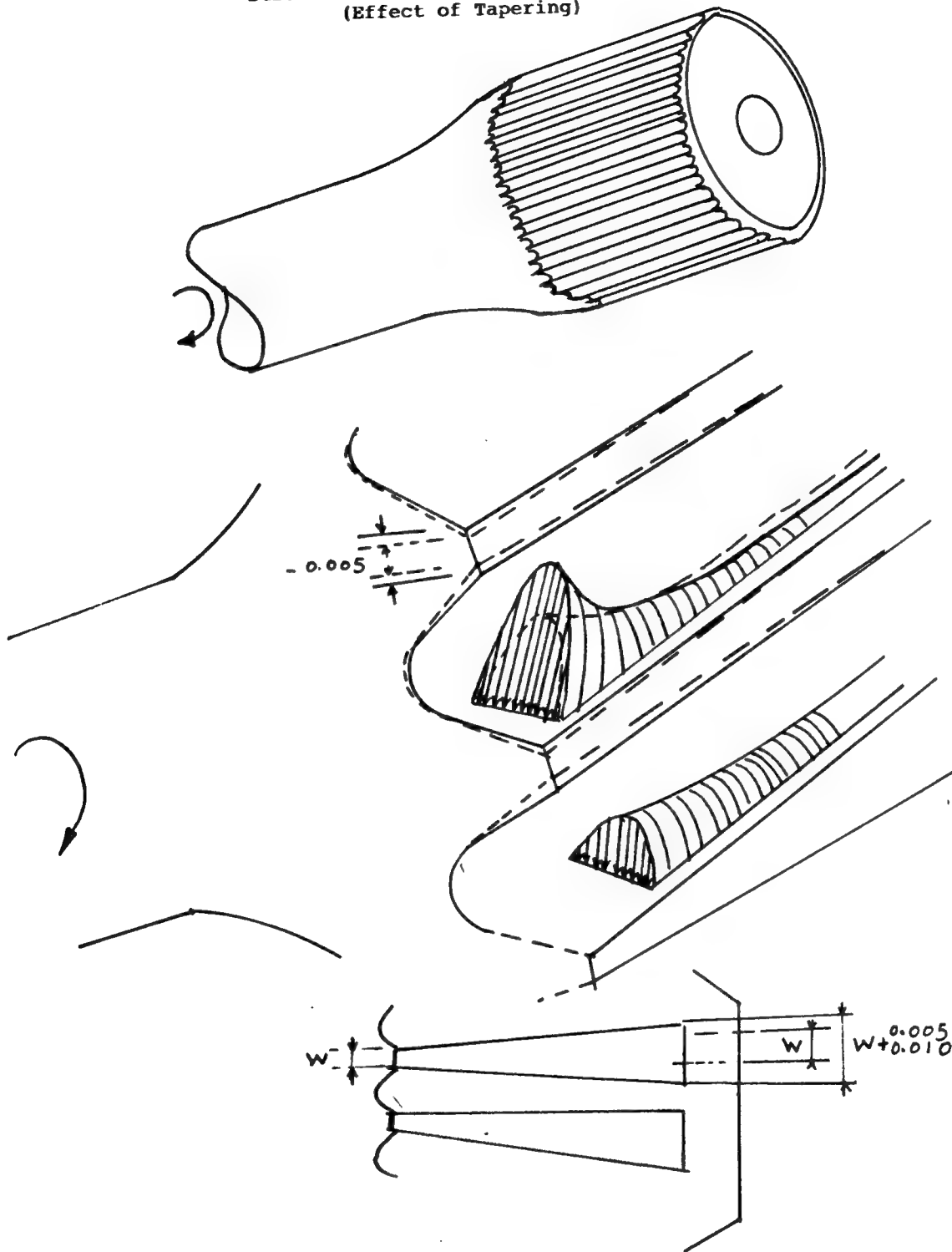Stress Distribution on Spline Teeth
(Effect of Tapering)
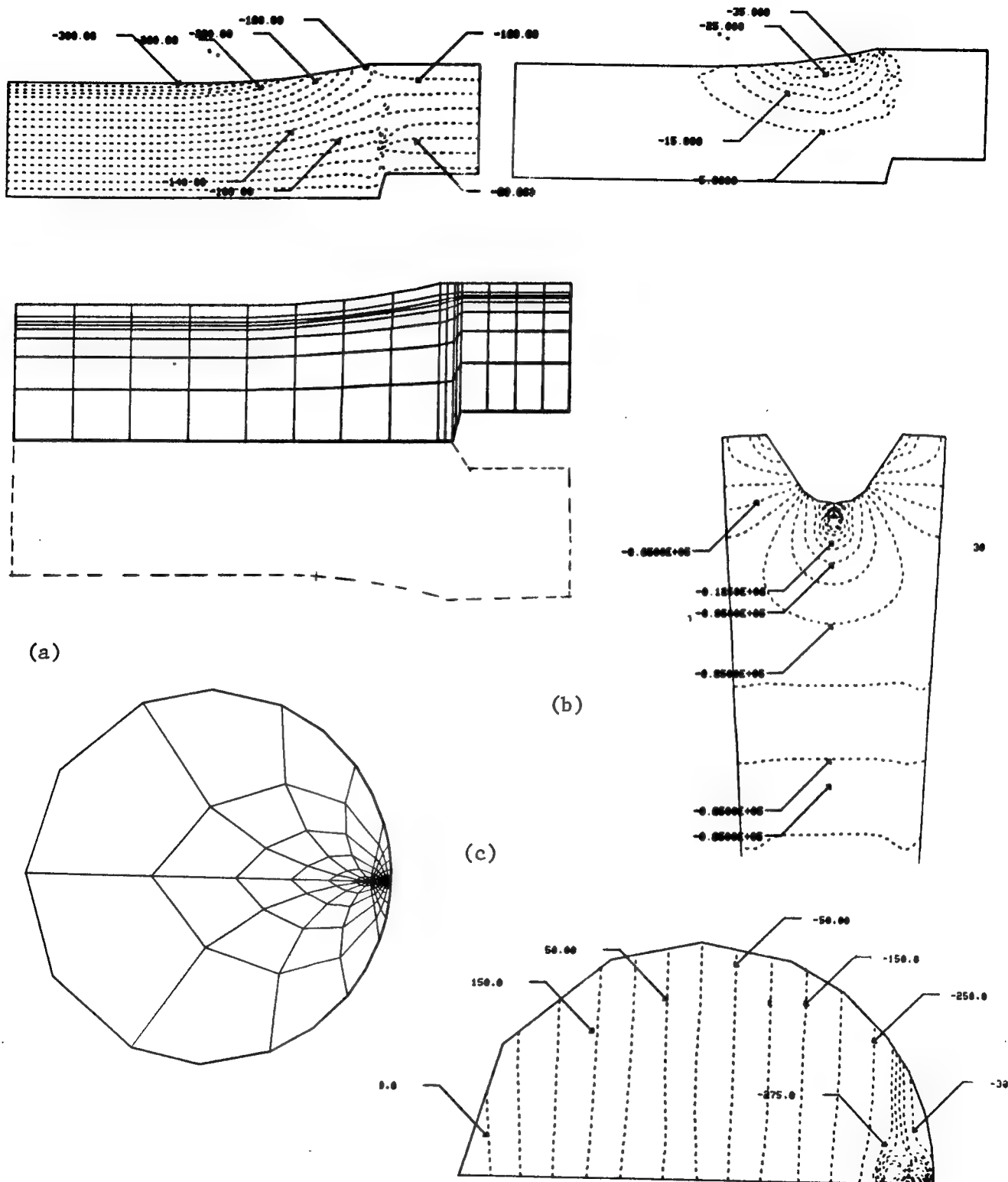

Figure 5   Redesign of Spline Teeth

179

Figure 4   Torsional Stresses
                (a) Non uniform C.S.,   (b) Crack in Spline
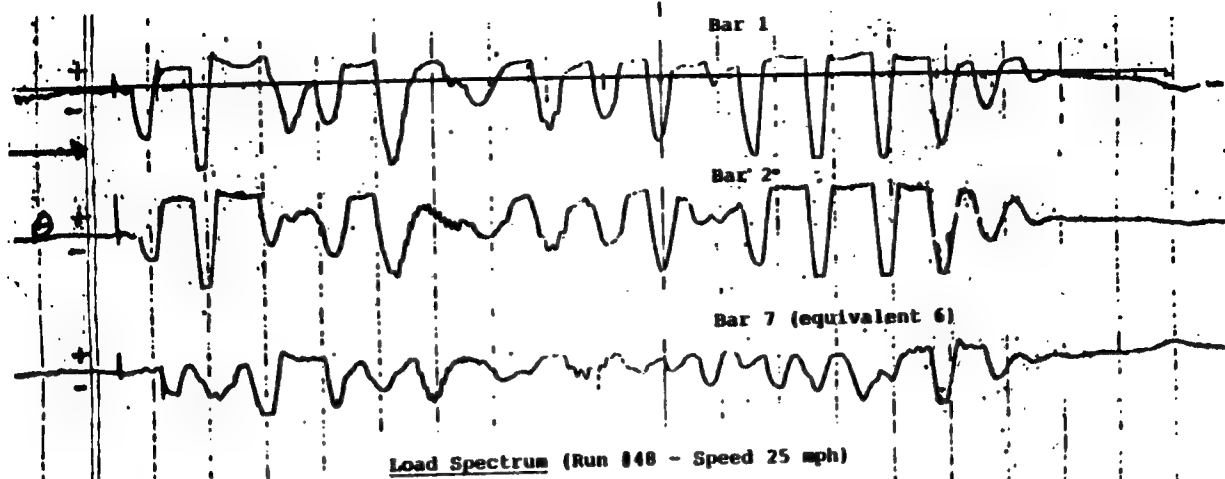   (c) Subsurface Crack in Shaft

Bar 1

Bar 2

Bar 7 (equivalent 6)

Load Spectrum (Run #48 - Speed 25 mph)

FIGURE 6a

Course Length 462 ft

AMPLITUDE DISTRIBUTION DATA RUN 48 (25 MPH)

	+ Peak	- Peak	+ 99%	- 99%	+ 66%	- 66%	+ 50%	+ 25%	- 25%
BAR 1	15.47	-30.71	15.33	-28.44	8.81	-3.51	3.00	-8.04	10.91
BAR 2	21.70	-28.92	21.42	-26.80	8.41	-7.43	-1.06	-11.53	13.92
BAR 7	13.91	-30.61	13.76	-30.47	6.63	-2.39	2.56	- 7.19	8.35

FIGURE 6b

Beta Distribution

Probability Density

Spectrum Load Representation (Run #48 - 25 mph)
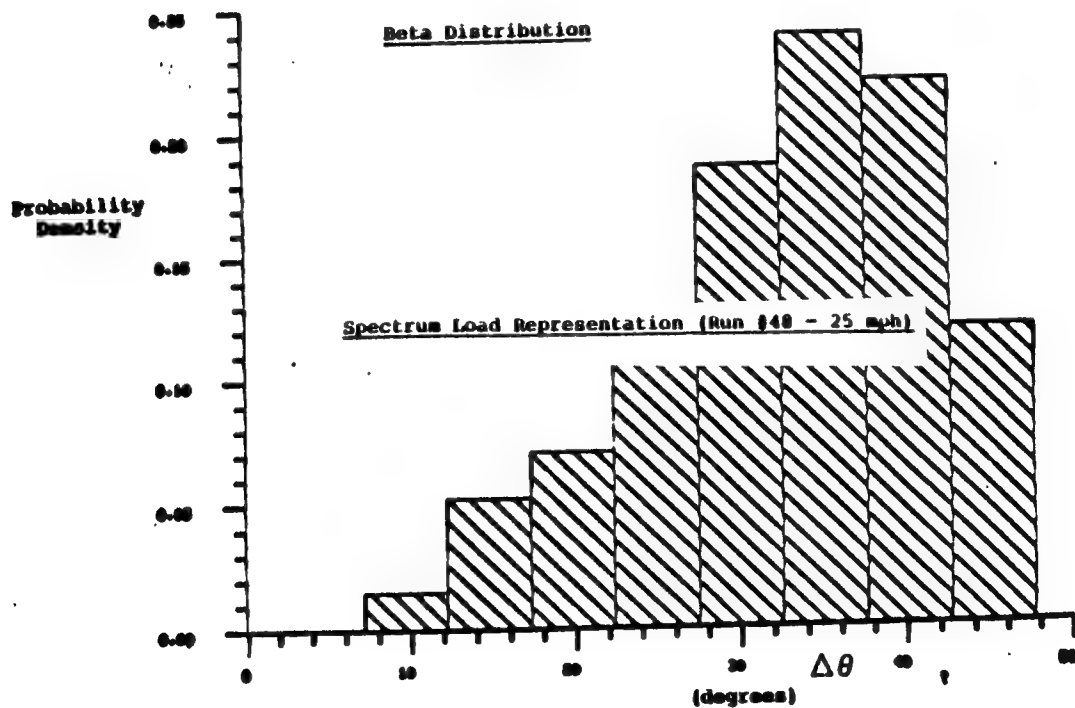
$\Delta\theta$
(degrees)

FIGURE 7

M60A3-APG12 COURSE-18MPH-ROADARM 1L ROTATION

YMAX = 0.40993

YMIN = -0.65729
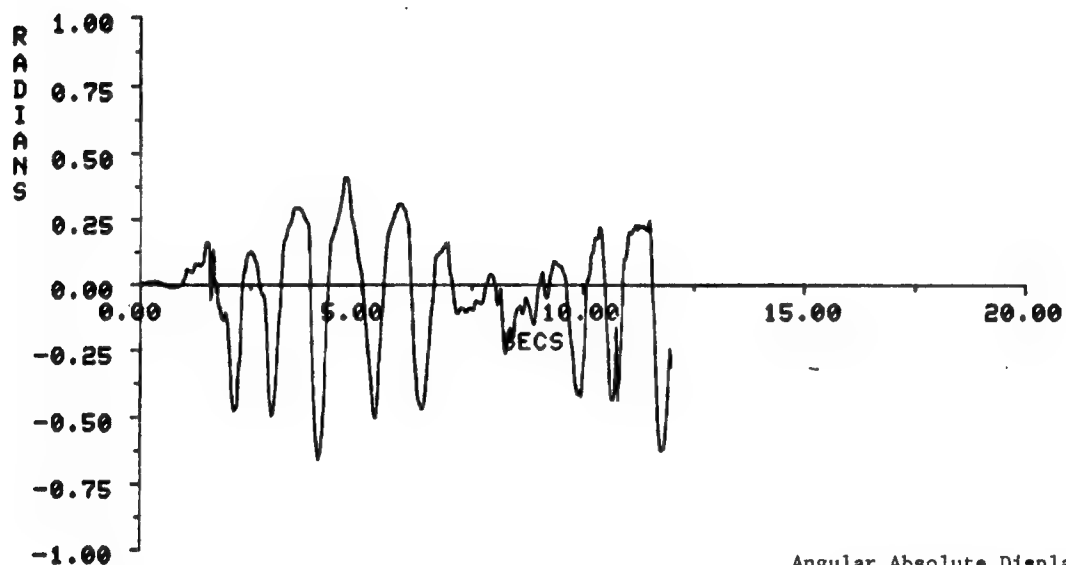
Figure 8

Angular Absolute Displacement
in Radians Δθ
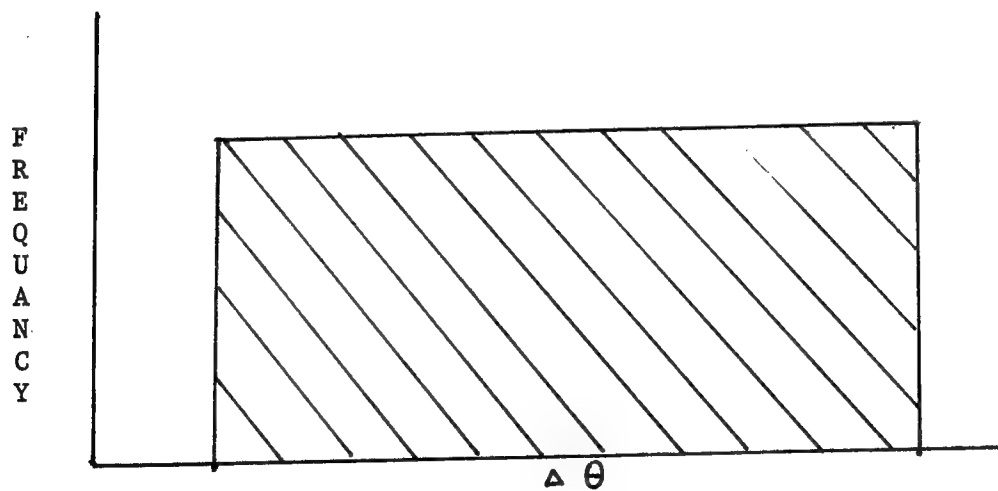
5.79	35.98
7.66	39.65
7.16	41.78
9.20	44.21
14.72	49.78
22.37	62.01
30.02	
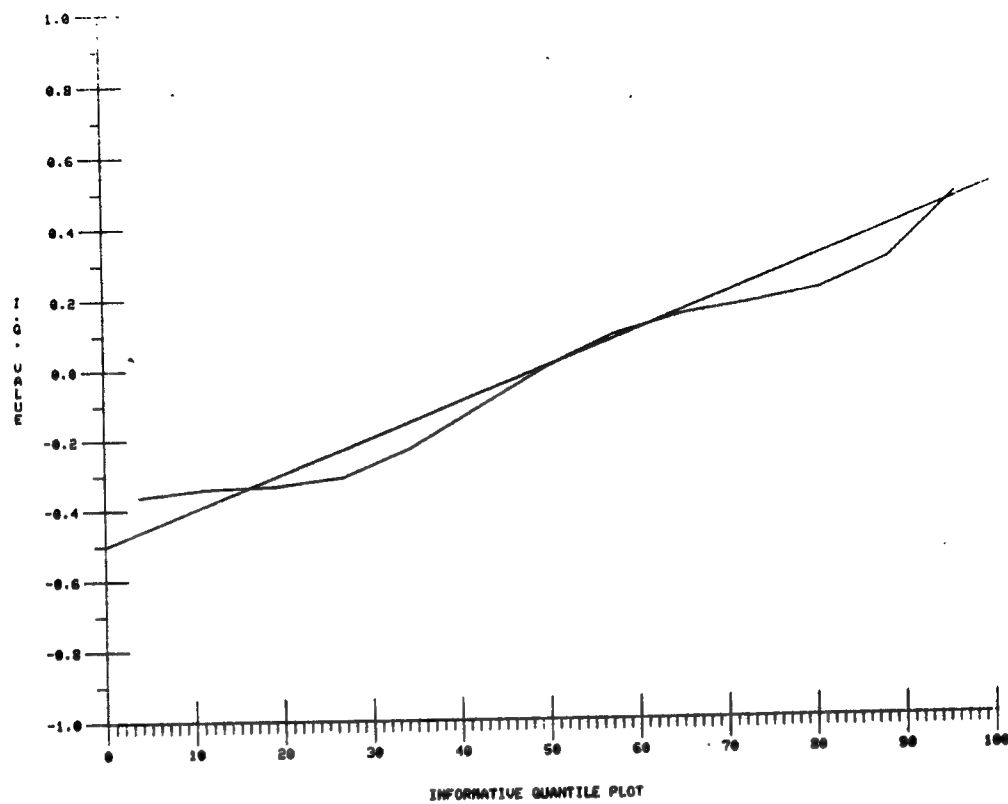
(a) I.Q. Plot (18 mph/1L)

(b) Uniform Distribution

Figure 9

183

Cycles to Failure Relation
$Log_{10}N = B - D \Lambda\theta$

Torsional Fatigue Life

Current Design (B = 8.06, D = .068)
Adjusted From Base Line Data to
Agree with Scranton's Torsional Tests

B = 8.06, D = .0618 (10% Reduction in Bar Stress)

B = 8.06, D = .0567 (20% Reduction in Bar Stress)

Base Line Data
(B = 7.70 and D = .068)
4340 – 230 KSI Yield
Based on Smooth Spec. Data
Mean Stress = 0 (R = -1)
Room Temp. Lab. Air
Shoot Peened Surface

FIGURE 10

STRESS DATA EVALUATION PROGRAM

Mean = 5.206
Standard Deviation = .239

Design Allowable
A = 4.55
B = 4.83

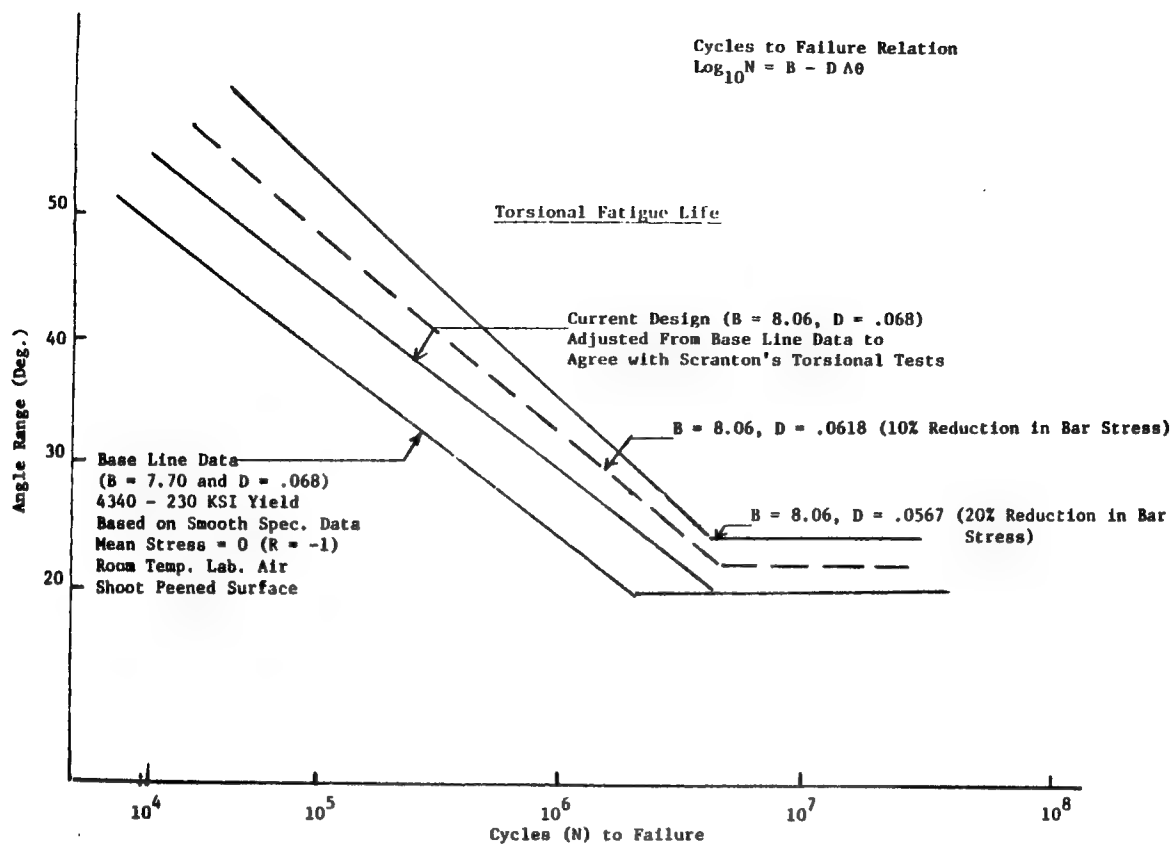Weibull
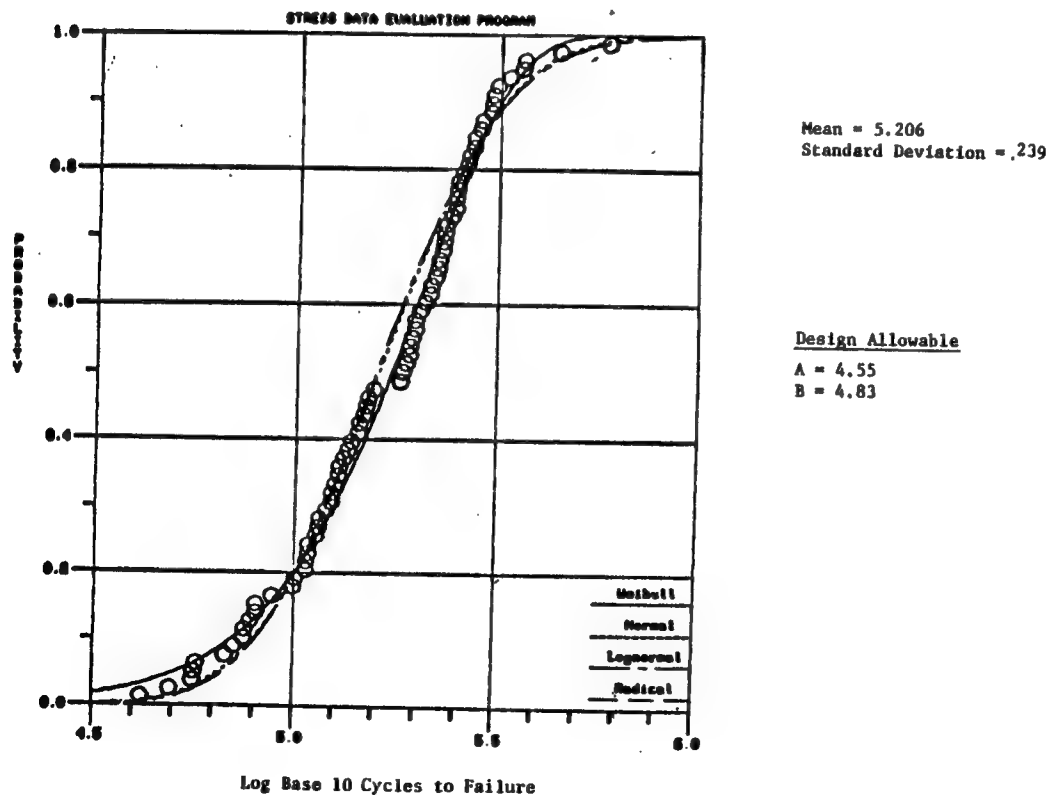Normal
Lognormal
Radical

Log Base 10 Cycles to Failure

FIGURE 11   M60 Torsion Bar Fatigue Test Results (Pooled Data 1977 to 1982)

184

Torsional Fatigue Life

Cycles to Failure Relation
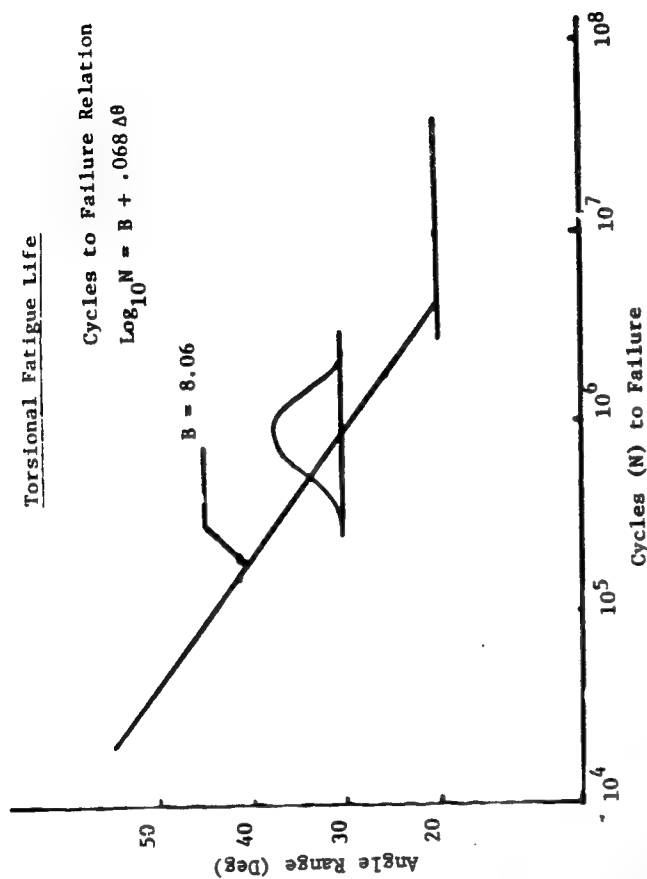
$Log_{10}N = B + .068 \Delta\theta$

B = 8.06

Angle Range (Deg)

Cycles (N) to Failure

FIGURE 12b

Simulation of B from S/N Curve Representation

Probability Density

S/N Curve $Log_{10}N = B + D\Delta\theta$

FIGURE 12a

Probability of Survival vs Miles
S/N Curve Results

Probability of remaining
life after 741 miles have
been completed.
$P_c = P_A/P_p$

Current
Design

20% Improvement in
Design (Stress
Reduction)

Probability
of
Survival

Miles (Run #4B - 25 mph)

FIGURE 13

Mean=2.331
S Dev=1.176

APG Reported Failure #1 Torsion Bars
(R and L together)

99% Survivability =
262 miles from
Weibull
Distribution

Miles to Failure $(x10^{-3})$
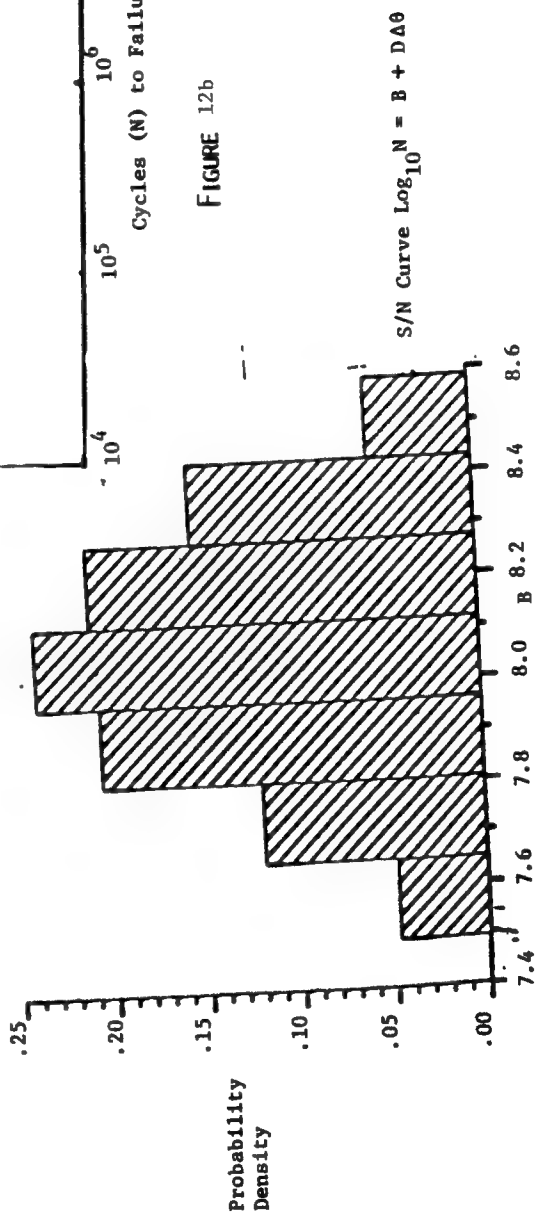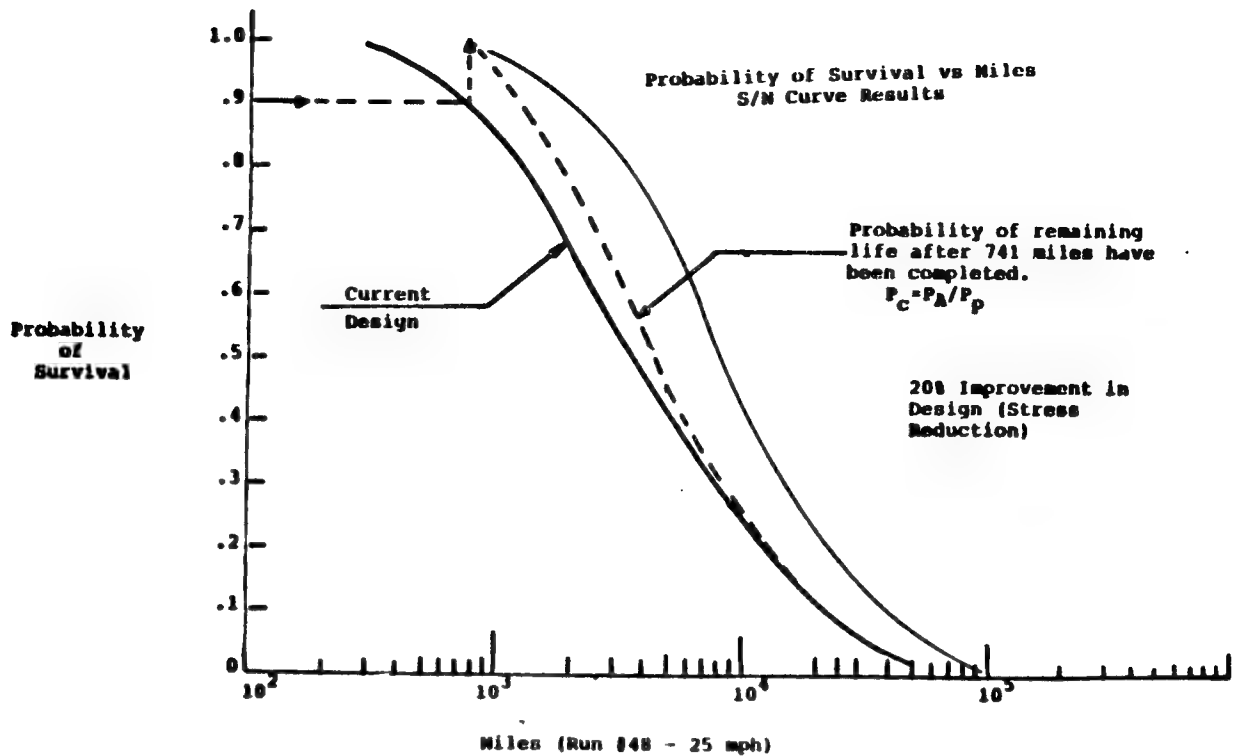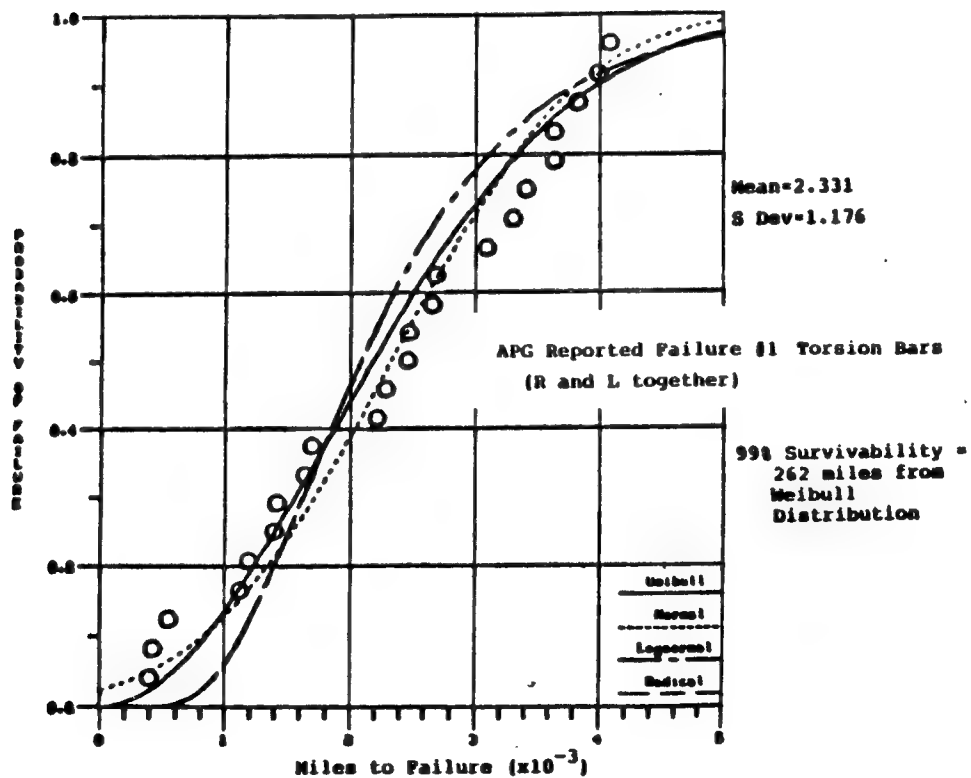
FIGURE 14

186

SESSION V: COMPOSITE APPLICATIONS — DESIGN ANALYSIS TEST AND EVALUATION

ANALYSIS OF TEXTILE STRUCTURAL COMPOSITES: AN OVERVIEW

Tsu-Wei Chou
Department of Mechanical
and Aerospace Engineering
University of Delaware
Newark, DE 19716

ABSTRACT

This paper reviews the recent development in the analytical modeling of the thermo-mechanical behavior of textile structural composites for 2-D and 3-D woven materials. In the case of 2-D fabric composites, three mechanistic models have been developed, to examine the elastic and thermo-elastic behavior of woven fabric composites, including elastic properties, knee behavior and the stress-strain curves, non-linear elastic behavior and thermal expansion coefficients.

In the analysis of 3-D fabric composite, the methodology is based upon the consideration of elastic strain energy and a Castigliano's theorem. Comparison between theory and experiments also have been made.

I. INTRODUCTION

Textile structural composites are gaining increasing technological importance. Textile forms used as reinforcements for composites can be designed to accommodate a variety of manipulative requirements, including dimensional stability, subtle conformability and deep-draw shapeability. Woven fabrics that are essentially two-dimensional constructions exhibit good stability in the mutually orthogonal warp and fill directions. Woven fabrics also provide more balanced properties in the fabric plane than unidirectional laminae; the bidirectional reinforcement in a single layer of a fabric gives rise to excellent impact resistance. The ease of handling and low fabrication cost have made fabrics attractive for structural applications. Triaxially woven fabrics, made from three sets of yarns which interlace at 60-degree angles, offer improved isotropy and higher in-plane shear rigidity. There are also other two-dimensional materials in the forms of knit fabric and weft-inserted warp knit constructions. These materials offer a much wider range of form and behavior than woven fabrics. It is possible to design composites with considerable flexibility in performance, from complete directional stability to engineered directional elongation. Another emerging area in textile composites is based upon three-dimensional integrated structural geometry. These materials can assume complex shapes and provide a high level of transverse shear strength and impact resistance.

This paper reviews the recent developments in the analytical modeling of the thermo-mechanical behavior of textile structural composites. In the area of two-dimensional fabrics, the focus has been on both biaxial and triaxial woven materials. In the area of three-dimensional textile structural composites, the methodology has

been established for modeling their stiffness and strength properties. Comparisons of the theoretical predictions with experimental results are also reported.

II. Analysis of Two-Dimensional Woven Fabric Composites

1. Geometric Characteristics

An orthogonal woven fabric consists of two sets of interlaced yarns. The length direction of the fabric is known as the warp, and the width direction is referred to as the fill or weft. Two basic geometrical parameters can be defined to characterize a fabric; n_{fg} denotes that a warp yarn is interlaced with every n_{fg}-th fill yarn, and n_{wg} denotes that a fill yarn is interlaced with every n_{wg}-th warp yarn. Here, we confine ourselves to non-hybrid fabrics and the case of $n_{wg} = n_{fg} = n_g$. Fabrics with $n_g \geq 4$ and where the interlaced regions are not connected are known as satin weaves. As defined by their n_g values, the fabrics are known as, for example, plain weave ($n_g = 2$), twill weave ($n_g = 3$), 4 harness satin ($n_g = 4$), and 8 harness satin ($n_g = 8$).

2. Methodology of Analysis

The theoretical basis of the present analysis is the classical laminated plate theory. Under the assumption of Kirchoff-Love hypothesis, the constitutive equations are written as:

$$
\begin{Bmatrix} N_i \\ M_i \end{Bmatrix} = \begin{bmatrix} A_{ij} & B_{ij} \\ B_{ij} & D_{ij} \end{bmatrix} \begin{Bmatrix} \varepsilon^o_j \\ \kappa_j \end{Bmatrix} - \Delta T \begin{Bmatrix} \tilde{A}_i \\ \tilde{B}_i \end{Bmatrix} \qquad (i,\ j = 1,\ 2,\ 6) \tag{1}
$$

Based upon the iso-stress and iso-strain assumptions, the above constitutive equations can be used to obtain the bounds of the thermo-elastic properties. The upper bounds of compliance constants are obtained from the iso-stress assumption; the lower bounds of stiffness constants are then obtained by taking the inversion of the compliance constant matrix. Similarly, the upper bounds of stiffness constants are derived from the iso-strain assumption; the lower bounds of compliance constants are then derived by inverting the stiffness constant matrix.

3. Elastic Properties

3.1 The Mosaic Model [1]

In general, a fabric composite idealized by the mosaic model can be regarded as an assemblage of pieces of asymmetric cross-ply laminates. Figure 1(a) shows the mosaic model of a unit cell for an eight-harness satin composite. The key simplification of the mosiac model is the omission of the fiber continuity and undulation (crimp) that exist in an actual fabric.

In the bound approach, the two-dimensional extent of the fabric composite plate is simplified by considering two one-dimensional models where the pieces of cross-ply laminates are either in parallel or in series as shown in Figs. 1 (c) and (d). The upper and lower bounds of elastic stiffness and compliance of fabric composite plates in such a "mosaic model" are obtained based upon the constant strain and constant stress assumption.

3.2 The Crimp (Fiber Undulation) Model [2, 3, 4]

The crimp model is developed in order to consider the continuity and undulations of fibers in a fabric composite. Although the formulation of the problem developed in the following is valid for all n_g values, the crimp model is particularly suited for fabrics with low n_g values. The crimp model also provides the basis of analysis for the bridging model.

Figure 2 depicts the geometry of the model where the undulation shape is defined by the parameters $h_1(x)$, $h_2(x)$, and a_u. The parameters $a_0 = (a - a_u)/2$ and $a_2 = (a + a_u)/2$ are automatically determined by specifying a_u, which is geometrically arbitrary in the range from 0 to a. Because a pure matrix region appears in the model, an "overall" fiber volume fraction, V_f, can be different from V_f in the yarn region.

The analytical results based upon the crimp model demonstrate that fiber undulation leads to a softening in the in-plane stiffness as compared to the mosaic model. The "crimp model", is particularly suited for predicting elastic properties of plain weave composites.

3.3 The Bridging Model [2, 3, 4]

The success of the threadwise analysis has led to the concept of a bridging model for general satin composites. Such a model is desirable in view of the fact that the interlaced regions in a satin weave are separated from one another. The hexagonal shape of the repeating unit in a satin weave, as shown in Fig. 3 (a), is modified to a square shape (Fig. 3 (b)) for simplicity of calculation. A schematic view of the bridging model is shown in Fig. 3 (c) for a repeating unit which consists of the interlaced region and its surrounding areas. This model is valid for only satin weaves where $n_g \geq 4$. The four regions labelled by A, B, D, and E consists of straight fill yarns, and hence can be regarded as pieces of cross-ply laminates of thickness h_t. Region C has an interlaced structure with an undulated fill yarn. Although the undulation and continuity in the warp yarns are ignored in this model, the effect is expected to be small because applied load is assumed to be in the fill direction.

The in-plane stiffness in region C where $n_g = 2$ has been found to be much lower than that of a cross-ply laminate. Therefore, regions B and D carry higher loads than regions A and E. Numerical results of the relationship between the in-plane elastic stiffness constants and $1/n_g$ can be found in Refs. [2, 3, 4]. The predictions of the present theory also show good agreements with experimental results.

4. Analysis of the Knee Behavior [2, 3, 4]

Both the crimp model and bridging model described above are now extended to the study of the stress-strain behavior of woven fabric composites after initial fiber failure, known as a knee phenomenon. The essential experimental fact for the knee phenomenon is that the breaking strain in the transverse layer, ε_2^b, is much smaller than that of the longitudinal layer in cross-ply laminates. Only the failure of the transverse yarns, which occurs in the warp direction in the present model, is considered. Thus, a failure criterion based upon maximum strain is adopted. Both bending deflection by the coupling effect and bending free condition have been examined.

We consider that the highest strain in the region exceeds the specified strain ε_2^b first, and it immediately leads to the failure of the adjacent area. The damaged area in the warp yarn then propagates as the load increases. It is assumed that classical laminate theory is still valid in this failure process, and that the effective elastic moduli of such a failed area in the warp yarn are much lower than those of a sound area.

The prediction for the bending-free condition compares very favorably with the finite element simulation. It is quite reasonable that the case with bending provides much lower stiffness because it is not subjected to lateral constraints.

Figure 4 compares numerical and experimental results for stress-strain curves of an 8-harness satin fabric plate of glass/polyester composites. The theoretical results for an 8-harness satin reinforced glass/polyimide composite compares extremely well with the experimental curve. It has been concluded that the bridging regions surrounding the interlaced regions are responsible for the higher stiffness and knee stress in satin composites than those in plain weave composites.

5. In-Plane Thermal Expansion and Thermal Bending Coefficients [5]

The constitutive equations of a laminated plate taking into account the effects due to a small uniform temperature change are given in Eqs. 1. The analytical techniques developed for the mosaic model, crimp model, and bridging model have been applied analyze the thermal problem.

Figure 5 shows numerical results of the analysis. The results show that the mosaic model provides a simple means for estimating thermal expansion and thermal bending coefficients. The one-dimensional crimp model predicts slightly higher in-plane thermal expansion coefficients and the same thermal bending coefficients as compared to those obtained from the mosaic model. The bridging model is particularly suited for the prediction of thermal expansion constants for satin composites. The experimental results on in-plane thermal expansion coefficients for a 5-harness satin composite agree well with the theory.

6. Hybrid Fabric Composites [6, 7]

The term "hybrid composites" is used to describe composite materials containing more than one type of fiber material. Hybrid

composites are attractive structural materials because they provide designers with a new degree of freedom in tailoring composites to achieve properties that cannot be obtained in binary systems, including a better balance of stiffness and strength and an increased elongation to failure. Hybrid composites also provide a more cost-effective means of using expensive fibers such as graphite and boron.

The three analytical models developed for the prediction of the elastic and thermal properties of the 2-D nonhybrid fabric composites can be readily applied to examine the elastic and thermal behviors of hybrid fabric composites. Upper and lower bounds of elastic stiffness and compliance of hybrid composites have been obtained based upon the iso-strain and iso-stress assumptions, respectively. The one-dimensional fiber undulation concept developed previously has been modified to treat the interlacing of two different types of fibers, and it has been incorporated into a general "bridging model" for pedicting thermo-elastic properties of hybrid fabric composites.

The predictions of elastic stiffness constants compare very favorably with experimental results of graphite/Kevlar/epoxy systems.

7.   Nonlinear Behavior of Woven Fabric Composites [8]

The non-linear elastic behavior of fabric composites is also examined. Three types of non-linearity including the shear deformation of fill threads, the extensional deformation of the pure matrix regions and transverse cracking of the warp regions have been taken into consideration. The non-linear constitutive relation developed by Hahn and Tsai is adopted in this analysis and the fiber undulation and bridging models developed above are also applied. Results of the analysis for a glass 8 harness satin/polyimide composite compares remarkably well with the experimental stress-strain curve. The analyses also show that the nonlinear effects are less pronounced for fabrics assuming larger geometrical repeating length due to the increasing influence of the "bridging effect". As a results, both knee stress and strain increase with the geometrical repeating length.

8.   Triaxial Fabric Composites [9]

Triaxially woven fabrics made from three sets of yarns which interlace at 60-degree angles, offer improved isotropy and higher in-plane shear rigidity. In the modeling process, the triaxial fabric composite is considered as an assemblage of three corrugated laminae. The classical laminated plate theory and the concept of crimp model are the basis of the analysis. This approach to triaxial fabric composite has been extended to consider the non-orthogonal biaxial woven structure where the deviation from orthogonality may come from fabrication process.

III.   ANALYSIS OF 3-D WOVEN FABRIC COMPOSITES [10]

1.   Geometric Characteristics

The structure and properties of three-dimensional (3-D) woven fiber composites are fabricated by a weaving or braiding technique. In comparing with two-dimensional (2-D) composites based upon fabrics

or unidirectional tapes, 3-D composites can be produced with considerable flexibility in their sizes along the length, width and thickness directions. The integral nature of these composites provides improved stiffness and strength in the thickness direction, along which interlaminated failure often occurs in 2-D composites.

In general, a 3-D fiber arrangement can be considered as composed of two types of structures: the baseline structure formed by weaving fibers along three mutually orthogonal directions and the interwoven or braided structure composed of fibers not orthogonal to one another. 3-D composites can be "designed" to meet the performance requirements in different directions through suitable spatial arrangements of the reinforcing fibers. The general features of the spatial arrangement can be better understood by focusing our attention on a typical location, for instance point d in Fig. 6, where the interwoven or interlocking of fibers may take place.

In order to facilitate the analysis, the 3-D diagonal composite rod structure of Fig. 6 is projected onto six mutually orthogonal planes along the +x, +y, and +z directions. For instance, in the z-projections, the upper half of the unit cell (above point d) is projected onto the -z plane and the lower half is projected once along each coordinate axis. The baseline rod structure, on the other hand, is projected only along the +x, +y, and +z directions. It is further assumed that the composite rods in each projection can be regarded as a 2-D plain weave material.

2. THE ELASTIC STRAIN ENERGY APPROACH

In considering the deformation of a unit cell, three types of elastic strain energies in the composite rods are taken into account. These include the strain energies due to bending, extension and compression over the region of fiber contact.

In the modeling process, the strain energies of the baseline composite rod structure are considered for the three plain weaves and the energies of the diagonal composite rod structures are examined for the six projections, which also assume two-dimensional woven configurations. The overall response of the unit cell structure to external loading is obtained by combining the responses of the baseline as well as the diagonal structures.

Figure 7 illustrates the predicted axial elastic modulus as a function of fiber volume fraction and fiber spatial orientation. The experimental data coincides rather well with predictions.

IV. Conclusion

Textile structural materials has emerged as a new reinforcement for advanced composite materials. Significant progress has been made to establish the methodology for modeling the linear and non linear constitutive relations, as well as the strength and failure behavior of both 2-D and 3-D textile composite constructions. The potential of textile composites for structural application is not fully realized and continuous effort is necessary for the understanding of this rapidly evolving field.

REFERENCES

1. Ishikawa, T., "Anti-Symmetric Elastic Properties of Composite Plates of Satin Weave Cloth," Fibre Science and Technology, V. 15, September 1981, 127-145.

2. Ishikawa, T., and T. W. Chou, "Stiffness and Strength Behavior of Woven Fabric Composites," Journal of Materials Science, V. 17, November 1982, 3211-3220.

3. Ishikawa, T., and T. W. Chou, "One-Dimensional Micromechanical Analysis of Woven Fabric Composites," AIAA Journal, V. 21, December 1983, 1714-1721.

4. Ishikawa, T., and T. W. Chou, Stiffness and Strength Properties of Woven Fabric Composites," Progress in Science and Engineering of Composite Materials, Proceedings of the Fourth International Conference on Composite Materials (1982).

5. Ishikawa, T., and T. W. Chou, "In-Plane Thermal Expansion and Thermal Bending Coefficients of Fabric Composites," Journal of Composite Materials, V. 17, March 1983, 92-104.

6. Ishikawa, T., and T. W. Chou, "Elastic Behavior of Woven Hybrid Composites," Journal of Composite Materials, V. 16, January 1982, 2-19.

7. Ishikawa, T., and T. W. Chou, "Thermoelastic Analysis of Hybrid Fabric Composites," Journal of Materials Science, V. 18, (1983), 2260-2268.

8. Ishikawa, T., and T. W. Chou, "Nonlinear Behavior of Woven Fabric Composites," Journal of Composite Materials, V. 17, September 1983, 399-413.

9. Yang, J. M., C. L. Ma, T. W. Chou, "Elastic Stiffness of Biaxial and Triaxial Woven Fabric Composites", Proceedings of the 29th SAMPE National Symposium, Reno, 1984.

10. Ma, C. L., Yang, J. M., Chou, T. W., "Elastic Stiffness of Three-Dimensional Woven Fiber Composites", presented at ASTM Symposium Testing and Design of Composite Materials, Philadelphia, 1984.
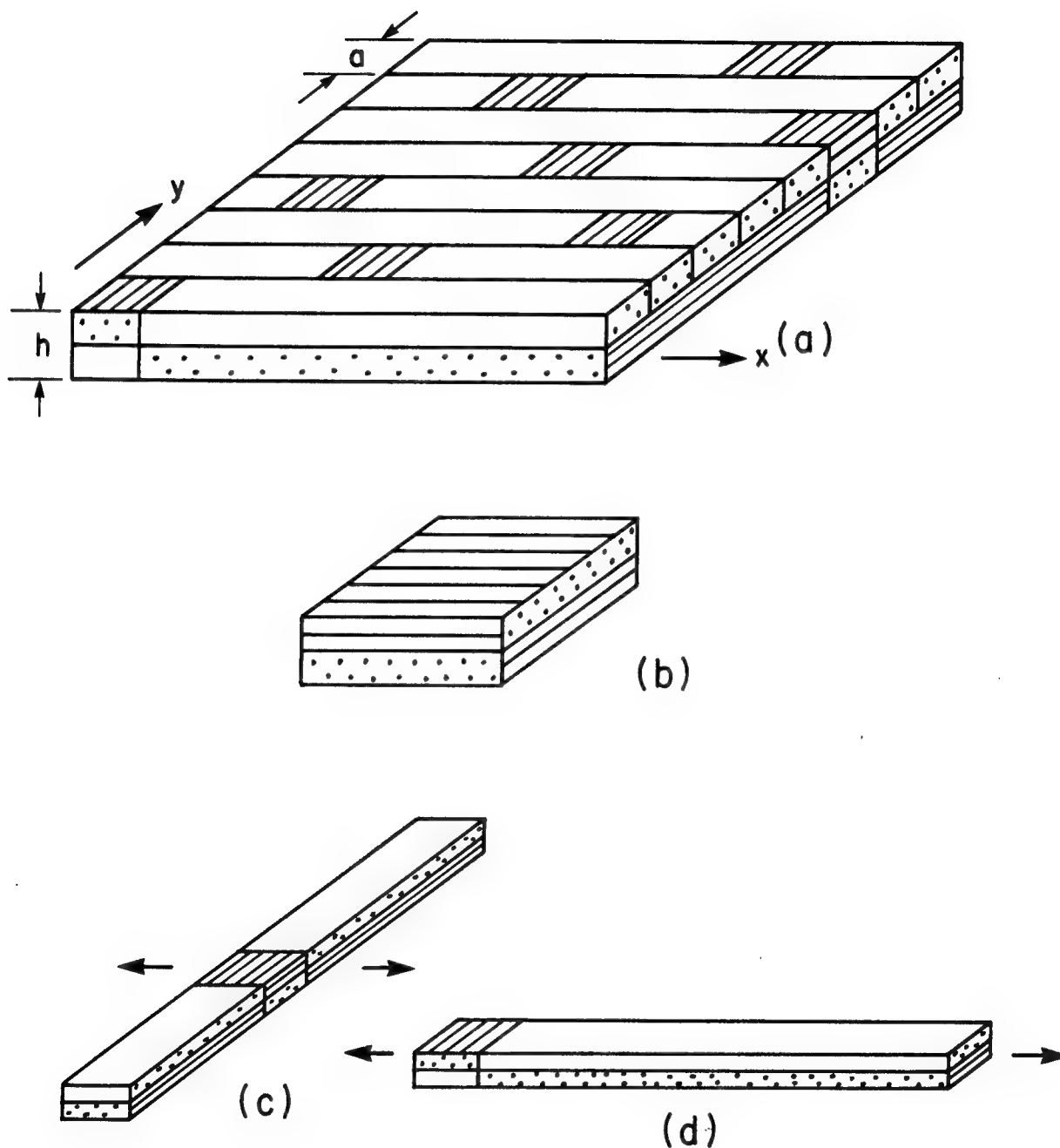
Figure 1   Mosaic model of (a) repeating region in an eighth harness
            satin composite, (b) a basic cross-ply laminate, (c)
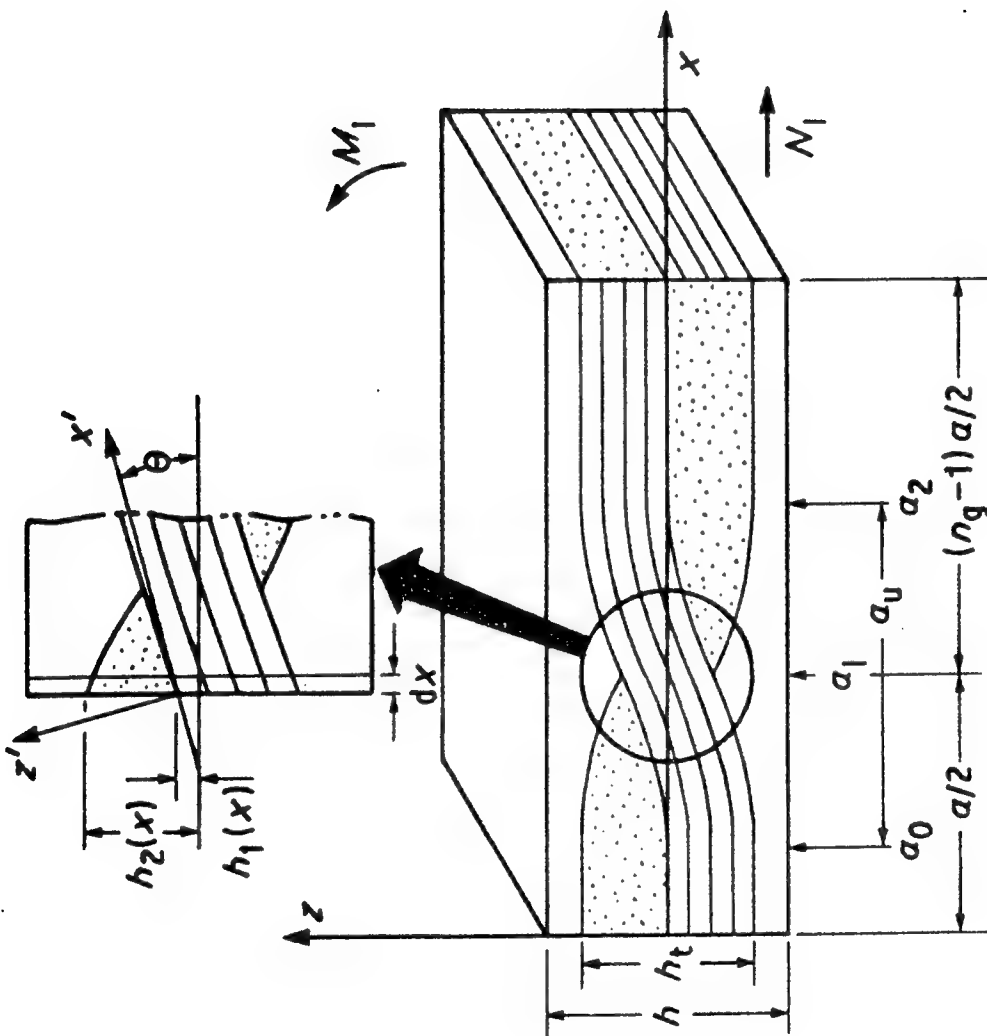   parallel model, (d) series model.

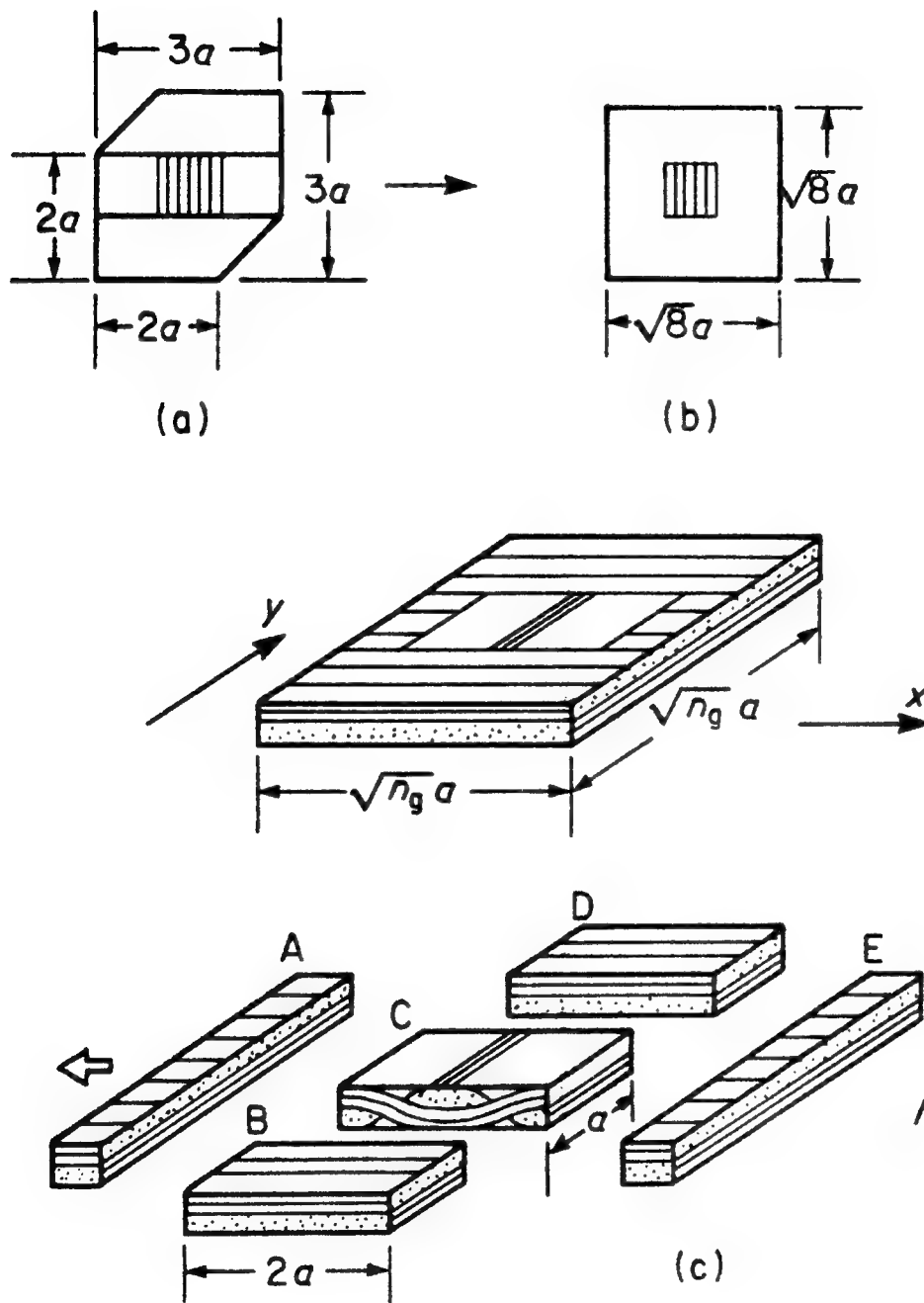Figure 2   Fiber Crimp Model

197

Figure 3 Concept of the bridging model, (a) shape of the repeating unit of 8 harness satin; (b) modified shape for the repeating unit; (c) idealization for the bridging model.
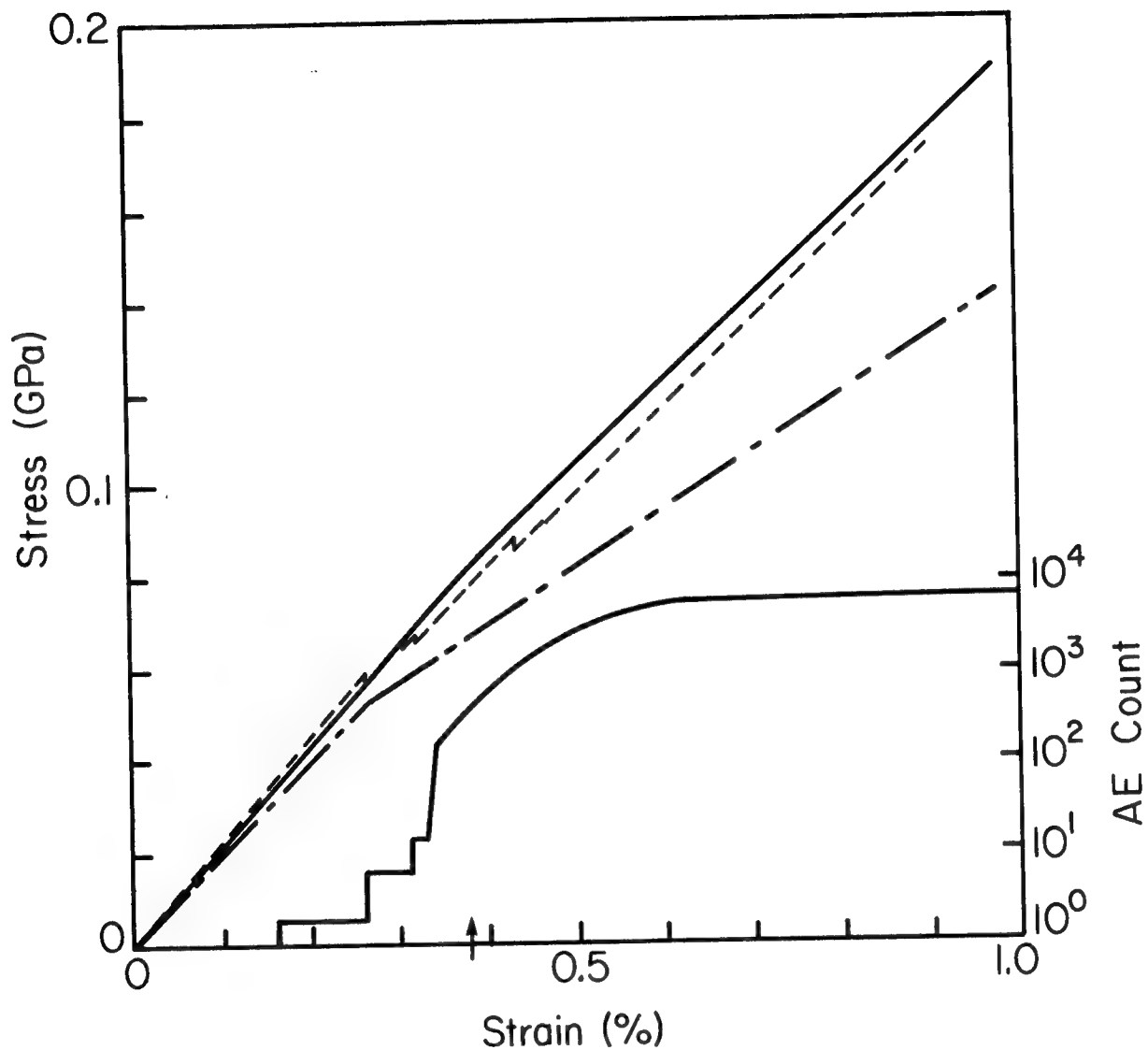
Figure 4 Stress-Strain curves for plain weave composites of glass/
polyester, V_f = 36.8% and experimental data of acoustic
emission. ——— Present results for the bending-free
condition;— · — Present results for the bending uncon-
strained condition; — — — Finite element simulation;
———Total count in acoustic emission measurement;
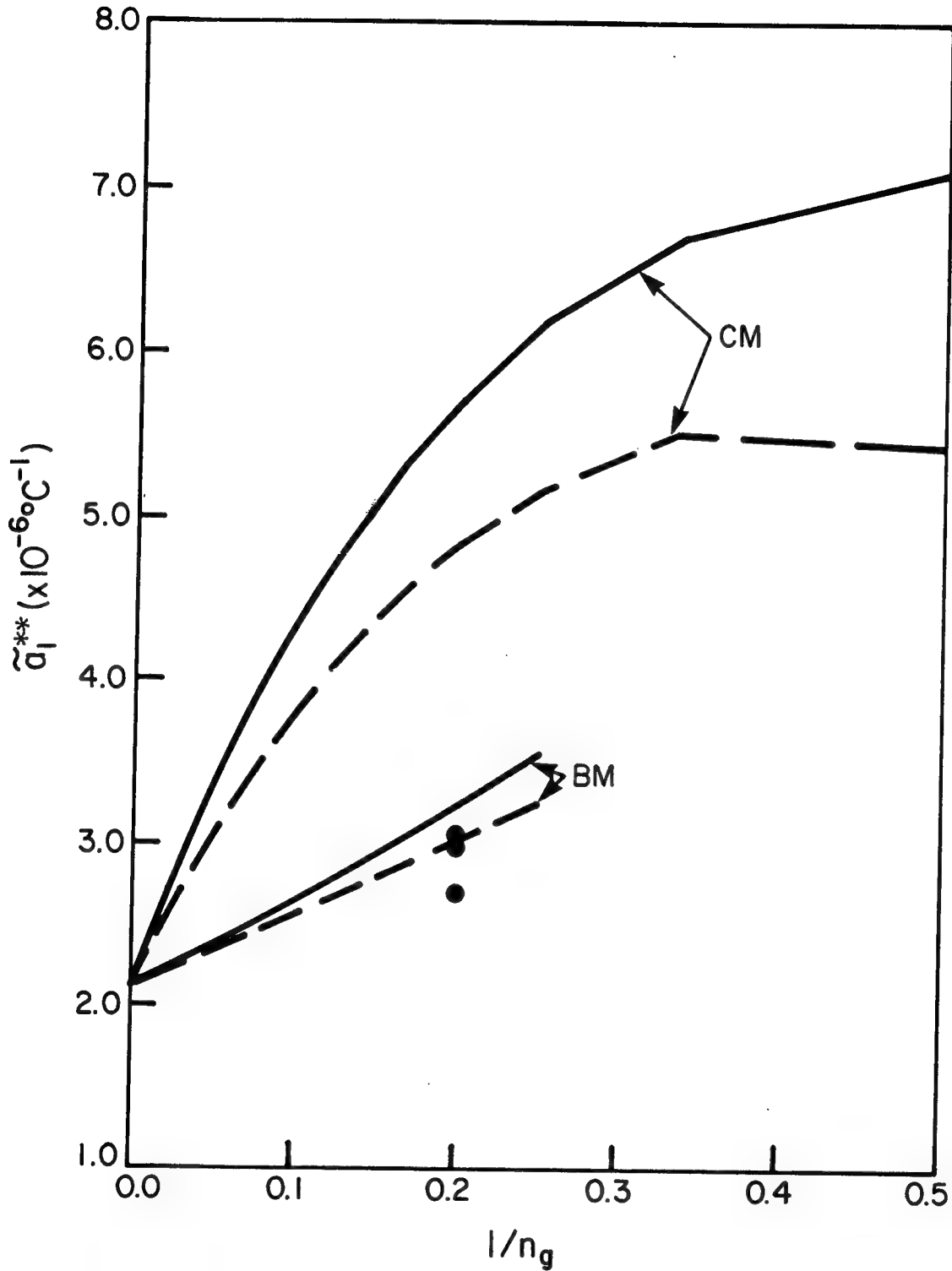and an arrow indicates the specified value of ε_2^b.

199

Figure 5 Comparison of theoretical predictions with the experimental results for 5 harness-satin graphite/epoxy composites. a/h = 3.75; ———, a/h = 7.5: – – –, and a_u/a = 1.0. CM and BM indicate fiber crimp and bridging models, respectively. ●: Experimental results at 300°K. n_g is defined in Sec. II.1.
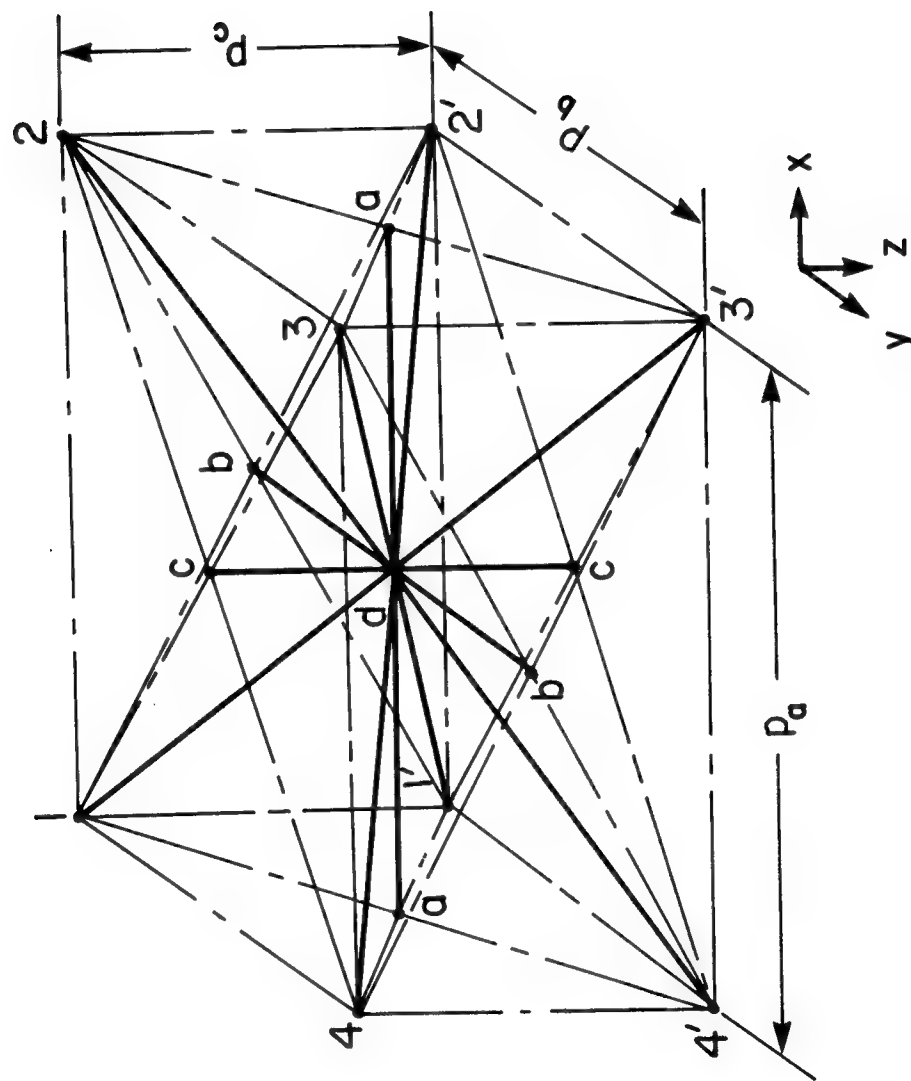
Figure 6 Unit cell geometry of 3-D woven composite. aa., bb and cc are baseline fibers, and 13', 42', 24' and 31' are diagonal fibers. d indicates the location of fiber interlock.
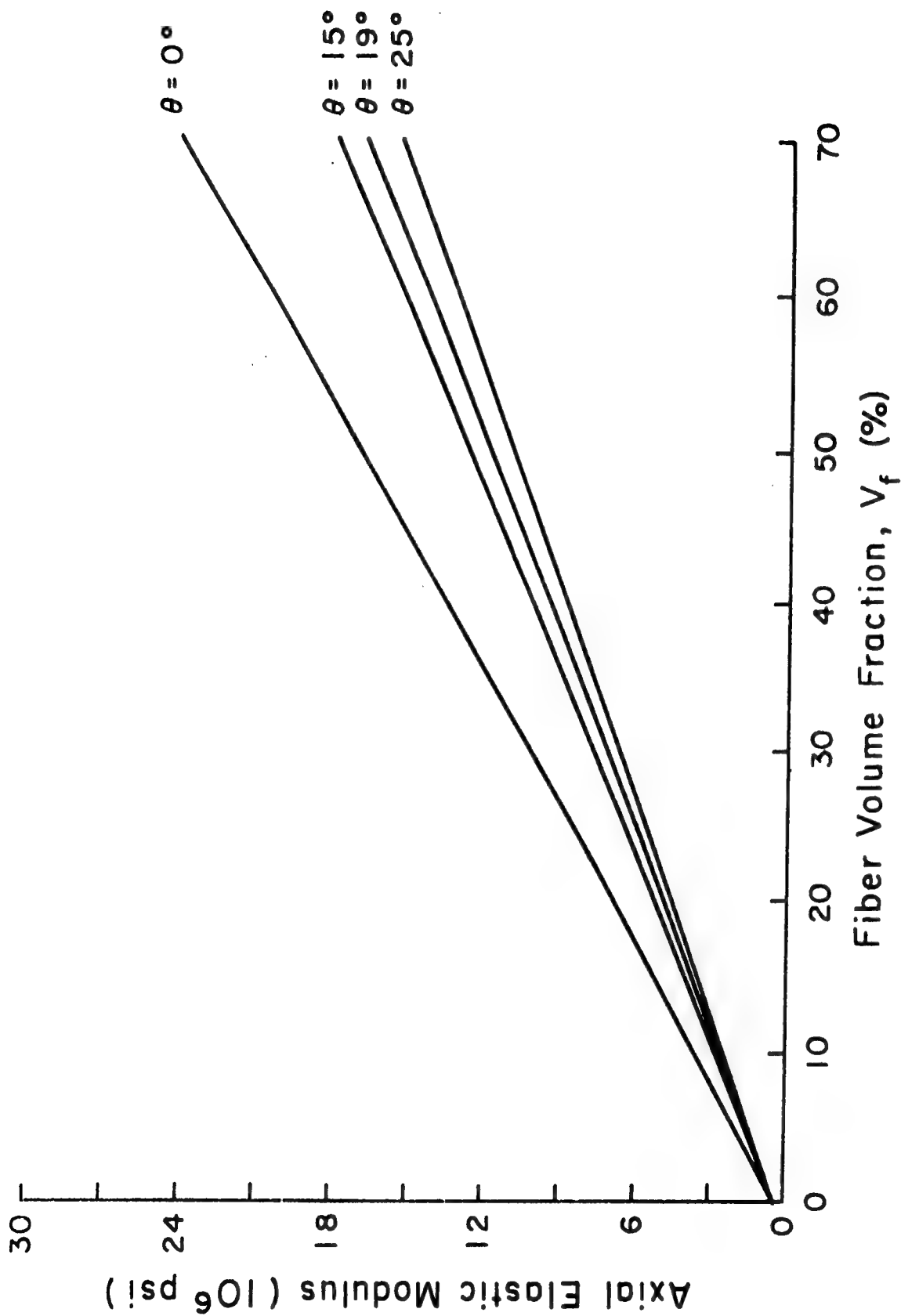
Figure 7 The predicted axial elastic modulus as functions of fiber orientation and fiber volume fraction for 3-D woven composite.

ANALYTICAL STUDIES ON A SLENDER COMPOSITE FRAMEWORK STRUCTURE FOR TENT APPLICATION

K .R. Gandhi and D. W. Oplinger
Army Materials & Mechanics Research Center
Watertown, MA 02172

ABSTRACT

This paper illustrates a practical approach in structural analysis and design of a slender composite framework. The result is a byproduct of Army effort directed at replacing the standard aluminum for a modular tent system framework by pultruded glass components. The initial analysis consisted of nonlinear large deformation finite element model for the fabric covering the frame but with linear response for the supporting framework. This was considered sufficient for initial design purposes. Subsequently a prototype was assembled and subjected to gravity type loading to simulate the snow loads. The test indicated ultra large deformations of the framework before final collapse. These large deformations also indicated that the linear structural design estimates were substantially unconservative. As the next logical step in analysis a special computer code was developed to model elastica-type behavior in framework. This involved numerical integration of the accurate nonlinear differential equation in combination with an iterative technique which converged on the final deformed geometry of the frame. This approach was helpful in checking the results later obtained by using commercially available codes claiming to accomplish the same through finite element approach. A comparative study using an identical case by the two different approaches has been presented. The effort also consisted of finite element studies using nonlinear elements with stress-stiffening in order to evaluate stability contribution of header and guy wires. Finally a near optimized design is arrived at with significant weight and cost reduction.

The results of the study illustrate the need for design approaches, in the case of composite structural system, that carefully account for special behavior characteristic of composites which rule out the use of conventional metal structure design philosophy.

1. INTRODUCTION

The Army TEMPER shelter system (Tent Expandible Modular Personal) structure to provide sheltered areas for kitchens, repair facilities and field hospitals (Fig.1). The TEMPER framework (Fig. 2) is a modular system which can be extended indefinitely. The essential components of the structure are polygonal frames refered to as arches, and purlins. The present configuration of the TEMPER involves a framework of extruded aluminum box sections for the

frames and circular tubing for purlins. This paper presents the analytical effort involved in studying the feasibility of replacing the current aluminum structural components with a glass polyester pultruded sections. It is expected that such a composite system will provide weight and cost reduction over the present design using aluminum.

Initial analytical efforts consisted of a finite element analysis to represent the tent structure consisting of two frames and fabric on it (Fig.2). This was done using a computer code NONFESA [1] wherein the fabric is treated as a membrane with nonlinear material and geometrical response with the possibility of large deformations, while the framework is assumed to deform linearly. The code is very much appropriate for use with the current metal framework which can be expected to be rigid enough to be adequately treated by ignoring the moderate geometrical changes in the shape of the supporting framework. In the case of the pultruded composite framework which was considerably more flexible than the aluminum version the assumption of linear framework response was found to be incorrect. As a result the application of the NONFESA code turned out to be very unconservative. In the absence of any other analytical tool it was considered useful to get some results from this code. For example the interaction of the fabric with the framework is a highly non-linear phenomenon and the NONFESA-type solution is needed to get an accurate calculation of framework loads. This aspect of the problem was addressed in [2]. The present paper provides for the extension of the prior work including the results from subsequent efforts leading to an optimum design.

A special in-house code CAN2 was also developed in order to treat very large deflections of the arches. This analysis which amounts to a numerical solution of the classical elastica Eq. (3) was useful in explaining the behavior of the tent frame under simulated snow load test performed on the prototype system. As the size and complexity of the system grew it was considered costwise efficient to use other commercially available systems. After some initial trial and error the computer code ANSYS developed by Swanson Analysis was investigated and found to check closely with the elastica -type solution yielded by CAN2. The analytical results for the stress state due to snow and wind loads along with the stiffening influence of cable is an important part of the effort. An attempt has been made towards optimizing the arch section design in order to yield a near minimum weight resulting in substantial weight and cost saving using the proposed composite alternative.

2. INITIAL ANALYSIS AND DESIGN

Initial analysis was done with the code NONFESA. This code treats the fabric as a membrane with three displacement degrees of freedom at each node. Further, it takes into account non-linear geometry and material behavior of the fabric. On the other hand, the supporting framework is treated by use of linear beam elements with 6 degrees of freedom at each node. The initial

analytical results were achieved with a one bay frame model (Fig.3) using the section properties of existing aluminum frame (Table 1). For the composite frame, solutions were obtained both for the case in which the section properties of Table 1 were assumed as well as for a weight-optimized section which is described later. The loads considered for these analyses were :(1) uniform vertical load intensity of 10 psf on the upper roof panels corresponding to the required snow load capability;(2) the pressure distribution shown in Fig. 4 corresponding to a 45 knot wind load. For computer simulation attention was restricted to only one bay (Fig.3). The solution is obtained from the NONFESA code is obtained in terms of nodal displacements, rotations and element forces. For the framework components, the outputs consist of 6 generalized forces(3 direct forces and three moments) at each end of a given beam element. An auxilliary routine was required to infer the interaction loads between the fabric covering and the framework, since these were not provided directly by NONFESA. The resulting loads are shown in Figs. 5 and 6 for aluminum and composite frames respectively for 10 lbs per sq ft. snowloading. It is interesting to note the difference in the two distributions. The vertical snow load distributes radically differently when the flexible composite frame is used instead of aluminum frame. This load redistribution reduces some of the moments especially in the purlins as one would expect. Further, the membrane behavior of the fabric also imposes loads in the horizontal plane due to the catenary effect. The concentrated loads on the arch frame were used for non-linear studies which are presented later in this paper.

3. PROTYPE CONSTRUCTION AND SIMULATED SNOW LOAD TESTING

On the basis of the initial analysis, a pultruded box section of outer dimensions 1.5"x1.5"x0.125" wall thickness was selected. As discussed in [2], this selection was made to allow for:(1) stress failure associated with moments caused by wind loading, which the initial analysis had indicated to be the critical loading case for that failure mode; (2) local buckling of the box section walls,associated with too small a ratio of wall thickness to width in the wall acting as compression flange: (3) Euler column buckling of the lower section of the arches, for column loads associated with the snow load case. The final section design which is discussed later was based on a similar combination of requirements, except for replacing the Euler column buckling condition with nonlinear collapse of the arch as a whole.

In order to verify the design, a two bay frame was constructed from commercially-supplied pultruded stock,using joints cannibalized from discarded aluminum frame components, and subjected to a simulated snow-loading test using canvas sheeting for representing distributed roof loads corresponding to the uniform-pressure snow loading requirement. About 70 canvas panels weighing 40-50 lb each were laid over the roof of the prototype system in two stages which took place over a period of about 1 1/2 months; in the first stage which required 7 days, a total load of 2560 lb corresponding to 10 psf (ie 100% of the design requirement) was applied; this was held fixed for 44 days,

following which an additional 500 lb of sheeting was added and again held fixed. Collapse of the structure occured 5 days after the final load was applied. Fig. 7 shows the prototype frame just at the beginning of the first load application step. Fig. 8 shows the load-deflection characteristics at the early stages of loading where relatively good comparison with the NONFESA analysis based on linear frame response is realized, together with the later stages where departure from linearity becomes apparent. Fig. 9 depicts a combination of deflection-vs-load for periods in which the load is being actively applied, together with deflection-vs-time for those periods during which the load is being held constant, while Fig. 10 shows the excessive deflection which occured at the later stages of the test.

Although the target load of 10 psf was achieved and held for the long period of time described above, the final load was considerably short of what had been predicted by the linear frame analysis provided by NONFESA. Creep behavior indicated by the drift in the deflections as a function of time as indicated in Fig. 9 may have exagerated the large-deflection behavior of the composite frame, but it appears that the large curvatures observed in Fig. 10 which occured as soon as the higher load levels were applied were sufficient to greatly exceed the range of deflections over which linear frame analysis could reasonably have been expected to apply.

4. NONLINEAR ANALYSIS

The test results thus showed that the method of analysis had to provide for excessive deformations in the composite framework. Initial investigation suggested that a large deformation analysis for a single arch would prove useful for providing insight into some of the important effects which were occuring in the failure of the composite frame. A numerical integration approach was applied to the differential equations used in the classical elastica problem [3]. A basic simplified frame geometry with pinned header connection and pinned leg supports as shown in Figure 11 was adopted. The loading shown in Figure 11 (c) is for 100% of the snow load condition ,which represents half the load being transferred from each half of a two-bay frame to the center arch. This we found later turned out to be a rather conservative assumption since the coupling effect of the purlins is quite significant at large frame deformations.

The method used to obtain an elastica-type solution relies on numerical integration of the exact differential equation for bending without any linearizing assumption. The analysis uses an arc length parameter S measured along the deformed frame (Fig.12) as the independent variable. This has the advantage of being able to deal with unlimited slope changes. The slope parameter, ϕ is the basic dependent variable in this approach.

The following basic equations were used:

$$\frac{d\phi}{dS} = \frac{M}{EI} \qquad (1)$$

where I is the moment of inertia, E the Youngs modulus of the frame material and M is the moment at any cross section due to horizontal and vertical loads. The moment is expressed as

$$M = \sum_j (x - X_j)\, F_{Vj} + \sum_k (y - Y_k)\, F_{Hk} \qquad (2)$$

where X_j is the horizontal position of a vertical load F_{Vj} while Y_k is the vertical position of horizontal load F_{Hk} and x and y are the horizontal and vertical positions of the observation point. The following equations define the shape

$$\phi = \int_0^S \frac{M}{EI} ds \qquad (3)$$

$$x = \int_0^S \cos\phi\; ds \qquad (4)$$

$$y = \int_0^S \sin\phi\; ds \qquad (5)$$

These equations are integrated numerically using Simpson's rule. The slope is found by numerically integrating Eq(1) starting with undeformed shape and taking moments of all forces. The symmetry condition at S=0 which is equivalent to maintaining a fixed slope there, determines the constant of integration.

Since the values of X_j and Y_k in Eq(2) vary as the frame deflects, an iterative process is needed to carry out the solution. A complicating issue is the fact that unknown horizontal force components (H_6 and H_{16} of Fig. 11(C) are present as constraints. (Note that the header brace attachment is pinned and has to be modelled as a condition of fixed horizontal distance from the vertical centerline of the arch. The program which was developed involved iterations within iterations, the inner loop providing for updating of the horizontal coordinates of the known-load application points, X_j, while two outer loops provided for independent adjustment of constraint forces H_6 and H_{16}. The X_j's were calculated as results of numerical integrations; using the undeformed shape of the frame as a starting point, successive iterations gave successive changes in the X_j's which eventually settled out.

The constraint loads, on the other hand, had to be treated as input parameters to the solution, and were selected by establishing a sensitivity matrix relating changes in X_6 and X_{16} to corresponding changes in H_6 and H_{16}. The resulting method of updating the constraint forces amounted to a difference representation of the Newton Raphson approach. Inner loop iteration was judged complete when no appreciable changes in the X_j's took place from one iteration to the next, while outer loop iterations were terminated when the resulting values of the Y_k's at the constraint locations were close enough to the required values to satisfy a particular error criterion.

This multiple iteration scheme was successful for all cases except those so close to snap-through of the frame as to cause instability.

This treatment of nonlinear deformation limits attention to the arches as discussed earlier. It was decided to do this in order to avoid undue complication in the investigation of large deformation effects. It will be seen that the analysis gave a good representation of the qualitative features of large arch deflections, especially in predicting the existence of loads at which snap-through would take place. The main draw-back was in ignoring the presence of coupling between arches which is produced by the purlins. A simple scheme for taking this into account gives a reasonable account of the discrepancies between test results and the nonlinear analyses which were conducted, not only with the elastica-type analysis but with the finite element approaches which are discussed later.

Figure 13 shows the deformed geometry that was predicted for 50% and 70% of the target snow load which was 10 lb/ft^2. The arch was assumed to be made of 1.5" square box, with 0.125" wall thickness of pultruded glass polyester. Using the above technique it was possible to increment the load up to 74% of the target load when finally the frame became unstable. The reason for this was that this iterative scheme at that load was unable to follow through the transition from Mode 1 to Mode 2 as shown in Fig. 11 (B). Similar computations were made for 2" square box section and the same wall thickness. It is interesting to see (Fig. 14) the variation of nonlinear moment as a function of percentage of the target load. The maximum moment in the arch occurs at the header attachment point which is presented as a function of the snow load for the two candidate sections.

The upper curves in Fig. 14 show the ratio of nonlinear moment (M_{NL}) predicted by using the elastica analysis to that predicted if geometrical nonlinearity was completely ignored (M_{LIN}). It is interesting to note that for 1-1/2" square section the moment ratio increases rapidly almost to infinity whereas for 2" square section the moment is considerably lower and closer to linear range. The obvious reason for this is the increased stiffness of the 2" square frame which precludes large distortions. For this section there are two-fold benefits, one because non-linear effects are

reduced considerably and secondly higher strength, ie larger section modulus.

5. APPLICATION OF ANSYS

The in-house elastica code was quite satisfactory for solutions involving up-to two imposed displacements and for the symmetric deformation state corresponding to snow loading. For a larger degree of indeterminacy which was anticipated in cases such as wind load involving nonsymmetric deformation, cable constraint and other restraints inherent in a non simplified practical structure, the iterative approach used in the elastica solution was considered a bit cumbersome. Hence a more labor-effective approach of using a commercial code with the necessary capability was adopted. Such a code would have to qualify by solving a proven test case with an acceptable degree of accuracy. In order to accomplish that the code should not only have a large deformation analysis capability but also provide for stress stiffening effects. The code ANSYS was tried out, wherein a solution was computed by using that code and compared with the same problem solved by the elastica approach. The parameter selected for comparison was the apex deflection. The results from both the cases are shown in Fig. 15, which certainly gave confidence in the capability of ANSYS to yield credible solutions for highly flexible frameworks like the composite tent frame in question. As a step toward optimized design, three choices of square box section were analysed-- 1-1/2", 1-3/4", 2". Results of the snow loading analyses are presented in Fig. 16 (A) with snow load carrying capacity plotted against the EI for the section. The top curve shows the collapse load at which its geometry of the frame became unstable. This in fact is the upper bound of the frame capacity if there is no limitation on bending stress of the material. The final design solutions are restricted to lie below the lower line which represent the bending stress failure limitation. As regard the wind loads, the design pressure corresponding to 45 knots wind was considered as 100% wind (Fig. 16(B)). The wind pressure was suitable converted into concentrated nodal loads. The computer solution is plotted in lower Fig. 16(B). In this case a designer need only consider the bending load failure, since the restraining effect of the cable never allows the frame to become unstable in the range of loads considered. Large displacements are expected to be a factor in practical uses of pultruded composite frames because of their inherent low stiffness when low-cost (ie glass-reinforced) materials are used. Maximum deformations were computed for different load intensities and presented in Figs.17-19. In a pultruded composite frame the magnitude of displacements is a matter of special concern, hence a study of maximum displacement at various load levels for the snow load case is presented in Fig. 17. It should be noted that the 10 psf snow load is an extreme condition with relatively low probability of occurence , whereas 3-5 psf snow load would be more typical and the curves of Fig. 17 should be interpreted with this in mind. Maximum horizontal displacements for the wind load case are shown in Fig. 19.

6. FINAL WEIGHT-OPTIMIZED ARCH SECTION DESIGN

An initial weight-optimization cycle was discussed in Sect. 3 based on the initial linear-frame analyisis approach. With the completion of the nonlinear version of the frame analysis it became apparent that the weight-optimized section could be achieved by a similar multi-condition analysis of the required section properties, except that Euler column buckling of the lower arch section had to be replaced by a statement reflecting the arch frame collapse condition. Thus the optimum section was one which gave the minimum area section providing adequate margin against:(1) bending stress failure;(2) local buckling of the compression flange of the section under high bending loads, and;(3) arch collapse corresponding to snap-through buckling of the overall arch.

Table 2 indicates some results of interest which are characteristic of the optimization exercise. The tabulated values of section height and width correspond to choices for which the EI of the section is a constant, the latter insuring that the same margin against collapse will be maintained, for a fixed wall thickness of the section. As h and w (section height and width) vary within this tabulation, the section modulus and section area change, leading to variations in bending stress and weight per unit length of the member. The acceptable section is required to have a bending stress below 24ksi to provide adequate margin with respect to a tensile stress capability of 35ksi for the pultruded material. The recommended section discussed in the lower part of the table provided a compromise between off-the-shelf pultruded stock availablility and an exact optimum.The 0.125" wall thickness of the section was calculated to provide a safety margin against local buckling of the compression flange(wall labeled "w" in the table) amounting to 100%.

7. CONCLUSIONS

The paper brings out some relevant lessons for a composite design engineer when he is attempting to make a transition from a metal design to a light weight low cost composite for a given product. Initial temptation to all is to follow the same tried and true, straight-forward methodology derived from the past metal design experiences with probably minor modifications. This paper indicates how such a seemingly rational approach could in many cases lead one to erroneous conclusions. It is a wise approach to test the initial design by prototype construction both under anticipated severe environments and under simulated expected loads. The structural performance could often alert the design engineer to new physical phenomena requiring radically different analytical tools. This is exemplified in this paper by the gross redistribution of forces one observes occurring in the composite structure. In the case considered for purlin design the redistribution turned out to be favorable, whereas for the arch frame design the non-linear moments turned out to be almost twice the magnitude of the linear values.
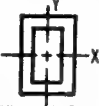
8. ACKNOWLEDGEMENTS

9. REFERENCES

1. O'Callahan, J.C., "NONFESA-Nonlinear Finite Element Structural Analysis Code for the Analysis of Stresses and Deflections in Frame Supported Tents", Bolt, Beranek and Newman Report 2803, Contract DAAG17-73-C-0107, March 1975.

2. D.W. Oplinger, J. Plumer and K.R. Gandhi "Design, Fabrication and Testing of a Pultruded Framework for Tent Applications" 28th Natiional SAMPE Symposium April 12-16, 1983.

3. HANDBOOK OF ENGINEERING MECHANICS, ed by W.Flugge, Sect. 45, p. 45-3 (1962) McGraw-Hill, New York.

TABLE I, PROPERTIES OF SECTION

Critical Element	Cross Section	Moment of Inertia I_{xx}	Moment of Inertia I_{yy}	Area in.^{2}	Ultimate Bending Strength @21000 psi	
					M_{xx}	M_{yy}
Main Frame Box Section 2-1/2"×1-1/4"×1/8"		0.678	0.219	0.875	11400.0	7300.0
Purlin 1-1/2" Dia. Tubing		0.093	0.093	0.369	2600.0	2600.0
Cross Ties Channel Section 1-1/2"×1"		0.140	0.039	0.412		

TABLE 2 COMPOSITE ARCH SECTION SELECTION

COMPOSITE SECTION PROPERTIES
FOR EI EQUIVALENT TO
2" SQUARE
$(I = 0.55 \text{ in}^4)$
APPLIED MOMENT AT 10 psf   126 in-K$_{ip}$
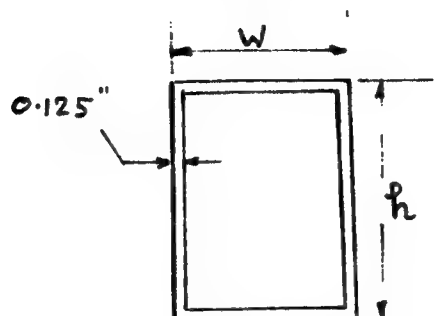
h (in)	2.0	2.2	2.4	2.6
w (in)	2.0	1.54	1.11	0.76
BEND STRESS (ksi)	22.9	25.2	27.5	29.9
WT/LENGTH, lb/ft	0.856	0.785	0.737	0.706

RECOMMENDED SECTION

$h = 2.5"$; $w = 1.25"$; $t = 0.125"$ $I = 0.68 \text{ in}^4$

BEND STRESS AT
10psf SNOW LOAD = 23.7 KSI
DISPLACEMENT = 5.1" AT 10 psf

WT/LENGTH = 0.79 lb/ft

Margin of Safety= $\dfrac{35.0 - 23.7}{23.7}$ =47%

FIG. I TEMPER TENT SYSTEM
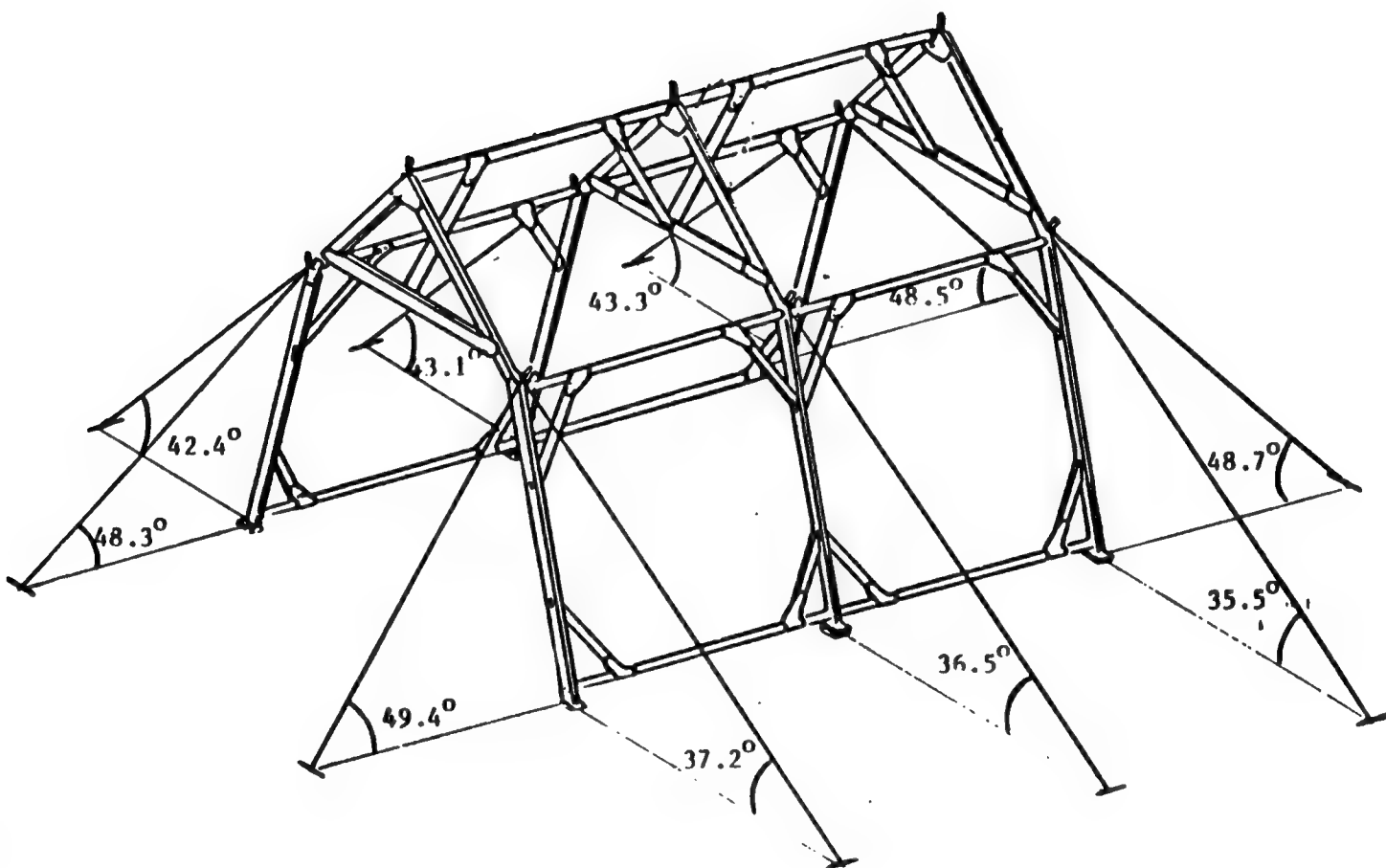
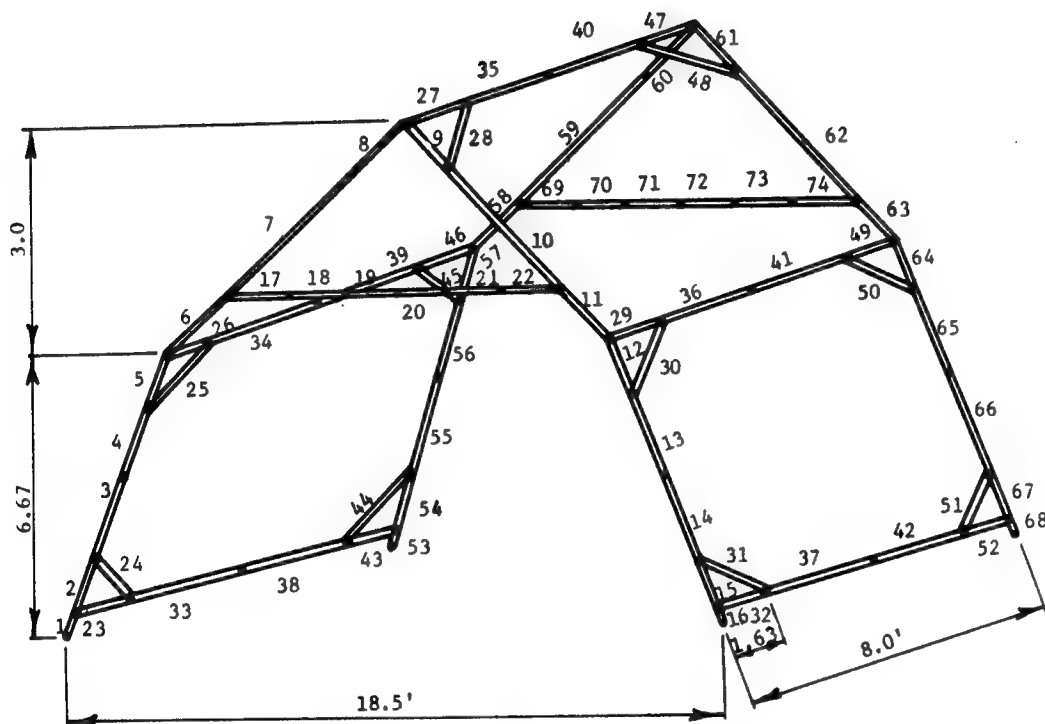FIG. 2 CONFIGURATION OF MODULAR TEMPER FRAMEWORK
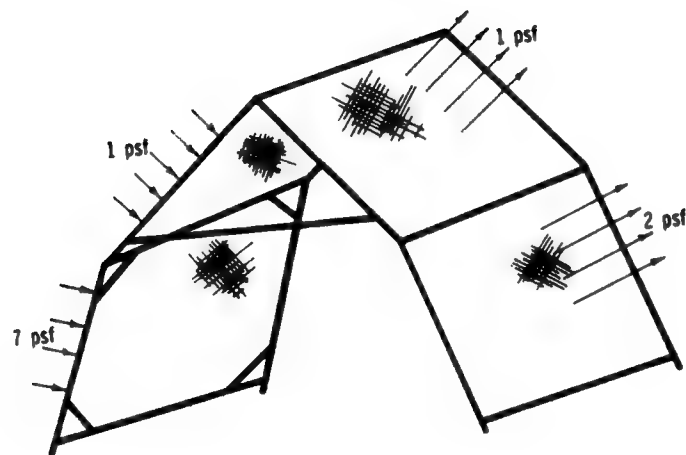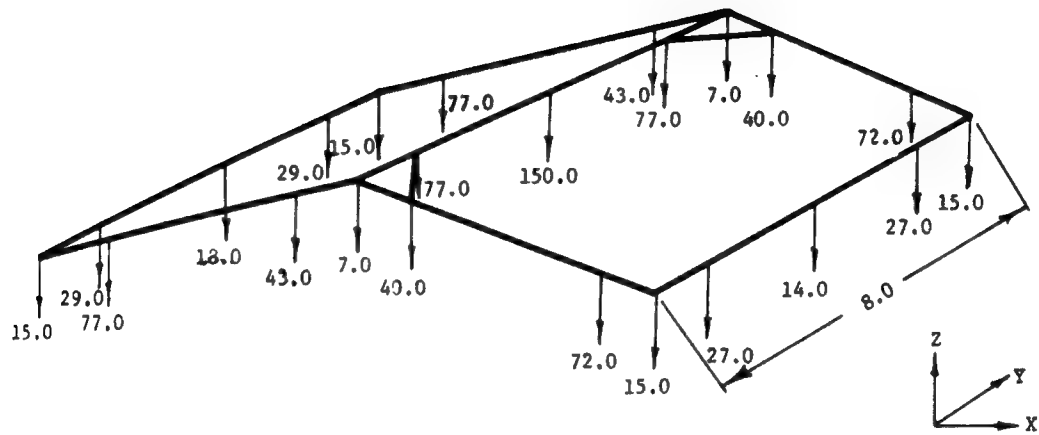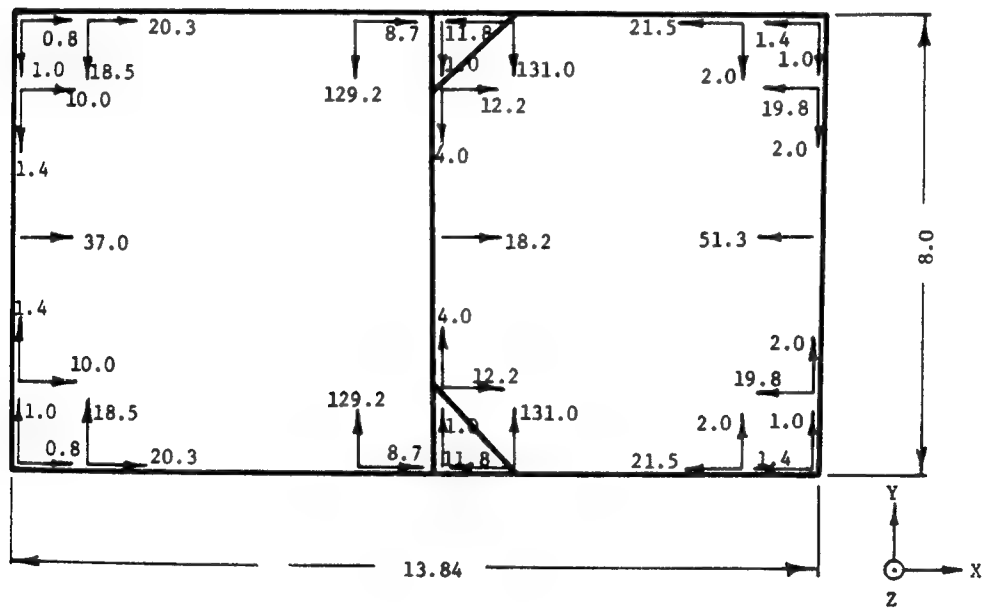
215

FIG. 3 LAYOUT OF TENT FRAME ELEMENTS
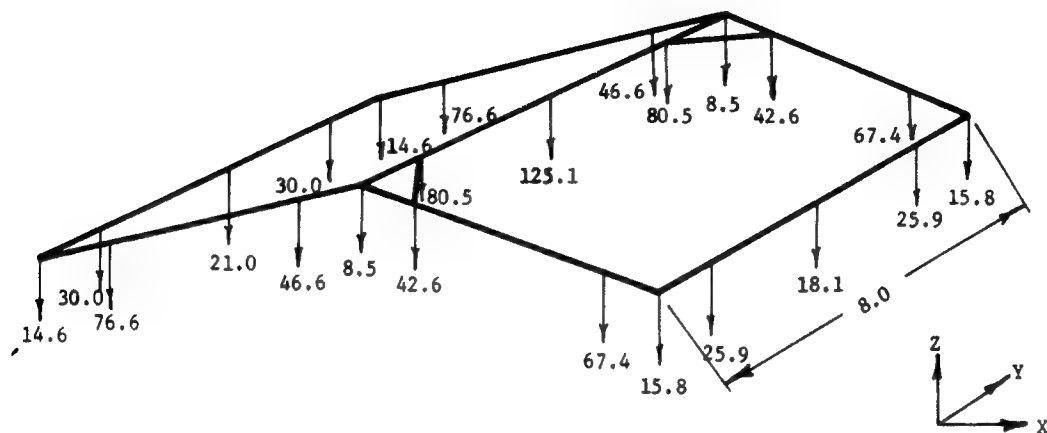
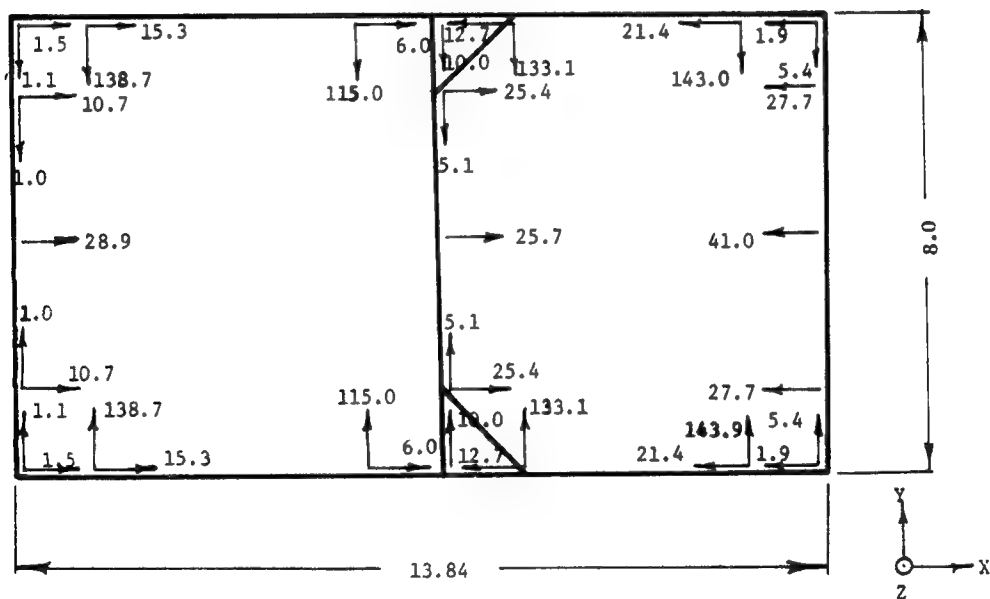FIG. 4   WIND PRESSURE INTENSITY ON TEMPER TENT

SNOW LOAD IN Z-DIRECTION

LOADS IN X&Y DIRECTION

FIG. 5 FRAME LOADS DETERMINED FROM NONFESA SOLUTION-ALUMINUM

SNOW LOAD IN Z-DIRECTION

LOADS IN X & Y DIRECTION

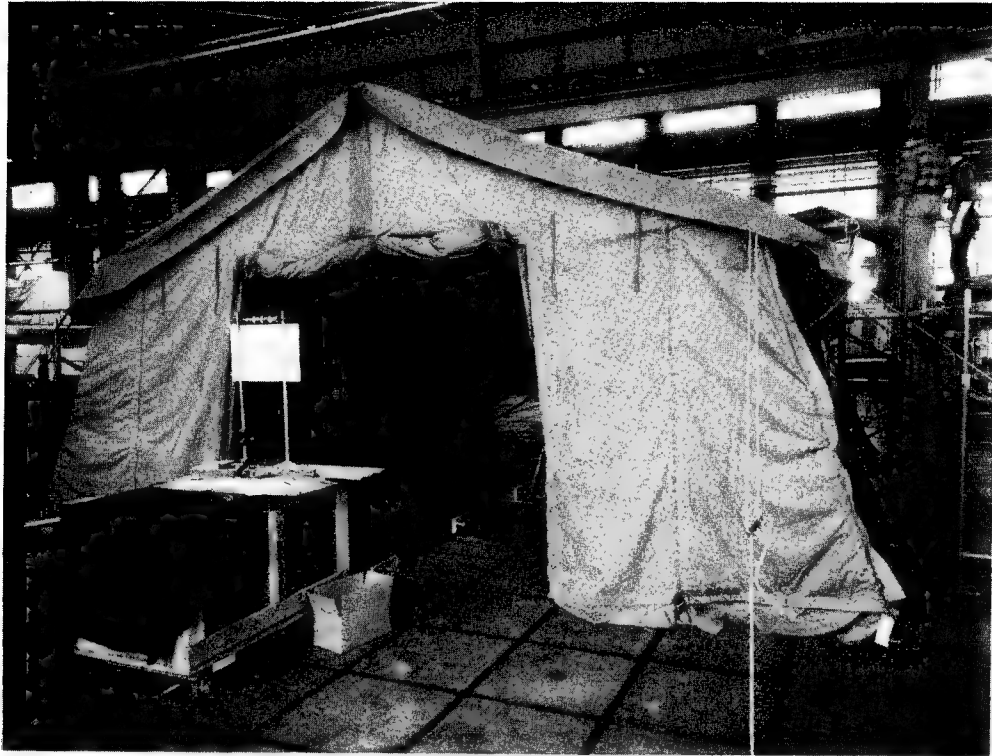FIG. 6 FRAME LOADS DETERMINED FROM NONFESA SOLUTION-COMPOSITE

FIG. 7 COMPOSITE FRAME TENT AT INITIATION OF
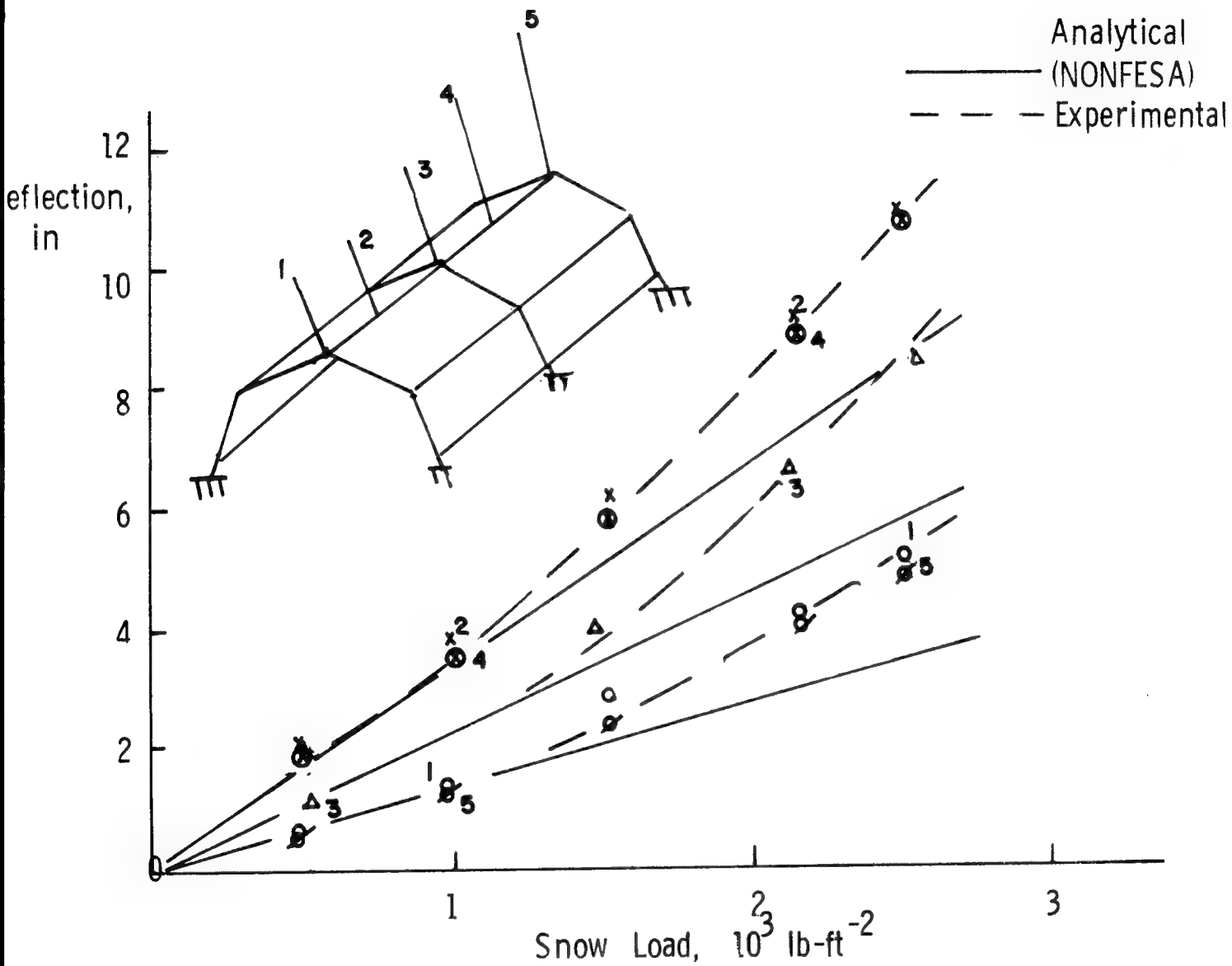SIMULATED SNOW LOADING

FIG. 8 COMPARISON OF NONFESA PREDICTIONS AND OBSERVED
DEFLECTIONS, SNOW LOAD TEST.

1 -- End Arch
2 --Purlin Center
3 --Center Arch
4 --Purlin Center
5 --End Arch

Deflection, in

20

10

Creep
21 Dec -- 3 Feb 82

Target
10 lb-ft^{-2}
Snow Load

Final
Load

Load, 10^3 lb

1   2   3

Days from Final Load Application
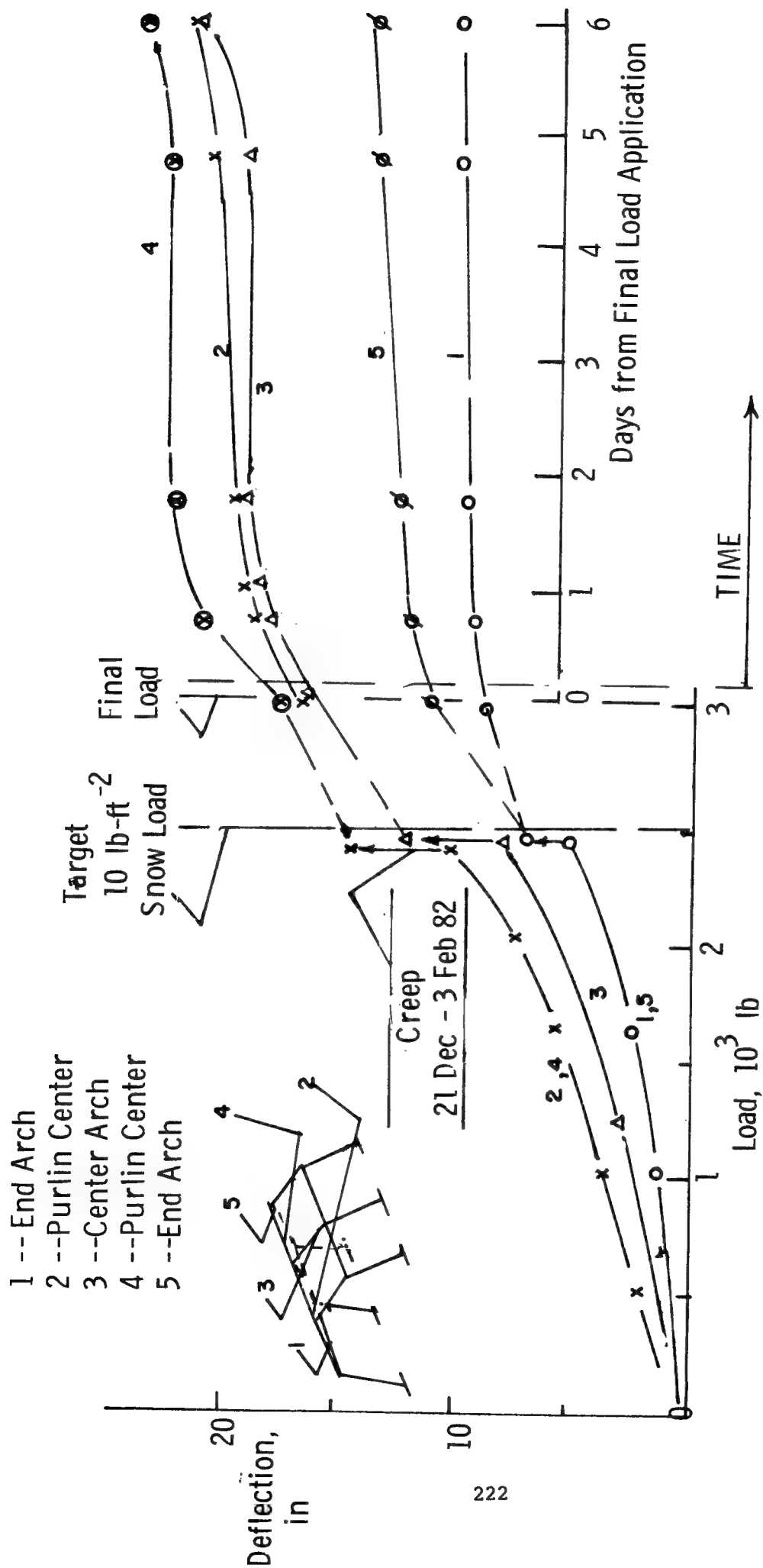
TIME

1   2   3   4   5   6

FIG. 9   LOADING SEQUENCE IN SIMULATED SNOW LOAD
TEST ON COMPOSITE FRAME

222
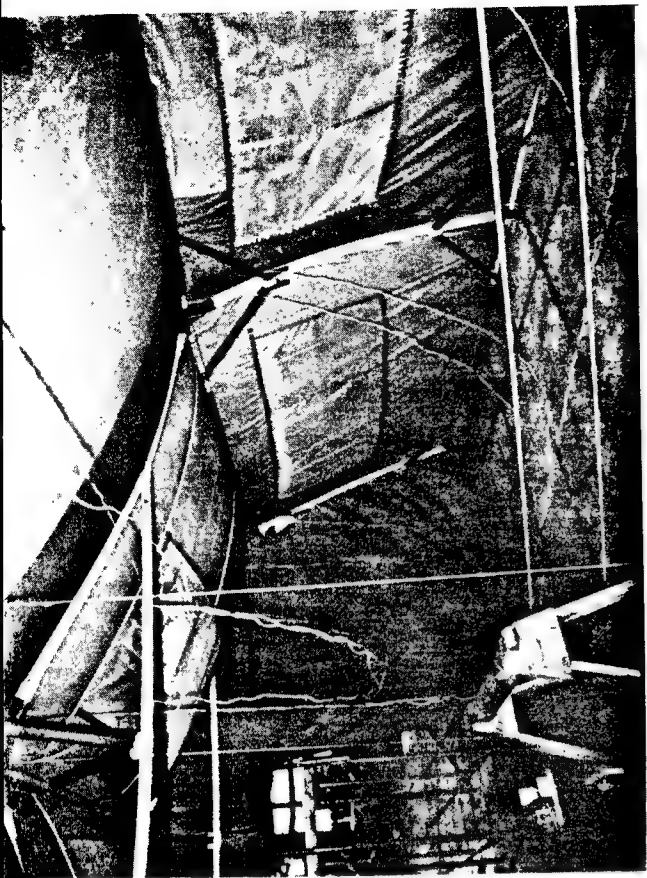
FIG. 10   INTERIOR VIEW OF THE LOADED COMPOSITE TENT. NOTE THE LARGE DISTORTIONS OF FRAMEWORK

(A) Rotation of Foot Load Vector with Increasing Load

Low Loads

High Loads

Mode 1

(B) Mode Jump for Snap-Through Buckling

"Floor" Level

Mode 2

94.2   149.4   112.3

H6

(C) Assumed Load System for Large Deflection Analysis

659

H16
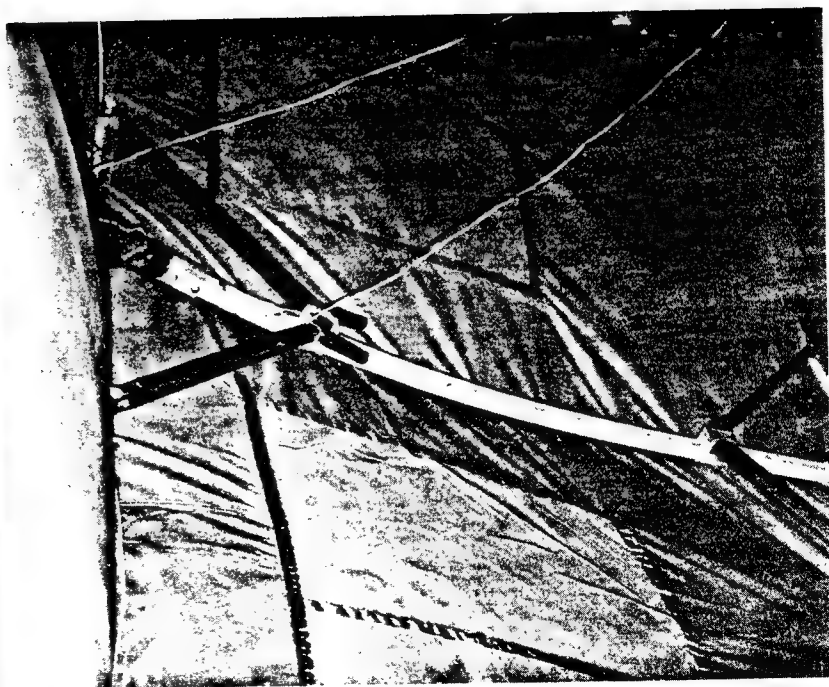
FIG. II CHARACTERISTICS OF NONLINEAR ARCH DEFORMATION
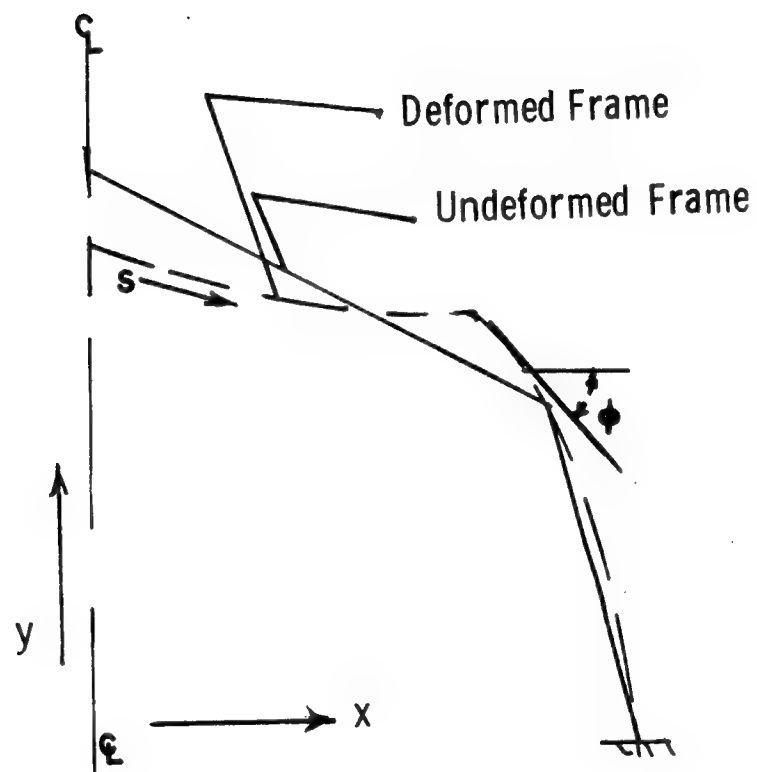
FIG. 12 COORDINATE SYSTEM FOR NONLINEAR ARCH ANALYSIS
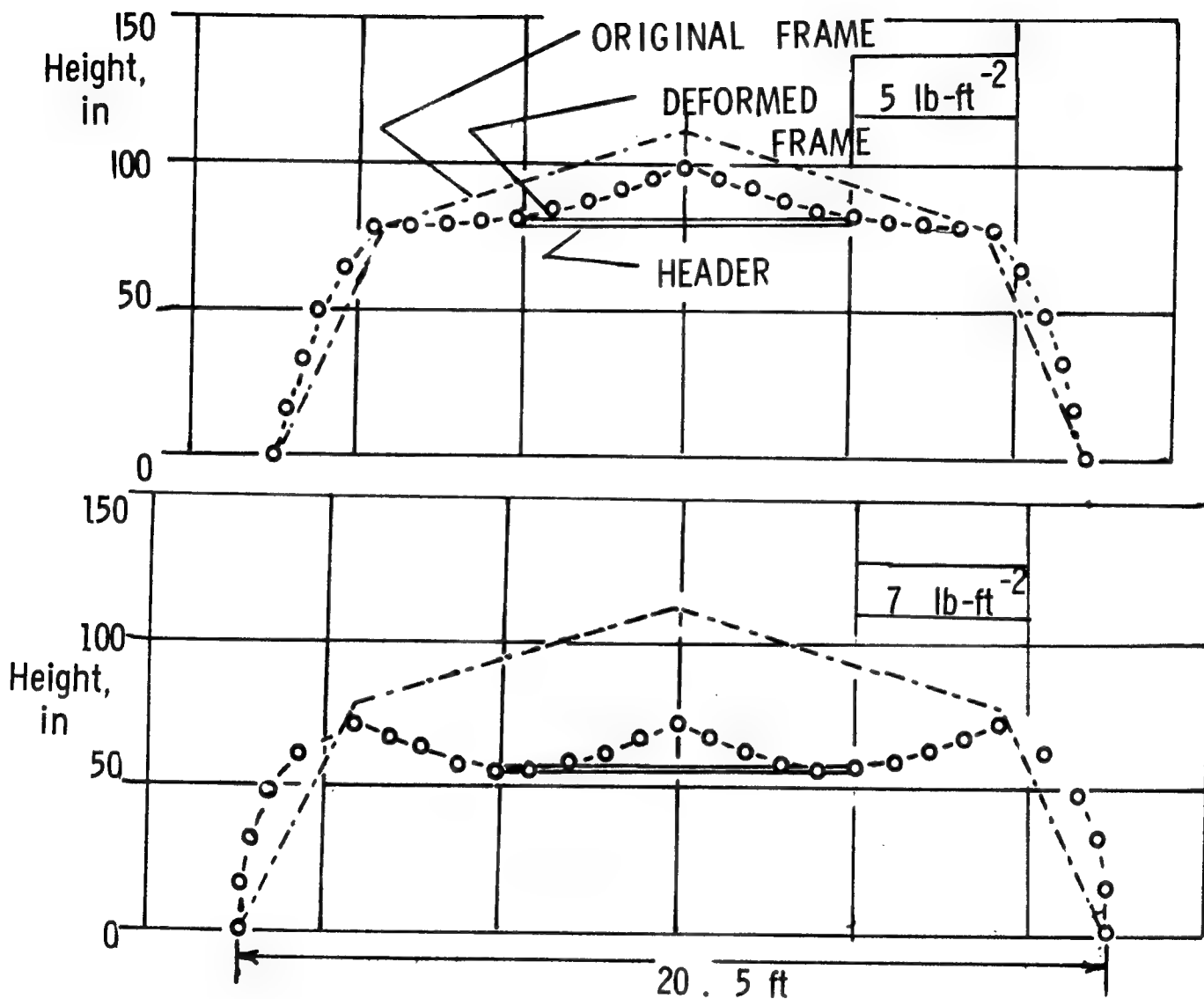
FIG. 13 PREDICTED NONLINEAR DEFORMATIONS OF ARCH
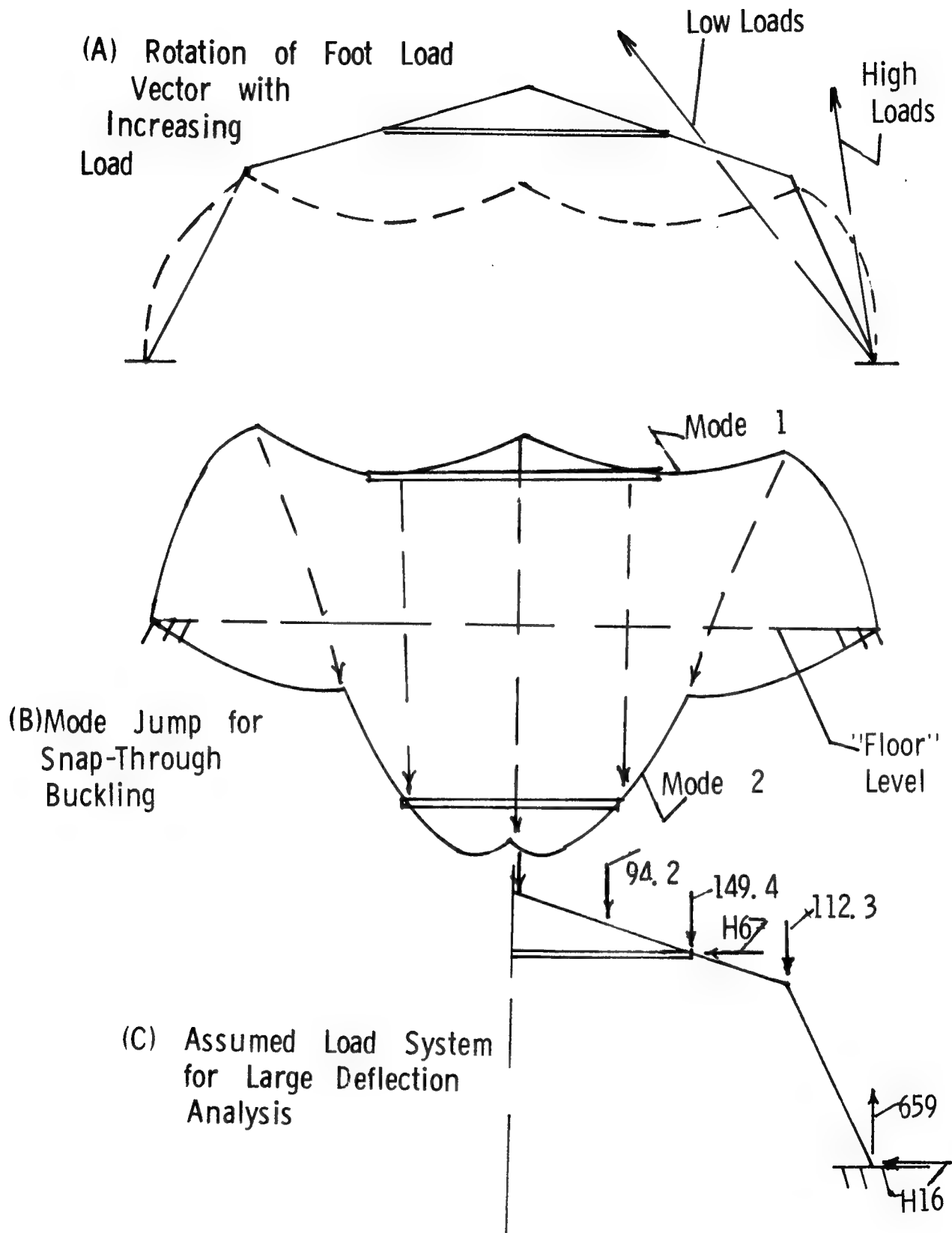
FIG. 14 VARIATION OF MAXIMUM MOMENT IN ARCH WITH LOAD
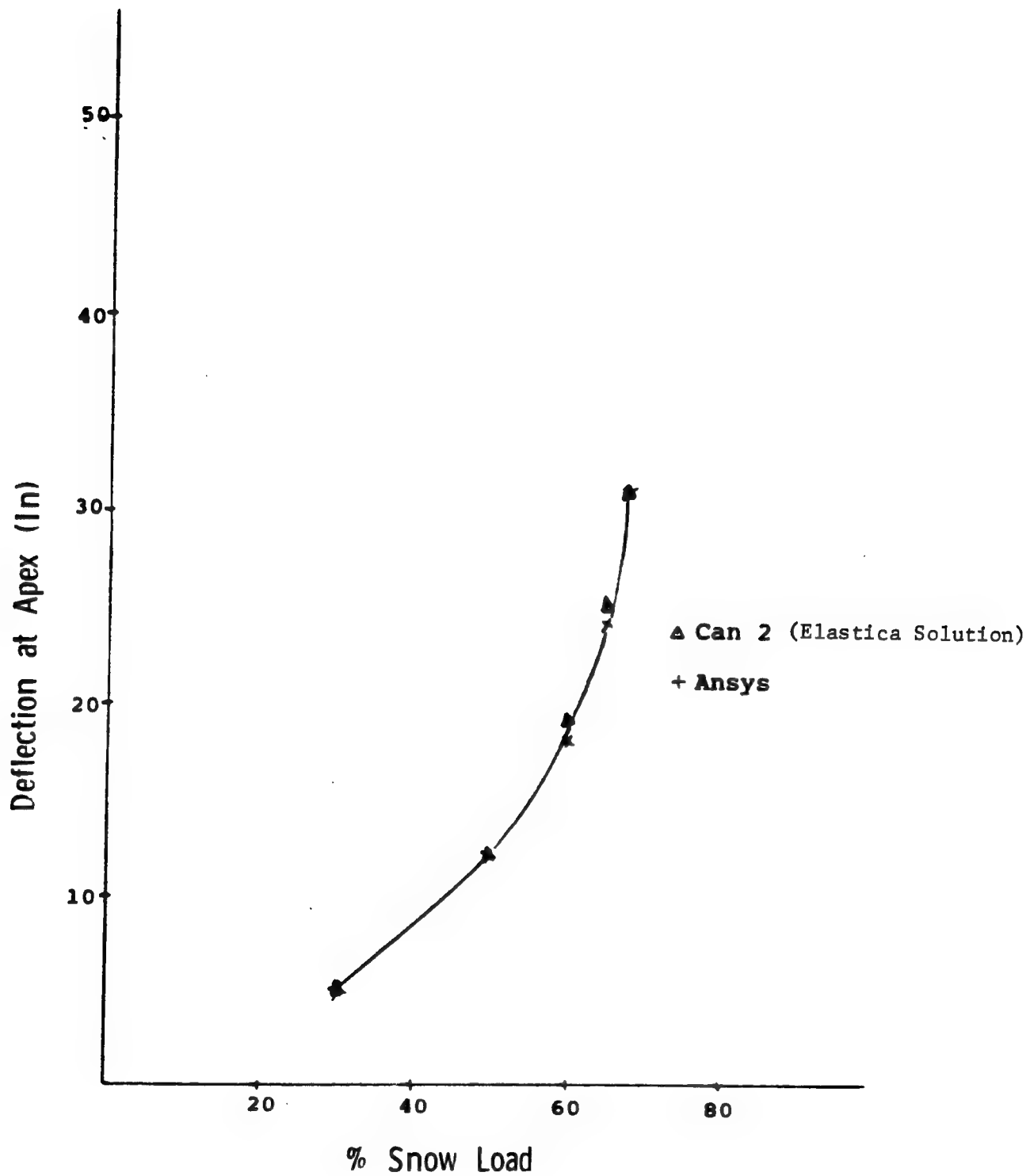
FIG 15 COMPARISON OF CAN 2 AND ANSYS SOLUTIONS 1-5" SQ

FIG. 16 STRUCTURAL PERFORMANCE VS EI OF ARCH SECTIONS
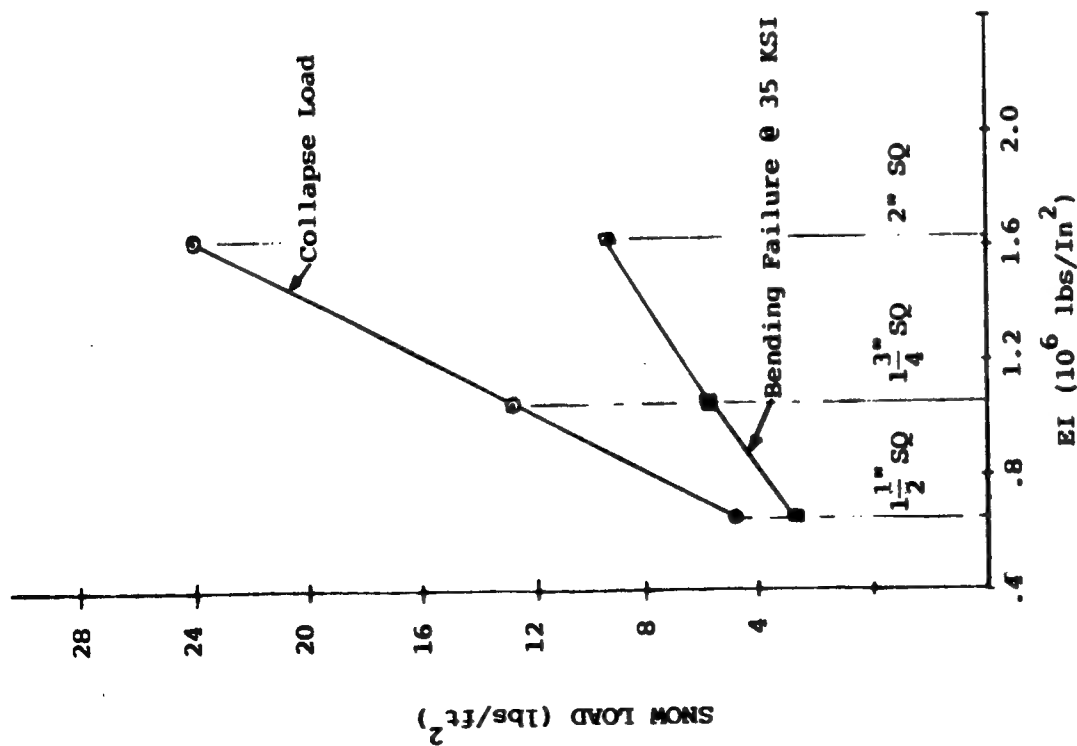
(A) Snow Load Capacity vs EI
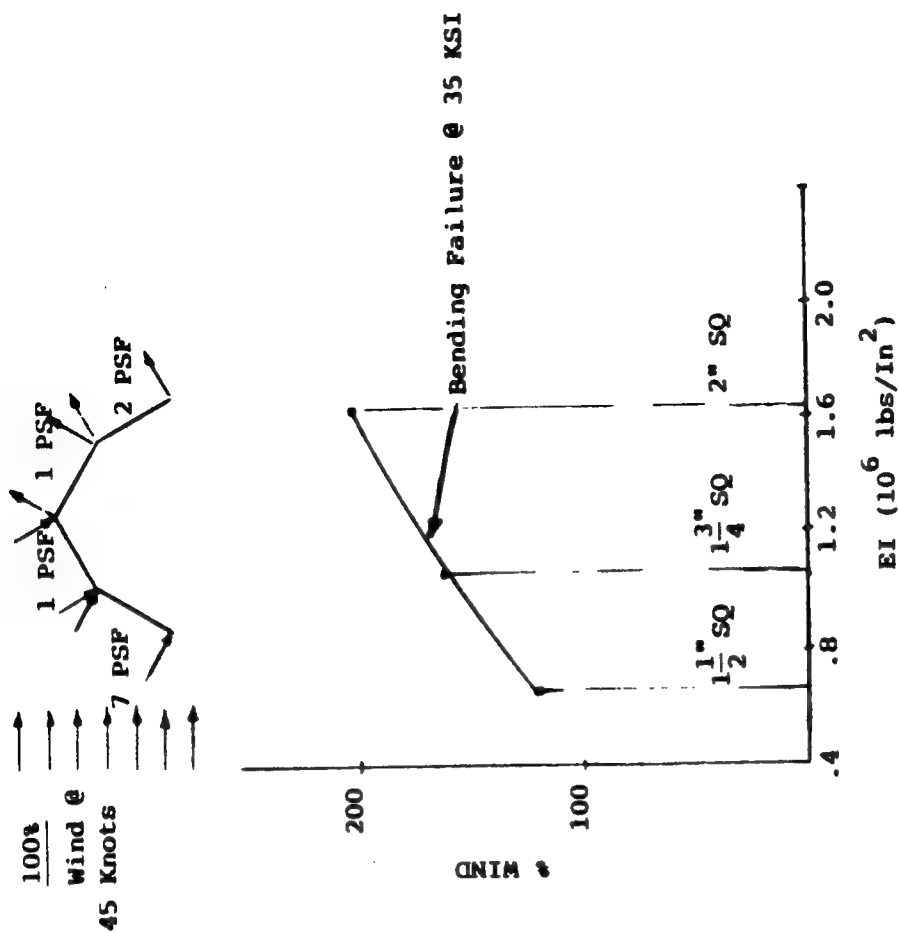
(B) Wind Load Capacity vs EI

Fig 17 Maximum Downward Displacement Vs Snow Load

FIG. 18 MAXIMUM DISPLACEMENT AT VARIOUS LEVELS OF SNOW LOADS

231

FIG. 19 MAXIMUM HORIZONTAL DISPLACEMENT UNDER WIND PRESSURE

SCALE MODEL SHOCK TUBE TESTING OF BLAST
HARDENED COMPOSITE SHELTER PANELS

Jerome P. Fanucci
Roger W. Milligan

Kaman AviDyne
Burlington, Massachusetts   01803

ABSTRACT

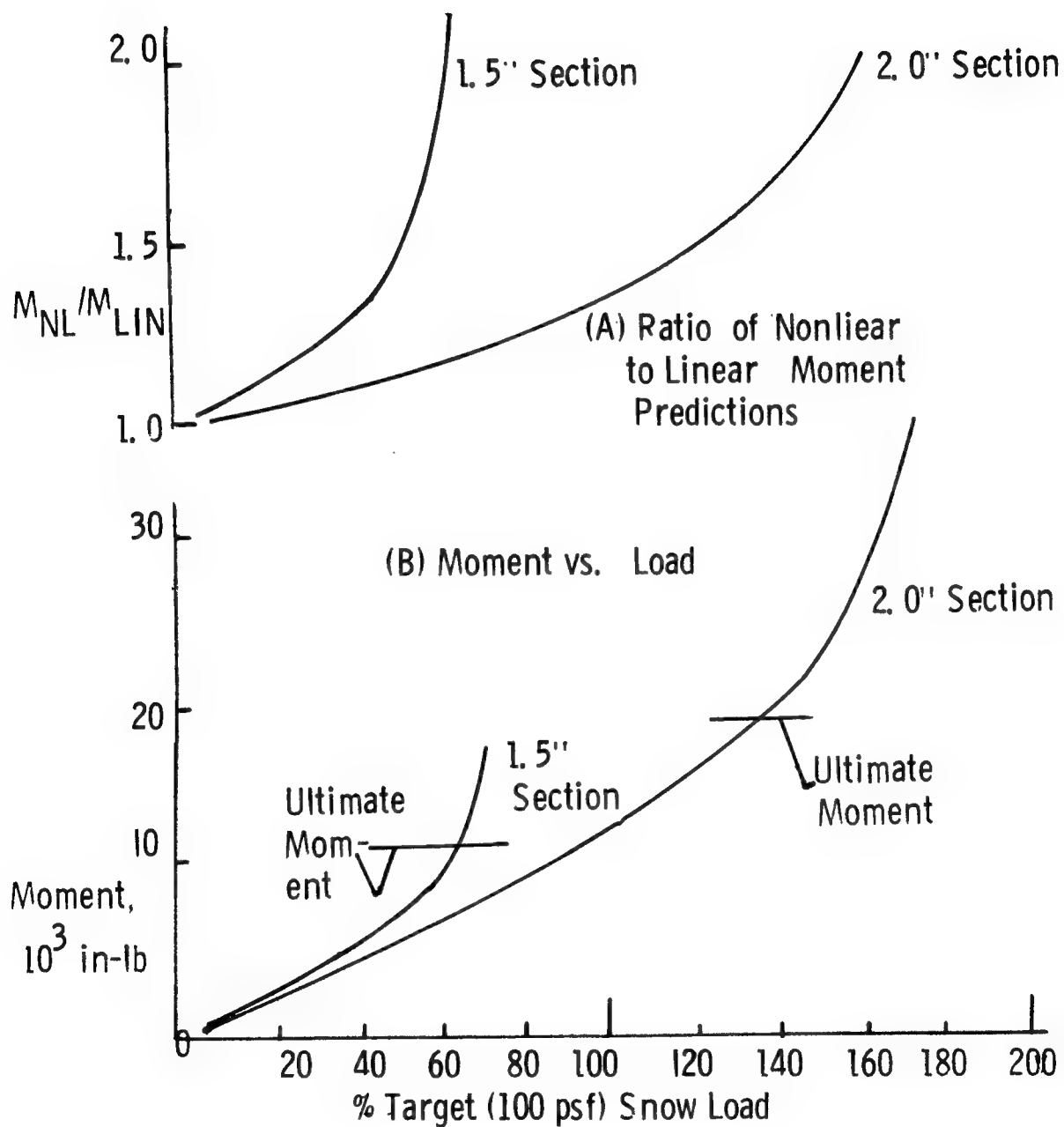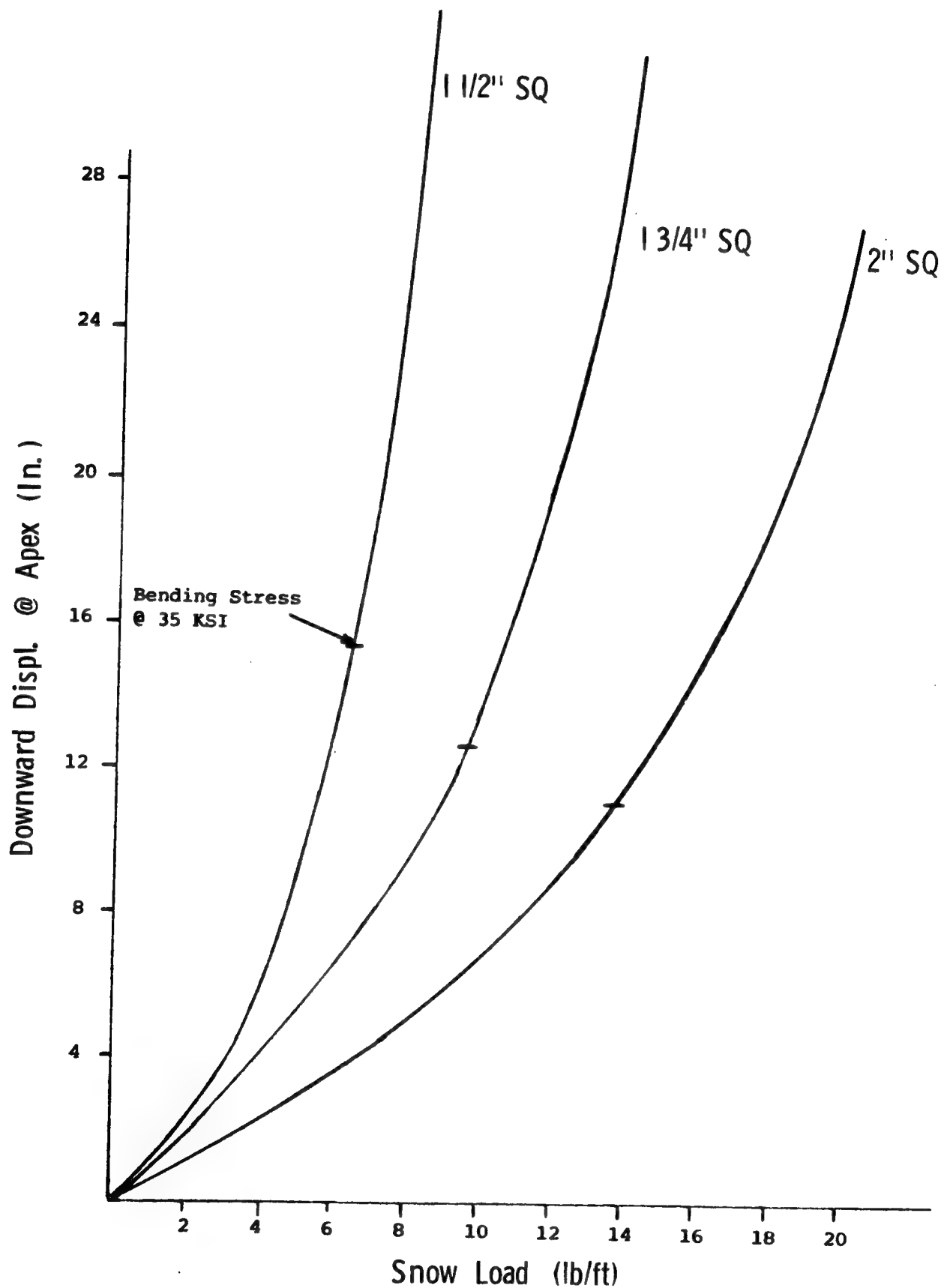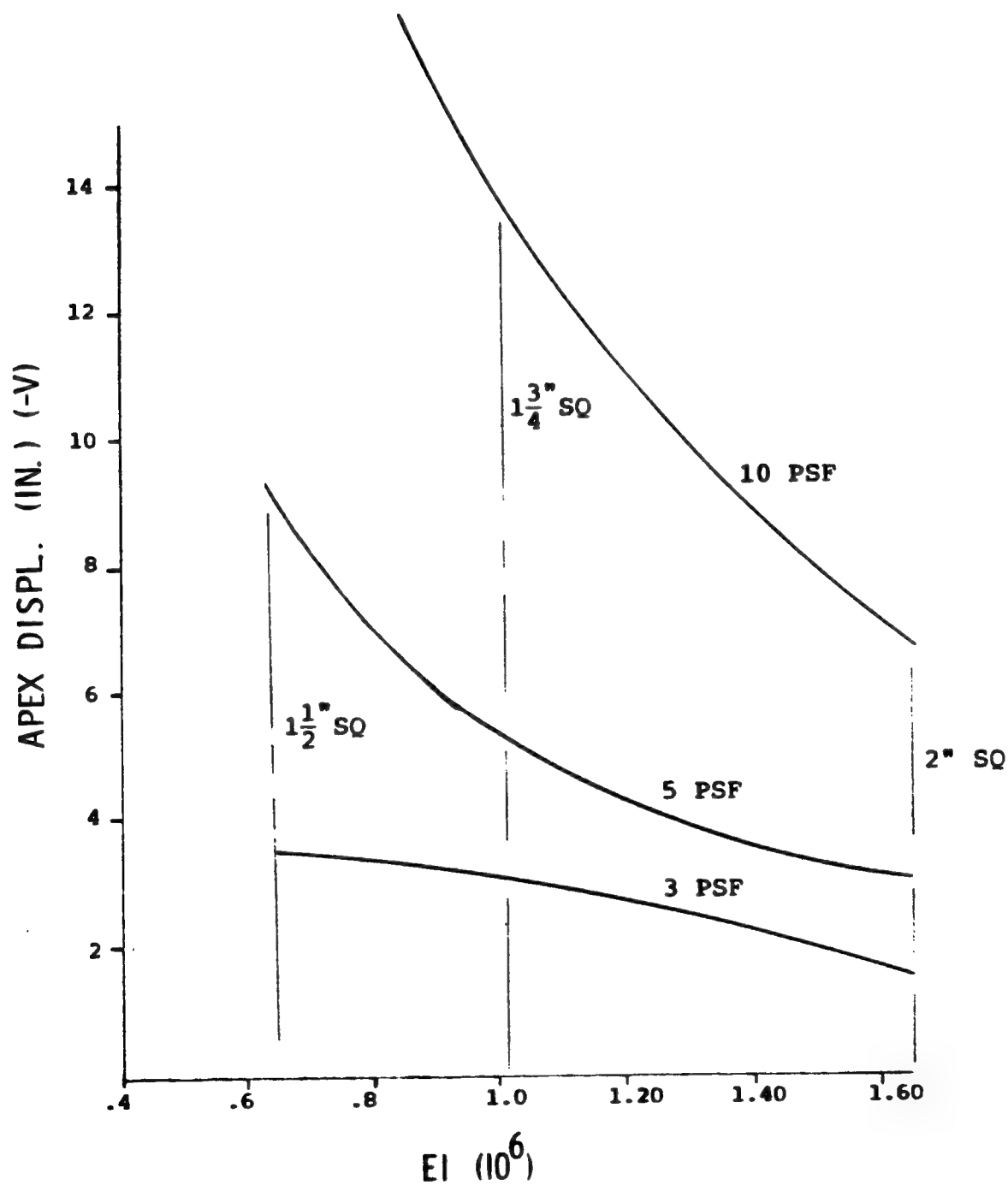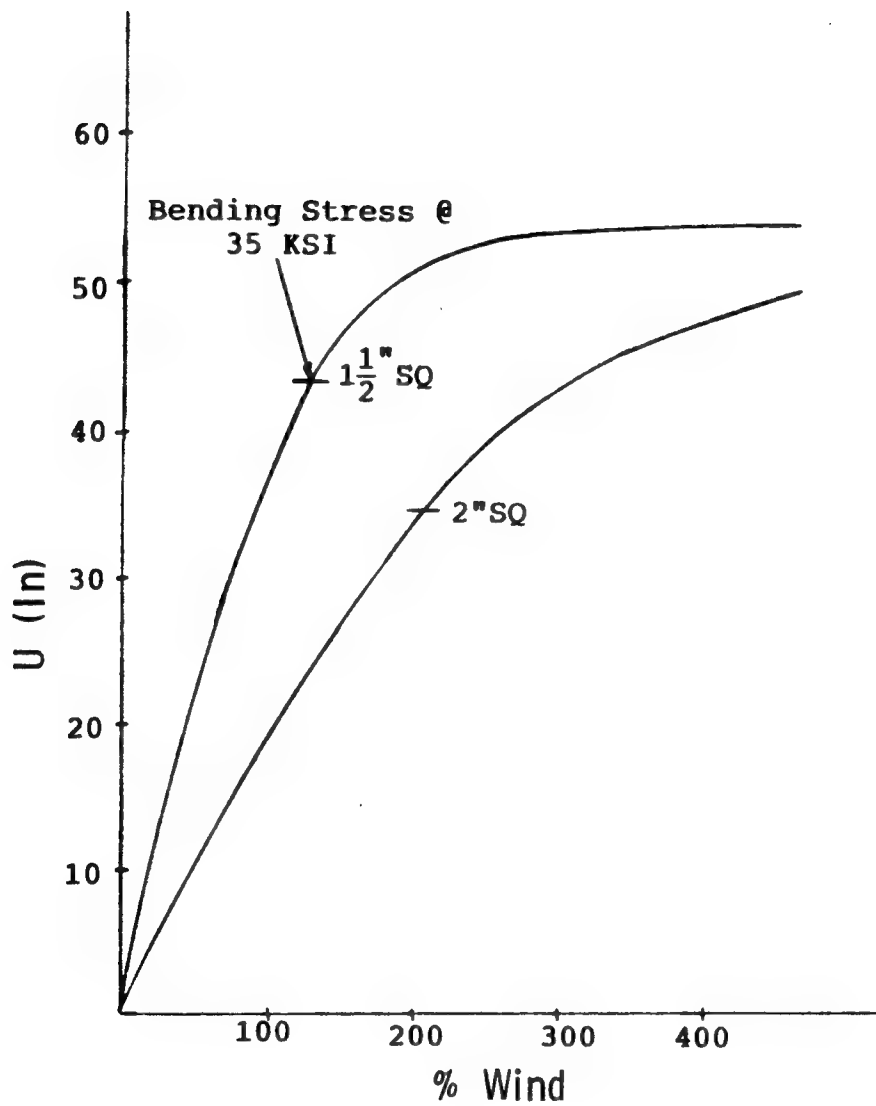Scale models of five competing aluminum, graphite/epoxy, Kevlar/epoxy and S-glass/epoxy shelter panels were tested in an 8 foot diameter shock tube. Each configuration had been sized to withstand blast loading effects. Testing verified the design techniques and analysis tools and provided a data base for future shelter projects. Results of the test program showed that both the conventional aluminum configuration and the composite material designs could withstand the blast condition. Measured dynamic strain histories were compared with ADINA finite element predictions. Correlation with strain measurements was good; however, correlation with time to peak strain was less accurate even when the complete support structure and shock tube wall were modeled. This work was sponsored by the Natick Army Research and Development Center.

INTRODUCTION

The battlefield survival of electronic command, control and communications systems is vital for the successful completion of many military missions. The importance of these systems has led to the imposition of blast hardness requirements on the mobile tactical shelters which house the equipment in the field. Blast loading places the most severe structural design requirement on a shelter. Hardening against blast effects can result in an unacceptably large weight increase and corresponding loss in payload. In an attempt to minimize the weight increase resulting from blast hardening, Natick Labs has sponsored a program which investigates alternatives to the conventional aluminum honeycomb structure currently used in unhardened designs. The work described in this paper will discuss one phase of this program, the experimental comparison of four competing advanced shelter wall designs and a conventional aluminum structure.

Following the design of ten full size shelter panels (1), a cost/ weight trade study (2) was used to select the five most interesting concepts for further experimental comparison and design verification. Testing of full size shelter panels, while possible (3,4), is prohibitively expensive. For this program, scaling techniques were used to produce approximately half size models of aluminum, S-glass, Kevlar and graphite/ epoxy shear stiffened sandwich panels and a graphite hat-stiffened membrane skin design.

Shock tube testing of the models was conducted in two stages. In the first stage, panels were subjected to blast loads approximately 30% lower than their design limit load, followed by exposure to limit load. All four sandwich designs passed limit load testing with little or no damage observed. The graphite hat-stiffened membrane design showed some evidence of stiffener debonding near test fixture corners. The second stage of testing consisted of exposure of previously untested models to an ultimate load blast level. These shots produced varying degrees of damage in the models. The tests demonstrated that the panels met the design requirements.

Data from the tests were reduced from 3 channels of pressure and 10 channels of strain instrumentation. Pressure levels on the panel were as expected for the initial second of the test. The design blast loading produces a step rise in overpressure on a shelter wall, followed by an exponential decrease to the value of the free field pressure behind the shock. A typical structure will reach maximum stress levels in a very short time, often 10 msec or less, after being subjected to this type of load. The response of panels to the initial phase of the pressure load was adequately simulated by the shock tube tests. Measured strain levels agreed well with predictions at the edge and center of the panel. Measured time to peak was usually lower than analytically predicted. Attempts to correlate measured frequency data with refined finite element structural analysis models did not significantly improve phase predictions.

SPECIMEN MODELING

Five candidate designs for blast hardened tactical shelter wall panels were chosen from a number of alternatives described in References 1 and 2. Selections were based on results of a trade study (Reference 5) which considered estimates of manufacturing and life cycle cost as well as weight reduction. Composite designs were highly rated for their ability to reduce or eliminate corrosion problems associated with water leakage through seams in standard aluminum honeycomb panels, a major problem with this type of construction. Table 1 lists details of the five full size designs chosen for experimental study. Four of these designs consisted of variations of the standard stiffened honeycomb sandwich panel currently in use on shelters. The aluminum design was sized to carry the blast loads without exceeding a 2% strain limit. Composite sandwich designs investigated the impact of material variation on weight of the standard configuration. The fifth configuration, a hat-stiffened graphite design, represented an alternative to current shelter panel geometry.

Blast testing of full size designs is prohibitively expensive for a comparative study. Since major objectives of the program were the generation of an experimental response data base for the verification of current and future structural dynamics analysis methods as well as direct design comparison, testing of reduced size specimens could be employed to produce useful results. Model testing in a controlled laboratory environment allowed much better definition of panel edge conditions than could be obtained in full scale field studies.

TABLE 1

FULL SIZE PANEL AND MODEL DETAILS

	Aluminum Sandwich	S-Glass Sandwich	Graphite Sandwich	Kevlar Sandwich	Graphite Hat-Stiffened
Outside Skin Laminate					
Full Size	6061-T6	$(\pm45/0_3/90_{1.5})_s$	$(\pm45/0_3/90_{1.5})_s$	$(\pm45/0_6/90_{1.5})_s$	$(\pm45/0_6/90_2)_s$
Model	6061-T6	$(0_2/90/\pm45)_s$	$(0_2/90/\pm45)_s$	$(0_3/90/\pm45)_s$	$(0_4/\pm45/90_{1.5})_s$
Outside Skin Thickness (in.)					
Full Size	0.090	0.104	0.072	0.152	0.110
Model	0.051	0.080	0.055	0.096	0.083
Inside Skin Laminate					
Full Size	6061-T6	$(\pm45/90_3/0_{5.5})_s$	$(\pm45/0_3/90_{1.5})_s$	$(\pm45/0_{12}/90_{3.5})_s$	$(51\%0°,49\%\pm45°)$ [1]
Model	6061-T6	$(0_3/90_2/\pm45)_s$	$(0_2/90/\pm45)_s$	$(0_6/90_2/\pm45)_s$	$(47\%0°,53\%\pm45°)$ [1]
Inside Skin Thickness (in)					
Full Size	0.090	0.168	0.072	0.280	0.345
Model	0.051	0.112	0.055	0.160	0.209
Stiffener Wall Thickness (in.)					
Full Size	0.16	0.115	0.169	0.152	0.170
Model	0.09	0.080	0.090	0.082	0.110
Core Depth (in.)					
Full Size	5.5	5.5	5.5	5.5	4.0
Model	3.0	3.0	3.0	3.0	2.3
Panel Weight (lbs)[2]					
Full Size	673	605	369	610	352

(1) Stiffener cap area - laminate constructed from intermixed 0 and ±45° layers.
(2) Full size panels are 220 x 80 inches, models are 66 x 48 inches in plan view.

235

Testing was conducted in Ballistic Research Laboratory's (BRL) 8 foot diameter shock tube. This facility had the capability of producing a shock with a maximum incident overpressure of 15 psi. The largest practical panel size was approximately 4 x 5 feet. Two methods for testing reduced-size panels were considered. The first, testing a full depth section with reduced length and width dimensions, could not be used. In order to generate design skin stress levels in the full depth cross section, a incident test overpressure equal to the ratio (full size width/reduced size width)^2 times the design pressure would be needed. This value exceed the facility limit. A more important concern with this type of test was the need for a different multiplying factor to match core shear stress. It is not possible to simultaneously match both skin and core stresses using a reduced width, full depth test specimen.

Since it was important to experimentally match the state of stress in the panel to verify design procedures, testing a properly scaled model of the panel cross section was selected. With this method, all linear dimensions including panel depth were multiplied by the scale factor,

$$\lambda = \text{(model width/full size width)}.$$

Analysis of the scaling problem for blast loaded structures (References 6, 7, and 8) shows that the response of a model of scale, λ, will be related to that of an idealized full scale structure according to the parameters listed in Table 2.

TABLE 2

RELATIONSHIPS BETWEEN SCALE MODEL AND FULL SIZE RESPONSE
TO BLAST LOADING (FROM REFERENCE 8)

Physical Parameter	Scale Factor
Length	λ
Time	λ
Velocity	1
Acceleration	λ^{-1}
Mass	λ^3
Force	λ^2
Strain	1
Stress (Pressure)	1
Energy	1

This table shows that an ideally manufactured model of reduced size, λ, will exactly match the full size stress state when the model is loaded by the full size incident overpressure. Since time is shown to scale by a factor of λ, model frequencies will be higher than full size frequencies. This implies that strain rate can not be properly matched. This was felt to be of only minor concern at the moderate strain rates experienced in the test program.

236

A more significant deviation from model fidelity was imposed by the use of standard material thicknesses in both metal and composite designs in order to keep fabrication cost low. This requirement most directly impacted model laminate layups. All full size composite skins contained two sets of plies oriented at ±45 degrees to the panel width which carried inplane shear loads. These plies could not be properly modeled using off-the-shelf prepreg thicknesses. A second important deviation from an ideal model was the decision to reduce the aspect ratio of the panel, its ratio of length to width, from its 2.5 full size value to 1.4 in the model. This deviation permitted a deeper core that more accurately simulated cell buckling phenomena, and thicker skins to minimize laminate modeling errors. Analytical studies have shown that very little change in the biaxial load components occurs as aspect ratio increases above a value of approximately 1.5.

Details of the five test panels are compared to full size dimensions in Table 1. Figure 1 illustrates a typical sandwich panel configuration, along with test instrumentation locations. The aluminum, glass, graphite, and Kevlar sandwich panel designs each contained seven box-shaped stiffeners to assist the 3.8 lb/ft^3 paper honeycomb core in carrying the shear loads. The aluminum configuration used off-the-shelf extrusions for stiffeners. Stiffeners in the composite configurations were made by tape winding 3 inch wide unidirectional prepreg on a mandrel in alternating plus and minus 45 degree layers until the desired thickness of uncured material was built up, then curing the assembly in a outer mold line box to ensure control of the height dimension. Skins were fabricated from unidirectional tape and press cured.

Figure 2 illustrates the graphite/epoxy hat-stiffened design. This configuration differed from the other four concepts in that it had only an outer surface skin. Bending loads carried by the inner skin of the sandwich designs were instead supported by additional 0° fibers built into the caps of the 10 hat-stiffeners. Stiffeners were fabricated from unidirectional tape hand laid onto a mandrel and autoclave cured. Webs were composed entirely of ±45-degree plys which ran continuously from edge to edge. Seventeen 0° plies were added in the cap area. Panels were assembled in a secondary bonding operation, with aluminum clips used to connect the stiffeners to the metal edge-close-out members. Each panel had a total of 246 close-tolerance holes drilled along its upper and lower surface perimeters to facilitate mating with the panel support frame and shock tube interface with the best possible simulation of a clamped boundary. All panels were fabricated by Bonded Technology, Inc. of Cromwell, Connecticut.

EXPERIMENTAL PROCEDURE

Models were tested at BRL's 8 foot diameter shock tube. This facility, located in Aberdeen, Maryland, consists of a 232 foot long steel tube closed at the test specimen end by a heavily reinforced plate. The tube is mounted on tracks which allow axial motion and is restrained longitudinally 122 feet upstream from the test specimen location. In
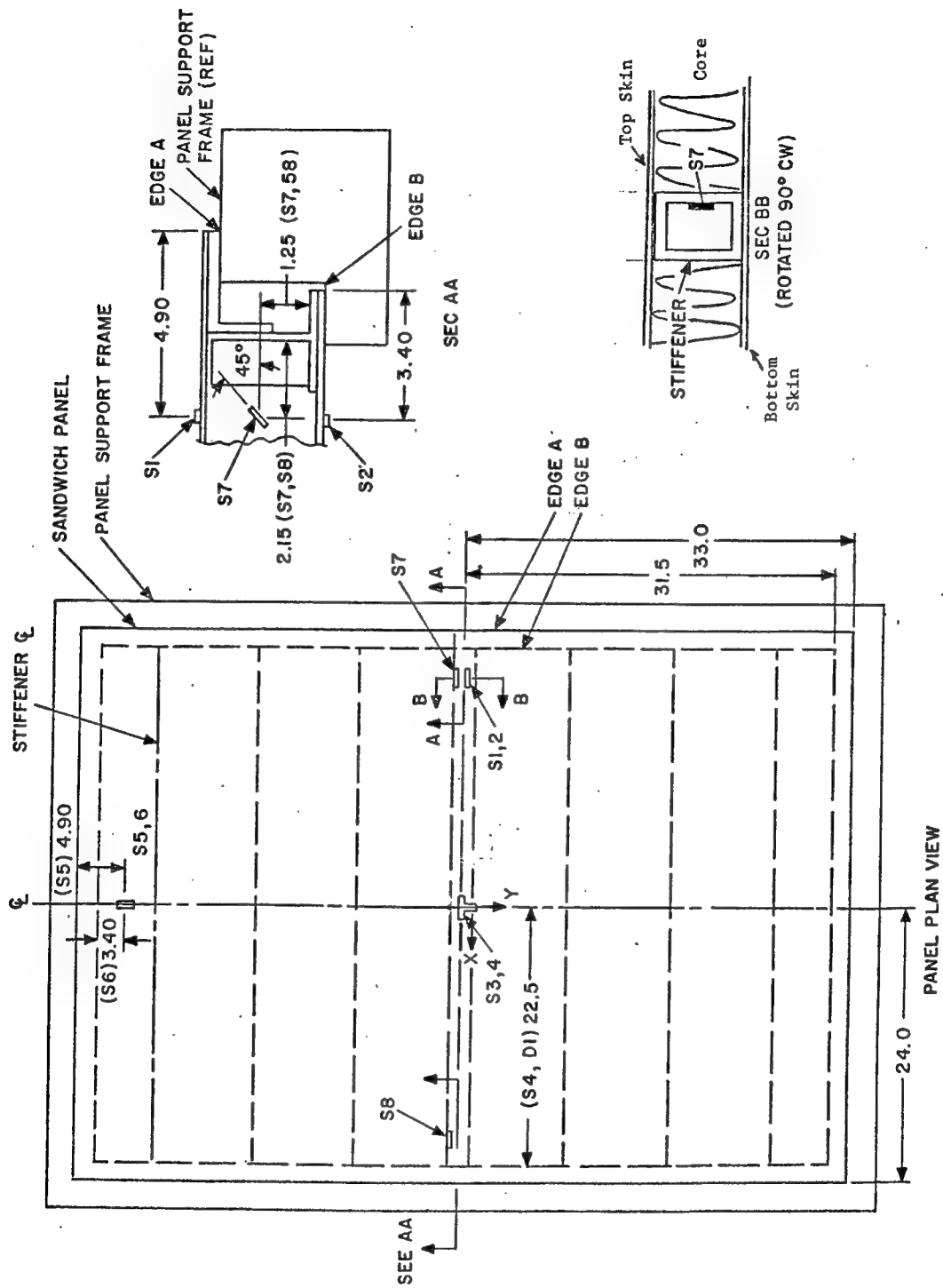
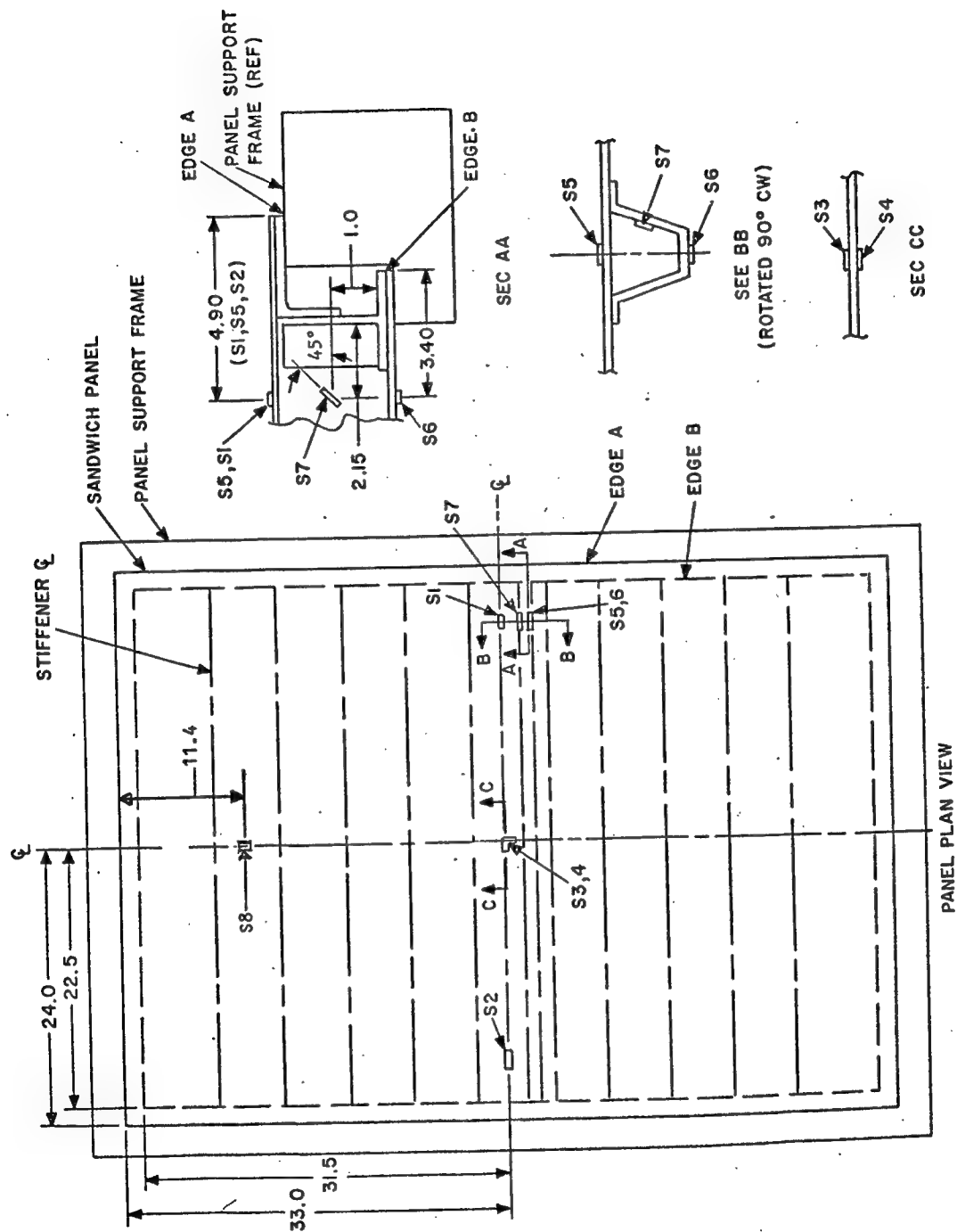Figure 1. Typical Sandwich Panel Fabrication and Instrumentation Details

Figure 2. Graphite/Epoxy Hat-Stiffened Panel Fabrication and Instrumentation Details

239

addition, the end closure is mounted on tracks to allow access for specimen mounting. For this program an intermediate steel fixture was built to interface test panels with the existing closure. The 1500 pound fixture was designed to provided the best possible simulation of clamped boundary conditions yet attach to the closure at only four pre-existing lugs. Panels were mounted in the fixture outside the tube. The panel/fixture combination was then bolted to the tunnel end closure, and the entire assemble moved into position at the end of the tube. A wooden spacer was attached inside the tube to raise the interior surface to the level of the panel. This minimized air flow disturbances during shock reflection. Figure 3 shows a test specimen attached to the fixture in the process of being mounted onto the tube closeout.

The end of the tube opposite the specimen contained a plenum chamber sealed by a metal diaphragm. After pressurizing the chamber, a shot was initiated by rupturing the diaphragm with explosive cord. A shock wave would then propagate down the tube and strike the end closure/test specimen combination. This procedure was expected to produce a single step rise in pressure at a level equal to the reflected overpressure value, followed by a gradual decay to ambient conditions. All previous testing conducted by BRL had employed specimens which did not completely seal the tube. An unexpected result of the complete blockage of the end closure for this program was the generation of as many as five additional step loadings of significant level as the initial shock reflected up and down the tunnel. Prior to the initial shot it was felt that leakage from the many access holes and other small openings in the tube would reduce the magnitude of the secondary shocks. The effect of the multiple loading on observed panel damage is uncertain.

Pressure and strain measurements for each shot were sampled at 1.0 and 5.0 µmsec intervals, respectively, and stored for later analysis on two 14 track tape recorders. Strip chart records of key channels were available for immediate study. Test instrumentation consisted of two pressure transducers mounted near the panel surface to measure the reflected overpressure value, and an upstream gage to measure the incident value. Ten channels of strain were also monitored. Figure 1 shows strain gage locations for the four sandwich panel configurations marked as S1 through S8. S3 and S4 are biaxial gages which require two instrumentation channels each. Strains were measured at all design critical locations, with backup gages for the most important points. Biaxial readings are necessary for the optimized composite designs. The strain in the fiber direction of the stiffener was also measured. Figure 2 shows similar locations on the hat-stiffened design.

TEST CORRELATION

In order to evaluate analytical methods for predicting the dynamic response of sandwich panels under blast loading, the test panels were modeled using the ADINA (Ref. 9) finite element code and analytical results compared with the test data. As will be shown, first cut modeling efforts based on the test panel supported only by its mounting frame gave reasonable correlation with measured values for peak strain; however, the calculated response was not in phase with the test data. In an effort to
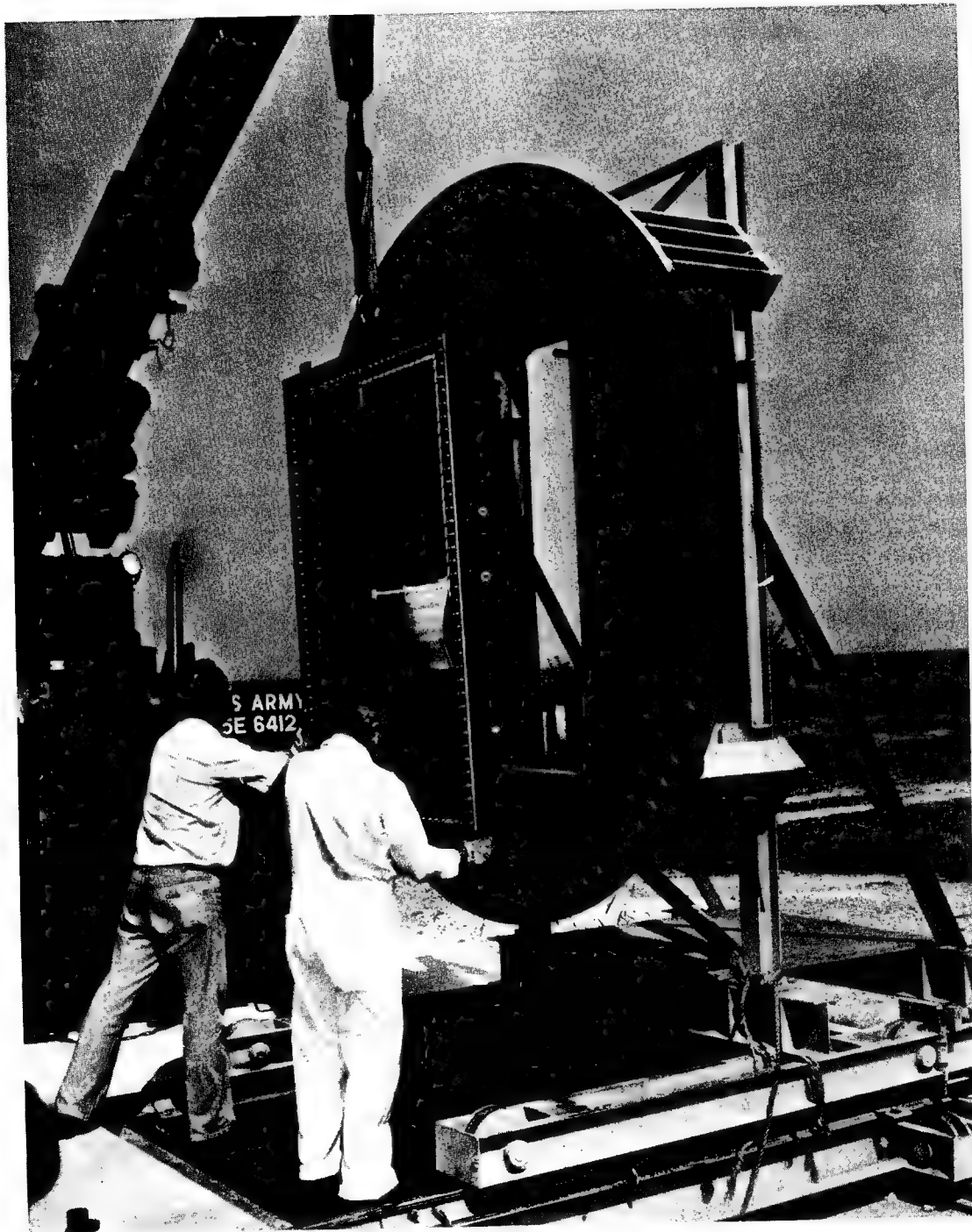
Figure 3.   Installation of panel/frame combination onto BRL shock tube
fixture

241

improve the time history correlation, a more sophisticated analytical model was developed which also includes the effects on panel response of the BRL support fixture and the shock tube. Details of the analytical models are described below together with the associated panel response and its correlation with test data. Results are presented for the aluminum and graphite sandwich panels only. Because of the well established values for material properties, the aluminum panel provides the best baseline configuration for evaluating analytical methods. Of the composite sandwich panels tested, the graphite panel results are presented because this configuration is of particular interest for advanced shelter applications (Ref. 5).

Shown in Figure 4 are details of the finite element model (FEM) for the test panel supported by the steel support frame. The schematic identifies the principal components of the sandwich panel which include face skins, core, shear beams and the panel end closure. Table 2 summarizes model details regarding the number of elements and the ADINA element type for each component. As shown, the sandwich honeycomb core and the core beam components were modeled using a 16 noded, 3D solid element. All other panel components were modeled using an 8 node, 2D solid, plane stress element. As shown in Figure 1, the shear beam at the panel center was instrumented with strain gages on the webs at either end. For this beam, a geometrically exact model was obtained using 2D, plane stress elements (See Figure 4). At other core beam locations, 3D solid elements were used to define an equivalent layer beam which matched the shear and bending stiffnesses of the actual beam. Similarly, the honeycomb core was modeled via equivalent layer elements. As noted in Figure 4, the support frame was also modeled via 3D elements. Geometry for this item included the "stepped cross sectional" detail (See Figure 1, Sec. AA). Due to symmetry considerations, it was only necessary to model one quarter of the panel and support. A simple support boundary was assumed at the frame/fixture interface as indicated by the nodal lines of support shown in Figure 4. For this model, pressure was applied only to the panel surface facing the shock wave – i.e., the pressure surface.

As noted previously, the panel/frame assembly interfaced with the BRL support fixture attached to the end of the shock tube. Details of the modeling of these items is shown in Figure 5. One observes that 3D solid elements were used to model the BRL plate. The reinforcing beam on the ambient side of the plate was modeled as follows: 2D solid, plane stress elements were used to model the web of the beam; the beam flange adjacent to the beam was modeled using 3D solid elements; finally, the outstanding beam flange was modeled using truss elements. Sixteen axial truss elements were used to model the extensional stiffness of the shock tube. Due to symmetry, it was only necessary to model one quarter of the BRL plate/tube assembly. A clamped boundary was assumed at the joint between the BRL plate and the shock tube.

For the complete model – i.e., panel/frame integrated with the BRL fixture/shock tube, the panel frame was joined with the BRL plate at nodes corresponding to the shaded area shown in Figure 5. Pressure loading was applied to the total "pressure surface" area of the panel plus frame and to
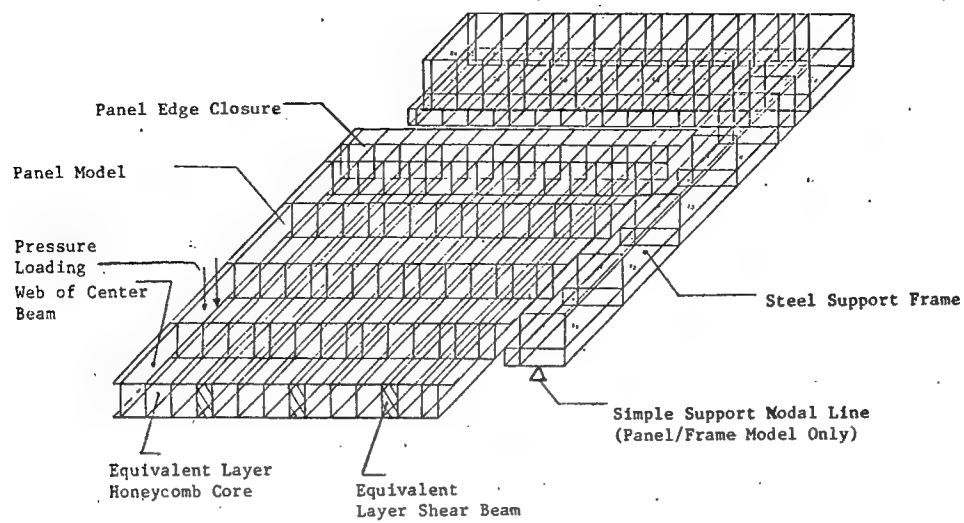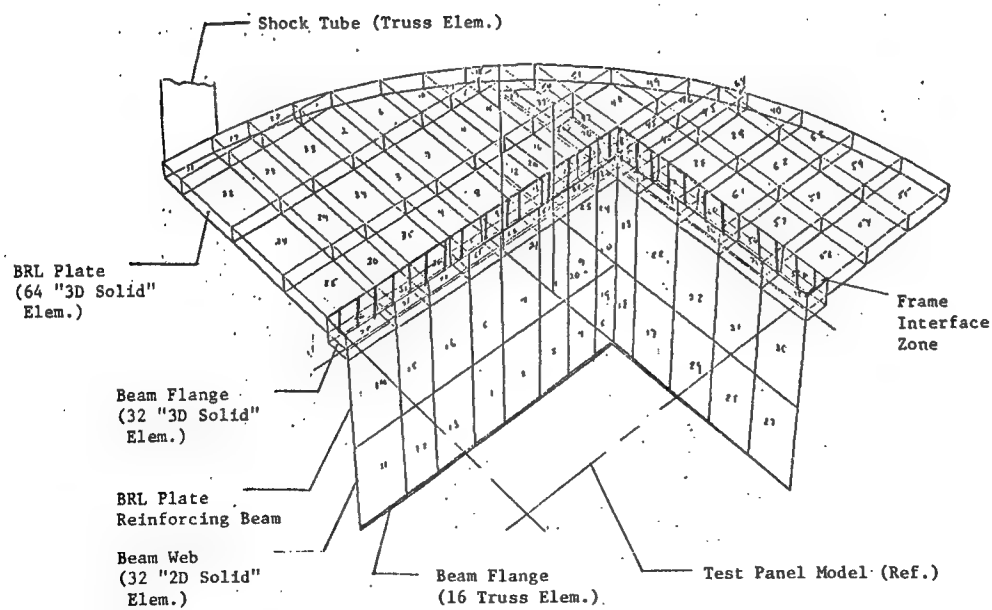
Figure 4. Sandwich Panel/Support Frame Model

Figure 5. BRL Fixture/Shock Tube Model

TABLE 2

Finite Element Details for Sandwich Panel/Support Frame
(See Figure 4)

Item	Components	Model Description
Sandwich Panel	Pressure face	96 2D Solid, plane stress elements (8 nodes)
	Ambient face	75 2D Solid, plane stress elements (8 nodes)
	Shear beam at panel centerline	5 2D Solid, plane stress elements (8 nodes)
	Other shear beams	15 3D Solid elements (16 nodes)
	Honeycomb core	55 3D Solid elements (16 nodes)
	Edge closure	20 2D Solid, plane stress elements (8 nodes)
Support Frame		67 3D Solid elements (16 nodes)

the pressure surface of the BRL fixture (not including the shaded area of Figure 5). The outside diameter of the model for the BRL fixture corresponds to the bolt circle for fixture/plate attachments and is greater than the actual pressure area of the BRL plate as represented by the shock tube inside diameter. A geometry correction factor was applied to the pressure loading on the BRL plate model (but not the panel model) to preserve the correct total axial load.

As noted above, the test section end of the shock tube is free to move in a longitudinal direction; hence, motions generated at the shock tube/BRL support fixture interface could influence the dynamic response of the panel. Some BRL test date (Ref. 10) was available from a previous test program where measurements were made of motions at the test section. This data is shown in Figure 6. Also shown is the calculated axial deflection of the tube for the same reflected pressure (applied as a step function input) and based on the complete dynamic model described above. One observes that there is excellent agreement between analysis and test data for both peak deflection and time to peak deflection. This result demonstrates that the model accurately accounts for motions induced by the pressure loading at the shock tube/BRL fixture interface.

Figure 7 presents a typical reflected pressure time history measured near the surface of the aluminum sandwich panel. In this case the reflected pressure was 27.5 psi and was determined by integrating the area under the pressure curve up to four milliseconds and dividing by the time. One observes a sharp drop in pressure at approximately 0.1 msc. This behavior was attributed to air leakage at the shock tube/BRL fixture joint (Ref. 11). Panel response curves shown below were determined by approximating the actual pressure time history curve by a step pressure input where the peak pressure magnitude equaled the measured reflected pressure. Preliminary panel response analyses were made with both the actual and approximate pressure histories and established the validity of the method.

For selected strain gage locations, the dynamic response of the aluminum sandwich panel to the blast loading is shown in Figures 8 through 10. In the figures, the calculated dynamic response is shown based on two dynamic models labeled "frame/panel" or "complete model". The frame/panel model corresponds to the panel supported only by the base frame, whereas the "complete model" also includes the BRL support plate and the shock tube. Also given in each figure is a curve of the measured panel strain response at the indicated panel location. Comparison of the response curves indicates how well the analysis for each dynamic model predicts the measured panel response. Gage locations selected for presentation correspond to critical panel design points and include sandwich face stress near the panel boundary and panel center, and also shear related strain near the beam ends.

Figure 8 presents strain correlation results for a gage (S2X) located on the panel centerline near the panel boundary. (See the schematic in the figure for strain gage location). The measured response at the gage location (solid line) shows a peak strain of -1725 μst occurring at 1.55
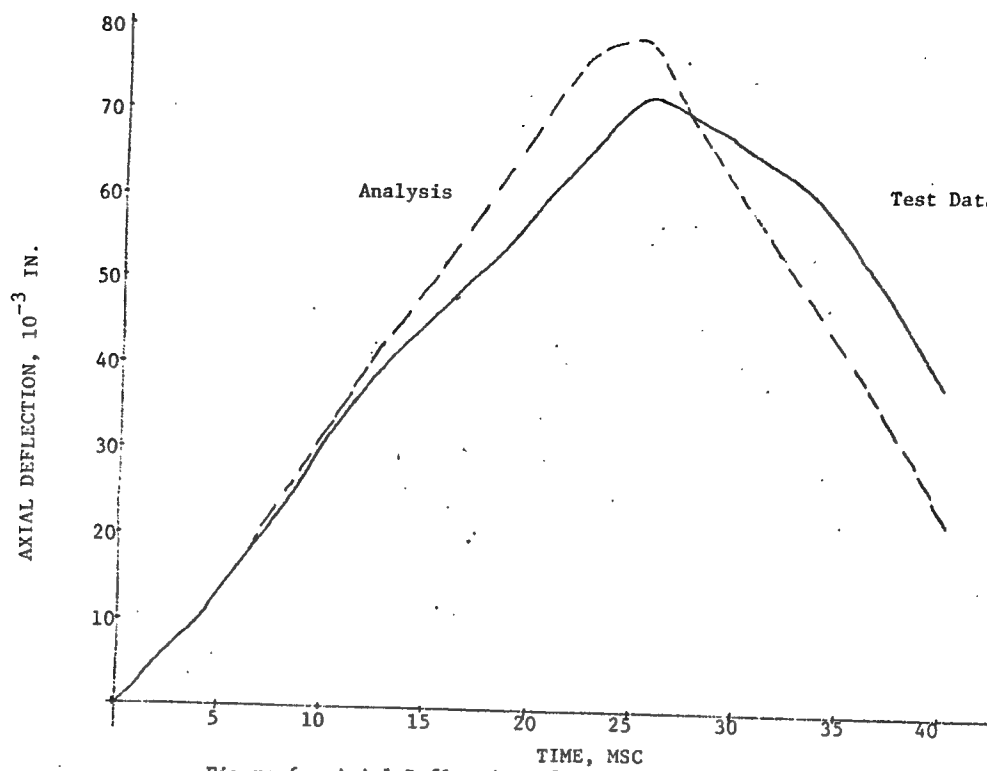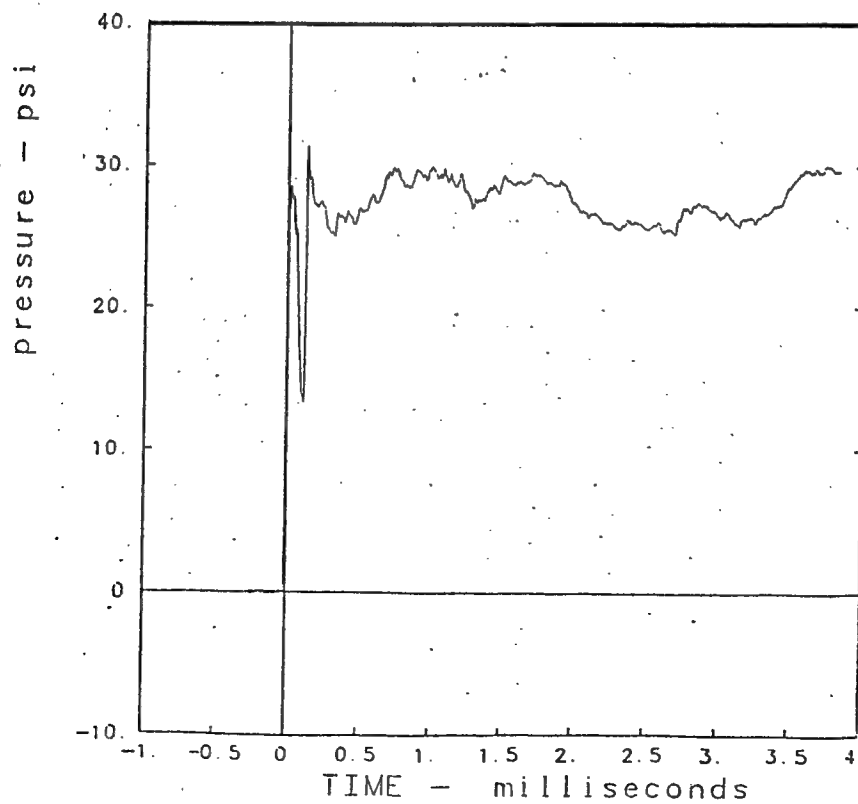
Figure 6.   Axial Deflection of BRL Shock Tube for HATS Panel Test
(Reflected Pressure = 14.5 psi)

Figure 7.   Reflected Pressure Loading for the Aluminum Sandwich
Panel (Reflected Pressure = 27.5 psi)

Figure 9. Aluminum Panel Face Strain at Panel Center – Gage S3X
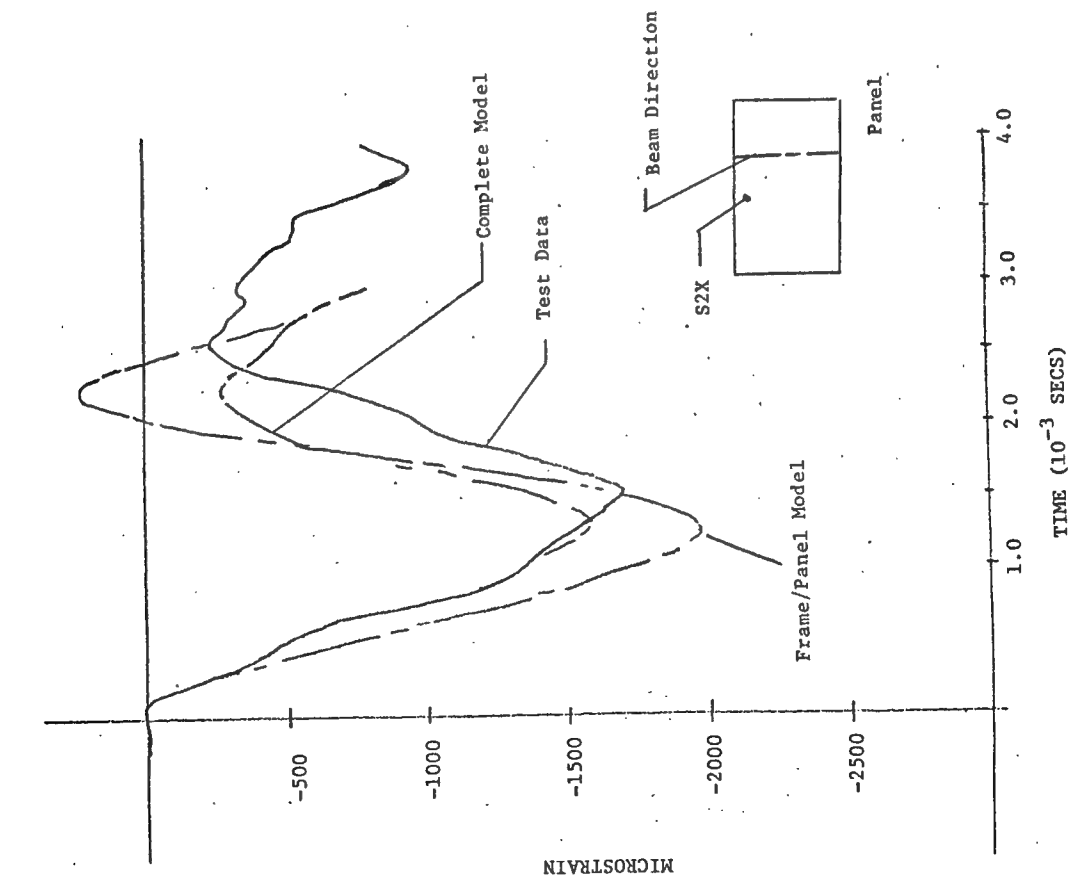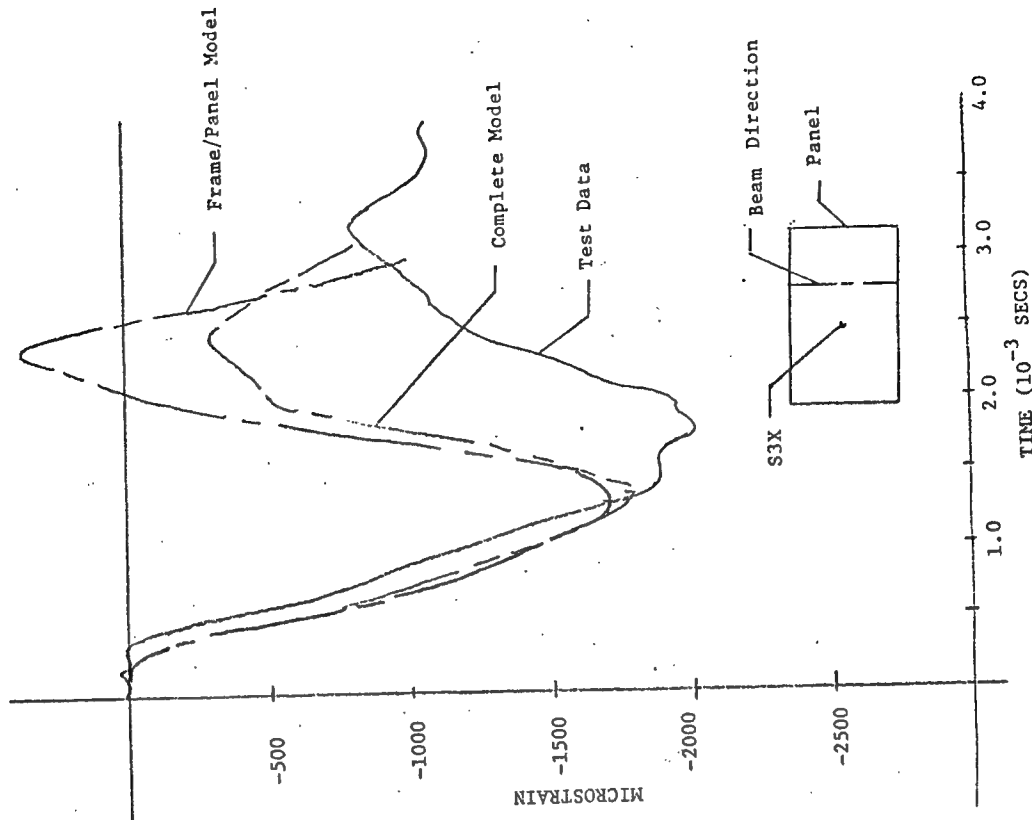(Reflected Pressure = 27.5 psi)

Figure 8. Aluminum Panel Face Strain at Panel Edge–Gage S2X
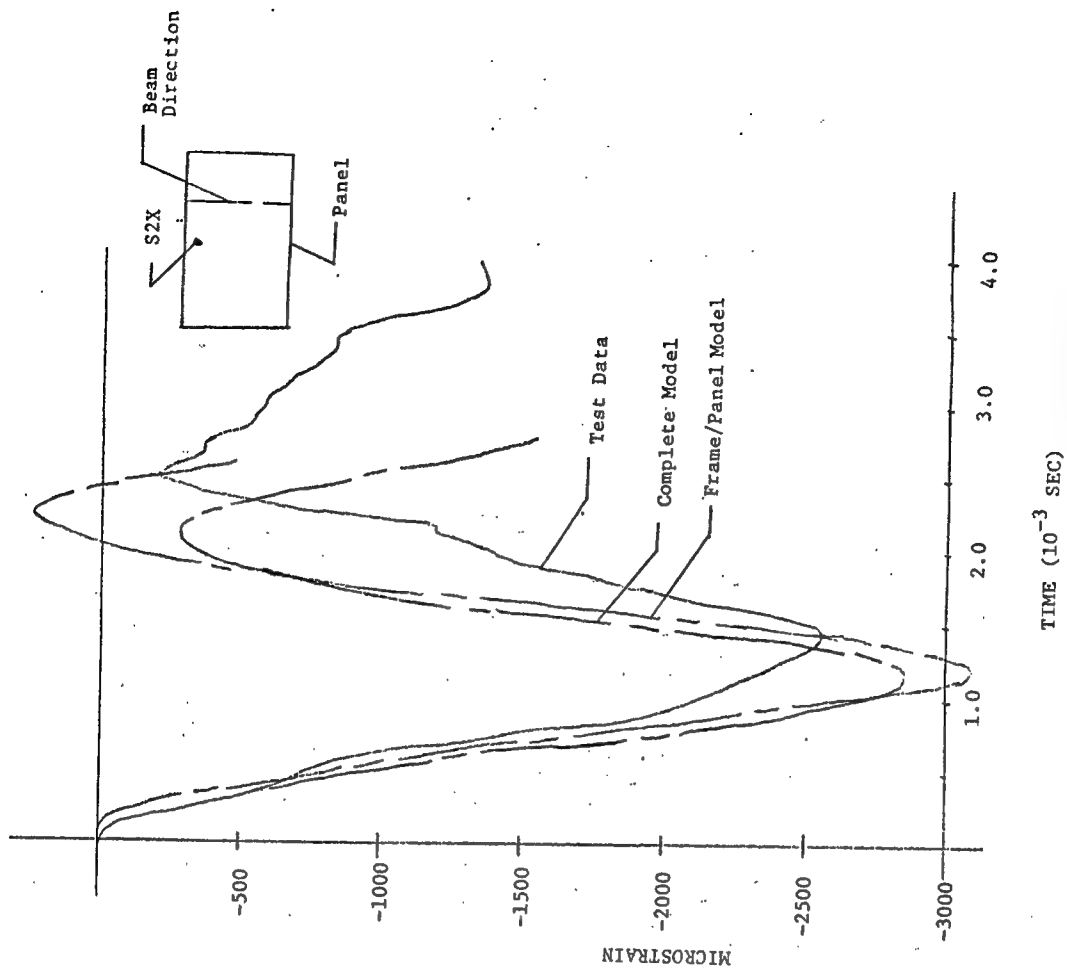(Reflected Pressure = 27.5 psi)

247

Figure 11. Graphite Sandwich Panel Face Strain at Panel Edge - Gage S2X (Reflected Pressure = 27.3 psi)
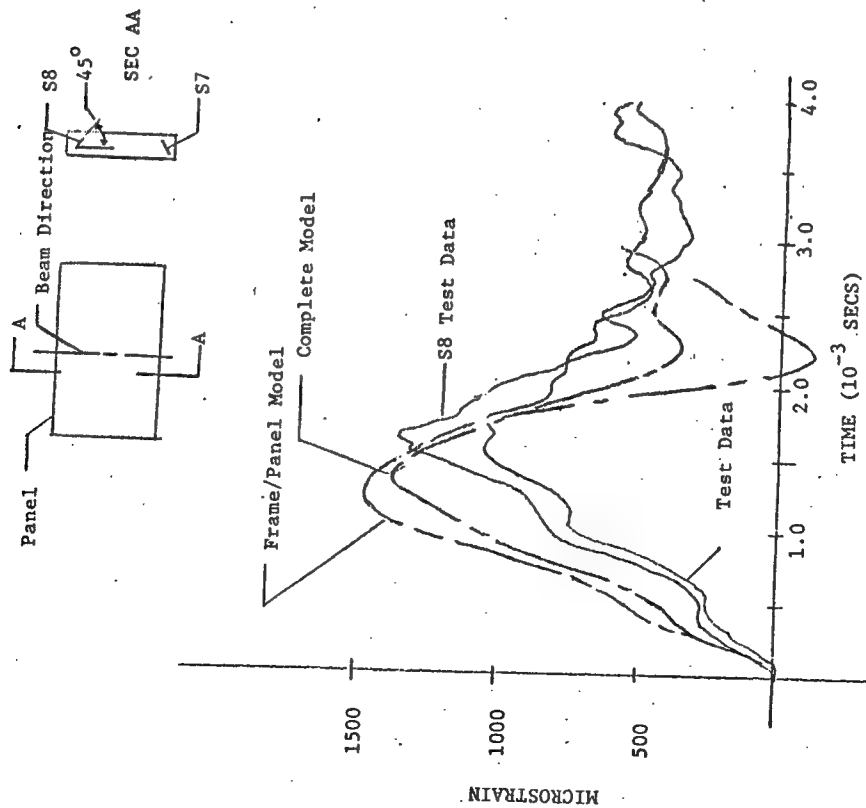

Figure 10. Aluminum Sandwich Panel Strain In Shear Beam Ends - Gage S7 and S8 (Reflected Pressure = 27.5 psi)

248

msc. Results based on the frame/panel model overpredict the maximum strain by approximately 14.5%. In addition, the time for maximum response is much earlier (1.25 vs 1.55 msc). Note also that the strain time history for this model rapidly decreases to zero strain after the peak value. For this gage an analysis based on the complete model made a significant improvement in the calculated gage response. For example, the maximum calculated strain is 9% less than the measured value and the peak response time is closer to the measure value (1.35 vs 1.55 msc.). The strain characteristics after the peak value also follow those of the measured data.

Similar comparisons can be made for the aluminum sandwich panel response at a face strain gage located at the panel center (See Fig. 9) and for beam shear gages located near the ends of the centerline shear beam (See Fig. 10). In addition a corresponding set of curves is presented for the graphite sandwich panel (See Figures 11, 12, and 13).

The relative accuracy of the two dynamic models is summarized by the data of Table 3. For each panel type and gage location, the table presents ratios of calculated time for maximum response and associated strain as compared to the corresponding test data. A value of 1.0 for this ratio would indicate that the analysis exactly predicts the test result. For the two shear strain gages, the test data results were averaged for the time and strain parameters. In addition to time and strain ratios for each individual gage, an average value for time and strain ratio is given in the table based on all the gages. This latter value gives a measure of the accuracy of the calculated versus test results for all the gage locations.

One observes from the table that based on the average time and strain ratios for all the gages that the complete model gave improved correlation with test results for both the aluminum and graphite panels. For the complete model, it is noted that on the average the maximum strain results were accurately predicted. However the associated time for maximum response was approximately 15% less than that indicated by the test data.

CONCLUSIONS

(1) Shock tube testing of scale models is an attractive alternative to the full scale field simulation of blast loaded panels. Properly designed and tested models will experience full scale stress levels, allowing direct confirmation of analytical results. Low cost, comparative studies can be conducted in well controlled laboratory conditions. Full size testing should be used for final design verification, since proper experimental boundary conditions are difficult to attain.

(2) Results of the current test program confirmed that the composite designs are capable of surviving the design loading as well as conventional aluminum honeycomb sandwich panels.

(3) Agreement between finite element strain predictions and measured data indicate that standard analysis techniques can predict panel response to blast loading. Improvement in correlation obtained by modeling the panel/frame/test fixture combination demonstrated the importance of properly modeling end conditions in finite element analysis.
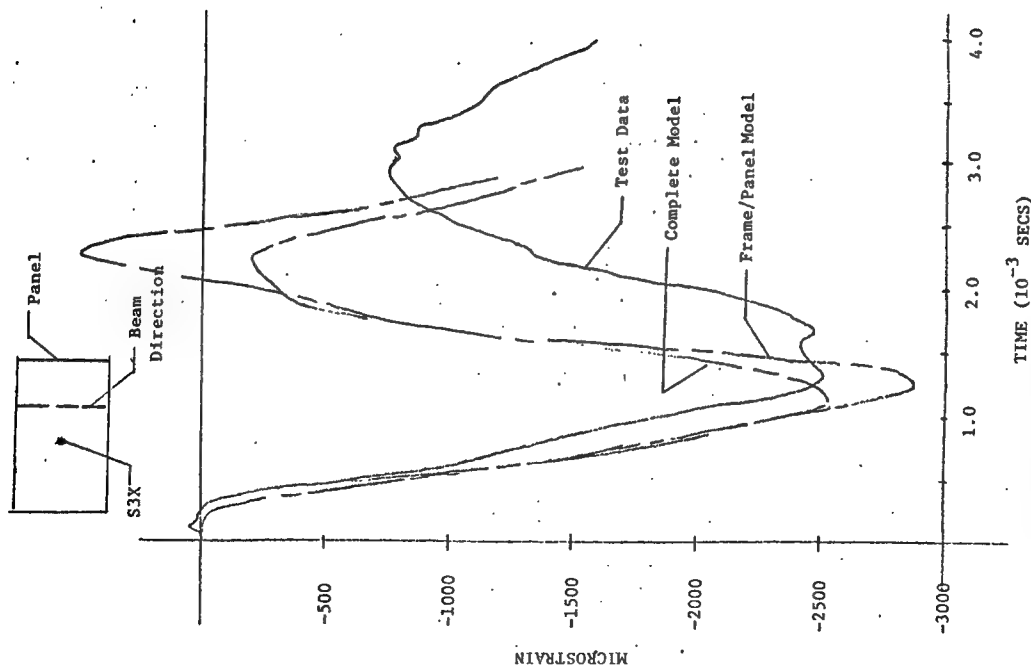
249

Figure 13. Graphite Sandwich Panel Strain Near Shear Beam Ends - S7 and S8 (Reflected Pressure = 27.3 psi)

Figure 12. Graphite Sandwich Panel Face Strain at Panel Center Gage S3X (Reflected Pressure = 27.3 psf)

250

TABLE 3

Comparison of Analytical Predictions and Test Results
for Aluminum and Graphite Sandwich Panels

Panel	Gage	Frame/Panel Model		Complete Model	
		t^*_r	ε^*_r	t_r	ε_r
Aluminum	S2X	.807	1.145	.871	.916
	S3X	.722	.840	.722	.889
	(S7,S8)av.	$\dfrac{.75}{.76**}$	$\dfrac{1.226}{1.07}$	$\dfrac{.844}{.812}$	$\dfrac{1.143}{.983}$
Graphite	S2X	.833	1.212	.833	1.118
	S3X	.947	1.146	.871	1.010
	(S7,S8)av.	$\dfrac{.747}{.842}$	$\dfrac{.977}{1.112}$	$\dfrac{.833}{.846}$	$\dfrac{.913}{1.014}$

* t_r = Calculated time for peak response/test data time for peak response

     ε_r = Calculated maximum strain/test data maximum strain

**   Average of result for all gages

REFERENCES

1. Milligan, Roger W., Fanucci, Jerome P., Rodal, Jose J.A., and Lawrence J. Mente, "Research and Development of an ISO Rigid Wall Hardened Shelter", Kaman AviDyne Report KA TR-187, July 1981.

2. Milligan, Roger W., Fanucci, Jerome P. and Allen M. Lush, "Technology Base Development for Nuclear Hardened Tactical Shelters, Volume II - Experimental and Analytical Evaluation of Blast Hardened Concepts", Kaman AviDyne Report KA TR-205, July 1984.

3. Milligan, Roger W., Lush, Allen and William L. Crenshaw, "Blast Response of a Hardened Army ISO Shelter", Supplement to the Proceedings of the Army Symposium on Solid Mechanics, 1982 - Critical Mechanics Problems in System Design, Supplement to AMMRC MS 82-4, September 1982.

4. Schuman, W.J., Jr., Zartarian, G., Yeghiayan, R.P. and W.D. Allison, "C^3 Shelter Designs for the Tactical Battlefield", Proceedings of the Army Symposium on Solid Mechanics, 1980 - Designing for Extremes: Environment, Loading, and Structural Behavior, AMMRC MS 80-4, September 1980, pg. 46.

5. Fanucci, J.P., "Composite Material Structures for Tactical Shelters: A Cost/Weight Study", Proceedings of the Army Symposium on Solid Mechanics, 1982 - Critical Mechanics Problems in System Design, AMMRC MS 82-4, September 1982, pg. 257.

6. Baker, W.E., Westine, P.S. and Dodge, F.T., Similarity Methods in Engineering Dynamics, Hayden Book Company, Inc., Rochelle Park, New Jersey, 1973.

7. Schuring D.J., Scale Models in Engineering, Pergamon Press, New York, 1977.

8. San Miguel, A., "Composite Tank Floor Armor", Proceedings of the Army Symposium on Solid Mechanics, 1980 - Design for Extremes: Environment, Loading and Structural Behavior, AMMRC MS 80-4, September 1980, pp. 65-83.

9. Bathe, Klaus-Jurgen, "ADINA-A Finite Element Program for Automatic Dynamic Incremental Nonlinear Analysis," M.I.T. Report AE81-1, September 1981.

10. Letter from William D. Allison, U.S. Army Ballistic Research Laboratory, to Roger W. Milligan, Kaman AviDyne dated March 1, 1984.

11. Allison, William D., "Shock Tube Tests of Natick Hardened Shelter Panels," U.S. Army Ballistic Research Laboratory Report, to be published.

EXPERIMENTAL AND ANALYTICAL EVALUATION OF SURFACE COATINGS FOR PROTECTION AGAINST HIGH INTENSITY THERMAL PULSES

Jerome P. Fanucci
Brian D. Boyer
Roger W. Milligan

Kaman AviDyne
Burlington, Massachusetts   01803

ABSTRACT

The ability of 21 thermal coatings to protect a structure against a high intensity thermal pulse was investigated. Nearly 200 tests were conducted at a solar furnace facility using both aluminum and graphite/epoxy substrates covered with thin layers of candidate materials. Thermophysical properties of each material were estimated by iterating assumed properties until analytical predictions found using the TRAP code matched experimental measurements in a number of different tests. The empirically derived properties were used to calculate the thickness of each material required to protect against a specified nuclear thermal pulse, which differed from the test conditions. A trade study that considered coating cost, weight and a number of other practical considerations important for Army field operations showed that several materials could perform satisfactorily, with an intumescent ablator scoring highest. This work was sponsored by the Natick Army Research and Development Center.

INTRODUCTION

Mobile tactical shelters are used to house command, control and communication equipment vital to the successful completion of many military missions. Due to the importance of the electronic equipment they contain, many of these shelters are required to be hardened against the effects of tactical nuclear weapons. One important aspect of overall nuclear hardness is thermal pulse survivability. A nuclear thermal pulse radiantly heats the structural surfaces and can induce damage by reducing material strength and stiffness properties or by creating thermal stresses. The elevated temperature effects render the structure more vulnerable to the nuclear blast loading which immediately follows the heating period.

As part of a larger Natick Lab sponsored shelter hardening program, an experimental and analytical investigation of homogeneous, filled and reinforced polymer thermal protection materials was undertaken. From this large group twenty-one different commercially available thermal coatings were selected for study at Sandia Labs' Flux Gage Calibration Station (FCGS), a solar furnace facility. Table 1 lists details of the materials tested. Each material was exposed to a high-flux, square thermal pulse simulating the nuclear heating environment. Coatings were tested by

TABLE 1

MATERIALS SUBJECTED TO SOLAR FURNACE TESTING

Material Trade Name	Supplier	Composition	Type of Protective Material
*1. Korotherm	DeSoto	Acrylic/Isocyanate	Ablative Sublimer
*2. Thermolag 330-1	Quantum Group	Epoxy Mastic	Ablative Sublimer
3. Chartek 59	AVCO Specialty Materials	Epoxy Mastic	Ablative Intumescer
*4. Flamarest 1600 BTX	AVCO Specialty Material	Epoxy Mastic	Ablative Intumescer
*5. Flexfram	Fiber Materials, Inc.	Filled Epoxy Polyamide	Ablative Char Former
*6. AVCOAT II	AVCO Systems Division	Epoxy Polyamide	Ablative Char Former
*7. AVCOAT 8039	AVCO Systems Division	Epoxy	Ablative Char Former
*8. E-400	Flamemaster	Epoxy	Ablative Char Former
*9. DE-380	Flamemaster	Epoxy	Ablative Char Former
*10. DE-370	Flamemaster	Epoxy	Ablative Char Former
11. DE-350	Flamemaster	Epoxy	Ablative Char Former
12. AVCOAT 8021	AVCO Systems Division	Epoxy Urethane	Ablative Char Former
13. AVCOAT 893	AVCO Systems Division	Cork/Phenolic	Ablative Char Former
14. P-50	Sheller Globe	Cork/Phenolic	Ablative Char Former
15. Belcobalsa	Baltek	End-grain Balsa	Albative Char Former
16. MA-25S	Martin Marietta	Elastomeric Silicone	Ablative Char Former
17. E-68	B.F. Goodrich	EPDM Rubber	Ablative Char Former
18. Syncore 9822	Dexter/Hysol	Syntactic Epoxy/ Glass Microballons	Ablative Char Former
*19. Kevlar	Dupont	Kevlar Fabric/ Aramid Resin	Ablative Char Former
*20. AS4/3501-6 Graphite Epoxy	Hercules	Graphite Fiber/ Epoxy Resin	Ablative Char Former
21. Polyurethane Paint	DeSoto		Ablative Char Former

*Materials selected for post-test analysis.

254

applying different thicknesses of each candidate to 6061-T6 aluminum and AS/3501-6 graphite/epoxy substrates. Thermocouples were used to monitor specimen temperatures during exposure. Readings from the instrumentation were recorded with an automatic data acquisition and reduction system. Plots of temperature versus time were digitized and compared to the response predicted using TRAP (Reference 1), a thermal/structural analysis code developed by Kaman AviDyne.

Correlations were generated by iterating assumed material properties for one coating thickness/substrate combination until satisfactory comparison was obtained. The material properties which produced a good correlation at one thickness were then checked against test results of other coating thicknesses, and refined until agreement for all tests of each material occurred. These final properties were used to predict a thermal coating thickness that would produce the desired protection for the design nuclear pulse, which differed in both peak magnitude and shape from the experimental thermal loading.

Results of this study show that the thermal protection of both composite and metallic shelter walls can be obtained by the application of thin, sprayable coatings of commercially available heat shielding materials. Thicknesses on the order of 20 mils were found to be adequate for the scenario investigated. Some of the materials tested have previous service experience demonstrating their ability to satisfy other considerations such as maintainability and durability. A trade study found that a number of coatings could provide adequate thermal protection, with Chartek 59, an intumescing ablator, scoring highest.
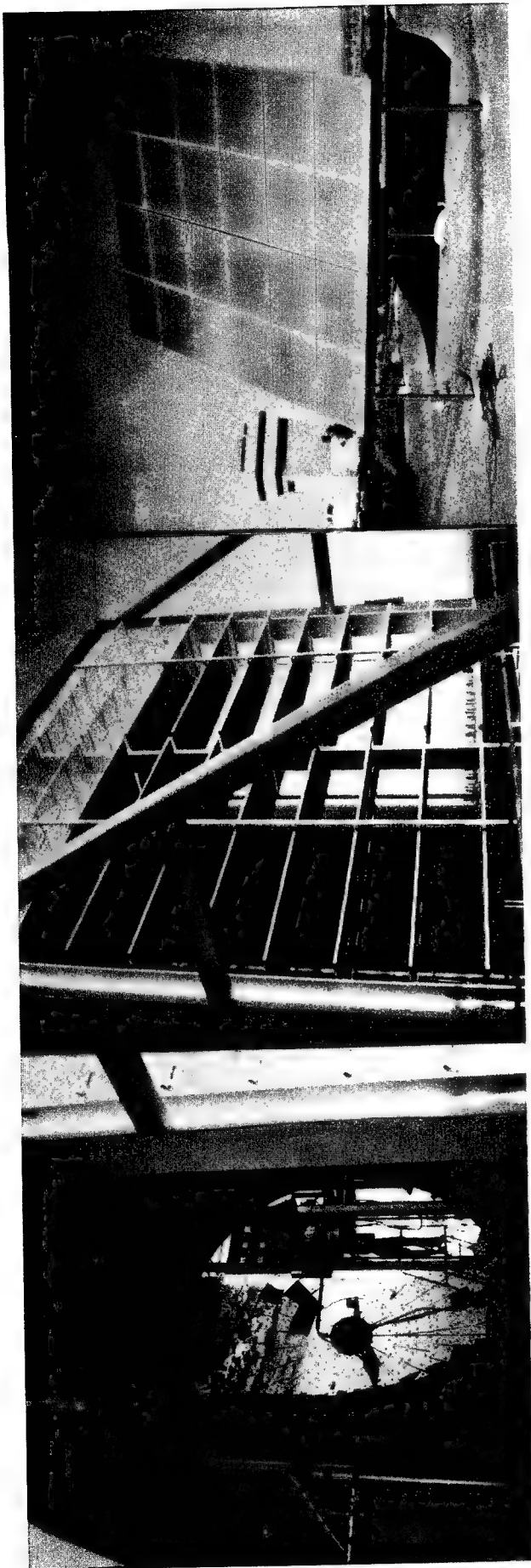

EXPERIMENTAL

Approximately 178 4.4 x 3.8 inch 6061-T6 aluminum and 48 AS4/3501-6 graphite/epoxy substrates were fabricated for this test program. Except for calibration, paint test and for virgin graphite or Kevlar/epoxy specimens, all substrates were top-coated with one of three different thicknesses of protective material. Details of the specimens are described in Reference 2. Pre-test calculations for each protective material, made using assumed thermophysical properties, were run to establish a baseline thickness estimated to provide the desired level of thermal shielding. Each manufacturer applied its own coatings. Duplicate copies of each material/thickness combination were produced. Materials that seemed most promising in pre-test analysis were also tested on graphite/epoxy substrates to investigate the difference in response observed with low conductivity backings.

Each 0.063" thick aluminum substrate had a single 5-mil Teflon-insulated Type-K thermocouple welded and bonded to the center of its back face. Composite specimens had 2 or 3 thermocouples installed. Six Kevlar/aluminum hybrid coupons were constructed with 2, 4 or 8 layers of Style 181 Kevlar cloth cocured at 250°F with Dow 324 resin and bonded to basic aluminum substrates. In addition to the thermocouple mounted on the back face of the aluminum, these specimens had a second thermocouple built in during layup to the ply interface midway through the thickness.

AS4/3501-6 graphite/epoxy specimens were press cured, 13-ply layups of alternating 0 and 90 degree unidirectional material. Two thermocouples were built into these substrates during the layup procedure, one in the second ply from the surface and one in the seventh. Plies containing thermocouples were split along the fibers and butted against each side of the instrumentation to minimize thickness buildup. Twelve of the 48 composite substrate specimens had additional composite material added to their outer surface. Six graphite/Kevlar hybrids were made with the same three thicknesses of Kevlar as used on the aluminum substrate specimens described previously. Another 6 of the basic graphite blanks had 3, 6 or 12 extra plies of 0/90 AS4/3501-6 added. All 12 of these extra material composite specimens had a third thermocouple cured into the center of the added plies. All specimens were sprayed with a 0.001 inch coating of flat black paint to equalize their initial absorptivity and to better simulate the actual service environment. The nominal cured per-ply thickness of the graphite/epoxy used in this program was specified by the manufacturer as 0.00525 inches, while average measured ply thickness was found to be 0.0050 inches. This suggests that the cured graphite laminates were somewhat resin poor. Average measured thickness of the Kevlar cloth was 0.0105 inches per ply.

An experimental program was conducted at Sandia National Laboratories' flux gage calibration station, located in Albuquerque, New Mexico. This solar furnace facility, illustrated in Figure 1, consists of a 24-foot square heliostat and a 22-foot diameter parabolic concentrator. A louvered attenuator placed between the heliostat and focusing mirrors controls the magnitude of the flux delivered to the specimen. A fast acting shutter creates a nearly square edged pulse. The 228 mirrors that form the concentrating array are aligned to produce a beam with a peak flux in the uniform 0.4 inch diameter central spot of 50 to 55 cal/cm^2/sec. Figure 2 diagrams the nearly Gaussian, cylindrically symmetric energy distribution at the focus of the beam. Test sequencing, data acquisition and reduction at the facility were computer controlled. Thermocouples were read and recorded at approximately 4 millisecond intervals during exposure to the thermal pulse. Time versus temperature plots were produced following each day of testing. Points from selected specimen response curves were digitized for use in later analytical work.

Tests were conducted as follows: the thermal pulse level was set prior to a shot by adjusting an attenuator opening until the desired flux was measured with a radiometer temporarily located at the focal point of the beam. A test specimen was then moved into position and exposed to a thermal pulse. Most tests used a sharp-edged, flat-topped pulses of the type illustrated in curve A of Figure 3. The start and stop times of the pulse were produced by an iris-type shutter which required approximately 0.15 seconds to travel from full open to full closed position. Most specimens were received a nominal 50 cal/cm^2/sec maximum flux, 100 cal/cm^2 total fluence exposure. During data reduction the exact level of each shot was adjusted to account for local atmospheric conditions at the time of the test, an amount that varied at most 10%. A few spare specimens were exposed to pulses B and C of Figure 3 to study the effect of flux rate on response, but results were inconclusive.

A) Parabolic Collecting and
   Focusing Mirror

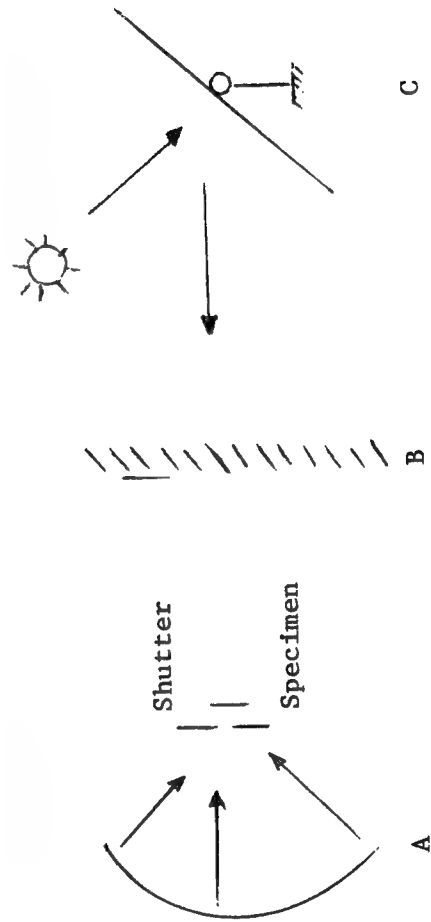B) Power Attenuator

C) Tracking Heliostat
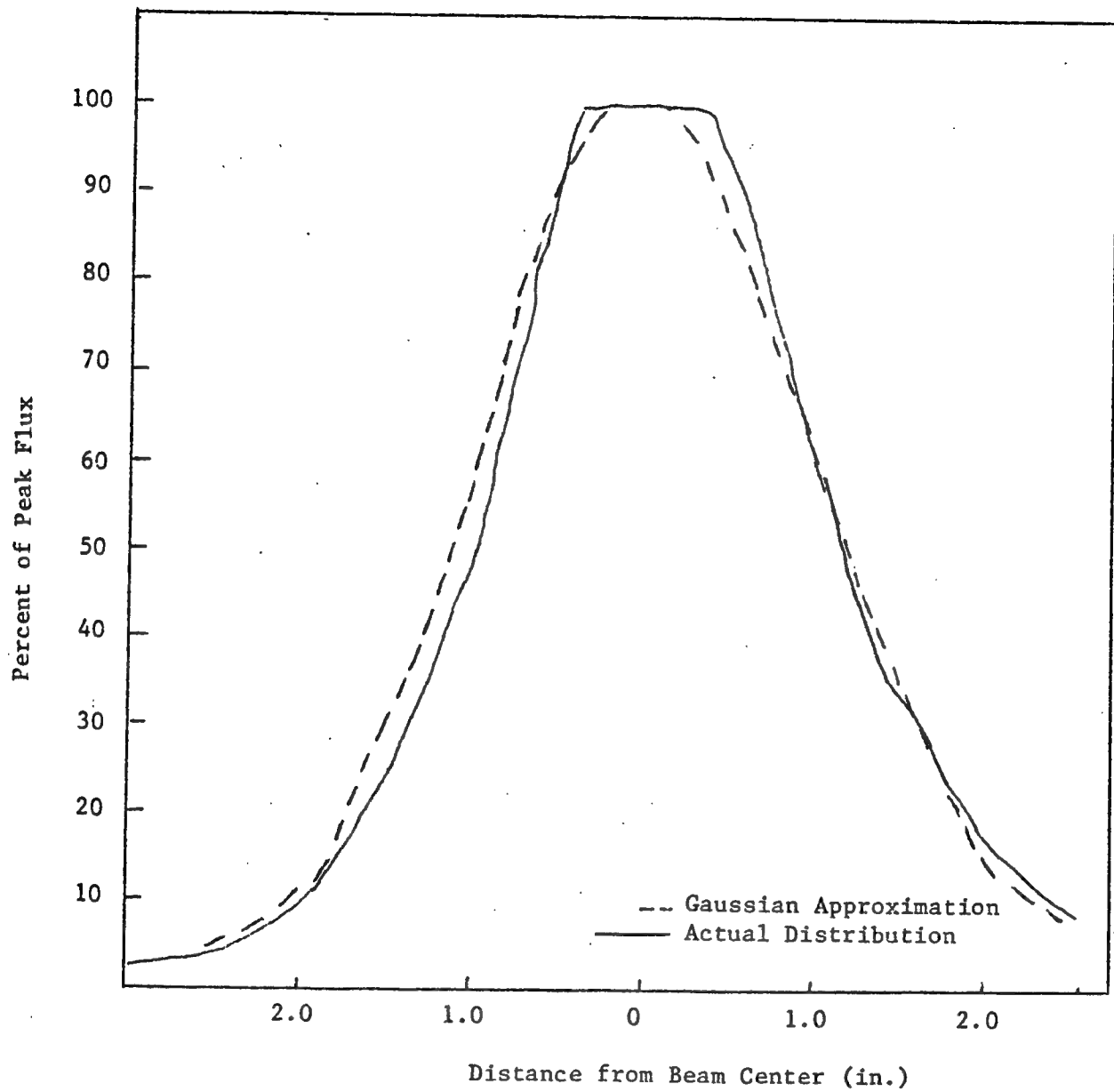
Figure 1. Flux Gage Calibration Facility Details
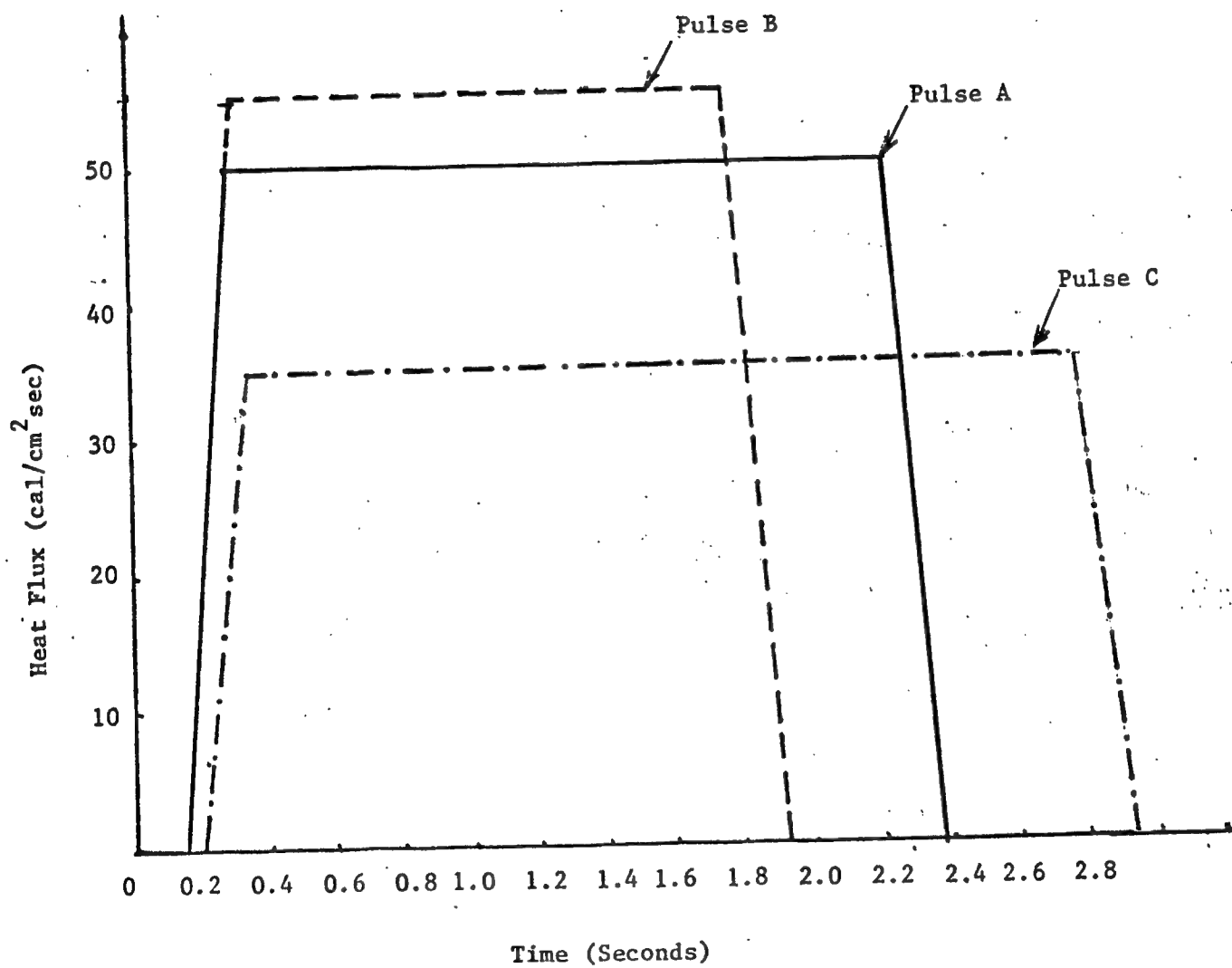
257

Figure 2. Flux Distribution in FGCS Beam

Figure 3. Flux Time History of Experimental Pulses

All tests were conduced with free air convective cooling. Video tapes of the experiments showed that smoke, which formed in many of the tests, usually cleared from the specimen rapidly. Density of the smoke varied from nearly transparent to semi-opaque, suggesting that some blockage of thermal radiation occurred. The production of smoke was considered to be a viable thermal protection mechanism for the tactical shelter application of interest to this program. Several of the specimens were observed to ignite during exposure. Flames were self-extinguishing in all cases.

ANALYSIS

Since testing with the correct shape and peak flux of the design nuclear pulse was not experimentally possible, an important aspect of the test program was the generation of thermophysical properties that could be used to analytically predict the response of protective coatings. This approach assumed that properties derived from testing with a square pulse will apply to the case of a nuclear shaped pulse. The experimental program was designed to minimize this concern by choosing the parameters of the square pulse such that it produced analytically similar results when compared to calculations performed with the proper nuclear shape. Figure 4 shows a typical analytical comparison of an identical substrate/protective coating combination exposed to the square experimental pulse and the design nuclear pulse. The small difference in response was judged to be acceptable.

The TRAP code was used to extract material property information from the measured thermal response data. TRAP is a 2-dimensional finite difference thermo/structural analysis code originally developed by Kaman AviDyne to study vulnerability of complex aircraft components subjected to thermal load from laser or nuclear weapons. An analytical correction for cylindrical symmetry, included in the code, was exercised for this study. In its current form TRAP can analyze structures with multiple layers of different materials through the thickness. Consideration of transient temperature dependent strength, stiffness and thermophysical properties along with ablation characteristics, can be incorporated in the analysis. Some materials, such as Kevlar and graphite/epoxy and char forming ablators, undergo chemical change prior to reaching the temperature required to produce complete ablation. The endothermic reactions occurring before layer removal are simulated by artificially elevating the specific heat curve over the range of temperatures at which the reaction occurs, as illustrated in Figure 5. When using this method, excess energy stored by the mathematical model in the C_p bump will be lost either when the fibers or char layer ablates, or the specimen begins to cool. Layers that are cooling follow the lower hysteresis curve, preventing the energy that was artificially stored from being dumped back into the structure. The conductivity curve can also adjust to reflect the properties of the charred epoxy. Both the effects of energy blocked by smoke and added by flames are analytically included in the artificially elevated C_p curve. For this reason, results of this program should be used with caution for applications where high free stream velocities clear smoke rapidly.
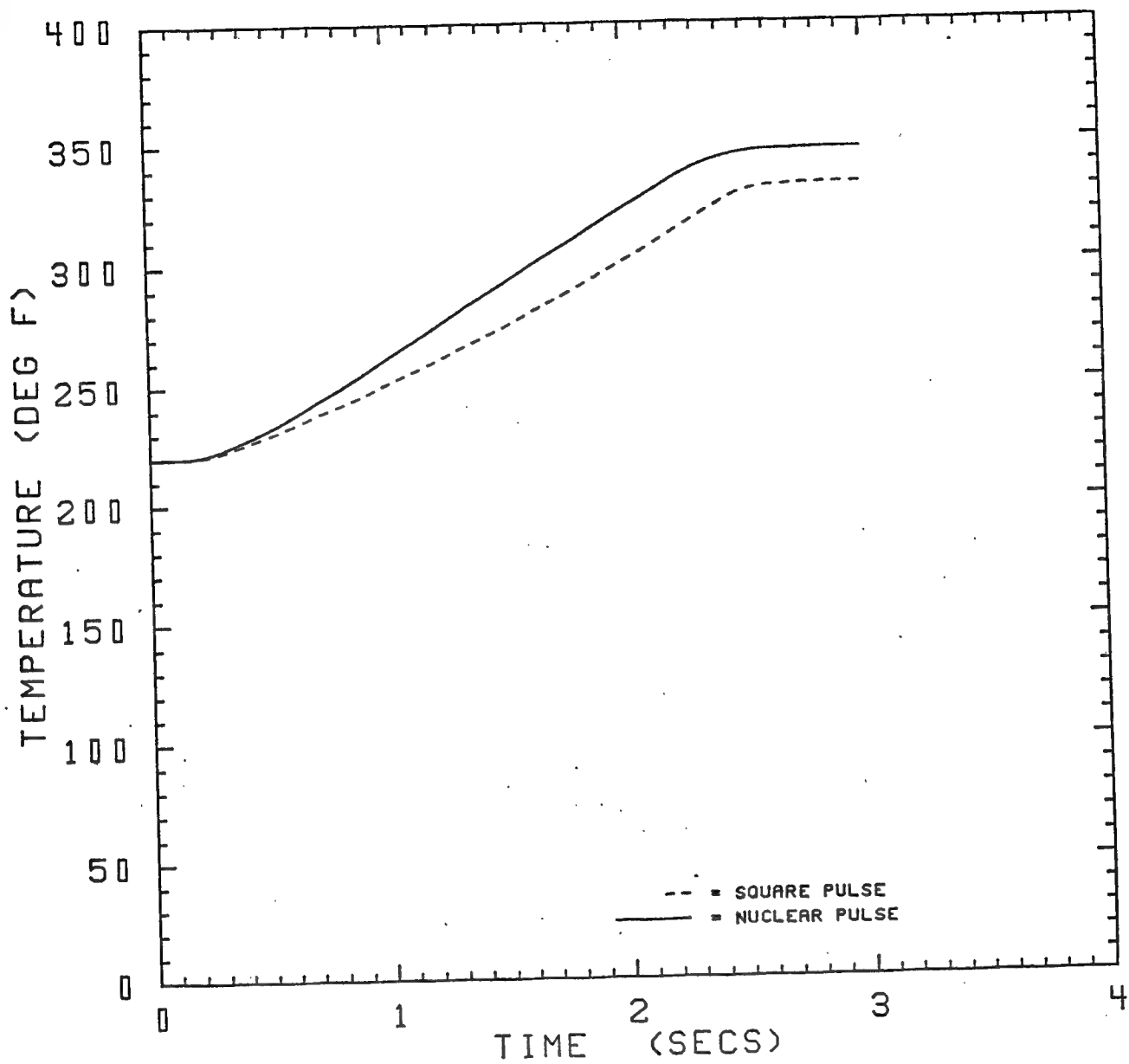
COMPARISON OF NUCLEAR AND SQUARE PULSE
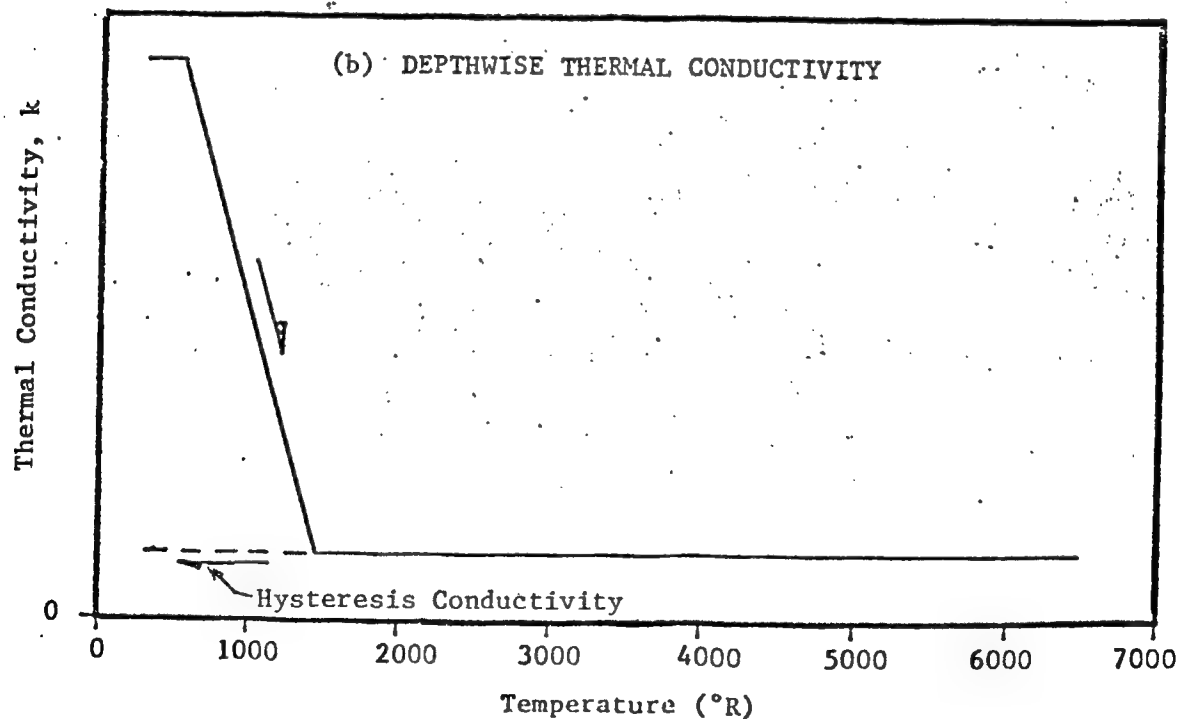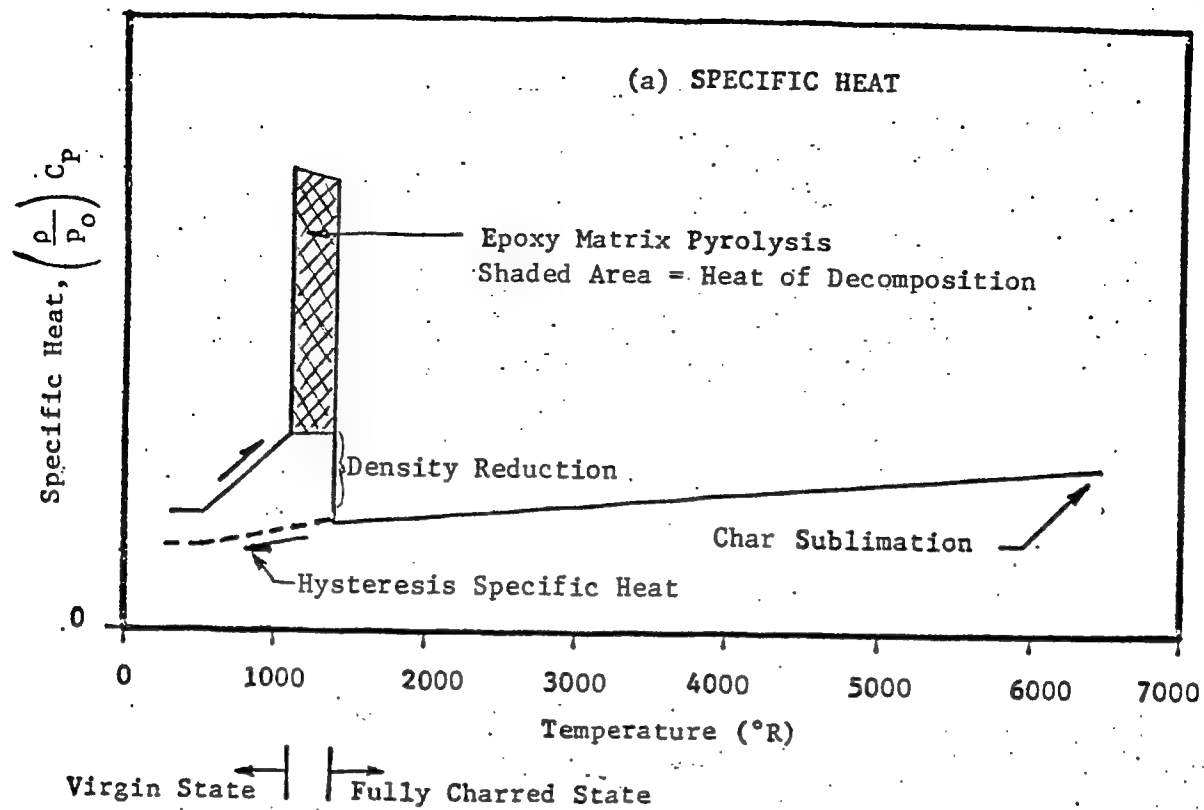THERMOLAG 330-1 ON ALUMINUM

Figure 4

Figure 5. Piecewise Linear Conductivity and Specific
Heat Curves for Generic Char Forming Ablator

The method used to deduce material properties from the test data involved an iterative sequence of material property assumption, analysis of a particular combination of specimen geometry and test conditions, comparison of analytical and experimental results, and modification of the assumed properties in an attempt to improve the correlation. Properties were further refined by continuing the above procedure until a number of specimen/pulse combinations all had good correlation using the same set of material properties. This empirical method is not the most accurate procedure for determining the temperature dependent thermophysical properties of a material. Individual tests for conductivity, specific heat, heat of ablation and other important parameters could produce more refined results. For screening the large number of materials considered by this program, however, this combination analytical/experimental procedure was deemed sufficiently accurate, and could be performed at a much lower cost than detailed measurement of individual properties.

RESULTS

Based on preliminary analysis of the thermal test results and practical considerations such as cost, ease of application, maintainability, durability and weather resistance, ten of the most promising materials were selected for detailed property determination. The selected materials are indicated by a * in Table 1. These studies showed that all the top candidates could be classified into one of three categories, distinguished both by observed physical response and the form of the derived material property data which resulted in the best correlation. These categories were:

1. Subliming Ablators - These materials decomposed with no significant char residue. They provided a majority of their protective capability by absorbing energy with an endothermic decomposition reaction and by removal of heated material at a specific temperature. These materials were modeled with the TRAP code by specifying an ablation temperature and corresponding heat of vaporization.

2. Char Forming Ablators - These materials employed the high energy decomposition reaction of the subliming ablators with the formation of a carbonized char residue after initial decomposition. This residue provided protection by two mechanisms: reduced conductivity and high reradiation of energy. Reradiation became a significant factor since the temperature of vaporization of the carbon layer, approximately 6000°F, allowed it to reach high temperatures, estimated at nearly 4000°F in some cases, during the thermal pulse. TRAP modeled these materials with the elevated C_p technique described in the previous section.

3. Intumescing Ablators - In addition to the above mechanisms, these materials underwent significant swelling during heating. Post-test observation of test specimens showed that some coatings had swelled to nearly 50 times their pre-test thickness. This reaction results in the thermal isolation of the highly heated

char material from the underlying structure. These materials were modeled with both the elevated C_p technique and by significantly reducing their conductivity at the decomposition temperature.

A typical correlation for tests of three different thicknesses of a single protective coating material is shown in Figure 6. In this figure the symbols represent test data measured at the back face of an aluminum substrate protected by 0.013, 0.023 and 0.030 inches of Flamemaster DE-380, while the solid lines show analytical predictions. The same set of analytically derived properties was used to generate all three prediction curves. Data acquisition began at time 0 in the figure. The command to open the shutter, which initiates exposure of the specimen, was issued 0.15 seconds later. The shutter reached its full open position at 0.3 seconds on the plot. The shutter was closed at 2.4 seconds. For the shelter application of interest to this project, it was desired to determine the protective coating thickness that would limit the outer substrate surface temperature rise at a particular time during thermal exposure to 120°F. Using the material properties derived from test data and the specified nuclear pulse, the thickness of this particular material required to satisfy the design requirement was found, after a few additional TRAP calculations, to be 0.012 inches. Similar calculations were performed for all ten materials to first determine realistic material properties, and then to select a design thickness.

Similar techniques were used to correlate results of tests performed using coated graphite/epoxy substrates. Only three of the top ten materials had been tested on graphite. Tests on graphite substrates differed from the previously described aluminum substrate tests in several regards. The much lower thermal conductivity of the composite substrate caused more of the energy to be retained at the surface, resulting in a more rapid rise of protective material temperature. The thermally thin aluminum specimens had almost no temperature gradient between the inner and outer aluminum faces. The mass of the material provided a heat sink capability to the aluminum structure which helped it meet the outer face 120°F temperature rise criterion more easily than the graphite substrate specimens, which heated rapidly near the surface while they interior remained cool. This difference is best appreciated by noting that 0.021 inches of DE-380 were required to meet the outer surface temperature rise specification on graphite, but only 0.012 inches were needed on aluminum.

Correlation of TRAP results on graphite were complicated by the fact that the thermophysical properties of the composite are much less well defined than similar aluminum properties, adding an additional uncertainty to the analysis. Other workers have published graphite/epoxy thermophysical property data generated using similar test data/analysis correlation techniques (References 3 and 4). These reports describe results obtained in highly convective wind tunnel environments where smoke clearing and char-layer removal is more significant. In addition, these reports present results obtained by correlating with thermocouple readings 4 or more plys below the surface, while data measured just below the exposed surface ply was used in the current study. This location, near or sometimes in the decomposition region, can be more sensitive to the values
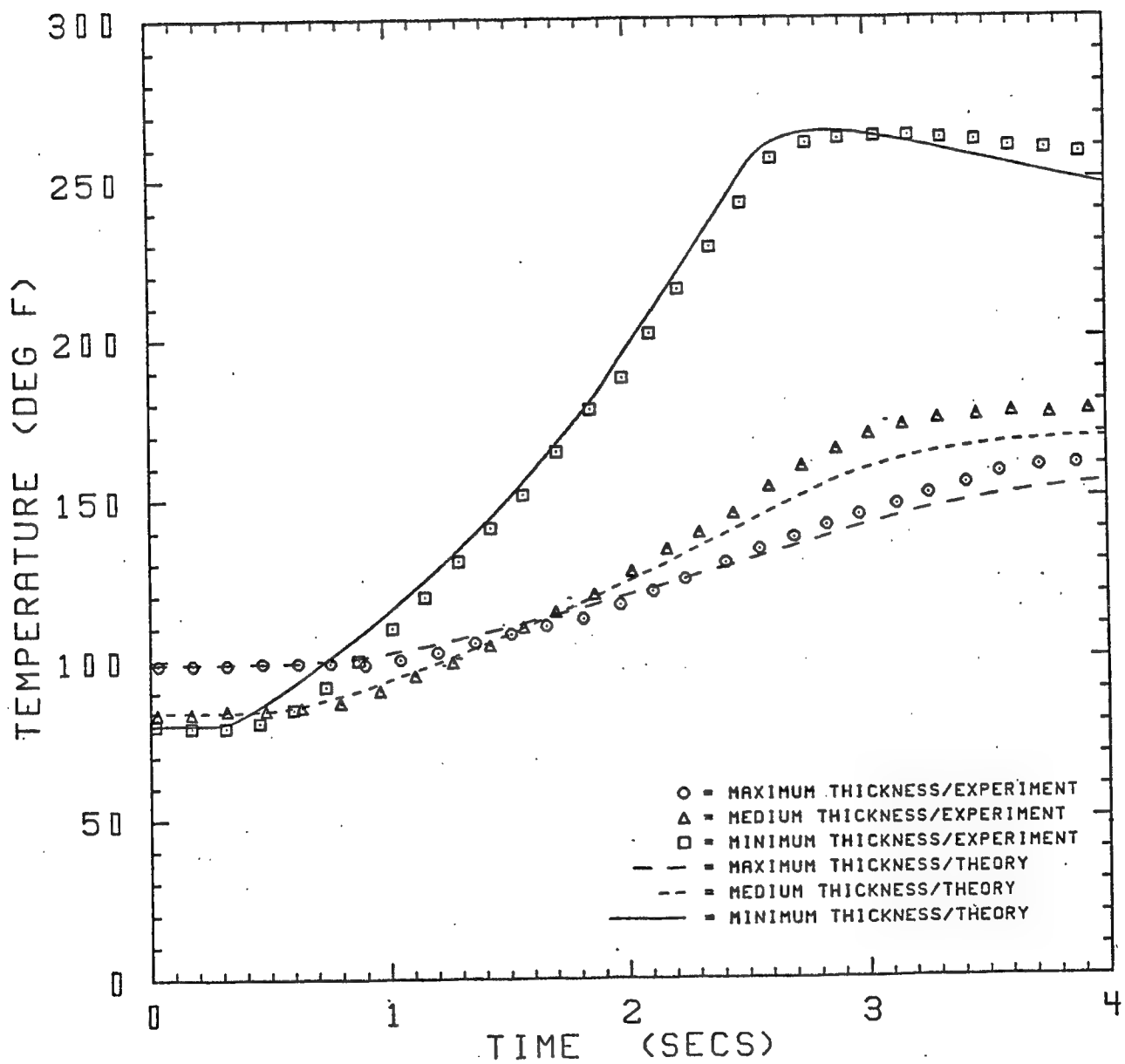
264

Figure 6. Typical Comparison of Experimental Measurement and Analytical Correlation

of the ablation parameters. The major difference between graphite/epoxy thermophysical properties reported by other investigators and those derived from tests of unprotected graphite/epoxy conducted during this study is the magnitude of the C_p elevation used to model epoxy ablation. The difference in this value, a factor of two or more greater in the current study than previously reported, can be attributed to differences in radiation blockage due to smoke, char removal and the lower than normal epoxy content of the graphite laminate. Graphite/epoxy material properties, along with Kevlar/epoxy properties measured by a similar technique, are summarized in Table 2.

Figure 7 shows the much more complicated behavior typical of unprotected graphite/epoxy specimens exposed to a 50 cal/cm^2/sec flux. Squares in this figure represent the response measured by the thermocouple located in the second ply of the specimen and circles the thermocouple in the center of the laminate. TRAP predictions obtained using the Table 2 properties are plotted as lines. Material in the outer plys smooths the inner thermocouple response by acting in a manner similar to the coating material on the aluminum substrate previously illustrated in Figure 6. The response of the outer thermocouple, buried in the epoxy decomposition zone of the laminate, is much more complicated. The temperature in this ply rises rapidly to approximately 500°F. The effect of resin decomposition in the outer ply then begins to slow the rate of temperature increase by absorbing its decomposition energy. When all the epoxy above the thermocouple has been pyrolyzed, the temperature again begins to rise rapidly until the beam is turned off at 2.4 seconds. The dip in the experimental data near the peak temperature is thought to be caused by delamination near the thermocouple.

A trade study was used to quantitatively rank the top ten coating materials and Kevlar/epoxy for thermal hardening capability and other practical concerns. Table 3 presents results for aluminum, while Table 4 shows results for composite substrates. Material rankings differed slightly on the two substrates due to the difference in performance of the coatings on high versus low conductivity materials. Cost and weight scoring, based on numerical results, are explained in the tables. Scores in the other more qualitive categories are based on estimated relative performance of each material, and could potentially change as more data becomes available. Materials with the largest point value, listed in the two rightmost columns of each table, are judged to be the best performers for shelter applications. The scoring system adopted for this trade study suggested that a number of commercially available materials are suitable, with Chartek 59 scoring the highest on both metal and composite substrates.

SUMMARY

This study determined that a number of commercially available coatings can provide thermal pulse protection to hardened tactical shelters. Ablative materials were found to be the best class of performers, with Chartek 59, an intumescing ablator scoring highest in a trade study. Several other commercially available materials were also found to be suitable. It was found that very little data was routinely available from

TABLE 2A

AS4/3501-6 GRAPHITE EPOXY THERMOPHYSICAL PROPERTIES

Transverse Virgin Conductivity

K(Btu/in Sec°F)	T (°F)
1.00×10^{-5}	80
1.00×10^{-5}	650
2.315×10^{-6}	949
2.315×10^{-6}	6000

Transverse Char Conductivity

K(Btu/in Sec°F)	T (°F)
2.315×10^{-6}	80
2.315×10^{-6}	6000

Virgin Specific Heat

$(p/p_o) \, C_p$ (Btu/1bm°F)	T (°F)
0.30	80
0.45	259
0.51	499
0.442	649
7.0	650
7.0	949
0.274	950
0.285	968
0.432	6000

Char Specific Heat

$(p/p_o) \, C_p$ (Btu/1bm°F)	T (°F)
0.274	80
0.274	950
0.285	968
0.432	6000

Additional Properties

1) Heat of Decomposition ($c_p \, \Delta T$) = 2100 Btu/1bm
2) Graphite Ablation Temperature = 6000°F
3) Graphite Heat of Sublimation = 13310 Btu/1bm
4) Virgin Density = .054 1bm/in^3
5) Density Reduction after Decomposition = 72%
6) Surface Absorptivity = 0.9

   (at all wavelengths & temperatures)

TABLE 2B

KEVLAR/EPOXY THERMOPHYSICAL PROPERTIES

Virgin Conductivity

K(Btu/in Sec°F)	T (°F)
2.5×10^{-6}	80
2.3×10^{-6}	800
1.0×10^{-6}	1100
1.0×10^{-6}	2500

Char Conductivity

K(Btu/in Sec°F)	T (°F)
1.0×10^{-6}	80
1.0×10^{-6}	2500

Virgin Specific Heat

$(p/p_o) \; C_p$ (Btu/lbm°F)	T (°F)
0.28	80
0.36	600
0.45	800
14.0	801
14.0	1100
0.3	1101
0.45	2500

Char Specific Heat

$(p/p_o) \; C_p$ (Btu/lbm°F)	T (°F)
0.30	80
0.30	1100
0.45	2500

Additional Properties

1) Heat of Decomposition ($c_p \, \Delta T$) = 4200 Btu/lbm
2) Char Ablation Temperature = 2500°F
3) Char Heat of Sublimation = 1.0 Btu/lbm
4) Virgin Density = .044 lbm/in^3
5) Density Reduction after Decomposition = 66%
6) Surface Absorptivity = 0.92

   (at all wavelengths & temperatures)
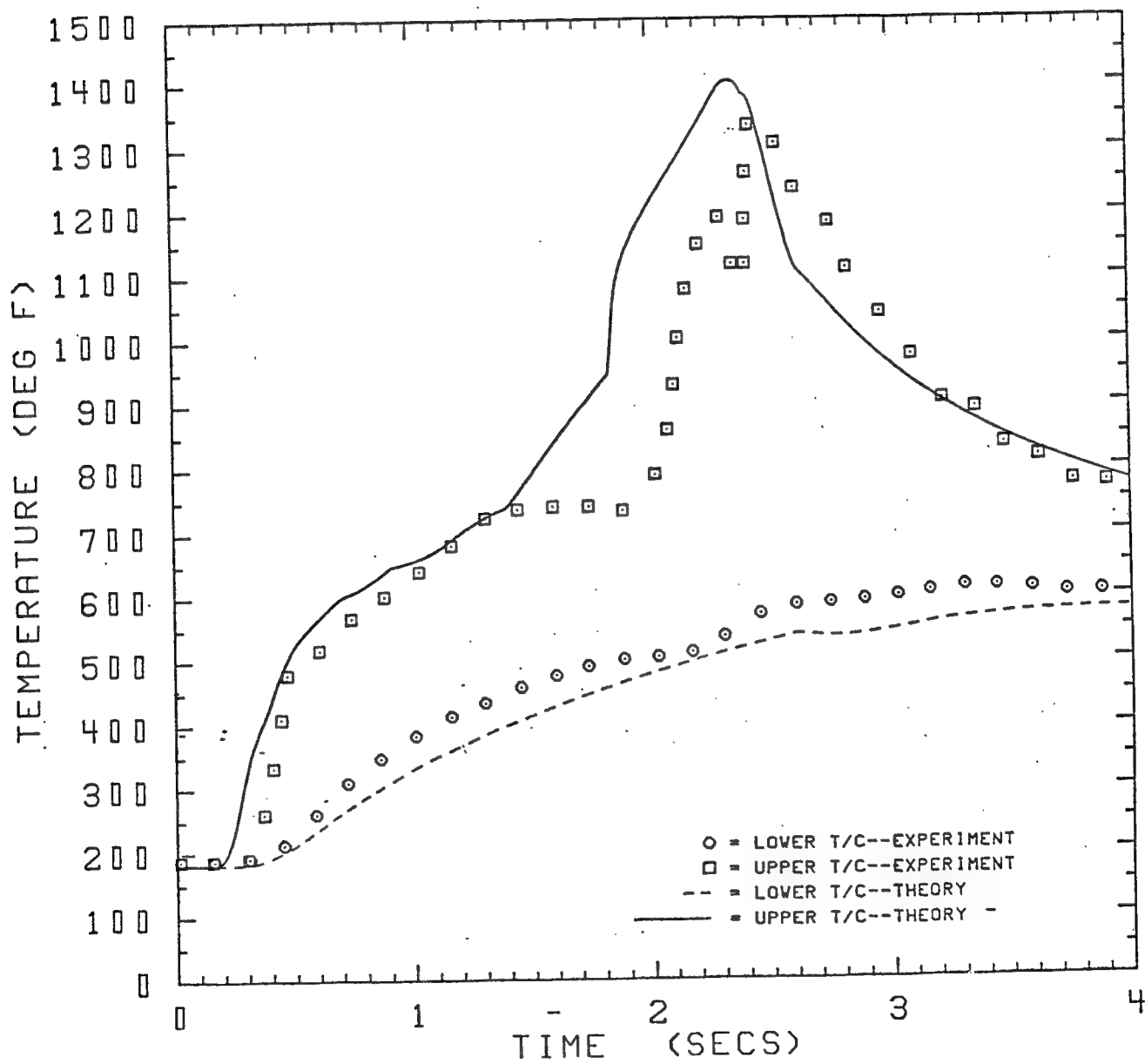
Figure 7.   50 cal/cm^{2}sec Exposure of Graphite/Epoxy

TABLE 3

MATERIAL PERFORMANCE RATINGS FOR ALUMINUM SUBSTRATE

Material	Thickness	Weight[1]	Rating[2]	Cost[3]	Rating[4]	Durability	Weatherability	Maintainability	Ease of Handling	Chemical Resistance	Total, Scheme #1	Total, Scheme #2
Korotherm	.010"	9	3	$95	2	1	ND*	0	1	ND	15	14
E-400	.013"	11	3	165	1	1	3	1	2	2	20	18
DE-380	.012"	10	3	85	2	1	2	1	3	2	22	21
DE-370	.013"	11	3	95	2	1	2	1	3	2	22	21
Flamarest 1600 BTX	.010"	10	3	90	2	2	1	1	2	ND	19	18
Chartex 59	.012"	14	2	45	3	2	3	1	3	3	24	25
Flexfram	.017"	19	1	95	2	2	3	1	2	1	16	17
AVCOAT II	.012"	10	3	85	2	2	ND	0	2	ND	18	17
AVCOAT 8039	.014"	14	2	85	2	2	ND	0	2	ND	14	14
Thermolag 330	.012"	13	3	40	3	1	3	1	1	3	24	24
Kevlar/Epoxy	.022"	22	1	440	1	3	3	0	0	3	24	14

1) Coating weight at design thickness on a 20 x 8 foot panel, lbs.
2) Weight rating criteria: 10 to 13 lbs = 3, 13 to 16 lbs = 2, over 16 lbs = 1
3) Material cost at design thickness on a 20 x 8 foot panel, $
4) Cost rating criteria: $0 to 50 = 3, $50 to 100 = 2, over $100 = 1
   Weighting scheme #1 = 3 x weight rating + 2 x cost rating + other factors
   Weighting scheme #2 = 2 x weight rating + 3 x cost rating + other factors
*) ND = no data

270

TABLE 4

MATERIAL PERFORMANCE RATINGS FOR GRAPHITE/EPOXY SUBSTRATE

Material	Thickness	Weight[1]	Rating[2]	Cost[3]	Rating[4]	Durability	Weatherability	Maintainability	Ease of Handling	Total, Scheme #1	Total, Scheme #2
Korotherm	.021"	19	2	$200	1	1	ND*	0	1	10	9
E-400	.019"	16	2	245	1	1	3	1	2	17	16
DE-380	.021"	17	2	150	2	1	2	1	3	19	19
DE-370	.019"	16	2	135	2	1	2	1	3	19	19
Flamarest 1600 BTX	.016"	16	2	140	2	2	1	1	2	16	16
Chartex 59	.018"	18	2	60	3	2	3	1	3	24	25
Flexfram	.025"	28	1	140	2	2	3	1	2	16	17
AVCOAT II	.017"	14	3	120	2	2	ND	0	2	18	17
AVCOAT 8039	.026"	26	1	155	2	2	ND	0	2	11	12
Thermolag 330	.026"	27	1	85	3	1	3	1	1	18	20
Kevlar/Epoxy	.036"	36	1	720	1	3	3	0	0	14	14

1) Coating weight at design thickness on a 20 x 8 foot panel, lbs.
2) Weight rating criteria: 10 to 15 lbs = 3, 15 to 20 lbs = 2, over 20 lbs = 1
3) Material cost at design thickness on a 20 x 8 foot panel, $
4) Cost rating criteria: $0 to 100 = 3, $100 to 200 = 2, over $200 = 1
   Weighting scheme #1 = 3 x weight rating + 2 x cost rating + other factors
   Weighting scheme #2 = 2 x weight rating + 3 x cost rating + other factors
*) ND = no data

271

manufacturers regarding either the thermophysical properties of their materials, or their response to normal service environments. A combined analytical/experimental techinque for modeling a material's thermal response with sufficient accuracy for comparative design was demonstrated as a cost saving alternative to individual measurement of specific material properties. This technique was used to estimate thermophysical properties of graphite and Kevlar/epoxy composites as well as ablative coatings. It was observed that smoke generated during exposure to a thermal pulse may result in significant radiation blockage, a fact that should be considered when applications with high free stream velocities are of interest.

Thermal effects directly influence the mechanical design of hardened shelters. This program showed that a Kevlar fragment shield located outside a load carrying skin of a structure with ballistic as well as nuclear hardening requirements provides adequate thermal protection without any additional surface treatment. Thin coatings were shown to be capable of controlling the temperature rise of exposed structure in shelters without ballistic barriers. The temperature of the load bearing material in a shelter wall at the time of blast arrival is a critical design parameter. Strength and stiffness properties of the composite and metal materials considered for use in shelter construction degrade with temperature. Limiting the temperature rise produced by a nuclear thermal pulse reduces the amount of material needed to survive a blast, and with it a shelter's cost and weight.

REFERENCES

1. McManus, Hugh and Dennis C. Coyne, "TRAP4 - A Digital Computer Program for Calculating the Response of Mechanically and Termallly Loaded Aircraft Structures to the Thermal Radiation of a Nuclear Explosion or High Energy Laser", Kaman AviDyne Technical Memorandum KA TM-141, October 1982.

2. Fanucci, Jerome P., Boyer, Brian D. and Roger W. Milligan, "Technology Base Development for Nuclear Hardened Tactical Shelters Volume IV - Thermal Protection Concepts, Part A - Analytical and Experimental Results", Kaman AviDyne KA TR-219, April 1984.

3. Griffis, C.A., Masumura, R.A., and C.I. Chang, "Thermal Response of Graphite Epoxy Composite Subjected to Rapid Heating", Naval Research Lab, Memorandum Report 4479, March 31, 1981.

4. Menousek, J.F. and D.L. Monin, "Laser Thermal Modeling of Graphite Epoxy", Naval Weapons Center Technical Memorandum 3834, June 1979.

NOTES

SESSION VI: SPECIAL SESSIONS ON COMPOSITES

COMPOSITE APPLICATIONS IN VEHICLES

ANALYSIS AND DESIGN

FABRICATION AND TESTING OF LARGE CALIBER (105mm) COMPOSITE
SABOT SPECIMENS
D. M. Granville, AMMRC and M. A. Scavullo, Benet Weapons Lab

DESIGN AND DEVELOPMENT OF COMPOSITE OFF-ROAD VEHICLES FOR
MINI BAJA EAST
Roy Richard, Professor, University of Lowell

CHALLENGES TO APPLYING COMPOSITES TO MILITARY GROUND VEHICLES

Presented At

Army Symposium on Solid Mechanics

1-3 October 1984

By

J. R. Plumer*
D. Oplinger*
J. McElman**
J. Chevalier***
J. Hamell****

*Army Materials and Mechanics Research Center
Watertown, MA

**University of Lowell
Lowell, MA

***Research & Development Center
US Army Tank Automotive Command
Warren, MI

****PM, Heavy Truck
US Army Tank Automotive Command
Warren, MI

I INTRODUCTION

Current interest in applying fibrous composite materials to military ground vehicles stems from objectives such as that incorporated in STRATEGIC ARMY DOCTRINE, "AIRLAND 2000" which stresses the need for air transportability and rapid deployment using helicopter and fixed wing aircraft. In addition the typical commercial market has objectives such as reduced costs, fuel economy improvement through reduced weight, and improved component/vehicle performance. Some of the specific advantages of fiber reinforced plastic (FRP) materials are discussed in Section III.

The purpose of this paper is to discuss the problems and challenges facing the designer who is tasked with applying fibrous structural materials to ground vehicle systems. In typical instances metal component designers may take advantage of a solidly emplaced metals design and fabrication technology which is characteristic of the automotive industry. In the case of fibrous composite materials the designer must undergo considerable redirection in design philosophy because of differences in structural behavior between composite and metallic components, a much less advanced production technology base which is currently available to the automotive industry, and factors such as materials costs which currently tend to be greater than those encountered in metals.

A number of attributes of composite materials in addition to light weight (TABLE I) make them attractive for application to current and future military vehicle systems. AMMRC and TACOM have been engaged in joint studies of potential vehicle component applications for a number of years, in efforts which typically involve:

> -feasibility studies,
> -prototype design, and
> -fabrication of demonstration components

This paper will discuss the typical problem areas involved in successful design of automotive composite structures in the military scenario. In addition, typical case histories of component structural design and fabrication efforts which have been conducted, as well as potential future applications (TABLE II) will be described. Finally, a wheeled vehicle test bed program involving evaluation of previously developed components in addition to development of additional components will be proposed.

II SUMMARY OF PRESENTATION

ADVANTAGES OF COMPOSITE MATERIALS

The advantages of fiber reinforced materials for vehicle applications, as summarized in TABLE I, include:

> Corrosion resistance
> Good ballistic resistance per unit weight
> Light weight
> Design flexibility
> Reduced maintenance
> Improved mobility and fuel economy resulting from low weight
> Potential cost reduction (acquisition and life cycle)

DESIGN CHALLENGES

Problem areas which arise in the design of composite structures include:

> Design for orthotropic behavior
> Radical differences in failure criteria from those used in metals
> Joint and attachment design
> Need for iterative design procedures involving tradeoffs between selected materials, fabrication approaches and design considerations
> Allowance for low stiffness in materials selected for low cost
> Need for design ingenuity to provide cost savings where higher cost materials must be used.
> Lack of a mature production base leading to greater variability of material properties and dimensional tolerances than in the case of metals
> In armored vehicles, the need for combining good structural performance with good ballistic performance in integrated structure/armor designs

PREVIOUS DEVELOPMENT EFFORTS

TABLE II highlights a number of efforts which have been conducted jointly between AMMRC and TACOM on wheeled vehicles. These efforts and those from the automobile manufactures maybe summarized as follows:

Use of FRP in selected vehicle components to demonstrated definite improved performance, weight reduction, and successful incorporation into conventional vehicle construction.[2,3]

Design methodology, specification, and evaluation capabilities are maturing within the industry.

Corrosion resistance/increase durability is emerging as a primary driver affecting life cycle cost of tactical/support vehicles.

279

CASE STUDY - M871 TRAILER SIDE RACK DEVELOPMENT

Typical FEA (SAP IVA) employed at AMMRC in FRP design of vehicle components is described in References [2] & [3]. The objective of the study was to design a FRP Truck Trailer Side Rack panel (Fig 1) as a retrofit replacement part for the Army M-871 - M-872 trailers. The variables considered in the study included:

> Type of Plastic
> Type of Reinforcement
> Materials Properties
> Configurations and Cost

The FEA methodology produced configurations 25% lighter at an accompanying cost reduction of 50%. Prototypes were statically tested to clarify analytical prediction of stress and deflections prior to field testing.

OPPORTUNITIES AND AMMRC/TACOM INITIATIVES FOR FRP COMPOSITES IN MILITARY WHEELED VEHICLES

These application opportunities are listed in descending order of estimated economic pay back:

> -Corrosion Resistance - Increased component durability for decreased life cycle costs.

> -Weight Reduction - Reduction of existing fleet vehicles by redesign and replacement of components.

> -Increased Performance - Complete design of new concept vehicles maximizing reduction of unsprung weights, superior dynamics, and lower vehicle weights.

Three AMMRC/TACOM initiatives responsive to these opportunities, are discussed as follows:

> -Composite Plastics applications for the Heavy Expanded Mobility Tactical Truck (HEMTT); the vehicle currently employs a FRP battery box cover. Future composite applications are being planned for the cargo body sides panels tail gate, wheel chalk blocks and mud flaps. These components offer the best composite material application opportunities (cost versus payback) relative to (a) corrosion resistance (b) weight reduction (improved transportability and mobility) and (c) improved durability.

> -The second initiative is a joint TACOM/AMMRC effort to establish and maintain a wheeled vehicle test bed program. This effort would assemble instrument and evaluate numerous composite components designed and fabricated for the M-939 5 ton truck. Studies to include documentation of weight reduction, increases in durability, validation of structural dynamic finite element models, and life cycle data.

-The third initiative is a complete redesign study and prototype effort to be conducted jointly with TACOM/AMMRC - 9th Inf Division, Ft. Lewis, WA. The goals are to prototype in FRP selected components from the HMMWV for maximized weight reduction and increased performance.
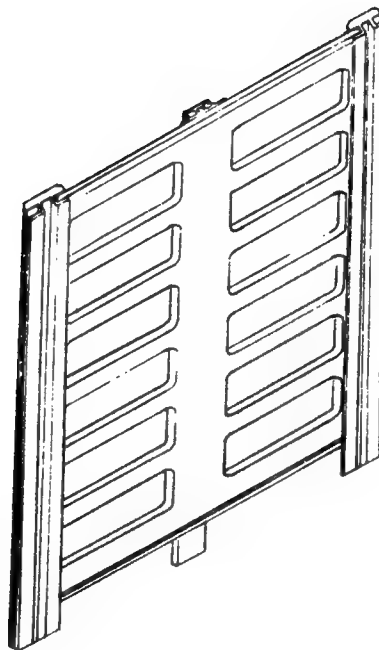
Figure I, FRP Trailer Side Rack for
M-871 Semi-Trailer

TABLE I

ADVANTAGES OF COMPOSITE MATERIALS TO
ARMY WHEELED VEHICLES

Specific Strength and Stiffness

Fatigue Resistance

Damage Tolerance

        Non-Spalling – No Vaporous Effects
        Equal Ballistic Protection at Reduced Weight

Corrosion Resistance

Design Flexibility

Economics

        Production Costs
        Life Cycle Costs
        Energy Conservation

TABLE II

TACTICAL VEHICLES

TRUCKS/TRAILERS

COMPONENT	PRESENT MATERIAL	COMPOSITE	% WT. SAVINGS
WINDSHIELD	SAFETY GLASS	ABR. RESIST. POLYCARBONATE	30
WHEEL	STEEL (100 LBS)	SMC (50 LBS)	50
TRAILER SIDE RACKS	WOOD (60 LBS)	SMC (40 LBS)	30
TROOP SEAT SLATS	HARDWOOD (.87 LB/FT)	GRP (BOX BEAM) (.67 LB/FT)	23
5 TON TRUCK HOOD & FENDER	STEEL (325 LBS)	FRP (162 LBS)	50
5 TON TRUCK PROPELLER SHAFT PN 11669147	STEEL (15 LBS)	FRP (8.72 LBS)	50
5 TON TRUCK REAR SPRING ASSEMBLY	STEEL (293.4 LBS)	FRP E TYPE FIBERGLASS/ EPOXY (142.3)	52

283

REFERENCES

1. E. M. Lenoe "Current Advanced Composite Applications in the Unived States", First Department of National Defense Composite Materials Workshop, Victoria, British Columbia, 13-15 July 1983.

2. J. R. Plumer et al., "Design and Fabrication of FRP Truck trailer Side Panels", 38th Annual Conference, Reinforced Plastics/Composites Institute, the Society of the Plastics Industry, Houston, TX, February 7-11, 1983.

3. J. R. Plumer et al., "Design and Fabrication of FRP Truck Trailer Side Racks", AMMRC TR 83-50, August, 1983.

DYNAMIC ANALYSIS OF THE BFV COMPOSITE TURRET

(extended abstract)

C.R.ORTLOFF

CENTRAL ENGINEERING LABORATORIES

FMC CORPORPORATION

1185 COLEMAN AVENUE

SANTA CLARA,CA 95052

Extended Abstract

Composite materials are being extensively employed in development programs sponsored by the government to replace metal parts on military vehicles. A leading example is the turret design to fit the FMC Bradley Fighting Vehicle. It consists of an aluminum substructure with a fiberglass/polyester shell which serves as both primary structure and armor. This design provides advantages in weight savings, ease of manufacture, ballistic protection and strength over the welded aluminum components it replaces. The lower modulus of the fiberglass/epoxy (FG/EP) shell, compared to its aluminum counterpart, engenders a host of new problems related to its greater flexibility and deflection under load. This leads to considerations of the dynamic behavior of the low modulus composite turret shell and the subsidiary effects related to vibration and the high damping characteristics of composites over aluminum shell structures.

As part of the AMMRC reinforced plastic turret program, a study to investigate composite turret dynamic behavior is in progress. Results from this program are based on ANSYS FEA models of a composite BFV turret (800 elements) mated to a BFV hull (1600 elements) with a suspension system (300 elements) consisting of torsion bars, roadarms, roadwheels, shock absorbers and track elements. Initially the natural frequencies and mode shapes of the BFV experimental composite turret were determined and compared to those of the existing all-aluminum turret; ANSYS calculations of the natural frequencies are based on displacement (but not rotation) constraints of the turret base ring. Since computed natural frequencies for the composite turret are approximately a factor of 7 lower than those for the all-aluminum turret, they can be excited by typical road/track/suspension system/hull input spectra thus causing excessive ISU and secondary gunsight vibration levels. Mode shapes reveal that the secondary sight, located near the center of the large composite top panel of the turret experiences significant amplitude vibratory motions. A sequence of turret internal stiffners are investigated as a means to increase natural frequencies out of the range of input excitation frequencies and limit deflections at sight locations. The effects of these stiffners on natural frequency values and mode shapes has been computed. To fully understand the total modal vibration picture, the turret FEA model was added to a full BFV FE hull model. Modal analysis of the total FE system was performed under free-free constraints, for both the all-aluminum and aluminum hull-composite turret vehicles. For the all-aluminum vehicle, hull stiffness is less than that of the turret and consequently contributes significantly to the low system natural frequencies. For the aluminum hull-composite turret system, both hull and turret are of comparable stiffness so that the system acts as a unit in determining natural frequencies. Mode shapes of the aluminum hull-composite turret system are computed to reveal these effects graphically. The composite turret-aluminum hull system mode shapes still indicate low frequency "drumhead" vibrations of the turret top plate similar to those observed from the more limited fixed base ring turret modal analysis. The "fix" of providing gusseting within the composite turret to connect the ISU and secondary sight zones rigidly to the turret aluminum substructure is recommended as local deflection amplitudes are locally reduced to acceptable values observed from the existing aluminum BFV turret. Outside of these zones, low frequency composite shell vibration still exists but no critical components are affected adversely.

The natural frequencies are also raised by addition of gusseting thus contributing to lowered turret excitation from suspension system/road interaction input excitation.

A further study of composite damping effects on turret vibration levels has been performed. Tests to determine the α, β ANSYS damping coefficients for aluminum and FG/EP test specimens were performed and incorporated into computations for the turret dynamic response to a 10 round burst from the 20 mm cannon. Computations compare the all-aluminum to composite turret response at trunnion and sight locations; this response is in the form of deflection and acceleration (g loading) time histories resulting from gun firing. Results indicate that damping is very rapid for the composite turret and all frequencies are damped to near zero amplitude values between successive shots (200 round/min). This further indicates that driven excitations input into the composite FG/EP turret produce a fatigue spectrum similar to the impulse train. This is unlike the case for the lightly damped all-aluminum structure for which a broad frequency range response to excitation exists and persists over long times and has energy distributed over many modes.

Further study of the composite turret vibration levels has been performed for the aluminum hull-composite turret-suspension system BFV FE ANSYS model. This model requires substructuring to improve computational efficiency. The model is run over a 1 foot radius ground obstacle at a given speed and the dynamic response of the hull, turret and suspension system determined. This response includes all deflections stresses and force components within the hull/turret/suspension system components at all times before, during and after vehicle encounter with the road obstacle. The g loading and vibration history of certain points on the turret has been determined for typical BFV-road obstacle encounters. The vibration time history then gives further information to understand the turret response spectrum from inputs originating from suspension system interaction with the ground being after modification by passage through the elastic hull. Results indicate that low frequency inputs to the turret result but are damped rapidly by both the suspension system shock absorbers and the damping effects of the FG/EP shell. Work is in progress to refine the model for vehicle-ground interaction effects by field verification tests.

ANSYS
7/27/84
10.3340
PREP7 ELEMENTS

AUTO SCALING
XU=-1
VU=1
ZU=1
DIST=107
XF=134
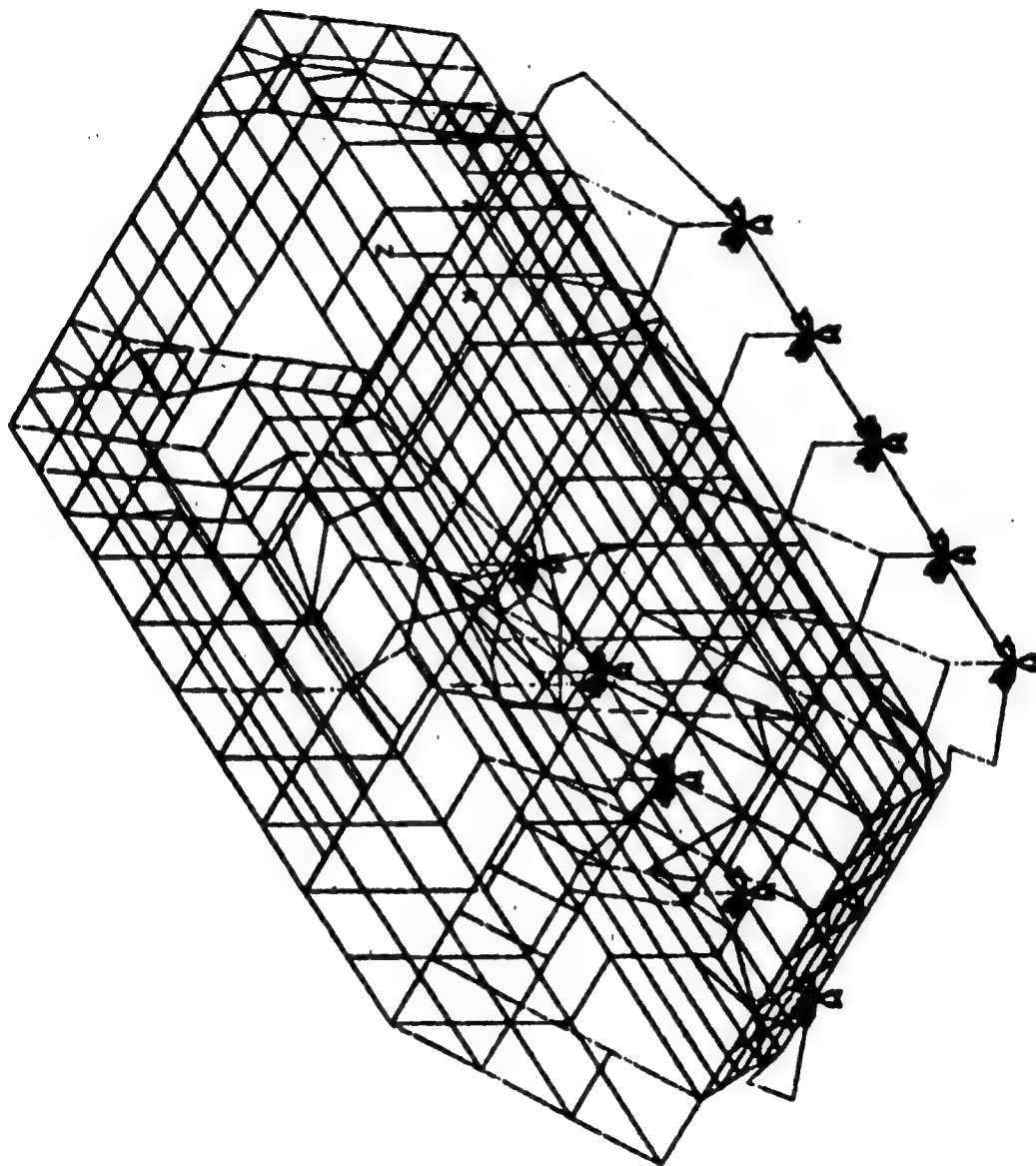YF=-.148
ZF=52.2
ANGL=90
HIDDEN

PREP7 -INP-

BFU NORMAL MODES ANALYSIS (TURRET MERGED TO HULL 4-18-84)

BRADLEY FIGHTING VEHICLE

FINITE ELEMENT MODEL
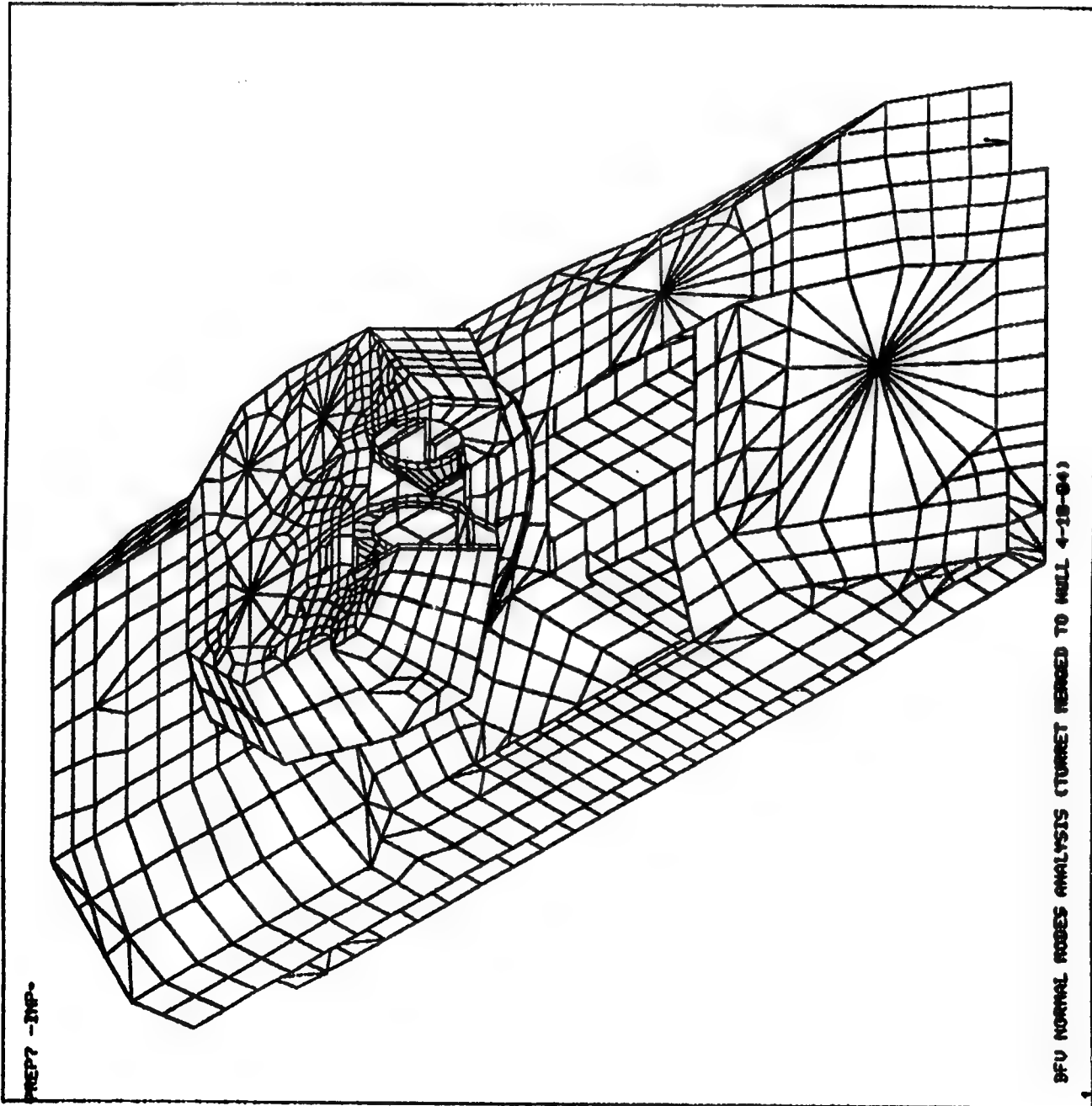
M113A2 FINITE ELEMENT
MODEL

FIBER-REINFORCED COMPOSITE WHEELS - STATUS UPDATE

JAMES A. WOELFEL
PRINCIPAL MATERIALS ENGINEER
MOTOR WHEEL CORPORATION
LANSING, MICHIGAN 48910

ABSTRACT

Composite wheels continue to find interest in the automotive original equipment market primarily as a potential replacement for aluminum wheels.

Development efforts have continued for the past several years to produce a fiber-reinforced passenger car composite wheel which will satisfy all of the current durability requirements of original equipment in domestic and foreign markets. Significant progress will be reported in the areas of durability testing and lug nut torque retention for a wheel designed for certain front wheel drive vehicles.

Several critical processing problems and their effect on laboratory fatigue and field durability have been studied. Field evaluation involving test track durability fleet testing and general consumer testing is continuing to show that the composite wheel is indeed dependable and serviceable.

Vehicle testing was initiated in 1978 and is continuing with over 4,000,000 miles accumulated thus far showing no serviceability problems.

New tests were developed to evaluate problems unique to composite materials during and after extensive exposure to high temperatures. Discussion will center on a major technological challenge which became the key to the composite wheel development. Lug nut torque retention was analyzed in detail. Subsequent testing confirmed a solution to torque loss with actual data from laboratory and road testing demonstrating a significant advance in the development of the composite wheel. A description of the tests and their relationship to actual vehicle performance on the road will be discussed.

Comparison will be made in weight, cost, and test data for steel, aluminum, magnesium, and composite wheels. Several benefits will be pointed out for a composite wheel used on passenger cars, including lighter weight and corrosion resistance.

As with many of the new products being developed today not only for the automotive industry, but also for consumer and aerospace as well, especially ones that are key structural components and safety related, an attempt is being made to answer all the technical questions before marketing. The composite wheel is one such product, but which is now ready for use by the automotive industry.

RECOVERY VEHICLES - THEIR FUNCTION AND FUNCTIONAL PROBLEMS

Lt. Col. D. Staley
Aberdeen Proving Ground, MD

Fast recovery and repair of damaged tanks are a little recognized but extremely important factor for ultimate success in battle. The recovery and towing operations for a heavy vehicle such as an M-1 or M-60 tank under usual battlefield conditions present a myriad of technical problems which tax to extremes the present capabilities of engineering materials and engineering design and analysis.

The recovery vehicle itself must combine traction greater than the mobility, ballistic protection and speed equivalent to that of the vehicle recovered. The traction problem alone combines machanics of soil behavior under the extremes of battlefield conditions with the still incompletely understood mechanics of tracks and track components.

The auxiliary equipment required for recovery and towing must be strong and rugged enough to handle the enormous vehicle, light enough to be handled in turn by a few soldiers and compact enough to be efficiently stored and carried on the vehicle - all mutually competing requirements.

This presentation will describe the battlefield significance of recovery vehicle operations, a variety of recovery and towing operations and a number of currently urgent problems.

Progress on the Advanced Composite Airframe Program

J. Goldberg Ph.D.

Sikorsky Aircraft
North Main Street
Stratford, CT 06602

The author will cover the current progress on the Advanced Composite Airframe Program (ACAP). This program is sponsored by the Applied Technology Laboratory of the U.S. Army and is intended to demonstrate the advantages of advanced composites as construction materials. A helicopter airframe that meets stringent military requirements was designed, fabricated and is now being tested. The airframe reduced weight and cost as compared to an equivalent metal baseline.

Demonstration testing of the completed airframe is now being initiated. The cost and weight goals required by the contract have been exceeded with ease of design and fabrication demonstrated. More importantly, producibility in rate production has been demonstrated as the program was oriented to high volume production. It is clear that the technology (in both design and production) transfers easily into other advanced transportation vehicles.

APPLICATION OF THE BOUNDARY ELEMENT METHOD TO
PROBLEMS IN COMPOSITE FASTENING

Enayet Mahajerin
Assistant Professor
David L. Sikarskie
Professor and Chairman
Michigan State University
East Lansing, Michigan 48824-21226

Extended Abstract

The purpose of the present study has been to develop an efficient numerical algorithm for use in the analysis of composite structures, principally mechanically fastened composites. The major analytical tool in stress and deformation calculations in composites has been the finite element method (FEM). In this paper a boundary element method (BEM) is developed, a compact and efficient computer code written, and the method compared directly with the FEM.

The heart of the computation scheme is the treatment of the following, general boundary integral

$$P_\beta (F) = a\, \delta_{\beta\gamma}\, R_\gamma (S) + \int_{\partial D} G_{\beta\gamma} (F,S)\, R_\gamma (S)\, dS \qquad (1)$$

$$\beta,\ \gamma = 1,2$$

Here F is the field point, S is source point, P_β is either the displacement, u_β or the traction t_β, R is the source strength (initially unknown) and G is the fundamental solution. Three different cases (boundary conditions) are considered:

(1) Pure displacement boundary condition;

    $a=0$, $P_\beta = u_\beta$, and $G_{\beta\gamma}$ = displacement fundamental solution.

(2) Pure traction boundary condition;

    $a = 1/2$, $P_\beta = t_\beta$, and $G_{\beta\gamma}$ = traction fundamental solution

(3) For mixed type boundary conditions, a suitable combination of (1) and (2) is used.

Equation (1) is descretized by considering the boundary ∂D to be a series of straight lines. For simplicity the unknown source is assumed constant over each subdivision. Equation (1) thus is reduced to the linear system of equations

$$\underset{\sim}{A}\ \underline{R} = \underline{P} \qquad (2)$$

where $\underset{\sim}{A}$ is a 2N x 2N influence matrix with N the number of boundary subdivisions. Once this system is solved for R the results are substituted back into equation (1) to determine displacements and stresses as follows:

(1) P_β are displacents, u_β, if we set;

   a = 0 and $G_{\beta\gamma}$ = displacement influence function for the appropriate anisotropic elastic material

(2) P_β are stresses $\sigma_{\alpha\beta}$, if we set;

   a = 0, and $G_{\beta\gamma}$ = stress influence function again for the appropriate anisotropic elastic material.

The accuracy of the results depends on how one constructs A. For F≠ S all elements of A are computed numerically using a four-point Harris-Evans quadrature rule, while for F→S, an analytical integration is developed for the orthotropic case which may be extended for fully anisotropic materials. Similar treatment is repeated in computing boundary stresses and displacements.

Two sample computations are shown in figure/table 1 and 2. The figures show the symmetric half of a single pin, loose fit lap joint fastener. Two boundary conditions in the pin contact areas are shown; a normal cosine traction distribution and a completely fixed displacement condition. Both of these are approximations of the effect of the pin on the composite structure. Note that the stress concentration at the edge of the hole is the bottom entry of the σ_{yy} stresses. The σ_{yy} distribution satisfies overall equilibrium and the stress concentration values agree with exact values where available (other cases including the isotropic have been run).

The comparison between the BEM and the FEM was done for an isotropic material with a known value for the stress concentration, i.e. K_I = 3.1352, for an aspect ratio of d/w = .1. The ANSYS FEM computer code had 134 quadratic elements while the BEM computer code had 57 boundary elements. This resulted in the same edge subdivision for both codes. The following resulted;

FEM	BEM
K_I = 3.1102	K_I = 3.0952
CPU = 177 sec.	CPU = 27 sec.

There is a reasonably clear indication, at least for the problems investigated in the present paper, that the BEM is the more efficient approach.

Figure/Table 1

Stresses along the ligament line ab
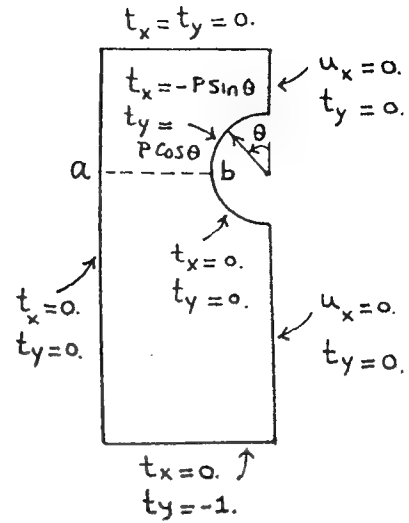for an orthotropic composite.
Cosine distribution of tractions on
the upper half of the hole, d/w = .5,
N = 60 (boundary subdivisions)

d = 0.5

e = 0.5

h = 1.5

w = 1.0

x	y	σ_{xx}	τ_{xy}	σ_{yy}
.02	1.5	.2160	-.1639	.7849
.04	1.5	.1100	-.1734	.9807
.06	1.5	.1555	-.1826	1.1347
.08	1.5	.2200	-.1826	1.2813
.1	1.5	.2775	-.1799	1.4318
.12	1.5	.3224	-.1643	1.5958
.14	1.5	.3531	-.1495	1.7830
.16	1.5	.3669	-.1323	2.0057
.18	1.5	.3575	-.1137	2.2820
.2	1.5	.3088	-.0949	2.6403
.21	1.5	.2595	-.8586	2.8645
.22	1.5	.1848	-.0770	3.1305
.23	1.5	.0826	-.0678	3.4528
.24	1.5	-.0037	-.0583	3.8640
.25	1.5	-.9524	-.2265	5.7545

Figure/Table 2

Stresses along the ligament line ab
for an orthotropic composite.
Fixed pin case, d/w = .5,
N = 60 (boundary subdivisions)
d = 0.5
e = 0.5
h = 1.5
w = 1.0
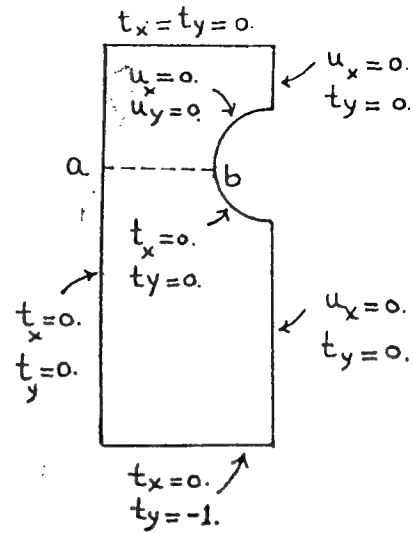
x	y	σ_{xx}	τ_{xy}	σ_{yy}
.02	1.5	.0019	-.0077	.8061
.04	1.5	.0232	-.0728	.8580
.06	1.5	.0324	-.1015	.9069
.08	1.5	.0390	-.1029	.9600
.1	1.5	.0442	-.1022	1.0203
.12	1.5	.0464	-.1007	1.0930
.14	1.5	.0432	-.0972	1.1815
.16	1.5	.0310	-.0913	1.3077
.18	1.5	.0040	-.758	1.4794
.2	1.5	-.0501	-.0467	1.7377
.21	1.5	-.0946	-.0221	1.9236
.22	1.5	-.1584	-.0116	2.1754
.23	1.5	-.2480	-.0527	2.5430
.24	1.5	-.3886	-.1264	3.2133
.25	1.5	-1.9566	-.9854	9.7269

DETERMINATION OF MEANINGFUL DESIGN ALLOWABLES FOR COMPOSITE MATERIALS

by

Donal Neal, Luciano Spiridigliozzi and E. M. Lenoe

AMMRC, Watertown, MA

Methodology for estimating material design allowables is described for three general applications, namely 1) for advanced composites for aircraft applications 2) lower cost composites for an anti-tank weapon, and finally 3) for composites produced via elastic reservoir molding.

For the aircraft quality materials a methodology for obtaining the "A" and "B" material design allowables using an extreme quantile modeling process is described. The allowables represent a value determined from a specified probability of survival with 95 percent confidence in the assertion. The survival probabilities are .99 for the "A" and .90 for the "B" allowable. The required tail probabilities are relatively small, therefore modeling the tail distribution provided a more accurate allowable estimate as compared to the conventional central region modeling. This was particularly so when the sample is contaminated (e.g. multi-modality and outliers) or limited in size.

The Bootstrap, exponential distribution and a data censoring procedure provided the models used in deteriming the tail probabilities and their corresponding confidence values. The Bootstrap method (see figure 1) was applied in order to obtain the variance for the lower percentile values and thereby provided the necessary reliability estimates and their corresponding confidence numbers used in the allowable computation. For small samples a regression scheme was introduced in order to obtain the lower ordered percentiles.

The exponential model represented selected truncations of the tail distribution from which the specified percentile numbers and their confidence interval were obtained. The truncations provided a sample of percentile estimates from which a robust estimate of the sample mean defined the allowable.

The Weibull distribution was applied to the upper ordered censored data (as much as 80 percent) in order to model the tail region of the data. All three methods showed the capability of resisting the effects of contamination in addition to accurately representing the important tail region of the data set in contrast to central region modeling which arbitrarily accepts the tail representation.

301

Allowables estimated from the Weibull (complete sample), normal, lognormal, Breiman, Bootstrap and non-parametric (N.P.) models were obtained for a simulated bimodal sample. Since the N.P. method is most reliable for the bimodal case, the results indicate the acceptability of the Breiman and Bootstrap methods in contrast to the conventional models. The approximate 23 percent error in determining A allowable by the normal and Weibull distributions is unacceptable.

The Weibull B allowable computation for the probability ranked sample was 1.06 KSI as compared to the N.P. computation of 1.33 KSI. Censoring the sample by 75 percent and using the Weibull model resulted in a B allowable of 1.30 KSI for the sample. The agreement with the N.P. solution is excellent.

A preliminary assessment of this research indicates tail distribution modeling can provide a universal tool for obtaining the material design allowable for aircraft models without the need for classifying a model for the complete sample.

For the non aircraft applications, the implications of batch-to-batch variations are explored and procedures for conservative design approaches are suggested.
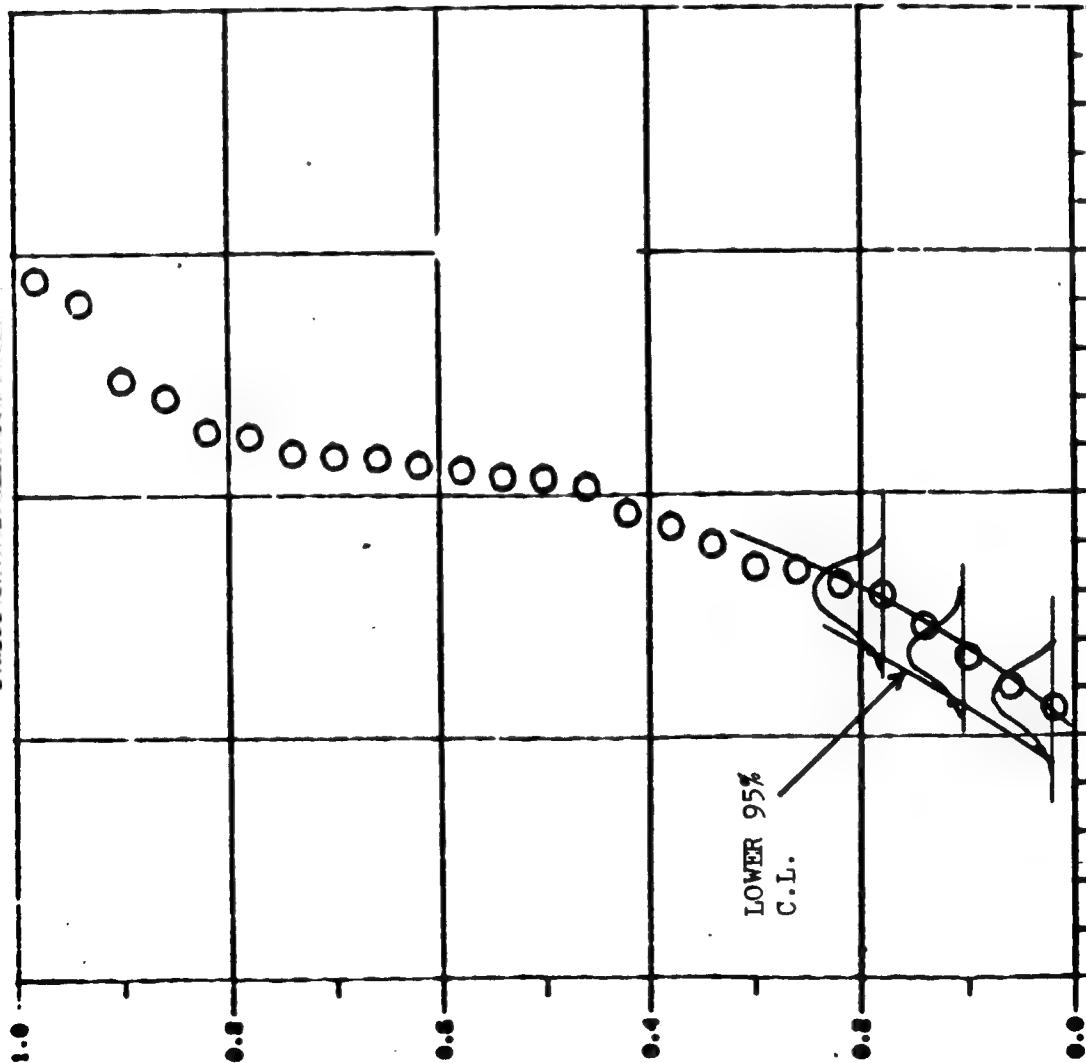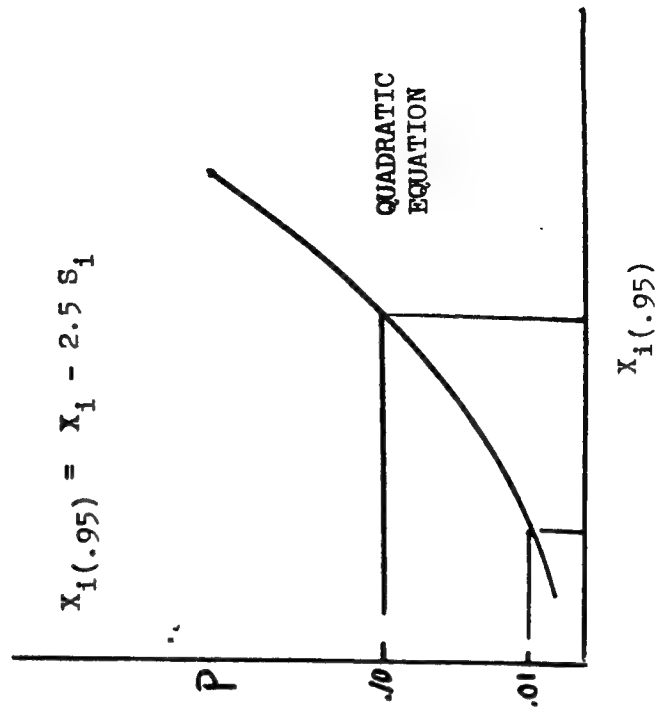
FIGURE 1

Design of Thin Composite Laminates

Raymond L. Foye

Aeronautics Department

US Naval Postgraduate School

Monterey, CA 93943

In the design of any composite structural component the choice of a satisfactory prepreg material is analogous to the choice of a metal alloy for use in a metal component design. This material choice is often aided by the fact that the required metal gage can be quickly estimated from a knowledge of the primary loads and stiffness requirements throughout the component. Sometimes bending and buckling requirements or the existence of redundant load paths will require more complex analysis. However, many material selection and sizing problems fall into the category of statically determinate membrane load states with simple stiffness requirements. This paper addresses that category of composite design problem.

When designing with composites both the choice of a prepreg material and the laminate sizing problem is complicated by the necessity of first selecting the fiber orientation for each ply. For strongly orthotropic material, anticipation of biaxial laminate response as a function of fiber orientation is beyond the intuition of even the most experienced designers and analysts. A laminate analysis is usually required to verify laminate mechanical properties. This calculation is relatively simple but is also tedious and error prone. It is an ideal task to relegate to a microcomputer. In fact, the microcomputer performs this task so efficiently that in a few minutes it can predict enough laminate property data to greatly simplify the problem of material selection, orientation, and sizing. This paper describes and illustrates the use of some elementary computer programs that provide much of the necessary information to the designer to select an efficient and practical laminate for use with a given prepreg material. The programs do not perform any extensive optimization in the usual structural sense. They only perform repeated laminate analyses and present the data in such a way as to simplify the final choice of a laminate. They allow common sense to prevail in the process and they also provide the means for estimating the penalties associated with the inevitable tradeoffs that are made for ease of fabrication, confidence, cost, and repairability, etc.

These programs consider only multiple biaxial load cases and symmetric laminates belonging to the common families of laminates that have been categorized as unidirectional (0_i), cross ply $(0_i/90_j)$, angle ply $(\pm 0_i)$, augmented angle ply $(0_i/\pm 0_j)$ or $(90_i/\pm 0_j)$, double angle ply $(\pm 0_i/\pm \phi_j)$, or zero-theta-ninety $(0_i/\pm 0_j 90_k)$. The majority of composite components use one or more of these laminate families and most composite data bases relate to these families. These families are all a subset of the double angle ply or zero-theta-ninety families. There is a separate design program for each of these two basic families. The unidirectional, cross ply, angle ply, and augmented angle plies can be investigated with either program.

With these programs the user first specifies the choice of prepreg material, the single ply properties, the failure criteria, the laminate family of choice, the stiffness requirements, the load cases, and the total ply thickness of interest. The programs analyze all possible ply orientations (using 1° increments of 0 and ϕ) for the family of interest and graphically display the minimum margin of safety for each design. The designer, observing these results, decides whether the choice of material and total laminate thickness was satisfactory. If the margins of safety are all inadequate the designer increases the laminate thickness or uses a material with improved properties. Similarly, if many of the margins are high he can reduce the number of plies or use of lower grade of material and run the program again. The programs are fully interactive. This process not only points out the least weight designs but it also indicates the safest minimum weight design and the price that must be paid in weight and (or) safety for using any other design. This enables the designer to make rational choices based on unspecified design constraints. For example, he can assess the penalty associated with the use of a laminate for which substantial test data and confidence already exists rather than use a theoretically better design that is lighter or carries a higher safety margin but has no existing test data to support its use.

These programs have been used by graduate students in aeronautics to bridge the gap between composite mechanics and component design. They may be expected to also help experienced designers, particularly in preliminary design. This paper describes these programs and gives examples of their use. They are equally applicable to unidirectional, bidirectional or woven prepreg materials.

ROLE OF DATA-BASED MANAGEMENT SYSTEMS IN COMPUTER-AIDED ENGINEERING

Charles L. Blackburn
Kentron Technical Center
Hampton, VA

Abstract not available.

COMPUTER-AIDED DESIGN OF HELICOPTER STRUCTURES

Joseph Goldberg
Sikorsky Aircraft Company
Stratford, CT

Abstract not available.

Fabrication and Testing of Large Caliber (105mm)
Composite Sabot Specimens

by

Dana M. Granville
Organic Materials Laboratory
Army Materials and Mechanics Research Center

and

Maurice A. Scavullo
Large Caliber Weapons Systems Laboratory
Benet Weapons Laboratory

INTRODUCTION

In recent years, increased emphasis has been placed on reduction of mass for discarding sabots. Lightweight sabots have the advantages of improving the performance of an armor piercing fin-stabilized projectile through higher projectile exit velocity and increased range.

Aluminum sabots (typically 7075-T6) of various designs have been used but significant weight reductions have not been possible due to its own material weight restrictions. Modern composites have evolved into cost-effective replacements for metals, having superior strength-to-weight ratios and the ability to have directional properties where needed in a sabot application such as the M774 (105mm) and M829 (120mm) systems.

An analytical study to determine the feasibility of using lightweight composites has been completed[1]. The study shows through finite element analysis that composites may realistically reduce the mass of a current sabot by 30 to 40%. In the application of composites, the Army Materials and Mechanics Research Center (AMMRC) has successfully fabricated orientations of glass/epoxy and graphite epoxy continuous fiber composites for testing at Benet Weapons Laboratory.

TEST APPARATUS

Figure 1 is a photograph of the simulation test equipment capable of applying 200,000 lbs of tensile load to a penetrator or shear load to the lugs of a sabot section. Past work with metal sabot specimens using this equipment[2,3] has given us the opportunity to determine the relative mechanical strength requirements for a composite sabot. The hydraulic cylinder at the base mores a load frame assembly as a unit. The tensile load is applied between the movable upper load frame (small columns) and the stationary lower

load frame (large columns). The load is applied to the specimen assembly (not shown) through the rods and end caps shown near the top of the photograph. A 200,000 lb strain gage type load cell mounted between the hydraulic cylinder and the upper load frame provides the load measurements.

Figure 2 shows the specimen assembly which is mounted in the simulation equipment. The loading rods and end caps apply the tensile load through the fixture to the sabot segments. The upper sabot segment transmits the load to the thread-like lugs on the penetrator in the same general way as in the launch of the projectile, the load being applied to the 7° faces of the lugs. The penetrator is made of maraging 250 steel with a yield strength much higher than the stresses required to shear the lugs and grooves from the sabot segments. The lower sabot segment is also made of the same maraging steel as the penetrator, insuring failure in the upper sabot segments. The lower sabot segment is loaded on the 45° face of the lug and is not tested in this apparatus.

COMPOSITE TEST SPECIMENS

Upper sabot segments having a test length equivalent to eleven (11) lugs and grooves were fabricated from glass-epoxy and graphite-epoxy prepreg tape. It is understood that if we were to fabricate a composite sabot for the maximum design potential of these composites, the baseline metal $45^\circ/7^\circ$ lug and groove geometry would not be used, but the launch simulation test equipment incorporated this conventional M774 (105mm) penetrator profile so that an excellent correlation of shear failure data between metal alloy sabots and organic material sabots could be obtained.

Prepreg (resin preimpregnated reinforcement) was chosen for this application because of its excellent handling characteristics and the consistently high volume fraction of fibers obtainable in such a thick composite. By using strictly unidirectional continuous fibers, volume fractions of 55% for glass and 60% for graphite were achieved. The use of woven prepregs, or the wet filament winding process simply could not achieve these levels of fiber loading in the precise orientations desired at the critical lug and groove interface.

The materials used were Scotchply SP-250 S2 glass-epoxy prepreg manufactured by 3M, and Magnamite AS-4/3501-6 graphite-epoxy prepreg manufactured by Hercules. Symmetrical 18" x 18" layups using the $+45^\circ/-45^\circ/0^\circ$ sequence were completed. Because of the difference in the per-ply thicknesses of glass and graphite prepregs, 180 plies of the glass prepreg were required to achieve the 1 3/8" thickness desired, while 250 plies of graphite prepreg were needed. Once the laminates were laid up, a debulking stage was completed using a two-platen compression press. Heat treated aluminum caul plates covered with tedlar release film were used to sandwich the thick laminates, which was then wrapped in bleeder-release cloth and burlap material. A nylon vacuum bag with a vacuum gland attachment was finally used to seal each wrapped laminate. Autoclave cure cycles were followed using a continuous vacuum throughout heating and cooldown.

The cured unwrapped laminates were cut into blocks using a diamond wheel, and placed in lathe fixtures for machining into the final configuration test specimens using specially sized C-type grinding wheels (Figure 3). Figure 4 shows a typical specimen with one section removed to show the lugs and grooves.

TEST RESULTS AND DISCUSSION

Three sets of $\pm45^{\circ}/0^{\circ}$ orientations with respect to the sabot's axial direction were machined to determine the actual relative effects of shear strength at the lug and groove interface. When all fibers were aligned perpendicular to the axial direction as shown in Figure 5, the shear failure was an interlaminar failure of the epoxy bond to the glass, with no visible damage to the glass fibers, resulting in a low ultimate shear load. By running the 0° fibers parallel to the axial direction (Figure 6), the shear failure load value more than tripled. Two-thirds of the volume fraction of fibers (the $\pm45^{\circ}$ component) were now running alongside of, and perpendicular to, the 45° side of the lug and groove profile (Figure 7). There was some fiber buckling, but the failure generally followed the direction of the discontinuous 0° fibers and the machined interface. Finally, by orienting the 0° fibers perpendicular to the axial direction as shown in Figure 8, the reinforcing fibers shared more of the shear load. Figure 9 shows the results of a load application to the sabot shear test fixture. The lugs were sheared off uniformly at the depth of engagement of the penetrator. More complete fiber buckling was observed, resulting in the highest shear failure load value of the glass-epoxy specimens.

The graphite-epoxy specimens that followed had the identical fiber orientation of the highest shear loaded glass-epoxy specimens. Because of the higher modulus graphite, a smaller strain was witnessed than with the glass-epoxy counterparts, and again a great deal of fiber buckling occured at the interface. These results were similar to those achieved with 7075 aluminum sabots. Figure 10 shows load-deflection plots for the aluminum in the T6 and T73 temper and for a graphite-epoxy specimen. The peak load for the graphite-epoxy was slightly less than for the aluminums, but at this first stage we are encouraged by sabot specimen results that are in the ballpark, despite significantly lower mass.

CONCLUSIONS

Because of the encouraging results from the graphite-epoxy specimen tests at BWL, AMMRC and BWL will continue to work with the new graphite/epoxy and graphite/polyether etherketone (PEEK) prepreg formulations that are becoming available. New high strain graphite fiber prepregs with higher strength and modulus than the AS-4 fiber (Tables 1 and 2) will soon be fabricated into specimens for further sabot testing. PEEK thermoplastic resin is also of particular interest because of its excellent long term moisture resistance and its high resistance to crack propagation[4].

Different "lug and groove" designs, including the use of variable pitch geometries to tailor the advantages of composites so that axial interfacial stress contours may be more uniformly redistributed under launch load conditions shall also be investigated, as well as isolated deposition of metal coatings on the lug and groove interface.

REFERENCES

1. Bletsis, Richard, "Feasibility of a Composite Sabot," 28th National SAMPE Symposium, April 1983.

2. Scavullo, Maurice and Underwood, John, "Service Simulation Test System for Kinetic Energy Penetrator Projectiles," TR ARLCB-TR-81007, February 1981.

3. Scavullo, Maurice and Underwood, John, "Laboratory Testing of Long Rod Penetrator and Sabot Components," TR ARLCB-TR-82036, October 1982.

4. Cogswell, F. N., "Continuous Fibre Reinforced Thermoplastics," ICI PLC, England, 1984.
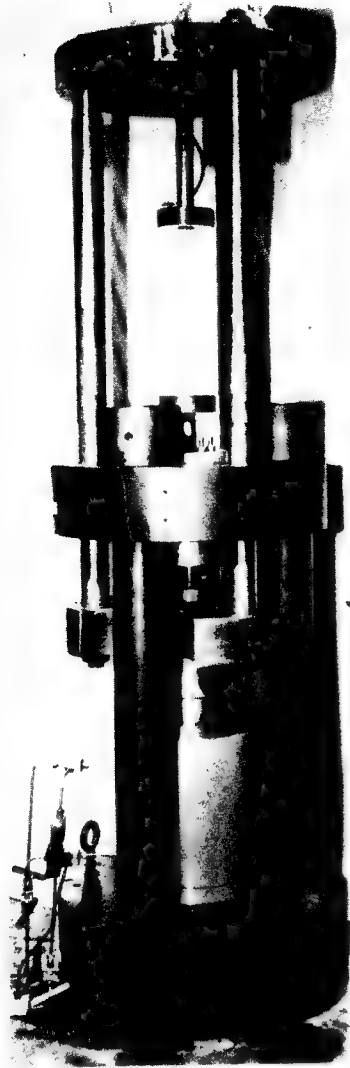
Figure 1. TWO HUNDRED THOUSAND POUND LAUNCH SIMULATION TEST SYSTEM FOR KINETIC ENERGY PENETRATOR ROUNDS
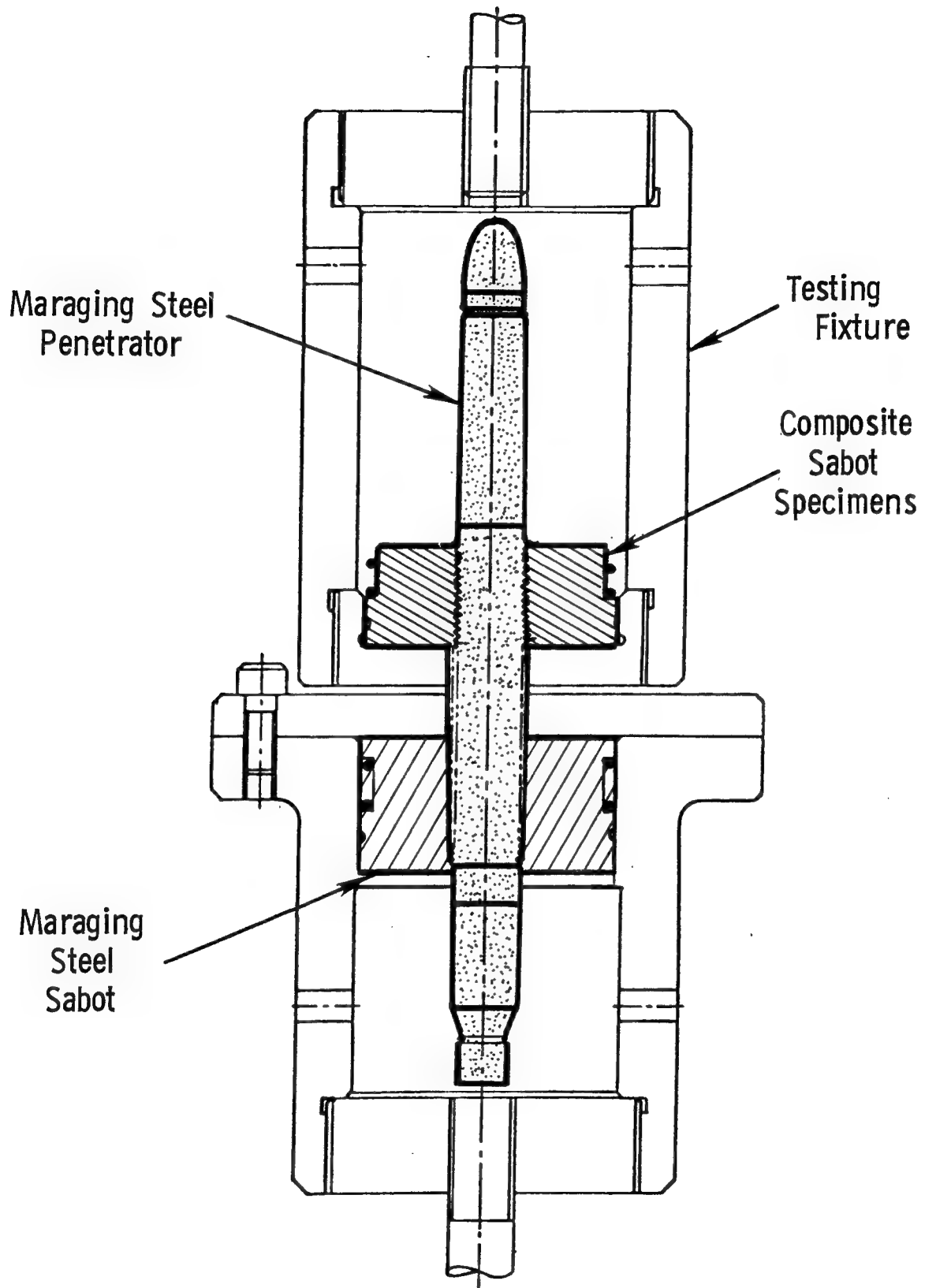
Figure 2. SPECIMEN ASSEMBLY FOR SABOT LUG SHEAR TEST

Labels in figure:
- Maraging Steel Penetrator
- Testing Fixture
- Composite Sabot Specimens
- Maraging Steel Sabot
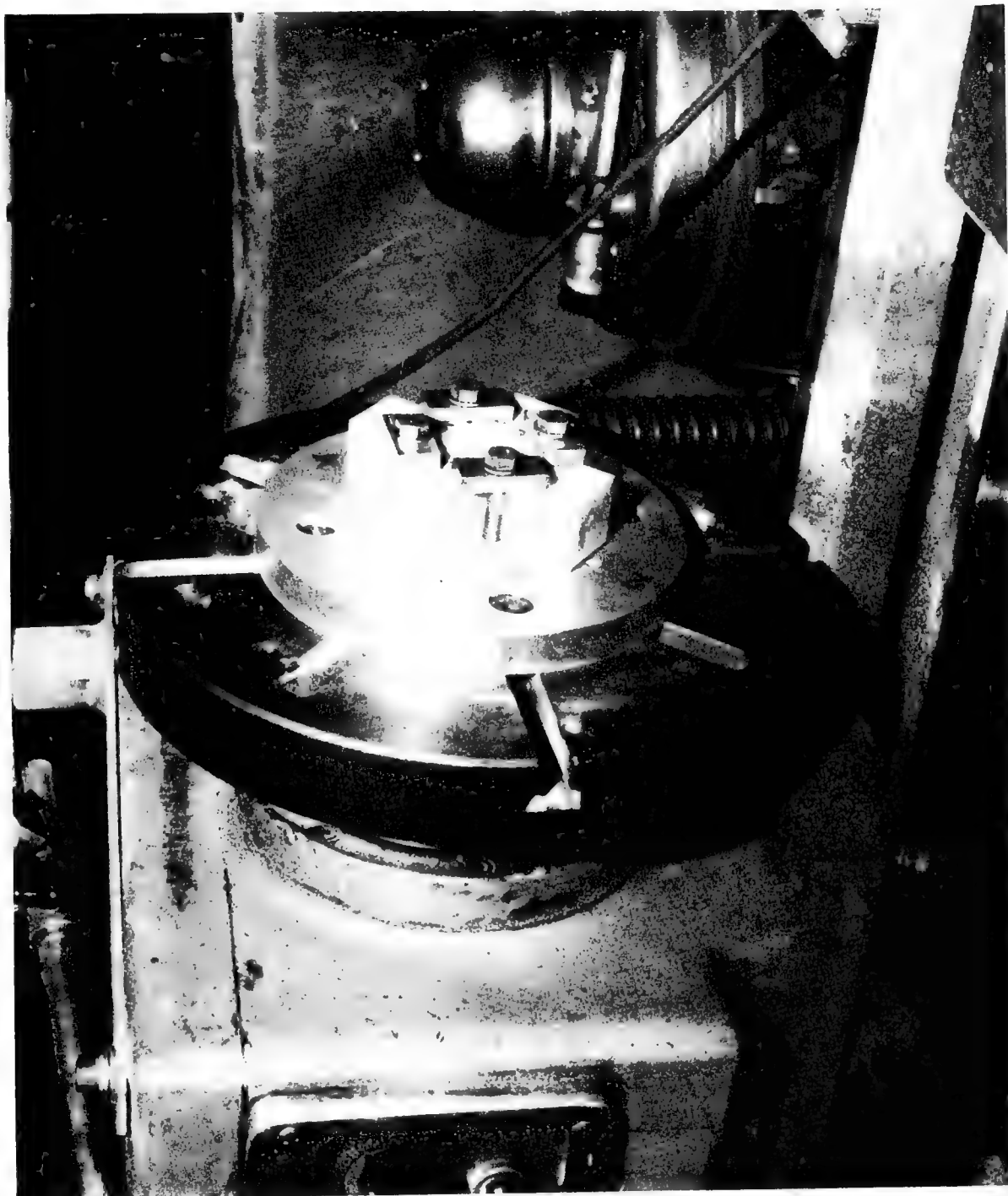
Figure 3. SPECIMENS BEING MACHINED USING A LATHE
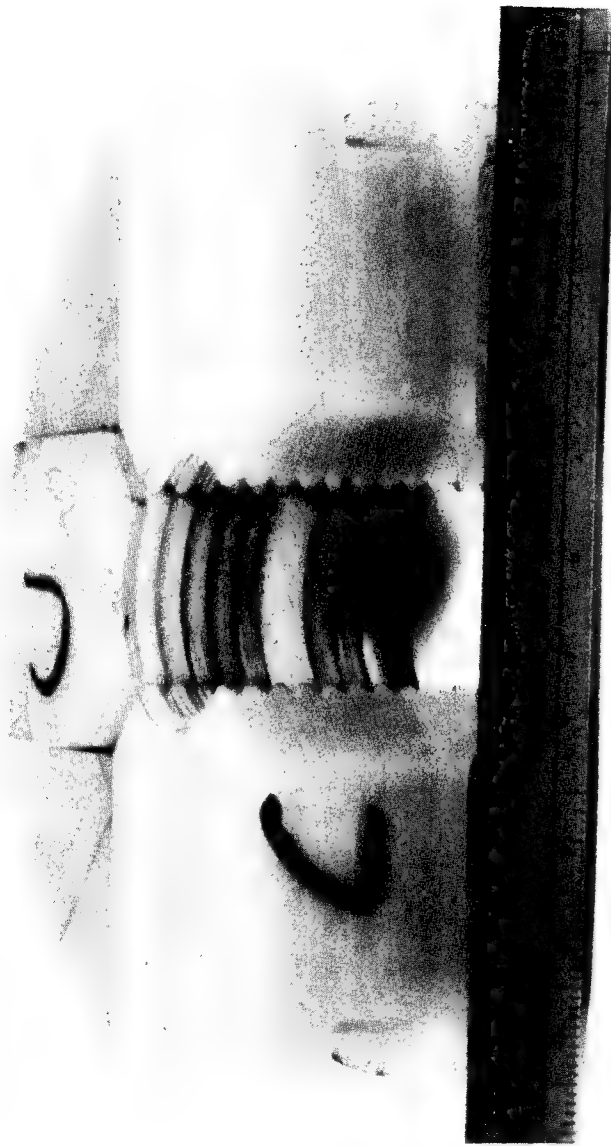
Figure 4.   TEST SPECIMEN WITH ONE SABOT SECTOR REMOVED TO SHOW LUGS AND GROOVES. GLASS-EPOXY COMPOSITE

S-2 Glass/Epoxy, $\pm 45°/0°$, All Directions $\perp$ to Axial Direction. Shear Load at Failure, 20,000 lb.

Comment: Specimen Failed Cleanly at Fiber-Resin Interface, No Fiber Damage (Delamination).
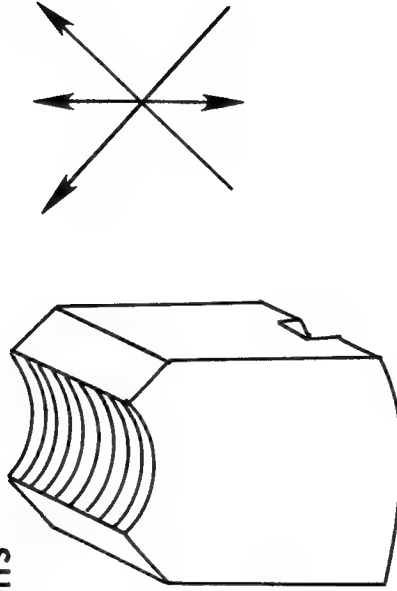
Figure 5. COMPOSITE SABOT SPECIMENS - ORIENTATION EFFECTS ON PROPERTIES

S-2 Glass/Epoxy $\pm 45^0/0^0$, 0^0 Direction
Only II to Axial Direction. Shear
Load at Failure, 66,000 lb.

Comment: Specimens Failed at Inter-
face Along 0^0 Direction Fibers.
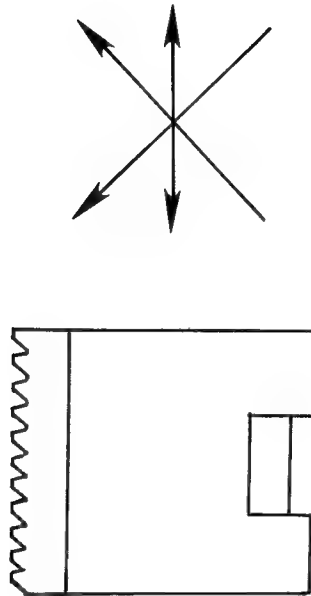
Figure 6.
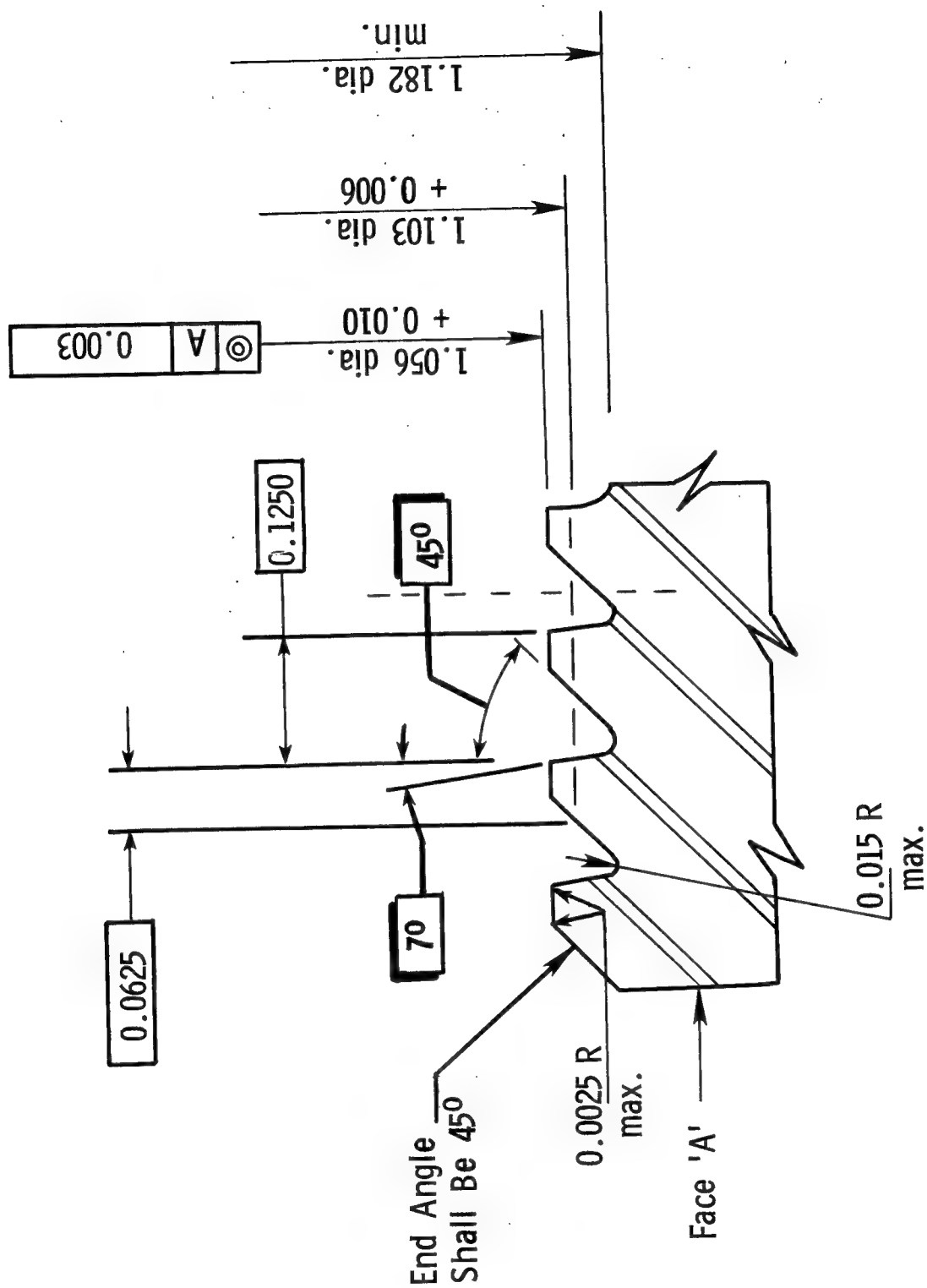
Figure 7. COMPOSITE SABOT (M774) LUG AND GROOVE DIMENSIONS

1.182 dia. min.

1.103 dia. + 0.006

1.056 dia. + 0.010

⌖ 0.003 A

0.1250

45⁰

0.0625

7⁰

End Angle
Shall Be 45⁰

0.0025 R
max.

Face 'A'

0.015 R
max.

S-2 Glass/Epoxy, ±45°/0°, 0° Direction Only ⊥ to Axial Direction. Shear Load at Failure, 94,000 lb.

Comment: Evidence of More Complete Fiber Buckling

AS-4 Graphite/Epoxy, ±45°/0°, 0° Direction Only ⊥ to Axial Direction. Shear Load at Failure, 112,000 lb.

Comment: Smaller Strain Evidenced than With Glass/Epoxy Counterparts, Again Good Fiber Buckling at Lug-and-Groove Interface.

Figure 8

322
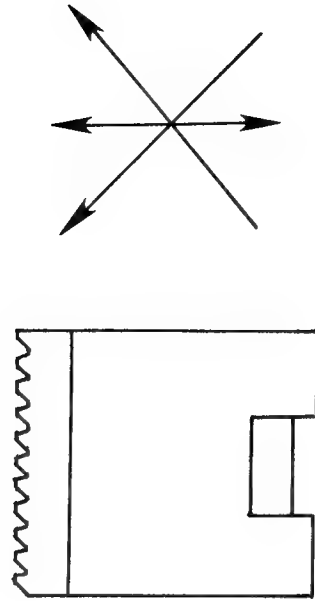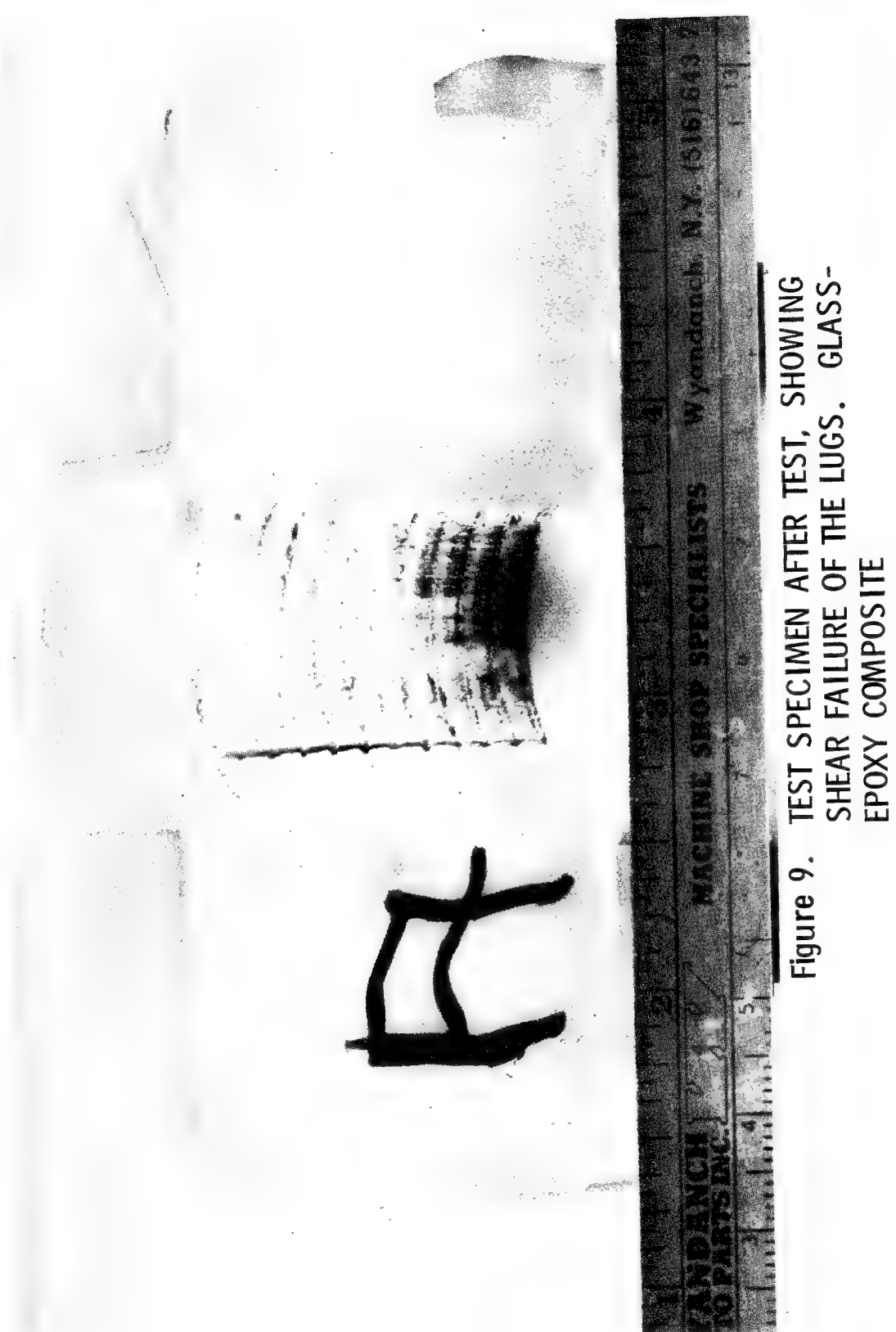
Figure 9. TEST SPECIMEN AFTER TEST, SHOWING SHEAR FAILURE OF THE LUGS. GLASS-EPOXY COMPOSITE

323
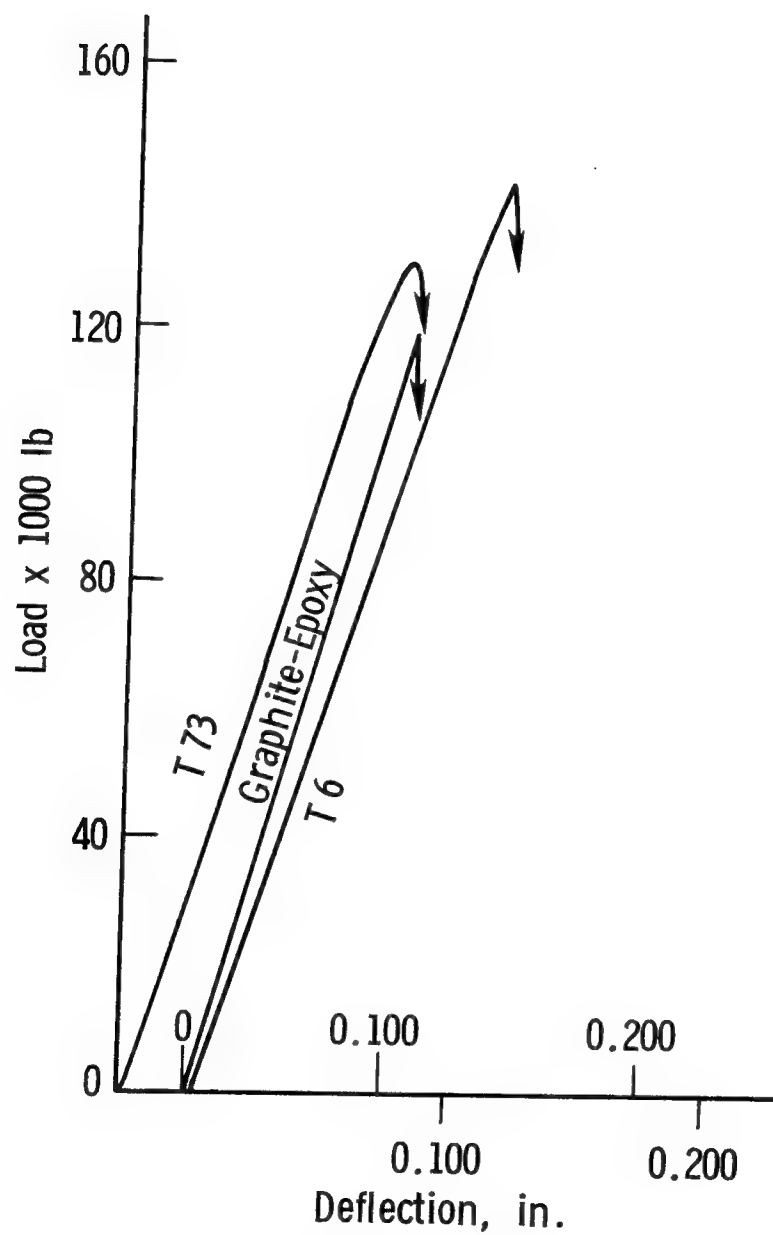
Figure 10.   LOAD-DEFLECTION PLOTS OBTAINED
FROM LUG SHEAR TESTS

DESIGN AND DEVELOPMENT
OF
COMPOSITE OFF-ROAD VEHICLES
FOR
MINI BAJA EAST
(A COLLEGIATE COMPETITION)

Roy Richard, Professor
University of Lowell, Lowell, Massachusetts

In September of 1982 students at the University of Lowell, Lowell, MA, began the design of an off-road vehicle for competition in the Annual Mini Baja East. Mini Baja is a collegiate design contest sponsored by S.A.E. and Briggs and Stratton. Participating schools are required to design and build a vehicle utilizing a Briggs and Stratton 8 HP motor for competition in off-road and deep water racing.

The University of Lowell's initial entry (KEVKAR) was a six-wheel skid steer vehicle utilizing an all composites body/frame. A second vehicle (KEVKAR TWO) was designed during the 1983-84 school year, again incorporating a composite structure.

Emphasis in this paper is on the use of computer-aided design system for the design and construction of a Kevlar-skinned/covered monocoque body. Fabrication techniques were developed by the students to allow easy fabrication of prototype vehicle bodies, utilizing unskilled (student) labor.

In particular, a low cost mold was developed utilizing the computer's ability to plot full-size templates, and allowing the use of inexpensive mold materials and one-off fabrication techniques.

Although structural analysis has been minimal to date, the use of CAD will allow for future finite element mesh generation and analysis by student investigators utilizing a packaged mesh generator capability.

SESSION VII: WORK IN PROGRESS

SHOCK FRACTURE AND RECOMPACTION OF COPPER

D. YAZIV and S. J. BLESS
University of Dayton Research Institute
Dayton, Ohio   45469

Spall fracture can occur under plate impact due to interaction of release waves generated by shock reflection from free surfaces. Spall fracture has been characterized for many materials (1, 2). In this paper we report a new technique for study of dynamic fracture by plate impact. Two flyer plates are separated by a small gap (Figure 1). The first plate causes spall in the target, as in a conventional experiment. The second plate is of highr shock impdance. Impact of the second plate closes the fracture. The advantage of this technique is that it allows determination of the properties of the damaged material in the spall region.

Prelimnary experiments have been conducted to demonstrate feasibility. A 2-inch (50mm) diameter compressed gas gun was used to launch 50mm diameter flyer plates. Target rear surface motion was measured with a VISAR. The wave interactions in the target and flyer plates were analyzed with the SWAP method of characteristics code (3). The target was fully annealed OFHC copper; spall properties of this material have been reported previously (4). The first flyer plate was 2024-T3 aluminum, and the second was copper or 1020 steel.

Five shots have been completed that demonstrated fracture/recompaction in copper. The velocity range ws 820 - 1300 ft/s (250 - 400 m/s). Targets were 0.16 in (4mm) thick and flyer plates were 0.08 in (2mm) thick. Shots 719 and 720 were typical; the velocities were 1200 and 1270 ft/s (365 and 388 m/s), respectively. Figure 2 shows the x,t diagram generated by the SWAP code for shot 719. In this shot and in shot 720, only half of the aluminum first flyer was backed by a copper second flyer; the other half was air backed. Figure 3 shows the appearance of the targets after impact. The two halves of the target display different damage, as predicted by the SWAP simulation. The single flyer plate impact produced partial spall (a region containing porosity), while no damage is readily visible opposite the two-flyer plate impact.

The free surface velocity record from shot 719 is shown in Figure 4. In addition to the conventional "spall signal" (point 3) there is an arrival from the second flyer impact (point 4) that has "leaked" through the damaged region, and a shock arrival (point 6) caused by final closure of the spall plane.

Work is continuing with this technique. Future tasks are to extend the experiments to brittle materials, and to develop constitutive models that describe the damaged region.

REFERENCES

1. J. N. Johnson, J. Appl. Phys. 52, 2812 (1981).

2. L. Davison, R. A. Graham, Phys. Rep. 55, (1979).

3. L. M. Barker, E. G. Young, SLA-74-0009, (1976).

4. S. J. Bless, D. L. Paisley, "Shock Waves in Condensed Matter-1983", APS Conference, Edited by J. R. Asay, et al, pp. 162-166.
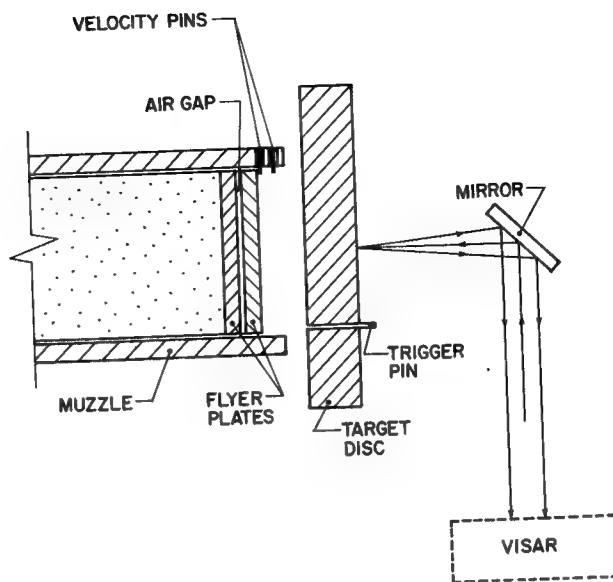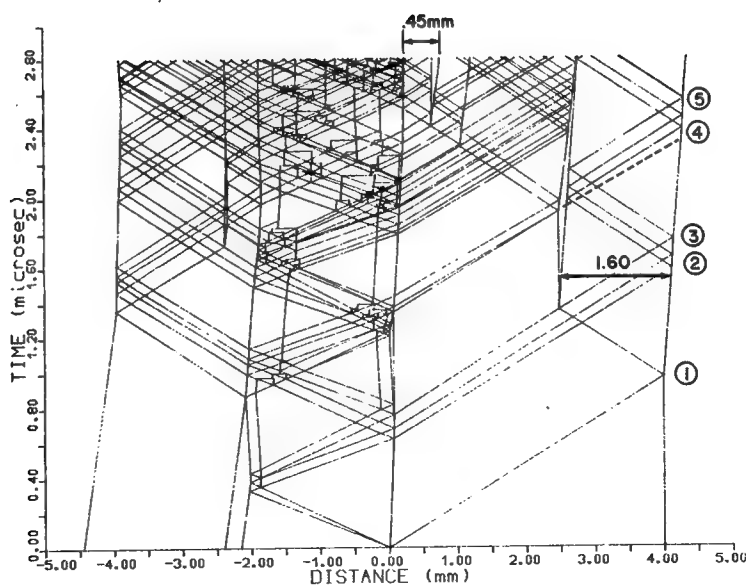
Figure 1.   Double Flyer Geometry.

Figure 2.   (x,t) Diagram for Double Flyer Impact, Shot 719.
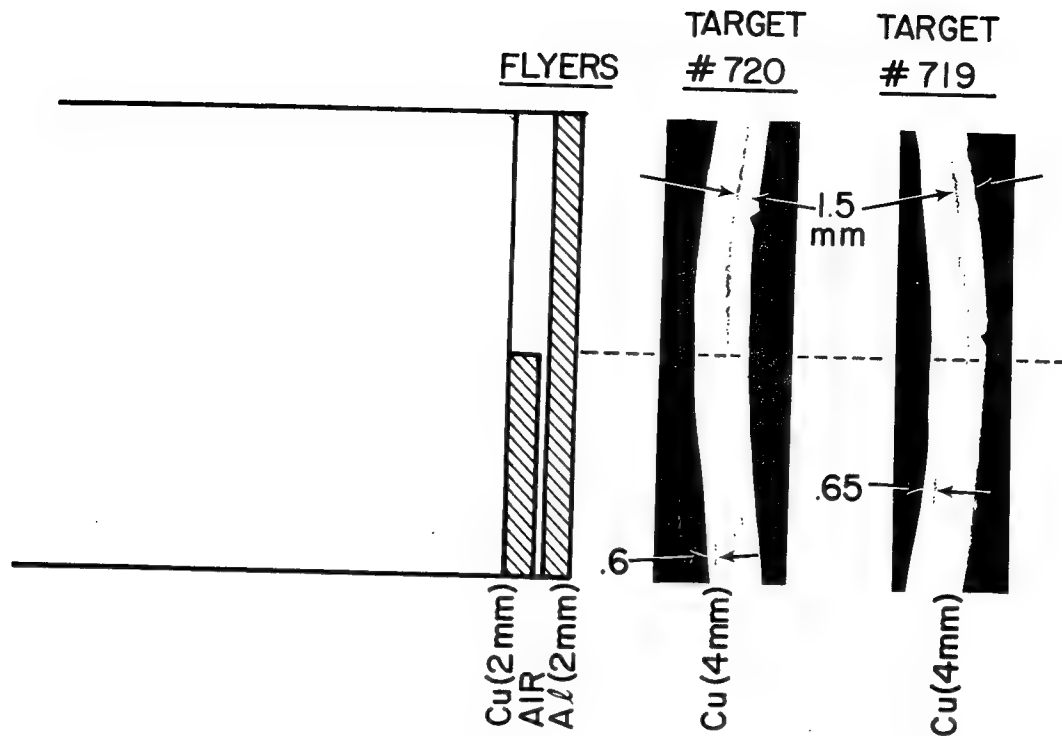
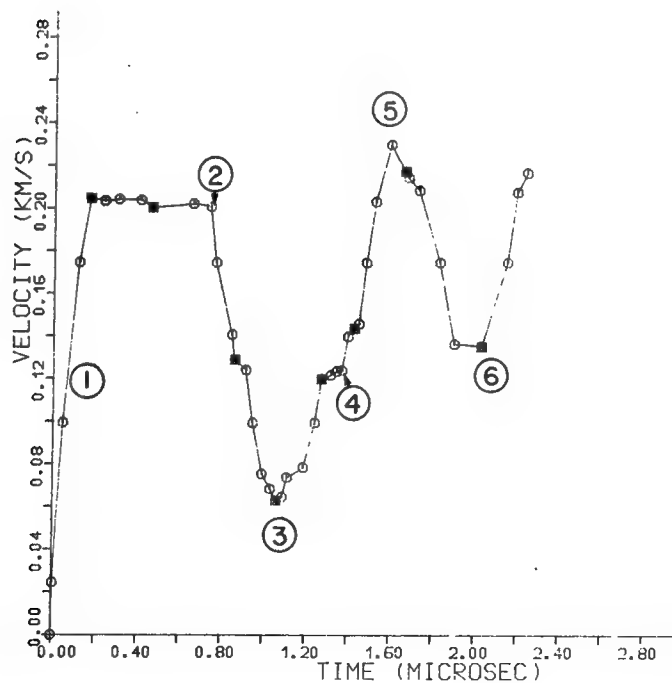Figure 3.   Damage Caused by Double and Single Flyer Impacts

Figure 4.   Free Overface Velocity in Shot 719.   Numbers Refer
            to Arrivals Indicated in Figure 2.

332

TORSIONAL IMPULSE STUDY IN ARTILLERY PROJECTILE

KOK Y. CHUNG
US Army Armaments Research and Development Center
Dover, New Jersey   07801-5001

Torsional impulse is a phenomenon recently recognized by the artillery projectile community as an important design criterion for large caliber weapon systems. In 1976, an investigation of the in-bore motion of gun launched projectiles was initiated after the failure of a threaded joint in an 8-inch rocket assisted projectile. The failure prompted various attempts by projectile designers to characterize the torsional environment that caused the mechanical failure of the joint. The basic factor that governs the magnitude of the torsional acceleration pulse was the presence of "free run" which is characterized by positive forward motion of a projctile before reaching th origin of gun tube rifling. The amount of "free run" is determined by the rotating band and obturator geometry, the forcing cone and gun tube wear in the vicinity of the inception of rifling. This factor permits the projectile to reach an appreciable axial velocity before the rotating band becomes effective and starts the rotational acceleration. The projectile must then undergo an abnormally high angular acceleration in order that the spin rate could maintain the fixed relationship with the axial velocity. This high torsional environment at a time of relatively low axial setback force could create potential problems for friction joints and friction driven components. It was also evident during this investigation that firing with propellant charge that has a fast rise time could increase the magnitude of torsional impulse significantly because of the higher axial velocity level attained early in the launch.

Early experiments were conducted using the wire-in-bore technique to provide transmission between the instruments on board the projectile and data acquisition ground station. Due to the high set-back and lateral forces, extraneous responses contained in the recorded signals made analysis of the data extremely difficult. Subsequently, the Technical Support Directorate and Large Caliber Weapon Systems Laboratory of ARDC developed a 155mm telemetry projectile system capable of measuring torsional impulse i a high G gun environment. The mechanical portion of the TM projectile (Figure 1) consisted of axial and tangential accelerometers located at the rear (near the rotating band) and the front of the projectile. The telemeter is housed in the main body and the antenna used for transmitting the telemetry signal is mounted on the ogive section with a protective covering. At the nose of the projectile is a parachute recovery module to soft recover the TM projectile.

The first firing was conducted with a worn NATO tube and trilateral stick charge (fast rise time). The test data gathered depicted various in-bore motions of the projectile. The accuracy of the data were independently verified by external measurements and compared well with similar firing by Sandia Laboratories (Figure 2). Additional firings are being planned to

scenario in gun firings. The dynamic condition of a rotating band being engraved must be determined such that engraving forces could be modeld accurately. The success of an analytical model will offer the projectile design community a powerful tool to evaluate a range of torsional impulse parameters, including US/NATO tubes, steel/chrome tubes, tube/projectile interfaces and propelling charge characteristics. Any worst case combination could be further investigated by actual instrumented firing.
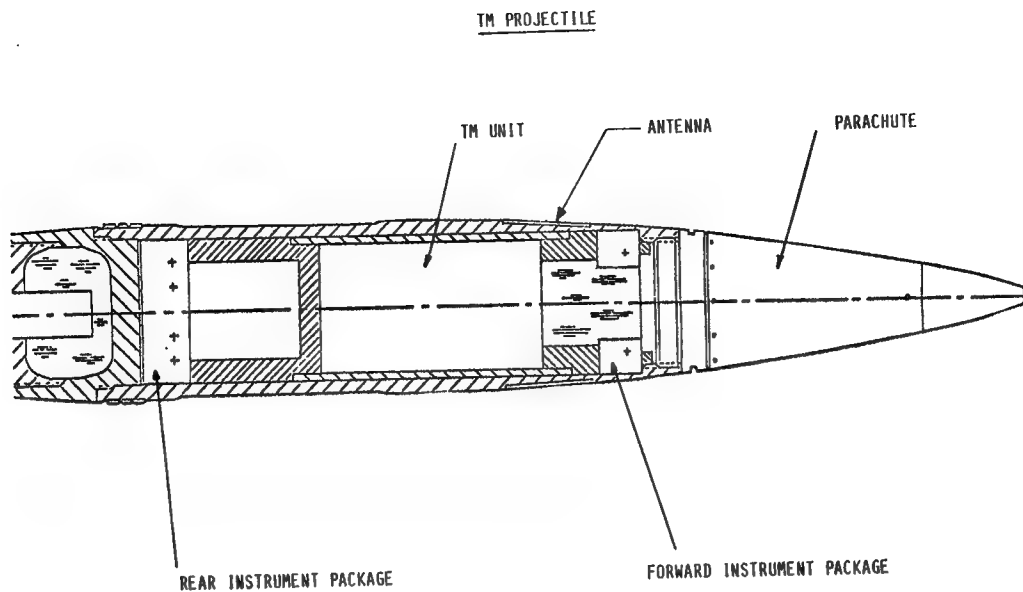
FIGURE 1

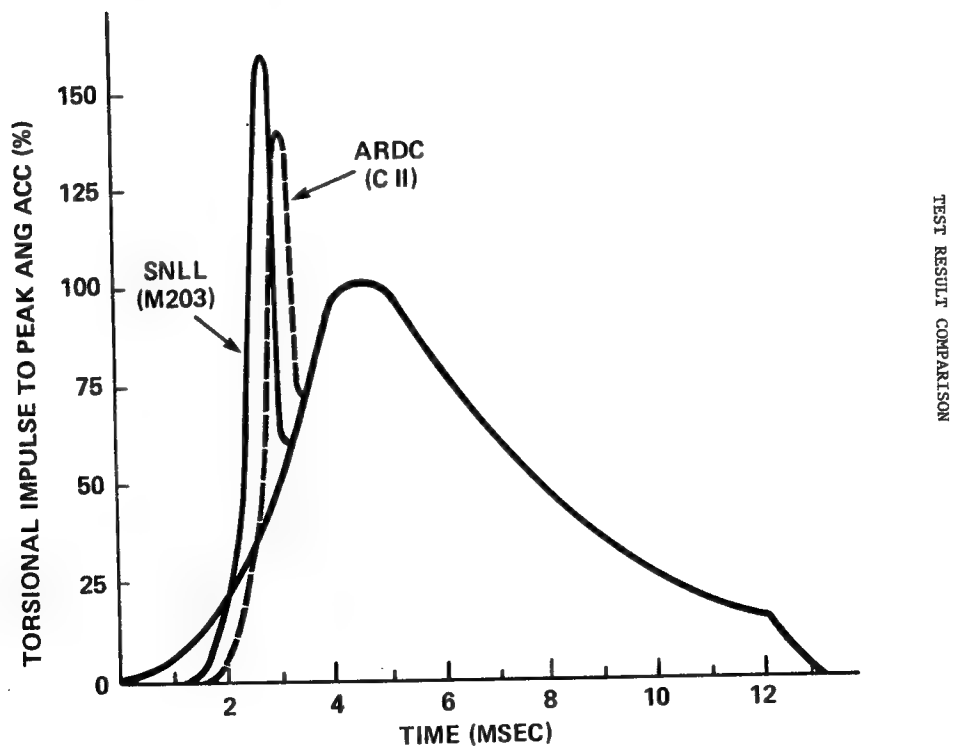# PT08 TORSIONAL IMPULSE

STICK CHARGE

FIGURE 2

EFFICIENT ANALYSIS FOR MULTI-LAYERED COMPOSITE SHELLS OF REVOLUTION WITH PARTICULAR APPLICATION TO HYBRID GUN BARRELS

A. Tessler and L. Spiridigliozzi
Army Materials and Mechanics Research Center
Watertown, Massachusetts 02172

EXTENDED ABSTRACT

Army design requirements pertaining to large caliber guns call for lightened barrels with improved shooting accuracy. These goals appear to be best attainable through utilization of advanced high strength/low weight composite materials. Efforts are currently under way to study the feasibility of applying organic and metal matrix composites to large caliber gun barrels.

Because of the composite/steel merging, these hybrid guns present a considerable challenge as far as the design and analysis are concerned. In particular, vibrational characteristics of such guns may be drastically different from those of the standard, monolithic steel barrels. Since gun vibrations are generally responsible for shooting inaccuracies (dispersion), it is essential that the vibrational properties are favorably designed and accurately predicted.

From the solid mechanics viewpoint, the large caliber barrels (e.g., 105mm and 155mm bore diameter) may be regarded as thick shells with axial geometric and material symmetry. Hence, a shear-deformable shell-of-revolution model may be appropriate and, perhaps, constitutes the most economical idealization for the eigenvalue/eigenvector (natural vibration) analysis.

The present effort is focused on a shell-of-revolution finite element approach for an efficient, undamped natural vibration analysis of large caliber hybrid barrels. Specifically, a linear, two-noded frustrum element is formulated on the basis of Naghdi's refined shell theory [1], extended herein to accommodate a multi-layered, heterogeneous wall lay-up. The displacement methodology is adopted. The five primary components of the kinematic field are interpolated along the circumferential and meridian coordinate directions (i.e., u—circumferential displacement, v—meridian displacement, w—transverse displacement, α and β—normal rotations about the meridian and circumferential directions, respectively; refer to Figure 1 for the notations). The latter approximation is achieved via a Fourier expansion which permits a general asymmetric shell response.

A special interpolation strategy, adopted from the works of Tessler and Dong [2] and Tessler [3], is invoked in the meridian direction. It is manifested by different degree polynomial assumptions for the kinematic variables, and a convenient degree-of-freedom reduction procedure, which is performed a priori to the element matrix integrations. A judicious choice of the meridian polynomial assumptions is governed by the meridian shear strain expression ($\gamma = w_{,s} + \beta$). In order to ensure proper element behavior for a

wide range of radius-to-thickness and length-to-radius ratios, the meridian slope, $w_{,s}$ and the corresponding normal rotation, β, are interpolated by the same polynomial forms. Thus, in the present, lowest order element, w is assumed to vary parabolically while the other four variables are taken to be linear. With these assumptions, the initial nodal configuration includes an 'extra' mid-span w degree of freedom. It is, however, conveniently condensed out by forcing the meridian shear strain, initially linear, to take a constant value. This procedure may alternatively be interpreted as an explicit enforcement of a higher order (in this case, linear) Kirchhoff mode (i.e., vanishing shear strain).

The result is a two-noded element configuration, where, for the most general case of an 'effective' anisotropic material, ten degrees-of-freedom are required at each node (i.e., the five kinematic variables possess two sets of coupled independent coefficients in the circumferential Fourier expansion). However, only five degrees of freedom per node (i.e., u_i, v_i, w_i, α_i, β_i) are necessary when the 'effective' properties constitute a generally orthotropic material. If the shell response is strictly axisymmetric, then three nodal degrees of freedom (i.e., v_i, w_i, β_i) describe the shell motion.

In the derivation of the element matrices, Hamilton's variational principle is employed. The element stiffness and consistent mass matrices are integrated exactly along the circumference and numerically along the meridian. In the latter case, minimum order Gaussian quadrature for the exact evaluation of the integrals is used.

A series of numerical tests is undertaken to assess the element performance for various geometric parameters and material properties. Furthermore, natural frequencies of vibration are computed for a 105mm Gr-Ep/Steel gun barrel and compared with those of the standard all-steel gun. The results depicted in Figure 2 correspond to a thirty-four element model.

The methodology developed herein is general enough to be applicable to a wide range of axisymmetric shell problems. Based on the numerical data available to date, the element performs equally well in the thin and thick flexure regimes. The formulation is variationally consistent, and the element computations are economical.

REFERENCES

1. Naghdi, P.M., Foundations of Elastic Theory. Progress in Solid Mechanics (Edited by I.N. Sneddon and R. Hill), Vol. IV, Chapter 1, North-Holland, Amsterdam (1963).

2. Tessler, A. and Dong, S.B., "On a Hierarchy of Conforming Timoshenko Beam Elements", Computers & Structures, 14, 335-344 (1981).

3. Tessler, A., "An Efficient, Conforming Axisymmetric Shell Element Including Transverse Shear and Rotary Inertia", Computers & Structures, 15, 567-574 (1982).
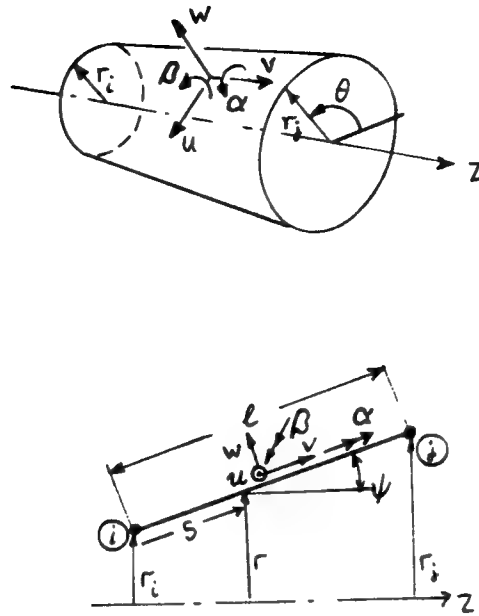
Figure 1. Conical Shell Element.
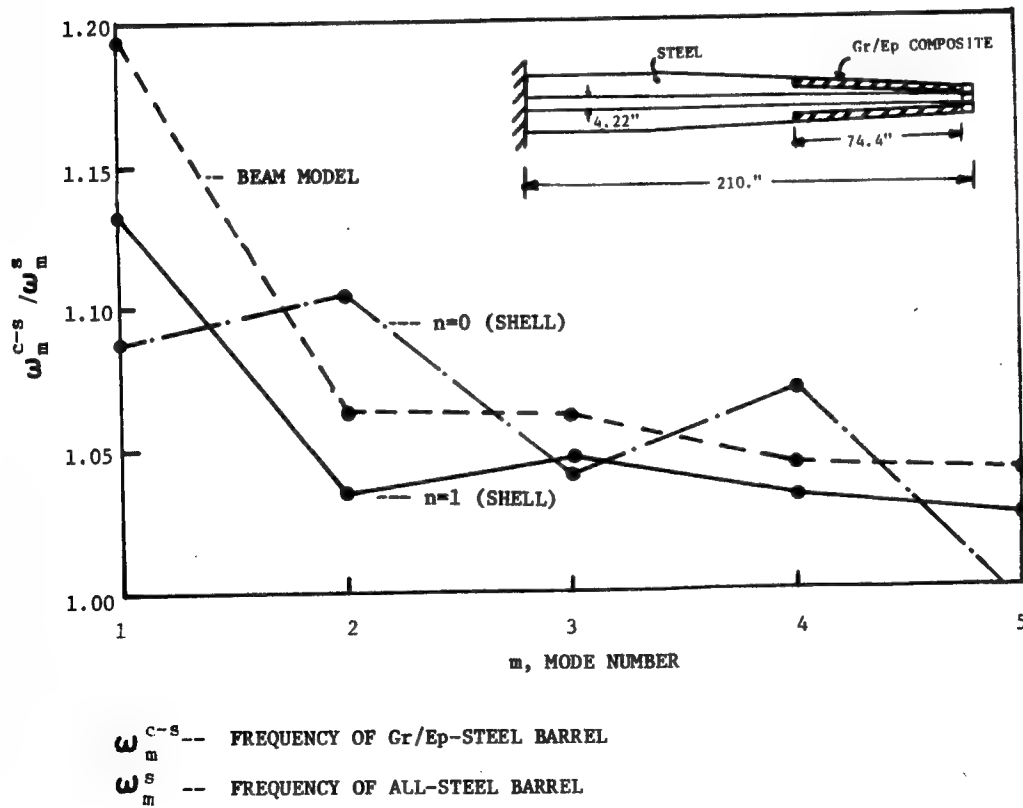Geometric and Kinematic Notations.

ω_m^{c-s} -- FREQUENCY OF Gr/Ep-STEEL BARREL

ω_m^s -- FREQUENCY OF ALL-STEEL BARREL

Figure 2. Normalized Natural Frequencies Versus
Longitudinal Mode Number for 105 mm Barrel.

DESIGN AND DEVELOPMENT OF HIGH STRAIN
COMPOSITE WING FOR NAVY AIRCRAFT

MARK LIBESKIND
AERO ENGINEER
NAVAL AIR DEVELOPMENT CENTER
WARMINSTER, PA 18974

EXTENDED ABSTRACT

INTRODUCTION

Composite wing structures currently in use on Navy aircraft are designed to strain levels substantially below the failure strains of the basic composite material to allow for the effects of strain concentrations (Figure 1). Reducing the effect of such concentrations offers the opportunity of increasing composite wing structural efficiency. Data collected from specimen tests at elevated temperature provide the basis for the current upper limit on design ultimate strain levels of 3500-4500 in/in for wing skins. Within this strain limitation, superior fatigue characteristics and acceptable damage tolerance and repairability are obtained.

The objective of this program is to develop composite design improvements, using existing fiber and resin systems, which will permit a substantial increase in composite wing design allowables without sacrificing fatigue life, damage tolerance, survivability, and repairability.

Design Criteria

A subsonic patrol multi-mission V-STOL aircraft (Grumman 698) was used as a baseline for the study. Criteria established for the program is shown (Figure 2). Previous design studies indicated that a 50% increase in working strain levels to 6000 in/in for tension and compression wing covers was necessary to achieve the weight reduction goal of 20% over the current state-of-the-art composite design. The environmental conditions were established based upon aircraft operating temperatures, mission profiles, and typical deployment areas. Damage tolerance requirements are similar to current design requirements. Survivability considerations required the structure to carry limit load following a single hit by a ballistic projectile and to tolerate hydraulic ram effects due to high energy impact. Supportability requirements established dictated that one cover be designed to be removable for maintenance and repair. This requirement eliminated the use of blind and interference type fasteners from the design. In addition, removable access panels for maintenance of wing internal systems was included in the design. Finally, the wing box is an integral fuel containing structure and thus was designed to withstand maximum fuel pressures which could be encountered during refueling or flight conditions.

Selected Design

During the initial phase of the program, various concepts and structural configurations were evaluated. These trade studies considered both multi-rib and multi-spar designs as well as variations in skin and substructure. The configuration selected for detailed development is a five-spar wing with 15 ribs. The graphite/epoxy (Gr/Ep) skins incorporate discrete caps, where 0° plies are concentrated over the spars resulting in a local spanwise pad (Figure 3). The 0° ply orientation coincides with the spar runs. To reduce the strain concentration at the fasteners S - glass/epoxy (Gl/Ep) softening strips are used in the cover to locally replace the 0° Gr/Ep plies whenever the laminate is penetrated. The rib attachments are made with fasteners, utilizing a local chordwise pad to drop the working strain to tolerable levels. Crack arrestment capability is provided by local Gl/Ep strips positioned on either side of each 0° concentration. The upper skin is attached to the spars with mechanical fasteners and gang channels. The spars are integrally cured with the lower skin and stitched together with Kevlar to provide reinforcement for out-of-plane loads. Stitching of the upper and lower wing covers prevents delaminations from propagating beyond the stitch lines and provides a blowout panel for survivability requirements.

Coupon/Element Tests

Coupon and element tests were performed prior to final design of the sub-component test specimen (Figure 4). The coupon specimen test results were used to provide basic materials data on the unique hybrid configuration and to provide a better analytical basis for the design. Coupon type specimens included simple tension and compression specimens with loaded holes to develop bearing/tension interaction curves for the softened laminate, bolt pull through specimens, and integral stitched substructure-to-cover specimens. Various element type specimens representative of critical areas of the design were tested to insure structural adequacy of the subcomponent. Element tests performed, but not shown in Figure 4, included combined longitudinal tension and flatwise tension beams of the wing skin/spar attachment, spar termination elements of the spar/rib intersection, and spar shear test specimens of the covers and spars. The results of these tests demonstrated the effectiveness of the 0° fiberglass/epoxy in locally increasing the strain allowable at fastener holes and validated design details, such as stitching and integral skin/substructure assembly. In general, these tests verified the effectiveness of the design in sustaining design ultimate strain levels in excess of 6000 μin/in. The durability of the design was demonstrated by fatigue tests of coupons and elements in excess of two lifetimes followed by residual static tests to failure above 6000 μin/in.

Damage Tolerance

Damage tolerance was achieved through a multi-path design utilizing crack-arrestment strips made of a compliant material to contain the damage and prevent catastrophic failure under design loads. Gl/Ep strips were selected as the crack-arrestment medium because of their high strain-to-failure. In addition, Kevlar stitches were incorporated through the crack-arrestment strips to stop delamination growth. Tests were performed to verify that minor low energy

342

impact damage which has grown to a significantly large size due to high operating strain levels, is arrested by the stitches while damage due to high energy impact (small ballistic threat) is arrested at the crack-arrestment strips. Three distinct sites on the wing skin are of interest; (1) between spars, (2) directly over the spar, and (3) near the edge of but not on the discrete cap/spar. One panel was impacted at increasing energy levels at the three sites, followed by NDI determination of the extent of the delamination. The results of this test (Figure 5) indicate that the stitches tend to stop the delamination growth caused by impact. Additional specimens, both two and three bay, were impacted and/or drilled at various locations to represent both damage types. Spectrum fatigue and static testing to design ultimate levels produced no significant damage propagation (Figure 5).

Survivability

A test was performed to determine the effectiveness of the design to contain and isolate damage resulting from hydraulic ram effects. Damage containment was accomplished through the use of a "blow-out" panel created by lines of stitching along the spars and ribs. The test box was impacted with a 5/8 in. steel ball representative of a missile fragment fired at 4500 ft/sec. The box was filled with JP-4 fuel and pressurized to 5.3 psi. The damage was essentially contained by the stitches thereby preventing propagation and catastrophic failure (Figure 6). Some fastener pullout was noted, however, damage was minimal. Survivability of the design was assessed by testing a large panel with simulated ballistic damage. The panel was representative of a three spar section of the wing tension skin with an 8 in. hole removing the center built up cap area (Figure 6). At 4200 μin/in far field strain, a combination crack/delamination initiated at the edge of the hole and propagated to the glass strips and was arrested. The panel was loaded to the maximum design fatigue load (4700 μ in/in) with no additional damage observed. The ability of the damaged panel to sustain design limit load provided some assurance of the survivability of the design. Obviously, actual ballistic tests are needed to fully demonstrate the design.

Subcomponent Fabrication and Test

In order to verify the overall design of the high strain wing, a subcomponent box is currently being fabricated (Figure 7). This component is representative of the wing center section and includes major areas of concern generic to multi-mission aircraft wings as well as the selected design. The subcomponent is a three-cell thru box and consists of two graphite/epoxy intermediate spars integrally molded and stitched to the lower cover at the discrete cap and mechanically attached to the upper cover through "S" glass softening strips also at the discrete cap. Front and rear spars are mechanically attached to both the upper and lower covers. Crack arrestment capability is being provided by local "S" glass strips with Kevlar/Epoxy stitches providing delamination control. An access door is located in the center bay. A fuel sealing groove is incorporated along the periphery of the box.

Testing, which will be performed at the Naval Air Development Center, will consist of internal fuel pressurization and mechanical static and fatigue loading representative of the most critical design conditions. Additional testing which may be performed includes demonstration of repair technology and/or battle damage tolerance capability.

OBTAIN SIGNIFICANT WEIGHT SAVINGS IN COMPOSITE
WING STRUCTURE BY DESIGN IMPROVEMENTS TO
INCREASE DESIGN STRAIN LEVELS.

DESIGN CONSIDERATIONS:

EFFECT OF HOLES ON STATIC
STRAIN CAPABILITIES

WEIGHT
COST
DAMAGE TOLERANCE
DURABILITY
SURVIVABILITY
MAINTENANCE
FUEL CONTAINMENT
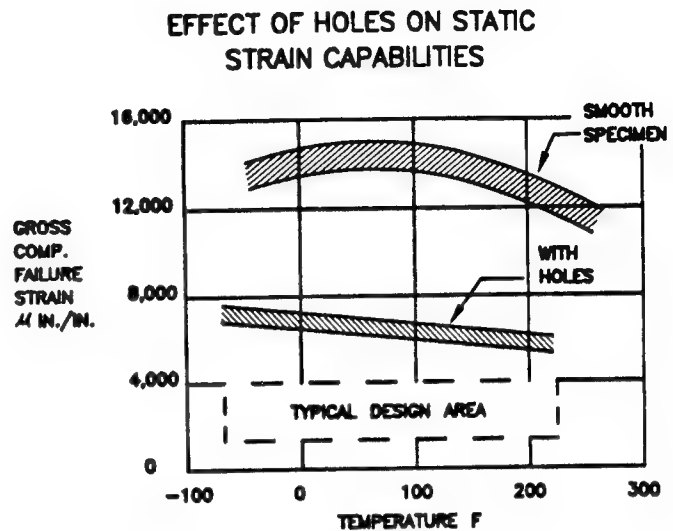
FIGURE 1 - OBJECTIVE/DESIGN CONSIDERATIONS

- **WEIGHT:** 20% WEIGHT REDUCTION FROM CURRENT
  SOA COMPOSITE DESIGN

- **STRAIN LEVEL:** 6000 MICRO-IN/IN DESIGN ULTIMATE STRAIN
  FOR TENSION AND COMPRESSION COVERS

- **ENVIRONMENTAL CONDITIONS:** 160 DEG. F AND 1.3% MOISTURE

- **DAMAGE TOLERANCE:** SUSTAIN DUL AFTER LOW ENERGY IMPACT

- **SURVIVABILITY:** • SINGLE BALLISTIC HIT AND SUSTAIN DLL
  • HYDRAULIC RAM EFFECTS

- **SUPPORTABILITY:** ONE COVER REMOVABLE FOR MAINTENANCE & REPAIR

- **FUEL CONTAINMENT:** WITHSTAND MAXIMUM FUEL PRESSURES

FIGURE 2 - DESIGN CRITERIA

345

1. MULTI—SPAR CONFIGURATION FOR SURVIVABILITY
2. STITCHING AND CRACK ARRESTMENT STRIPS FOR DAMAGE TOLERANCE
3. INTEGRAL LOWER COVER; COCURED AND STITCHED TO SUBSTRUCTURE
4. BOLTED UPPER COVER; S/GLASS AT BOLT HOLES
5. ALL 0° GR/EP OVER SPARS; ±45° GR/EP BETWEEN SPARS

FIGURE 3 - SELECTED DESIGN

FIGURE 4 - COUPON/ELEMENT TESTS

DAMAGE TOLERANT DESIGN

REPRESENTATIVE HIGH ENERGY

IMPACT DAMAGE
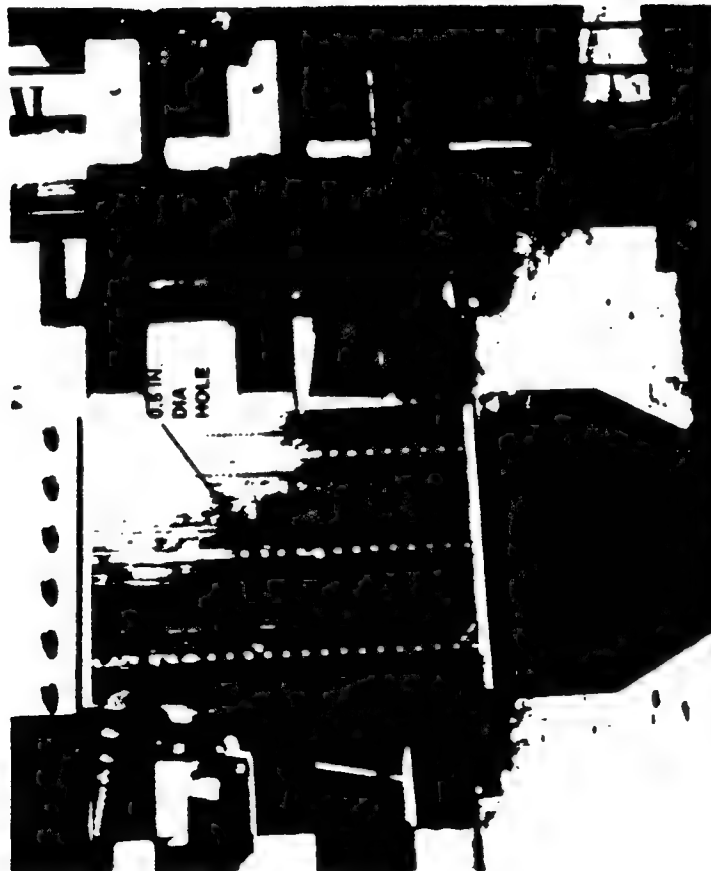
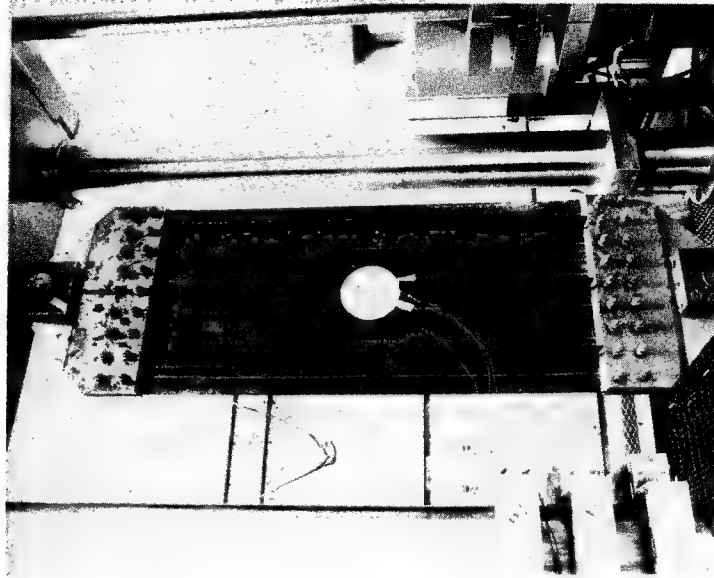## LOW ENERGY IMPACT SURVEY PANEL
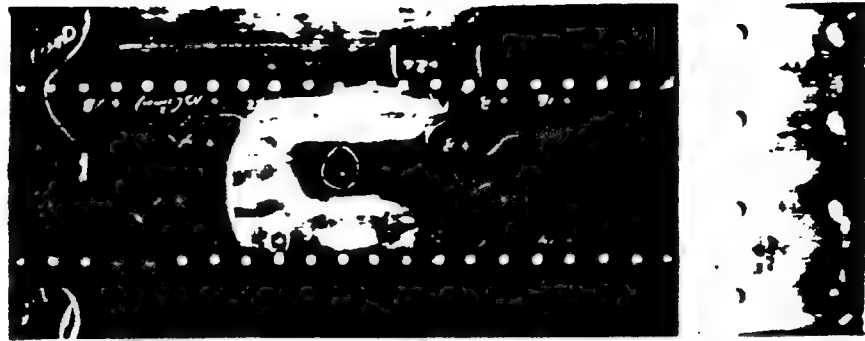
FIGURE 5 - DAMAGE TOLERANT DESIGN

347

ELEMENT TESTS
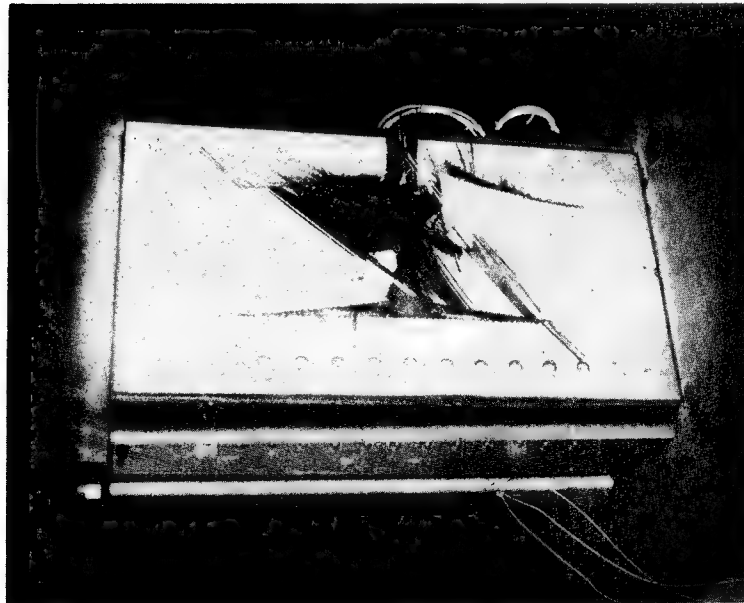
SURVIVABILITY

HYDRAULIC RAM

FIGURE 6 - HYDRAULIC RAM/SURVIVABILITY ELEMENT TESTS

FIGURE 7 - SUBCOMPONENT CONFIGURATION

ABSTRACT

LOADS ANALYSIS METHODOLOGY FOR DETERMINING
STRUCTURAL STRENGTH DESIGN CRITERIA FOR
LIGHT WEIGHT ARMORED COMBAT VEHICLES

Donald M. Anderson
Member Technical Staff

Laurence E. Reinhart
Member Technical Staff

Applied Mechanics Division, Jet Propulsion Laboratory,
California Institute of Technology

Methodology and preliminary results are presented for rationalizing the
selection of structural strength design criteria for light weight armored
combat vehicles (ACV's). Since the loading is stochastic, the methodology is
a probabilistic approach relating structural design criteria to performance
capability over rough terrain. This is in contrast to previous ground vehicle
design practice, which has been a somewhat arbitrary selection of structural
load factor based upon the empirical estimates of the design handbooks.

At JPL, a Structural Test Model (STM) hull of a typical light weight tracked
ACV has been designed and assembled. This structure serves as a demonstration
of advanced analytical design techniques in which structural analysts are
close-working partners with designers. Computer aided design (CAD) techniques
and sequenced finite element modeling of the evolving design were used to
generate a vehicle hull of relatively high structural efficiency, yet of low
cost conventional aluminum plate fabrication. The demonstration structure,
designed to the old consersative handbook loads, reflects the weight savings
resulting from a modern analytical (finite element) design process.
Application of the loads analysis discussed below would result in further
weight reduction and improved structural integrity, at the high performance
which the light weight makes possible.

Terrain induced dynamic loads in a light weight tracked ACV depend primarily upon vehicle speed, terrain roughness (or obstacle height), and the vehicle suspension system. While vehicle/suspension dynamics can be accurately modeled, the maximum expected terrain loads in projected operations are also functions of: (1) relevant terrain roughness characteristics and obstacle distribution statistics, (2) mission terrain/intensity projection or "mission profile", and (3) applicable human tolerance limitations. These three parameters are not well defined, yet they are critically influential in setting the structural design load requirements. For purpose of this analysis, these influential parameters are treated as key suppositions. In application of this methodology to a new vehicle design and procurement program, the key suppositions would be quantified as requirements or specified conditions, based upon collected experimental and field data and the results of the subject analysis. The analysis is described schematically in Figure 1, in which the key suppositions which constrain vehicle performance and influence load probabilities are shown.
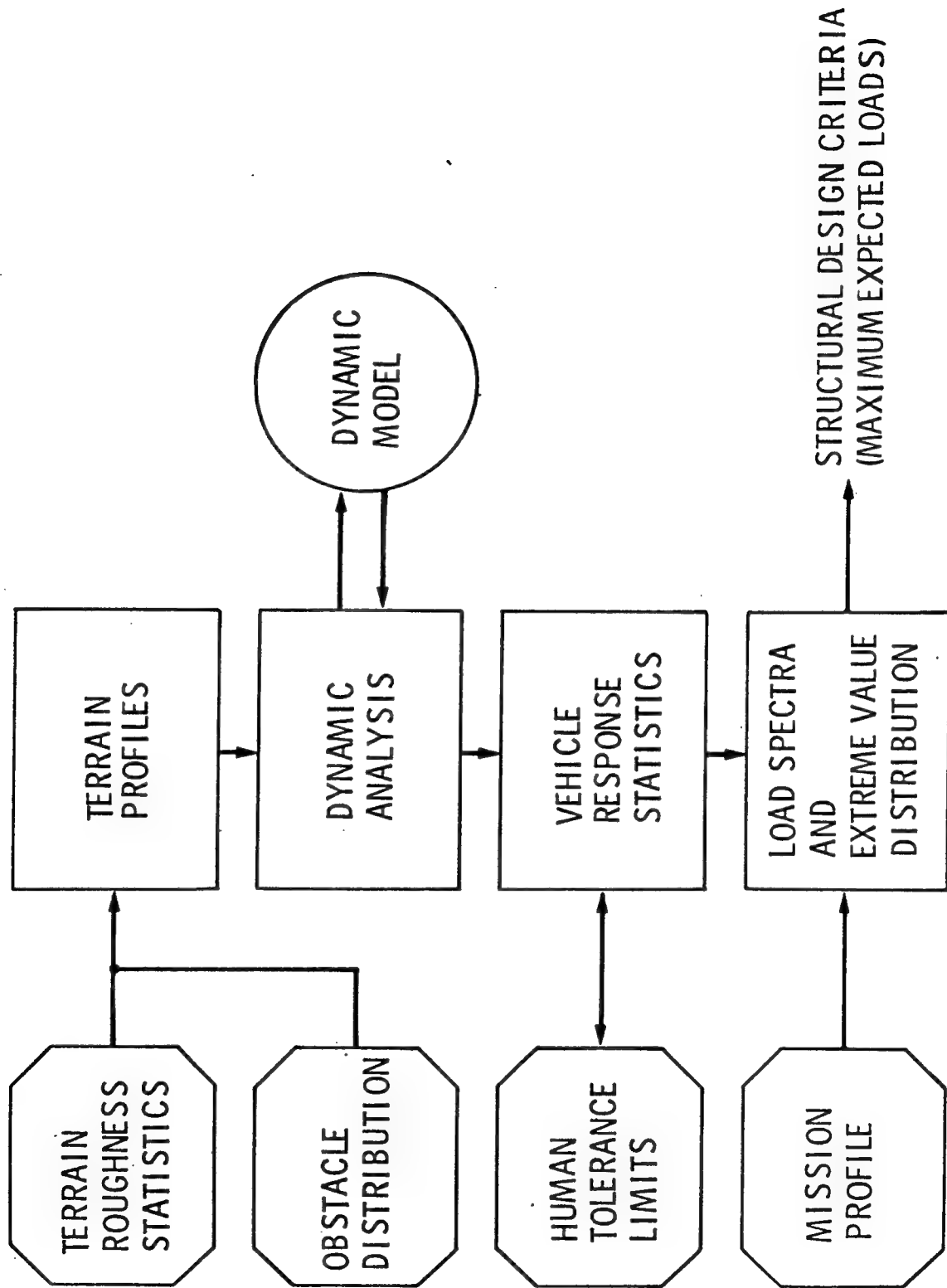
Since the objective is to determine probabilities of extreme loads as a function of performance, the vehicle dynamic analysis has utilized precise modeling of the non-linear behavior at load extremes. Because of these non-linearities, Monte Carlo techniques were required to obtain response statistics. It was therfore essential that each computer run be as low in cost as possible, without sacrificing required precision at the response extremes. Similar attention was given to the statistical quality of the computerized terrains used as input to the vehicle dynamic model. This is because the extreme value analysis includes statistical examination of the response data at three different levels: (1) the time-varying response function, (2) the distribution of the maxima of the response, and (3) the distribution of the extremes of the maxima when an extreme is determined for each of many sample terrain segments.

Computerized terrain profiles of actual test courses (at Aberdeen Proving Ground and Ft. Knox) were used as input time functions for comparing analytical model response with measured vehicle response over actual terrain. Synthesized terrain profiles were generated to meet prescribed roughness characteristics (power spectral density and rms height), which also satisfy desired statistical stationarity requirements. (Such stationarity is required for application of the extreme value theory used to determine load exceedence probabilities). Two different methods have been implemented for generating such random terrains, and a variety of statistical subroutines developed to evaluate the statistical characteristics of input and response.
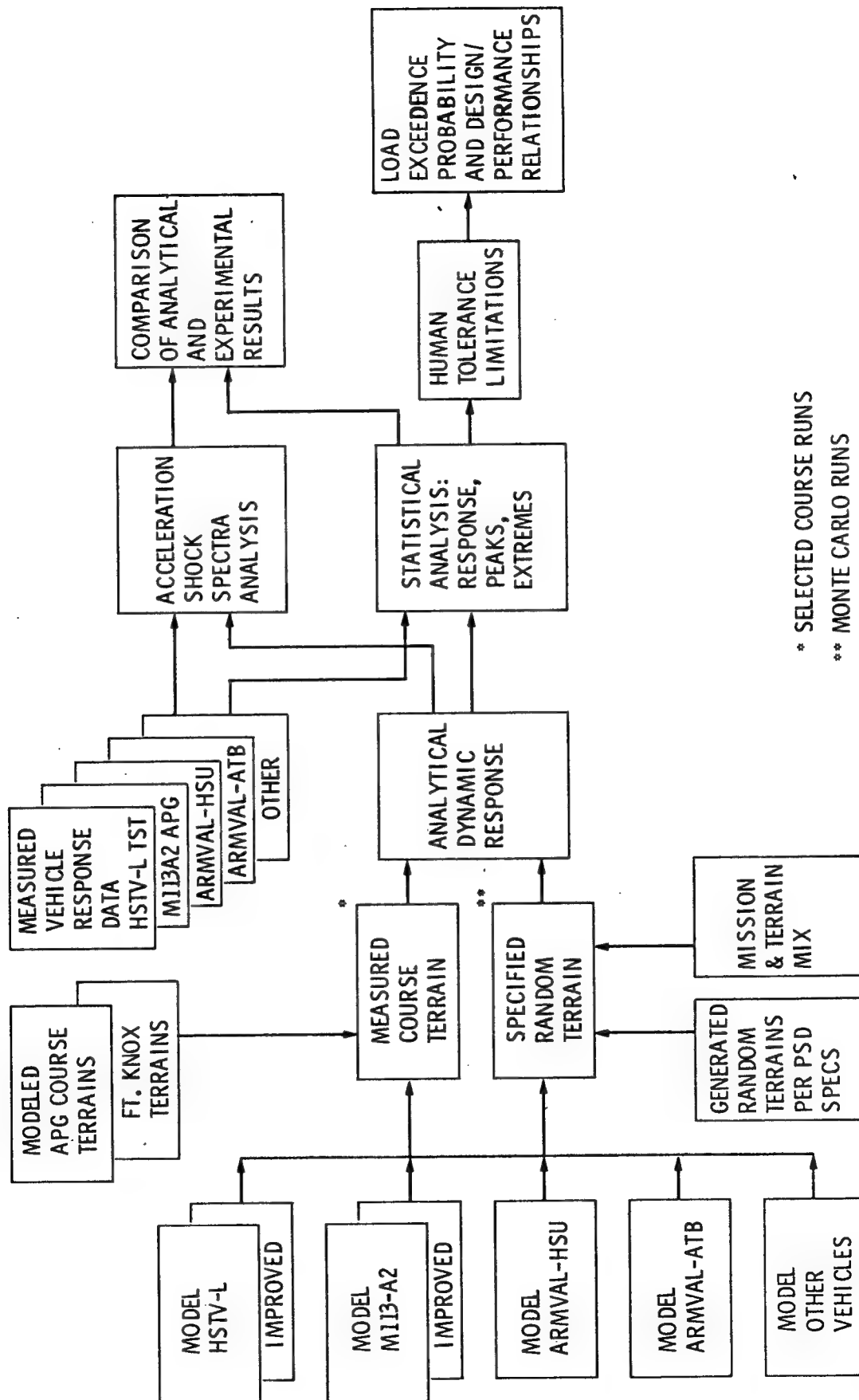
The synthesized random terrain profile was fed to the rigid body/suspension system dynamic model and the resulting vehicle response statistics (PSD and rms) related to that of the terrain input for the particular speed and vehicle. The analytical results were compared with actual vehicle test data for several vehicles: M113A2, M1, M60, HSTV-L, and two ARMVAL test vehicles. The overall task schematic is shown in Figure 2. Although an unorthodox utitlzation, acceleration shock spectra have proven of value for comparing analytical with actual vehicle response. A series of runs over each terrain profile at different speeds established the full range of vehicle response statistics for the terrain PSD represented by the (sufficiently long or randomly repeated) tailored profile. Vehicle response determinations include acceleration power absorbed at the driver's location, as well as load statistics, so that human tolerance levels can be applied. These general results (for a given vehicle) are compared with particular results (both measured and analytical) for performance over known terrain profiles such as Perryman III and APG Profile 4.

Statistical results obtained for each terrain type are combined according to the anticipated (selected) mix of terrain types and speeds to be expected on typical and maximum intensity missions, using a selected mission profile. An obstacle impact requirement, selected with the aid of computer simulation results, is imposed over the probabilistic load exceedence results, using a selected obstacle probability density distribution. The resulting overall load statistics, based upon the given mission profile, also provide load spectra useful for determining fatigue life estimates. The final load exceedence curves relate the probability of structural load extremes to vehicle performance and human tolorance level over expected terrain. This enables structural design load limits to be selected in conformity with human limits and the required performance over rough terrain, with known risk of exceeding structural limitations.

TERRAIN LOAD DESIGN CRITERIA

AMTD LOADS STUDY SCHEMATIC

JPL

* SELECTED COURSE RUNS
** MONTE CARLO RUNS

Boxes in the schematic:

- LOAD EXCEEDENCE PROBABILITY AND DESIGN/ PERFORMANCE RELATIONSHIPS
- COMPARISON OF ANALYTICAL AND EXPERIMENTAL RESULTS
- HUMAN TOLERANCE LIMITATIONS
- ACCELERATION SHOCK SPECTRA ANALYSIS
- STATISTICAL ANALYSIS: RESPONSE, PEAKS, EXTREMES
- MEASURED VEHICLE RESPONSE DATA HSTV-L TST M113A2 APG ARMVAL-HSU ARMVAL-ATB OTHER
- ANALYTICAL DYNAMIC RESPONSE
- MODELED APG COURSE TERRAINS FT. KNOX TERRAINS
- MEASURED COURSE TERRAIN
- SPECIFIED RANDOM TERRAIN
- MISSION & TERRAIN MIX
- GENERATED RANDOM TERRAINS PER PSD SPECS
- MODEL HSTV-L IMPROVED
- MODEL M113-A2 IMPROVED
- MODEL ARMVAL-HSU
- MODEL ARMVAL-ATB
- MODEL OTHER VEHICLES

355

TRANSIENT ANALYSIS AND TESTING OF A NONEXPANDABLE TACTICAL SHELTER SUBJECT TO RAIL IMPACT

A. R. Johnson*, J. R. Cullinane', L. P. Cuzzupe*,
and A. S. Lamontage*

EXTENDED ABSTRACT

Tactical shelters are nearing the completion of development and will be in general use by the Army in the near future. These shelters are transportable and meet both Army and International Standards Organization requirements for shipping containers. They are designed such that they can be adapted to a variety of missions. In order to insure that the adaptations will perform succesfully in the field it is necessary to develop structural design models which can be used to check the performance of the shelters for each special mission. The variations of the shelters from one mission to the next usually involve the mounting of different equipment internal to the shelter or possibly the addition of doors or access ports to the shelter. Although the overall construction of the shelter does not change,the effect of the modifications must be reliably determined in the design stage to allow the modified shelters to become available for field use without unjustified development delays.

In this effort a previously developed finite element model for a two-for-one shelter is used and extensively modified to make two new structural design models. The first model is for a nonexpandable shelter with no modifications. The second model is for a nonexpandable shelter designed for chemical and biological (CB) environments. Both models were made valid for dynamic analyses. The most recent drawing package for the Family of Tactical Rigid Wall Shelters was used to determine the structural elements in the finite element model. The model is tested by comparing numerical predictions of accelerations for a rail impact test with measured data. An extensive test plan was developed based on experience gained from a previous similar test. The test is to be conducted in September 1984 an has a twofold purpose. First, it will serve as a proof test of a preliminary design of a CB shelter. Second, it will provide acceleration and cable tie down load data for corelation with the design model.

FINITE ELEMENT MODEL OF CB SHELTER: The model of the shelter is shown in Figure 1. Minor changes are frequently made to the model to include new items or to determine the response at a specific location. The basic model consists of 352 beam elements, 12 rigid body elements, 227 plate elements, 466 nodes, 121 rigid link elements and, when assembled, has

* US Army Materials and Mechanics Research Center, Watertown, MA.
' US Army Natick Research and Development Center, Natick, MA.

about 1600 variables. There are 22 different types of beams and 6 different types of plates included in the model. The model is an updated version of a previously used model[1,2] for an expandable tactical shelter. This new model reflects recent updates to the structural drawings and the changes necessary to model the nonexpandable CB shelter, see Figure 2. Structural damping was included by constructing a global damping matrix which is proportional to the global stiffness matrix. The mass matrix is consistent with the displacement interpolation function and reflects the known mass distribution in the shelter. Several concentrated rigid body elements are used to model equipment inertial properties.

DYNAMIC LOADS: The rail impact test consists of attaching the shelter plus payload to a flatcar as indicated in Figure 3. The car is then brought to a velocity of 10 mph, released and allowed to couple with two stationary cars. During the impact test the shelter is dynamically loaded by the blocks and cables used to attach it to the flatcar and from the vertical motion of the flatcar resulting from the coupling. A first order estimate of the block and cable loads can be obtained using a two degree of freedom model of a shelter restrained by cables in tension and blocks in compression, see Figure 4. These loads plus additional loads to simulate the vertical acceleration can be applied in the finite element analysis to determine the structural response of the shelter.

TESTING: A test program was developed in which accelerations and cable forces will be measured as a function of time. Figure 5. indicates the general approach to be taken. Accelerometers will be placed at key locations on the shelter so that the global response of the shelter will be known. That is, accelerations at corner points, midpoints on edges, 1/3 points on panels, etc. will have accelerations measured with respect to a global coordinate system. Details of equipment response will also be measured, see Figure 6. for example. The acceleration data will be time sequenced so that numerical integration will yeild information on shelter racking or other structural deformations of the shelter.

REFERENCES:

1. Arthur R. Johnson,"Response of a Two-forOne Tactical Shelter to Racking Loads," US Army Natick Research and Development Laboratories, Natick, MA, 1981 (AD A102389).
2. Arthur R. Johnson III,"Analysis of Accelerations in a Dynamically Loaded Tactical Shelter," US Army Natick Research and Development Laboratories, Natick, MA, 1982 (AD A124378).
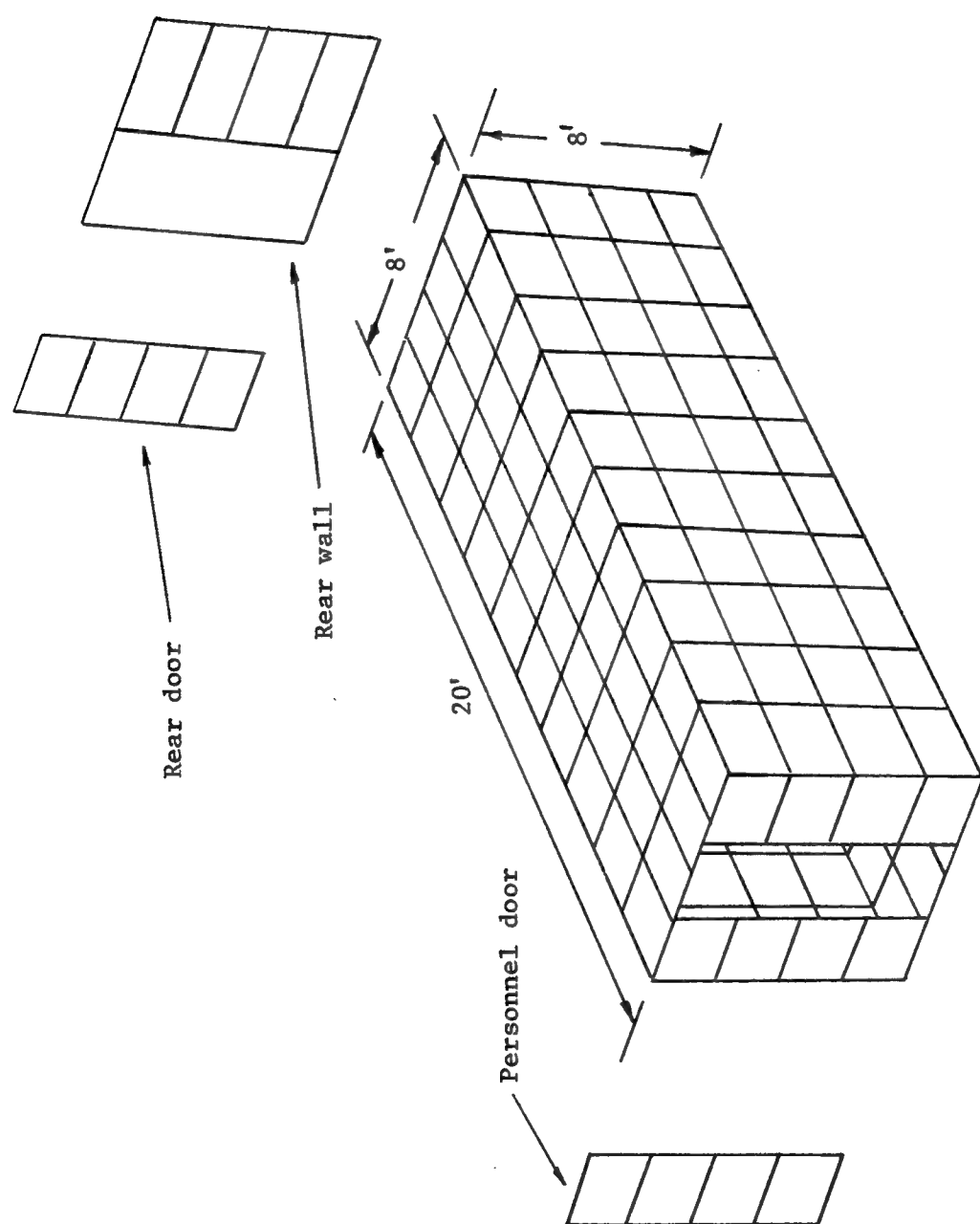
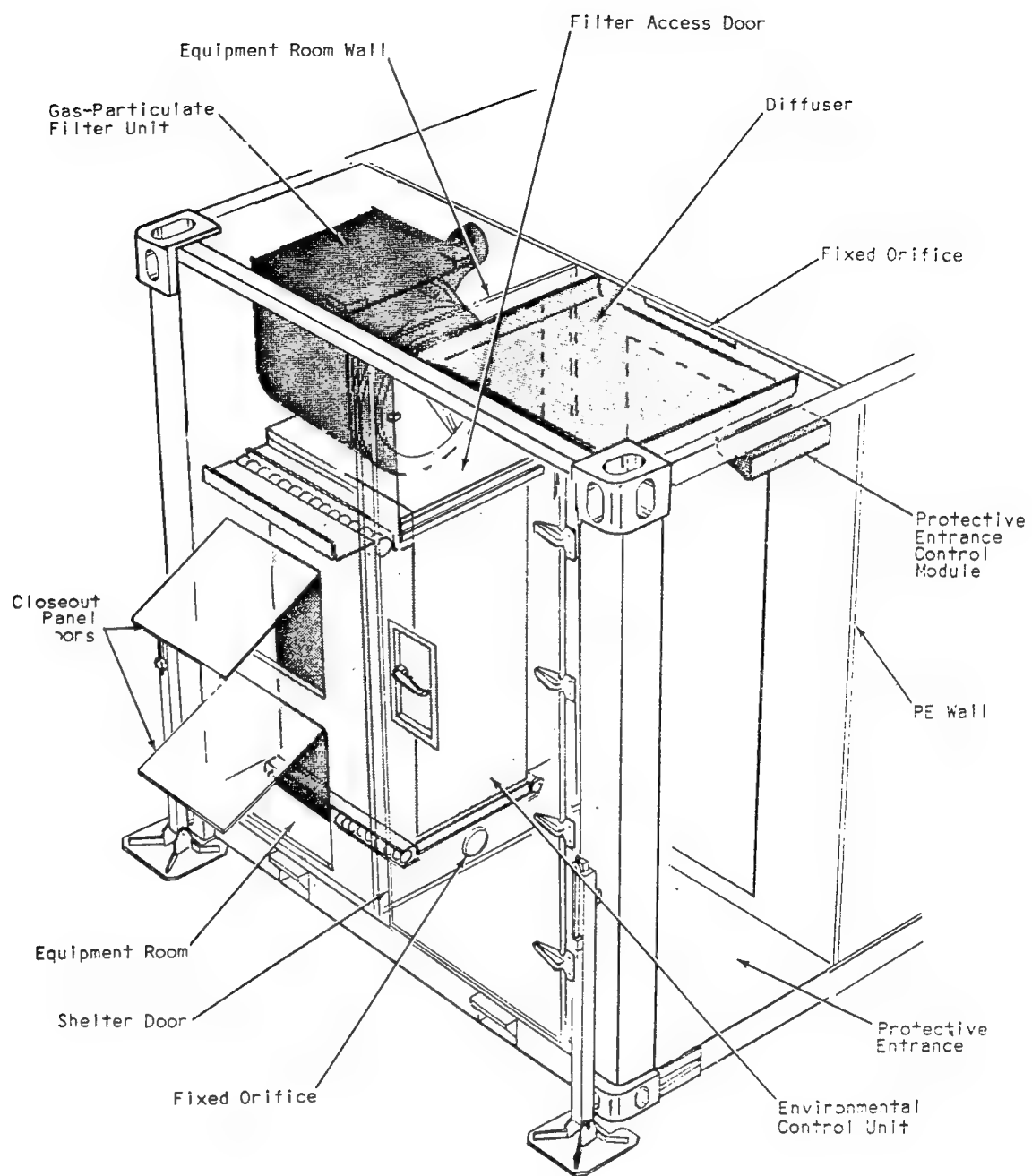Figure 1.   Finite element model of nonexpandable shelter.
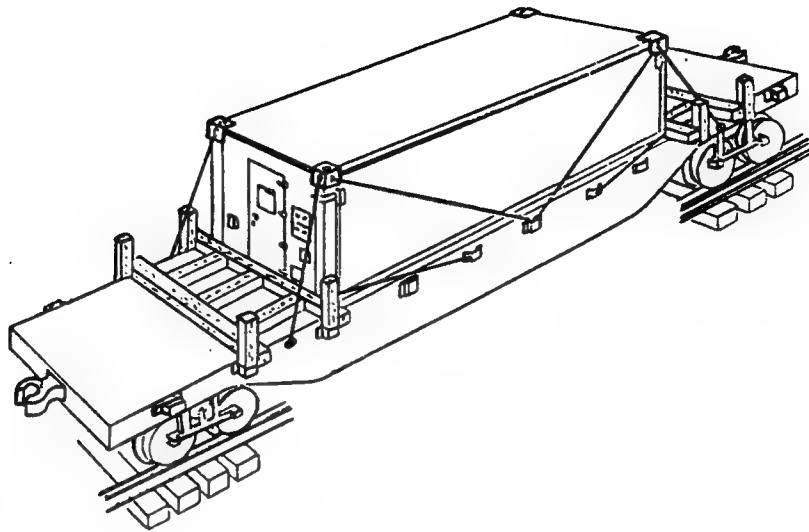
359

Figure 2. CB modification to shelter.
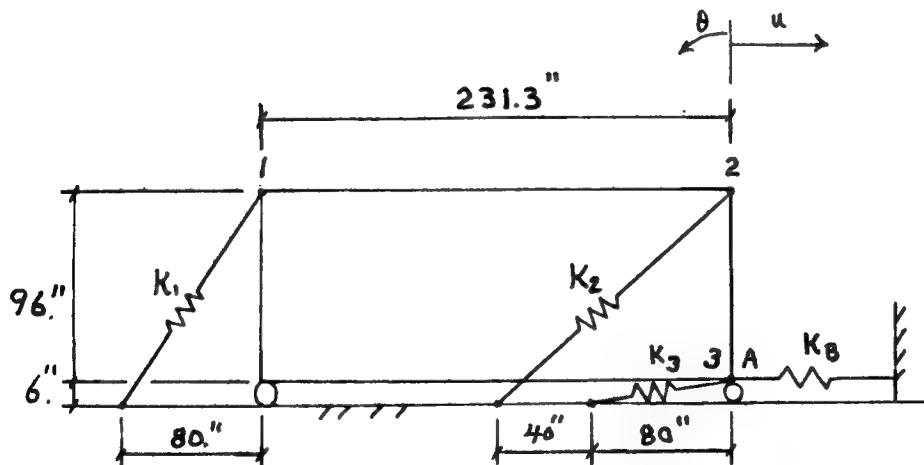
Figure 3.   Shelter in shipping mode on flatcar.

Figure 4.   Two degree of freedom model (u,θ) for shelter,
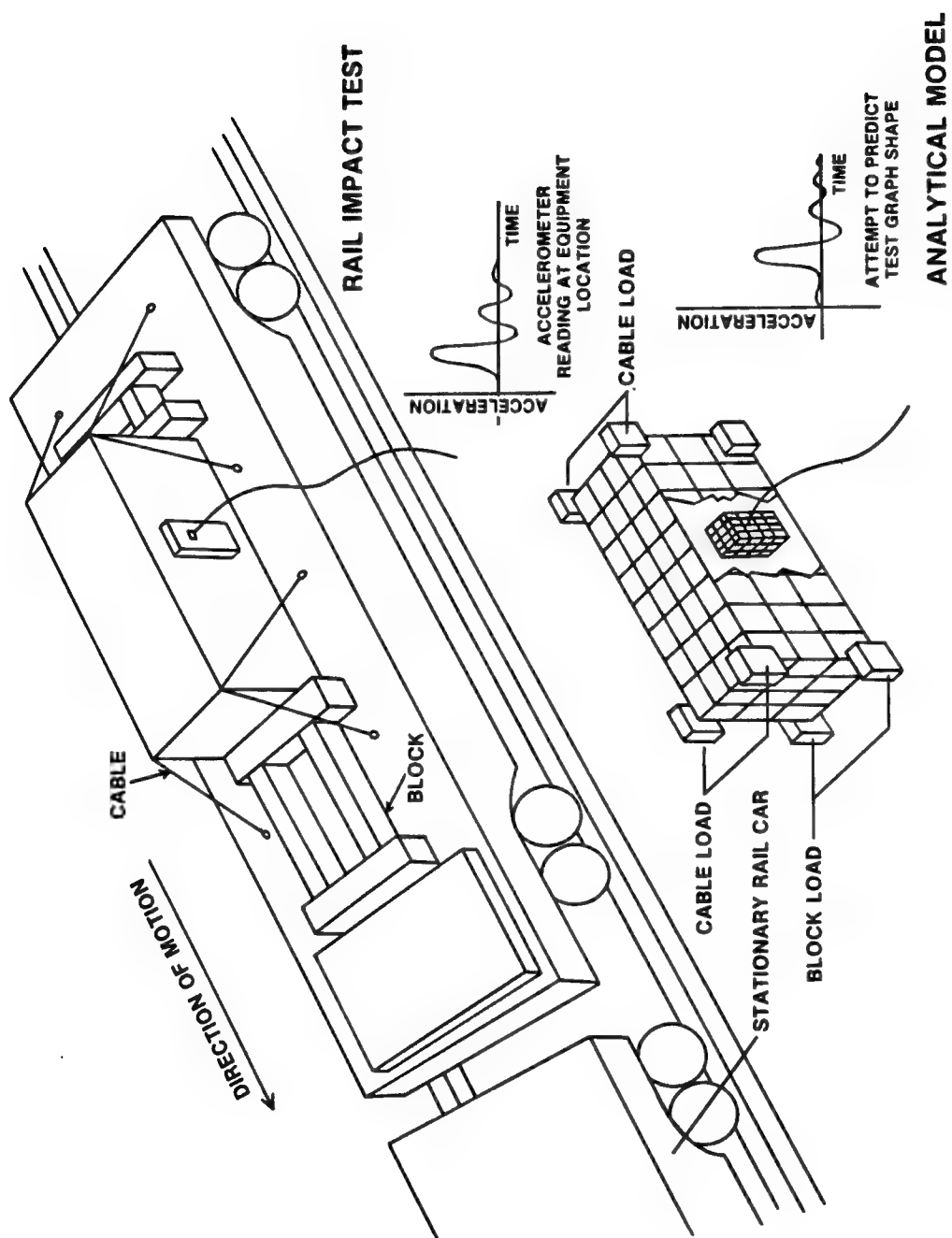   cables and blocks.

Figure 5. Rail impact test and analytical model.
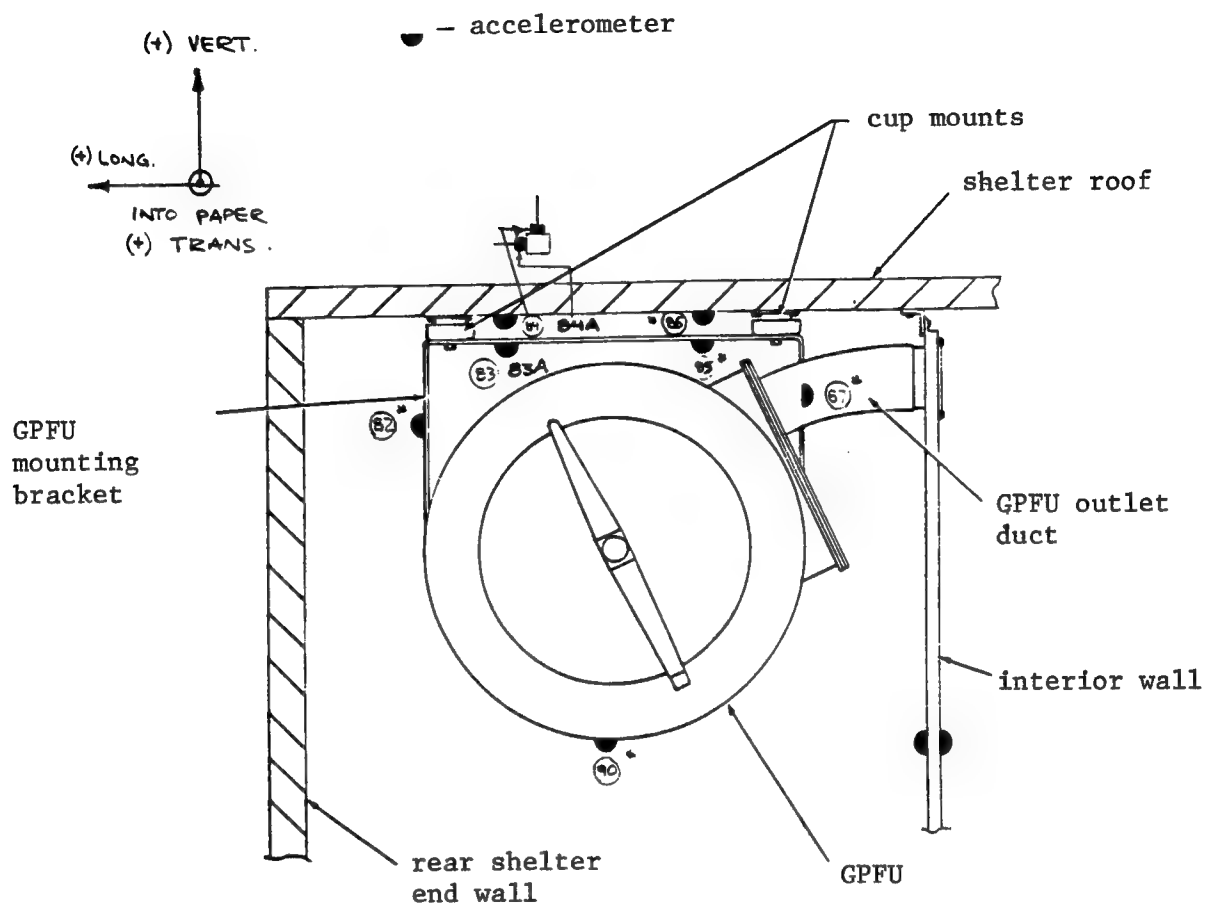
GAS-PARTICULATE FILTER UNIT (GPFU)

(side view)

Figure 6.   Accelerometers on gas-particulate filter unit.

363

A SEMI-AUTOMATED SYSTEM FOR MOIRE' STRAIN ANALYSIS

ALAN H. KATZ
Army Materials and Mechanics Research Center
Watertown, MA 02172

AMMRC utilizes Moire' techniques for strain analysis. Data reduction is laborious and time consuming. The system described uses Moire' fringe photographs as the input and produces strain profiles as output with greater speed and accuracy than possible with manual methods.

The AMMRC video digitizing system is composed of a Hamamatsu C1000 video digitizer and a Hewlett Packard 9845B desktop computer system.

A fringe photograph such as the one shown in Figure 1, is scanned by the digitizer which is under the control of the HP computer. Data which is acquired are the video intensities of the pixels examined (zero to 255). The system is capable of a maximum resolution of 1024 X 1024 pixels over the video field.

The data acquired is stored locally by the HP computer on its floppy disk for later uploading to a host computer for data reduction and analysis.

Uploading of the data is accomplished through the use of the HP computer's terminal emulator and a modem and telephone line. Data is sent at 1200 baud under the control of software on the host computer. This software incorporates limited error checking which is designed to detect errors by the telephone transmission.

After uploading is successfully accomplished all further reduction and analysis is performed by the host. This consists of filtering, fringe identification, strain analysis and graphic output.

Filtering is accomplished using a Fast Fourier Transform with an exponential low pass filter transfer function. The results are then displayed on a Tektronix graphics terminal. The data points, which up to now are defined only by their coordinates, are now interactively associated with the appropriate fringe values and stored in this form. The fringe ordering is the area of least automation.

A geometric mesh which is made up of triangular elements is then generated. Each element of the mesh should have some minimum number of data points within it. Smoothing by splines is performed in each element with continuity required at element boundaries. Differentiation of the smoothed data provides the strains.

Having obtained the strains, contours can be plotted using currently available in-house software. Strain profiles can also be plotted. A set of contours is shown in Figure 2.

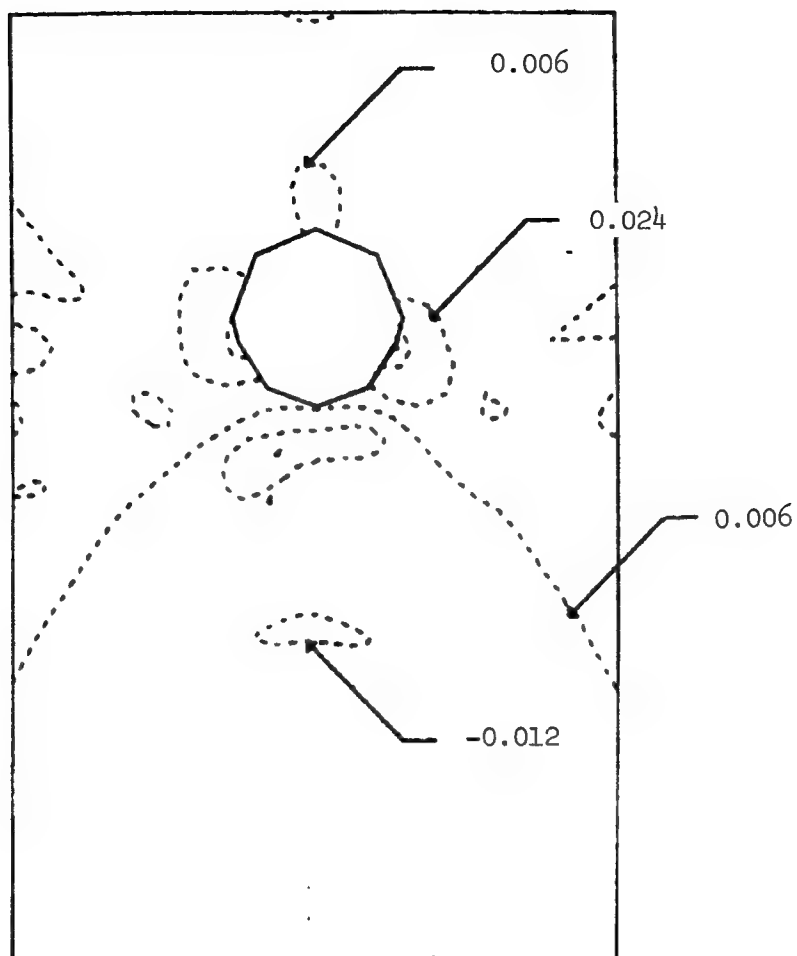FIGURE 1. MOIRE' FRINGE PHOTOGRAPH OF PIN-LOADED COMPOSITE SPECIMEN

FIGURE 2.   STRAIN CONTOURS OBTAINED FROM DATA IN FIGURE 1.

EXPERIMENTAL VERIFICATION OF ANALYTIC BOLTED JOINT METHODOLOGIES

STEVEN M. SERABIAN
Mechanical Engineer

Army Materials and Mechanics Research Center
Watertown, MA 02172

EXTENDED ABSTRACT

Past analytical and experimental work efforts pertaining to bolted joints at AMMRC by Oplinger, Gandhi, Parker and Katz have demonstrated that non-linear behavior plays a significant role in the response of 0/90 and +45 laminates in pinned and bolted joint configurations. Their application of classical Moire Techniques and linear finite element methods to pin-loaded aluminum and composite specimens have indicated that 0/90 laminates behave nonlinear in shear primarily in the region in front of the pin while +45 laminates behave nonlinear in tension primarily in the net-section area (1, 2).

In an effort to analytically investigate the effects of nonlinear intra-laminar shear behavior upon the nonlinear laminate response of composite joints, Oplinger, Freeze, and Gandhi applied a two dimensional, nonlinear, orthotropic finite element analysis to +45 and 0/90 laminates containing open holes and 0/90 pin-loaded laminates (3). In the analysis, nonlinear, intra-laminar shear stress-strain behavior is accounted for through the use of secant shear moduli in conjunction with laminate analysis to calculate effective constitutive properties. The elastic analysis is interative in nature and bases its final solution on the convergences of secant moduli. A perfectly fitted, frictionless pin that exerts its load through assumed displacement conditions is utilized.

Analytical results from Oplinger's nonlinear finite element techniques indicate a qualitative agreement with past experimental results for 0/90 pin-loaded laminates. Quantitative agreement is thought to be obtained through lamina mechanical properties characterization of the particular fiber/resin system being used. Analytical treatment of +45 pin-loaded laminates has not been undertaken to date.

In an effort to experimentally verify Oplinger's analytical assumptions pertaining to bolted joints, current experimental work at AMMRC has been centered primarily around the application of Classical Moire Techniques to +45 and 0/90 pin-loaded, S-glass/epoxy coupons. In these efforts, photo-printed 500 line/inch cross gratings on KODALITH transparent stripping film were cemented on the front surface of the composite coupon while strain gages were adhered to the back surface. The coupon was then pin-loaded to failure in a hydraulically actuated loading frame while deformed grating photographs and strain gage readings were taken at various load levels. These photographs were then processed on AMMRC's Classical Moire Optical Bench which is shown schematically in Figure 1. Variable mismatch, fringe multiplications, and U

and V field seperation techniques were performed with this system to obtain U and V displacement fields of the coupon at various load levels. So far to date 0/90 and +45 coupons have been tested while only 0/90 displacement contours have been processed. Correlation between strains obtained from these displacement contours and strain gage readings is good. Shown in Figure 2 is a sample of these results.

To provide an accurate mechanical property data base for the nonlinear, orthotropic finite element modeling of the pin-loaded coupons, mechanical testing of the fiber resin system has been undertaken. Tension testing of unidirectional SL-3 Streamline specimens in both fiber and matrix directions as well as Asymmetric Four Point Bend (AFPB) and +45 ASTM shear tests have been conducted (4 - 6). From these test, lamina mechanical properties as a function of strain have been found. These may be seen in figures 3.

Correlation between experimental Moire testing and analytical finite element analysis of the pin-loaded coupons will be done through an interactive displacement contour plotting algorithm developed by C. E. Freese (7). In this algorithm, finite element results may be displayed as Moire fringes where variable mismatch, fringe multiplication, U and V field seperation, and fringe shifting techniques may be applied. Utilizing this flexible display capability, computer generated displacement field Moire fringes will be compared to experimental Moire results.

Literature Cited

1) D. W. Oplinger, "Fibrous Composite in Structural Design", Edited by E. M. Lenoe and J. J. Burke, Plenum Press, New York, New York, p. 575-602.

2) D. W. Oplinger, B. S. Parker, and A. Katz, "Moire Measurement of Strain and Deformations in Pin-Loaded Composite Plates", Extended Summaries, 1979, SESA Spring Meeting, 14 Fairfield Drive, Brookfield, CT 06805.

3) D. W. Oplinger, C. E. Freese, and K. R. Gandhi, "Experimental and Analytical Evaluation of Nonlinear Mechanical Response in Notched Laminates", Proceedings of Ninth Annual Mechanics of Composites Review, Dayton, Ohio, October 24-26, 1983.

4) D. W. Oplinger, B. S. Parker, K. R. Gandhi, R. Lamothe and G. Folley, "Comparison of Tension Specimen Design for Static and Fatigue Testing of Composite Materials", Second US - Japan Symposium on Composite Materials, NASA Langley Research Center, Hampton, VA, June 8, 1983.

5) J. M. Slepetz, T. F. Nagaeski, and R. F. Novello, "In-Plane Shear Test for Composite Materials", AMMRC publication, document No. AMMRC TR 78-30, July 1978.

6) B. W. Rosen, "A Simple Procedure for Experimental Determination of the Longitudinal Shear Modulus of Unidirectional Composites", Journal of Composite Materials 6(October 1972) pp. 552-554.

7) Contour Plotting Module, February 1982, Developed by C. E. Freese at AMMRC, Watertown, MA 02172.
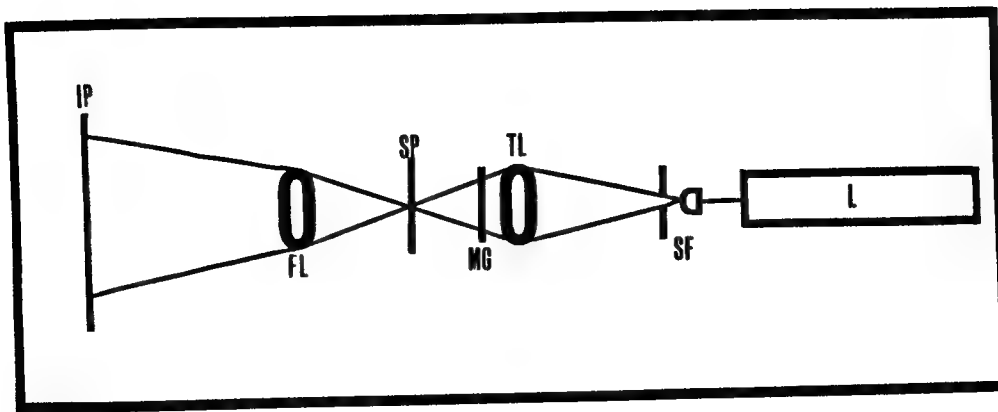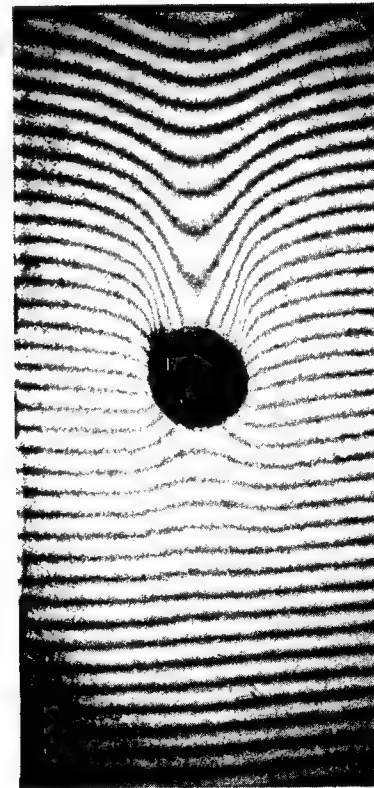
IP -- IMAGE PLANE

FL -- FIELD LENSE

L -- LASER

MG -- MOIRE GRATING

SF -- SPATIAL FILTER

SP -- SPECTRUM PLANE

TL -- TRANSFORM LENSE

Figure 1   AMMRC Classical Moire Optical Bench
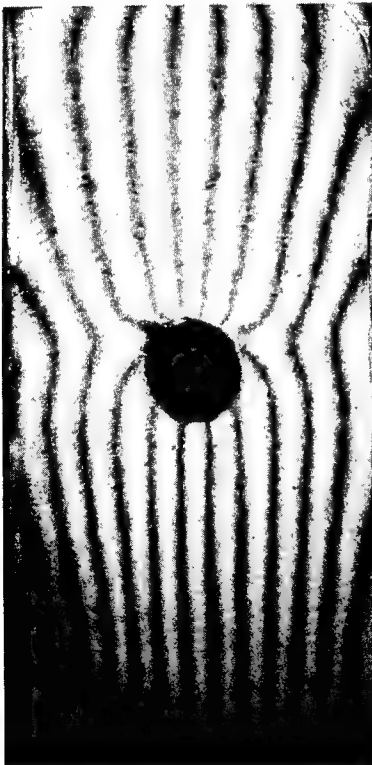
V-Field
1500 lbs (6672 N)
Mismatch +.010 in/in
.001 in/fringe (.00254 cm/fringe)

U-Field
1500 lbs (6672 N)
Mismatch +.016 in/in (
.001 in/fringe (.00254 cm/fringe)

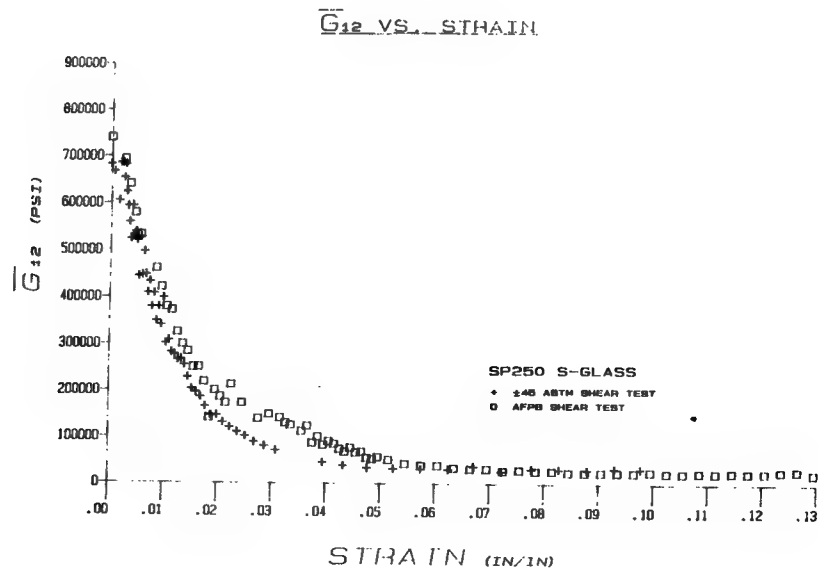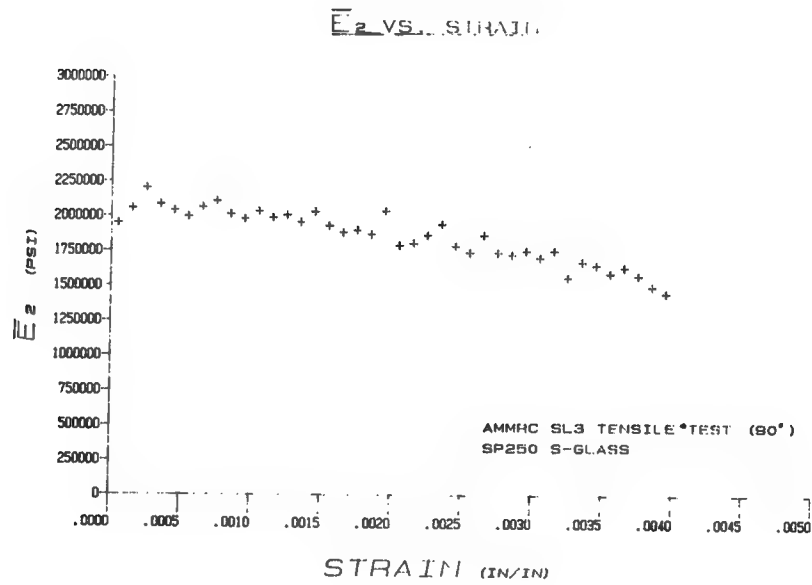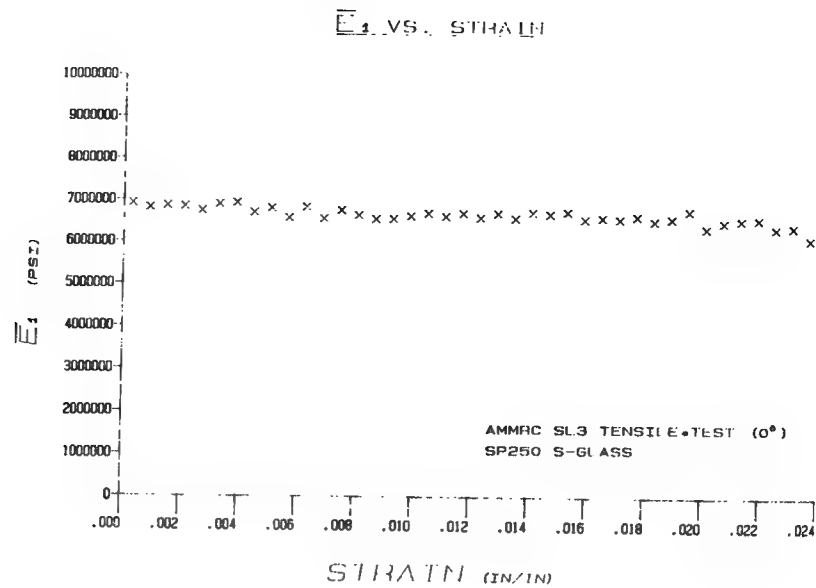Figure 2   Moire Fringe Patterns of 0/90 Pin-Loaded Coupon
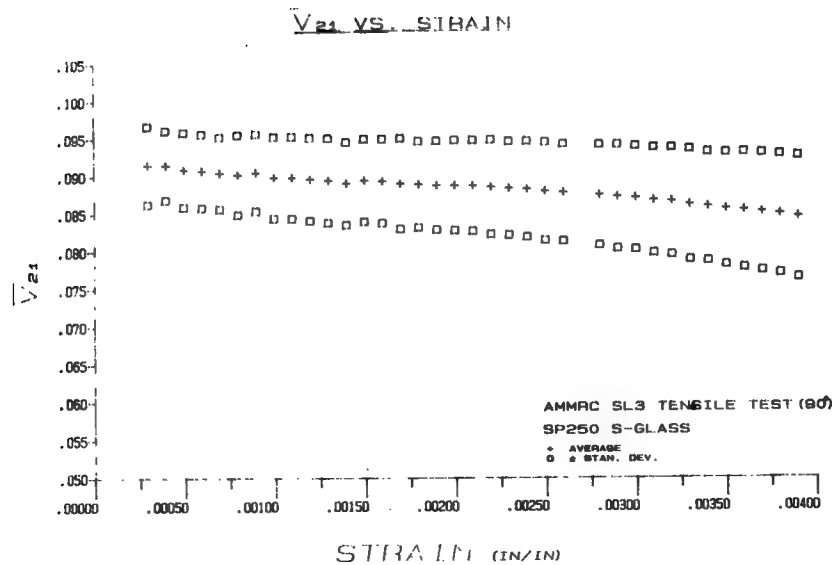
Figure 3   Lamina Mechanical Properties

372
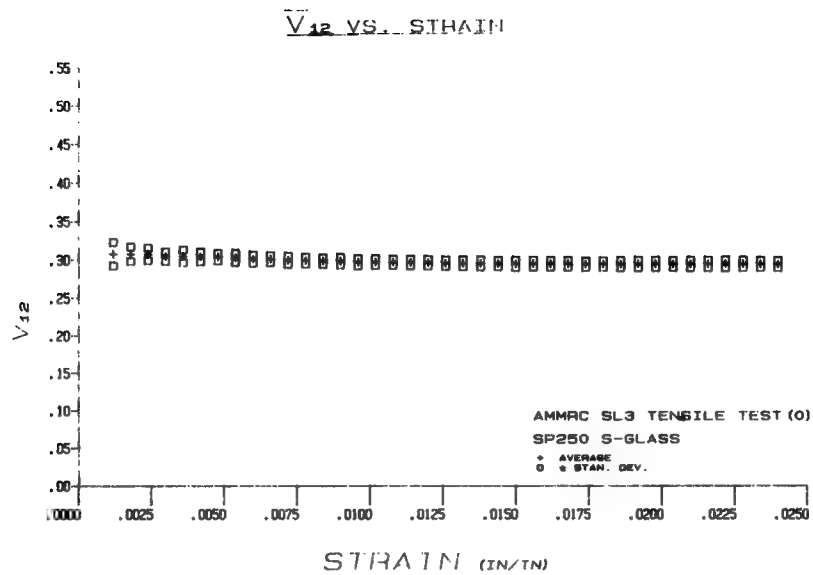
Figure 3   Lamina Mechanical Properties

EXPERIMENTAL STUDY OF MECHANICALLY-FASTENED COMPOSITES

Gary Cloud, Professor
Pedro Herrera, Research Assistant
Metallurgy, Mechanics and Materials Science Department
Michigan State University
East Lansing, MI 48824-1226

EXTENDED ABSTRACT

The mechanics of fasteners in composites were studied in a combined experimental-theoretical research program (1). The objectives were to gain fundamental insight into the stress-strain field in the vicinity of pin-type fasteners of various kinds and to provide sound guidance to designers responsible for the selection and sizing of fasteners for different applications. This paper concentrates on the experimental phase of the program.

EXPERIMENTAL METHODS

The primary experimental method utilizes Moire interference with optical Fourier processing of grid photoplates. Rugged grids are applied to the specimen by vacuum-deposition, and these grids are recorded for each state of the specimen using high-resolution techniques. Sequential recording of grating replicas and subsequent coherent optical processing to obtain enhanced fringe patterns, often with multiplied sensitivity, allow quantitative comparisons between any two states of the specimen at any later time. Such a procedure is especially advantageous in nonreversible structural testing. Complete descriptions of this approach appear in reports and papers by the authors' group (2-9), so further description is not needed here.

It soon became clear that the Moire technique as summarized above has a strain sensitivity which is marginal for work on composites, as was expected. Consequently, while this method was being used on the first specimen in this project, a program to extend the sensitivity by a factor of 10 or more was begun. In order to compare theoretical and experimental results in this project, the constitutive properties of the material studied had to be measured.

The material used was fiber glass-epoxy laminate with woven fibers (R1500/1581, 13 plies, 0.14 in thick) supplied by GIBA-GEIGY, Composite Materials Department, 10910 Talbert Avenue, Fountain Valley, California 92708. The dimensions of typical specimens are shown in Figure 1. Two-way metallized grids having 2000 lines per inch were applied to the specimen in the regions of the holes.

The specimen was then loaded and the grid photographed for each load increment using a Horseman view camera with a Zeiss s-planar lens of 120mm F.L. at F5.6. The resulting photoplates were superimposed with master gratings in a coherent Fourier optical processor to obtain Moire fringe patterns indicative of displacement. The fringes were digitized and fed to a computer to obtain the desired strain maps. Figure 2 is a typical fringe photo. Figures 3 and 4 are typical strain plots. Figure 5 shows a distribution of strain based on the results from the Moire fringes.

Experimental evaluation of elastic constants

Determination of E_1, E_2 and ν is quite straight forward. Two tensile tests are required, and for this purpose two specimens were constructed: one

with the warp fibers oriented along the direction of the loading (for determination of E_1 and ν_{12}) and the other with woven (weft) fibers in the direction of loading (for determination of E_2 and ν_{21}). Four single-element strain gages of type EA-13-075AA-120 from Micromeasurements were used to check the uniformity of the stress field. Strain gage rosettes on both faces of the specimen were also used (type CEA-06-062UR-120), first to determine any effect of bending on the specimen and then to obtain the measurements needed. The results obtained for Young's modulus and Poisson's ratio are as follows: $E_1 = 3.188 \times 10^6$ psi; $E_2 = 3.0824 \times 10^6$ psi; $\nu_{12} = 0.11$; $\nu_{21} = 0.11$.

DISCUSSION

From the many strain plots obtained we find that, in the area of contact between pin and composite, ε_y is highly compressive; but, as we move away from the edge of the hole towards the end of the specimen, its value decreases to an average value. Now, looking at the right hand edge of the hole, ε_y is of tensile nature; as we move away from the edge of the hole towards the edge of the specimen it decreases to an average value.

Much more information useful to the designer can be extracted from these Moire photographs. As an example, examine the areas shown in Figure 5 where the normal strain, ε_y, changes from tensile to compressive. Along that interface, we find a very high shear strain which in some cases can produce delamination and/or failure by shearing, especially along the transition zone from high compressive strain to tensile strain near the fastener. Such features of the Moire results allow the designer to get useful information anywhere on the surface of the specimen providing better criteria for the determination of the optimum combination of parameters such as distance from hole to edge, ratio of pin to hole diameters, fiber orientation, lay-up sequence, etc.

High-sensitivity Interferometric Moire Technique

From the results for ε_x (the smaller strain component), it is clear that the Moire technique as described has a marginally low strain sensitivity for work on composite materials.

An interferometric technique similar to that described by Post (10, 11) and Walker, Mckelvie and McDonach (12) was developed. In this interferometric Moire technique, the specimen grating is a phase-type grating. The analysis is carried out by using the overlapping beams of coherent light to create the specimen grating and the master grating which is projected onto the deformed specimen.

Important virtues of the system developed for this investigation are:

1. No rigid connection is required between the specimen and the system. This feature is relevant in view of the convenience of performing measurements in environments which are not so ideal as a vibration-free optics laboratory.

2. Measurements can be performed in three different directions, yielding a map of strains in the same number of directions and allowing calculations of maximum strains.

3. Grating frequencies are easily adjusted to suit the problem. Typical frequency for composite work is 20,000 lines per inch.

Preliminary testing of this technique has been conducted and the results are promising. Figures 6 shows Moire fringes of displacement in the x-direction (perpendicular to the direction of the loading).

COMPARISON BETWEEN EXPERIMENTAL AND NUMERICAL RESULTS

This paper describes the methodology of obtaining strain in the actual composite material by Moire techniques which are self-calibrating and which do not depend on assumptions of material behavior. Typical results are reported. A companion paper (13) describes a boundary-element approach to the problem and gives results from that method. Some finite element results are also computed and used for comparison of the two numerical approaches.

It is instructive and valuable to designer, theoretician and experimentalist to compare the results from these widely diverse approaches to the problem. Since the methods are so different, good agreement of results would imply that the results are probably correct. Disagreement would give an idea of the magnitudes of errors in either or both sets of results.

To perform the comparison, some strains measured by Moire were converted to stress by use of generalized Hooke's law. This procedure inserts an assumption of material behavior into the experimental findings, but it does facilitate comparison. It is probably more reasonable, but also more difficult, to use Hooke's law to convert the numerical results to strain. The conversion of experimental data was carried out for ϵ_y at selected points along the ligament line between hole boundary and specimen edge. These stresses were normalized, then plotted. They are compared with the matching finite element values. The comparison is shown graphically in Figure 7.

CLOSURE

The two Moire methods described above have a very broad range of potential application. In addition to the simple fastener geometry discussed herein, interesting results have been obtained for cases involving molded-in-place load-spreading inserts; and studies of hybrid joints and multiple-fastener arrays are beginning.

ACKNOWLEDGEMENT

REFERENCES

1. Cloud, G., Sikarskie, D., Mahajerin, E., Herrera, P., "Theoretical and Experimental Investigation of Mechanically Fastened Composites," contract report, U.S. Army Tank-Automotive Research Command TACOM, Warren, MI 48090, 1984.
2. Cloud, G., "Simple Optical Processing of Moire-grating Photographs," Exp. Mech., 20, 8, 265-272 (Aug. 1980).
3. G. Cloud, Radke, R., and Peiffer, J. "Moire Gratings for High Temperatures and Long Times," Exp. Mech. Vol. 19, No. 10, 19N-21N. Oct. 1979.
4. Cloud, G., Paleebut, "The Dimensional Nature of Strain Field Near Coldworked Holes." AFWAL-TR-80-4204, Wright-Patterson AFB, Ohio (1980).
5. Paleebut, Somnuek, "An Experimental Study of Three-dimensional Strain Around Coldworked Holes and in Thick Compact Tension Specimens," Ph.D. Thesis, Michigan State University, Department of Metallury, Mechanics and Materials Science, 1982.
6. Cloud, G., "Residual Surface Strain Distributions Near Holes Which are Coldworked to Various Degrees," Technical Report AFML-TR-78-153, Wright-Patterson AFB, Ohio (1980).
7. Cloud, G., "Measurement of Strain Fields Near Coldworked Holes," Experimental Mechanics, 20, 2, 9-16, (January 1980).

8. Cloud, G., and Sulaimana, R., "An Experimental Study of Large Compressive Loads Upon Residual Strain Fields and the Interaction Between Surface Strain Fields Created by Coldworking Fastener Holes," Technical Report AFML-TR-80-4206, Wright-Patterson AFB, Ohio (1980).
9. Cloud, G., and Tipton, M., "An Experimental Study of the Interaction of Strain Fields Between Coldworked Fastener Holes," Technical Report, AFML-TR-80-4205, Wright-Patterson AFB, Ohio (1980).
10. Post, D., "Optical Interference for Deformation Measurements-Classical, Holographic and Moire' Interferometry" Mechanics of Nondestructive Testing Proceedings, edited by W.W. Stinchcomb, Plenum Publishing Corp., NY (1980).
11. Post, D. and Baracat, W.A., "High Sensitivity Moire Interferometry--A Simplified Approach," Exp. Mech. 21, 3, 100-104 (March 1981).
12. McDonach, A., McKelvie, J., Mackenzie, P., and Walker, C.A., Proceedings of the V International Congress on Experimental Mechanics, Montreal, Canada June 10-15,1984 pp. 308-313.
13. Sikarskie, D., and Mahajerin, E., "Theoretical Studies of Mechanically-Fastened Composites," Proc. Army Symposium on Solid Mechanics, 1984, Oct. 1-3, Newport, RI, AMMRC, Watertown, MA.
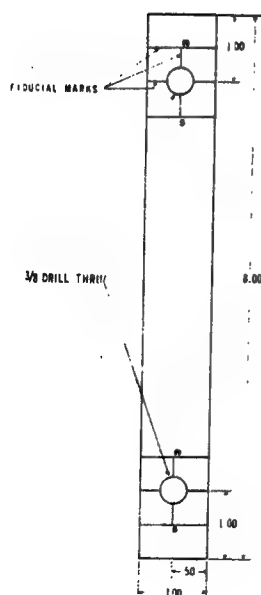
Figure 1. Dimensions of the test coupon
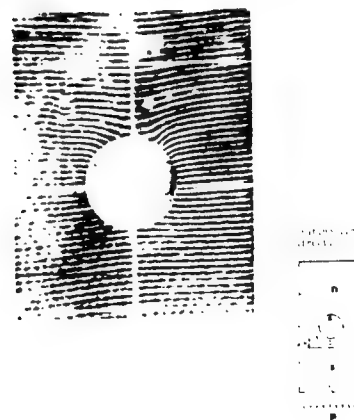
Figure 2. Photograph of Moire pattern showing displacements parallel to load line for 400 lb. load with pitch mismatch.
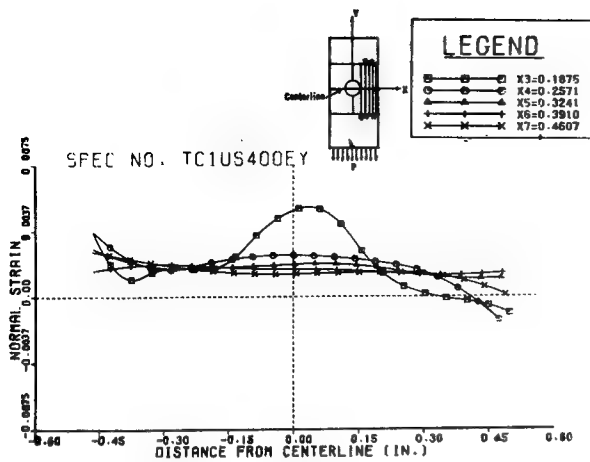
Figure 3. Strain parallel to load axis (ε_y) along several lines encompassing a ligament region.
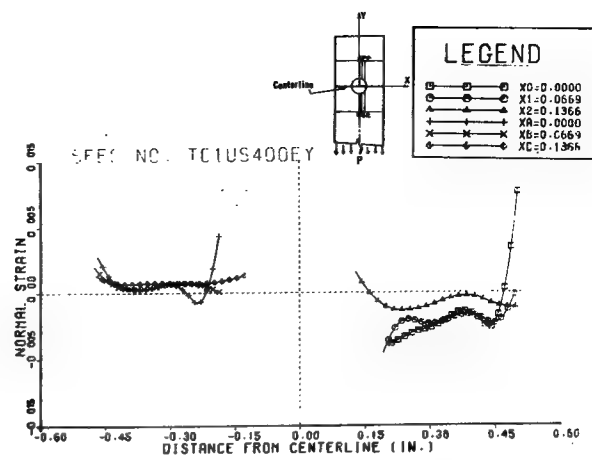

Figure 4. Strain parallel to load axis (ε_y) along several lines in and opposite to the bearing region.
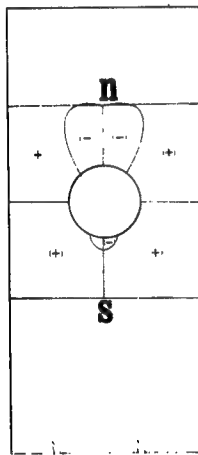

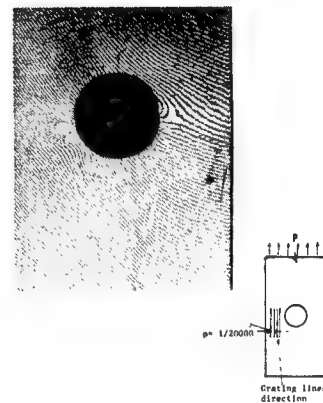Figure 5. Distribution of tensile and compressive strain (ε_y) near the fastener hole.

Figure 6. High sensitivity Moire fringes showing displacements perpendicular to the direction of loading for 130 lb. load with rotational mismatch.
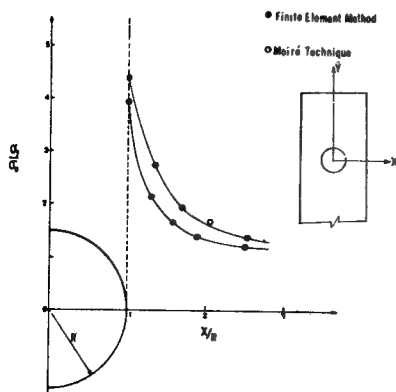

Figure 7. Comparison of stress concentration factors obtained by numerical and experimental techniques.

STRESS INTENSITY NEAR BLUNT FLAWS

D. M. TRACEY and C. E. FREESE
Army Materials and Mechanics Research Center
Watertown, MA 02172

The work is concerned with the stress state near the ends of cracklike flaws in elastic-plastic metals. The flaws being considered have rounded ends, but are cracklike in the sense that flaw length greatly exceeds the radius of curvature at the ends. Knowledge of the stress conditions ahead of such flaws is important to various strength and failure issues; e.g., the elongation of impurity debonding flaws and crack initiation ahead of machined flaws in fracture testing.

There has been very little work done on the elastic-plastic cracklike flaw problem. Plasticity effects are generally discussed in terms of the local slipline predictions, even though the limits of applicability of these predictions are often unknown. With fracture theories based upon stress averaging over microstructural dimensions, for instance, the need for refined solutions near a flaw is clear. There exists considerable information on the stress state ahead of mathematically sharp cracks. However, in many cases the desired information in the region of influence of the root geometry is not provided by the sharp crack singular solutions. There has been very noteworthy work published in the current literature on the solution ahead of cracks which have blunted as a result of large plastic deformations incurred during loading. In the present work, we are concerned with the flaw which is blunted in the stress-free state and which is not so sharp that finite deformation blunts it further in contained plasticity situations.

Computer methods of stress analysis are being used to perform the study. The single most difficult feature of the blunt flaw problem is accommodating the relative smallness of the root radius in the discretization. In the analysis of engineering notches or even sharp cracks, the controlling dimensions are usually of the same order of magnitude. In contrast, for the case that we preset below, the root radius is smaller than the crack length by a factor of 2000. Since details of the stress variations in the region influenced by the root geometry is desired, grid dimensions must be fractions of the root radius.

We have developed a special numerical formulation which can readily accommodate the blunt flaw problem. Elasticity theory complex stress function techniques are used to represent the solution everywhere except in the root region. In this region, finite elements are used to account for yielding and plastic deformation. Our attention has been directed to the problem of a flaw under low magnitude remote tensile loadings. Load magnitudes were such that the plastic zone extended no more than 4% of the flaw length from the ends of the flaw. The formulation allows treatment of infinite domains and thus the case of a flaw outside the influence of other boundaries. For the small plastic zone case, the discretization for refined root analysis is easily attained.

Results for a flaw with semi-circular root are presented in Figure 1. Numerical data are given for load levels from $T = 0.18Y$ to $.28Y$. Here T is the value of remote tension and Y is the yield stress of the nonhardening Prandtl-Reuss material which was modeled. The solid curve is the slipline prediction for this root geometry. It can be seen that neither the stress maximum nor its location is accurately predicted by slipline theory. The reason for this is related to the fact that fully plastic conditions do not develop at the top of the flaw surface, but only extend part way up the semi-circular root. The bottom slipline in the figure serves as a approximate demarcation line for the region that has reached fully developed plasticity conditions.

The discussion will include more details of the stress solutions, the evolution of the plastic zone, strain magnitudes and sensitivity of these results to root shape. Application of these results in fracture studies will be addressed. Finally, comparisons will be made with sharp crack solutions.
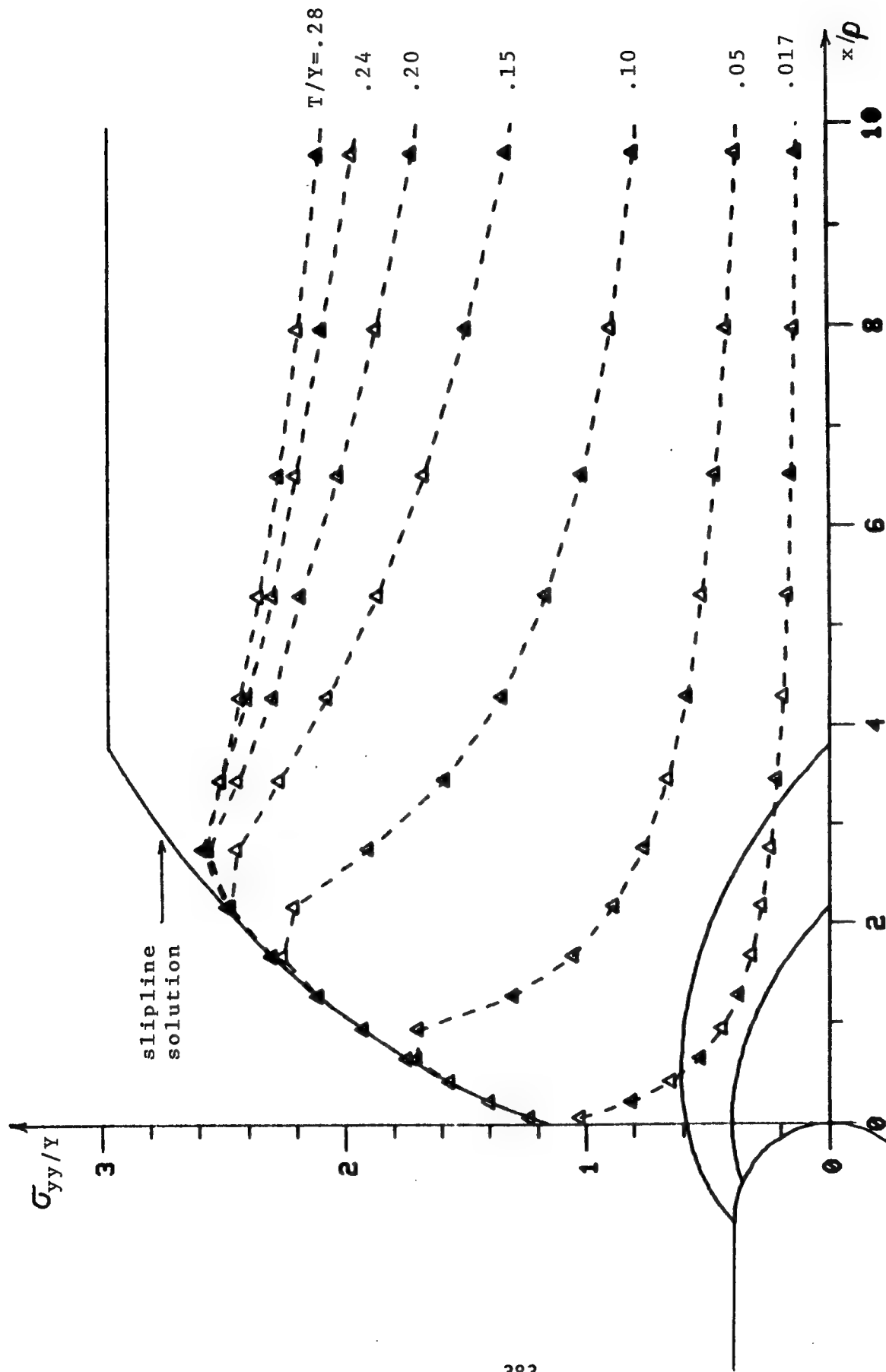
FIGURE 1. ELASTIC-PLASTIC STRESS DISTRIBUTIONS FOR BLUNT FLAW

MODELING BOUNDARY CONDITIONS IN ELASTIC-VISCOPLASTIC FORMING PROBLEMS

Daniel C. Peirce
Arthur D. Little, Inc.
Cambridge, MA. 02140

EXTENDED ABSTRACT

During the past decade, considerable progress has been made in computer modeling of large deformation forming problems. The most extensive work, done primarily at the University of California at Berkeley and Battelle's Columbus Laboratories, has employed a rigid-viscoplastic constitutive model. Such models, by neglecting the stiff response associated with elastic behavior, have enabled numerical analysts to solve highly nonlinear mechanics problems with larger and fewer increments. In problems with phenomena like spring back or high residual stresses, however, it is important that the elastic material response not be omitted from consideration. Research has continued on elastic-viscoplastic constitutive models, and schemes for implementing them more efficiently have been developed. A finite element code based on such methodology has been developed at Arthur D. Little, Inc., and has been applied to a number of prototype problems in forming of elastic-viscoplastic materials.

In order for such a computer code to be applicable in practical situations, it must be able to address the wide variety of boundary conditions that may arise: contact, release, frictional sliding, and curved boundaries are good examples. The work to date has focused on developing an appropriate framework for handling contact and release; the aim is to incorporate frictional behavior as the work continues.

The displacement finite element method on which the computer code is based makes use of the principle of virtual work in the following form:

$$\int_{Vo} \tau^{ij} \, \delta\dot{n}_{ij} \, dV = \int_{S_o} T^i \delta\dot{u}_i \, dS \tag{1}$$

Here, n_{ij} are increments of the components of Lagrangian strain, which are derivable from the displacements u_i as

$$\dot{n}_{ij} = 1/2(\dot{u}_{i,j} + \dot{u}_{j,i} + \dot{u}^k_{,i} u_{k,j} + u^k_{,i} \dot{u}_{k,j}) \tag{2}$$

where a comma denotes covariant differentiation in the reference coordinate system. Also in (1), τ^{ij} are the contravariant components of Kirchhoff stress on the current coordinates, T^i are components of the nominal traction vector, and V_o and S_o are volume and surface in

385

the reference configuration. Incrementally, the principle of virtual work in (1) becomes

$$\int_{V_0} (\dot{\tau}^{ij} \delta\dot{\eta}_{ij} + \tau^{ij} \dot{u}^k_{,i} \delta\dot{u}_{k,j}) \, dV =$$

$$\int_{S_0} \dot{T}^i \delta\dot{u}_i \, dS + \left[\int_{S_0} T^i \delta\dot{u}_i dS - \int_{V_0} \tau^{ij} \delta\dot{\eta}_{ij} \, dV \right] \quad . \quad (3)$$

The bracketed terms on the right of (3) serve as an equilibrium correction when (1) is not satisfied exactly at a particular stage of an incremental calculation; these terms also play an important role in our approach to contact and release.

During a forming operation, it is typical for a point on the boundary of a workpiece to be free initially and then to contact the tooling at a later stage of the process. When modeling this phenomenon incrementally, the contact will only be noticed at the end of a step, and then the point in question will have actually penetrated the tooling instead of stopping at its surface. This difficulty is overcome by altering the incremental displacement of the point in question so that it does in fact coincide with the tooling surface. In the next increment, the bracketed terms in (3) provide correction forces so that points in the vicinity of the adjusted point will also relocate appropriately.

Conversely, points already in contact with the tooling may release under conditions of negative pressure. Such points may be easily recognized by making use of (1). At any point on the surface of the workpiece, the nominal tractions at the end of an increment may be recovered by using the current stress state to calculate the left hand side of (1). These tractions may be simply related to the normal pressure, and the point will be released in the next increment if the pressure is negative.

A sample problem where the above considerations come into play is the heading of an axisymmetric tube, as shown in Figure 1. As a first cut at modeling this problem, five nine-node elements were used. Both initial and deformed configurations are shown in Figure 2. The curvature of the mesh compared to the sharp lines of the dies shows that more nodes, and hence more elements, are necessary to match the die shapes accurately. Nevertheless, the schemes outlined above limited the outward radial expansion of the tube, and dealt with the complex die shapes sucessfully.

STRESS DISTRIBUTION IN A STEEL MODEL OF
AN OVERLOADED BREECH RING

P. C. T. Chen and G. P. O'Hara
U. S. Army Armament, Munitions, and Chemical Command
Armament Research and Development Center
Large Caliber Weapon Systems Laboratory
Benet Weapons Laboratory
Watervliet, NY 12189

EXTENDED ABSTRACT

In guns with a sliding breech mechanism, breech ring failures have been observed originating from the lower fillet in the vicinity of the contact region. There have been a considerable number of photoelastic studies done on weapon breeches of this type. The observations indicate that high tensile stress produced by stress concentration at the fillet was responsible for the failure. Sometimes failure can be prevented by changing the geometry, adding more weight and/or using higher strength materials. Often it is either too expensive or simply not permitted to do so. Autofrettage has proved to be an efficient coldworking process in manufacturing gun barrels. The elastic carrying capacity and the fatigue life can be increased. The technique is based on the production of beneficial residual stresses through coldworking to counteract the high operating stresses induced by firing. An exploratory study on the autofrettage of a breech mechanism has been made using a two-dimensional polycarbonate material model. The residual stresses at the fillet of an overloaded breech ring have been determined by means of photoplasticity and finite element analysis (1).

This paper describes a further numerical study on a two-dimensional steel model of an overloaded breech ring. An experimental investigation of fillet stresses for this model was obtained by means of photoelastic coating technique (2). The maximum stress at the boundary was reported but no information about the stress distribution. The finite element program ADINA, developed by K. J. Bathe (3), is used for this purpose. The geometry of this two-dimensional steel model is discretized by 8-nodes isoparametric elements as shown in Figure 1. The material is assumed to obey the von Mises yield criterion, the Prandtl-Reuss flow theory, and the isotropic hardening rule. The numerical results of the stresses at all points were obtained as functions of loading history. There are three stress components at each of the 9N points where N is the number of elements and 3x3 points are used in carrying out the numerical integration. A stress contour at one stage of loading is shown in Figure 2. The location and magnitude for the maximum fillet stress have been found. The calculated boundary stress, determined by extrapolation, agrees very well with the experimental result as shown in Figure 3.

References:

1. P. C. T. Chen and Y. F. Cheng, "Stress Analysis of an Overloaded Breech Ring," ASME Century 2 Emerging Technology Conferences, Proc. Int'l Conf. on Reliability, Stress Analysis and Failure Prevention, Aug 1980, pp. 175-180.

2. Y. F. Cheng, "An Experimental Investigation of Stresses in a Steel Model of an Overloaded Breech Ring by Means of Photoelastic Coating Technique," ARLCB-TR-80038, Aug 1980.

3. K. J. Bathe, "ADINA Users' Manual," Report AE-81-1, ADINA Engineering, Inc, Watertown, MA, 1981.
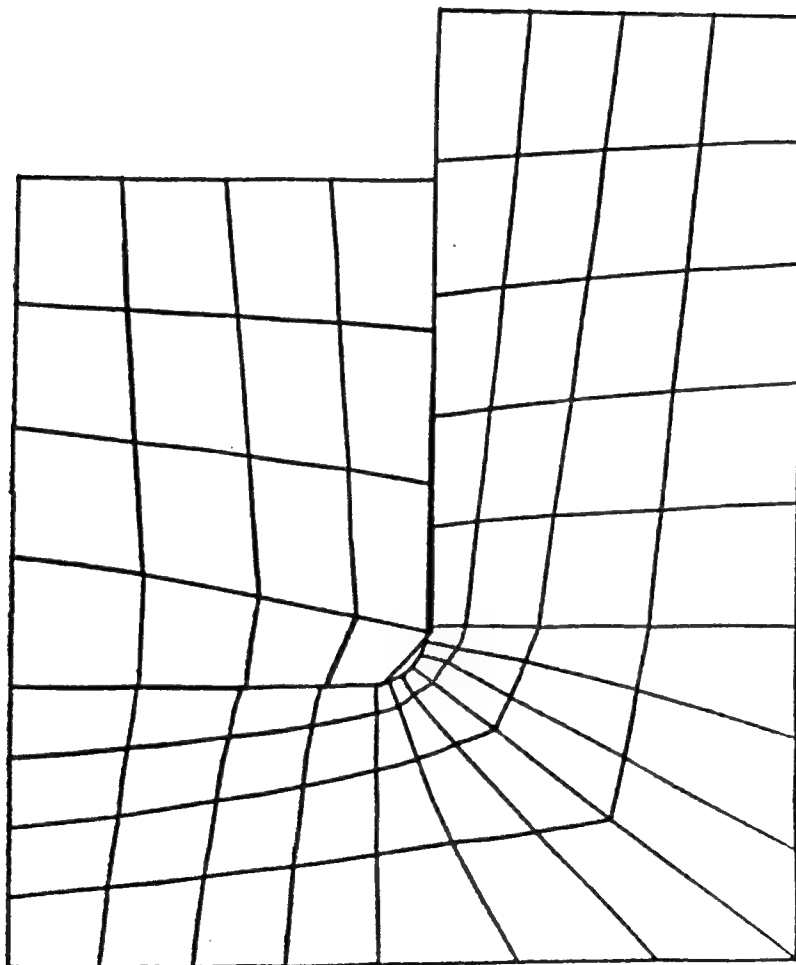
Figure 1. A finite element model for breech mechanism

Figure 3. Major principal stress along a radial direction.

L,M,N,O,P,Q = 10,20,30,40,50,60 ksi, respectively

Figure 2. Effective stress contour near the fillet.

HIGH STRAIN-RATE MATERIAL MODELING

A.M. Rajendran
Research Engineer

S.J. Bless
Research Physicist

University of Dayton Research Institute
Dayton, OH   45469

R. Garrison
Mechanical Engineer
David Taylor Naval Ship R&D Center
Code 1740.3, Maryland 20084

Our objective is to develop constitutive models for use in finite element/difference simulations of impact and explosive events. Such events involve complex load histories and high to ultra-high strain rates. Therefore, we have used test techniques that subject materials to both compressive and tensile stress states at a variety of strain rates. We have employed constitutive models that explicitly include history and strain rate dependencies.

Experiments were conducted with a split Hopkinson bar (SHB). The bar was used for compression and tension tests, using the techniques described in Reference 1. The state-variable-based constitutive model of Bodner and Partom (B-P) (Reference 2) was used to analyze the test results. The B-P model has been successfully programmed into the STEALTH finite difference code and MAGNA finite element code.

The B-P model expresses the plastic strain rate, $\dot{\varepsilon}^p_{ij}$, as follows:

$$\dot{\varepsilon}^p_{ij} = D_o \exp \left\{-\left(\frac{Z^2}{3J_2}\right)^n \left(\frac{n+1}{2n}\right)\right\} \quad \frac{S_{ij}}{\sqrt{J_2}} \tag{1}$$

where J_2 is the second invariant of the stress deviator S_{ij}. D_o and n are material constants. Z is a plastic work dependent state variable that takes the form

$$Z = Z_1 - (Z_1 - Z_o)e^{-mW_p} \tag{2}$$

where

$$W_p = \int \sigma_{ij} \dot{\varepsilon}^p_{ij} \, dt. \tag{3}$$

Z_o, Z_1, and m are material constants.

The materials investigated were C1008 steel and 7039-T851 aluminum. SHB data were obtained in tension and compression for many different strain rates. Each tensile test is at essentially constant strain rate; the strain rate decreases continually during each compression tests. The range of strain rates was 300/s to 3000/s. The data show that steel is strongly rate dependent, while aluminum is relatively rate independent. Because of their different behavior, these two materials provide a good test for the constitutive modeling technique.

An algorithm consisting of a series of programs was developed to derive the best values for B-P coefficients from tensile data. The validity of the model and coefficients was checked in two ways: by their ability to describe the observed tensile loading curves, and by their ability to predict the results of compression tests.

The values of the B-P parameters for these materials are given in Table 1. By both measures of success, the model performance was fully satisfactory. Comparisons with tensile data are shown in Figure la and lb, and with compression data in lc and ld. Quasi-static tensile data are also included in these figures to show the rate dependency of the materials,

This work has demonstrated the feasibility of employing general visco-plastic models that explicitly include history and strain rate effects. Procedures have been developed for evaluating and calibrating the models over a range of stress states and strain rates.

REFERENCES

1. Nicholas, T., "Material Behavior at High Strain Rates," Impact Dynamics, John Wiley, New York, Chapter 8, pp. 277-331, (1981).

2. Bodner, S. R. and Partom, Y., "Constitutive Equations for Elastic-Viscoplastic Strain Hardening Materials," J. Applied Mechanics, Vol. 42, pp. 385-389. (1975).

TABLE 1

BODNER-PARTOM MATERIAL CONSTANTS

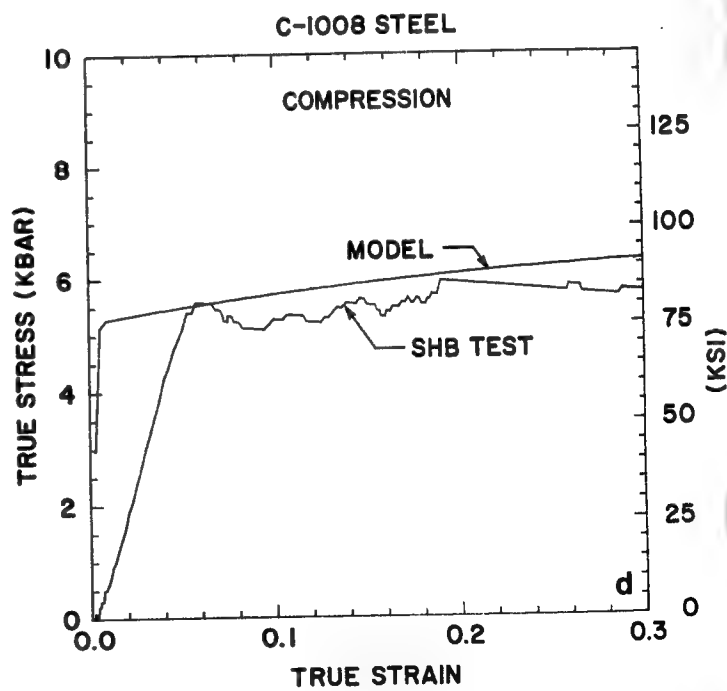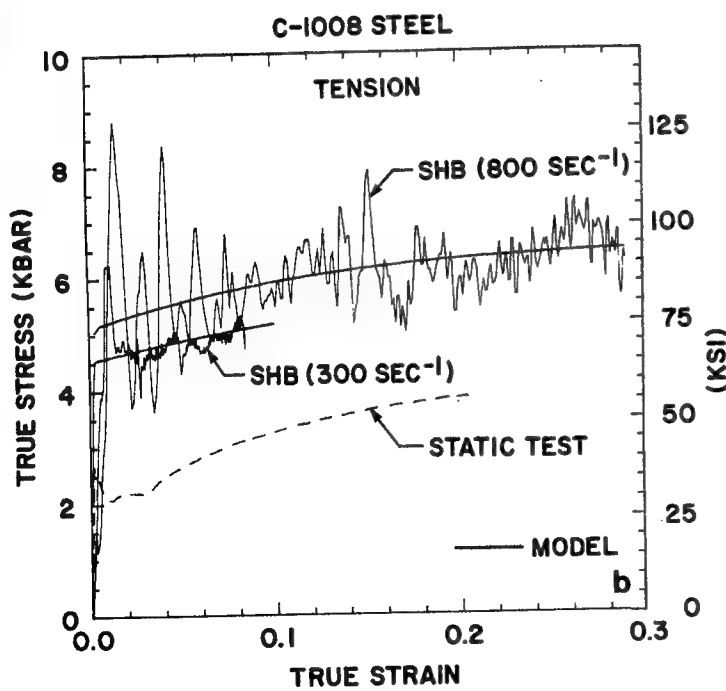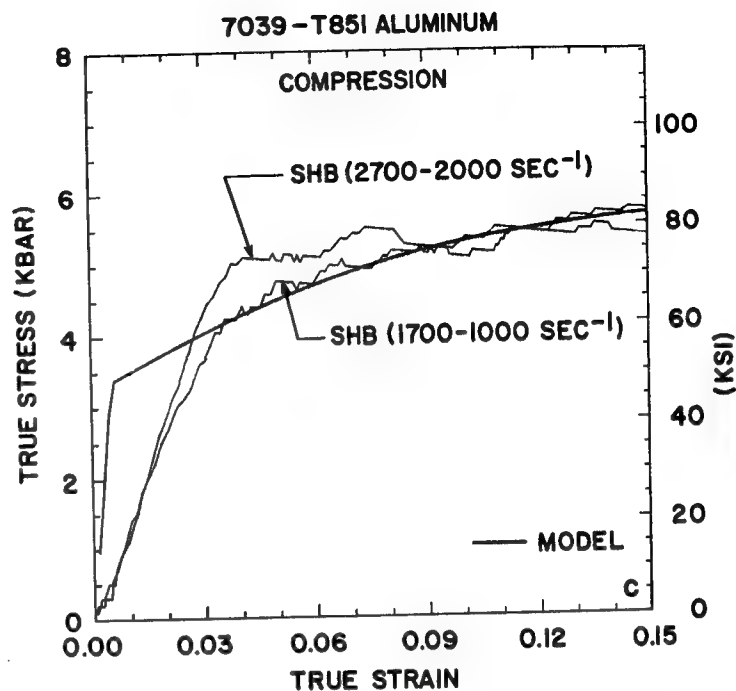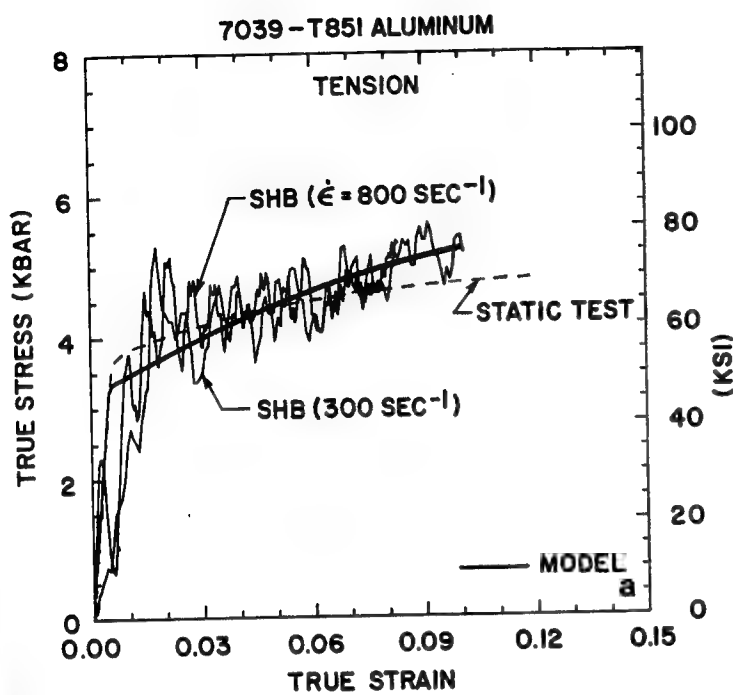| MATERIAL	n	m KSI^{-1} $(KBAR^{-1})$	Z_o KSI (KBAR)	Z_1 KSI (KBAR)	D_o sec^{-1}
C1008 Steel	0.4	0.1034 (1.5)	798 (55)	1015 (70)	10^8
7039-T851 Aluminum	5.0	0.2413 (3.5)	65 (4.5)	115 (7.9)	10^8

Figure 1.   Comparison of Bodner-Partom Model Predictions
With SHB Test Results.

PREDICTION OF ULTIMATE STRENGTH
OF COMPOSITE CURVED FRAME MEMBERS

ROCKY RICHARD ARNOLD, Ph.D.
Principal Engineer

JATIN C. PAREKH
Engineer

Anamet Laboratories, Inc.
San Carlos, California 94070

EXTENDED ABSTRACT

The research discussed herein concerns the development of a theoretical and analytical approach for the prediction of ultimate strength of composite curved frame members (Figure 1). The theoretical derivation includes important physically observable characteristics of composites not usually included in conventional elasticity theories, such as effects of transverse shear, nonlinear geometry, and nonlinear material behavior. The formulation utilizes an energy approach based on the Reissner variational principle [1] in which both dispacement and stress are taken to be variationally unknown. The resulting system of nonlinear algebraic equations can be easily programmed on a modern digital computer, providing the designer with an accurate and inexpensive method for the design of composite (or metal) curved frame members. Comparisons with available experimental test data from an on-going NASA-sponsored effort are used to substantiate the theoretical formulation.

This research is funded by NASA through the Small Business Innovative Research (SBIR) Program. The Phase I feasibility research has been completed. The Phase II principal research proposal has been submitted to NASA. During the Phase I effort the theoretical model for the curved frame was defined and the governing equations derived. These equations will be programmed during Phase II. Also, during Phase II, the computer program developed will be validated by additional experimental testing to be performed by Sikorsky Aircraft.

Currently, NASA is funding Sikorsky Aircraft (NAS1-16826) in an effort to design, fabricate and test composite curved frames for helicopter fuselage structures. To date, this program has followed a rather typical process for composite structures -- design, test, redesign and test with the newer designs showing small but meaningful improvements in structural performance. The inability to accurately predict performance and the influence of geometry

and materials on the overall behavior of the structure is certainly a major obstacle to further development efforts. For this reason, the present research is relevant and offers potentially substantial benefits to the manufacturers of aircraft.

To a large extent, the theoretical approach follows that of Arnold and Mayers [2] in which, for the first time, the postbuckling behavior of rectangular, flat laminated composite plates was accurately predicted to failure. The key elements of the approach are the inclusion of (1) material inelasticity in the anisotropic lamina (2) transverse shear in the laminate and (3) a simple failure criterion found by correlation to tests to be quite adequate. Through the use of the Reissner potential energy, a relatively general computerized algorithm that requires only the specification of the displacement and stress distributions was constructed. The final set of equations is quite imposing when written in their entirety; however, they represent a relatively small problem from the computational viewpoint. The computer program is fast, easy to use, and can operate in an interactive environment. Best of all, the solution is closed-form, that is, finite elements are not used.

All of the virtues of the nonlinear mechanics theory described above are retained in the present formulation for the composite curved frame member. The modeling approach consists of idealizing the curved frame member as an assembly of three basic structural elements (Figure 2). The top and bottom flanges are assumed to be curved plates. The web is assumed to be a shear resistant member with no out-of-plane displacement allowed. Finally, the uprights are present to carry the crushing loads that occur between the upper and lower flanges. Each element is a composite laminate composed of materially inelastic anisotropic laminae. The curved plate elements incorporate geometric nonlinearities. Constraint relations are introduced to account for the distributed internal forces between the flanges and the web and uprights.

The ultimate goal of this research is to provide NASA and the government with a design tool which is both accurate and cost-effective.

REFERENCES

1. Reissner, R. L., "On a Variational Theorem in Elasticity," Journal of Mathematics and Physics, Vol. XXIV, No. 2, July 1950, pp. 90-95.

2. Arnold, R. R., and Mayers, J., "Buckling, Postbuckling, and Crippling of Materially Nonlinear Laminated Composite Plates," accepted for publication in the International Journal of Solids and Structures.

3. Rich, M. J., and Lowry, D. W., "Design, Analysis and Test of Composite Curved Frames for Helicopter Fuselage Structure," Paper No. 83-1005, Proceedings of 24th AIAA/ASME/ASCE/AHS Structures, Structural Dynamics and Materials Conference, 1983, PP. 730-737.
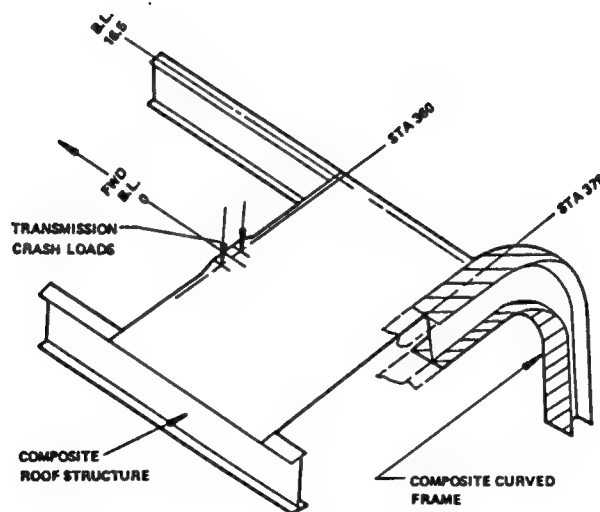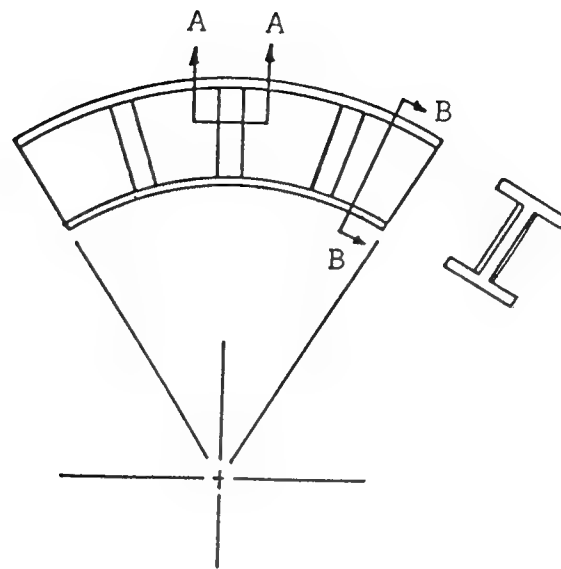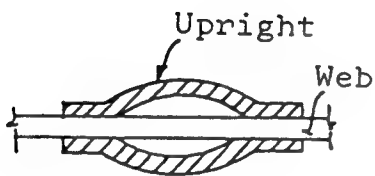
Figure 1   Composite Curved Frame Member Selected From
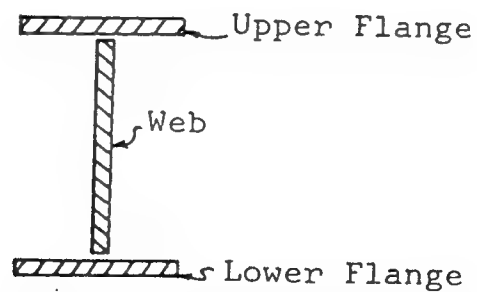BLACK HAWK Cabin Fuselage [3]

(a)   Basic CFM

(b) Upright Geometry (left) and Equivalent Model (right)

(c)   Flange/Web Structural Elements

Figure 2   Basic Structural Elements of the Composite
Curved Frame Member

Interaction of Rotating Band and Rifling Grooves

H.P. Chen
Post Doctoral Fellow
School of Aerospace Engineering
Georgia Institute of Technology
Atlanta, GA 30332

T. Tsui
Mechanical Engineer
Army Materials & Mechanics Research Center
Watertown, MA 02172

S. Hanagud
Professor
School of Aerospace Engineering
Georgia Institute of Technology
Atlanta, GA 30332

EXTENDED ABSTRACT

1. INTRODUCTION

The interaction, between the rotating bands and the rifling grooves, is usually used to provide the desired angular acceleration to a projectile as the projectile accelerates along the length of the barrel of a gun. This interaction is accomplished in the following way. Before entering the barrel, a fired projectile enters a "forcing cone". The outer diameter of the projectile is usually designed to be smaller than the minor diameter of the bore. However, the outer diameter of the rotating band which is located on the outer hard surface of the projectile is larger than the minor diameter of the bore. As a result, the radial dimensions of the rotating bands are reduced in the forcing cone. The reduction in the radial dimensions is followed by a circumferential flow into the rifling grooves and an axial flow along the length of the projectile. The rifling grooves have a twist along the length of the barrel. It is the combination of the aforementioned deformation of the rotating band and the designed twist of the rifling along the length of the barrel that results in an angular acceleration being imparted to the projectile as the projectile travels along the length of the barrel. Evaluations and improvements of the design of rotating bands need an understanding of the stresses and deformations of the rifling, the rotating band and the projectile combination in the forcing cone and the barrel.

2. PROBLEM SETTING AND PROGRESS

Before discussing the specific problems, it is noted that there are certain basic requirements on the rotating band material and geometry. The rotating band must have sufficient "plastic flow characteristics" to deform from its initial configuration to a shape dictated by the forcing cone and the rifling needs. At the same time, the rotating band must have sufficient strength to

(a) transmit the torque to the projectile,
(b) withstand the propellant gas pressure, and
(c) provide the needed attachment characteristics to the projectile.

403

As a consequence of these requirements, the current investigation of the stresses and deformations of the rotating band has considered the following specific parameters.

(a)   flow strength of the rotating band material, e.g., copper,

(b)   breathing strength of the cylinder,

(c)   depth of the rotating band, and

(d)   the interference.

Specifically, the first year studies have considered the circumferential flow of the rotating band material into the rifling grooves. It is to be noted that the axial flow problem alone has been studied in the past.

As discussed before, the circumferential flow results from the interaction of the rotating band and the rifling. The result of the interaction is the reduction of the radial dimensions of the rotating band and the flow of the rotating band material into the rifling grooves. In order to study the effect of the parameters such as the flow strength of the rotating band material, breathing strength of the projectile cylinder, depth of the rotating band and the interference on the circumferential flow, an approximate two-dimensional problem of the circumferential flow has been formulated. The approximate two dimensional plane strain problem is as shown in Figure 1. The gun barrel is assumed to move in the y direction into the rotating band. The initial velocity of the gun barrel has been calculated on the basis of the longitudinal velocity of the projectile and the amount of the interference. The gun barrel is assumed to be made of a specified steel. The rotating band is assumed to be made of copper and the projectile is assumed to be made of a titanium alloy. From the relative differences of the material properties assumed above, the following assumptions are made in the first stage of the analysis.

(a)   gun barrel and projectile are assumed to be rigid and

(b)   perfect bonding is assumed between the rotating band and the projectile.

From these assumptions, the final stage of the circumferential flow where the rifling grooves have interfaced with rotating band is shown in Figure 2. The dimensions for a specific case are shown in Figure 1. It is known that the strain rate effects are not very significant for copper that is usually used in the rotating band and is neglected in the analysis. The material model of the rotating band is assumed as an elastic-perfect plastic material.

3. SOLUTION TECHNIQUE

The problem described in Section 2 in general includes material nonlinearity and geometric nonlinearity. It is easily seen that analytical solutions, for such a transient dynamic response problem with finite deformation and elastic-plastic material, are very difficult to obtain. Suitable numerical methods have to be used to solve the problem. Finite difference techniques based on the Lax-Wendroff scheme and the modified version of Strang's method due to Morris and Gottlieb are used for the study of the transient dynamic response of elastic-plastic solids under conditions of finite deformations. The finite deformation formulation used in the gun barrel problem is a Cauchy stress formulation and updated Lagrangian approach. However, in such an approach, the finite difference meshes may distort with increasing time. Thus, the conventional finite difference schemes for spatial derivatives in which the meshes are fixed for all time are no longer suitable. A second order accurate numerical technique based on the Lax-Wendroff scheme, the modified Strang method and the contour MacCormack two-step procedure has been developed for use with deformable Lagrangian meshes at Georgia Institute of Technology [1]. This modified scheme is efficient and also is suitable for deformed meshes. Such a numerical technique has been used to solve the gun barrel problem.

Preliminary results are shown in Figures 5 to 7. In Figure 5, the velocity distribution in the plane strain problem for a specific time has been shown. The flow of the rotating band material into the rifling groove are seen in the figure. The principal stress distribution for a specific time are shown in figures 6 and 7. This phase of the project will be completed by the end of the first project period.

During the first phase of the project, preliminary work has been done in formulating the complete three dimensional problem and the needed solution procedure. Preliminary work has also been done to improve the computational efficiency by considering implicit methods and hybrid "explicit-implicit methods". The preliminary work has indicated that these methods have the potential of providing solution techniques to the three dimensional gun barrel problem that are computationally efficient.

REFERENCES

1. Chen, H. P. and Hanagud, S. "A Two Step Procedure for Numerical Solution of Hyperbolic Differential Equations Involving Deformable Lagrangian Meshes," paper presented at the U.S. Army Conference on Numerical Methods in Computing, R.P.I., Troy, New York, 1984.
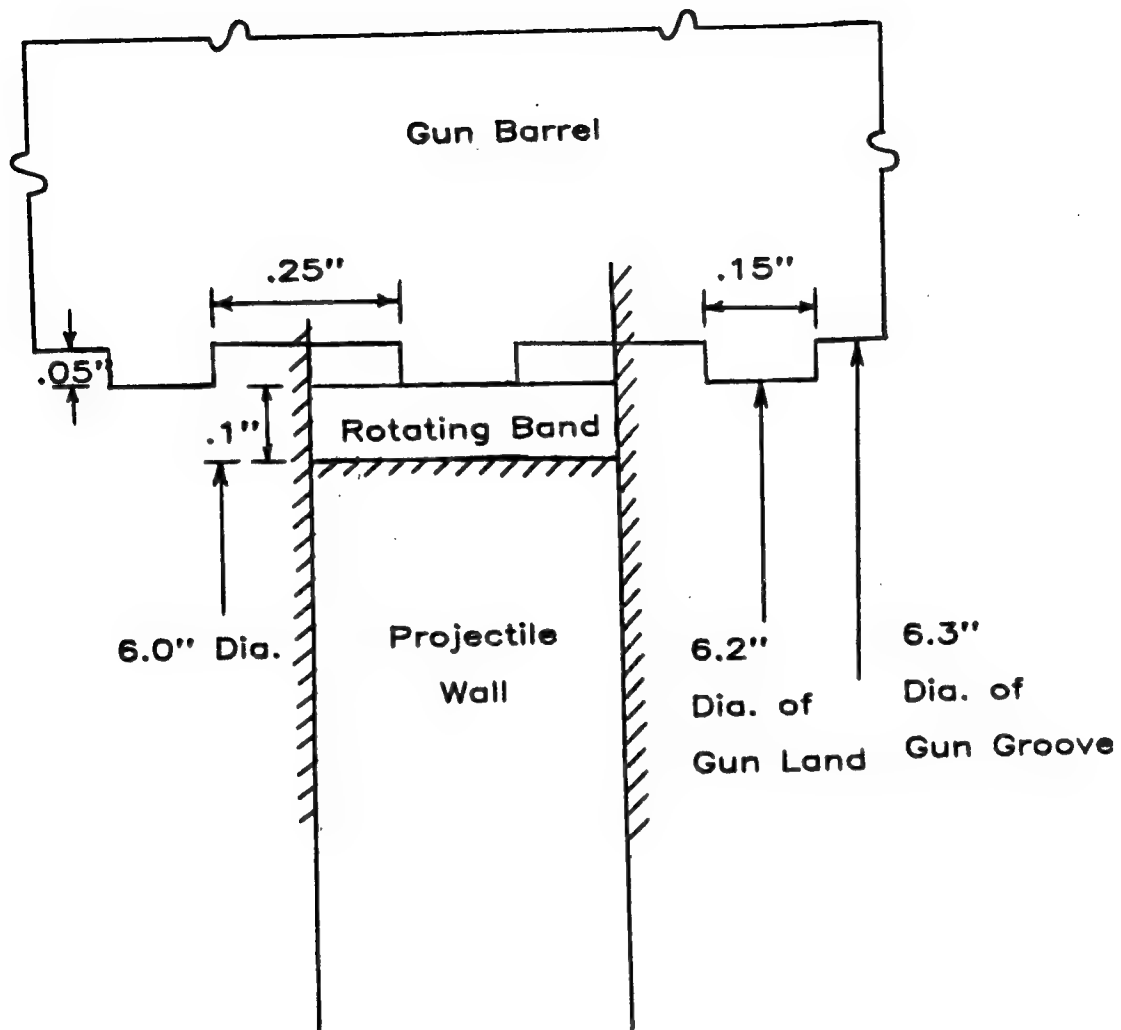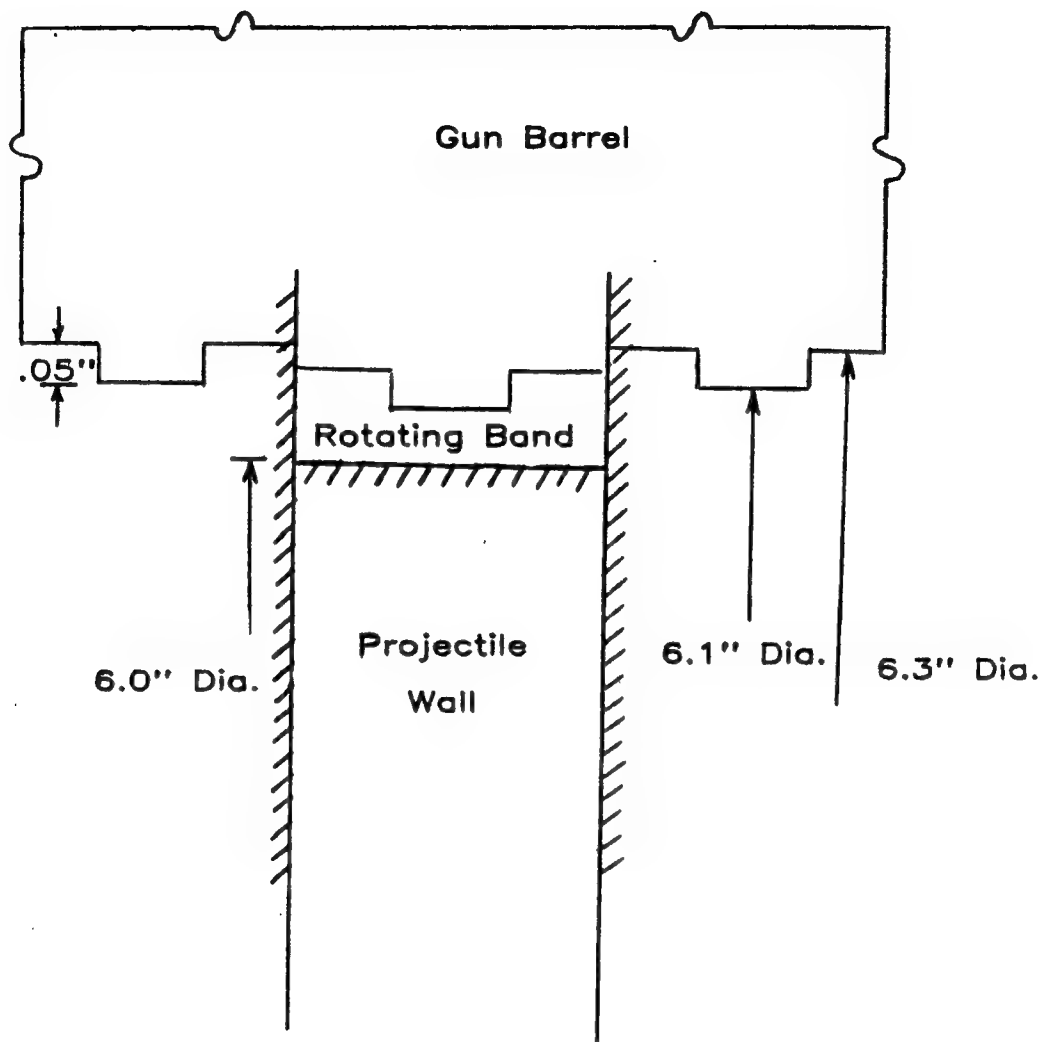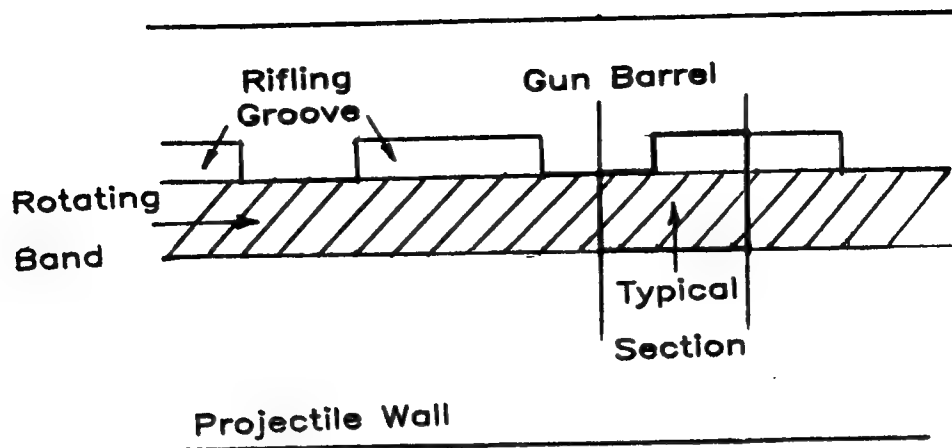
Figure 1. Before Loading

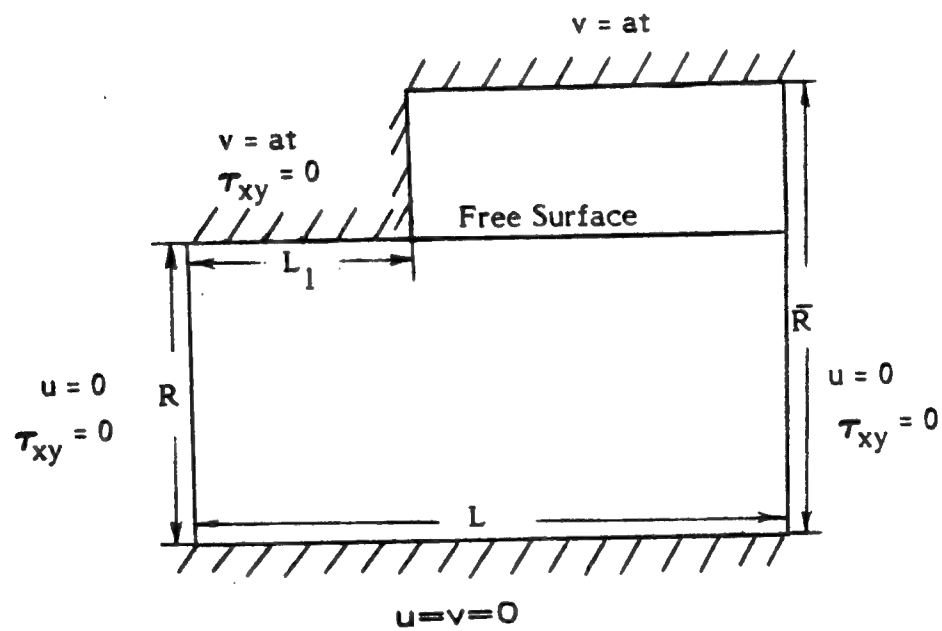Figure 2. After Loading

Figure 3. A Typical Section
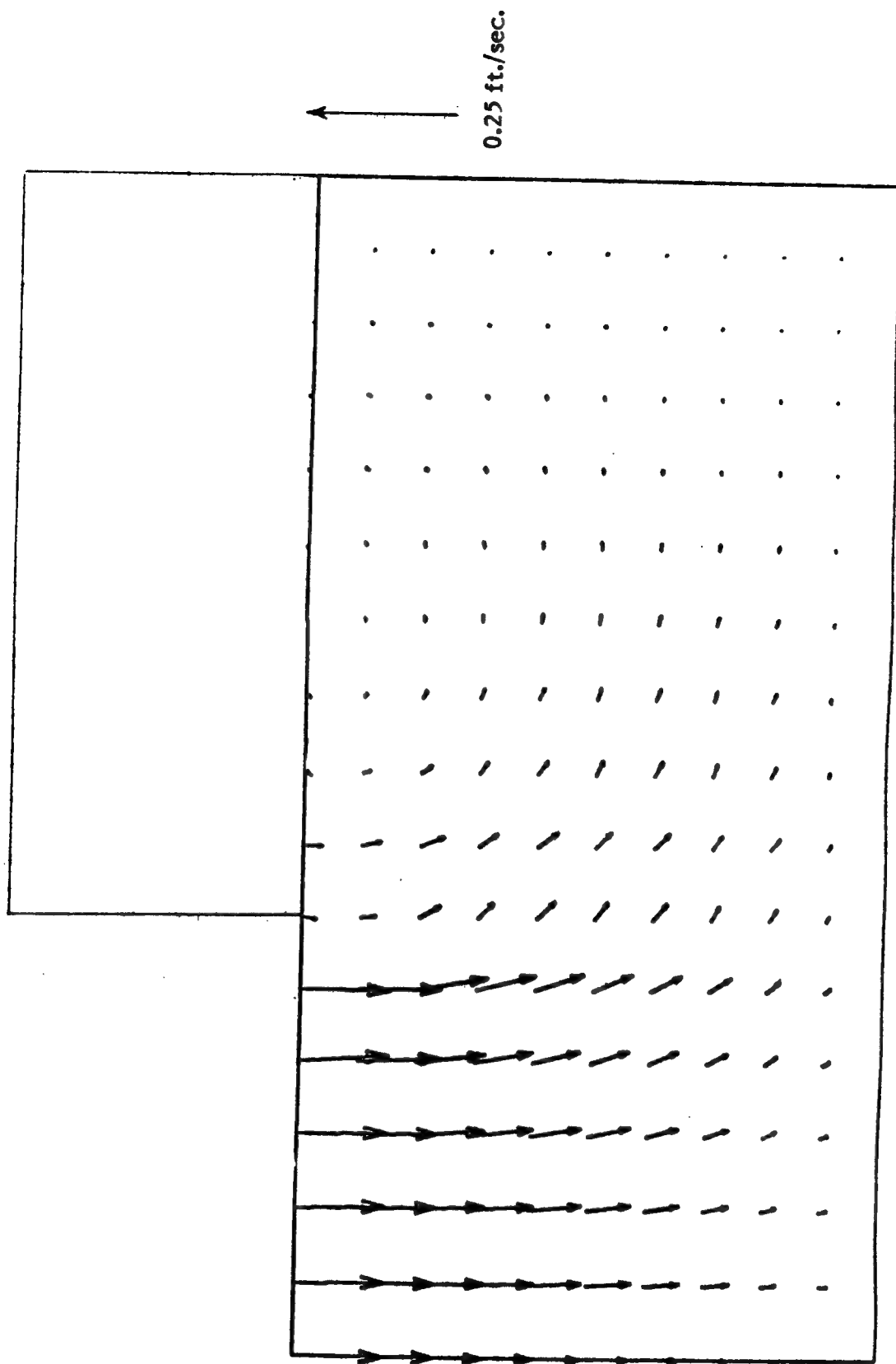

Figure 4. Boundary Conditions on Typical Section

409

0.25 ft./sec.
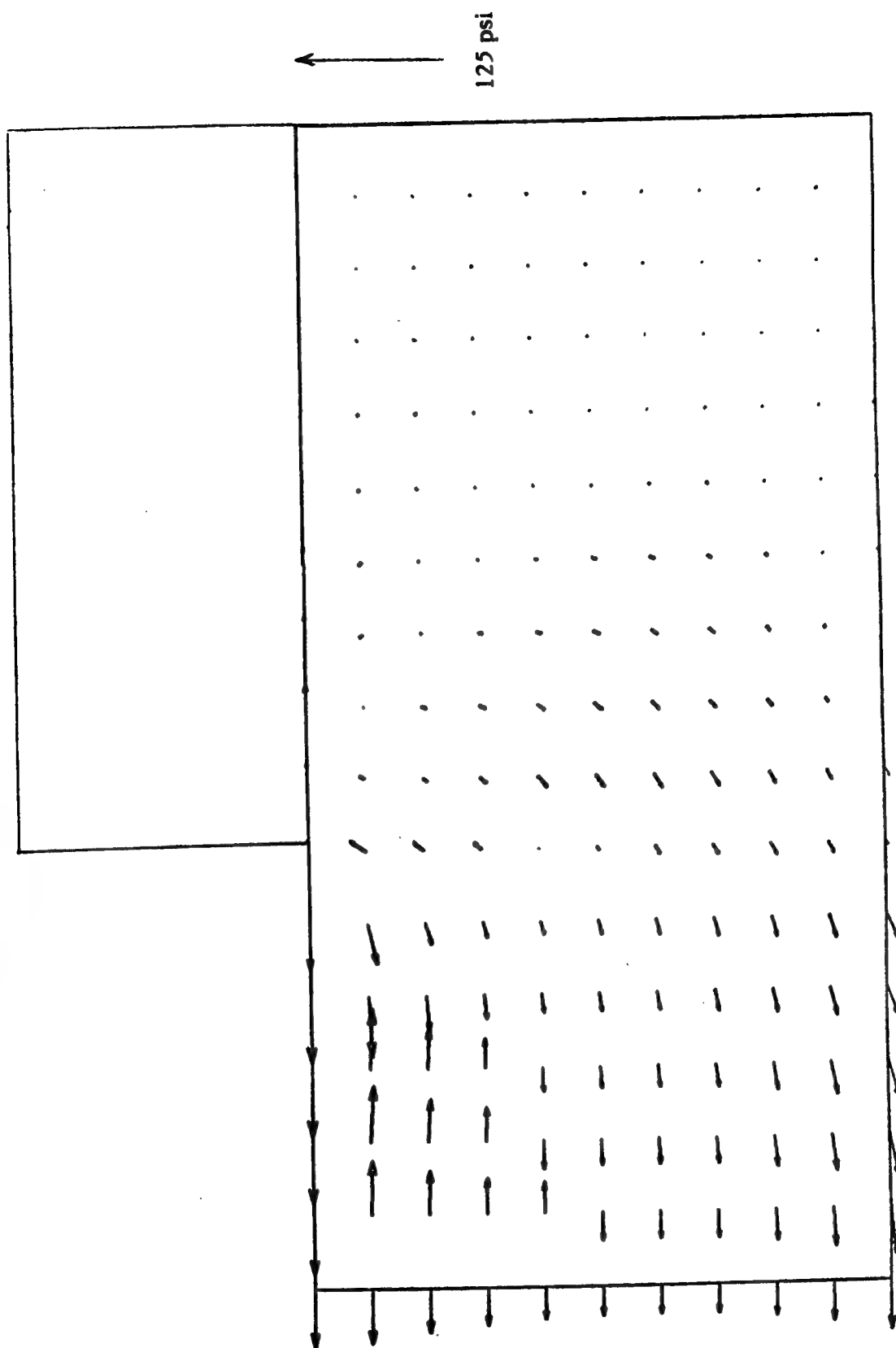
Figure 5. Velocity Field at a Specific Time   t = 2.962 μsec.

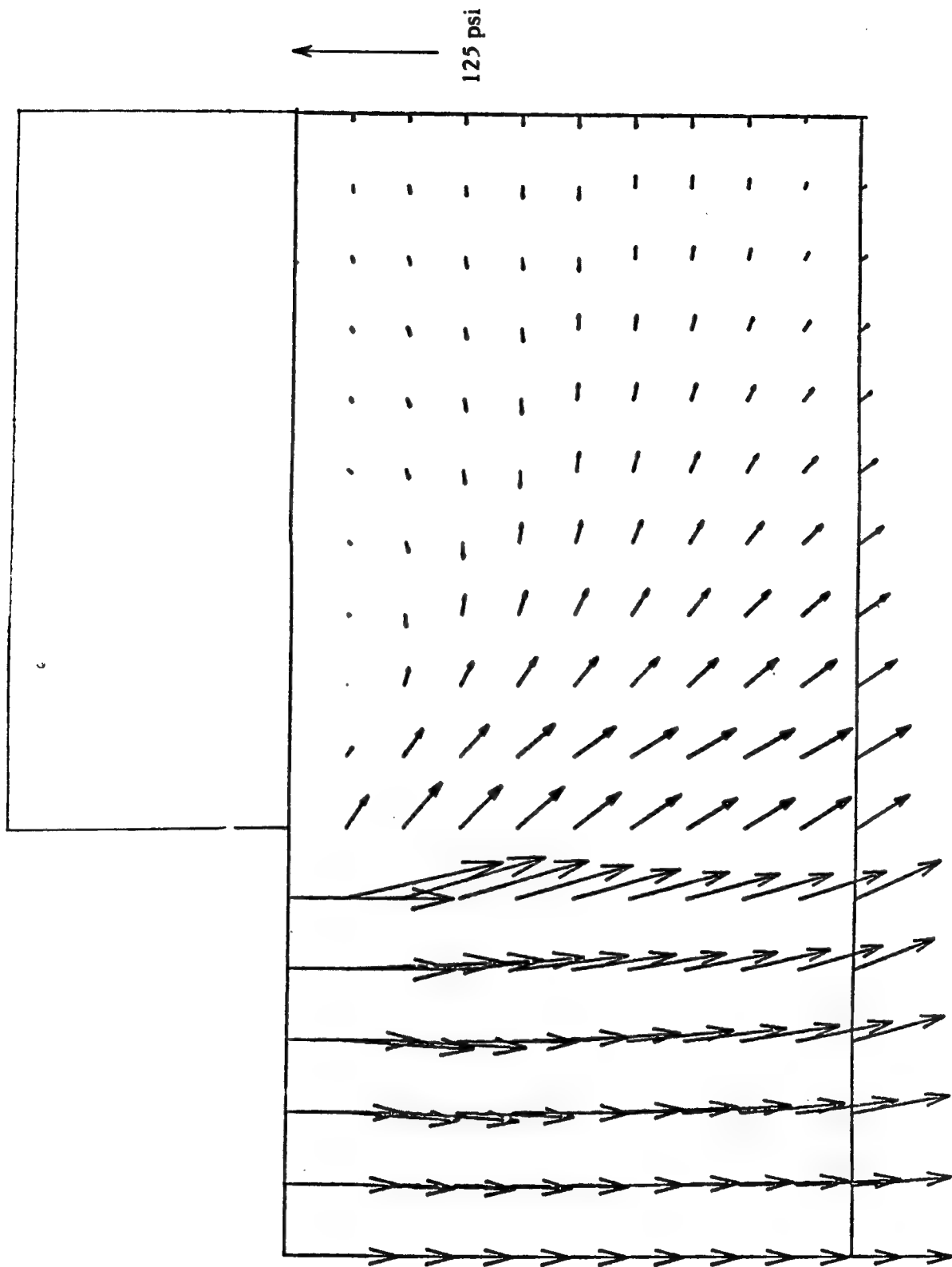Figure 6. The Principal Stress Field σ_1 at a Specific Time t = 2.962 μsec.

411

125 psi

Figure 7. The Principal Stress Field σ_2 at a Specific Time $t = 2.962$ μsec.

ABSTRACT

METHODOLOGY FOR TRACK FASTENING SYSTEM DESIGN

Henry W. Stoll
Professor of Mechanical Engineering
University of Wisconsin - Platteville

Donald M. Moore
Member of Techincal Staff
Applied Mechanicd Division, Jet Propulsion Laboratory
California Institute of Technology

Track fastening systems in current service on heavy tracked vehicles (i.e., M1/M60) require bolt-tightening and maintenace at intervals so frequent that combat readiness may be compromised. Track maintenance and repairs under field conditions could be significantly improved if track fasteners required simpler and less frequent maintenance and were easier to assemble and disassemble than current designs.

Although several approaches to solving the "track fastener problem" are possible (i.e., eliminate the need for track fasteners through major track redesign or design a good, general purpose, electrically powered wrench), this on-going research is aimed primarily at eliminating the disadvantages of current track fastening systems while at the same time avoiding significant change or redesign of existing track components. Under this constraint, the problem of track fastening system design becomes one of devising a method for connecting track components together in a way which permits no relative motion between parts, resists loosening, prevents separation of components under extremes of external load, and is at the same time, easy to assemble, disassemble, and maintain.

To prevent relative motion and joint component separation under extremes of external load, it is neccessary to preload the joined members. Preload may be defined as an internal force generated by the assembly of fastening system components which acts to resist joint component separation. The preload force is produced during assembly of the joint by elastic deformation of tensioned and compressed members comprising the fastening system. The magnitude of preload (P) developed is

$$P = R \, k \, \delta / (1+R) \tag{1}$$

where k is the stiffness of the tensioned member, δ is the elastic defomation, and R is defined as the ratio of compressed member stiffness to tensioned member stiffness.

For track fastening systems to be easy to assemble and disassemble, simple, positive locking, quick acting or snap-acting fasteners are preferred. These fastener types generally require less rigid, more flexible components. Equation (1) shows that as R and k are made small, the elastic deformation δ must become large to produce a desired preload. Since the maximum amount of deformation δ is limited by the material strength, it is seen that fast-acting fastening systems are not easily achieved when high preload is required. A further complication arises due to the accumulation of dimensional tolerances which acts to limit the amount of elastic deformation possible, even if material properties would permit additional deflection.

Because fastening systems are statically indeterminate, the minimum preload required to prevent joint separation depends on both the external load and on the stiffness ratio, R. The relationship between minimum preload, tensile and compressive external load, and stiffness ratio is shown in figure 1. It is clear from this figure that accurate knowledge of external loading is essential for proper preload specification and fastening system design.

At present, track fastener loading mechanisms are poorly understood and knowledge of load extremes is incomplete. Consequently, current track fastening system research at JPL is emphasizing the design and development of innovative track fastening systems which are easy to assemble and disassemble and are also capable of developing high preload. Based on a careful review and analysis of fastening system mechanics, the systematic synthesis approach shown in Table 1 has proven useful as a means for stimulating innovation and ensuring that all possibilities are considered. Using Table 1 a wide variety of conceptual designs can be quickly indentified simply by forming different combinations of elements chosen from the four functional areas delineated. For example, a combination of threaded fastener actuation, incline plane force generation, friction lock, and track pin rotation combined with preloading leads to the end connector currently used on M1 and M60 heavy tacked vehicles.

The use of an integrated detail design approach to optimize both performance and ease of assembly and disassembly has also proven fruitful. Typical plots of minimum preload versus stiffness ratio for the case where both tensile and compressive external load is applied are shown in Figure 2. These plots show that preload requirements can be reduced or minimized by sizing fastening system components to produce a stiffness ratio which falls within the range shown.

The design problems created by high preload requirements can be alleviated considerably by allowing selected components to deform plastically in a controlled way. This permits larger deformations and also allows the fastening system componets to be sized based on a desired stiffness ratio rather than on yield strength limiations. Plastic design does, of course, require added safeguards against reuse of permanently deformed parts.

Currently, JPL is in the process of designing and fabricating several promising track fastener concepts which have evolved from the work discussed above. These designs will be thoroughly tested and evaluated. Results thus far are encouraging and it appears that simple, low maintenance, positive locking, fast-acting track fastening systems which also satisfy the stringent requirements of heavy tracked vehicles are feasible.

MINIMUM REQUIRED PRELOAD vs
EXTERNAL LOAD & RELATIVE STIFFNESS
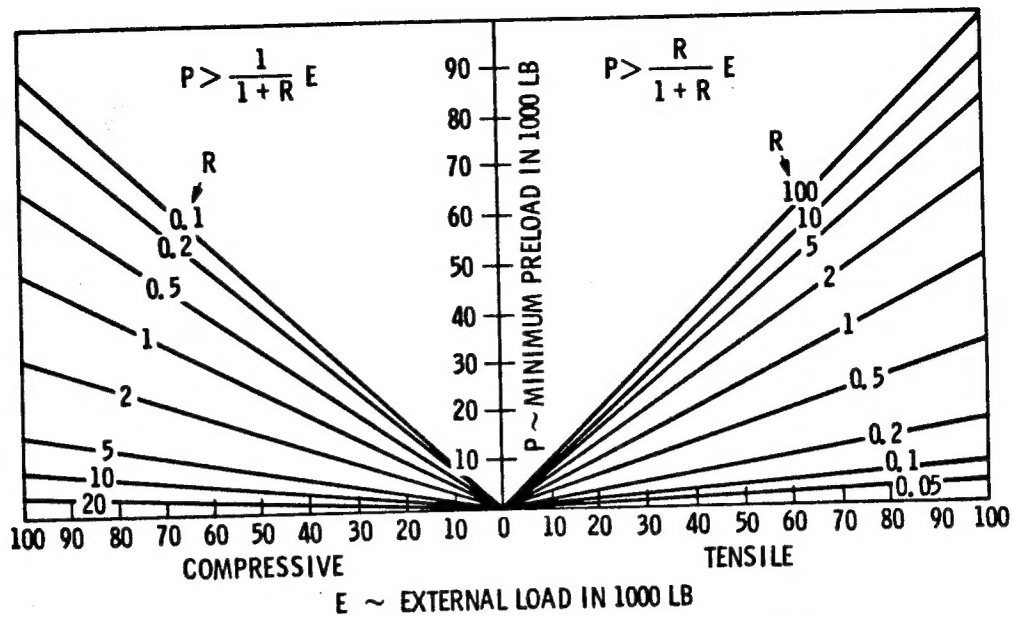

Figure 1.   Minimum Preload Vs. External Load

TABLE 1

SYSTEMATIC SYNTHESIS CHART

INSTALLATION / ACTUATION METHOD	FORCE GENERATOR	LOCKING PRINCIPLE	TRACK PIN ROTATION (END CONNECTOR ONLY)

• MULTI - STROKE
   1. THREADED DEVICES
   2. GEARED MECHANISMS
 	
• QUICK-ACTING
   1. CAM DEVICES
   2. SLIDER-CRANK
   3. 4-BAR LINKAGE
   4. QUARTER-TURN
 	
• EXTERNAL
   1. SPECIAL TOOL
   2. IMPACT LOADING
   3. MANUAL MANIPULATION
 	
• SNAP-ACTING
 	
• AUTOMATIC
   1. PYROTECHNICS
   2. CHEMICAL/THERMAL
   3. MEMORY METALS
   4. RATCHETING DEVICES
	• INCLINE PLANE
	
	• LEVER
	
	• GRAVITY
	
	• THERMAL
	   1. EXPANSION
	   2. CONTRACTION
	
	• ELECTRIC/MAGNETIC
	   1. SOLENOID
	   2. ELECTROSTATICS
	   3. PERMANENT MAGNET
	
	• EXPLOSIVE
		• FRICTION
		
		• OVER-CENTER
		
		• INTERFERENCE FIT
		
		• RETAINING LOCK
			• EXTERNAL
			
			   1. TOOL + FEATURE
			   2. TOOL + SNAP-ACTING
			   3. DRIVE OVER SPROCKET
			   4. INSTALL ON SPROCKET
			
			• COMBINED WITH PRELOADING
			
			• COMBINED WITH AXIAL INSTALLATION

JPL **MINIMUM PRELOAD VERSUS STIFFNESS RATIO**
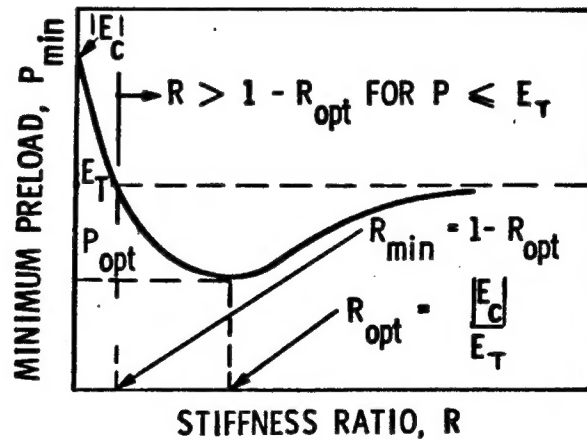
a) $E_T > |E_C|$
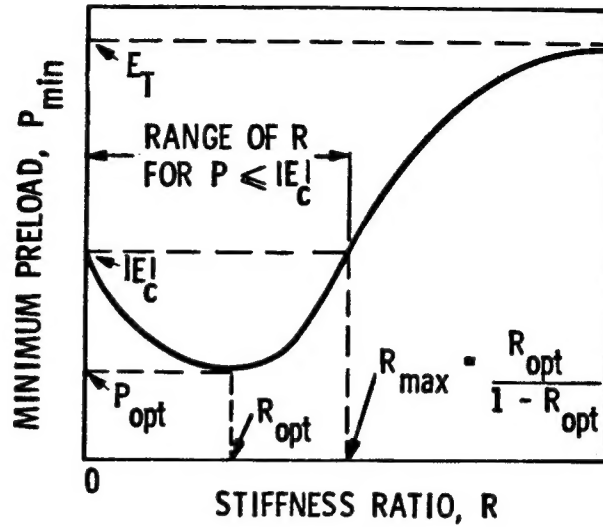
b) $|E_C| > E_T$

Figure 2. Minimum Preload Vs. Stiffness Ratio

SESSION VIII: DESIGN & ANALYSIS OF PROJECTILES & MUNITIONS

MODERATOR: J. I. Bluhm, AMMRC

PROJECTILE DESIGN TECHNOLOGY FOR LAUNCH

B. P. Burns & W. H. Drysdale, Ballistic Research Lab, Aberdeen, MD

PANEL DISCUSSION OF CRITICAL ISSUES IN ADVANCED SYSTEMS

- FRACTURE MECHANICS CONSIDERATION

J. Underwood, Benet Weapons Lab, Watervliet, NY

- COMPOSITES & THEIR IMPLICATION FOR SPECIAL CONCLUSIONS
  IN PROJECTILES

D. W. Oplinger, AMMRC

SESSION IX: SOLID MECHANICS IN PENETRATION PHENOMENA

MODERATOR: J. Mescall, AMMRC

COMPUTATIONAL ASPECTS OF PENETRATION MECHANICS — KINEMATICS &
MATERIALS ISSUES

J. Mescall, AMMRC

EXPERIMENTAL TECHNIQUES IN PENETRATION MECHANICS

S. Bless, University of Dayton Research Institute

BALLISTIC PENETRATION MODELS AS USED IN COMPUTER-AIDED-DESIGN
EVALUATIONS

R. Recht, University of Denver Research Institute

A REVIEW OF SOME RECENT RESULTS IN DYNAMIC PLASTICITY

J. Duffy, Brown University

THE SRI SNAG MODEL FOR SHEAR BANDING UNDER HIGH RATE LOADING

D. Shockey, Stanford Research Instiute

SYMPOSIUM COMMITTEE MEETING